Two-Phase Jet Loads

G. G. Weigand, S. L. Thompson, D. Tomasko

Prepared for
U. S. NUCLEAR REGULATORY COMMISSION

NOTICE

This report was prepared as an account of work sponsored by an agency of the United States Government. Neither the United States Government nor any agency thereof, or any of their employees, makes any warranty, expressed or implied, or assumes any legal liability or responsibility for any third party's use, or the results of such use, of any information, apparatus product or process disclosed in this report, or represents that its use by such third party would not infringe privately owned rights.

NUREG/CR-2913
SAND82-1935
R4

TWO-PHASE JET LOADS

G. G. Weigand
S. L. Thompson
D. Tomasko

Date Published: January 1983

Sandia National Laboratories
Albuquerque, New Mexico 87185
operated by
Sandia Corporation
for the
U. S. Department of Energy

ABSTRACT

A model has been developed for predicting two-phase, water
jet loadings on axisymmetric targets. The model ranges in
application from 60 to 170 bars pressure and 70°C subcooled
liquid to 0.75 (or greater) quality -- completely covering the
range of interest in pressurized water or boiling water
reactors. The model was developed using advanced two-
dimensional computational techniques to solve the governing
equations of mass, momentum, and energy. The model displays in
a series of tables and charts the target load and pressure
distributions as a function of vessel (or break) conditions;
this enables fast yet accurate "look up" for answers. For many
situations of practical interest, the model can predict sub-
cooled and saturated loadings in excess of the simple control
volume upper bounds of $2P_oA_e$ for nonflashing liquid and
$1.26P_oA_e$ for steam. Also, the results indicate that the
area of the loading on a flat target is often larger than
assumed by simplier models. Finally, approximate models are
given for estimating two-phase jet flow, expansion character-
istics, shock strengths, and stagnation pressures. These
approximate models could be used for estimating pressures on
targets not specifically addressed in this study.

CONTENTS

CONTENTS (Continued)

NOMENCLATURE

A	Area
A_E	Break area
C_S	Sound speed (sonic velocity)
D	Break diameter
E	Internal energy
F_r	Force on target
G	Mass flux
G_E	Break mass flux
H	Enthalphy
H_O	Stagnation enthalpy
L	Length from break exit to target
L_C	Length of exit fluid core
M	Mass flow rate
P	Pressure
P_A	Ambient pressure
P_O	Stagnation pressure
P_T	Target pressure
R	Target Radius
R_A	Target Radius where $P_T = P_A$
r	Radial coordinate direction
S	Entropy
S_O	Stagnation entropy
T	Temperature
T_O	Stagnation temperature

T_{sat}	Saturation temperature
ΔT_O	Degrees of subcooling $\Delta T_O = T_{sat} - T$
t	Time
t_c	Time constant for exit fluid core
V	Velocity
X	Steam:water quality
X_O	Stagnation steam:water quality
z	Axial coordinate direction
α	Parameter in load model
β	Parameter in load model
ρ	Density

1.0 INTRODUCTION

A nuclear power plant must be designed to ensure that the consequences of a pipe break (large or small) will be mitigated to prevent damage of any safety equipment or systems. A major concern in the event of a pipe break is the loading upon surrounding structures, equipment, etc., caused by the two-phase jet expanding from the break. These high energy jets have the potential to cause wide spread destruction.

In an attempt to prevent failures due to jet loading on any of the safety equipment or control systems, a complex system of jet deflectors, snubbers, and pipe restraints has been installed in plants. The design basis for much of these structural supports can be traced to Moody's one-dimensional jet load model[1]. Various interpretations of the actual zone of influence of the jet for this model have been made by others[2,3], but the one-dimensional force model from Reference 1 is nearly always applied. The error that could result from the one-dimensional approximation or the arbitrariness in deciding the zone of influence of the jet can result in costly overdesign, poor utilization of limited space inside of containment, or underdesign of restraint/barrier systems.

The use of simple one-dimensional modeling is inappropriate for two-phase jet load calculations; the jet is a complicated multidimensional flow. The high pressure and high temperature fluid that exits the break expands with supersonic velocities downstream of the break. Upon encountering a target (or obstacle) a shock wave forms in the flow field, and it is the thermodynamic properties downstream of this shock that determine the pressure field and load on the target. A multidimensional analysis, which is capable of treating strong shocks, is required to evaluate the thermodynamic properties downstream of these shocks.

Sandia National Laboratories, with the support of the U. S. Nuclear Regulatory Commission, has completed a study using modern multidimensional computational methods to evaluate the two-phase jet load on target geometries. The governing equations of mass, momentum, and energy were solved with a high resolution Eulerian method for all calculations. The calculations form a computational data base for evaluating jet and target pressures for axisymmetric target geometries. This data base covers the range of pressures, temperatures, and distances to the target present in both pressurized water (PWR) and boiling water (BWR) reactor designs. A two-phase jet load model, which provides both pressure and load distributions, was developed using the computational data base. In addition to the load model, approximate models were developed for estimating the jet expansion, shock, and target load.

1

At the beginning of this modeling effort, it was generally believed that current analysis methods[3] were overly conservative. Considerable design and manufacturing cost reductions would result from a more accurate model, and overall safety could be improved by a reduction in the complexity of the system. This was not the case. For many situations of practical interest, the new model can predict subcooled and saturated loading in excess of the simple control volume upper bounds currently employed[3]. The results also indicate that the area of the loading on a flat target is often larger than assumed by the simpler model.

Persons only interested in applying the two-phase jet load model should go directly to Chapter 2; the remaining chapters contain modeling discussions and derivations and model verification. Chapter 2 contains a discussion of the load model and the figures and charts that display the model; furthermore, two tutorial examples are provided.

Chapter 3 provides a discussion of the general characteristics of two-phase jets; their general behavior, geometry, governing equations, boundary conditions, and expansion characteristics are given. In Chapter 4 the computer model is developed and the computational data base is given; several examples, taken from the data base, are graphically illustrated. Chapter 5 provides charts for evaluating the thermodynamic properties of water and critical flow conditions. Chapter 6 contains the derivations and discussions of the approximate models: free jet expansion, standing shock, and target load. Model comparisons with both the computational data base and experimental data are given. Finally, Chapter 7 provides and discusses the details of the final load model; in addition, model versus experimental data comparisons are included. Four appendices provide the data needed for routine application of the model.

2.0 TWO-PHASE JET LOAD MODEL: CONCLUSIONS AND APPLICATION

This chapter and Appendices A, B, C, and D provide the jet load model. The model, at the request of the Nuclear Regulatory Commission, is given in the form of charts that provide the radial pressure and load distributions as functions of the break flow stagnation conditions and distance to the target. Chapter 7 describes the theoretical methods utilized in developing this model. This chapter will first discuss the load model and then conclude with an example calculation and tutorial discussion of the model. In this study, the development of a two-phase jet load model, we only considered initial conditions that result in two-phase flows (steam:water mixtures) at pressures above ambient conditions. Cold water jets were not considered, although parts of the model describe some of the behavior exhibited by highly subcooled, nonflashing jets.

2.1 Model Description

This section gives a brief summary of the load model. Appendix A contains a complete set of charts showing target pressure and load distributions for break flow stagnation conditions of

<div align="center">

60 to 170 bars

</div>

$$\left\{ \begin{array}{l} 0 \text{ to } 70 \text{ degrees of subcooling or} \\ 0 \text{ to } .75 \text{ quality } * \end{array} \right\}$$

and L/D's ranging between 0.50 to about 10. Appendix B contains the centerline target pressure distributions for the above conditions. Appendix C contains figures describing the jet exit-core length (L_c/D), and Appendix D contains figures describing the jet inlet-region thermodynamics and flow and associated water properties charts.

Figure 2.1 shows the geometry for this model; the geometry is axisymmetric. A list of the nomenclature used in Figure 2.1 and the figures describing the load model is given below as a convenience to the reader.

A_e	break exit area
D	break exit diameter
F_r	force on target
G_e	exit mass flux
L	length from break exit to target
L_c	length of break exit core, see Sections 3.6 and 4.2

---

*A larger range of qualities was considered in this study; a larger range is not reported because the normalized target pressure distribution is a weak function of quality for $X_o > .75$.
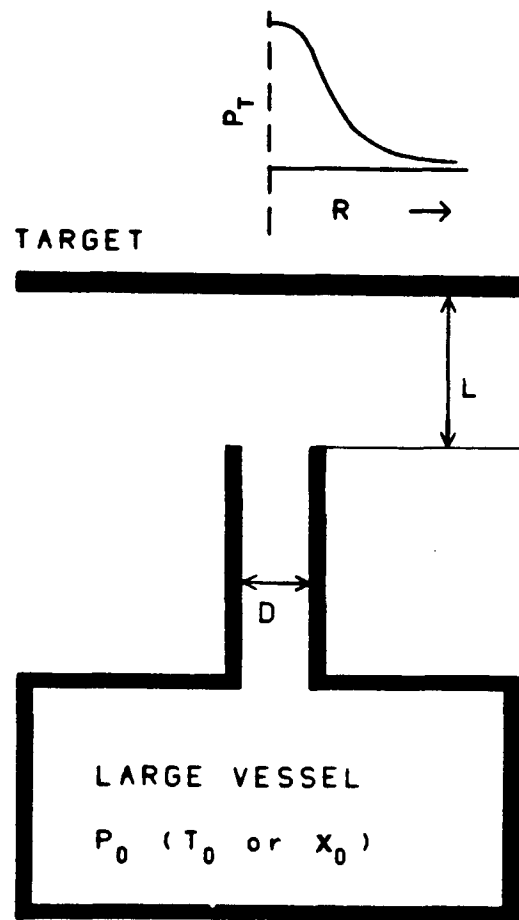
Figure 2.1   Two-Phase jet load model geometry.

P_O stagnation pressure at break
P_T target pressure
ΔT_O subcooling of stagnation temperature at break
X_O stagnation quality at break
R radius measured on the target

Figures 2.2 through 2.7 illustrate the features of the model.

Figures 2.2 and 2.5 give the target pressure distribution in bars as a function of target radius for stagnation conditions of P_O = 130 bars with ΔT_O = 35°C and X_O = 0.333 respectively. The target L/D associated with each curve is listed in the upper right hand corner of the figure; the lowest L/D value corresponds to the uppermost curve, e.g., in Figure 2.2 the curve with the highest centerline pressure is for L/D = 1.50 and the curve with the lowest centerline pressure is for L/D = 10.0.

Figures 2.3 and 2.6 give the target load distribution as a function of target radius for the same conditions noted above; in fact, Figures 2.2 and 2.5 are the integral of the pressure distributions in Figures 2.3 and 2.6. F_r is the total normal force acting on a circular disk target of radius R. These integrations are valid for target radii up to the point where the pressure on the target equals the ambient pressure. Far-field phenomena, the consequences of neglecting them, and the details of the load integration are given in Section 7.2. Figures 2.4 and 2.7 are composite contours of the target pressure. These figures display the extent of the exit core along with a letter indicator for pressure on a Cartesian grid of length to target (L/D) versus target radius (RADIUS/D): A = 1 bar, B = 2.5 bars, C = 5 bars, D = 10 bars, E = 15 bars, F = 20 bars, G = 25 bars, H = 30 bars, etc. Any target within the exit core (the shaded area) will be loaded by the vessel stagnation pressure, P_O. These curves are only informational and useful for quick scoping calculations; serious calculations should always be performed using Figures 2.2, 2.3, 2.5, and 2.6.

Use of the two-phase jet load model (figures in Appendix A) is not limited to targets with large radii. Except for a small subsonic region of flow near the center of the target, flow on the target is supersonic, thus edge effects are negligible. In other words, for nearly all problems of interest the solution is independent of target radius; one simply evaluates target loadings using the appropriate target R/D.

In this model there are three items that must be noted. First, when subcooling existed ($\Delta T_O > 0$ °C) and the target was located close to the break (L/D small) the loads predicted exceeded the simple control-volume limit of $F_r/P_O A_e$ = 2. This occurs because of the wide jet expansion from the break and because of far-field, supersonic phenomena. In subcooled cases the expansion is large enough to produce
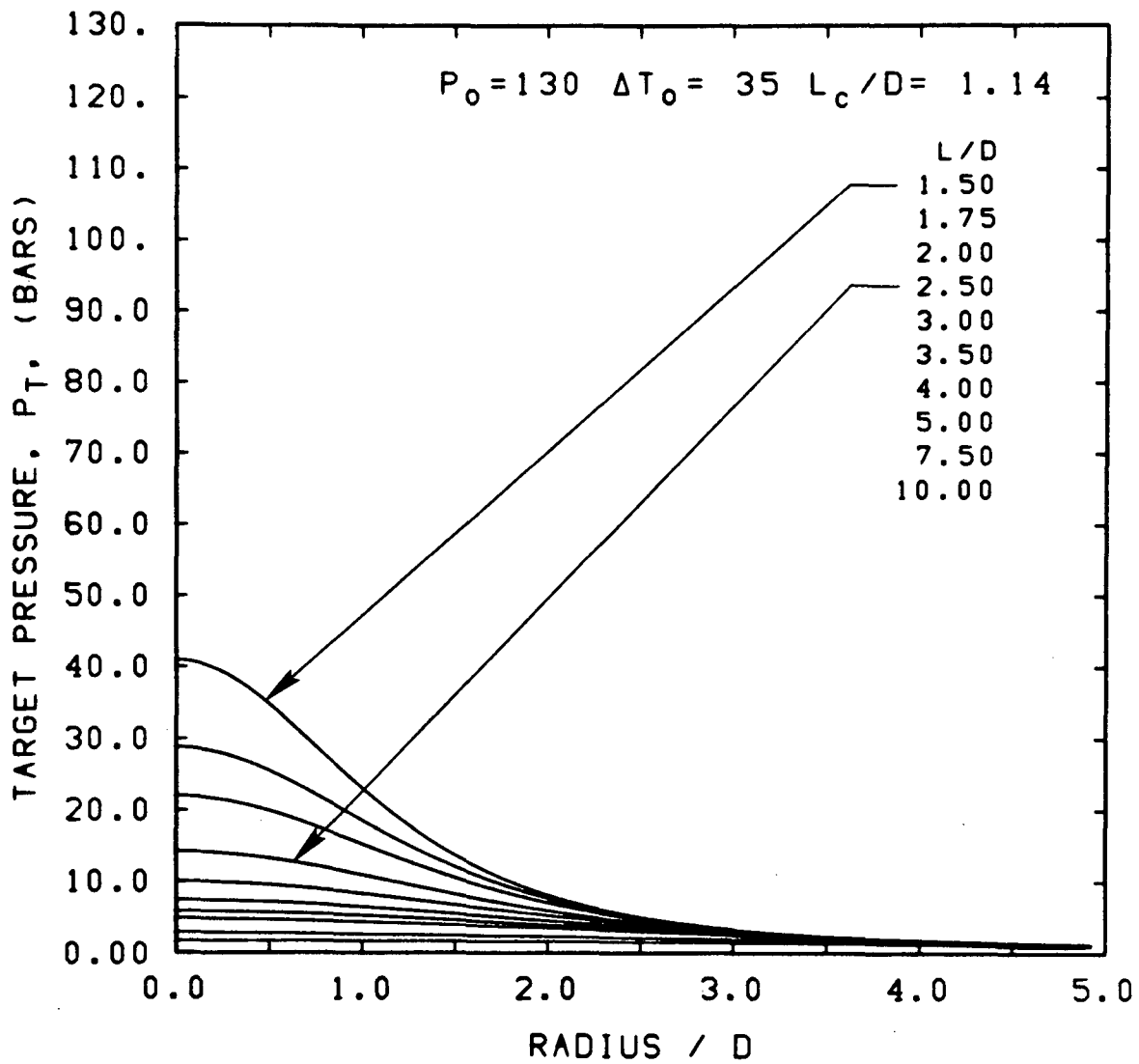
Figure 2.2   Target pressure distributions for stagnation
conditions of P_O = 130 bars and ΔT_O = 35°C.
The target L/D associated with each curve is
listed in the upper-right-corner key; the
lowest L/D value corresponds to the uppermost
curve.

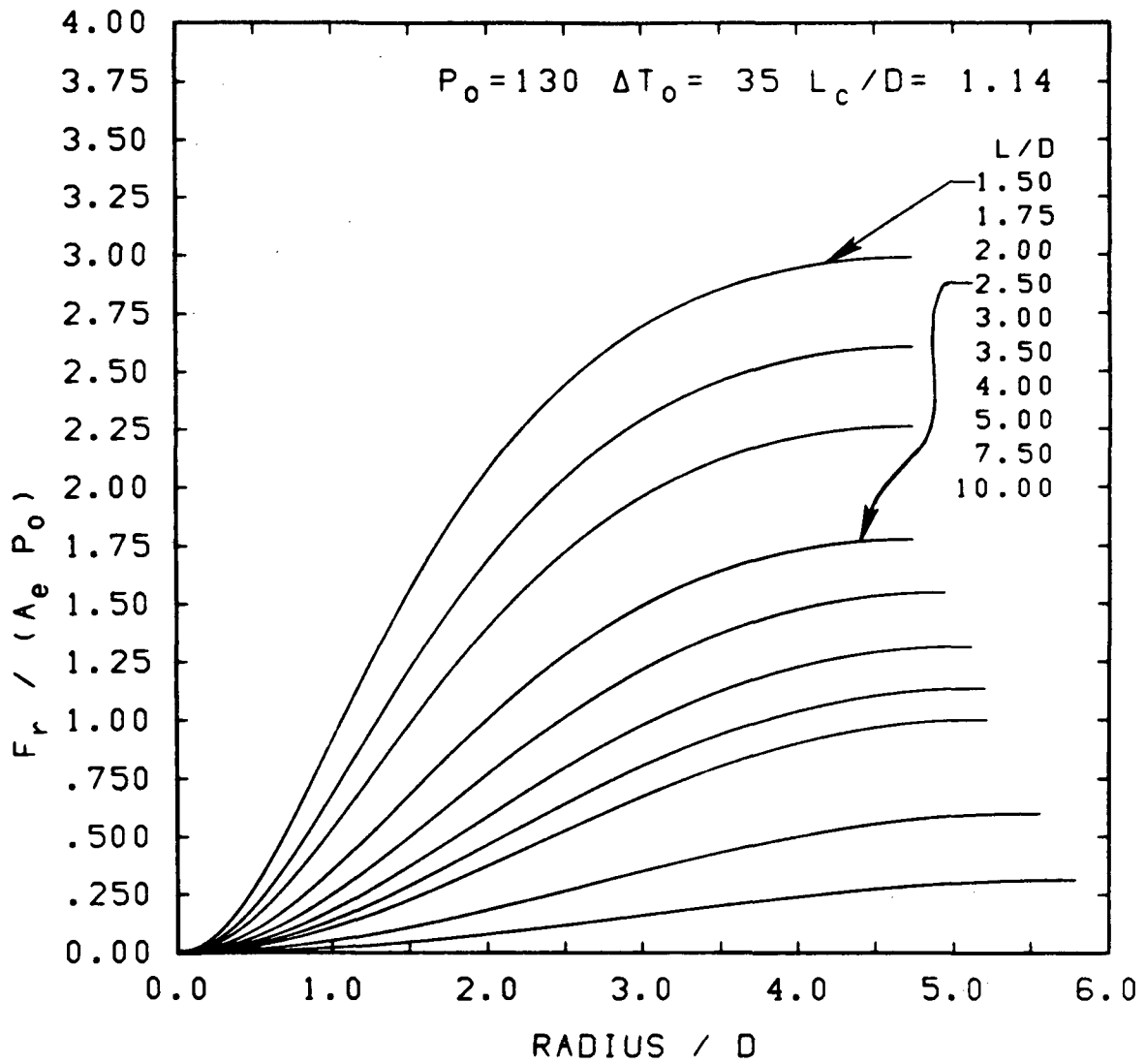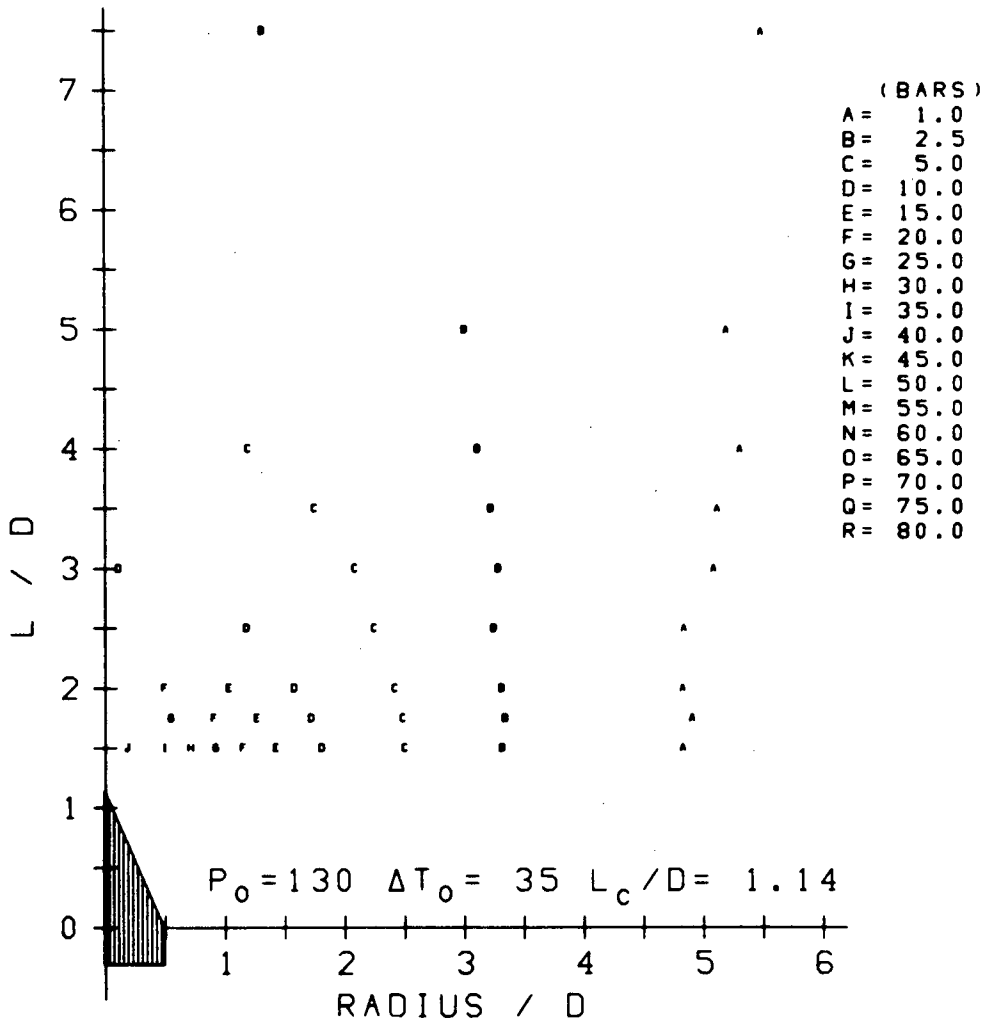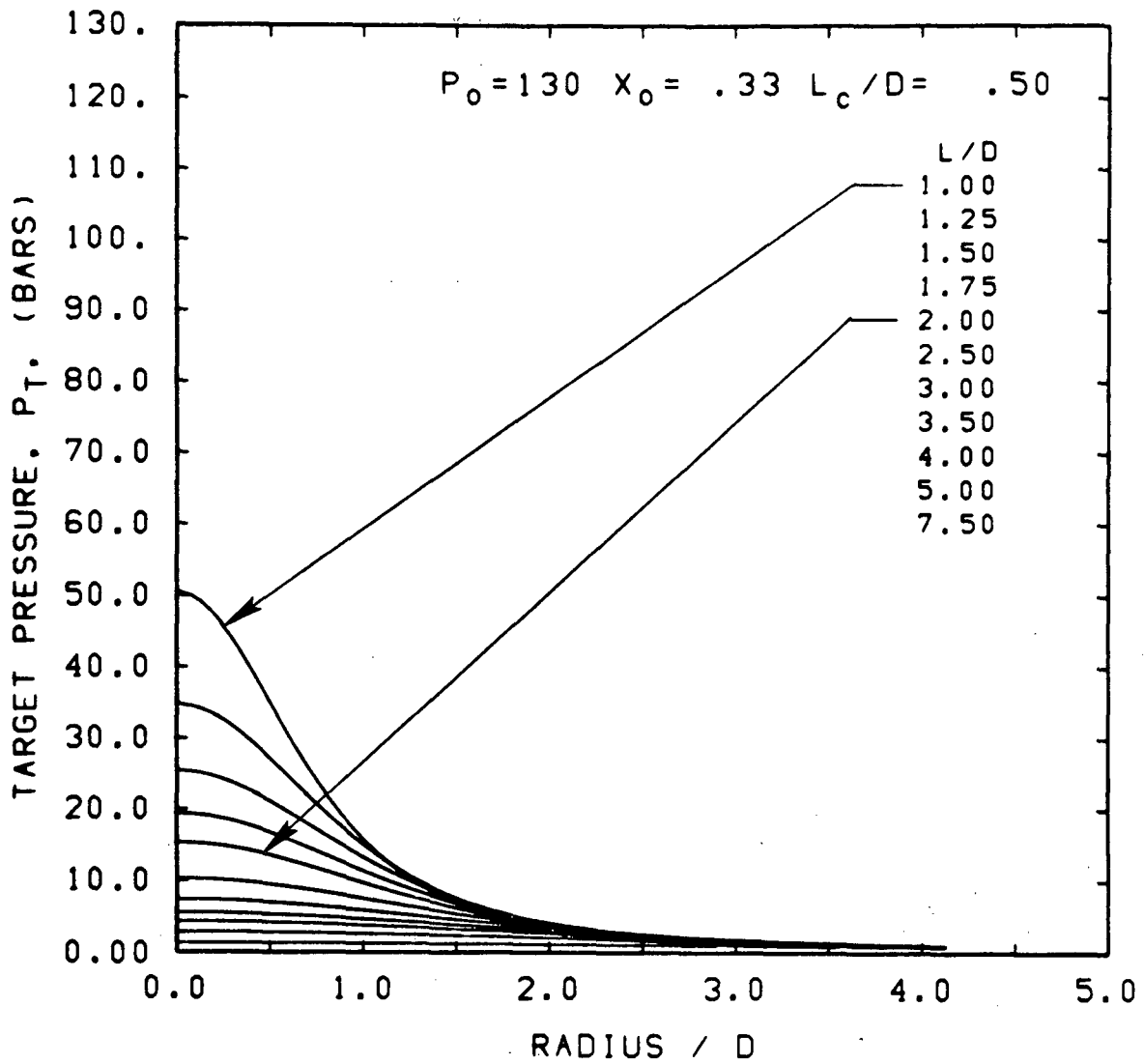Figure 2.3   Target load distributions for stagnation
conditions of P_O = 130 bars and ΔT_O = 35°C.
The target L/D associated with each curve is
listed in the upper-right-corner key; the
lowest L/D value corresponds to the uppermost
curve.

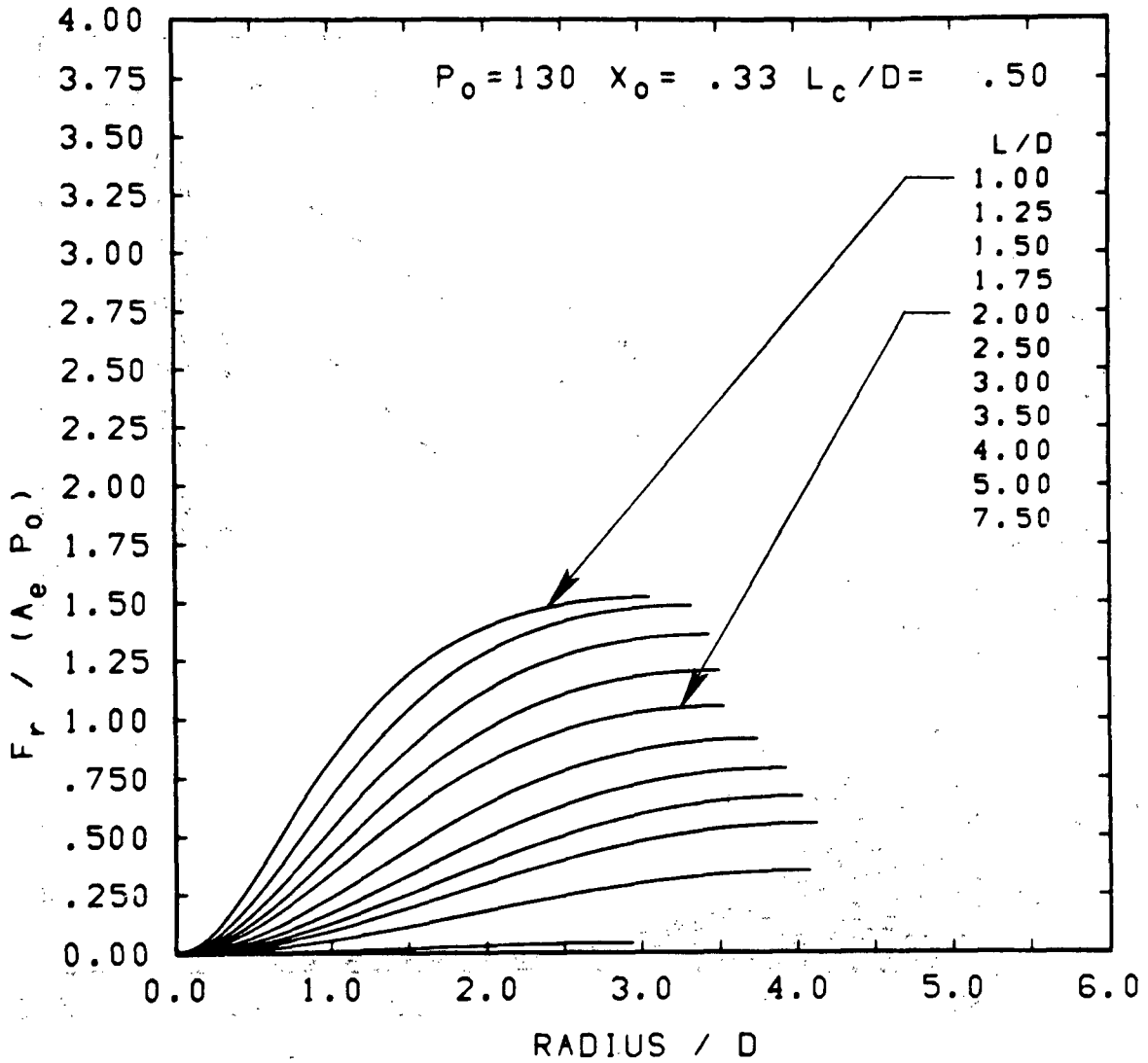Figure 2.4   Composite target pressure contours as a
              function of target L/D and target RADIUS/D
              for stagnation conditions of P_O = 130 bars
              and ΔT_O = 35°C. Smooth lines connecting like
              alphabetic letters form an approximate pressure
              contour corresponding, in bars, to the pressure
              versus alphabetic letter key. This contour
              plot is approximate and is only informational;
              it is useful for scoping calculations.

Figure 2.5 Target pressure distributions for stagnation
conditions of P_O = 130 bars and X_O = 0.33.
The target L/D associated with each curve is
listed in the upper-right-corner key; the
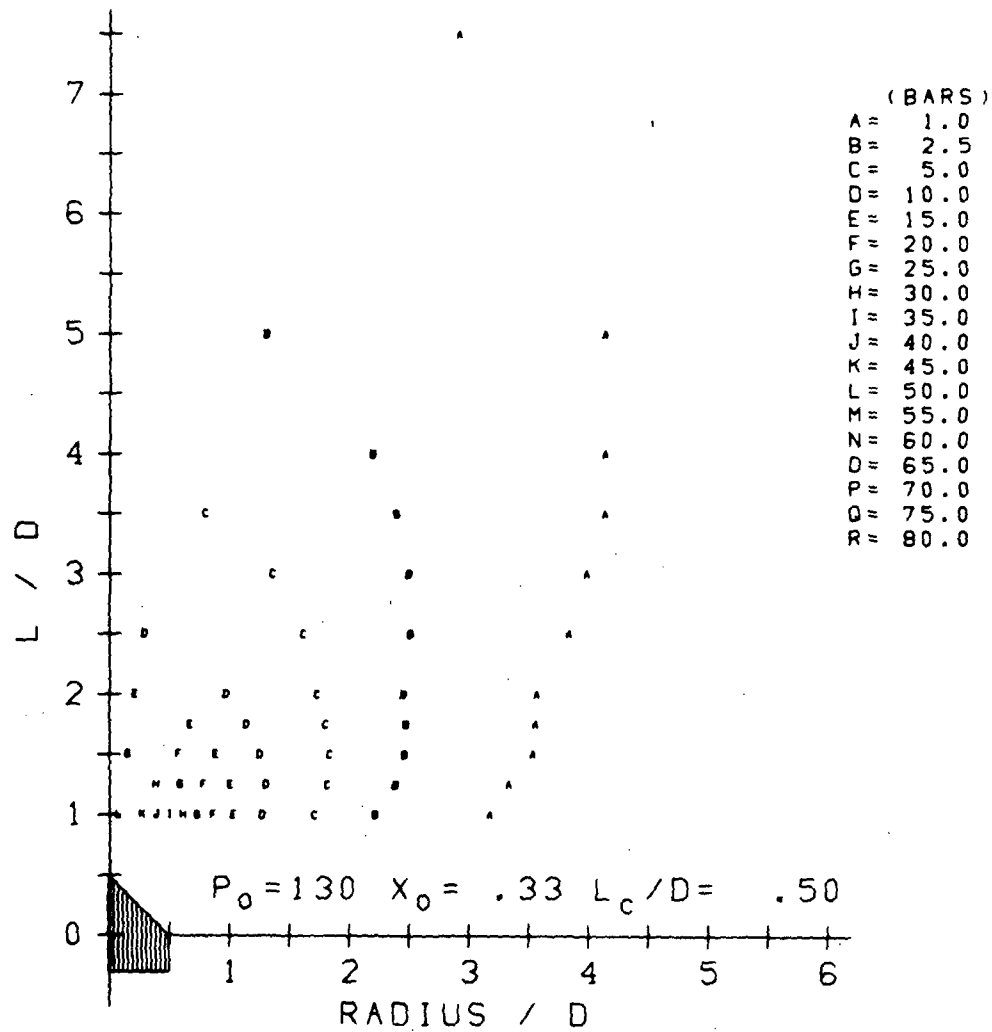lowest L/D value corresponds to the uppermost
curve.

Figure 2.6 Target load distributions for stagnation
conditions of $P_0 = 130$ bars and $X_0 = 0.33$.
The target L/D associated with each curve
is listed in the upper-right-corner key; the
lowest L/D value corresponds to the uppermost
curve.

Figure 2.7   Composite target pressure contours as a
             function of target L/D and target RADIUS/D
             for stagnation conditions of P_O = 130 bars
             and X_O = 0.33.   Smooth lines connecting like
             alphabetic letters form an approximate
             pressure contour corresponding, in bars, to
             the pressure versus alphabetic letter key.
             This contour plot is approximate and is only
             informational; it is useful for scoping cal-
             culations.

11

velocities with components opposite to the break flow. Secondly, because the target area increases as the square of the radius, at large radii a small error in pressure can result in a significant load change; consequently, some judgment must be used in evaluating the loads on large targets with large L/D's. Finally, because the computational data base used to develop this model was sparse for low pressure, highly subcooled flows, some care should also be exercised when making load predictions for highly subcooled flows ($L_c/D > 3.0$, where L_c is the jet core length given in Figure 3.14.)

2.2 Model Application

This section provides both an example of applying the above model and a tutorial. There are two principal methods of application. For both, the stagnation conditions at the break position are the important parameters. When only the peak loads are of interest, it is reasonable to assume that the stagnation conditions are those in the pipe or vessel prior to the pipe break. Since these conditions are the model's independent variables, the load and pressure distribution can be read directly from the graphs in Appendix A.

When there is interest in the time-dependent behavior or pipe friction effects, then the procedure becomes more difficult. The reality that faces the model user in this case is that pipe break information will be supplied by system codes such as TRAC[4], RELAP[5], and RETRAN[6]. These codes provide blow-down histories of the break flow and some thermodynamic properties upstream of the break. The bridge linking these system code histories and the two-phase jet model has been performed and is detailed in Chapter 5. Briefly, we developed a set of thermodynamic charts plus a set of HEM critical flow charts that relate the static thermodynamic properties just upstream of the break and the break flow to the stagnation properties. It is not necessary that the system code use the HEM model. The two following examples illustrate the use of the figures in Appendices A, B, C, and D by both of the above methods.

Consider the case where the two-phase jet load was of interest at two points in a blow-down calculation. The system code supplied the following break flow and thermodynamic state just upstream of the break:

1. G_e = 6.15 Kg/cm^2 s   2. G_e = 1.71 Kg/cm^2 s

   P = 120.0 bars   P = 50.9 bars

   T = 598.5 $^\circ$K   T = 538.1 $^\circ$K

   ρ = 0.653 g/cm^3 ρ = 0.0663 g/cm^3

12

For the first point the entropy is read from Appendix D Figure D.1, $S = 35 \times 10^6$ ergs/g $^{\circ}$K. Then using the break flow (G_e) and the entropy the stagnation temperature is located in Figure D.4, $T_0 = 600.4$ $^{\circ}$K. Finally, the stagnation pressure is located in Figure D.6, $P_0 = 150$ bars. The saturation temperature at 150 bars is $T_{sat} = 615.4$ $^{\circ}$K, thus the stagnation conditions at the break for the first point are

$$P_0 = 150 \text{ bars}, \quad \Delta T_0 = 15^{\circ}C$$

The target pressure and load distributions for this stagnation condition were found in Appendix A and are given in Figures 2.8 and 2.9. Consider an axisymmetric target with R/D = 3 and L/D = 1. From Figure 2.8 the target pressures at R/D's of 0, 1, 2 and 3 are 66.5, 25.0, 6.0, and 2.0 bars, respectively; from Figure 2.9 the total cumulative loads (F_r/P_0A_e) at R/D's of 0, 1, 2, and 3 are 0., 1.08, 1.9, and 2.16, respectively.

For the second point the entropy is read from Figure D.3, $S = 40.5 \times 10^6$ ergs/g $^{\circ}$K. Then using the break flow and the entropy the stagnation temperature is located in Figure D.5, $T_0 = 568$ $^{\circ}$K and lays in the two-phase region. Finally, the stagnation quality is located in Figure D.7, $X_0 = .333$. Thus the stagnation conditions at the break for the second point are

$$P_0 = 80 \text{ bars}, \quad \Delta T_0 = 0 \; ^{\circ}C, \quad X_0 = 0.333$$

The target pressure and load distributions for this stagnation condition were found in Appendix A and are given in Figures 2.10 and 2.11. Consider the same axisymmetric target with R/D = 3 and L/D = 1. From Figure 2.10 the target pressures at R/D's of 0, 1, 2 and 3 are 30.75, 9.5, 2.25, and 1.0 bars, respectively; from Figure 2.11 the total cumulative loads (F_r/P_0A_e) at R/D's of 0, 1, 2 and 3 are 0, .81, 1.3, and 1.35, respectively.

These two examples illustrate the use of the tables and charts in Appendix A and Appendix D. Both examples conveniently fell on existing curves. When this is not the case linear interpolation is recommended.
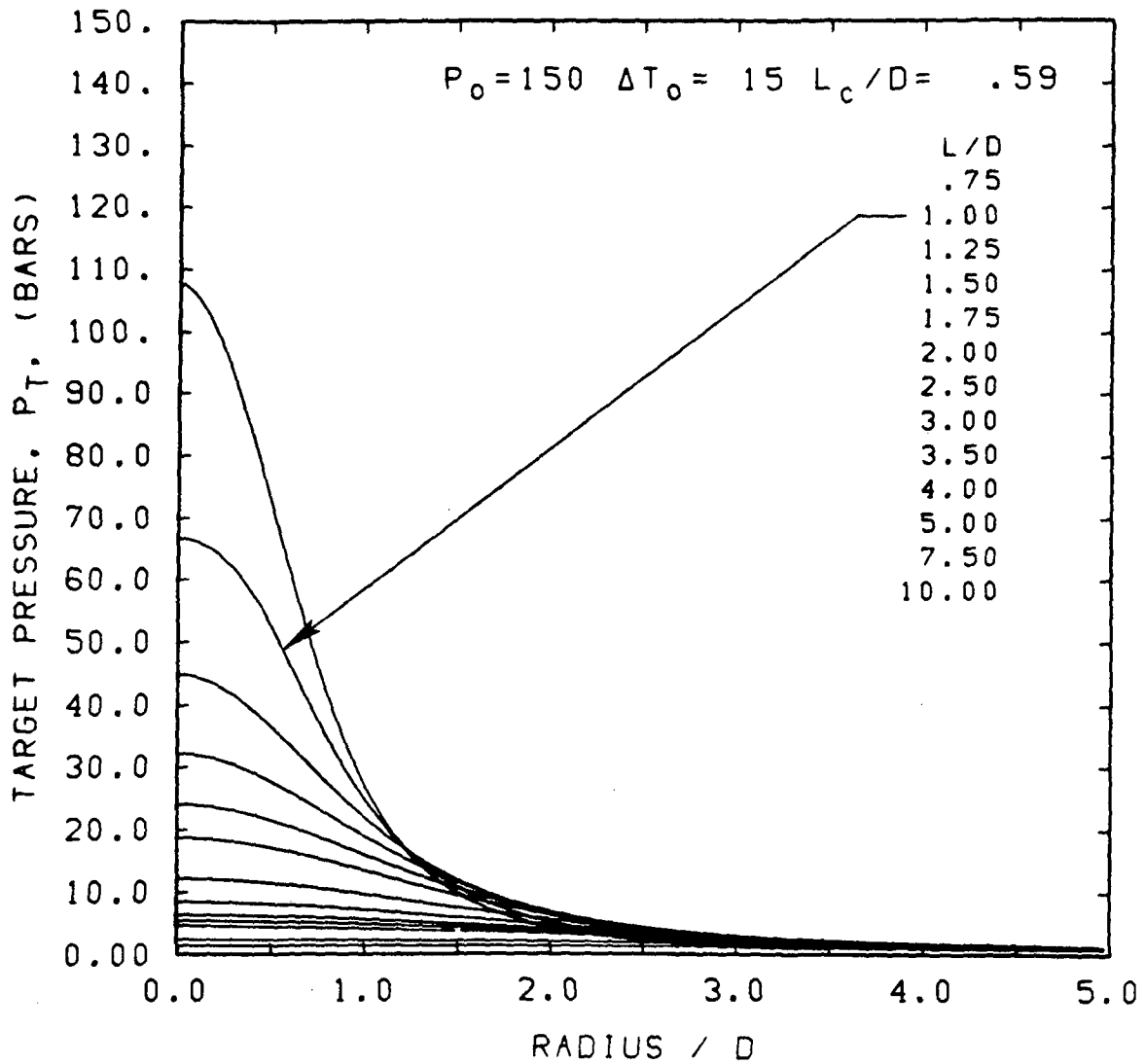
Figure 2.8 Target pressure distributions for stagnation conditions of $P_O = 150$ bars and $T_O = 15^\circ C$. The target L/D associated with each curve is listed in the upper-right-corner key; the lowest L/D value corresponds to the uppermost curve.
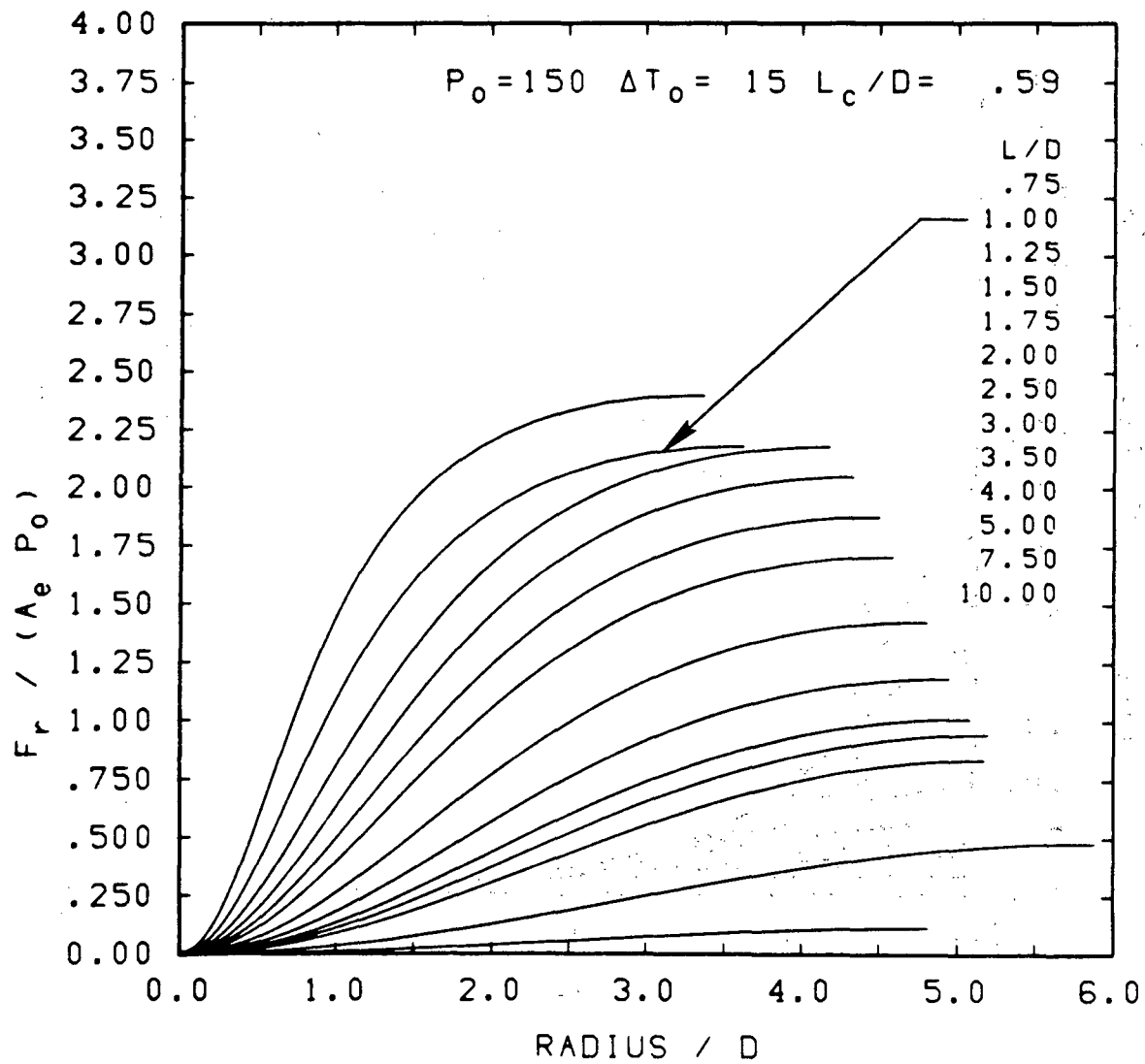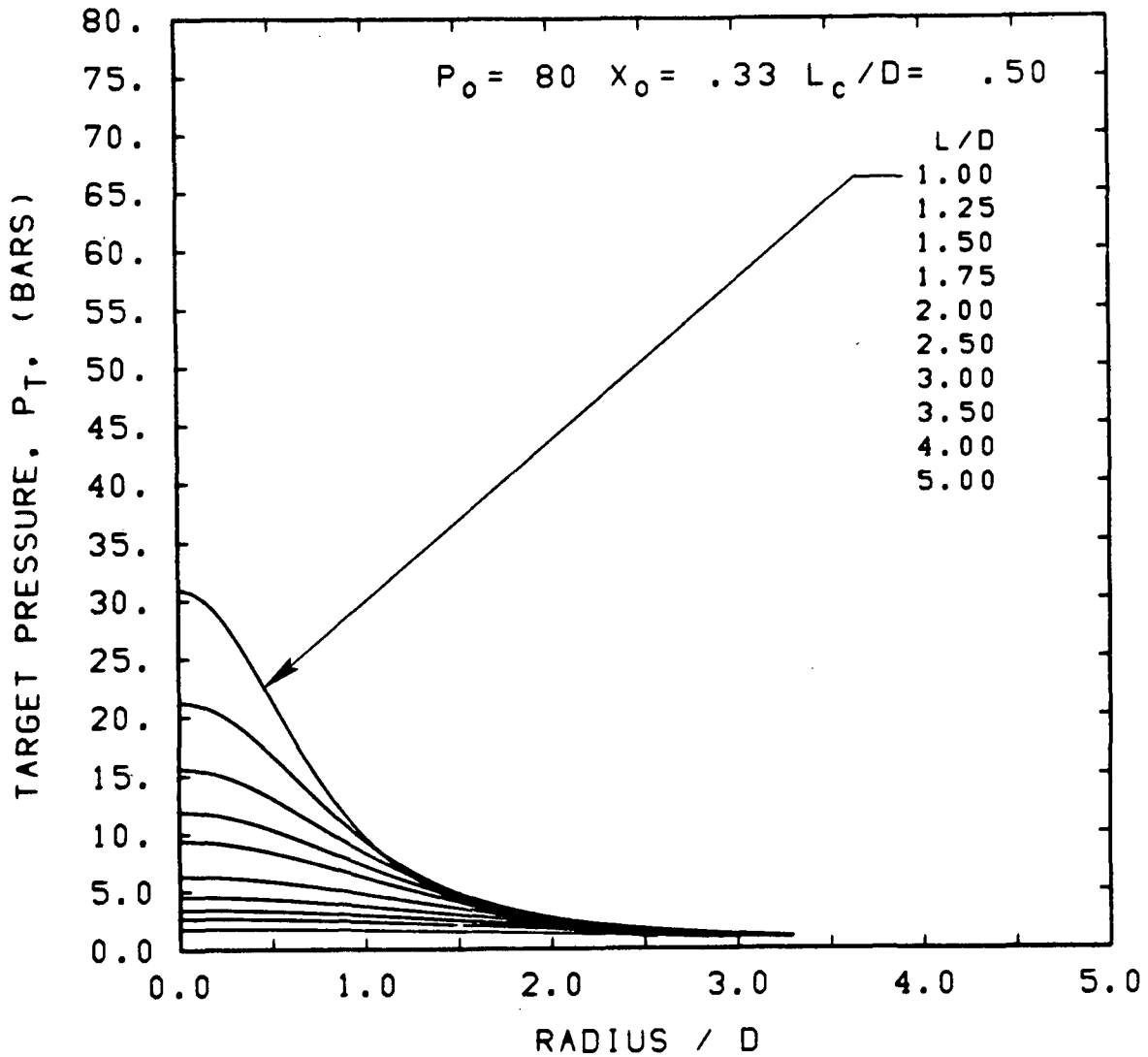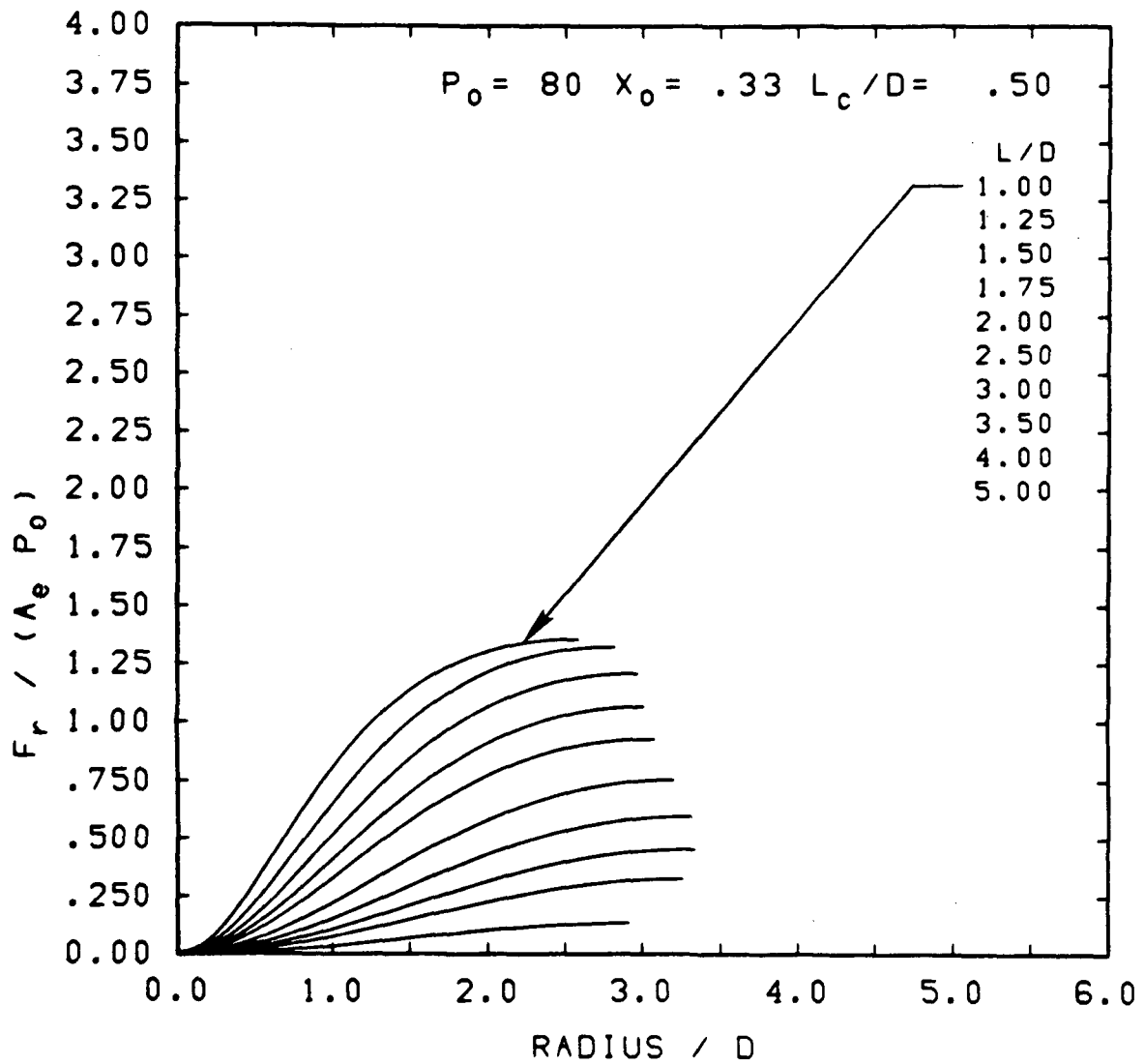
Figure 2.9   Target load distributions for stagnation
              conditions of P_O = 150 bars and ΔT_O = 15°C.
              The target L/D associated with each curve
              is listed in the upper-right-corner key; the
              lowest L/D value corresponds to the uppermost
              curve.

Figure 2.10   Target pressure distributions for stagnation
conditions of P_O = 80 bars and X_O = 0.33.
The target L/D associated with each curve
is listed in the upper-right-corner key; the
lowest L/D value corresponds to the uppermost
curve.

Figure 2.11   Target load distributions for stagnation
conditions of P_o = 80 bars and X_o = 0.33.
The target L/D associated with each curve
is listed in the upper-right-corner key;
the lowest L/D value corresponds to the
uppermost curve.

3.0 CHARACTERISTICS OF TWO-PHASE JETS

3.1 Generalized Two-Phase Jet Behavior

In this study we found that the flow field for two-phase jets impinging on axisymmetric targets is extremely complicated. However, regions of this complicated flow field can be explained using simple concepts, e.g., isentropic flow, normal shock theory, HEM choked flow, and others. Figure 3.1 illustrates the expected pressure behavior along the centerline of the jet. Figure 3.1a is a spatial illustration of the pressure field in a two-phase, impinging jet. The heavy solid lines in Figure 3.1a describe solid boundaries that depict the vessel, break nozzle, and target. The small plot on the right in Figure 3.1a describes the pressure-expansion in the vessel and piping and in the jet outside the vessel. The conditions at the dashed vertical line are the conditions at the break (pipe exit). The section of the graph to the left of the vertical dashed line corresponds to conditions outside of the pipe exit. Moving to the left corresponds to an increase in the target to pipe spacing. The points labeled 2,3, and 4 in 3.1a correspond to the pressures for one pipe spacing given the conditions at points 0 and 1. Figure 3.1b shows an actual pressure-expansion calculation for $P_O = 100$ bars, $\Delta T_O = 0$ $^{\circ}C$.

In the jet flow field there are three natural divisions of the field; each will be described in detail in later sections. There is a nozzle (or break) region where the flow chokes. In this region there is a core at choked flow thermodynamic properties that projects a distance downstream of the nozzle depending upon the degree of subcooling. Downstream of this region there is the free jet region. Here the jet expands almost as a free, isentropic expansion. The flow is supersonic throughout this entire region. The free jet region terminates at a stationary shock wave near the target. This shock wave arises because of the need for the target to propagate pressure waves upstream and, thus, produce a pressure gradient that will direct the fluid around the target. Downstream of the shock is the target region where the local flow field imposes the pressure loading on the target.

The pressure P_O is the vessel stagnation pressure, and P_1 is the choke pressure in the break nozzle. The pressure P_2 denotes a family of isentropic expansion pressures describing the centerline jet expansion upstream of the shock wave, and P_3 describes a family of pressures downstream of the shock wave that correspond to a normal-shock Hugoniot calculation from the jet-expansion state P_2. Finally, P_4 describes the family of stagnation pressures that correspond to each of the P_3 normal-shock Hugoniot calculations. Notice
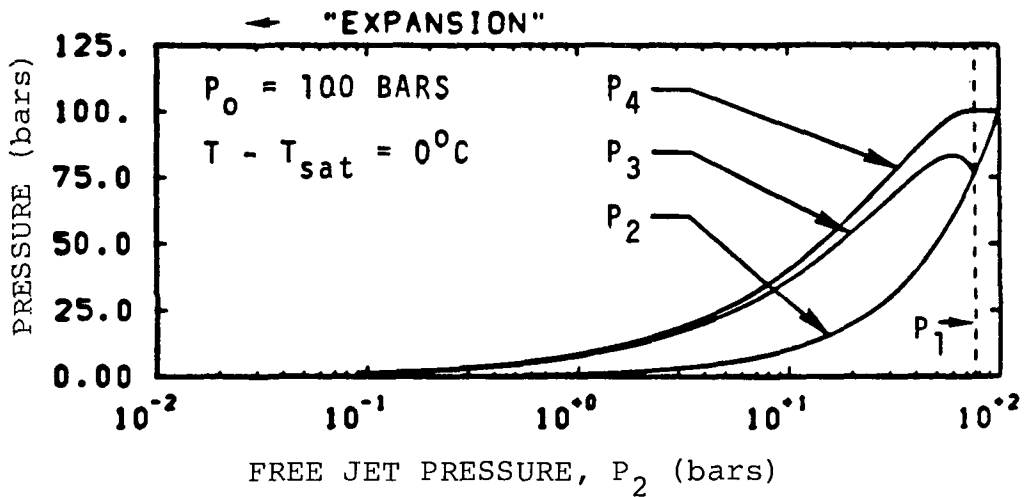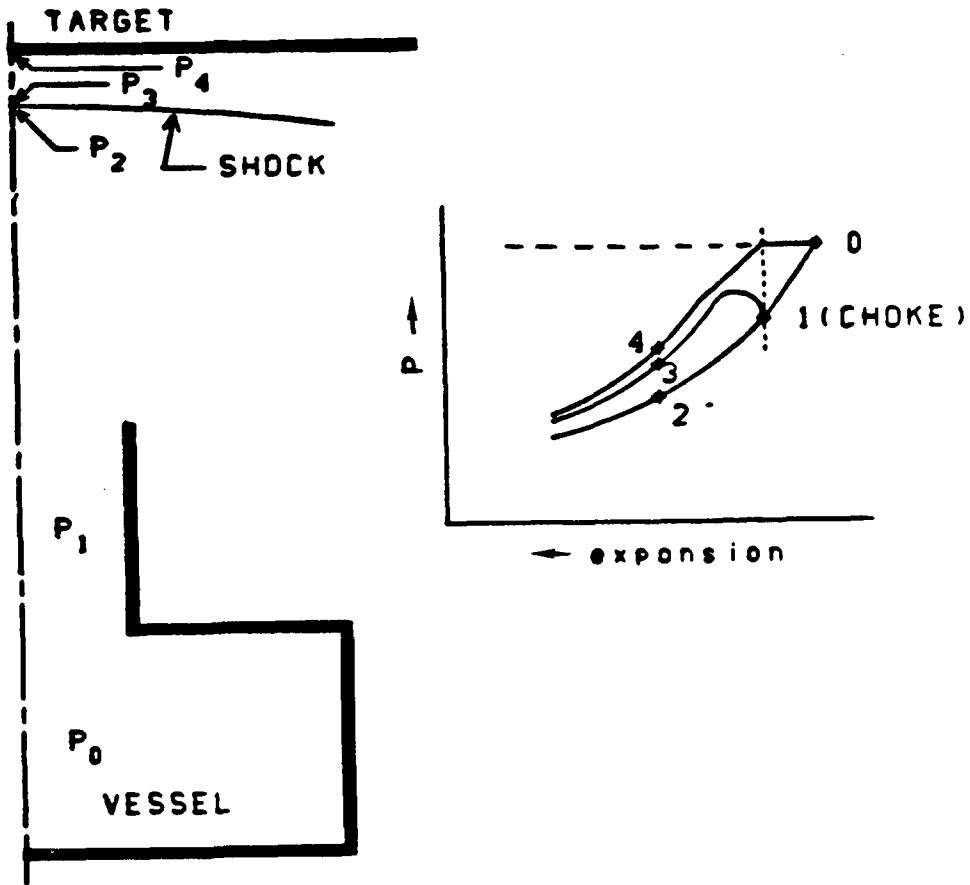
19

Figure 3.1   Illustration of the expected pressure
behavior along the centerline of a two-
phase jet impinging on targets.

20

that the shock wave causes a substantial stagnation pressure loss for highly expanded jets. This stagnation pressure loss is due to the non-isentropic processes in the shock and should not be confused with the very small viscous and entrainment losses. Figure 3.1b shows a set of actual jet pressure families for P_O = 100 bars and saturated liquid conditions.

3.2 Idealized Configuration

The idealized configuration used in this study is shown in Figure 3.2. A large vessel is uniformly filled with water with known thermodynamic properties. An exit pipe of diameter D is the only flow path out of the vessel. A target is located a distance L from the end of the pipe; the target has no curvature and has a radius that is large enough so that the fluid exiting its edge has expanded to containment pressure.

This piping configuration is equivalent to an offset guillotine break. The second pipe exit will be ignored for this study. It is assumed that there is no interaction between the two jets. Of course this could not be the case very early in the break history when the pipe sections are separating. However, this phase of the problem is beyond the current scope of this effort. Performing calculations early in the break history would require a number of specific configuration properties: pipe rigidity, restraint positions, and other items necessary to determine pipe whip.

This idealized configuration assumes that the exit pipe initially has fluid with the same thermodynamic state as the vessel, i.e., there is no initial motion. At time zero the pipe exit opens instantaneously to the outside or containment environment. The exit flow history that would be expected is illustrated in Figure 3.3 The initial steps in the flow are the result of the wave propagation from the pipe exit to the vessel and return. The length of time involved is approximately 2 L_p/C_s where L_p is the exit pipe length and C_s is the sound speed in the fluid. Multiple steps of decreasing amplitude would be expected.

After these initial steps, the maximum exit flow will develop. Further decreases in the flow would result as the vessel depressurizes. If the vessel is sufficiently large, then there will be a relatively long period of time where the rate of change in the flow is small. It is this period of the blowdown history that will be of main interest in this study. Points in this blowdown correspond to different initial vessel conditions.
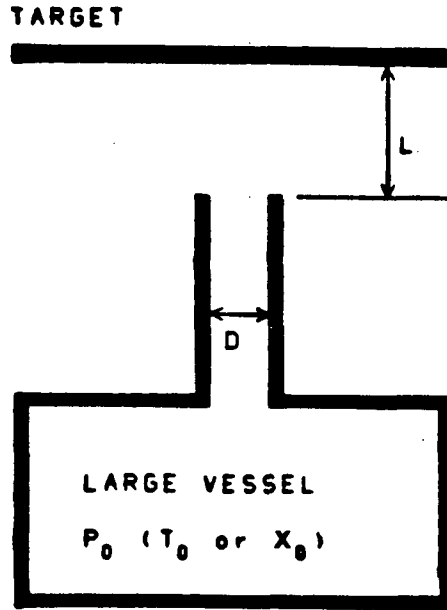
21

TARGET

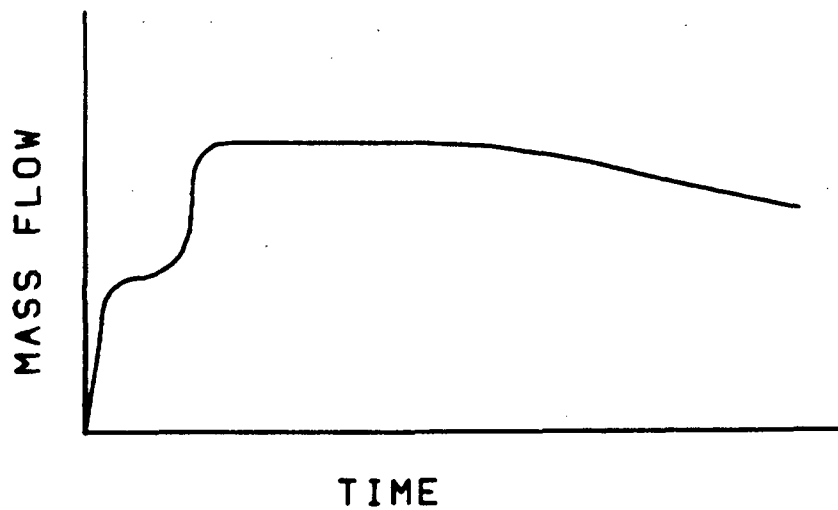Figure 3.2 Idealized two-phase jet loads geometry

Figure 3.3   Typical break flow history (instantaneous
double-ended guillotine break)

22

The flow conditions in the jet outside of the pipe adjust to the exit flow conditions much faster than the rate of change of conditions in the vessel. This is a consequence of the extremely high velocities that are developed as the jet expands downstream of the exit. For this reason, the two-phase jet was assumed to be quasi-steady, i.e., the time scale of the jet was assumed to be much smaller than the time scale of the vessel blowdown. The jet properties and loads can now be calculated while holding the vessel properties constant.

Using the quasi-steady approach makes the problem tractable. An unsteady model, which would be needed to calculate the initial transient, would need to consider not only the break and the target but also the flow in the vessel and associated piping. The time required on modern computers to carry out a large number of these calculations is simply prohibitive. It should be made clear that the modeling codes used in this study have the capability of evaluating the entire time-dependent blowdown. These type of calculations, however, require several hours of CDC 7600 time to advance the solution through the period of interest. The quasi-steady approach, on the other hand, allows the blowdown to be calculated independent of the jet problem; the time-dependent behavior of the vessel (reactor system) is analyzed over small time intervals using steady state calculations.

At this point an example that demonstrates the validity of using the quasi-steady assumption will be given. Figure 3.4 shows a typical blowdown history[7]; this history is actual data from a Marviken[8] free jet test. Figure 3.5 is an axial velocity distribution, computed with the model code, for the conditions of Figure 3.4 at about 5 sec -- a point where the pressure slope in the blowdown history was steep. The nozzle exit velocity was about 6000 cm/sec (196 ft/sec), and the downstream velocity was about 35,000 cm/sec (1148 ft/sec), thus an average axial velocity would be about 20,000 cm/sec (656 ft/sec). A particle leaving the nozzle would therefore travel about 200 meters (656 ft) in one second, or stated in another way, the time needed for a particle leaving a 1 ft diameter nozzle to traverse an L/D of about 6 is nine thousandths of a second (0.009 sec). Clearly the time scale in the flow outside of the nozzle is much different than the time scale of the blowdown given in Figure 3.4.

In this report, only two-dimensional axisymmetric geometries (targets) are considered. The extension of these models to other types of targets is beyond the scope of this investigation. However, the development of the HEM critical
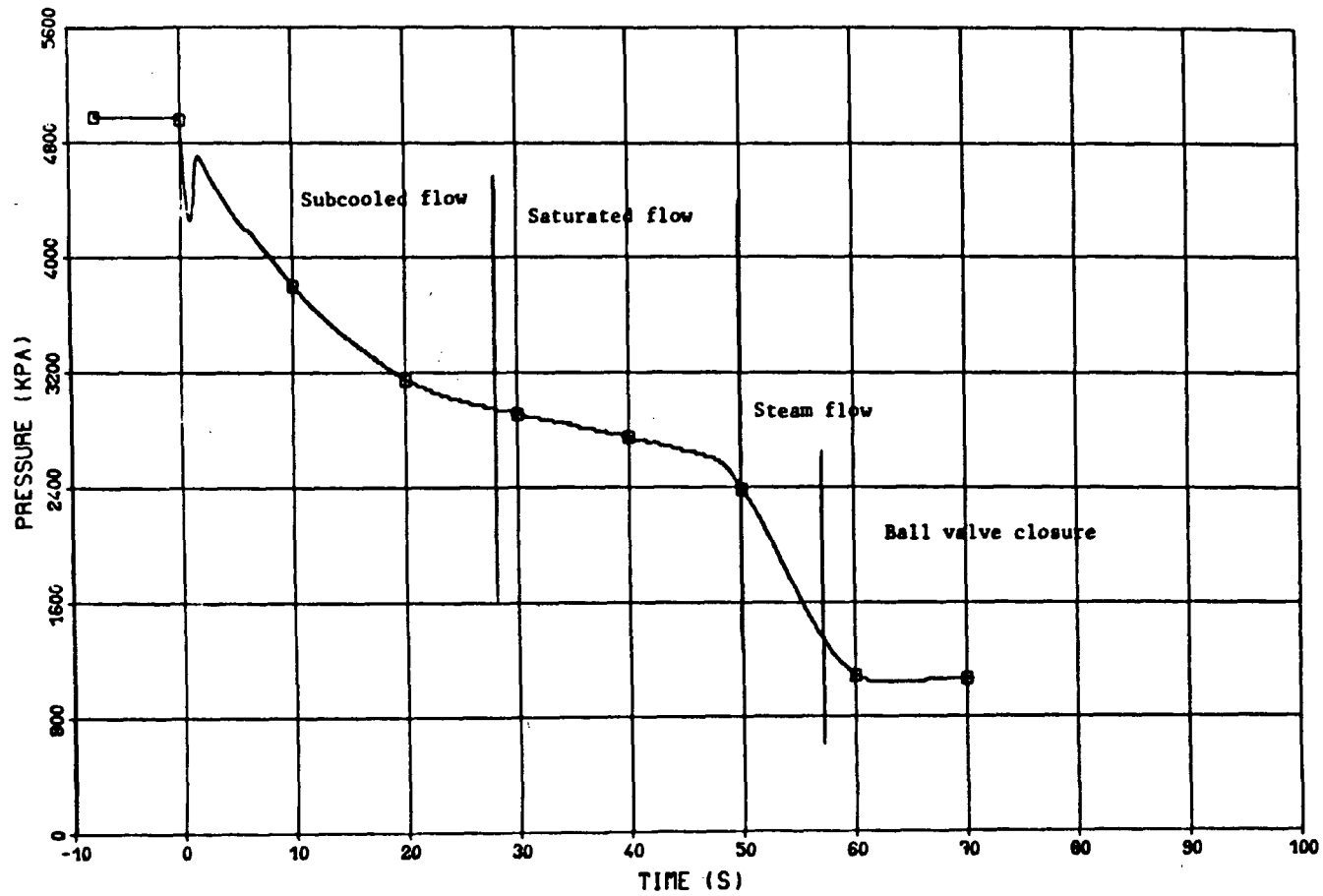
Figure 3.4   Typical blowdown vessel pressure history -- Marviken 1
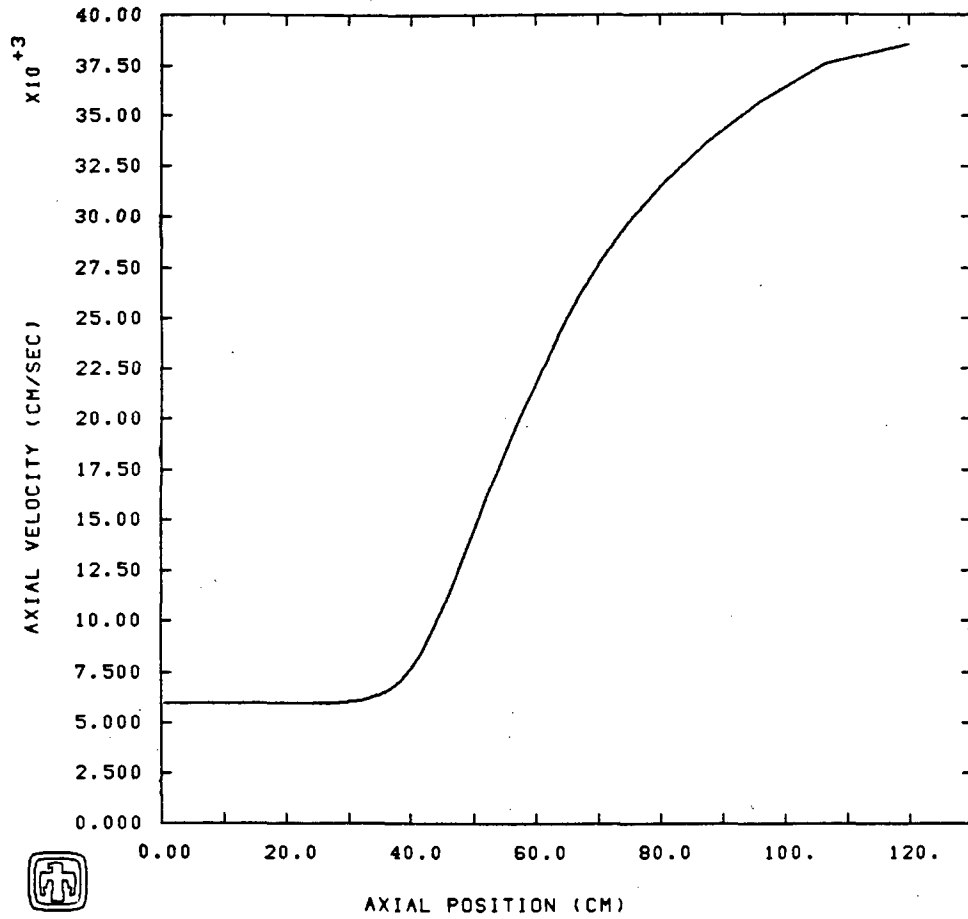   vessel pressure history from Reference 7.

Figure 3.5 Axial velocity distribution computed with
the model code for the vessel conditions
of Marviken 1 (Figure 3.4) at 5s.

flow model, the development of a method for considering the total pressure behind standoff shocks, and the development of methods for calculating the free jet properties are technologies that can be applied immediately to perform upper limit calculations for any target geometry. These features depend only on the thermodynamic properties of water.

3.3 Governing Equations

In the early part of the two-phase jet loads program, considerable effort was expended in finding a suitable model for describing the region between the pipe break and the target. This effort was twofold: a) use existing computer codes on available data and test problems, and b) use simple engineering equations and correlations to estimate jet effects. One-dimensional models were developed from first principles for the two-phase jet[9,10]. These models proved incapable of predicting the behavior of the jet because of the strong multidimensional behavior of the jet near the nozzle exit. It was only after considerable amounts of finite difference code calculations had been completed that progress was made in this area.

An expensive and lengthy code assessment, using a few two-phase jet problems was conducted; the results are given in References 9, 11, and 12. BEACON/MOD2,[13] BEACON/MOD3,[14] SOLA,[15] RELAP,[5] CSQ,[16] and TRAC[4] were all evaluated for their capability to treat various aspects of this problem. The final conclusion reached in the code evaluation was that none of the above codes, with the exception of CSQ, was capable of accurately treating the desired two-phase jet configuration without considerable code modifications; CSQ would only require minor modification. Because CSQ calculations also had proven to be the most reliable over the widest range of parameters and initial conditions, it was selected for use in this study. Nodalization studies also indicated that the meshing required to treat this problem was far in excess of the capabilities of any of the codes except CSQ.

The CSQ code is a finite difference code which solves a homogeneous, equilibrium set of equations for a specified flow field; the code has multi-material capabilities and uses an accurate equation of state for water[17]. Our choice of an equilibrium system of equations is discussed near the end of this section.

The governing equations are the conservation of mass, momentum and energy. These relations written in cylindrical coordinates for axisymmetric configurations are:

$$\frac{\partial \vec{U}}{\partial t} + \frac{\partial \vec{M}}{\partial r} + \frac{\partial \vec{N}}{\partial z} + \vec{Q} = 0, \qquad (3.1)$$

26

where the vectors are:

$$\vec{M} = r \begin{cases} \rho V_r \\ \rho V_r^2 + P \\ \rho V_r V_z \\ \rho V_r (E + P/\rho) \end{cases}$$

$$\vec{N} = r \begin{cases} \rho V_z \\ \rho V_z V_r \\ \rho V_z^2 + P \\ \rho V_z (E + P/\rho) \end{cases}$$

$$\vec{U} = r \begin{cases} \rho \\ \rho V_r \\ \rho V_z \\ \rho E \end{cases}$$

and

$$\vec{Q} = \begin{Bmatrix} 0 \\ -P \\ 0 \\ 0 \end{Bmatrix}$$

In these relations ρ is the density, V is the velocity, P is the pressure, E is the specific internal energy, t is the time, r is the radius from the center line of symmetry, and z is the axial coordinate. These equations when combined with the thermodynamic equation of state form a closed system of equations. For the present purpose, the equation of state simply relates the values of P, E and ρ. Two independent thermodynamic variables determine the complete state description.

27

The above relations may be simplified under certain conditions. When heat transport with the fluid is not important, one of the above relations can be eliminated in favor of the statement that the entropy (S) at a fluid fixed location is constant. For uniform initial conditions, this implies that the space fixed entropy value is also constant at positions where equation (3.1) is applicable, thus

$$S = S_O .$$
(3.2)

It should be noted that these relations do not apply at all positions in a jet field. Modifications are necessary for the description of nonisentropic behavior such as shock waves.

For the steady state situation in which all of the time derivatives in (3.1) vanish, there is another interesting solution. In vector form the energy equation becomes

$$\vec{V} \cdot \nabla(H + \frac{1}{2} \vec{V} \cdot \vec{V}) = 0 ,$$
(3.3)

where H is the enthalpy and V is the velocity. It then follows that

$$H + \frac{1}{2} \vec{V} \cdot \vec{V} = H_O = \text{constant} .$$
(3.4)

Additionally, when the steady state form of equation (3.1) is used the absolute length dependency may be scaled from the problem. In other words the form of the governing equations remains unchanged when distance scales are modified. For example, if the scaled position coordinates

$$r' = \frac{r}{\eta} \text{ and } z' = \frac{z}{\eta}$$
(3.5)

are introduced into the steady state form of (3.1) then the form of the resulting equations are the same as before the transformation. The scaling distance η vanishes from the

expressions. This scaling property can be employed in the engineering model to eliminate one of the independent parameters (jet size). The obvious choice in this problem for η is $\eta = D$ (the exit pipe diameter).

Most applications of these equations require numerical solution. In general, the equation of state relation is quite complex and not suited for linearized treatment. The main problem area is the phase change regions where very large discontinuities in some thermodynamic relations are encountered. The numerical methods used in the detail calculations for this study were developed in other studies at Sandia National Laboratories.[16]

As earlier noted, this above system of equations is an equilibrium system. Questions have always been raised about the validity of such a model when it is applied to situations where nonequilibrium conditions may exist. Our previous two-phase jet experience shows that the equilibrium relations, when properly applied in multidimensional geometries, are capable of accurately describing the two-phase jet without empirical correlation. It should be noted here that many times in the past what was thought to be nonequilibrium effects were actually multidimensional effects.[18] Finally, the equilibrium behavior should be completely investigated before expensive nonequilibrium calculations are attempted.

There are some additional properties of the above relations that can be developed and are of interest to the present problem. Choke flow is considered in the next section and shock wave relations are considered in Section 3.5.

3.4 Breakflow Conditions

The present computational models developed for analyzing two-phase jets require the flow conditions at the pipe break. The types of breaks addressed in this report result in what is commonly referred to as choked or critical flow. The calculation of two-phase choked flow for the purpose of estimating breakflow rates is a subject that has had considerable attention in the past[19,20,21]. As a result, numerous models have been published and debated. Because there is a scarcity of both existing and planned two-phase, choked flow experiments[22], there is no universal consensus about which of the choked flow models is best. In this study, the homogeneous equilibrium flow model (HEM) is used. This model was selected because it is thermodynamically consistent with the jet model, and moreover, earlier critical flow studies[10] showed that the HEM model provides the fluid's thermodynamic state at the break and is applicable to a wide range of initial conditions.

29

The properties of choked flows are a thermodynamic consequence; consequently, the geometry of the situation need not be considered until the final step. This last step is, however, very important when multidimensional choking occurs and the local geometry can have significant impact upon the break-flow rate. Reference 10 reported a good example of the effect geometry has. Several guard pipe calculations were performed where the two-dimensional structure at the break location was considered. The result was a homogeneous equilibrium flow rate that was about forty percent less than the flow predicted using the HEM critical flow model, applied as a one-dimensional model, i.e., a discharge coefficient $M_S = 0.60$.

Discharge coefficients were not used in this study at any time to correct flow rates for geometry effects. This practice has no thermodynamic justification since the fluid's thermodynamic state at the break would also need to be corrected. This is rarely done and cannot be done in a thermodynamically consistent manner.

Consider a flow in a pipe or a nozzle. The mass flux vector is defined by

$$\vec{G} = \rho \vec{V} , \tag{3.6}$$

where ρ is the density and V is the velocity. The total mass flow in the pipe can be written as

$$M = \int \vec{G} \cdot d\vec{A} , \tag{3.7}$$

where dA is the normal surface unit vector. The surface in question can be any surface which covers the pipe exit.

For homogeneous-equilibrium, inviscid flow

$$H_O = H + \frac{1}{2} (\vec{V} \cdot \vec{V}) \quad \text{and} \quad S = S_O , \tag{3.8}$$

where H is the enthalpy and S is the entropy. Note that the flow is isentropic. The mass flux may now be expressed as a function of the density and the enthalpy by combining equations (3.6) and (3.8), thus

30

$$G = \rho \sqrt{2 (H_O - H)} \qquad . \qquad\qquad (3.9)$$

For the HEM model, the mass flux depends only on the thermodynamic state of the fluid; consequently, the maximum mass flux (critical flow) must also only depend upon the fluid's local thermodynamic state.

Choking is defined as the state in the fluid where changes in the downstream properties do not alter the mass flow rate or any properties upstream of the break. The fluid at this state (or position) is supersonic, i.e., the magnitude of the fluid velocity vector is equal to or exceeds the local sound speed. Now if the upstream fluid is subsonic (the situation that exists in power reactor piping), then choking will occur at the position of the transition to supersonic flow:

$$\left[\frac{V}{C_s} < 1 \right] \text{ switches to } \left[\frac{V}{C_s} \geq 1 \right] \qquad . \qquad\qquad (3.10)$$

An absolute equality was specifically avoided in the above equation. Moreover, when the flow involves a phase change an equality does not exist and many of the acceptable definitions for choked flow breakdown because of the discontinuous behavior in the property derivatives at the saturation line. Consider the generally acceptable definition of choked flow

$$\left. \frac{\partial G}{\partial \rho} \right)_s = 0 \qquad . \qquad\qquad (3.11)$$

This definition seems to express mathematically the above definition for choked flow; however, equation (3.11) may not be valid at a phase boundary. This is easily seen from the following derivation.

Consider the square of equation (3.9) and differentiate this relation with respect to density while holding the entropy constant. The result is

31

$$G \left. \frac{\partial G}{\partial \rho} \right)_s = 2 (H_o - H)\rho - \rho^2 \left. \frac{\partial H}{\partial \rho} \right)_s . \qquad (3.12)$$

The enthalpy can be expressed as a function of internal energy, E, pressure, P, and density, ρ

$$H = E + P/\rho \quad , \quad \rho \left. \frac{\partial H}{\partial \rho} \right)_s = \left. \frac{\partial P}{\partial \rho} \right)_s . \qquad (3.13)$$

Thus equation (3.12) becomes

$$\frac{G}{\rho} \left. \frac{\partial G}{\partial \rho} \right)_s = 2 (H_o - H) - \left. \frac{\partial P}{\partial \rho} \right)_s . \qquad (3.14)$$

Substitution of equation (3.6) and (3.9) into equation (3.14) and following some rearrangement gives

$$\left. \frac{\partial G}{\partial \rho} \right)_s = \frac{V^2 - C_s^2}{V} \quad ; \quad C_s = \sqrt{\left. \frac{\partial P}{\partial \rho} \right)_s} , \qquad (3.15)$$

where C_s is the local sound speed. This above expression, the one generally applied to locate a choke point, will obviously fail the test in equation (3.11) when the sound speed behaves discontinuously.

A computer code was developed which determines the choke location defined by equation (3.10) for the various single and mixed phases of water. Additionally, the code will generate the fluid properties all along the isentrope in question. As long as no shocks are encountered in the flow field downstream of the choke point, this isentrope remains valid and represents the allowable thermodynamic states for the expanding fluid. This result is not insignificant, because if the jet is assumed to be isentropic, the thermodynamic behavior of the jet becomes known. What will not be known is the spatial dependence of these thermodynamic states. Two examples are given.

Figure 3.6 shows the flux versus density behavior which would result along an isentrope that crosses a phase boundary. This curve was produced using

$$G = \rho \sqrt{2 \ (H_O - H)} \ , \ S = constant \ . \qquad (3.16)$$

The initial stagnation conditions (P_O, T_O) were 100 bars and saturated liquid. The density and mass flux marked by the broken line is the choke point. Figure 3.7 shows the V/C_S ratio as a function of density for the same isentrope ($S = 3.3598 \times 10^7$ ergs/g^{O}C). In this region of the water phase diagram, where the sound speed is continuous, note that the choke occurs at $V/C_S = 1$. Equation (3.11) would have worked satisfactorily for this case.

Now consider the case where the water is initially subcooled. Figure 3.8 shows the mass flux versus density behavior for $P_O = 100$ bars and $\Delta T_O = 35^O$C. For this case, equation (3.15) becomes negative at the saturated liquid line without going through zero due to the discontinuous behavior of the sound speed there, thus choking occurs at this point. Figure 3.9 shows the discontinuous behavior in V/C_S that occurred with choking. Note the value of V/C_S ($V/C_S \simeq 2.6$) at the choke point and also note the behavior of V/C_S downstream ($\rho < \rho_{crt}$) of the critical flow point. Equation (3.11) would not have worked for this case.

3.5 Standing Shock at the Target

Simple modeling and CSQ calculations have shown the existence of a shock wave that stands a small distance from the target. The existence of such a shock wave was not unexpected; their existence and strength is well documented in single phase flows[23]. These types of shock waves exist because the fluid is required to deaccelerate rapidly in a very short distance. A shock wave may be characterized as an instantaneous, irreversible compression of the fluid. The energy for performing this rapid compression comes from the fluid's upstream kinetic energy; consequently, since the process is irreversible, the kinetic energy leaving the shock is less than would have existed for an isentropic compression. In other words the entropy changes (increases) across an adiabatic shock and the stagnation pressure decreases.

33
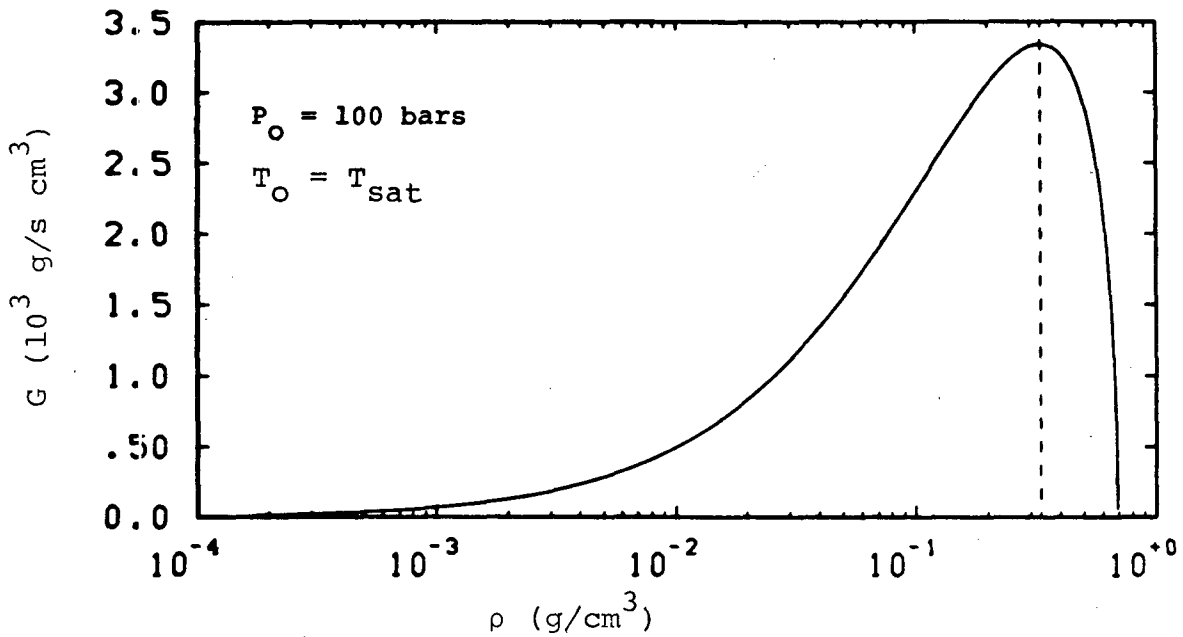
Figure 3.6   HEM mass flux as a function of density for
              stagnation conditions of P_o = 100 bars and
              saturated liquid, equation (3.16). Choking
              occurs at the vertical broken line.
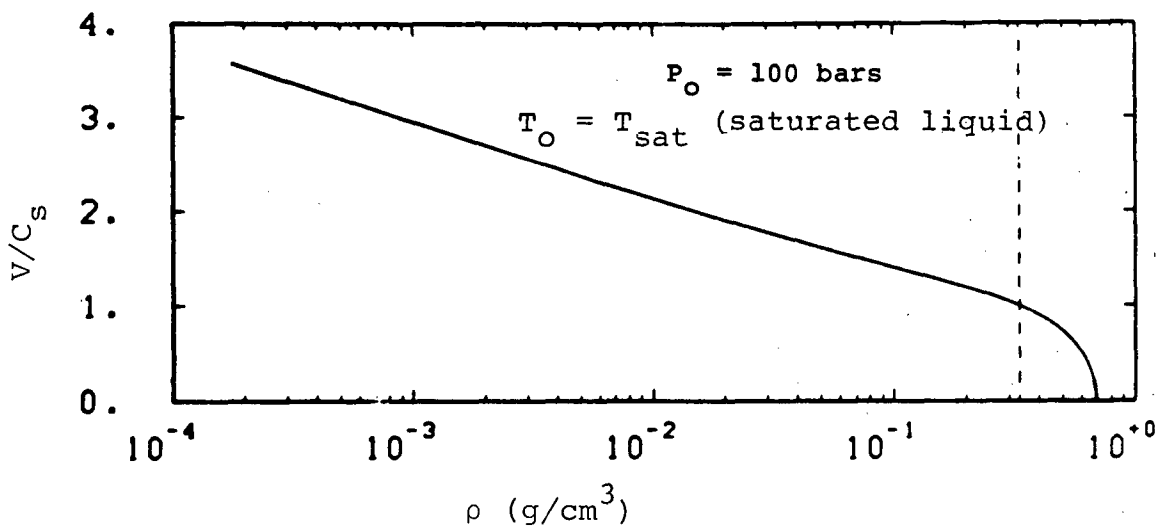
Figure 3.7   HEM velocity to sound speed ratio for stagnation
              conditions of P_o = 100 bars and saturated liquid.
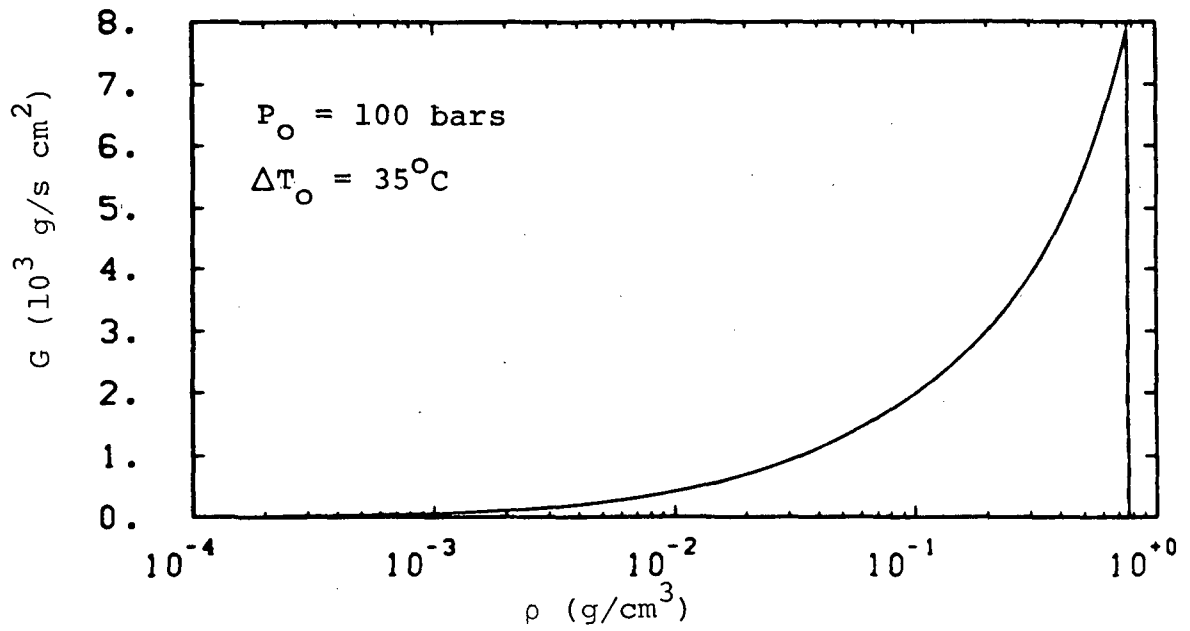
Figure 3.8   HEM mass flux as a function of density for
stagnation conditions of P_o = 100 bars and
ΔT_o = 35°C.
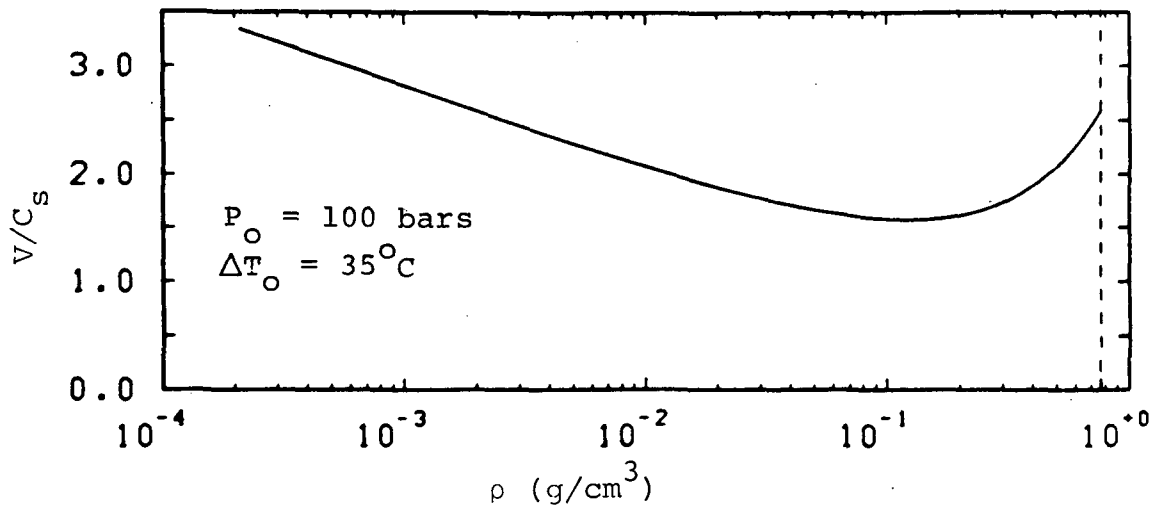
Figure 3.9   HEM velocity to sound speed ratio for stagnation
conditions of P_o = 100 bars and ΔT_o = 35°C.

If this is the case, then the homogeneous equilibrium flows in Section 3.5 become the input for the shock calculation. For the present discussion, consider the shock to be a normal shock. This assumption is quite reasonable since (a) we are endeavoring at this point to consider what happens to peak centerline stagnation pressure, and (b) independent of target shape, the shock is normal in character at some point (flow lines perpendicular to the shock).

Consider then the two-phase flow of a homogeneous, equilibrium, and isentropic fluid shown in Figure 3.10. The following equations express conservation of mass, momentum and energy for a stationary normal shock:

$$\rho_U V_U = \rho_D V_D \ , \tag{3.17}$$

$$P_U + \rho_U V_U^2 = P_D + \rho_D V_D^2 \ , \tag{3.18}$$

and

$$E_D - E_U = \frac{1}{2} \left(P_D + P_U \right) \left(\frac{1}{\rho_U} - \frac{1}{\rho_D} \right) \ , \tag{3.19}$$

where ρ, V, P, E are the density, velocity, static pressure and internal energy, respectively, and the subscripts U and D indicate upstream and downstream of the normal shock. These above equations are simply the Rankine-Hugoniot relations expressed for a stationary adiabatic shock. A code was developed to solve the above normal shock equations given the HEM input from Section 3.5

Consider the target and pressure nomenclature given in Figure 3.11. Figure 3.12a shows a sample calculation performed where the stagnation conditions were $P_O = 100$ bars and saturated liquid. Figure 3.12b shows a sample calculation performed where the stagnation conditions were $P_O = 100$ bars and a subcooling of 35°C. These curves show the pressures that would exist due to an isentropically expanding jet at the general point just upstream of the shock (P_2), the point just downstream of the shock (P_3), and the stagnation point on the target (P_4). The three

36
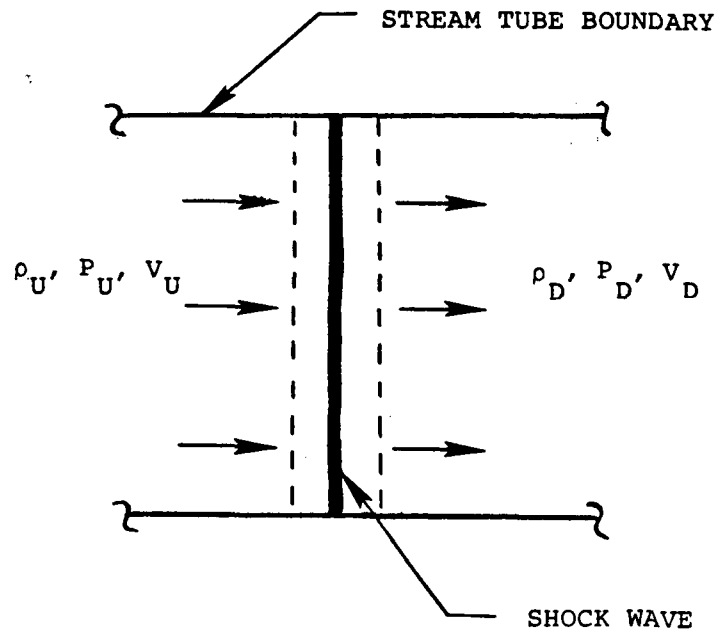
Figure 3.10 Illustration showing the control surface
for a stationary normal shock.

The labels in the figure: STREAM TUBE BOUNDARY, SHOCK WAVE, ρ_U, P_U, V_U, ρ_D, P_D, V_D
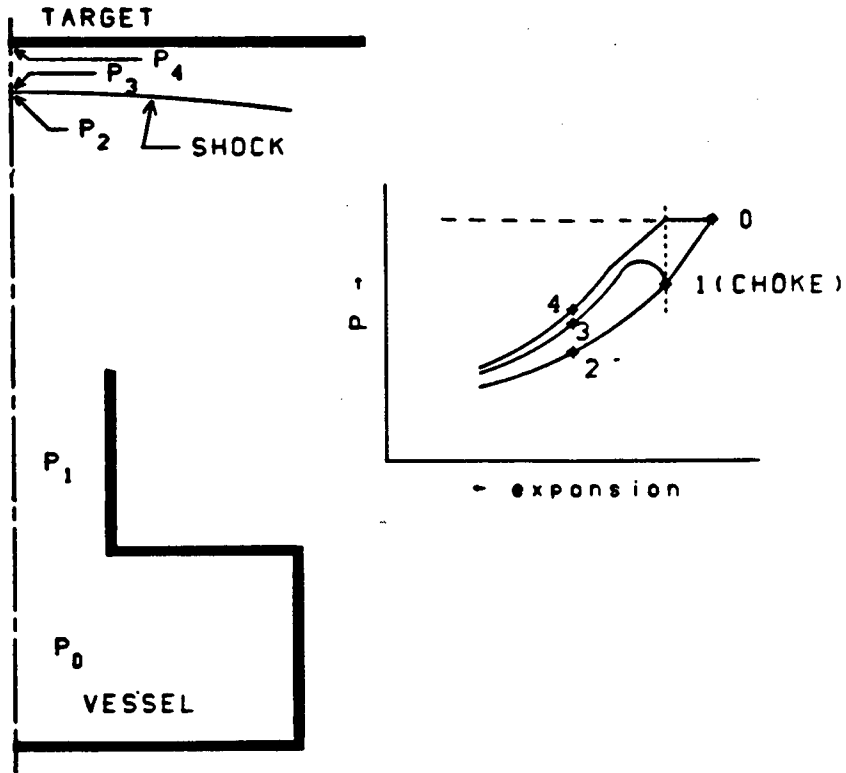
Figure 3.11 Pressure definitions and shock wave definition
for the centerline shock model.
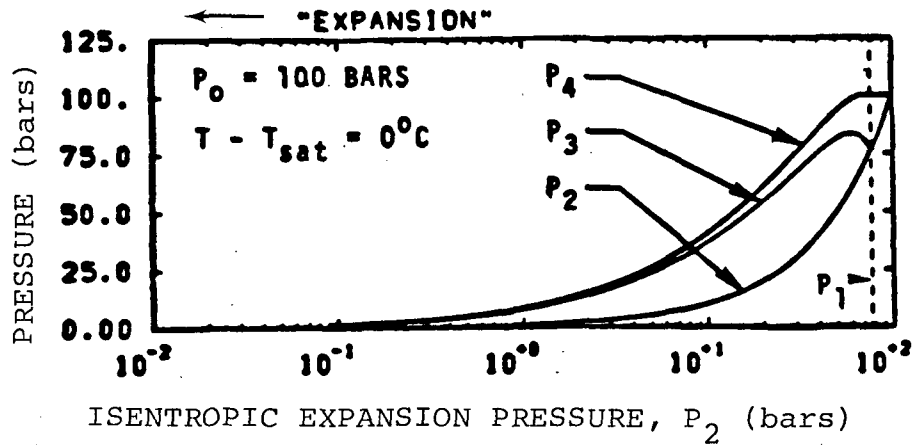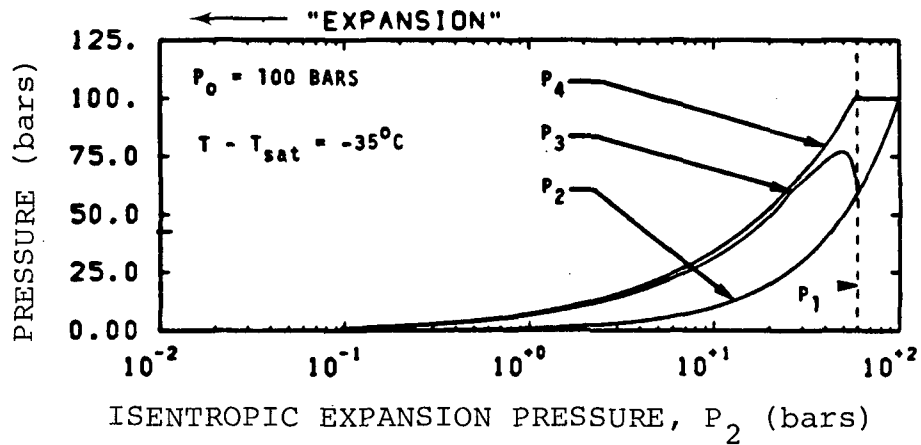
Figure 3.12   Calculation of the shock pressure P_3 and stagnation pressure behind the shock P_4 for the isentropic expansion pressure P_2 and for vessel stagnation conditions of a) P_0 = 100 bars, ΔT_0 = $0^{\circ}C$ and b) P_0 = 100 bars, ΔT_0 = $35^{\circ}C$.

corresponding pressures are all plotted at the same abscissa position. Note the rather significant (and rapid) fall off in stagnation pressure on the target as the jet expands. For both curves when P_2 is about one to five bars static pressure, the magnitude of the shock is such that the stagnation pressure behind the shock is only slightly higher than the approach static pressure, P_2.

Figure 3.13 shows a typical centerline pressure distribution for a two-phase free jet calculated using the CSQ code. This calculation models a Marviken[8] free jet test; the data points are actual Marviken data. Note the rapid decrease in static pressure that occurs axially in the free jet. This behavior confirms the pressure behavior given in Figure 3.12 and is the result of thermodynamic phenomena and not viscous dissipation phenomena. Also, this behavior in a free jet coupled with the above shock model indicates that for many flows at several diameters away from the break exit, the stagnation pressure on a target would not be significantly different from the static pressure of the free jet.

The shock structure has implications beyond this two-phase jet loads study. Experimentalists need to consider the influence of such a shock on their pressure measuring instruments.

3.6 Pipe Exit Core

The fluid exiting the pipe break will always be in a supersonic flow state for the conditions of interest in this study. This will create a conical exit core that will remain at critical flow conditions beyond the nozzle. This is a result of multidimensional behavior and has nothing to do with non-equilibrium effects.

The length of this exit core, L_c, depends on the time it takes for a pressure wave to travel from the outer edge of the exit nozzle to the center of the flow. This time is

$$t_c = D/2C_s \quad , \tag{3.20}$$

where C_s is the sound speed at the exit. If V_1 is the exit flow velocity, then the core length is

$$L_c = V_1 t_c \quad . \tag{3.21}$$

Combining (3.20) and (3.21), we find that

$$L_c/D = V_1/2C_s \quad . \tag{3.22}$$

The point on the centerline L_c from the pipe exit is the first point downstream of the pipe break where pressure information
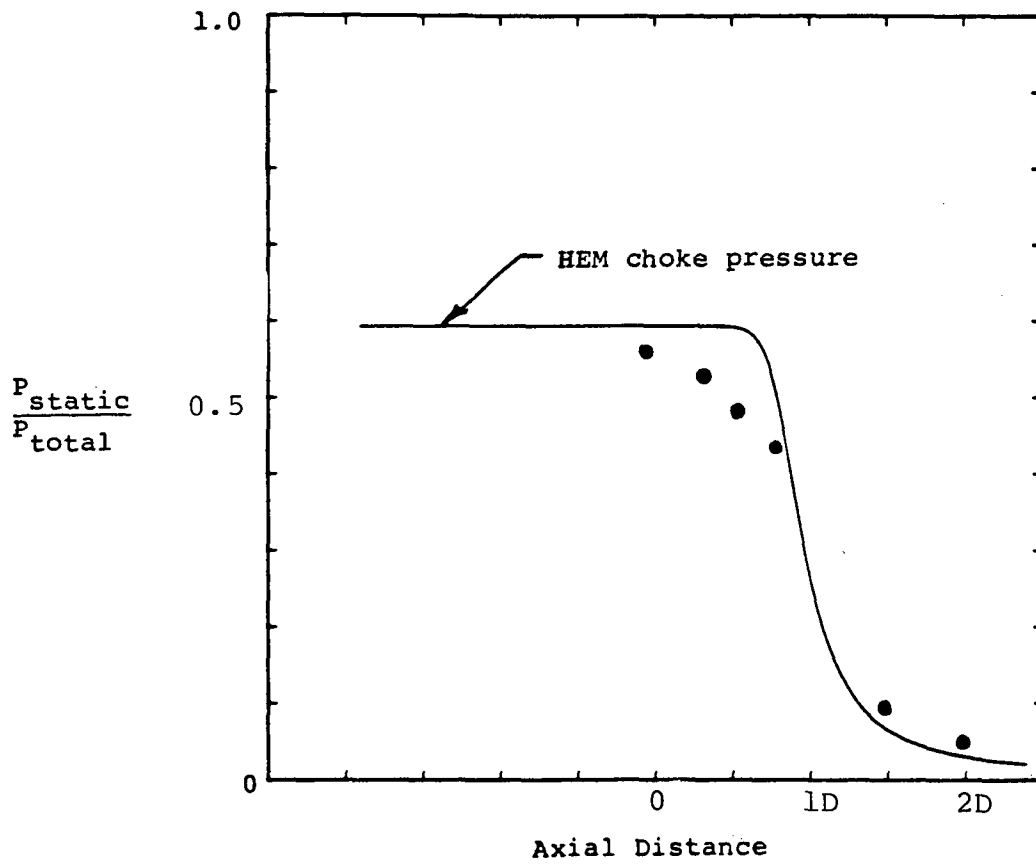
Figure 3.13 Typical axial pressure distribution in a two-phase jet calculated using CSQ[16]. Also shown are Marviken[8] free jet test data.

originating outside of the pipe would be communicated (via waves traveling at C_S) to the fluid that exited at the pipe center. For distances along the centerline less than L_C, the thermodynamic state of the fluid is the same as that inside the pipe. This conical core region with length L_C is shown in Figure 3.14. The structure of the core region has several dominating features that will be discussed in Section 4.2.

There are several things that should be noted about (3.22). First, since the critical flow parameters are thermodynamic in nature, it follows that L_C/D is also purely a thermodynamic property. Secondly, L_C/D will always be greater than or equal to 1/2 because the flow is sonic or supersonic at the choke surface. In Chapter 4, charts will be provided that show L_C/D = 1/2 for saturated stagnation conditions and L_C/D > 1/2 for subcooled conditions. For highly subcooled conditions, the L_C/D can be large.

3.7   Far Field Relaxation to Ambient Pressure

In the flow field far away from the nozzle (large radii), the pressure must relieve to the ambient pressure, P_A. The flow is supersonic and this relaxation to P_A occurs after the flow has expanded to pressures below P_A. This over-expanded region of the flow is terminated by a standing shock followed by a subsonic relaxation to P_A. Figure 3.15 illustrates the expected pressure loading on a flat target. In Figure 3.15 the scales have been purposely distorted to emphasize the overexpansion and shock. This far field shock wave is generally located at large radial positions for the two-phase problems of interest here. The exact position is, however, highly dependent on the exit flow conditions, target location, and ambient pressure.

The pressure involved in the overshoot and shock is relatively small ($\leq$ 1 bar). However, because of the large radii and large associated areas, the total integrated load can be appreciably affected by the far field shock phenomena.

No attempt was made in this study to accurately model the far field shock and flow behavior. It was present in all of the calculations but adequate numerical resolution was not used because of calculational expense considerations.

The load distributions were only evaluated up to the point where the pressure on the target reached ambient conditions. Further details about the load calculations performed in this report and their relationship to the far field shock phenomena are given in Section 7.2.

TARGET

$D = 2R$

$$L_C = \frac{RV_1}{C_S}$$

L_C

V_1

P_1

R

$P_0 \cdot T_0 \cdot \rho_0$

VESSEL

CL
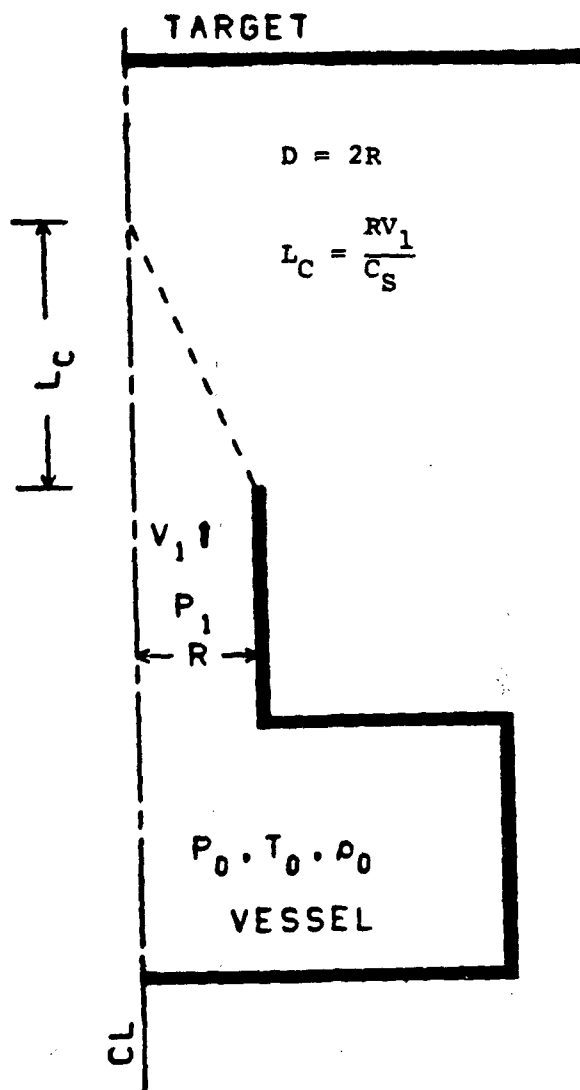
Figure 3.14   Illustration of conical core region
with equations for its length, L_c.
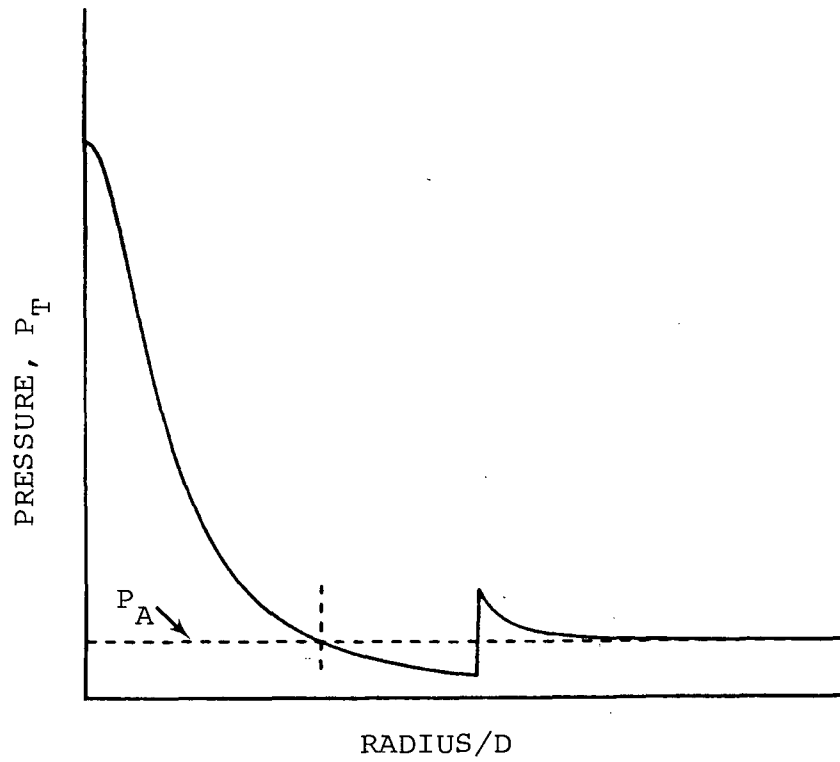
Figure 3.15   Illustration showing the expected pressure
loading on a flat target for a two-phase,
flashing jet.

3.8 External Choke

Up to this point, choking was assumed to occur in the system piping. This may not always be the case. As the target is moved closer and closer to the pipe exit, a point is reached where the choke point will move from inside the pipe to an external surface formed between the edge of the pipe and the target. The external choke phenomena is highly two-dimensional and it occurs almost instantaneously as the target moves toward the pipe exit. The flow can no longer maintain the choke surface in the piping. The shock that occurs near the target moves up into the vessel and an external choke surface forms.

Under these circumstances the idealized model introduced in Section 3.3 loses its validity. The external choking problem was not extensively investigated in this study; solutions of this type were beyond the present scope. However, this type of calculation can be performed without modification to the computer model. The total pressure at the centerline of the target would be P_O; therefore one interim approach would be to assume a uniform pressure distribution of magnitude P_O on the target for some appropriate radius.

4.0 TWO PHASE JET COMPUTER LOAD MODEL

Once it was established that CSQ[16] would be modified (see Section 3.5) for the two-phase jet problem a matrix of calculations was developed to establish a computational data base. This data base covers the following range of initial conditions

pressures of 60 to 170 bars

$$\left\{ \begin{array}{l} \text{subcooling of 0 to 70 } ^\circ\text{C} \\ \text{qualities of 0 to 0.75} \end{array} \right\}$$

L/D's of 0.50 to 15.0

This chapter contains the description of the computer model and presents typical data-base calculations and their consequences.

4.1 Computer Model

The advanced, two-dimensional computer code CSQ was used to develop the two-phase jet load data base. The calculations were conducted for the geometry shown in Figure 4.1.

Briefly, the model can be described as a steady constant property vessel blowing down through a nozzle of diameter D. The jet develops outside of the nozzle and strikes a target at a distance L from the pipe exit. The break flow from the vessel is evaluated using the HEM critical flow model; consequently, the break flow only depends upon the vessel stagnation properties. (The discharge coefficient at the nozzle exit is assumed to be unity.) The wall loading then becomes a function of four independent variables:

$$P_T = P_t(R/D, \ P_o, \ T_o, \ L/D) \qquad (4.1)$$

or

$$P_T = P_t(R/D, \ P_o, \ X_o, \ L/D) \ , \qquad (4.2)$$

where P_T is the pressure on the target, R is the radius (measured on the target), P_o is the stagnation pressure, T_o is the stagnation temperature, and X_o is the stagnation quality.

Figure 4.2 defines three regions within the geometry of Figure 4.1. Region I, inside the pipe, consists of an inlet boundary zone where the flow conditions are driven using the HEM critical flow velocity and thermodynamic properties (P_1, T_1, etc.). Throughout this entire region, the flow is uniform and nozzle geometry effects are neglected.
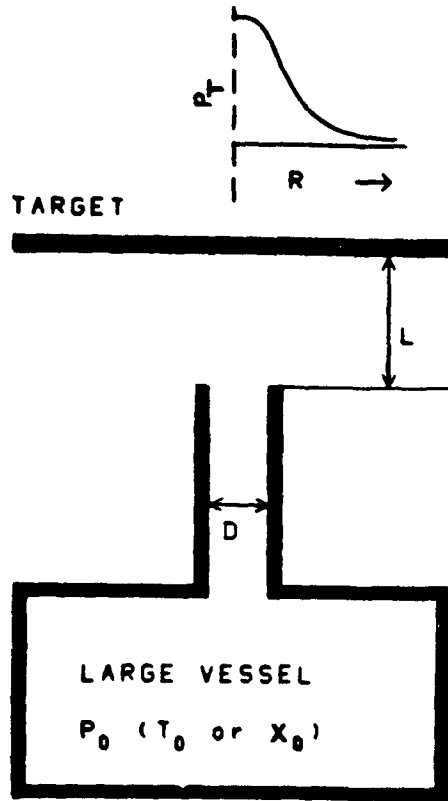
Figure 4.1   Model Geometry for Two-Phase Jet Load
Calculations
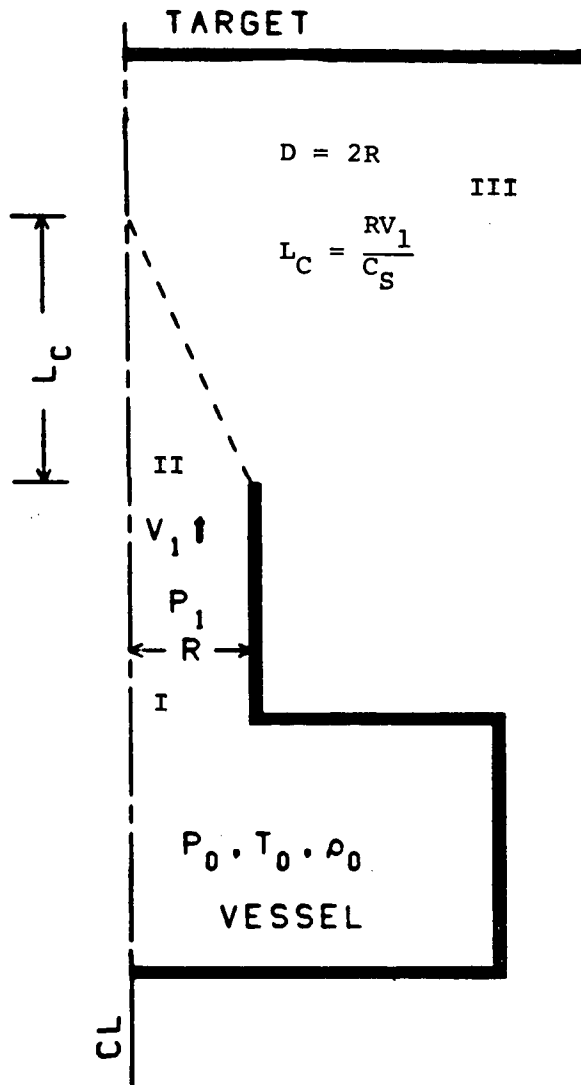
Figure 4.2 Illustration of vessel and target showing the three computational regions: I, HEM boundary; II, Exit Core; III, Jet Environment

Region II, the pipe exit core, consists of a conical core of fluid which remains at HEM critical flow conditions beyond the nozzle (or break). This core of fluid is traveling at supersonic velocity and was discussed in Section 3.6.

Region III, the jet environment, is the main solution region. In this region, the inviscid equations of motion are solved; the result is not only the wall pressure distribution, but the velocities, temperatures, pressures, etc., for each point in Region III. As earlier noted in Section 3.4, there is a distinct shock structure present near the wall in Region III. Our calculations define both the strength and shape of this shock.

4.2   Some Consequences of the Exit Core

There are three distinct (and obvious) possibilities that can occur with the exit core region, Region II: L_C greater than, equal to, or less than L. Consider first the case where $L_C > L$. Here, theoretically, the exit core touches the wall. In practice, there is a weak shock and the fluid recovers, for all practical purposes, the vessel's total pressure P_O. Using the HEM model, once given an L/D ratio and the system's stagnation properties, it is possible to determine if the peak pressure on the target will be the vessel pressure, i.e., if $L_C > L$. The charts in Figures 4.3 and 4.4 give L_C/D as a function of stagnation pressure and temperature; degree of subcooling is also shown. Consider the case where L/D = 2.0 and two operating points were P_O = 100 bars $\Delta T_O = 70^O$K and P_O = 100 bars, T_O = 560 K. For the first operating point L_C/D is about 2.7, thus the peak target pressure would be 100 bars. For the second operating point, L_C/D is about 1.0 and the flow field would have a strong shock, thus the peak target pressure would be less than 100 bars. Since L/D = 2, any vessel stagnation properties that generate an $L_C/D > 2$ would recover the stagnation pressure P_O at the target centerline.

The case where $L_C = L$ should theoretically recover the vessel pressure P_O. This case has not been thoroughly investigated in this study because the gradients in this region are very large and would require a very fine grid. However, calculations on either side of this point show clearly that as L_C approaches L, the peak pressure approaches P_O.

In the cases where $L_C < L$, a strong standing shock exists in the flow field near the wall and, depending upon the amount of jet expansion (see Figure 4.2), there is a loss of total pressure.

4.3   Modifications of CSQ for the Two-Phase Jet Impingement Study

The CSQ[16] code is a multi-purpose code that was developed at Sandia National Laboratories to handle a wide spectrum of material response problems. The next few lines, taken from the introduction in Reference 16, briefly describe the code's versatility.

50
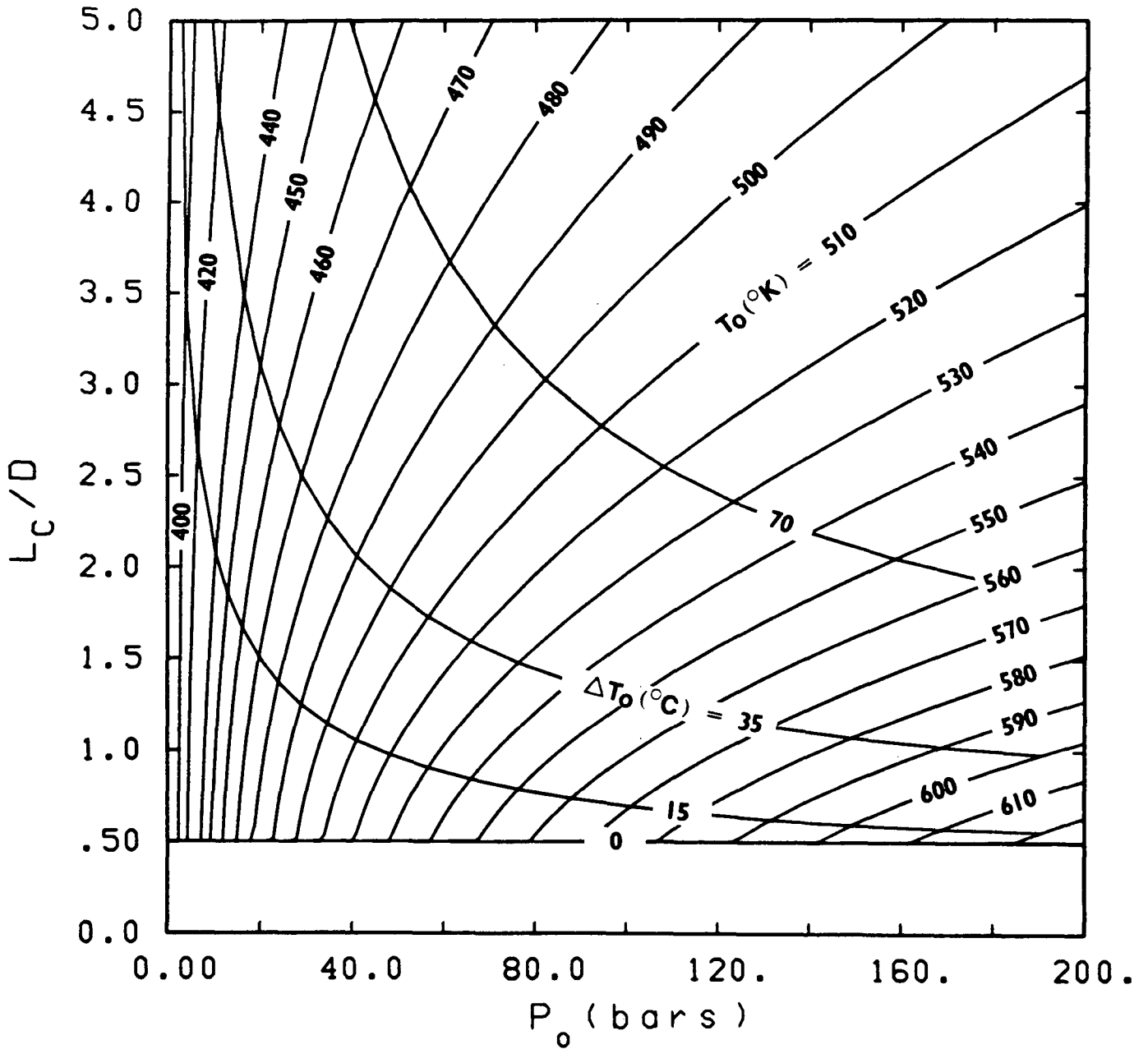
Figure 4.3   Two-phase, jet-exit core (L_C/D) as a function
of stagnation pressure and stagnation tempera-
ture or subcooling.

51
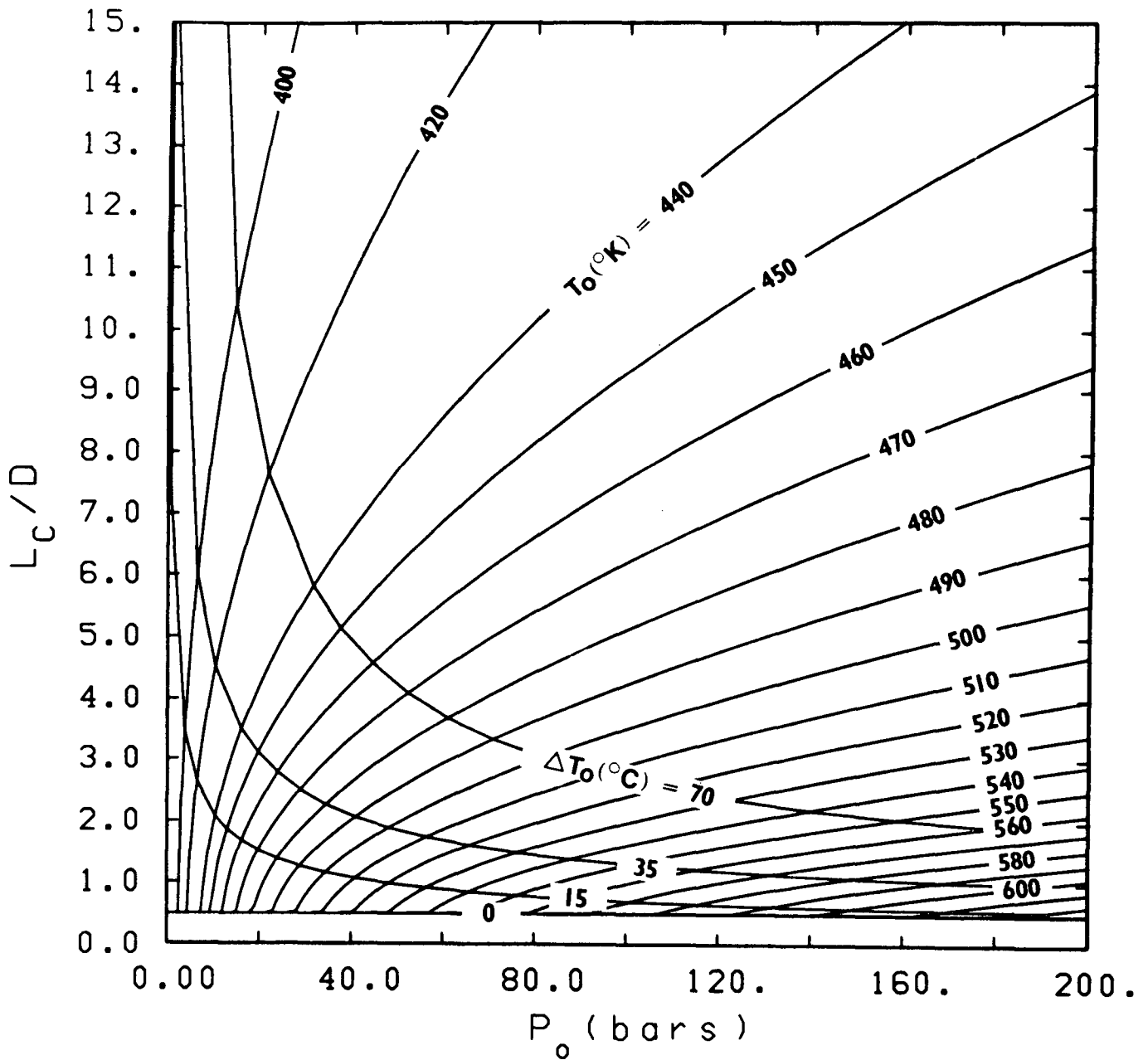
Figure 4.4   Two-phase, jet-exit core (L_c/D) as a function of stagnation pressure and stagnation temperature or subcooling.

CSQ is a FORTRAN program for computation of two-dimensional material response. An Eulerian finite difference method is employed in either rectangular or cylindrical coordinates. Models are included to treat an extremely wide range of problems, from solid dynamics to totally stripped plasmas. Portable editing and graphics programs are available to aid in analyzing the computed behavior.

Because the models in CSQ are general and apply to a wide range of problems with different time scales, it is possible to increase the computational speed for a given problem by selectively modifying the code to best suit the problem of current interest -- two-phase jets.

Modifications of CSQ were performed as part of this study; additionally, a version of CSQ was used which incorporated a second-order-accurate numerical convection algorithm for performing inter-cell transport of mass, momentum, and energy.[24] The modifications performed and a slight change in input parameters resulted in over a factor of 20 in calculation speed for the two-phase jet problem. Typical calculations with 10 to 25 cells across the break exit require about 20 minutes of CDC 7600 CPU time before the code reaches convergence in the jet field; this illustrates the importance of the factor of 20 increase in speed. The two main areas responsible for most of the speed increase are:

(1)   improved numerical methods for the equation of state description for water in two-phase states;

(2)   changes in input parameters for the viscosity computation;

Several other modifications to the standard CSQ code were also included for user convenience for these calculations, but the above were the only modifications related to computational speed and accuracy.

For the jet impingement calculations, CSQ was modified to use the thermodynamic description (equation of state, EOS) of water from Reference 17. The analytic form used is a complex function of density and temperature. Mixed-phase states were evaluated using the Gibbs phase rules with an iteration on the single phase surface. The end result was that an average of about 10 single-phase EOS evaluations were required for each mixed-phase state. Since for two-phase jets, a large fraction of the total computational mesh is mixed phase, the code was using a very large fraction of the total execution time in EOS evaluations.

This problem was solved by carefully fitting the thermodynamic properties along the mixed-phase boundaries. A very dense array of points and standard interpolation methods was used. All required EOS data were included so that no evaluations of the single phase

53

functions were required for any mixed-phase state. The net result was an increase in overall computational speed by a factor of about 2.5.

The second change concerned the use of viscosity in CSQ. CSQ was developed in projects where strong shock waves propagated through much of the two-dimensional grid. To smooth the results in the vicinity of the strong shock waves, the viscosity coefficients were given values considerable higher than the real physical viscosity. This is the standard procedure for this type of calculation (strong shocks) and results in very sharp wave fronts being spread over a number of computation cells.

The existence of a standing shock wave positioned very close to the target was discussed in Section 3.5. The large viscosity coefficients, which are the default input in CSQ, caused the need for a large number of cells near the target to obtain a mesh size converged solution. Since the computational time of the code is a linear function of the number of cells and the time step is Courant limited, the fine resolution was expensive. (See also Reference 24 for further discussion and examples of the effect these viscosity coefficients have on run time and nodalizations.)

The extent of the viscosity "difficulty" was discovered during a series of tests to determine mesh sizes for the final impingement matrix. A separate study was conducted to determine the appropriate correction. The study found that minor changes to the code input would eliminate the problem; no other code changes were necessary. A factor of approximately eight in overall computational speed was realized for this change. Nodalizations as coarse as $\Delta z/D \sim \Delta r/D \sim 1/20$ are now being used (20 cells across the pipe diameter). The larger viscosity coefficients required less than half of that cell dimension.

4.4 Model Calculations

Table 4.1 shows the variable ranges selected for study; note, however, that initial calculation experience has shown that some of the flow combinations are outside of the model's capabilities, i.e., double choking, etc.

Figure 4.5 shows a typical coarse grid which is used to initiate the calculations; finer zoning is later used to obtain fully converged solutions. Although for the present modeling purposes only the target pressures are of interest, the code actually provides the flow solution between the break and the target. Two examples will be provided. Axial position 0.0 is the break-exit plane.

Example one has a stagnation pressure and temperature of 170 bars and 555.52 K (70 °C subcooled). The target L/D is 2.0 and L_c/D is 1.98; thus we expect to recover nearly the initial

54

Table 4.1

Two-Phase Jet Model Calculational Matrix Base

Temperatures/Quality	subcooling, ΔT_O (^{O}C)	70, 50, 35, 15, 0
	qualities	0, 0.01, 0.05, 0.1, 0.2, 0.333, 0.75, 0.99
Pressures	pressure, P_O (bars)	60, 80, 100, 130, 150, 170
Position	target position L/D	0.5, 0.75, 1.0, 1.25, 1.50, 1.75, 2.0, 2.5, 3.0, 4.0, 8.0
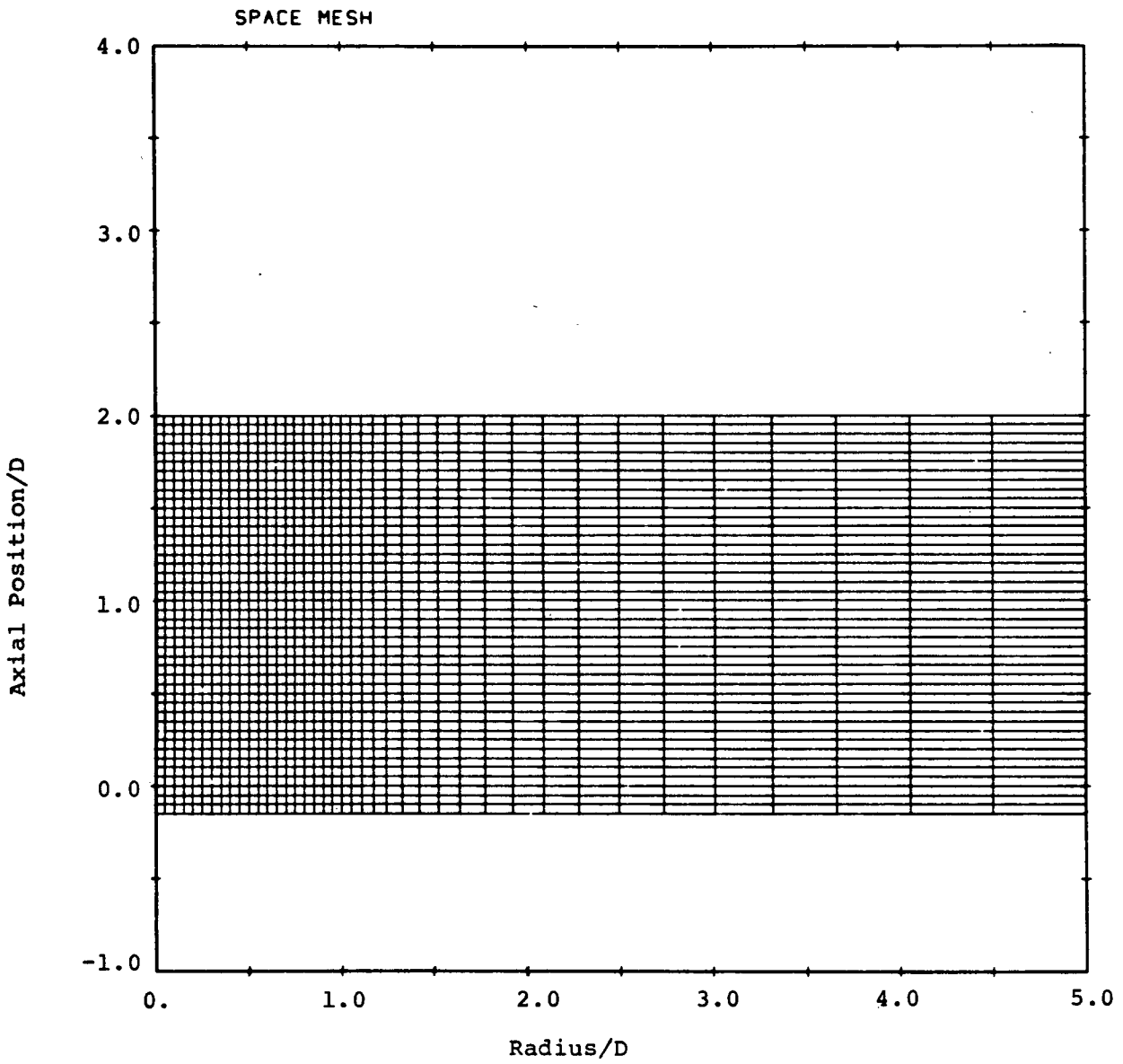
Figure 4.5   Typical coarse computational grid used in
              CSQ model calculations.

stagnation pressure at the target centerline. Figure 4.6 shows the resulting pressure contours and Figure 4.7 shows the density contours. The ordinate and abscissa in these two figures are the nondimensional axial and radial coordinates. The target is located at $L/D = 2.0$. Figure 4.8 shows the velocity, sound speed, temperature, and pressure on the target as a function of radius. Of particular interest is the pressure. The distribution of pressure with radius is typical of the distributions observed when $L_C/D > L/D$. note how rapidly the pressure falls off in the radial direction. Figure 4.9 shows the density, temperature, and pressure along the jet's centerline; note that large pressure gradients exist near the target and that the centerline target pressure is indeed about 170 bars.

Example two has a stagnation pressure and temperature of 150 bars and 615.39 K (0°C subcooling). The target L/D is 2.0 and L_C/D is 0.5. In this example, the strong shock structure will appear. Figure 4.10 shows the pressure contours and Figure 4.11 shows the density contours. These contours show a very rapid supersonic expansion of the jet just outside of the break. This is the same behavior observed for free jets. The expansion of the jet is very rapid; within about a pipe diameter beyond the exit core, the static pressure has dropped to less than 5 bars. Figure 4.12 shows the velocity, sound speed, temperature, and pressure on the target as a function of the target radius. The bell shaped curve for the pressure, observed in numerous calculations, was expected. Figure 4.13 shows the density, temperature, and pressure along the jet's centerline. In the pressure curve the shock, which occurs near the wall, is clearly visible. Figure 4.14 displays the velocity field. The length of each arrow is proportional to the velocity magnitude. Notice the well-defined shock where the velocity field changes direction discontinuously. Figure 4.15 shows the target pressure distribution (including the stagnation centerline value) on a scale which includes the vessel stagnation pressure, $P_O = 150$ bars. The shock structure, which stands off from the target, has a significant impact upon the local magnitude of the load. Finally, Figure 4.16 is a three-dimensional illustration of the pressure field; the jet expansion followed by a compression is clearly shown. The last curve in the foreground in Figure 4.16 is the wall pressure distribution.

The possibility of using some dimensionless correlation to represent the computer results was investigated. To date this has not been successful. This is mainly attributable to the change in behavior of the solution in the region of the shock and the change in the types of wall pressure distributions seen when the value of L_C/D becomes greater than or slightly smaller than L/D. The fluid upstream of the shock is a two-phase mixture while the downstream fluid is pure liquid. The fluid near the center of the target is also in a pure liquid state. The fluid flashes as it expands radially along the target. This results in a pronounced change of the shape of the target pressure distribution as shown in Figure 4.8.

E = 100 bars L = 35 bars
F = 90   M = 30
G = 80   N = 25
H = 70   O = 20
I = 60   P = 15
J = 50   Q = 10
K = 40   R = 5
         S = 2.5

Axial Position/D

Radius/D
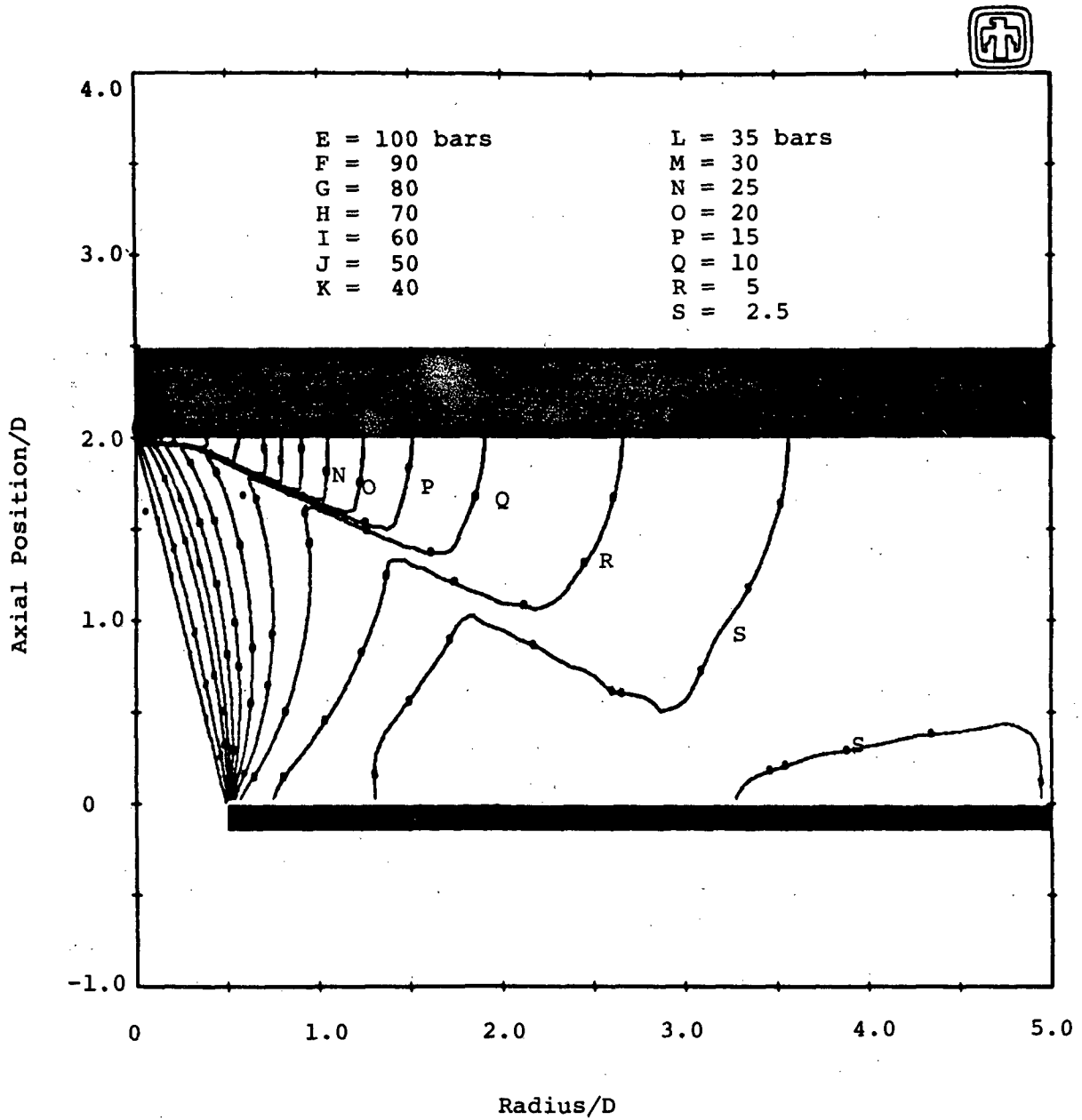
Figure 4.6 Pressure contours for subcooled stagnation properties (P_o = 170 bars, ΔT_o = 70 $^\circ$C). Note that the exit core extended to the wall, thus stagnation conditions were present at the center of the target.

58
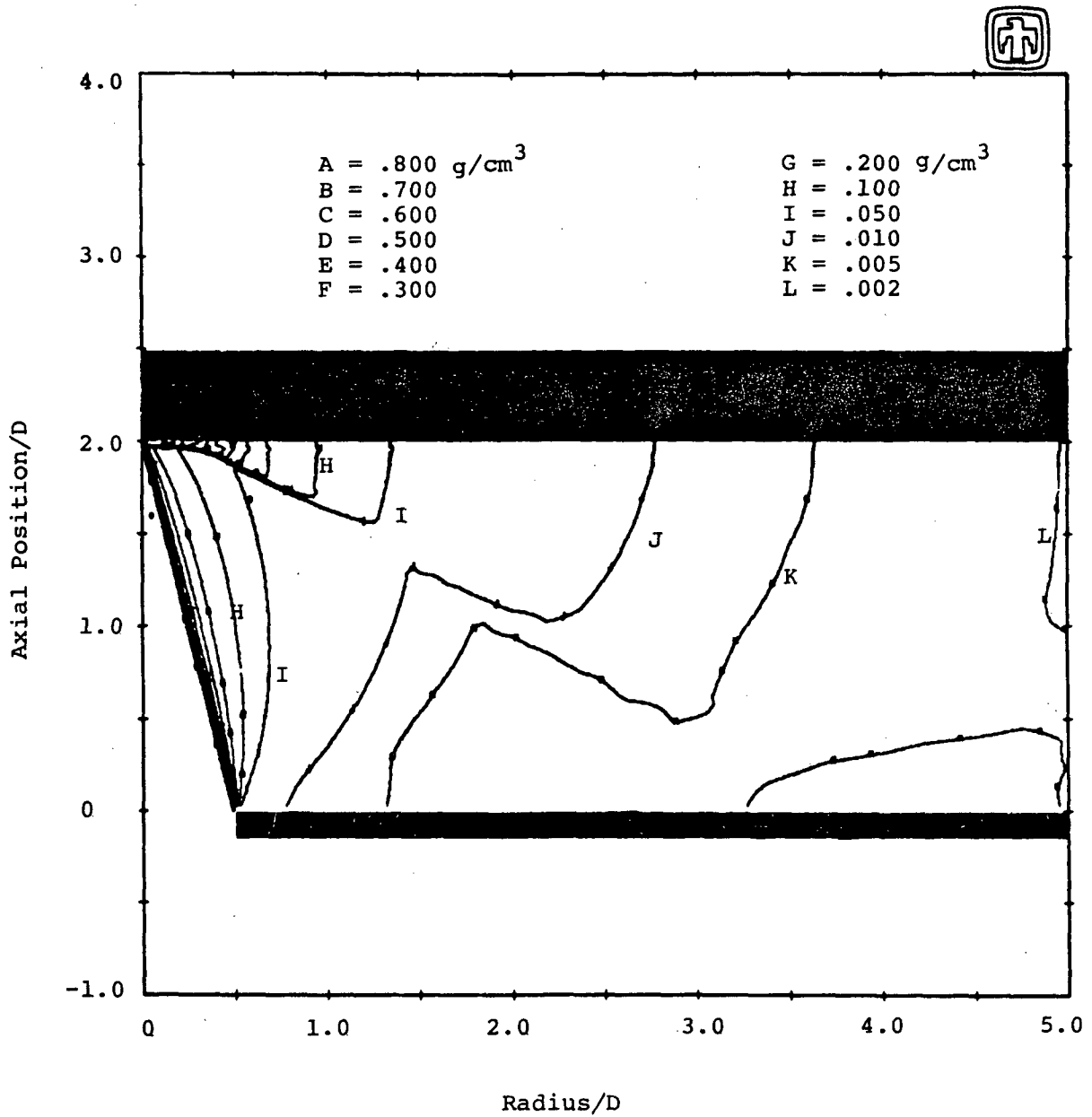
Figure 4.7 Density contours for subcooled stagnation properties (P_o = 170 bars, ΔT_o = 70°C). Note that the exit core extended to the wall, thus stagnation conditions were present at the center of the target.
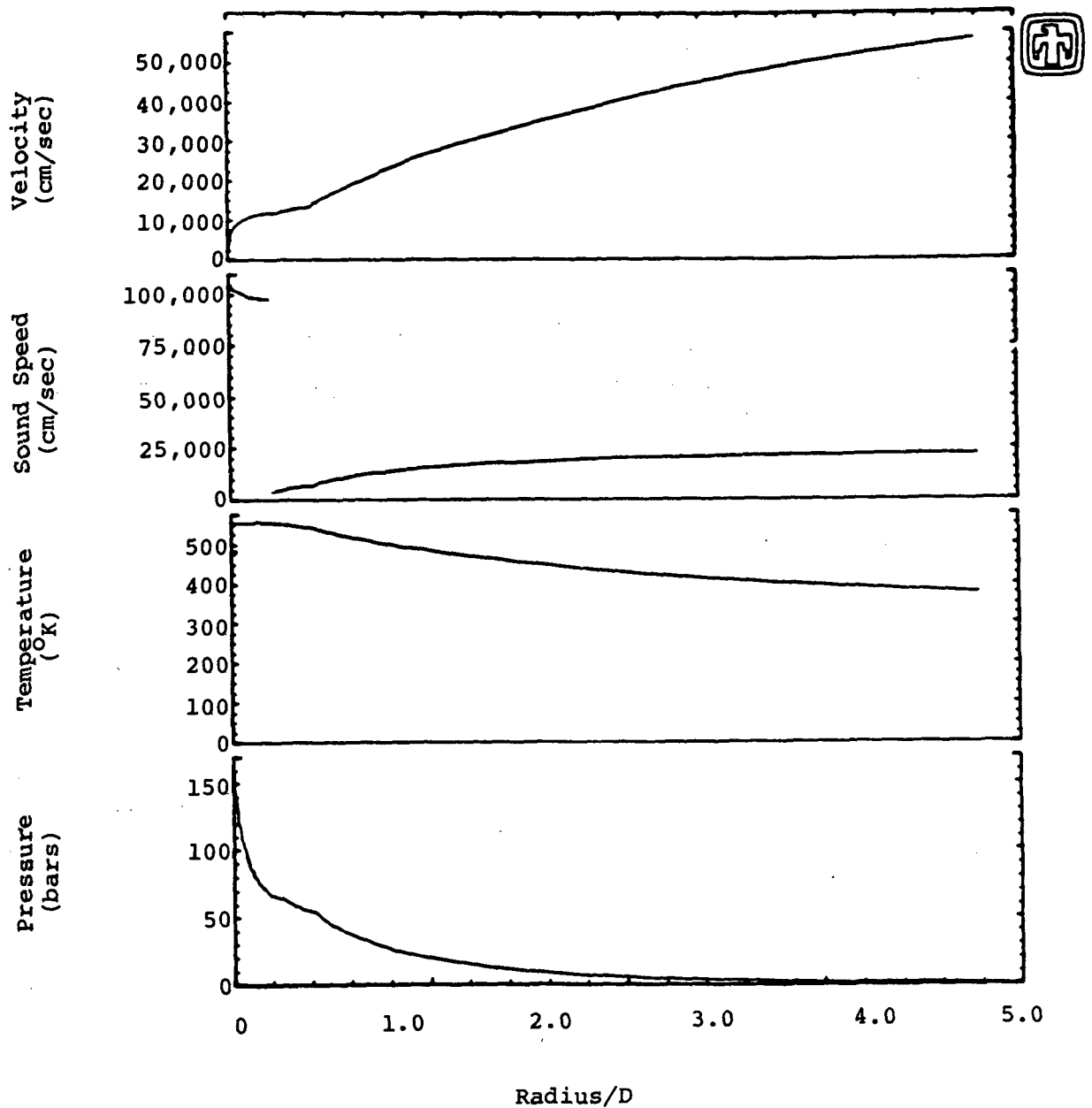
Figure 4.8 Velocity magnitude, sound speed, temperature and pressure distributions along the radius of the target for subcooled vessel stagnation conditions (P_o = 170 bars, ΔT_o = 70°C) where, the exit core extended to the wall.
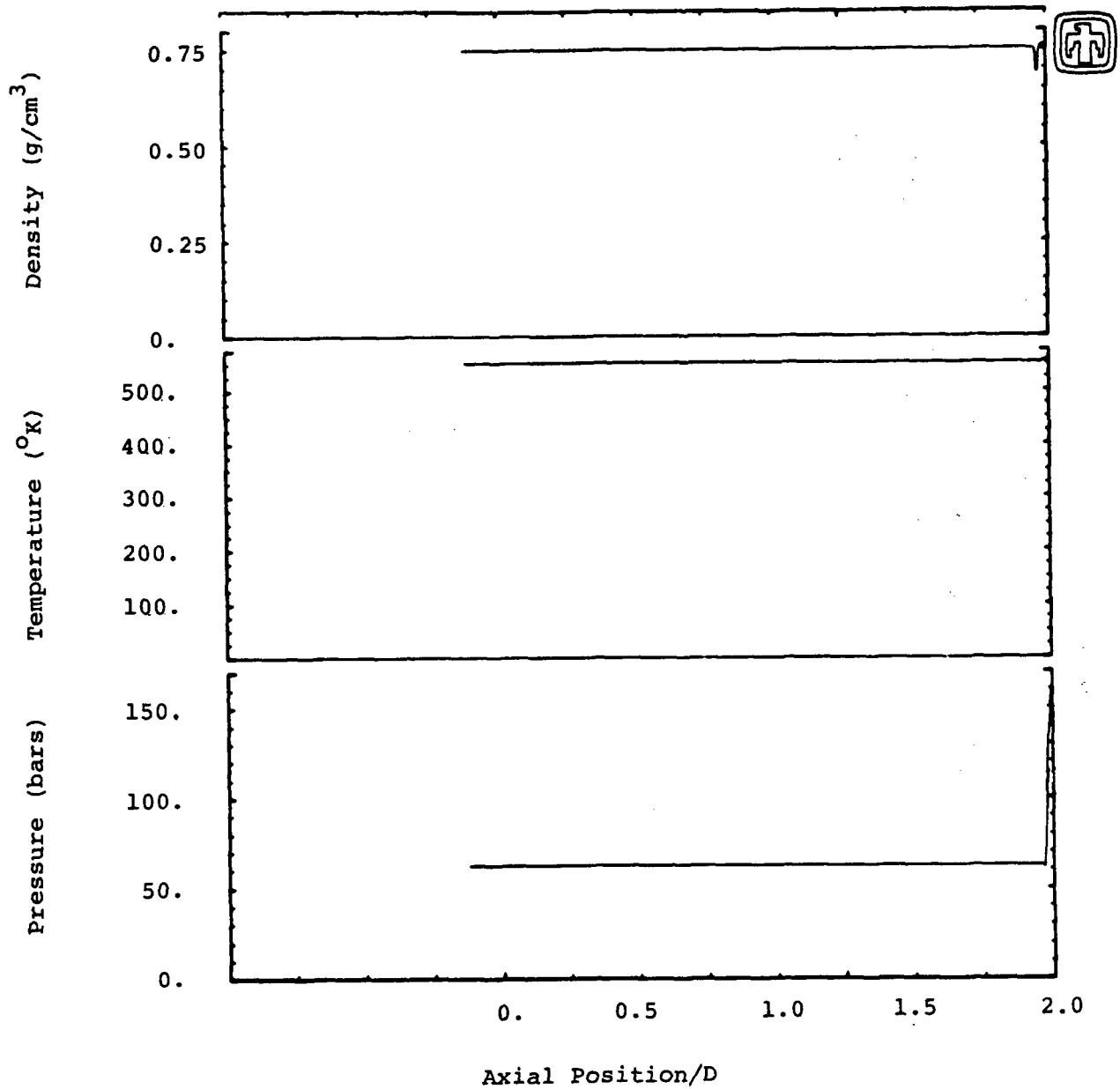
Figure 4.9 Density, temperature, and pressure distributions
along the centerline of the two-phase jet for
subcooled vessel stagnation conditions (P_o = 170
bars, ΔT_o = 70°C). Note that the exit core
extended to the wall and that the stagnation
conditions at the target (L/D = 2.0) are the
vessel conditions.

61
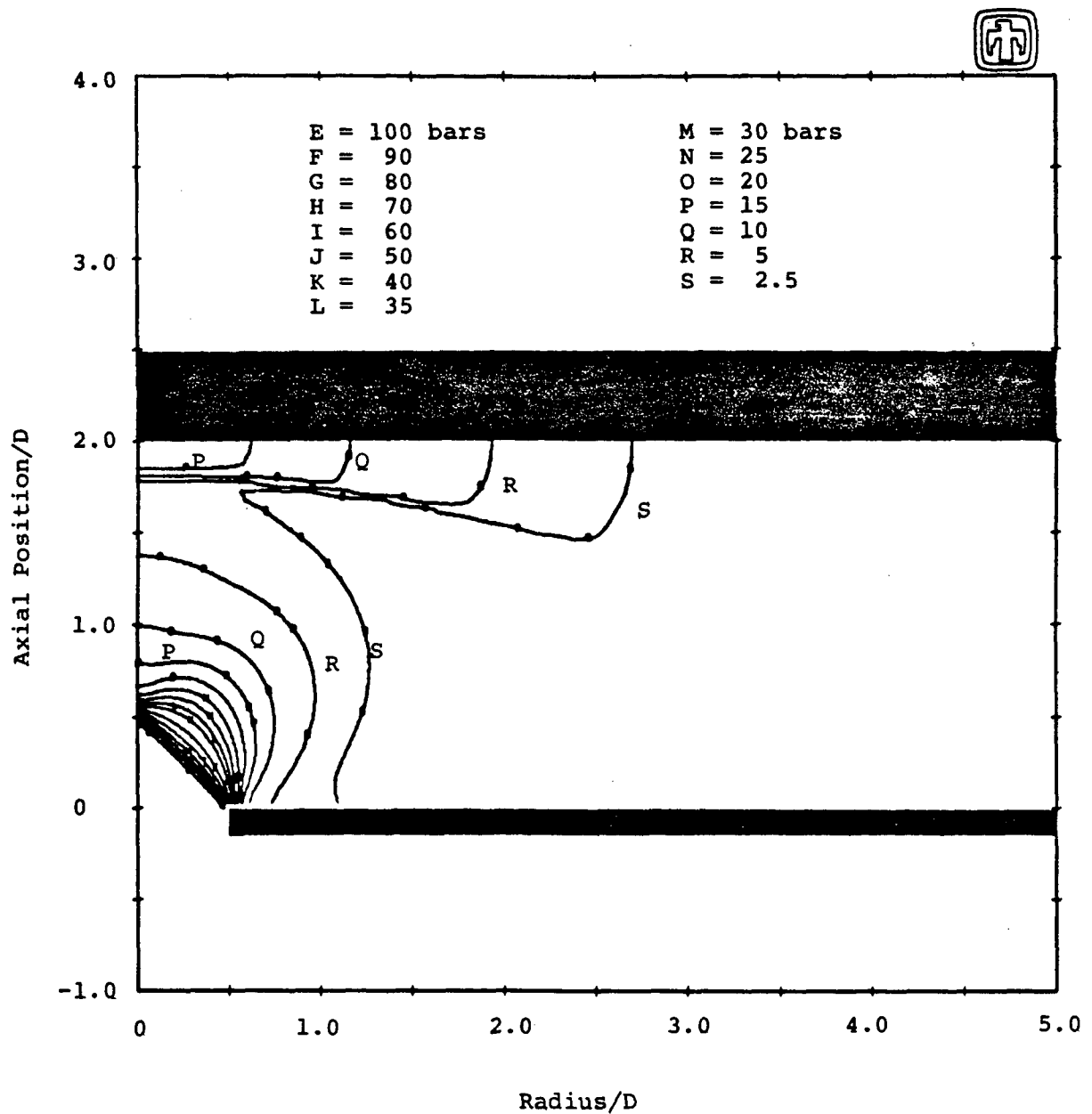
Figure 4.10   Pressure contours for saturated liquid
              stagnation conditions (P_O = 150 bars
              ΔT_O = 0°C). L_C/D = 0.50
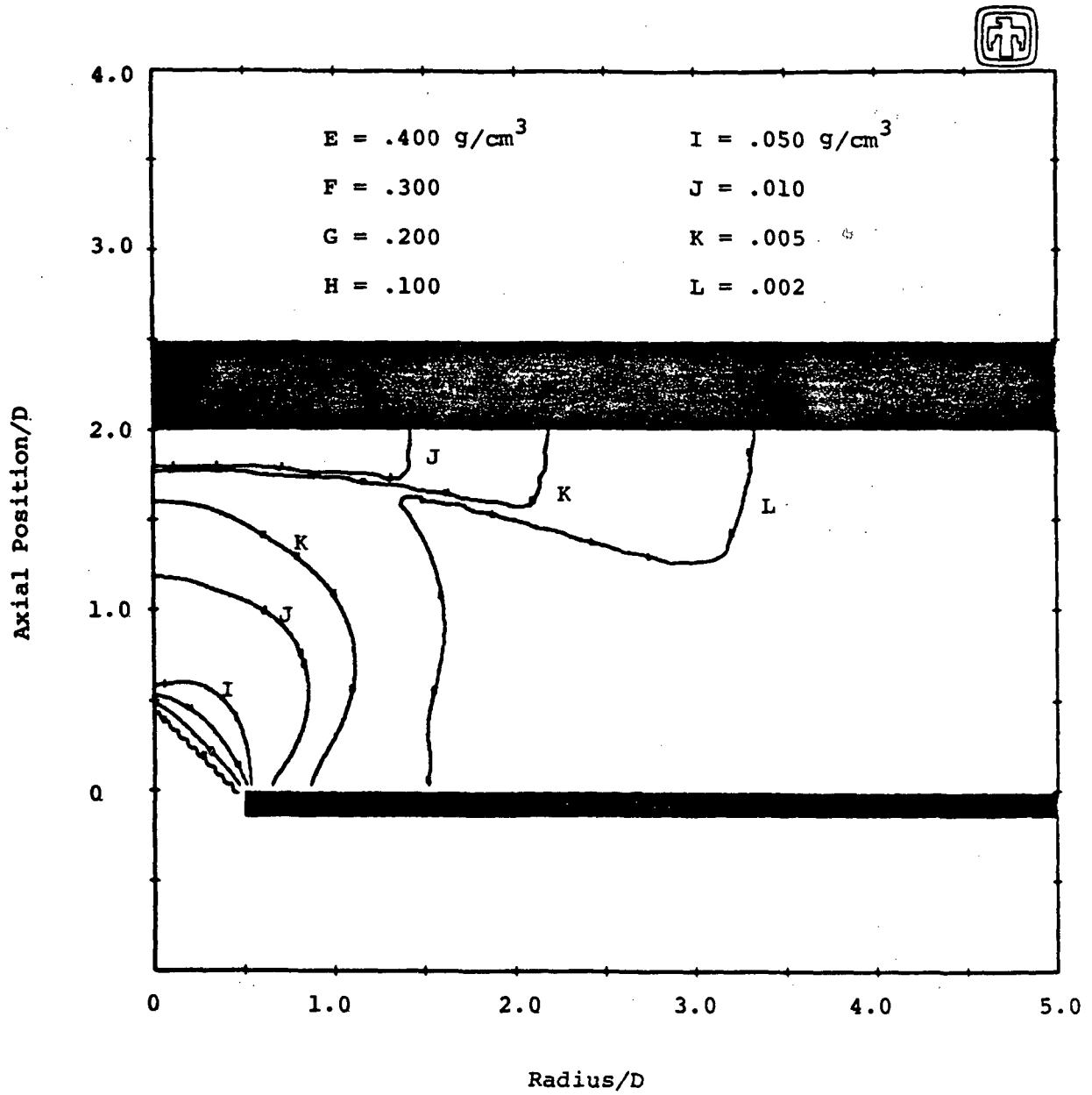
Figure 4.11   Density contours for saturated liquid
stagnation conditions (P_O = 150 bars,
ΔT_O = 0^OC). L_C/D = 0.50
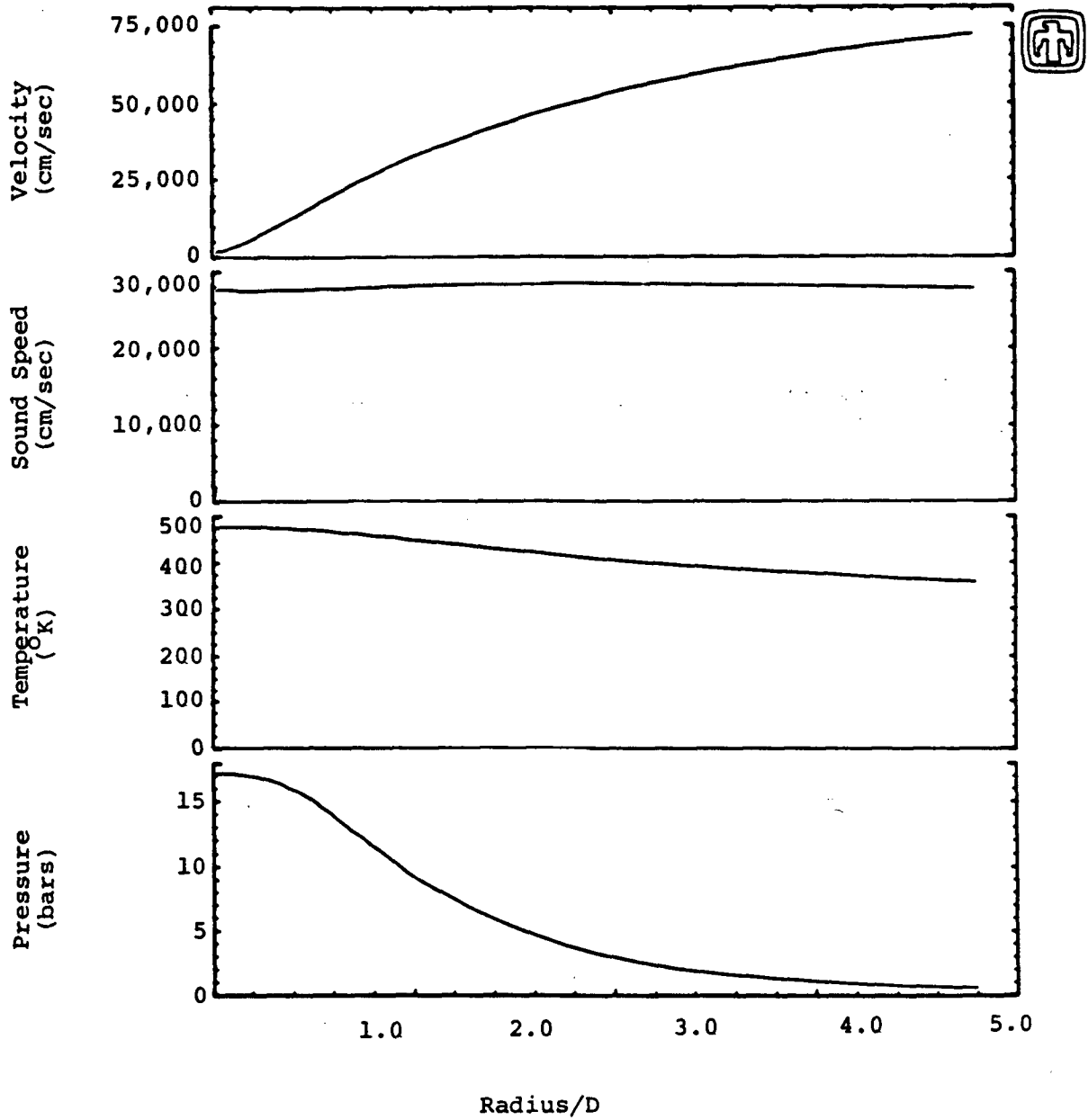
Figure 4.12   Velocity magnitude, sound speed, temperature
and pressure distributions along the radius
of the target for saturated liquid stagnation
conditions (P_O = 150 bars, ΔT_O = 0°C).
L_C/D = 0.5
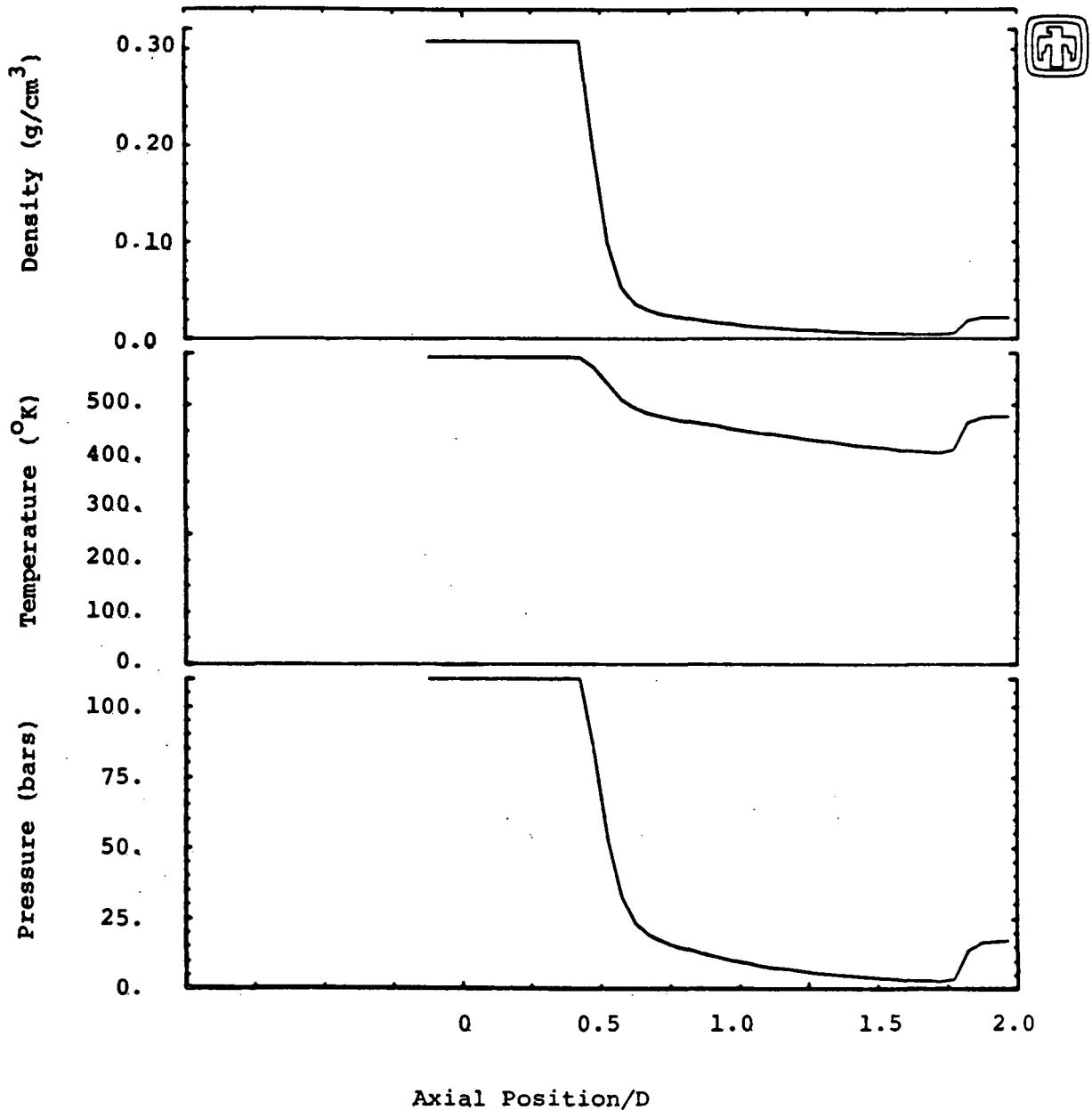
Figure 4.13 Density, temperature, and pressure distri-
butions along the centerline of the two-phase
jet for saturated liquid stagnation conditions
(P_O = 150 bars, ΔT_O = 0°C). L_C/D = 0.5

VELOCITY

Axial Position

Radius
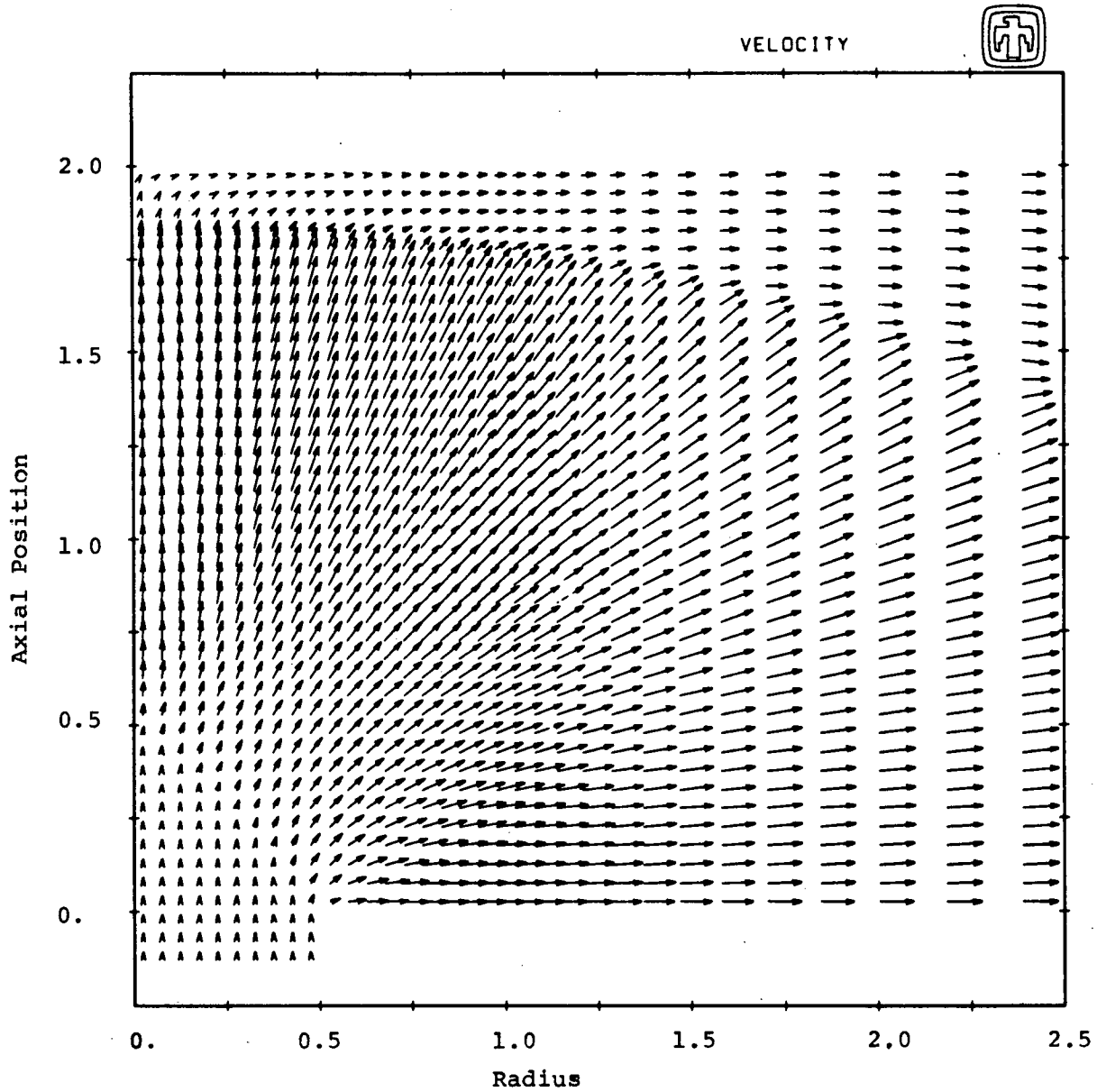
Figure 4.14   Velocity field for a two-phase, impinging jet
at stagnation conditions of P_o = 150 bars and
saturated liquid.   L/D = 2.0 and the axis are
the axial and radial coordinates measured in
centimeters.   Velocity magnitude is proportioned
to the length of each vector.
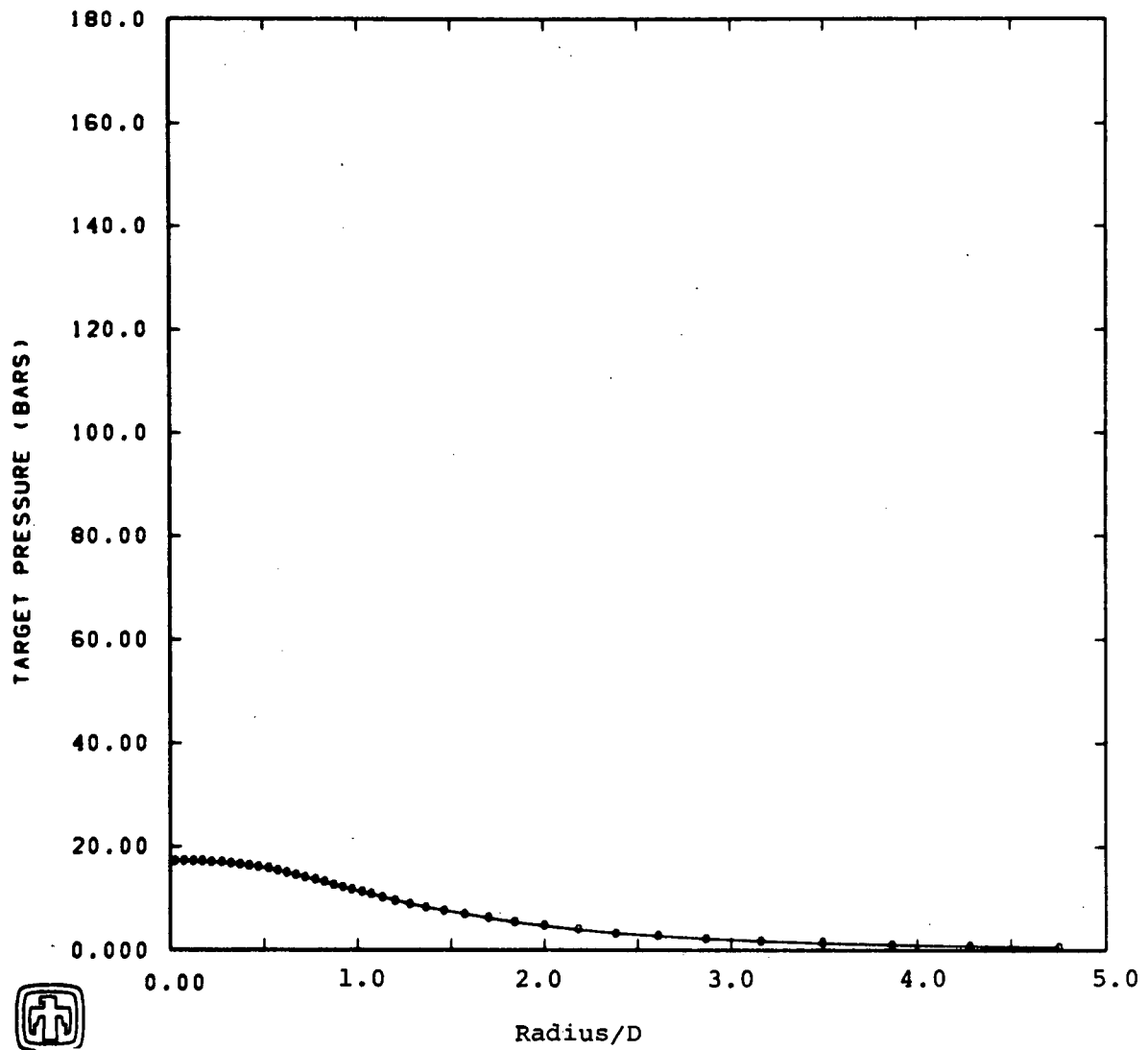
Figure 4.15   Target pressure distribution as a function of
the radial position for L/D = 2.0 and for vessel
stagnation conditions of P_o = 150 bars and
saturated liquid (ΔT_o = 0).

67
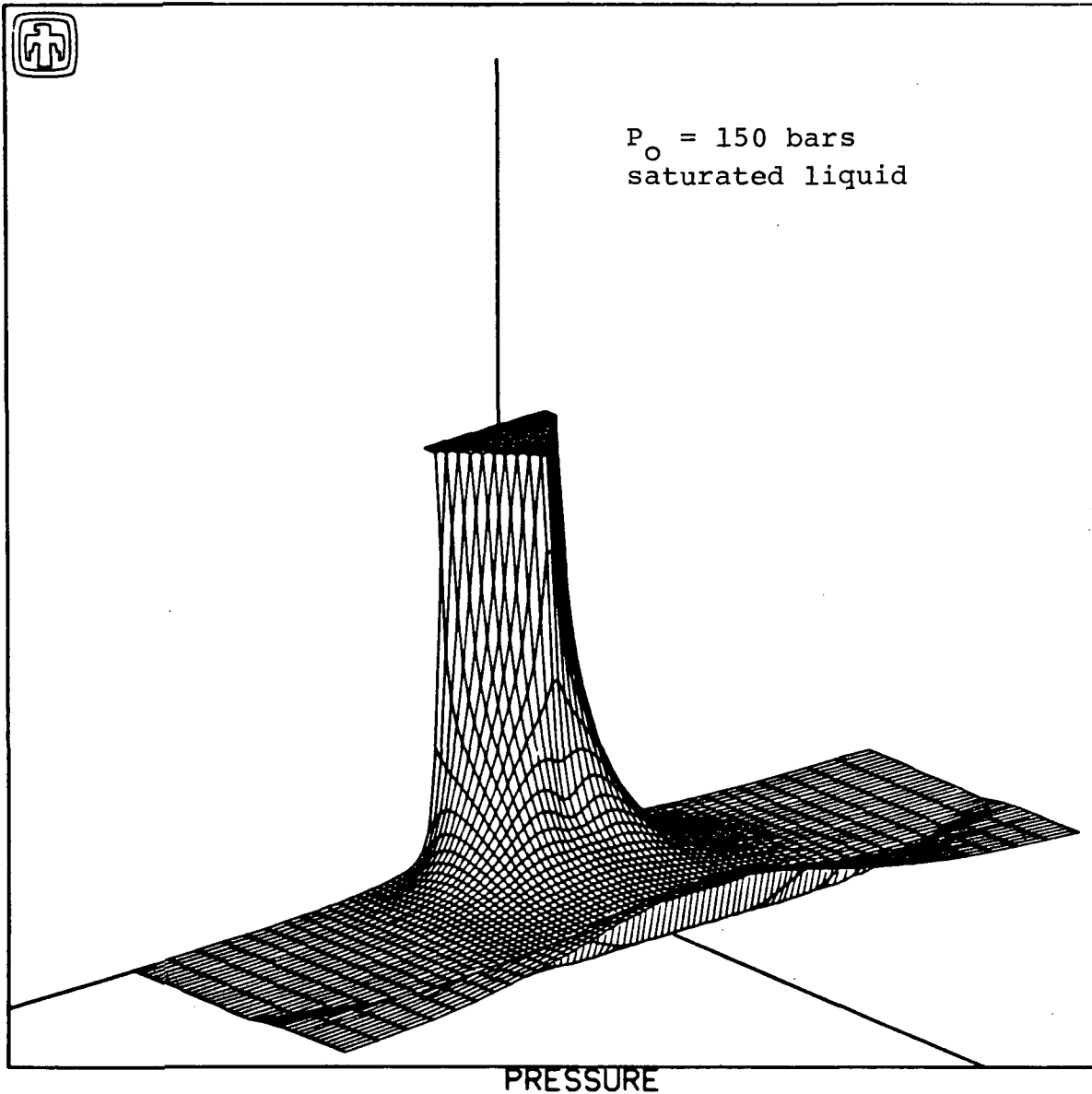
Figure 4.16   Three-dimensional pressure field contour
              for L/D = 2.0 and for vessel stagnation
              conditions of P_O = 150 bars and saturated
              liquid.

4.5 Data Base Calculations

In this section a small number of illustrative data base calculations will be given; this section will be kept brief because the calculations shown are a small subset of the figures in Appendix A. These figures illustrate the range of calculations performed.

Figure 4.17 shows the effect of target position with respect to the pipe break; the figure shows the target pressure distributions for several L/D ratios. The vessel stagnation conditions were $P_O = 150$ bars and 35°C subcooling. The curve for L/D = 1 is an example where L/D was less than L_C/D ($L_C/D = 1.07$); note that the wall stagnation pressure was P_O. The change in the shape of the pressure profile for L/D = 1 at about R/D = 0.50 is due to a phase change in the fluid at that point. Figure 4.18 shows the static pressure behavior along the jet's centerline for the same flow and geometric conditions of Figure 4.17. This figure shows an overlay of five centerline pressure distributions as a function of nondimensionalized axial position for five different target locations (L/D = 1.00, 1.25, 1.50, 2.00, and 4.00). Note that each curve ends with the stagnation pressure on the target. The jet behaves characteristically as a free jet up to the shock, which occurs near the target. Figure 4.19 illustrates three-dimensionally an overlay of both the wall and centerline pressure distributions given by Figures 4.17 and 4.18. The rapid fall in centerline stagnation pressure on the wall is observed in all L/D studies. For this particular group of calculations, $P_4/P_O \simeq .17$ at L/D = 2.0 and $P_4/P_O \simeq .05$ at L/D = 4.0 where P_4 is the centerline stagnation (wall) pressure. This trend is easily explained by the shock theory introduced earlier in Section 3.5.

Figure 4.20 shows the effect the upstream stagnation pressure, P_O, can have on the target's pressure distribution; the figure shows the wall pressure distribution as a function of the radial position. The vessel pressure P_O was varied between 60 and 170 bars, L/D was 2.0 and there was a constant 35°C subcooling.

Figures 4.21 and 4.22 show the effect of subcooling for two different vessel pressures. Figure 4.21 shows the target pressure distributions at L/D = 2.0 for $P_O = 170$ bars and several different stagnation temperatures; Figure 4.22 shows the wall pressure distributions at L/D = 2.0 for $P_O = 130$ bars. The centerline pressure distributions that correspond to the target pressure distributions given in Figure 4.21 are given in Figure 4.23. Notice the effect the stagnation conditions have on the break (pipe exit) pressure; again these distributions are characteristic of free jet behavior except for the points near the shock at the target.
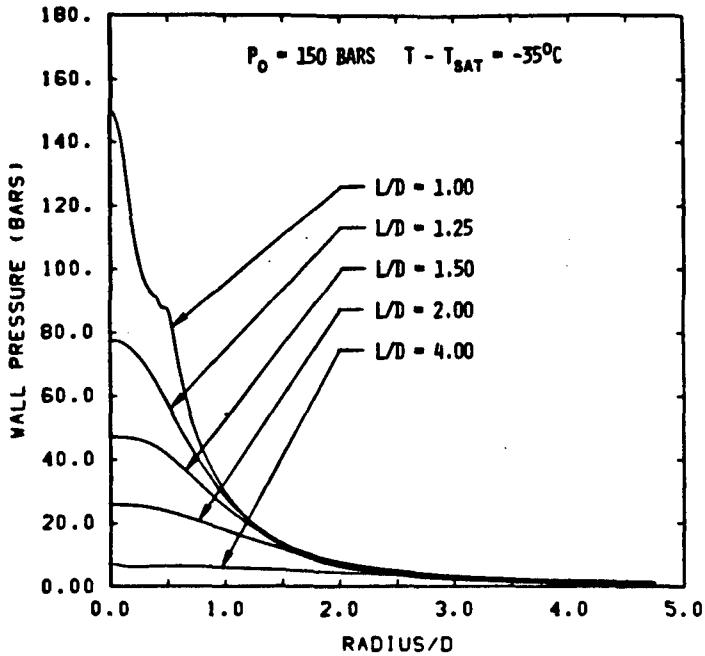
Figure 4.17   Wall pressure distribution for several L/D ratios
and for vessel stagnation conditions P_O = 150 bars
and 35° subcooled liquid.
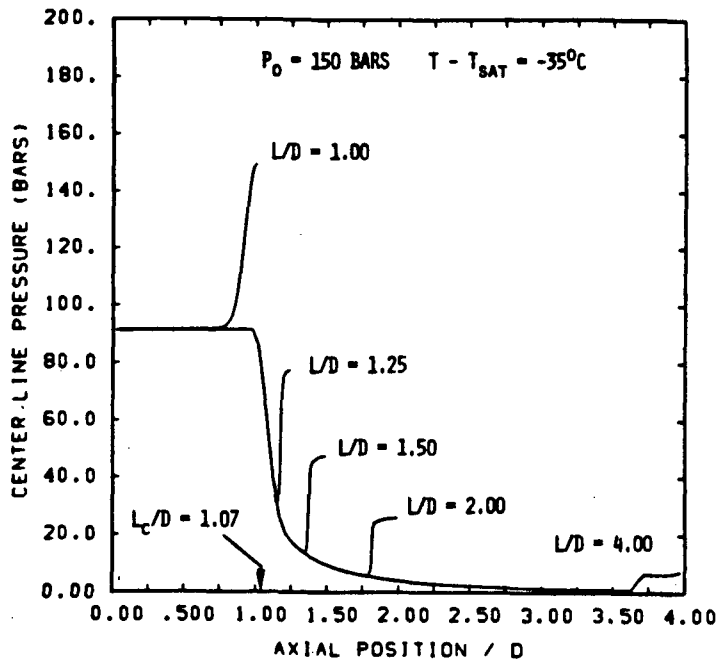
Figure 4.18   Overlay of five centerline pressure distributions
as a function of the non-dimensional axial position
showing the effect of target position (L/D).

70
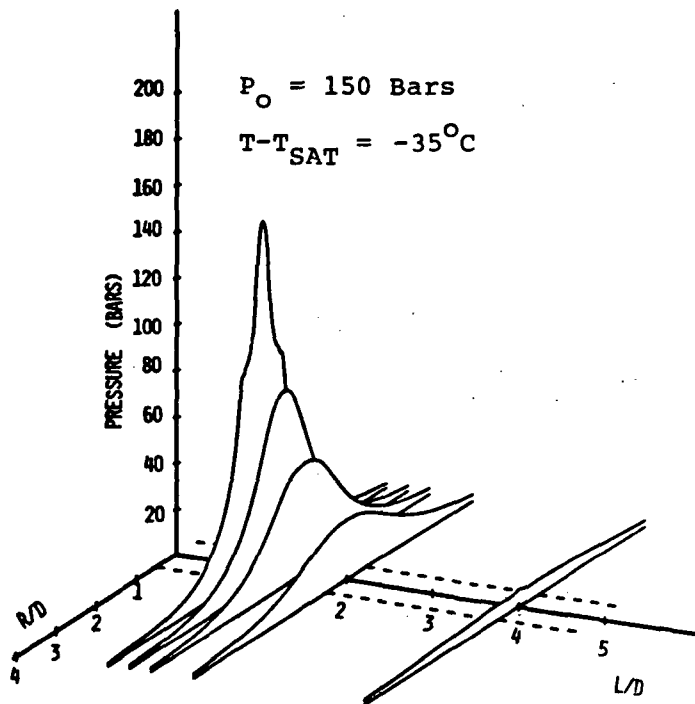
Figure 4.19   3-D illustration of five wall pressure distributions
as a function of target radius each at a different L/D.
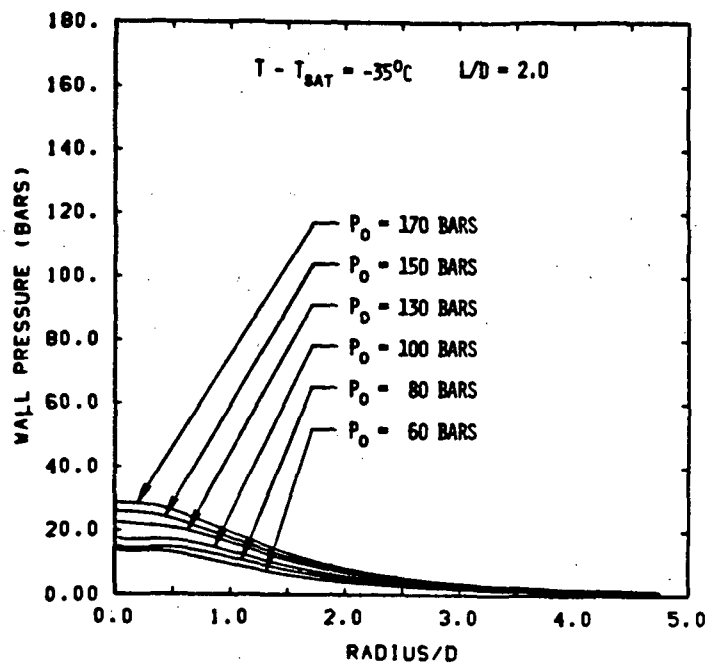
Figure 4.20   Stagnation pressure effect on target (wall)
pressure distributions at L/D = 2.

71
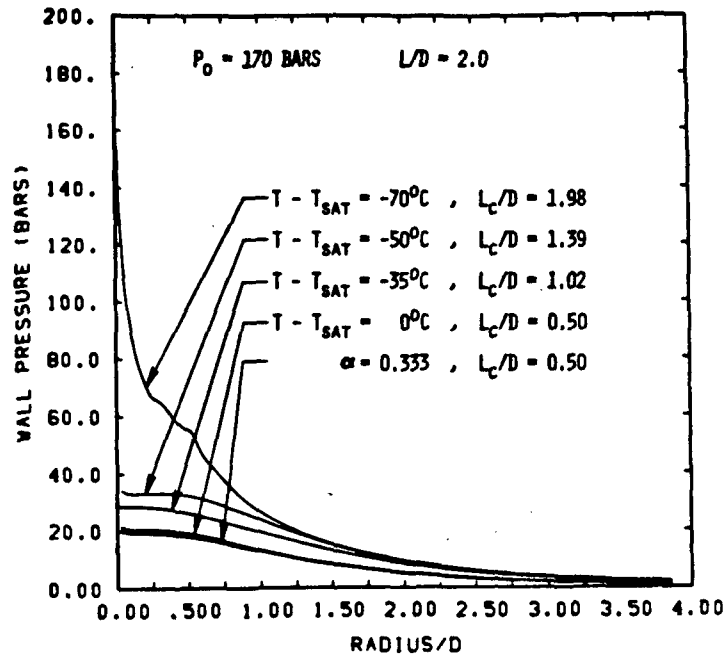
Figure 4.21   Effect of subcooling on target (wall pressure
at P_O = 170 bars and L/D = 2.
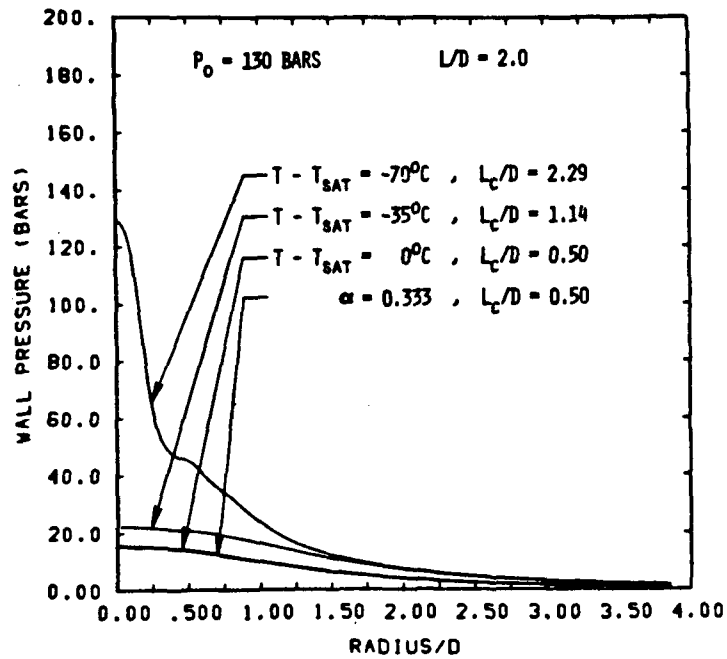
Figure 4.22   Effect of subcooling on target (wall) pressure
at P_O = 130 bars and L/D = 2.
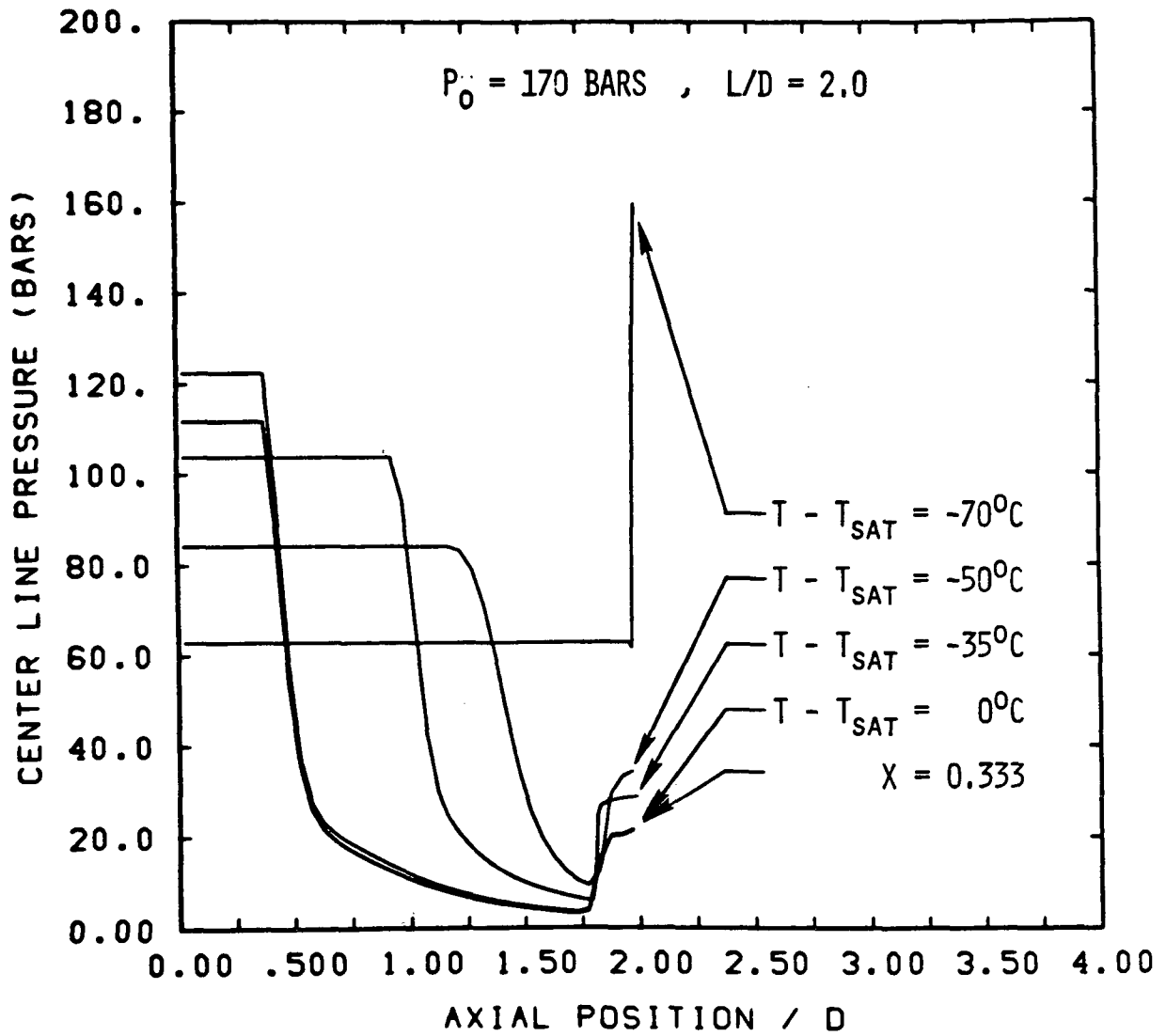
Figure 4.23   Effect of vessel subcooling on centerline
pressure at L/C = 2.0 and for a vessel
stagnation pressure P_o = 170 bars.

5.0 THERMODYNAMIC AND CRITICAL FLOW PROPERTIES

In this chapter we show figures that provide a description of the thermodynamic behavior of water. These charts are very accurate, and the relations used to develop them are used in both the CSQ model described in Chapter 4 and the approximate model that will be developed in Chapter 6. The defining relations for critical flow were developed in Chapter 3.

The HEM critical flow model is defined by the governing equations (3.8), (3.9) and (3.10). This model provides a consistent (isentropic) thermodynamic connection of the properties and flow upstream of and at the break. The critical flow charts relate the mass flux and the break thermodynamic properties to the upstream stagnation conditions.

These charts are given in Figures 5.1 through 5.9. Figures 5.1, 5.2, and 5.3 provide the properties of subcooled and saturated water for the pressure and temperature ranges of interest in this report. Figure 5.1 gives the temperature as a function of pressure (1 bar = .1 MPa) and entropy (1 erg/g^{o}K = 10^{-7} kJ/kg ^{o}K) for subcooled water; Figure 5.2 gives the temperature as a function of the density (1 g/cm^3 = 10^3 kg/m^3) and entropy for saturated water. Figure 5.2 also includes a bounding 200 bar isobar. Figure 5.3 gives the temperature as a function of density and entropy but at low densities (ρ = 0.001 to 0.1 g/cm^3). Figures 5.4 through 5.9 relate various thermodynamic properties to the HEM mass flux. Figures 5.4 and 5.5 show the HEM mass flux (1 kg/cm^{2}s = 10^{-4} kg/m^{2}s) as a function of the entropy and stagnation temperature; Figure 5.4 emphasizes the region with subcooled stagnation conditions while Figure 5.5 emphasizes the region with saturated stagnation conditions. Figure 5.6 shows the HEM mass flux as a function of the stagnation pressure and the stagnation temperature; these curves are used where the stagnation conditions are saturated. Figure 5.7 and 5.8 show the HEM mass flux as a function of the stagnation quality and stagnation temperature; these curves are used where the stagnation conditions are saturated. Figure 5.9 shows the HEM mass flux as a function of the stagnation density and the stagnation temperature, and Figure 5.10 shows the critical flow density as a function of the stagnation density and stagnation temperature. These charts provide a means for finding the break flow and break properties when given the stagnation or upstream properties, or for finding the stagnation properties when given the break flow and break or upstream properties. For example, the water properties figures (5.1, 5.2, and 5.3) can be used to determine the entropy just upstream of the break. Then using this entropy and the break flow rate the stagnation temperature is located in
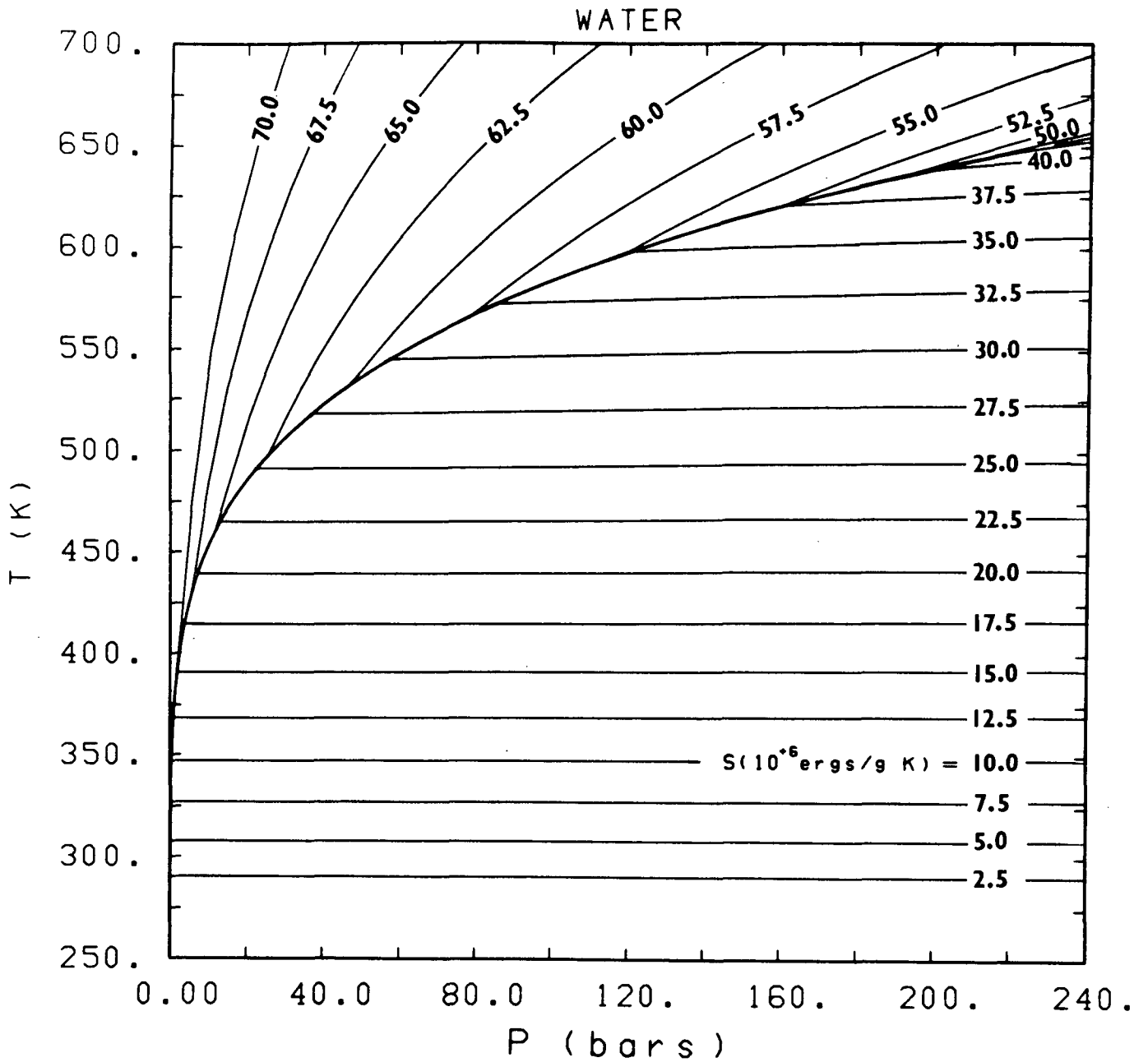
Figure 5.1   Thermodynamic properties of water.
Temperature as a function of pressure
and entropy for a range of pressure and
entropy that emphasizes subcooled
conditions.
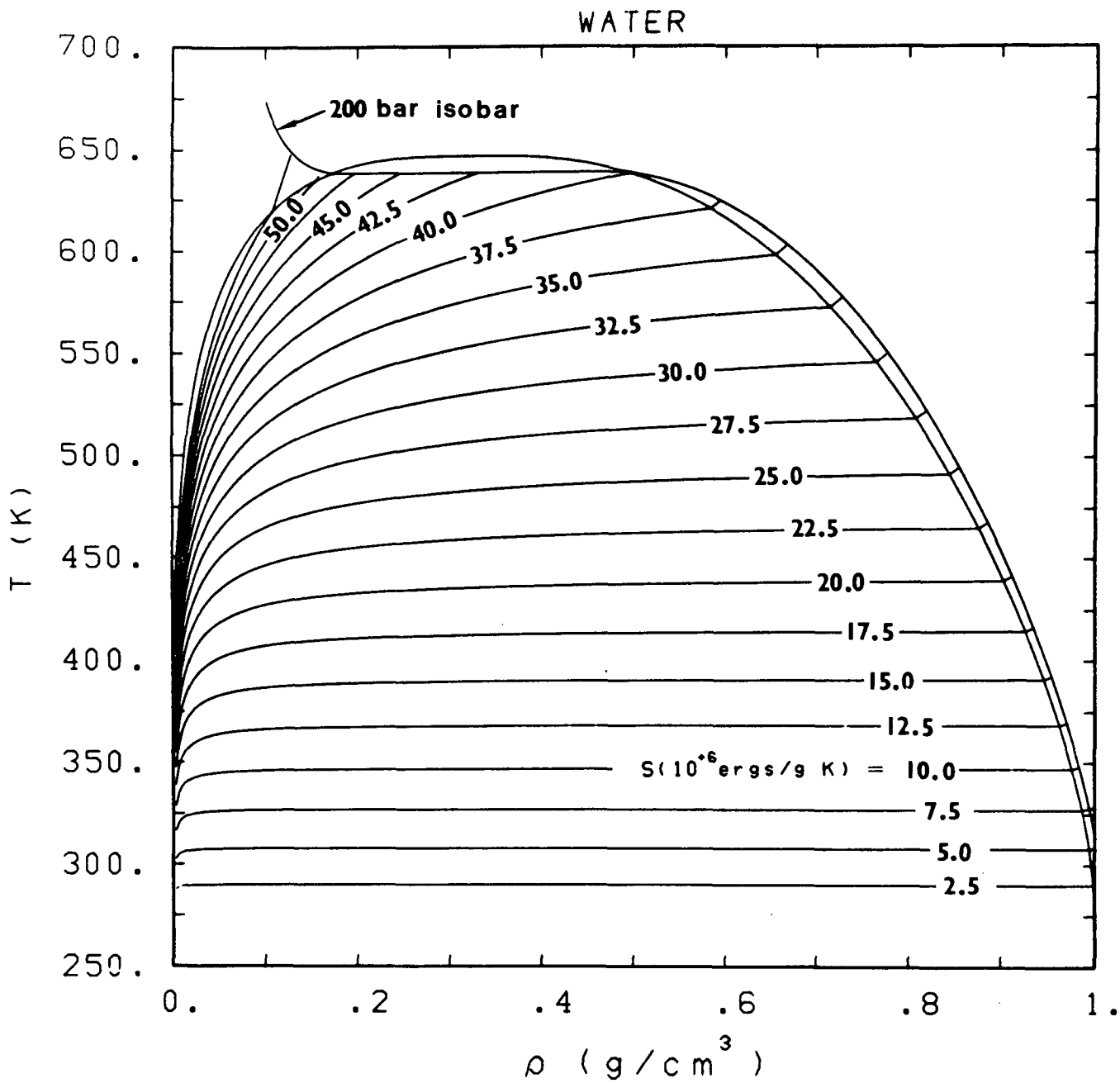
Figure 5.2   Thermodynamic properties of water.
Temperature as a function of density and
entropy for a range of density and entropy
that emphasizes saturated conditions.
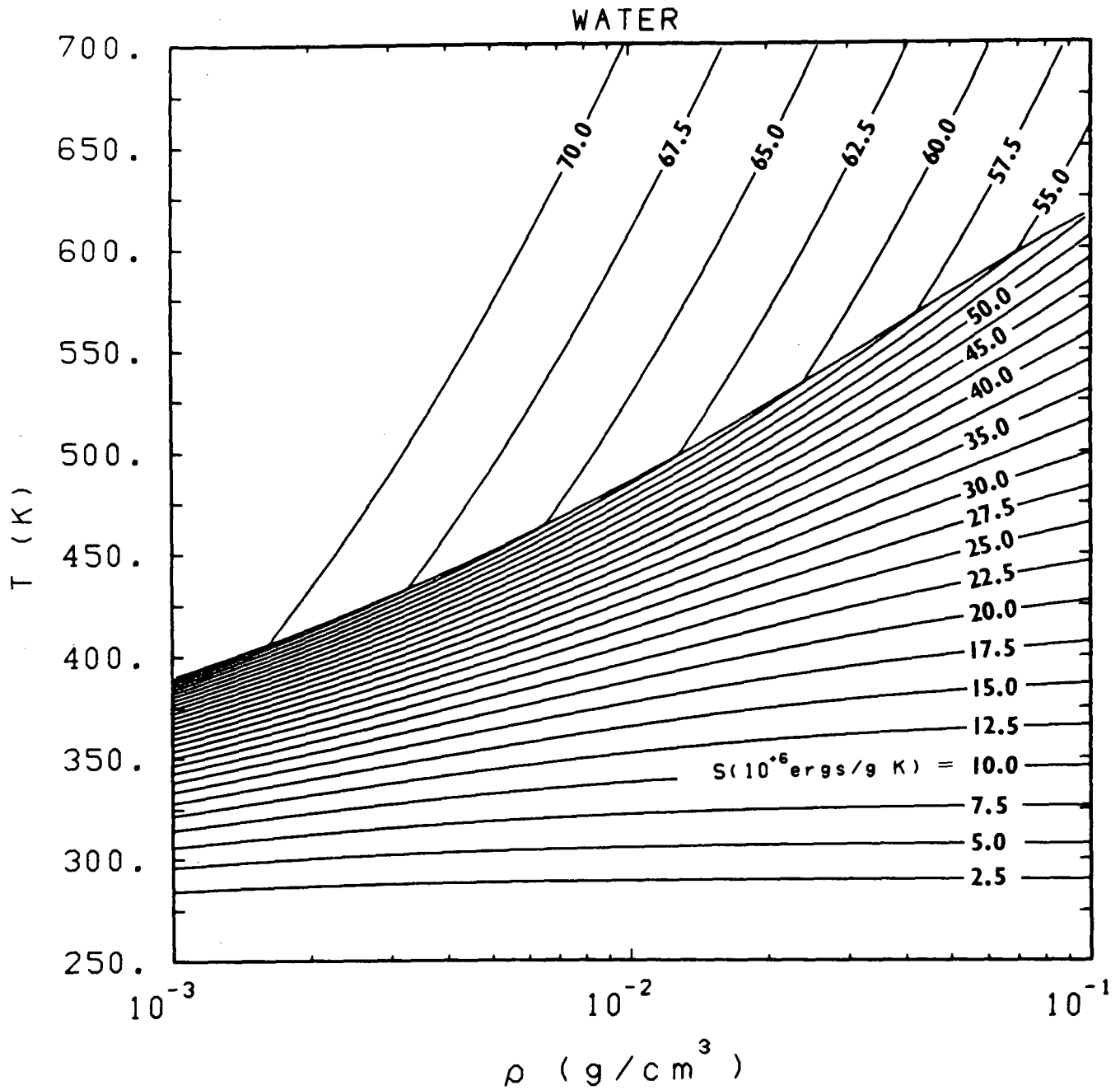
Figure 5.3　Thermodynamic properties of water.
Temperature as a function of density
and entropy for low densities.

78
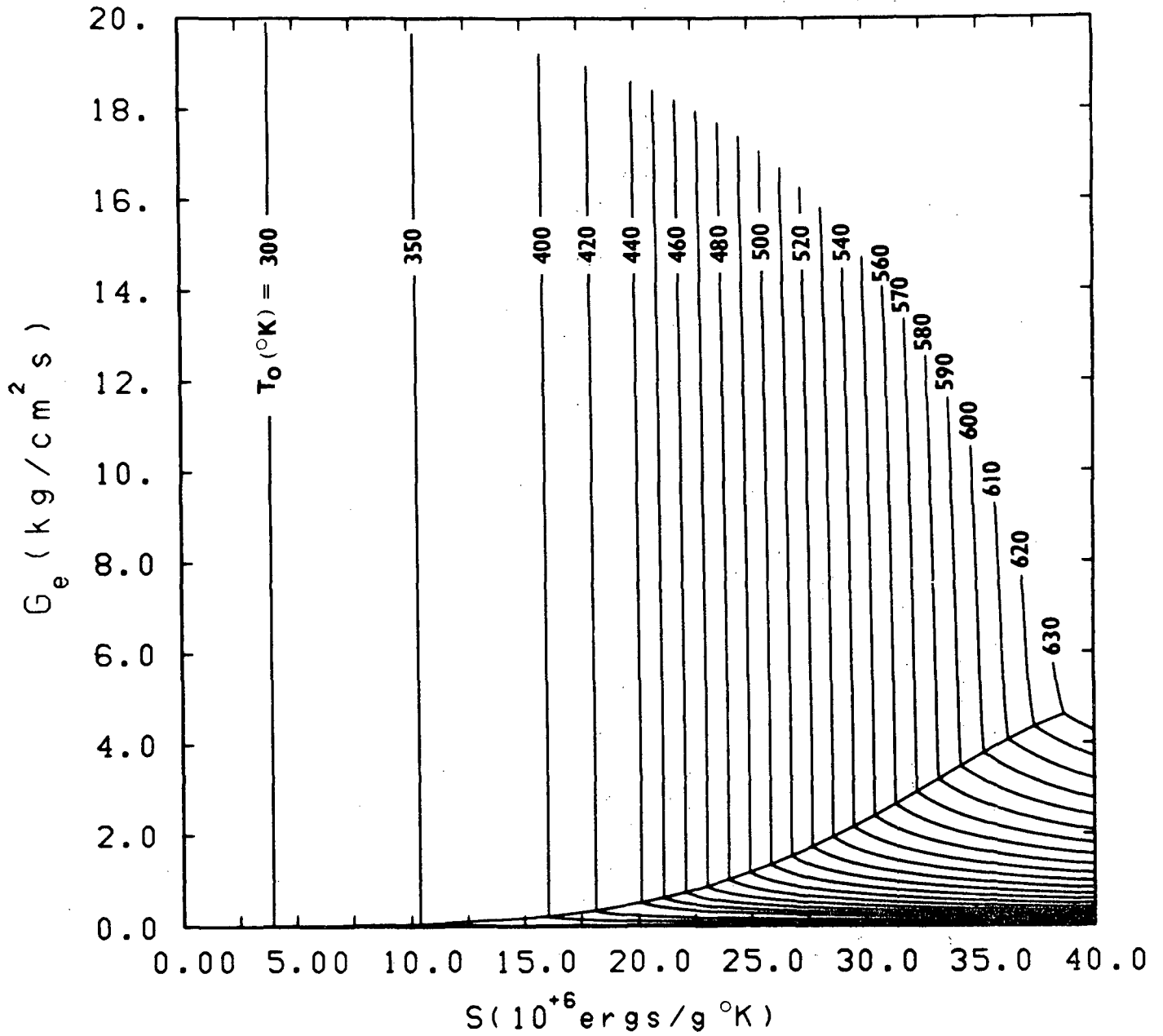
Figure 5.4   HEM mass flux as a function of entropy and
stagnation temperature for a range of entropy
that emphasizes subcooled stagnation conditions.
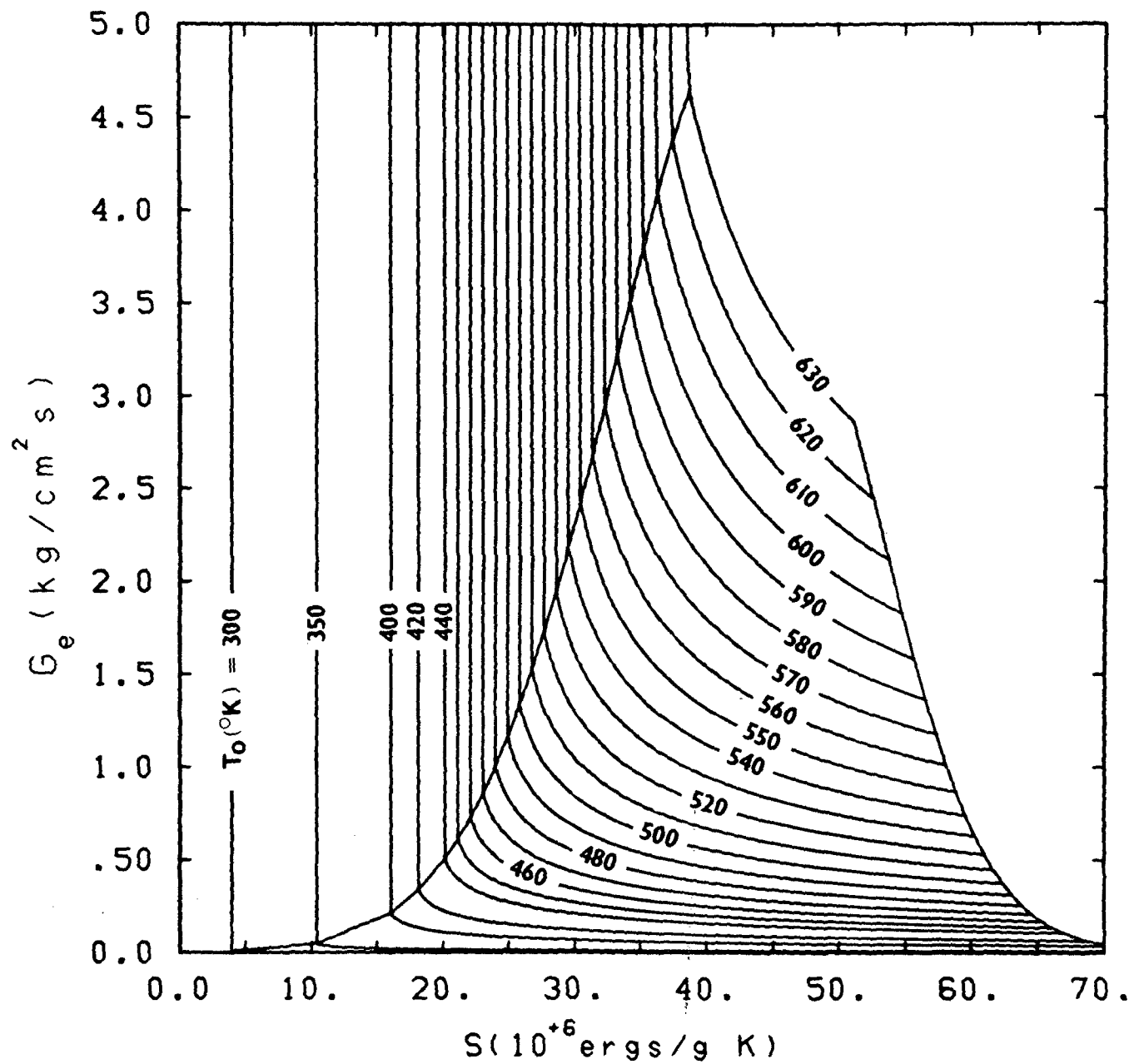
Figure 5.5   HEM mass flux as a function of entropy and
              stagnation temperature for a range of entropy
              that emphasizes saturated stagnation conditions.
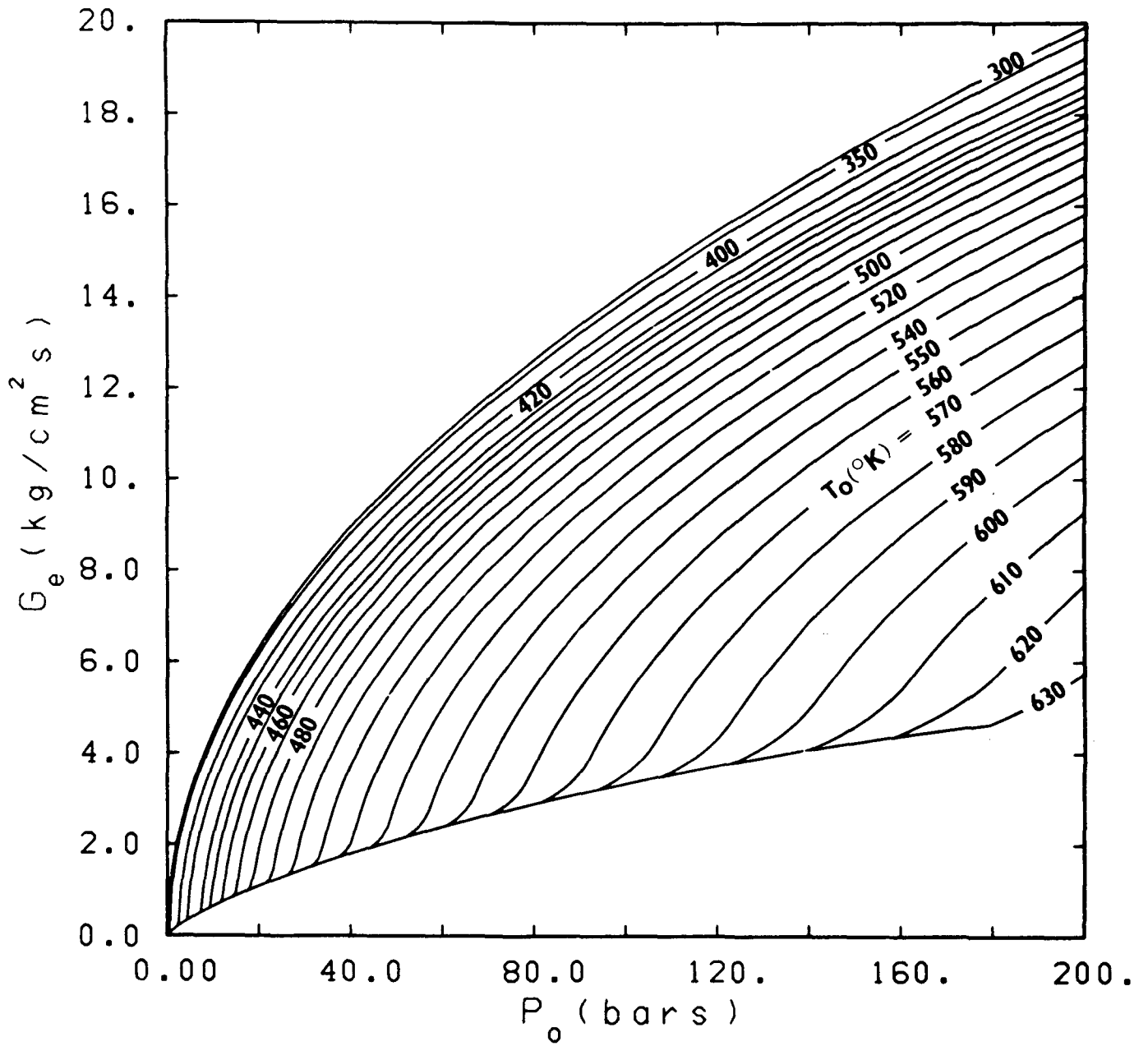
Figure 5.6   HEM mass flux as a function of stagnation
pressure and stagnation temperature.
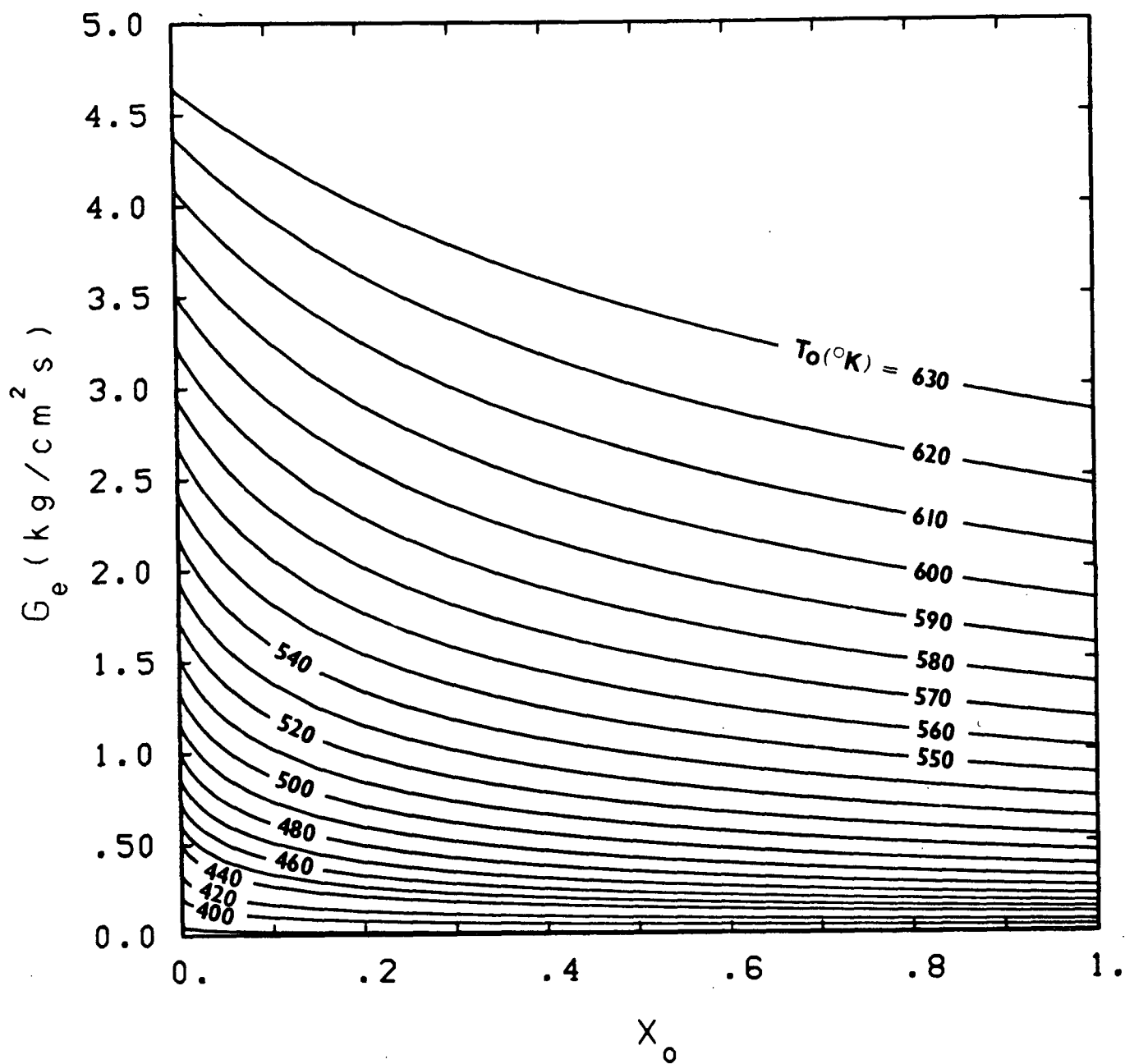
Figure 5.7 HEM Mass flux as a function of stagnation quality
         and stagnation temperature.
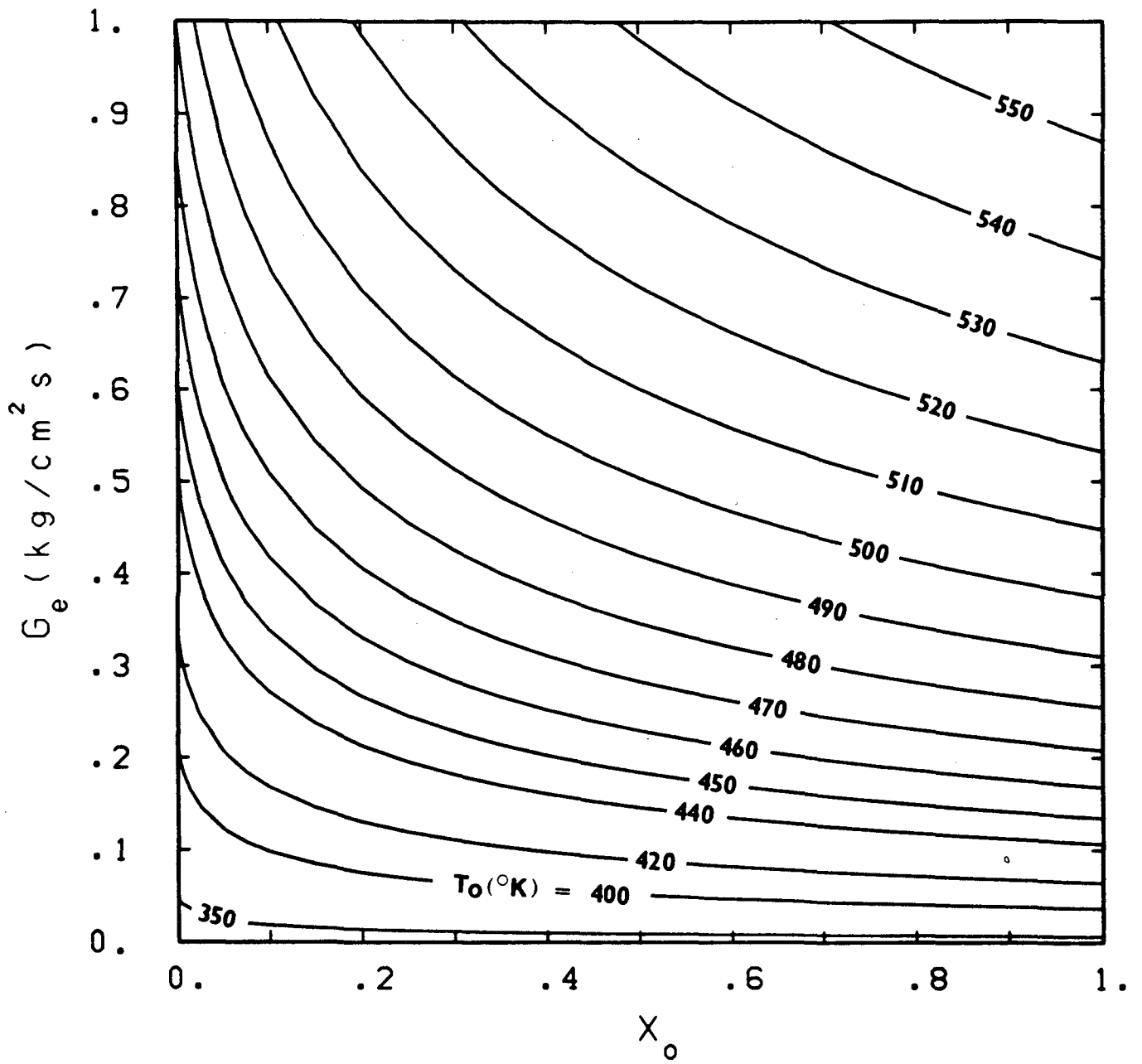
Figure 5.8   HEM mass flux as a function of the stagnation
quality and stagnation temperature.
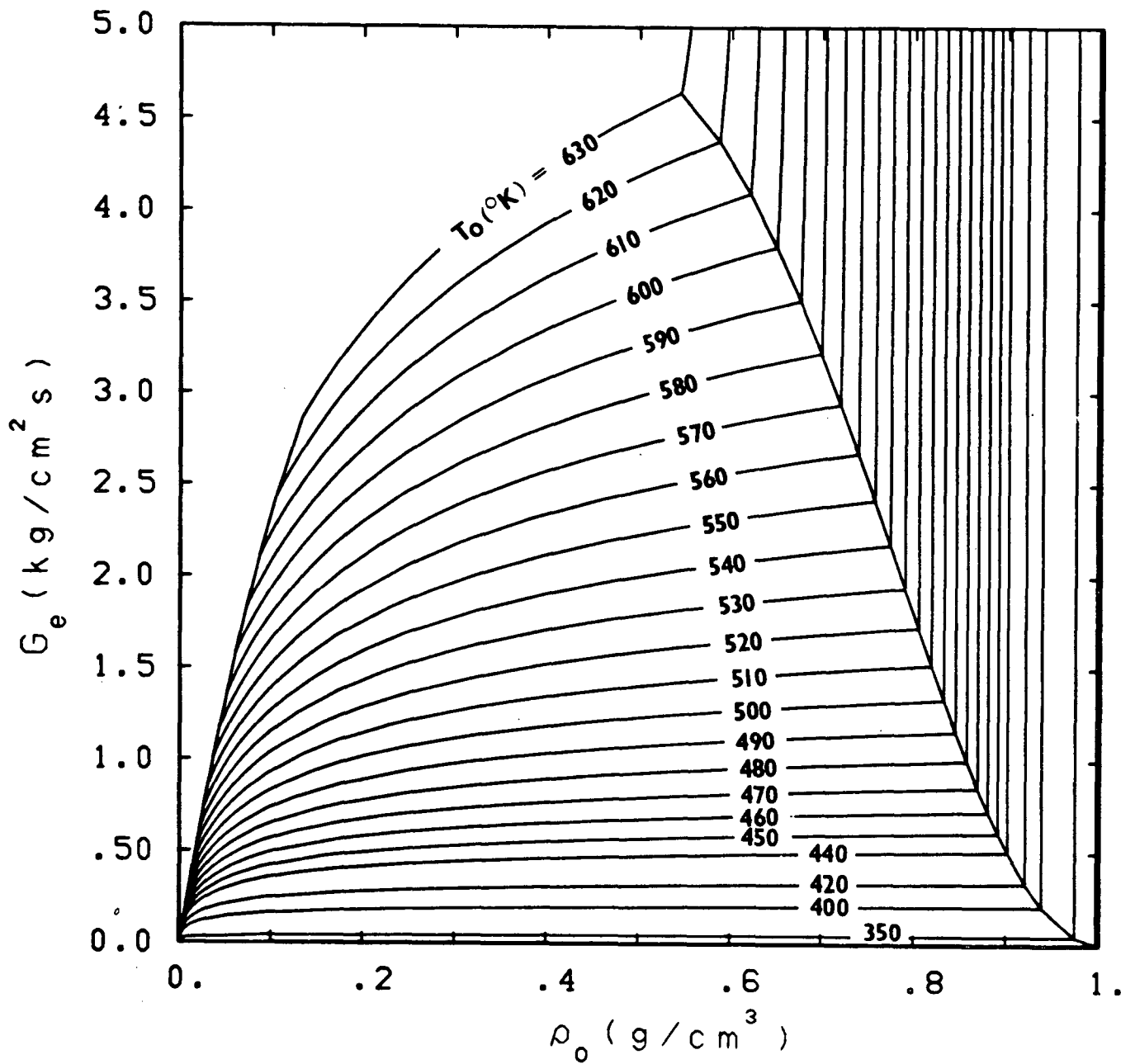
Figure 5.9   HEM mass flux as a function of the stagnation
density and stagnation temperature.
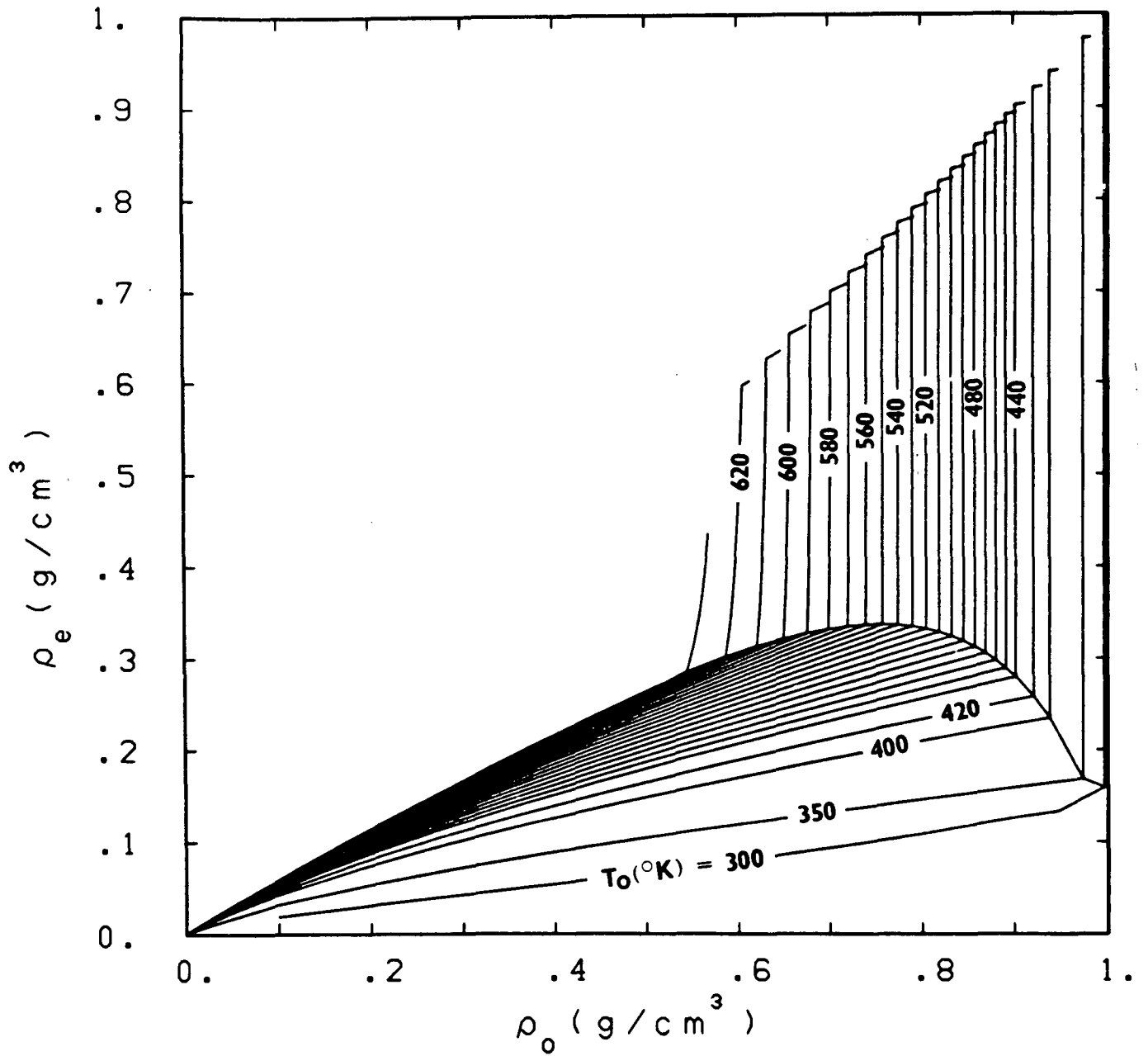
Figure 5.10   HEM critical flow density as a function of
stagnation density and stagnation temperature.

Figures 5.4 and 5.5. Finally, using the stagnation temperature
and the break flow, Figures 5.6 or 5.7 are used to find the
stagnation pressure or stagnation quality (whichever is
applicable). Although this procedure is given here in graphic
form, it is not difficult to computerize the entire procedure.

6.0   APPROXIMATE MODELS

The data base established using CSQ was sparse because of the wide range of initial conditions investigated with the resources available. Since the data base was sparse it became necessary to interpolate (curve fit) within the computational data base to arrive at complete sets of loading curves for a wide range of desired initial conditions. Simple interpolative strategies proved to be unsuccessful; the computational data base was too sparse and the two-phase jet impingement solutions were too complicated. Consequently, several approximate models, which contained much of the physics required to describe the basic phenomena occurring in the two-phase jet, had to be developed; these models were then used to perform the interpolation within the computational data base. This chapter describes jet and shock models for calculating both axial and target pressure distributions. These approximate models when combined are capable of predicting, with less accuracy than the model introduced in Chapter 2, two-phase jet loads, and are useful for fast scoping calculations.

6.1   Centerline Free-Jet Expansion Model

This model approximates the free jet expansion along the centerline of a two-phase jet.

The geometry for this model is given in Figure 6.1. A detailed description of this geometry was given in Chapter 3. Briefly, we are assuming the blowdown is quasi-steady. The vessel pressure P_0 is the upstream stagnation pressure; P_1 is the break pressure; P_2 is the centerline pressure in the jet upstream of any shock phenomena; P_3 is the pressure in the jet downstream of the shock; and finally, P_4 is the stagnation pressure at the target. Homogeneous-equilibrium (HEM) choked flow conditions are assumed for the break.

Consider the problem of determining the centerline pressure in an expanding jet for a general point 2, P_2. Since this point is upstream of the standing shock wave, it is essentially unaffected by the target's presence. (Once the full state of conditions are known at 2, then the centerline properties at 3 and 4 are completely determined provided the shock standoff distance is small.)

A large number of both free jet and target calculations were run as a part of this two-phase jet study. Results from these calculations and detailed discussions were given in Chapter 4. From observing the basic behavior of the thermodynamic property contours and the centerline pressure behavior we found that the following relation approximates the free jet expansions for flows with saturated stagnation conditions:
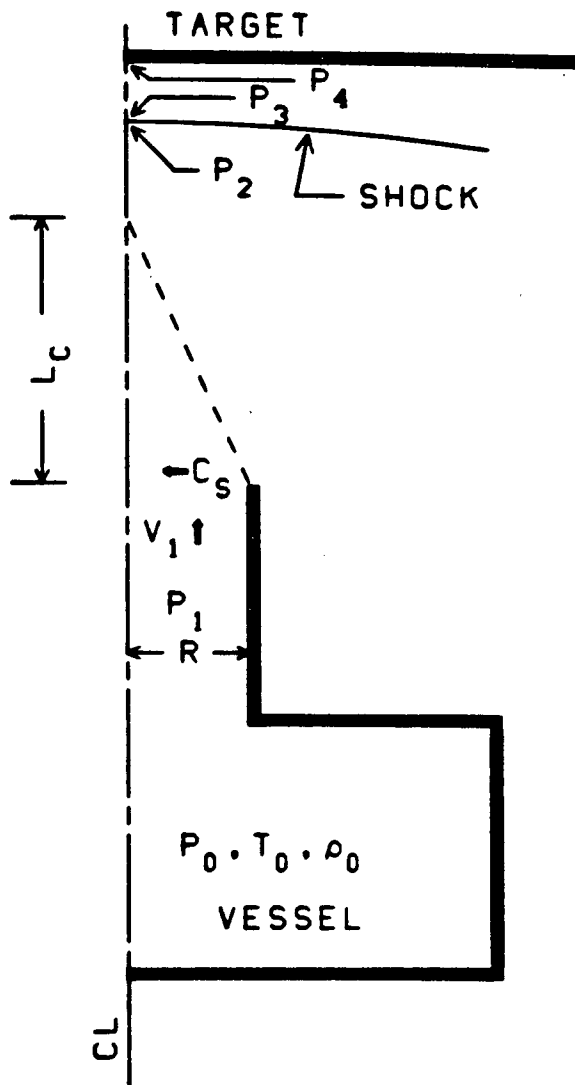
Figure 6.1 Geometry and definitions for the free
jet expansion model and the centerline
shock model.

$$(\rho V)_2 = (\rho V)_1 \left(\frac{D}{2z}\right)^2 \quad , \quad z \geq \frac{1}{2}D \quad , \qquad (6.1)$$

where ρ is the density of the two-phase mixture, V is the axial velocity, z is the axial distance to point 2, and the subscripts 2 and 1 refer to conditions at point 2 and the pipe exit, respectively (see Figure 6.1).

Arguments can be made for an approximate derivation of equation (6.1) if two assumptions are made about the two-phase jet expansion. Neither is absolutely true, but the errors appear to cancel. First assume that the jet has a well defined boundary described by a 45° expansion angle, then assume that the axial component of the mass flux is not a function of radius. These two assumptions are illustrated in Figure 6.2. Mass conservation then yields

$$(\rho V A)_2 = (\rho V A)_1 \quad , \qquad (6.2)$$

where A is the cross-sectional area of the jet. Since

$$A_1 = \frac{1}{4}\pi D^2 \qquad (6.3)$$

and

$$A_2 = \pi z^2 \quad , \qquad (6.4)$$

equation (6.2) will reduce to equation (6.1). Relation (6.4) uses the 45° expansion angle. Again, note that this relation is only approximately true along the axis of symmetry.

When subcooled stagnation conditions exist, the model in equation (6.1) does not account for the core length L_c. For subcooled stagnation conditions, the core length is greater than $D/2$. (The HEM core length L_c was discussed and a method for calculating L_c was given in Section 3.6.) Equation (6.1) can be modified to account for this behavior. This new approximate expression applicable in the range $D/2 \leq L_c \leq z$ is given by

$$(\rho V)_2 = (\rho V)_1 \left\{ \frac{(D/2z)^2}{1 - (L_c/z)^\beta [1 - (D/2L_c)^2]} \right\} \quad , \quad (6.5)$$

89
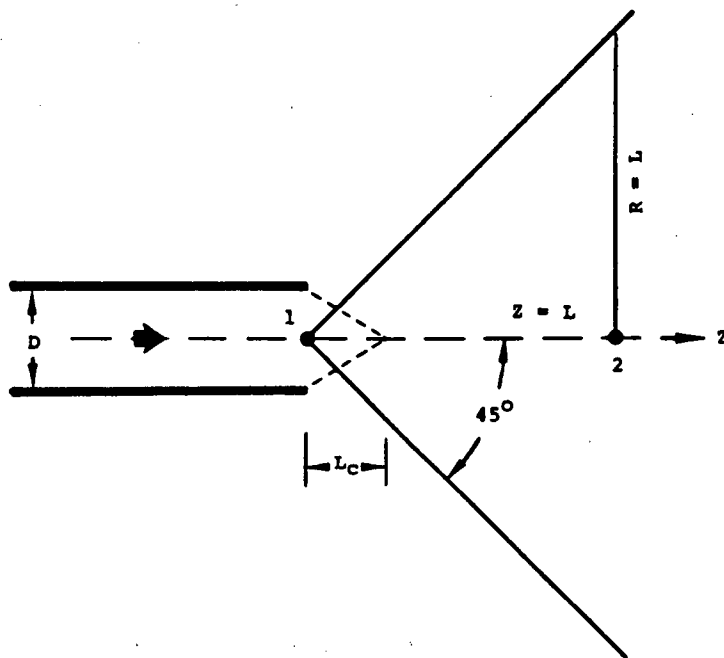
Figure 6.2   Illustration showing the geometry and
definitions used for developing the
algebraic free jet expansion model.

where β is a constant that must be evaluated using comparisons with data or calculations. A value of $\beta \simeq 14$ describes most of the calculations of interest. In both the simple model, equation (6.1), and the modified model, equation (6.5), HEM choked flow properties exist for $0 \le z \le L_C$. For saturated stagnation conditions, $L_C = D/2$.

The procedure for using the above relations to determine the free field jet parameters is straightforward. The exit conditions are calculated using the HEM critical flow model described in Chapter 3 or the charts in Chapter 5. The other relations which apply to the free field fluid are

$$H_O = H_z + \frac{1}{2} V_z^2 \qquad (6.6)$$

and

$$S_O = S_z \quad , \qquad (6.7)$$

where H is the enthalpy and S is the entropy; the model assumes an isentropic expansion. The three relations [(6.1) or (6.5)], (6.6) and (6.7) can be solved with the thermodynamic equation of state for water to complete the description of all thermodynamic variables and the velocity along the axis of symmetry. The numerical method is simple but was performed on a computer because of the nonlinear, complicated equation of state for water. (This same computer program was used to develop some of the thermodynamic charts shown in Chapter 5.)

Figure 6.3 shows the results from a sample calculation using (6.1) for a vessel stagnation pressure of $P_O = 150$ bars and $35^{O}C$ of subcooling ($\Delta T_O = 35^{O}C$). These initial conditions were selected to emphasize that equation (6.1) should be carefully applied when the stagnation conditions are not saturated. The curve labeled P_2 is the free jet expansion pressure calculated using equation (6.1); curves P_3 and P_4 will be discussed later in this report. Figure 6.4 shows the results obtained using equation (6.5) for the same stagnation conditions. The correction for the effect of the HEM boundary core is evident upon inspection. Finally, Figure 6.5 shows the comparison of the curves P_2 and P_4 from Figure 6.4 with the 2-D axisymmetric results from Section 4.5. The approximate model, P_2 from equation (6.5), compares quite well with the 2-D calculations for the entire length of the expansion.
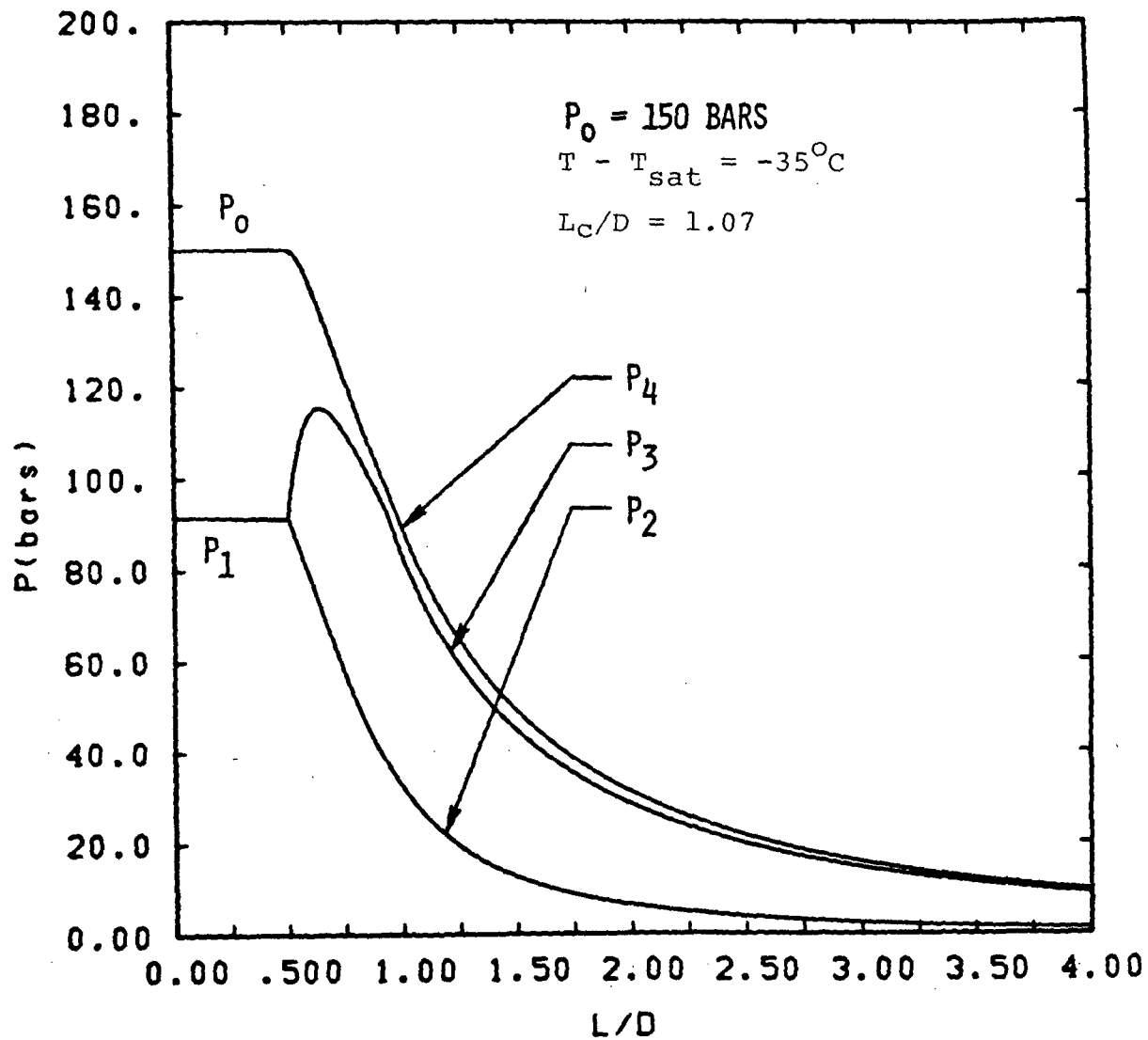
Figure 6.3   Pressure variation along the axis of
symmetry of a two-phase jet for the free
jet, equation (6.1), and shock models.
P_0 is the vessel pressure; P_1 is the exit
HEM pressure, P_2 is the jet pressure,
equation (6.1); P_3 is the Hugoniot pressure;
and P_4 is the target pressure.

92
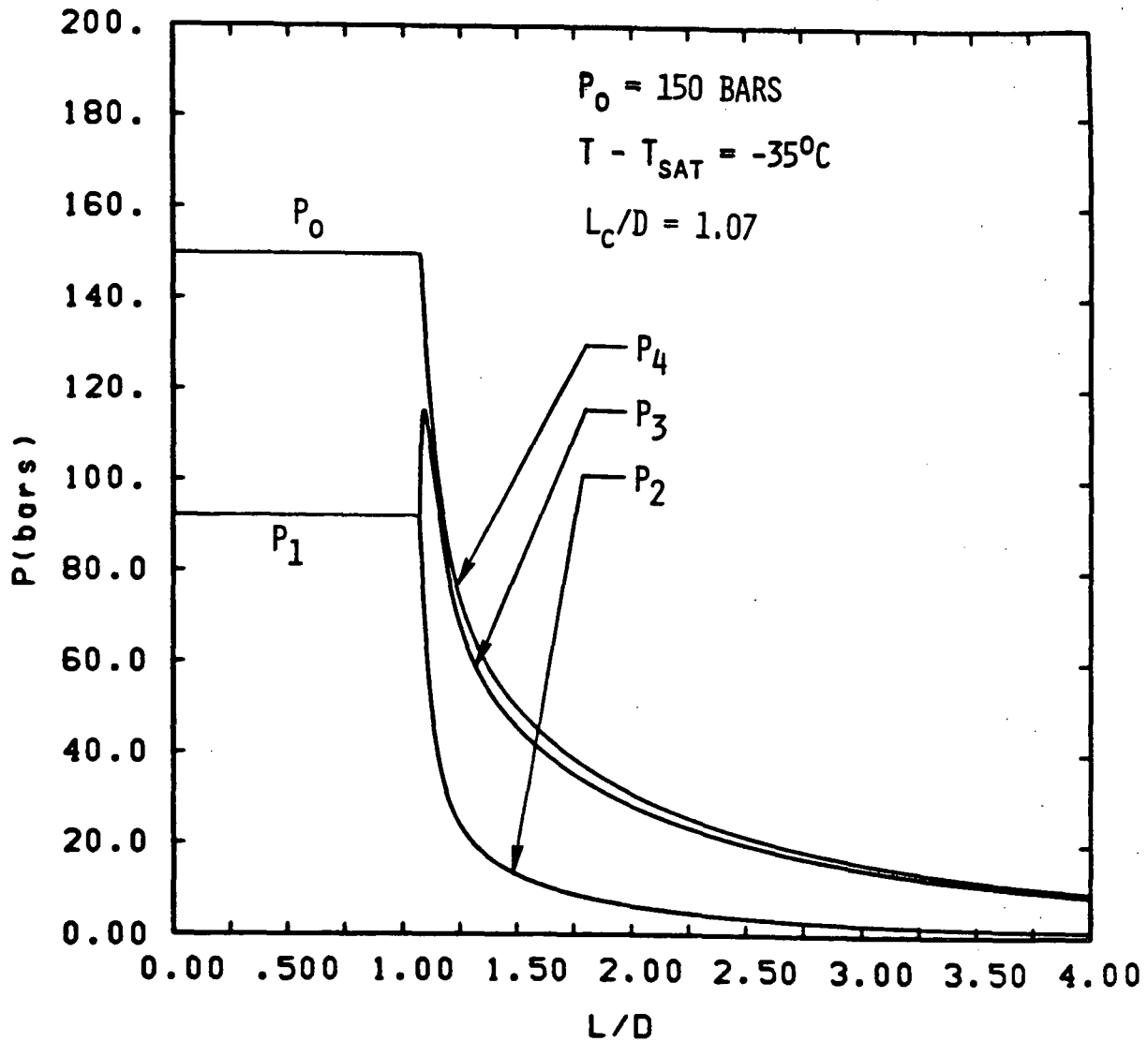
Figure 6.4   Pressure variation along the axis of
symmetry of a two-phase jet for the free
jet, equation (6.5), and shock models.
P_0 is the vessel pressure; P_1 is the exit
HEM pressure, P_2 is the jet pressure,
equation (6.5); P_3 is the Hugoniot pressure
and P_4 is the target pressure.
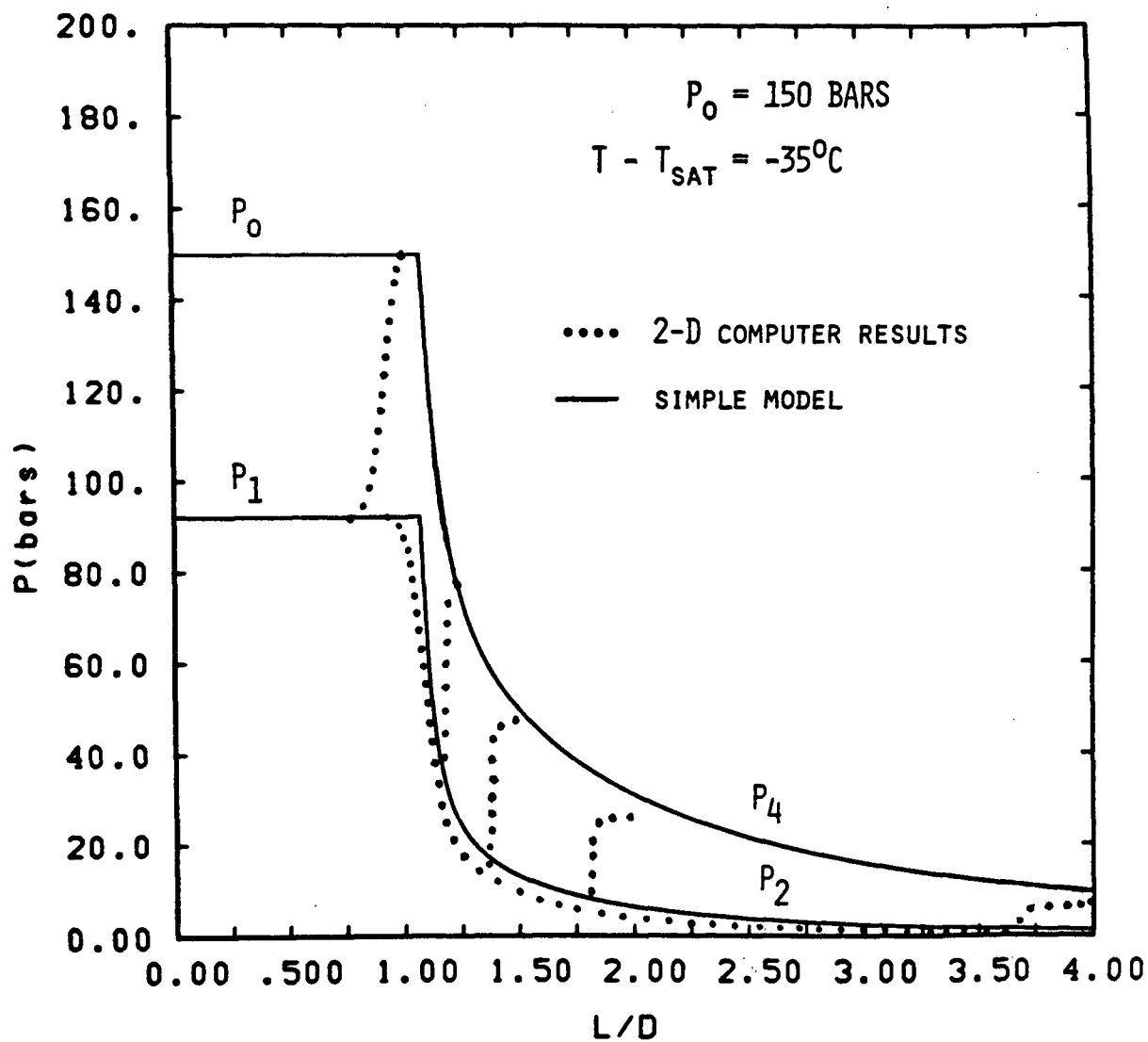
Figure 6.5   Comparison of centerline results from
              Section 4.5 Figure 4.18 with the free jet,
              equation (6.5), and the shock models.
              Curves for P_2 and P_4 are identical to
              the curves shown in Figure 6.4.

94

The above jet expansion model, using equation (6.1), has been compared to experimental data from the small-scale Ontario-Hydro tests[25] and from the near full-scale Marviken tests[8]. These data comparisons are presented without the benefit of labeled axes because the data at this writing was proprietary. Figures 6.6 to 6.13 show model and data comparisons for Ontario-Hydro tests for three nozzle diameters and three different initial stagnation conditions. For these comparisons the ambient pressures were unavailable to us; consequently, the model pressures at large z/D may represent expansion beyond the experimental ambient value. Figures 6.9 to 6.13 show the model and data comparisons for the Marviken tests; the experimental data was taken from pressure histories recorded in tests 1-3. Thus, the model was applied in a quasi-steady fashion. The conditions in the vessel were assumed to be the stagnation conditions at the pipe exit; the justification for making these assumptions is given in Chapter 3. For these Marviken data comparisons several different times in the pressure histories were selected to cover the range of slightly subcooled to fully saturated stagnation conditions.

The above data comparisons produce reasonably good agreement with data over a wide range of operating conditions; the model also compares favorably with the 2-D analytical predictions from Section 4.4.

6.2 Centerline Target Pressure Model

As the expanding jet approaches the target (or any stationary object) a standing shock wave forms near the target. Along the centerline this shock is normal to the target. The shock wave forms because the two-phase jet cannot sense the target's presence. The supersonic velocities in the jet prevent pressure signals from the target from propagating upstream. At a shock, kinetic energy is irreversibly exchanged for thermal energy; thus, there is a decrease in stagnation pressure across the shock.

At the target center we assume that the shock is normal and coincident with the target surface. Normal shock equations give the pressures P_3 and P_4 behind the shock. For a stationary normal shock in a two-phase, homogeneous, and equilibrium fluid the governing equations of mass, momentum, and energy are given as

$$\rho_2 V_2 = \rho_3 V_3 \quad , \qquad\qquad (6.8)$$

$$P_2 + \rho_2 V_2^2 = P_3 + \rho_3 V_3^2 \quad , \qquad\qquad (6.9)$$
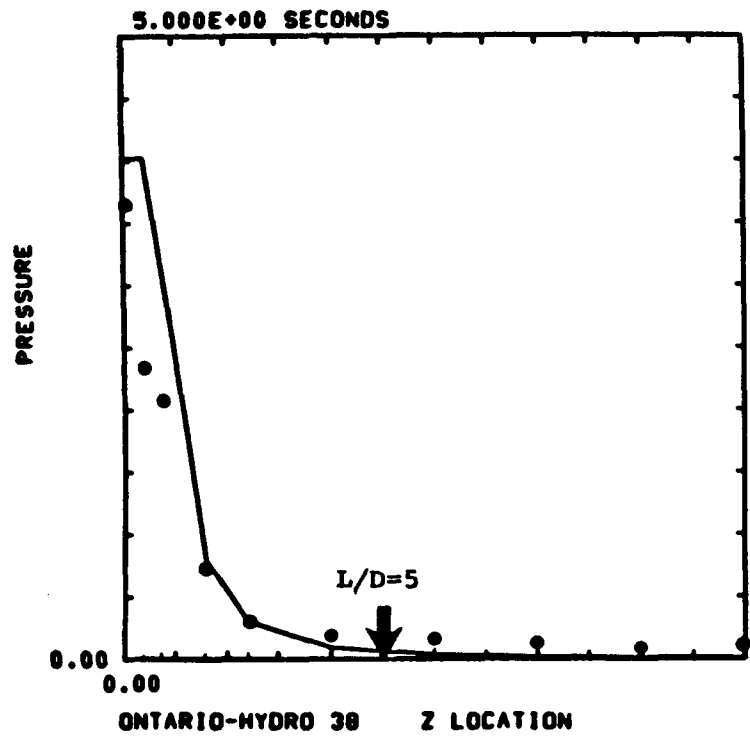
Figure 6.6 Free jet model comparison with Ontario-Hydro data.
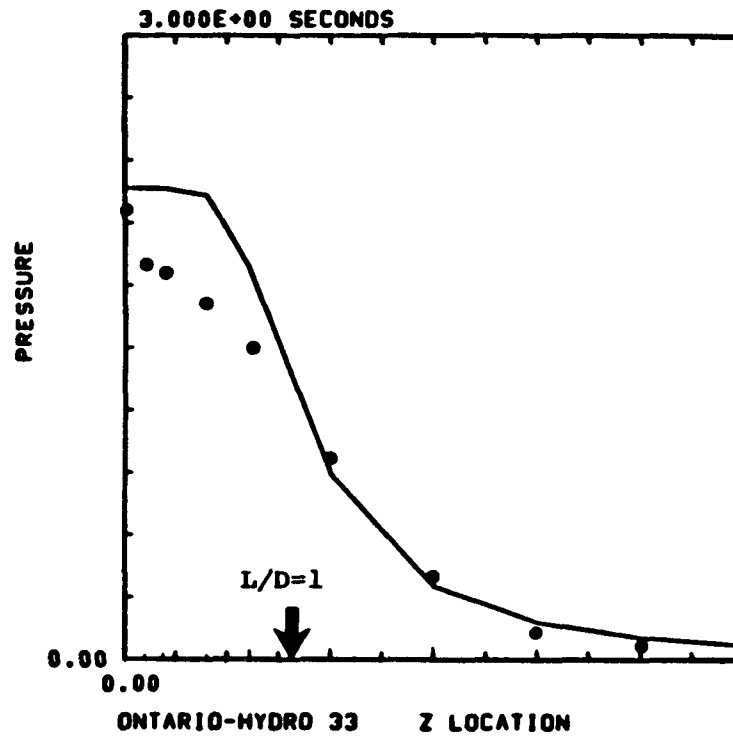
Figure 6.7 Free jet model comparison with Ontario-Hydro data.

3.500E+00 SECONDS

PRESSURE

L/D=1

0.0

0.00

ONTARIO-HYDRO 26   Z LOCATION

5.000E+00 SECONDS

PRESSURE

L/D=1

0.00

0.00

MARVIKEN 1   Z LOCATION
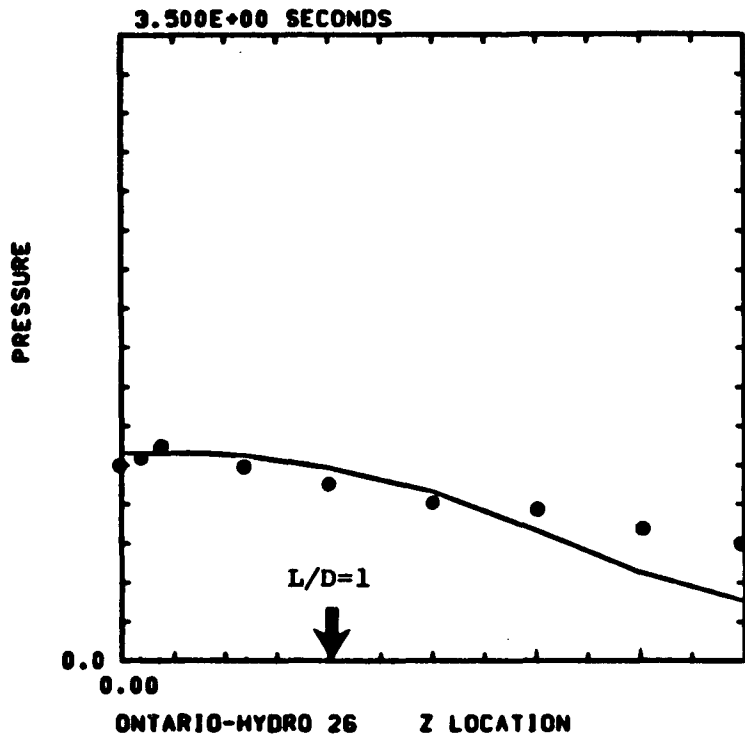
Figure 6.8 Free jet expansion comparison with Ontario-Hydro data.
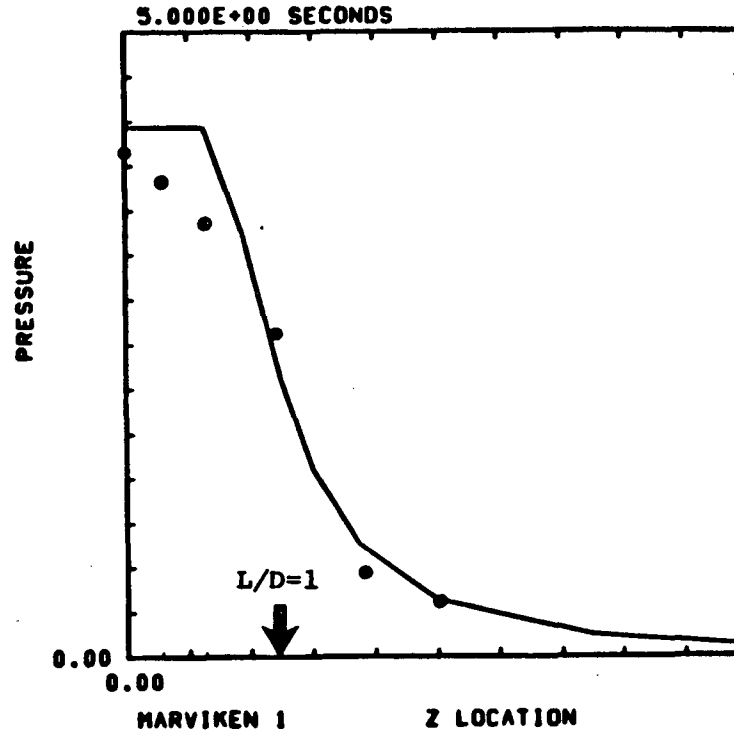
Figure 6.9 Free jet expansion comparison with Marviken data.

2.000E+01 SECONDS

PRESSURE

L/D=1

0.00

0.00

MARVIKEN 1   Z LOCATION

3.500E+01 SECONDS

PRESSURE

L/D=2

0.00

0.00

MARVIKEN 1   Z LOCATION
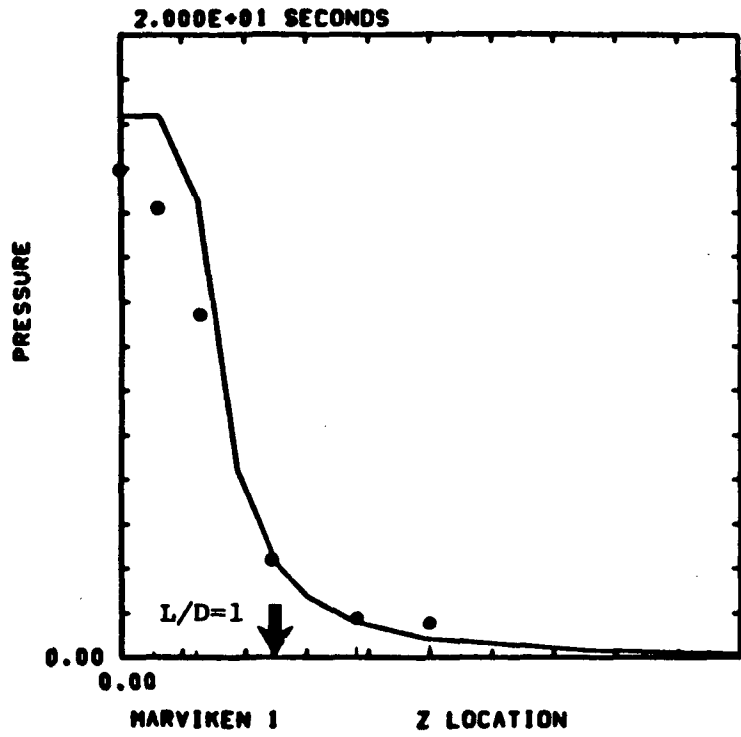
Figure 6.10   Free jet model comparison
with Marviken data.
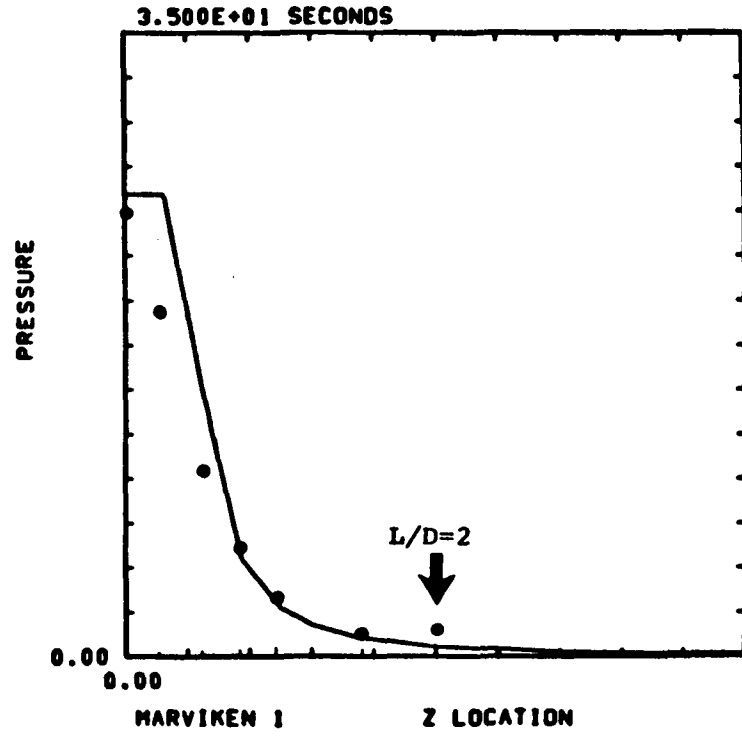
Figure 6.11   Free jet model comparison
with Marviken data.

3.000E+01 SECONDS

PRESSURE

L/D=2

0.00

0.00

MARVIKEN 2   Z LOCATION

2.000E+00 SECONDS

PRESSURE

L/D=1

0.00

0.00

MARVIKEN 3   Z LOCATION
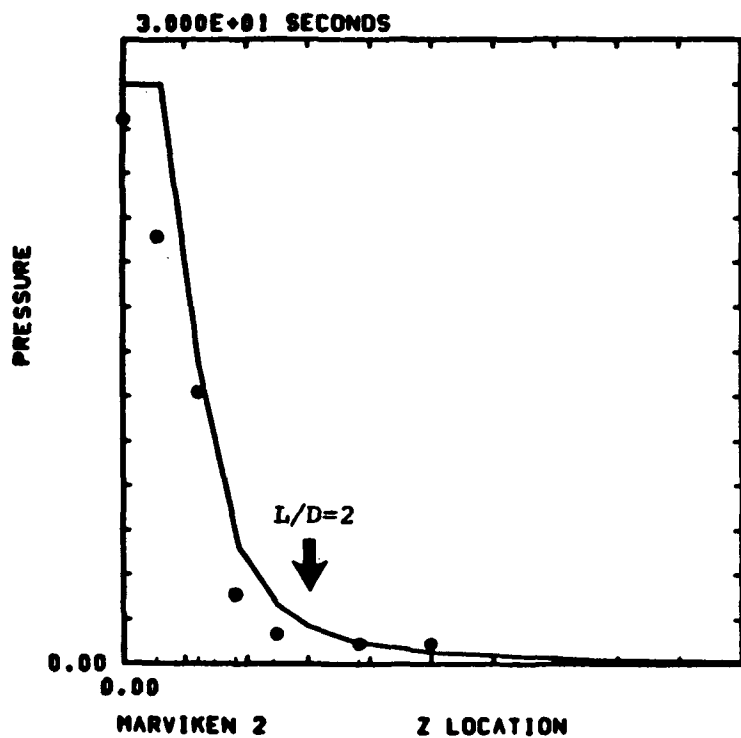
Figure 6.12   Free jet model comparison
with Marviken data.
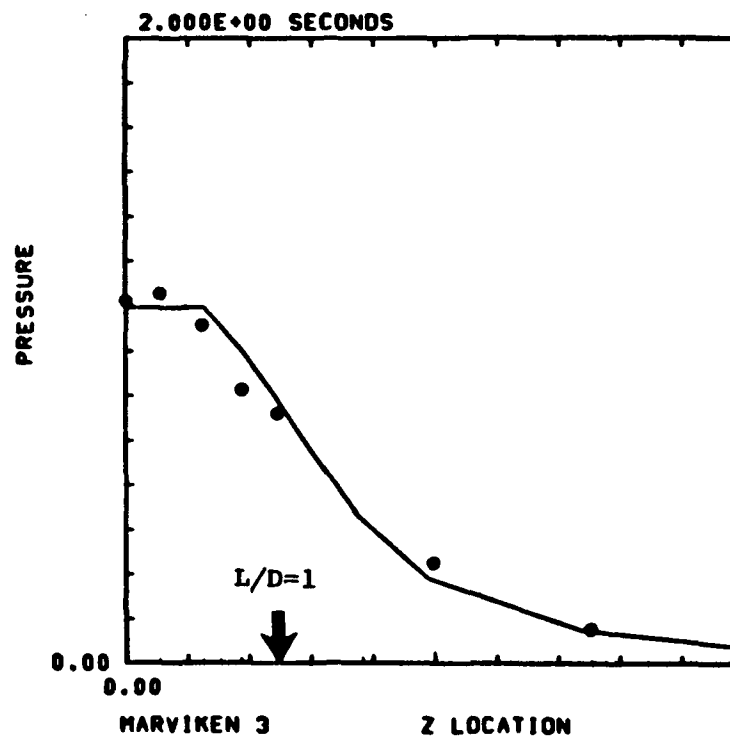
Figure 6.13   Free jet model comparison
with Marviken data.

and

$$E_3 - E_2 = \frac{1}{2} (P_3 + P_2) \left(\frac{1}{\rho_2} - \frac{1}{\rho_3} \right) \, , \qquad (6.10)$$

where ρ is the density, P is the pressure, V is the velocity, E is the internal energy and the subscripts 2 and 3 refer to points 2 and 3 in Figure 6.1.

State 2 in equations (6.8) to (6.10) is the expansion state given by equations [(6.1) or (6.5)], (6.6) and (6.7). The system of equations (6.8) to (6.10), then can be solved for state 3 (P_3) on the material Hugoniot. Once we know state 3, the total pressure downstream of the shock, P_4, is simply the isentropic stagnation pressure.

Equations (6.8) to (6.10) have been solved for the free jet example given in the last section (P_0 = 150 bars, ΔT_0 = 35°C); these results are given in Figures 6.3, 6.4, and 6.5. Figures 6.3 and 6.4 show P_3 plus the stagnation (target) pressure P_4 calculated using each of the simple jet model equations. Figure 6.5 shows a comparison of the target pressure P_4 calculated using the simple model and the target pressures from the 2-D calculations of Section 4.5. (Note that the 2-D curve is an overlay of five entire centerline distributions; P_4 is the final point on each of the broken curves).

A comparison between the stagnation pressure predicted with the combined free jet expansion and shock model and Marviken experimental data[8] is given in Figures 6.14 to 6.16. The data are shown without the benefit of labeled axes for the reason already given; however, a blow down typical of Marviken free jet tests was given earlier in Figure 3.4. This blow down is illustrative of Marviken stagnation pressures versus time at the break. Again, the engineering models show good agreement. The Marviken data given in Figures 6.14 to 6.16 are the stagnation pressures behind the shock that formed in front of the pressure recording instrument; therefore the stagnation pressure in the free jet was close or equal to the vessel stagnation pressure P_0. These data comparisons are further proof that viscous effects in the jet are small and that shock waves in the jet field are responsible for the stagnation pressure losses. Ultimately in an unconfined free jet there will be an over-expansion and subsequent shock wave formed allowing the jet to adjust to the ambient pressure conditions. (This particular phenomena was discussed in more detail in Section 3.7). Neglecting these shock waves leads to a misinterpretation of the stagnation conditions in two-phase jets.

100

2.000E+00 SECONDS

STAGNATION PRESSURE

L/D=1

0.0
0.00

MARVIKEN 3   Z LOCATION

4.000E+00 SECONDS

STAGNATION PRESSURE

L/D=1

0.0
0.00

MARVIKEN 3   Z LOCATION
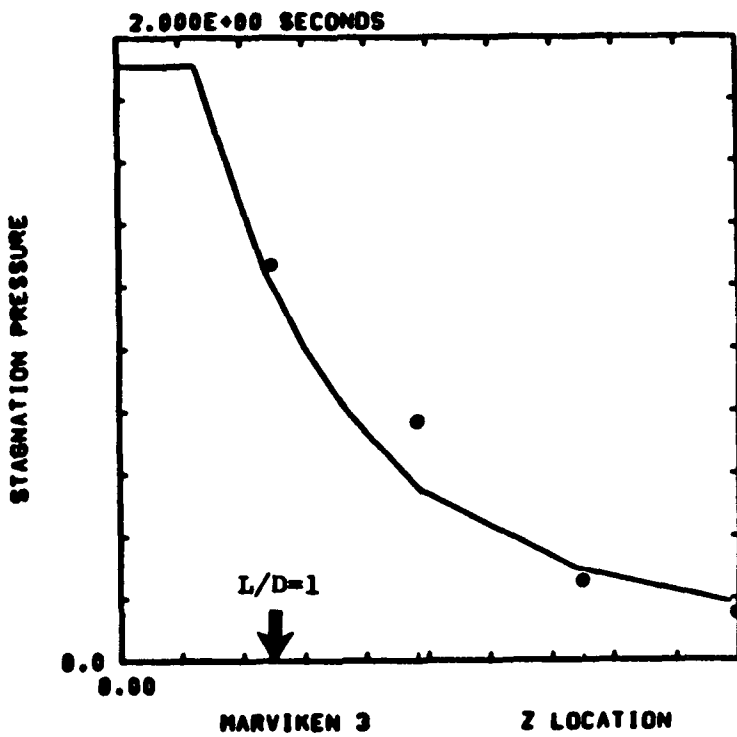
Figure 6.14   Stagnation Pressure Model
Comparison with Marviken Data
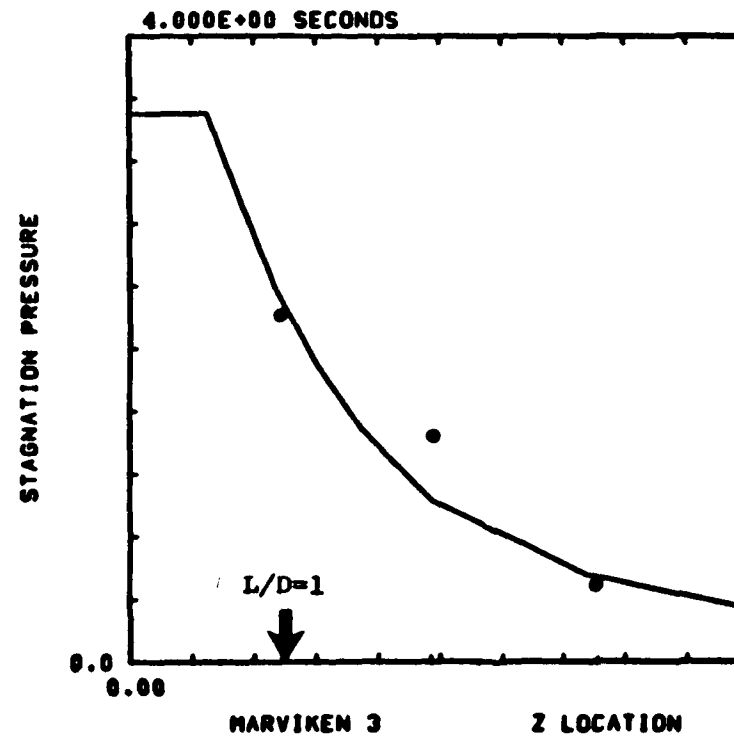
Figure 6.15   Stagnation Pressure Model
Comparison with Marviken Data

6.000E+00 SECONDS

STAGNATION PRESSURE

L/D=1

0.0

0.00

MARVIKEN 3

Z LOCATION
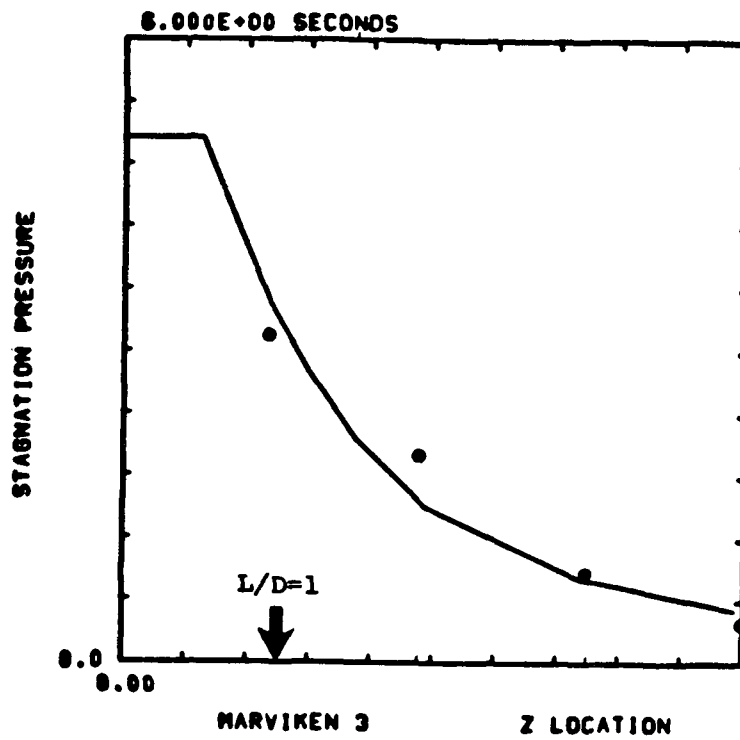
Figure 6.16 Stagnation Pressure Model
Comparison with Marviken Data

102

6.3 Target Radial Pressure Model

A review of the computational data base showed that the radial pressure loadings on a target were not nondimensionally similar. Subcooling and target spacing (L) had a strong influence on the shape of the pressure distribution. Consequently, one universal pressure profile will not describe the radial pressure behavior. In this section a model, which combines the free-jet expansion and shock wave features of the previous two sections, will be given for the radial pressure distribution on axisymmetric targets.

As indicated in Section 6.2 a shock forms in front of the target. At the center of the target the shock behaves as a normal shock but at target radii greater than zero the shock becomes oblique to the flow. Oblique shocks are governed by the same equations as normal shocks when using the component of velocity normal to the oblique shock.

Figure 6.17 illustrates the geometry for the radial model. Although CSQ calculations showed that there was a slight curvature to the bow shock (see Figure 4.14), the radial pressure model assumes that the target and shock are coincident. The properties upstream of the shock (P_2, T_2, V_2, etc.) are evaluated with the centerline expansion model, equation (6.1), using the expansion length of L' where

$$L' = \sqrt{L^2 + R^2} \quad .$$

(6.11)

The properties downstream of the shock are evaluated with the normal shock model, equations (6.8), (6.9), and (6.10) using the component of velocity normal to the oblique shock. Finally, the pressure on the target is found by isentropically stagnating the velocity normal to the wall behind the shock. The above process is repeated for the various radii until the pressure on the target reaches the ambient pressure; ambient pressure is then assumed beyond this point.

Figure 6.18 shows a comparison between the simple radial pressure model and radial pressure profiles from the computational data base (CSQ calculations); the case shown here is for stagnation conditions $P_O = 150$, $\Delta T_O = 35^{\circ}C$ and for L/D's of 1.25, 1.5, 2.0 and 4.0. The agreement shown in Figure 6.18 is typical of a wide range of stagnation conditions. The comparison is best at large L/D's where the target is away from the strong multi-dimensional effects near the break exit. Additionally, at small L/D's the standoff distance of the bow shock becomes significant with respect to the target spacing L and the shock wave exhibits a significant amount of curvature.

103

Figure 6.17   Geometry for the radial load model
              (approximate model).
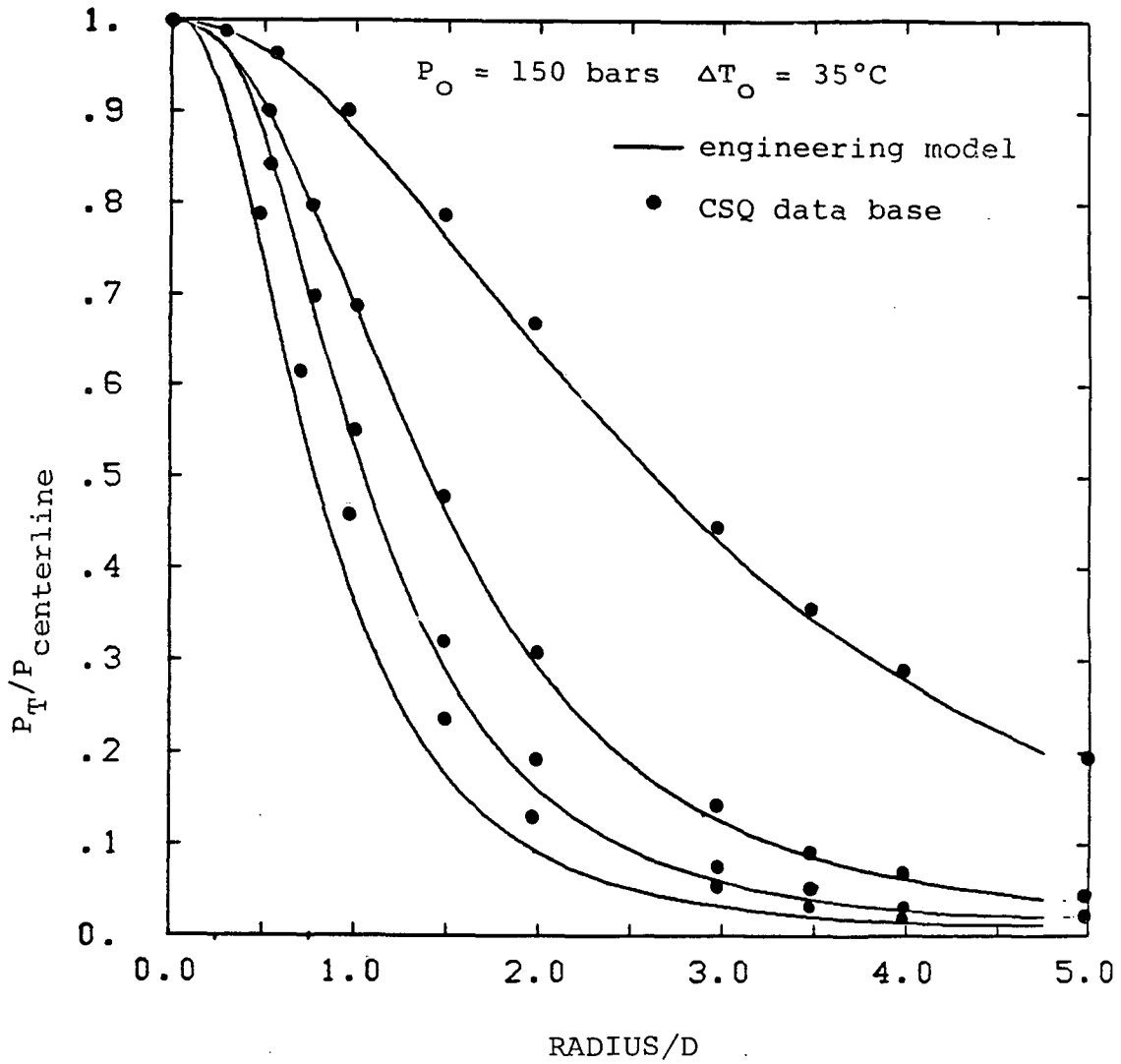
Figure 6.18 Radial pressure model (approximate)
comparison with the computational data
base (CSQ calculations).

7.0 ENGINEERING MODEL

The two-phase jet problem was too difficult to treat with approximate models, but at the same time it is impractical to run a two-dimensional, Eulerian finite difference calculation each time load calculations are made.

In Chapter 6 several approximate models were introduced. These models compared well with both data and CSQ calculations. This chapter describes the development of procedures for interpolating within the sparse computational data base using the approximate models. The result of this modeling was a description of the centerline pressure distribution and radial target pressure distribution for a wide range of vessel conditions and target spacings. These results have been provided in graphical form (see Appendixes A and B) and in dimensional variables when possible, thus the result forms a quick reference set of loading and pressure charts for a range of parameters applicable to most PWR's or BWR's.

7.1 Centerline Stagnation Pressure Model

The centerline stagnation pressure model was obtained by fitting the analytical data (CSQ data base) with the approximate model, equation (6.5), centerline function

$$(\rho V)_2 = (\rho V)_1 \left\{ \frac{(D/2z)^{\alpha}}{1 - (L_c/z)^{\beta} \left[1 - (D/2L_c)^{\alpha} \right]} \right\} . \qquad (7.1)$$

The parameters α and β were determined using a nonlinear least squares surface fitting technique [26] where

$$\alpha = \alpha (P_0, \Delta T_0, L/D, L_c/D) , \qquad (7.2)$$

$$\lim_{L/D \to \infty} \alpha = 2 , \qquad \lim_{\Delta T \to 0} \alpha = 2$$

and

$$\beta = \beta (P_0, \Delta T_0, L/D, L_c/D) . \qquad (7.3)$$

The resulting centerline pressure model is given in Figures 7.1 through 7.6 (see also Appendix B). Figures 7.1 through 7.6 show the
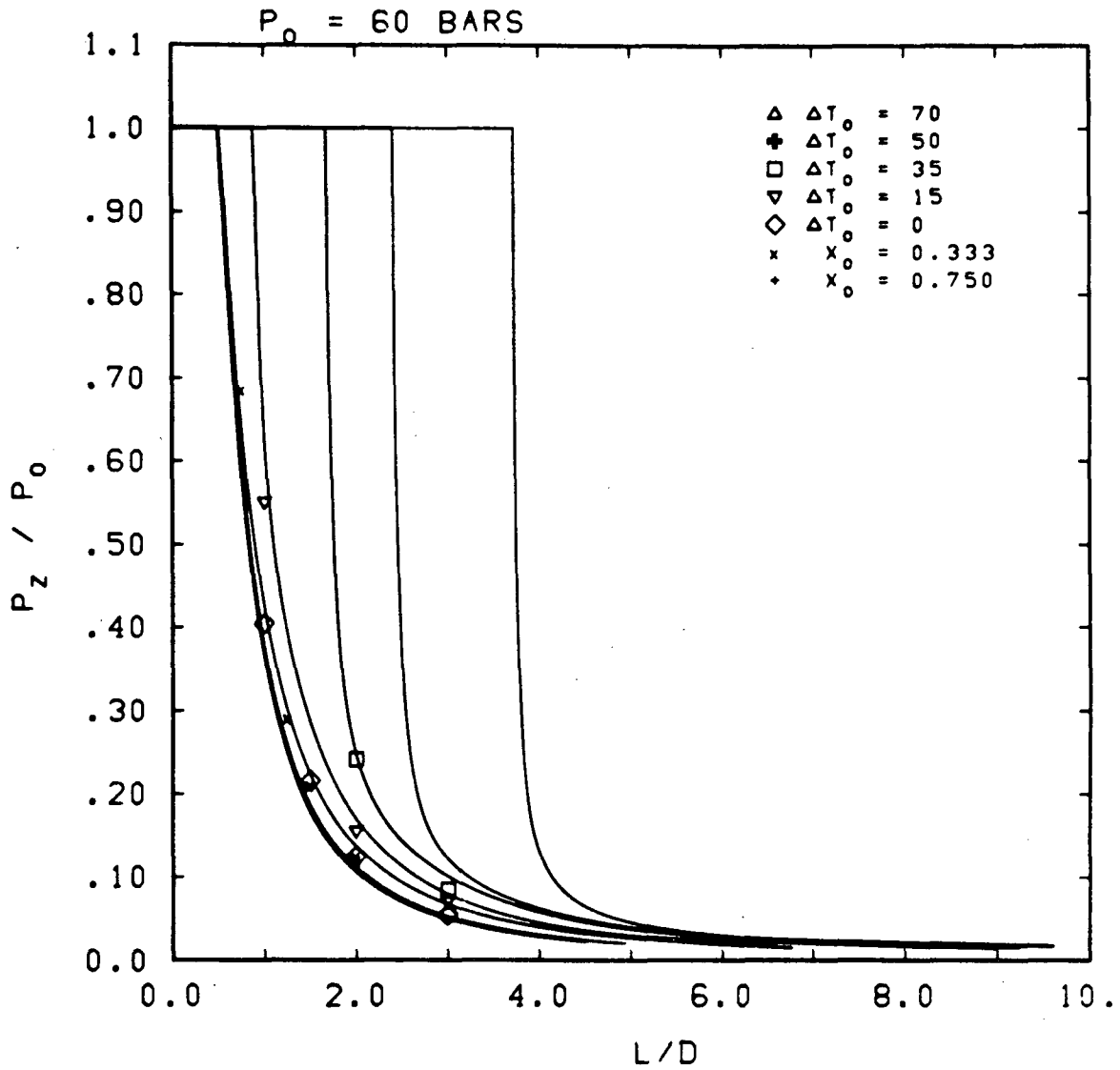
Figure 7.1 Centerline target pressure as a function of the
distance to the target (L/D) and the stagnation
properties. Comparison of the jet load model
with computational data base.
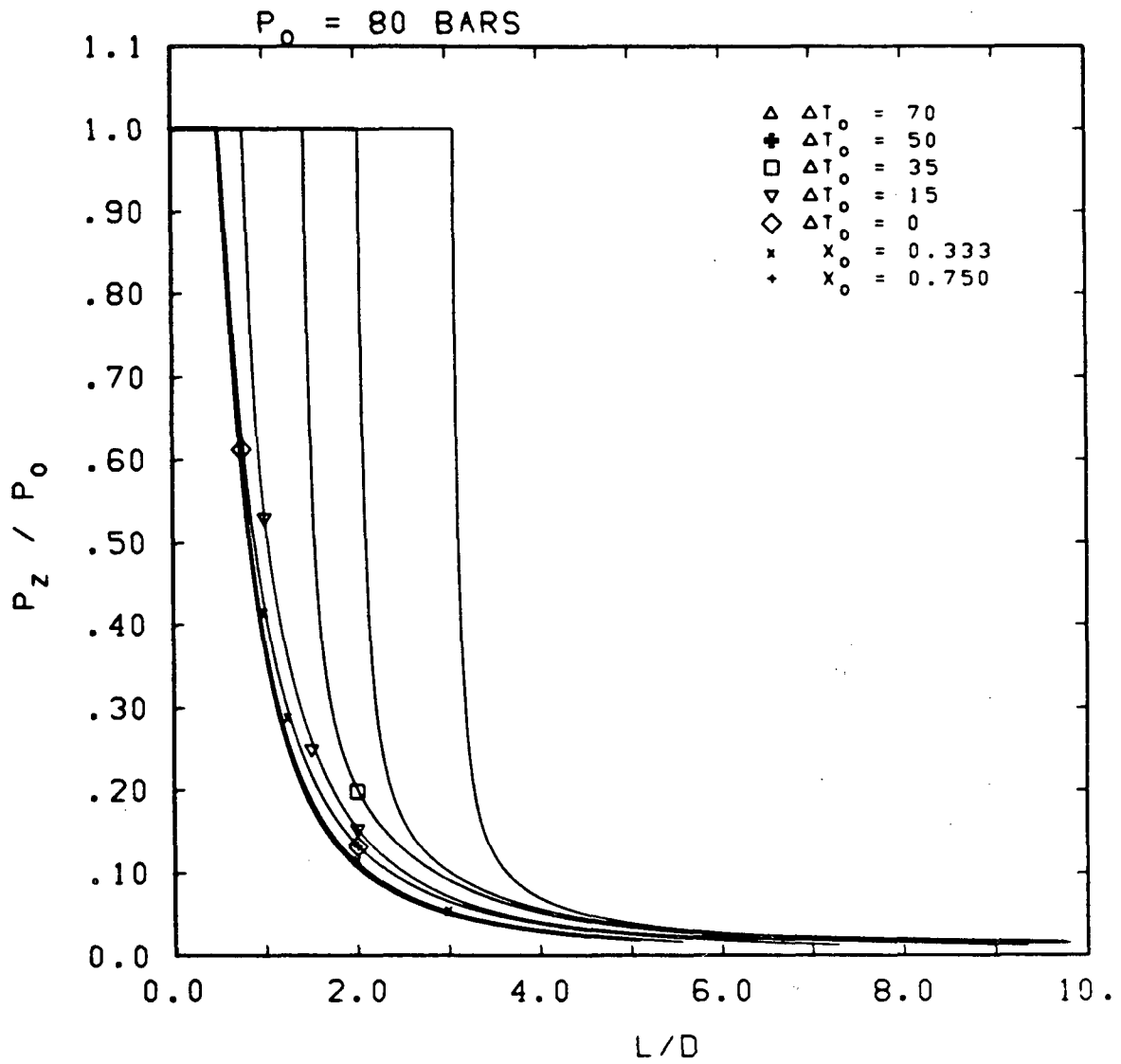
Figure 7.2 Centerline target pressure as a function of the distance to the target (L/D) and the stagnation properties. Comparison of the jet load model with computational data base.
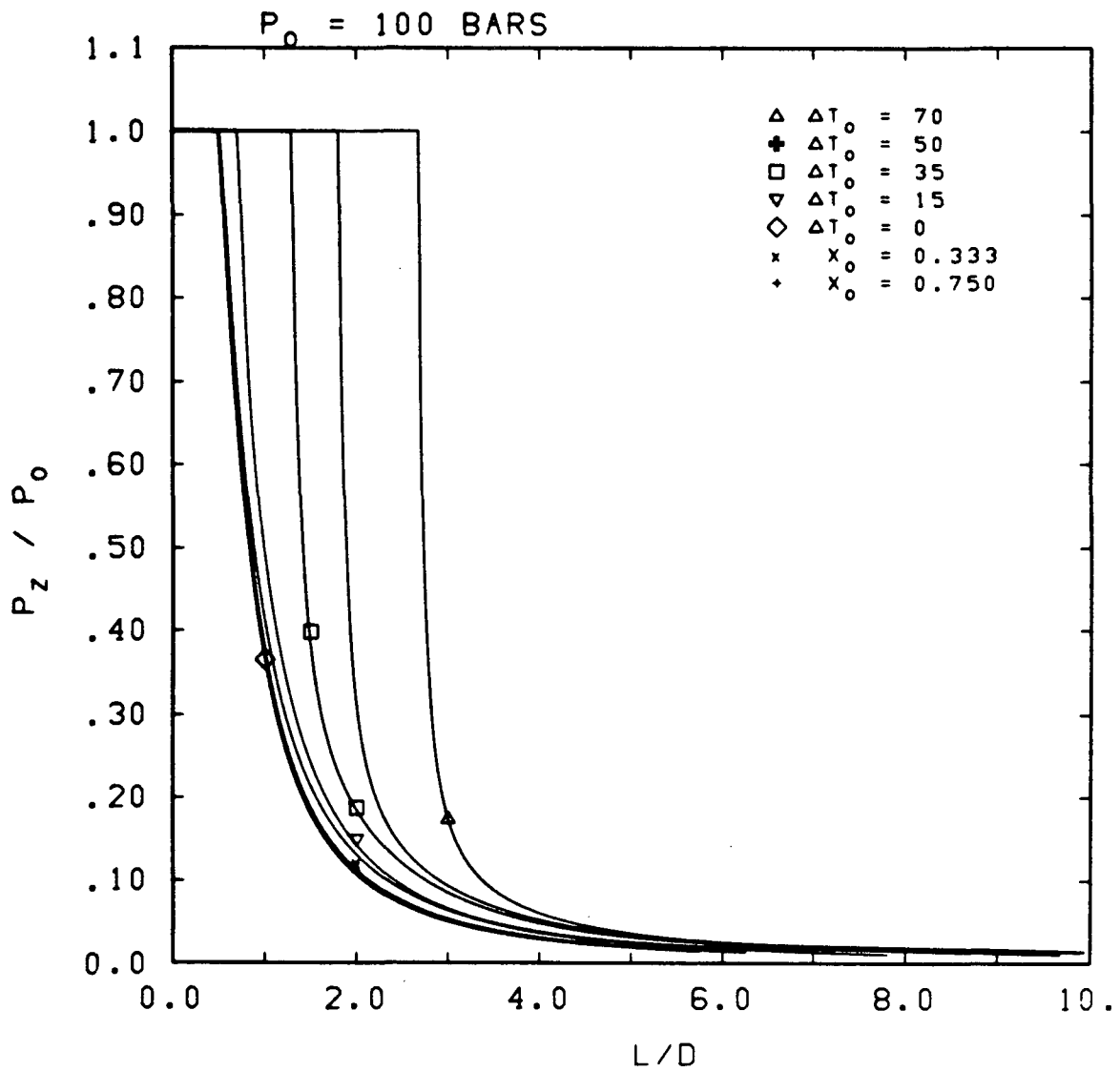
Figure 7.3 Centerline target pressure as a function of the
         distance to the target (L/D) and the stagnation
         properties. Comparison of the jet load model
         with computational data base.

110
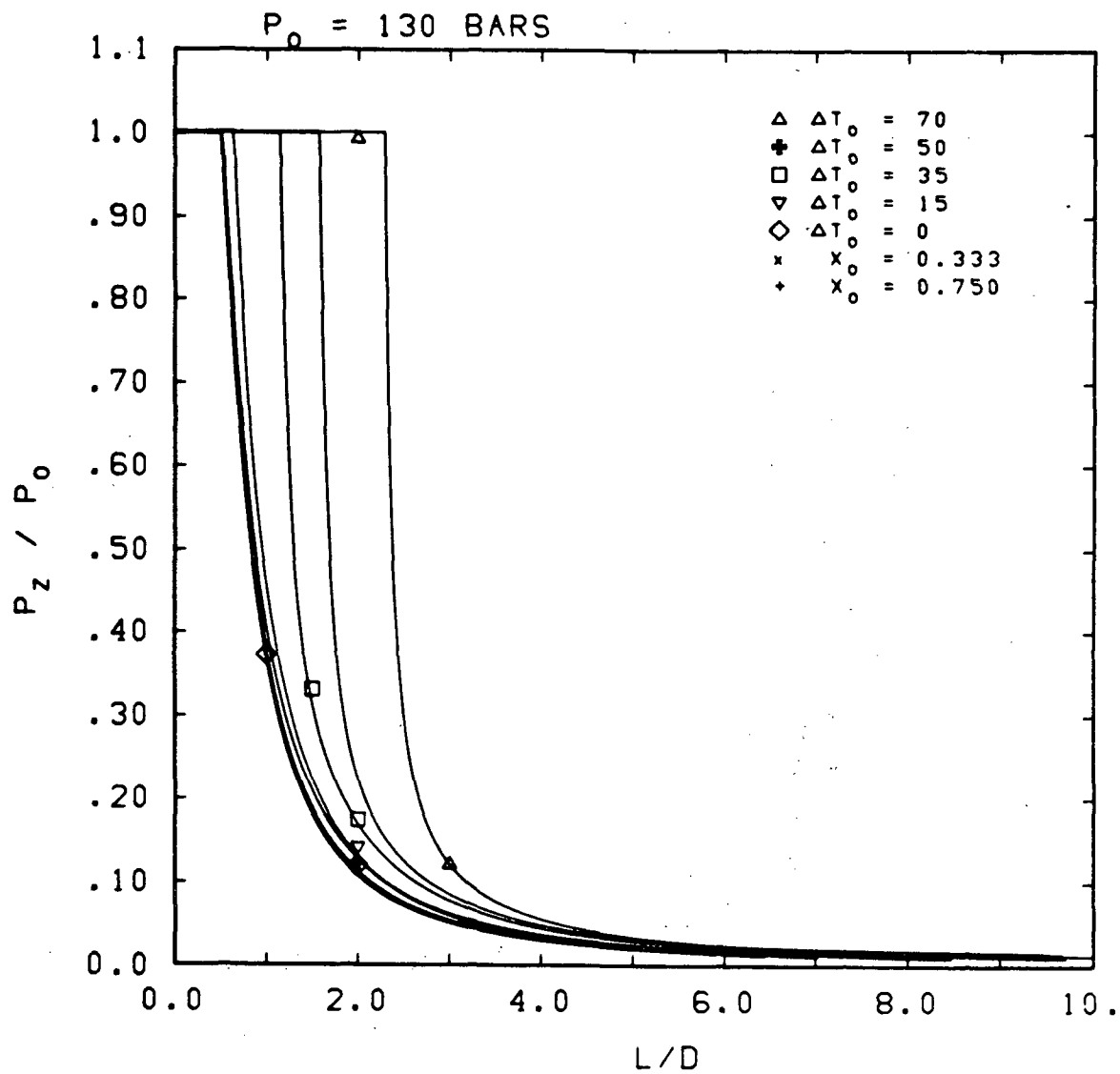
Figure 7.4   Centerline target pressure as a function of the distance to the target (L/D) and the stagnation properties. Comparison of the jet load model with computational data base.
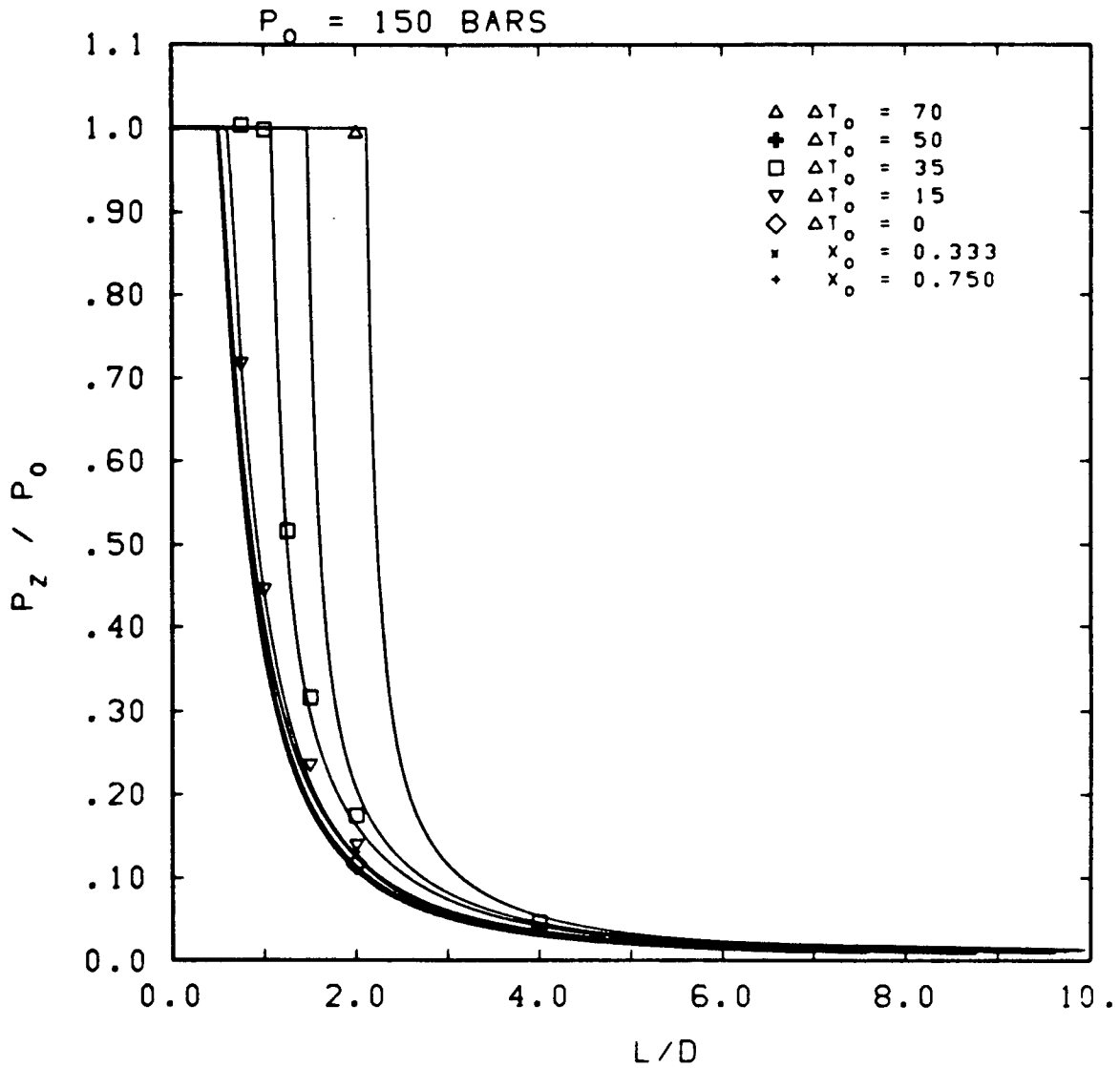
Figure 7.5   Centerline target pressure as a function of the
distance to the target (L/D) and the stagnation
properties. Comparison of the jet load model
with computational data base.
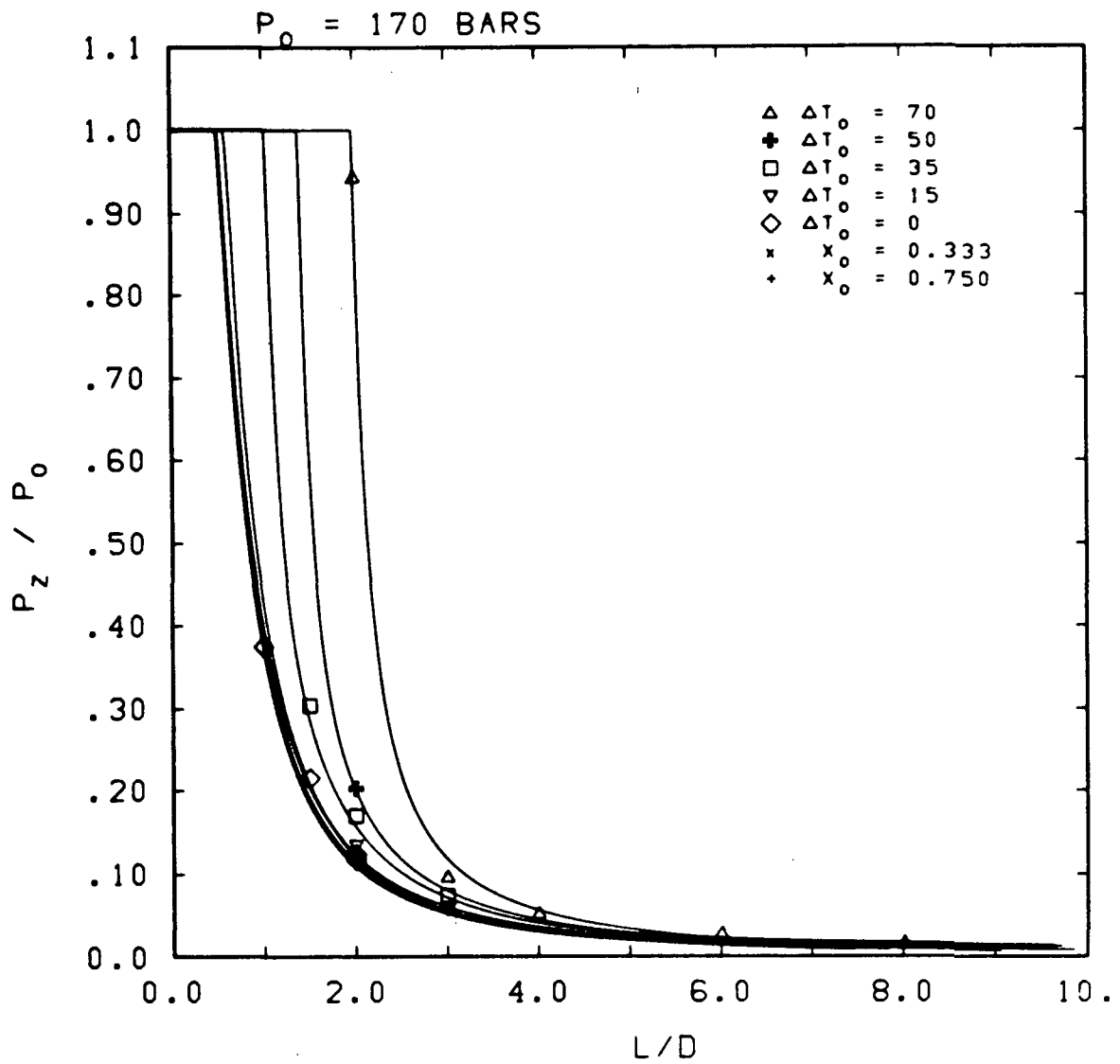
Figure 7.6   Centerline target pressure as a function of the
distance to the target (L/D) and the stagnation
properties.   Comparison of the jet load model
with computational data base.

113

centerline-target, stagnation pressure as a function of distance from the break (L/D) for stagnation pressures between 60 and 170 bars and both saturated and subcooled stagnation temperatures (ΔT_O = 70 ^{O}C to X_O = .75). The data symbols in the figures indicate centerline target pressures taken from the CSQ data base and used to obtain values for α and β in equations (7.2) and (7.3). Note the very rapid fall off in target pressure when L/D is slightly larger than L_C/D. This behavior can easily account for wide disparity in experimental results that were run under "identical" conditions. Additionally, these results re-emphasize the results of Section 4.2 where it was shown that powerfully destructive pressures occur on targets existing at L/D's less than L_C/D.

7.2 Radial Stagnation Pressure Model

The analytic radial load model introduced in Section 6.3 coupled with a curve fitting procedure forms the radial stagnation pressure model. This model provides a family of profiles that are a function of the break stagnation conditions and L/D. This approximate model was shown to agree well with data and the computational data base for saturated stagnation conditions (agreement best at large L/D's, L/D > 4). However, for subcooled stagnation conditions that have small L/D's the comparison between the approximate models and the CSQ data base was not good. Curve fitting was performed to increase the comparison between the approximate model and the CSQ data base. A brief description of the radial model follows; details of the approximate models were given in Chapter 5.

The centerline model in Section 6.2 uses z, the coordinate length normal to length along the target, to evaluate the thermodynamic conditions just upstream of the shock. Then the normal shock equations and isentropic compression relations are used to evaluate the stagnation conditions downstream of the shock. The radial stagnation pressure model uses equation (6.1) and assumes an isentropic expansion, thus

$$S = S_O = \text{constant} \tag{7.4}$$

and

$$(\rho V)_2 = (\rho V)_1 \, \frac{D}{2z^*} \quad , \quad z^* \geq \frac{1}{2} D \quad , \tag{7.5}$$

where z^* is the absolute value of the vectorial sum of the two coordinate lengths (z,r) describing points on the target, thus

$$z^* = \sqrt{z^2 + r^2} \, .$$

Figure 7.7 shows the geometry used in the radial jet expansion model. The oblique shock surface found in all of the baseline

114
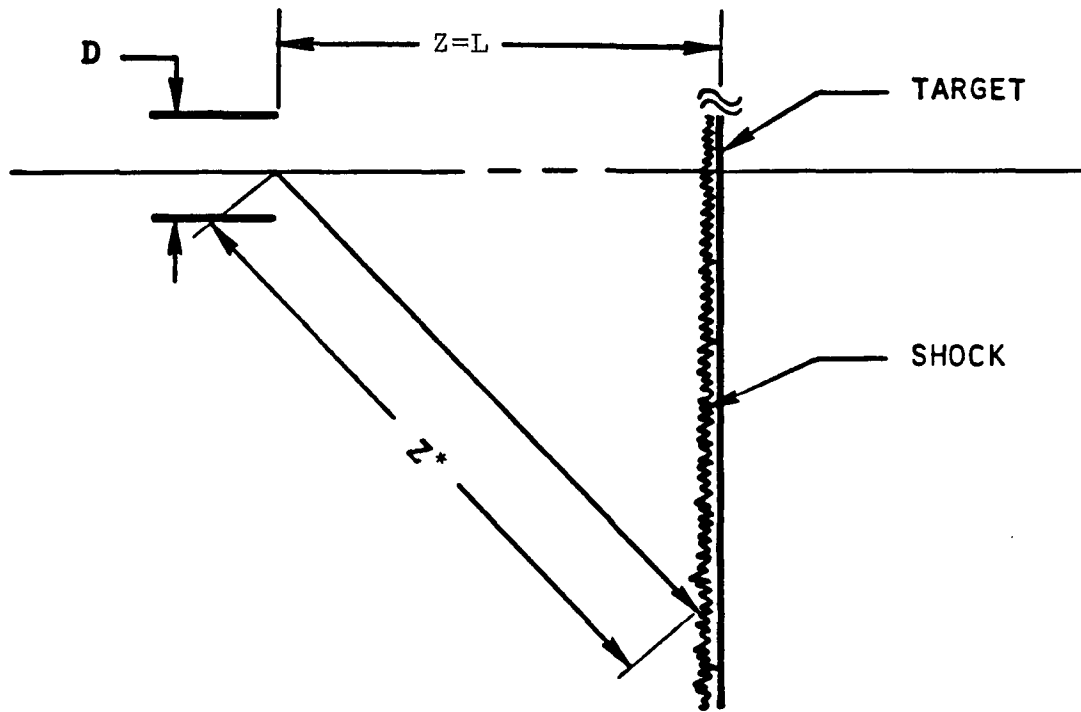
Figure 7.7 Geometry for the radial two-phase
jet load model.

CSQ calculations was modeled as a planer surface normal to the break centerline at a distance L from the pipe break, i.e., the shock surface and target surface are coincident. The conditions downstream of the shock are evaluated using

$$\rho_2 \, V_2 \, \sin\phi = \rho_3 \, V_3 \, \sin\phi$$

$$P_2 + \rho_2 \, V_2^2 \, \sin^2\phi = P_3 + \rho_3 \, V_3^2 \, \sin^2\phi \qquad (7.6)$$

where $\phi = \tan^{-1}(z/r)$; $z = L$, $0 < r < R$.

The stagnation conditions on the target are evaluated using the conditions downstream of the shock and by imposing an isentropic compression where the velocity normal to the target ($V_3 \sin\phi$) is brought to rest. The resulting pressure distributions were normalized using the centerline pressure evaluated with the engineering model; the final pressure distributions were then calculated from these normalized curves using the centerline pressure model in Section 7.2.

Target loads are then calculated by integrating the stagnation pressure distribution

$$F_r = 2\pi \int_0^R (P_T - P_A)r\,dr \; ; \; 0 \leq R \leq R_A \; , \qquad (7.7)$$

where P_T Target Pressure
  P_A Ambient Pressure
  R_A Radius where $P_T = P_A$

The ambient pressure, P_A, in this study was held fixed at 1.0 bar. Therefore, the radial pressure curves were only integrated out to a $R = R_A$ where $P_T = 1.0$ bar. For all radii greater than R_A the pressure was assumed to be constant and equal to P_A. This is only an approximation of the actual behavior of the target pressure for $r > R_A$; the actual behavior was discussed earlier in Section 3.7 and is illustrated in Figure 7.8a. The pressure on the target drops below P_A because of an over expansion of the jet flow; this over expansion of the flow is followed by a shock wave to provide for merging of the pressure in the jet with the ambient condition. The area on the target where ($P_T - P_A$) is negative acts to reduce the target load as shown in Figure 7.8b. In this region of the target a small negative value of ($P_T - P_A$) can have a significant effect on the load calculation because of the large areas associated with radii greater than R_A. This effect was neglected in this model and all model load calculations were halted when the maximum load, illustrated in Figure 7.8b, was reached. The

116

TARGET PRESSURE, P_T

P_A

RADIUS/D

(a)

TARGET LOAD

RADIUS/D
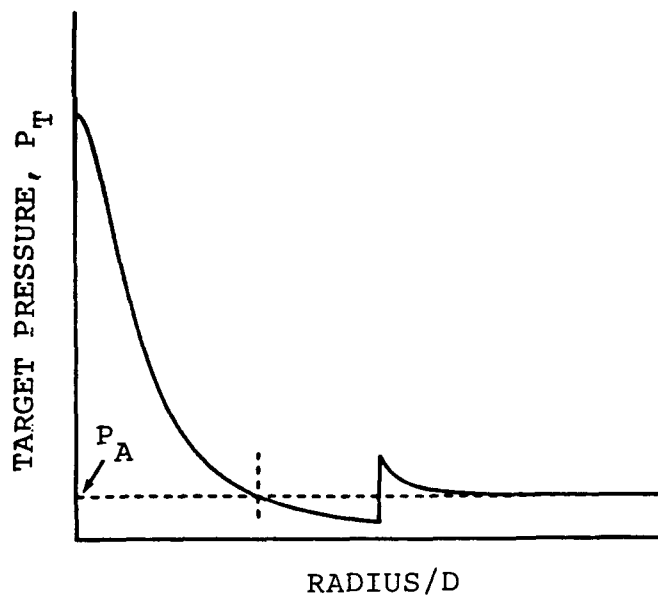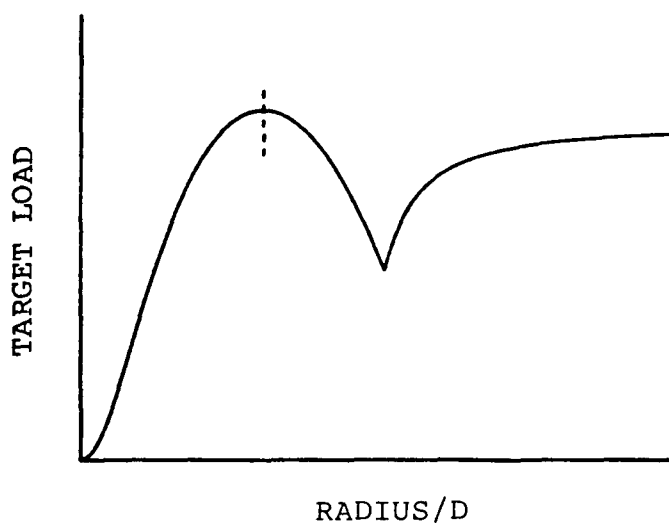
(b)

Figure 7.8 Illustration showing the two-phase jet behavior at large radii. Note the shock wave that forms because the jet expands beyond the ambient pressure.

1.0 bar pressure cut off occurred mostly in the range $4 \leq R/D \leq 10$, depending upon the initial conditions, but the shock occurs at large R -- R/D > 10 to 20. The calculations were cut off at the 1.0 bar limit because to accurately compute the solutions out to and beyond the shock would require a large grid, thus greatly increasing the costs to produce one point in the data base. Also the shock location does not easily scale and would ultimately lead to another parameter in the load model. Finally, because the flow is supersonic at the point where $P_T = 1.0$ bar a correction for ambient pressures other than 1.0 bar would be to simply add to the load, equation (7.5), the value $(1.0 - P_A) \pi R^2$. This correction is only valid when $(1.0 - P_A)$ is small.

Comparison of this radial model to the CSQ baseline calculations showed an excellent agreement of both radial profiles and radial loading for saturated flow at the break; however, in the case of subcooled flows when L/D was small (< 4) the agreement between the model and baseline calculations was poor. To correct the model for subcooled flow at small values of L/D a parametric fitting procedure, similar to the one used in Section 7.2, was used to improve the comparison between the baseline CSQ data base and the load model. Basically, the procedure was to minimize the least squared error of the target load between the CSQ data base and the load model by sliding the model's pressure distribution along the radial axis an amount ΔR where

$$\lim_{R \to 0} \Delta R = 0,$$

and for R>>0, $\Delta R \longrightarrow$ constant.

The final model was presented in Chapter 2 and detailed charts for a wide range of PWR and BWR applications are provided in Appendix A.

One final note concerns the sensitivity of the load curves at large radii. Because the area is large at large radii, a small change or error in the pressure will result in a significant change in the cumulative load $(\sim \pi \Delta P R^2)$. Therefore some care is necessary when applying the load model to large targets, especially for targets with large L/D's.

7.3 Experimental Verification

Experimental verification of the final two-phase jet load model is not straightforward because of the small amount of experimental data that exists with stagnation pressures in the 60-170 bar range. Also, most data in the 60-170 bar range was recorded in small scale facilities. A certain amount of the experimental data base, such as Marviken data[8] or Ontario Hydro data,[25] was utilized in verifying the methods used to obtain the approximate model, but

118

cannot be used to verify the final load model because the pressures
are too low. The data taken at the higher pressures and used here
to verify the load model are reported in References 27, 28, and 29.
Reference 27 reports Kraftwerk Union (KWU) data for steady impinging
jets operating at saturated conditions for stagnation pressures
varying between 30 to 100 bars; a schematic illustrating the test
arrangement is shown in Figure 7.9. References 28 and 29 report
blow-down tests performed by Battelle-Frankfurt for virtually
identical initial conditions of 140 bars and 30°C subcooled
(~ 300°C); a schematic illustrating the test arrangement is
shown in Figure 7.10. Additional discussion of both of these sets
of data can be found in Reference 9.

Figures 7.11 to 7.14 show the KWU data comparisons. The
stagnation conditions for these data were nominally 100 bars and
saturated liquid; however, in each case the actual data showed
vessel stagnation conditions between 92 and 96 bars. Because the
listed experimental pressure uncertainty was about 10% and because
there is some total pressure loss between the vessel and the nozzle,
the exact stagnation pressure is not precisely known; however, it
does range between 80 to 100 bars. Therefore, in Figures 7.11 to
7.14 target pressure distribution curves for stagnation conditions
of 80 to 100 bars and saturated liquid are plotted. Figures 7.11 to
7.14 show the data comparisons for L/D's of 1, 2, 3 and 5,
respectively; the comparison is very good. These data were not
connected, in any way, with the model development -- only the CSQ
data base was used. Additionally, the good comparison between the
model and experiment confirms the nondimensional behavior of the jet
for different L's and D's indicated by the equations in Section 3.3.

The data comparisons for the Battelle-Frankfurt data were more
difficult to perform than the KWU data comparisons; this was because
the blow-down network was complicated (consisting of two inter-
connected vessels), and the measurements reported in References 28
and 29 did not provide the necessary upstream total conditions. The
facility diagram in Figure 7.10 showed two vessels -- a pressure
vessel and a surge flask (small vessel). It is the stagnation
conditions in the small vessel that govern the load on the target.
There is, however, no reporting of the conditions in the small
vessel in References 28 and 29. Additionally, a clear definition of
the target L/D is not possible.

Figure 7.15 shows the nozzle geometry. CSQ calculations
(Chapter 4) have shown that highly subcooled jet flows expand at
large half angles, most with a half angle greater than 80 to 90
degrees. However, the geometry in Figure 7.15 shows that the jet is
confined by a nozzle half angle of 30 degrees for 40 mm (0.4 D). As
a result the nozzle has an effective L/D that lays between L/D = 2.0
and L/D = 2.4 depending upon the vessel conditions; the higher the

119
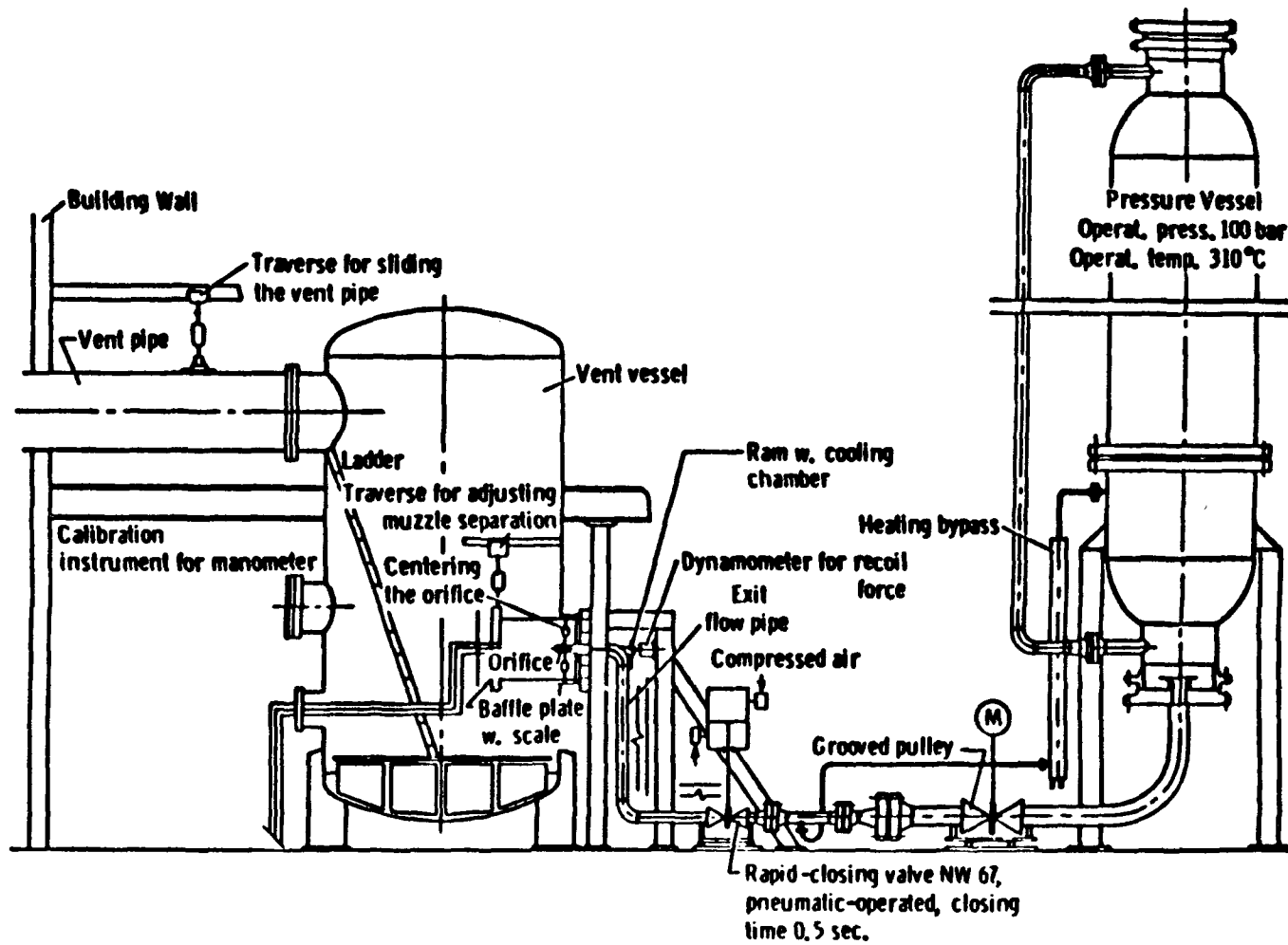
Figure 7.9   Kraftwerk Union blow down and two-phase
             jet load test facility (see Reference 27).
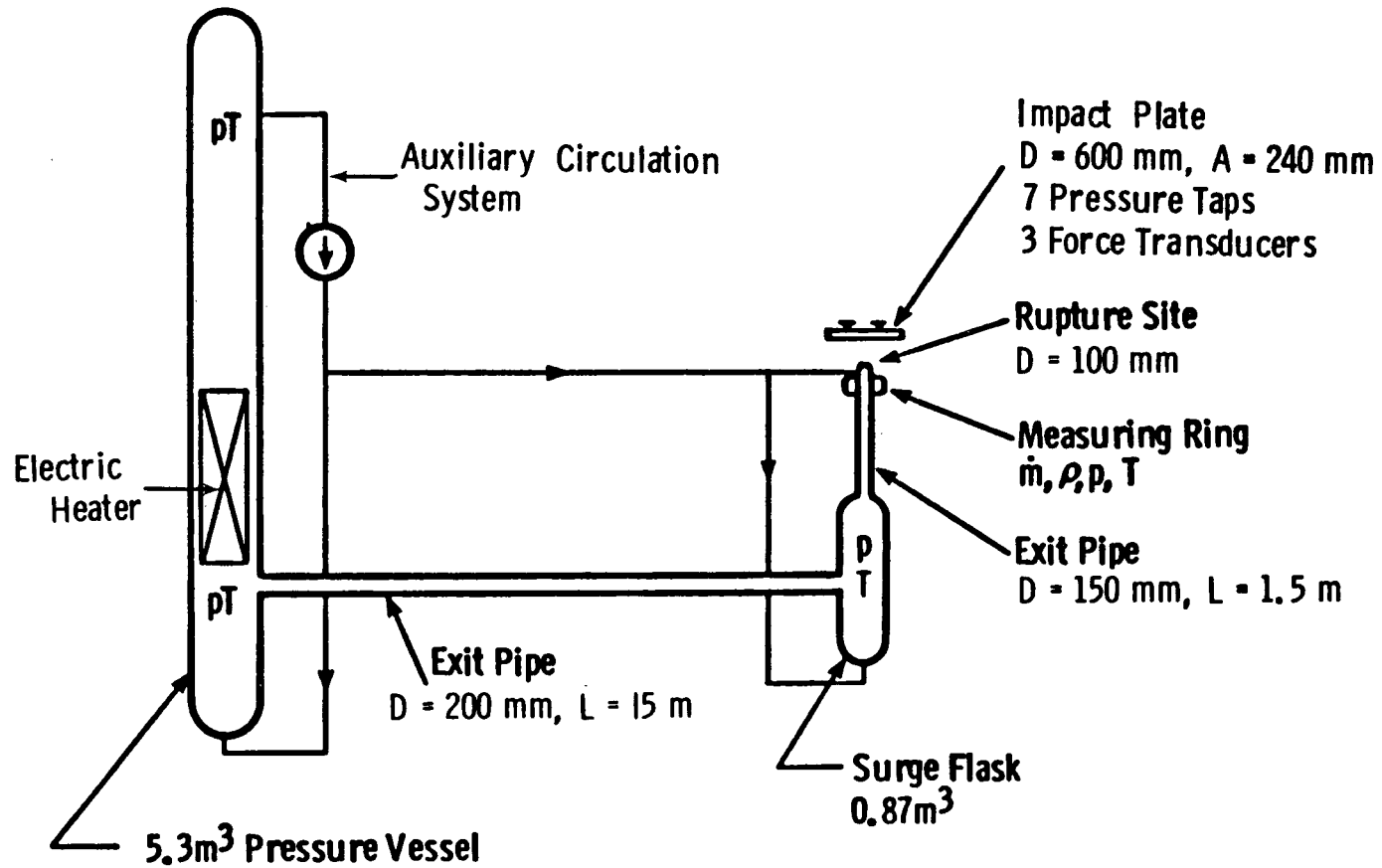
Figure 7.10   Illustration showing the Battelle-Frankfurt RS-50
test system.
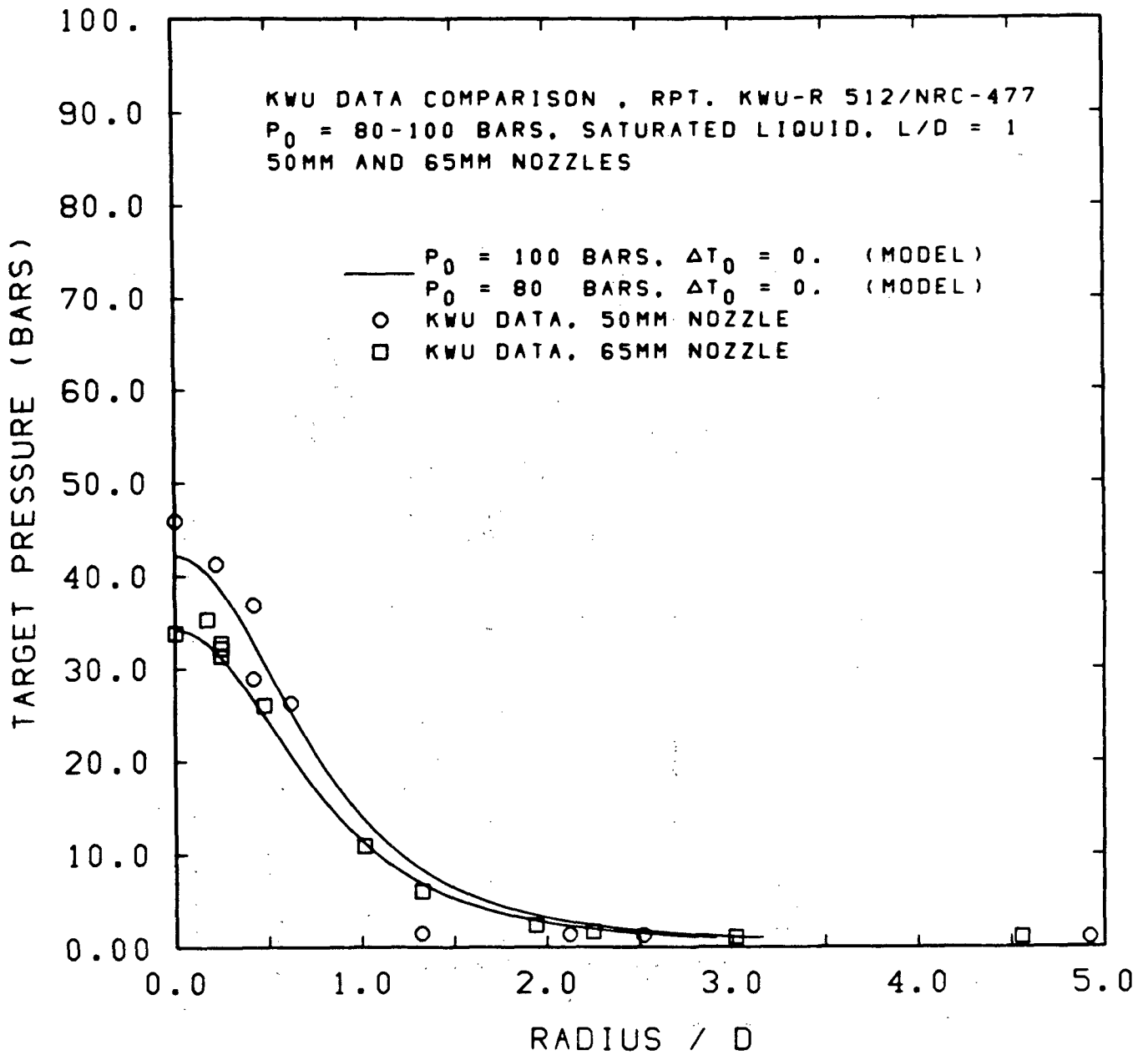
Figure 7.11 Comparison between KWU data and the two-phase jet load model for L/D = 1.
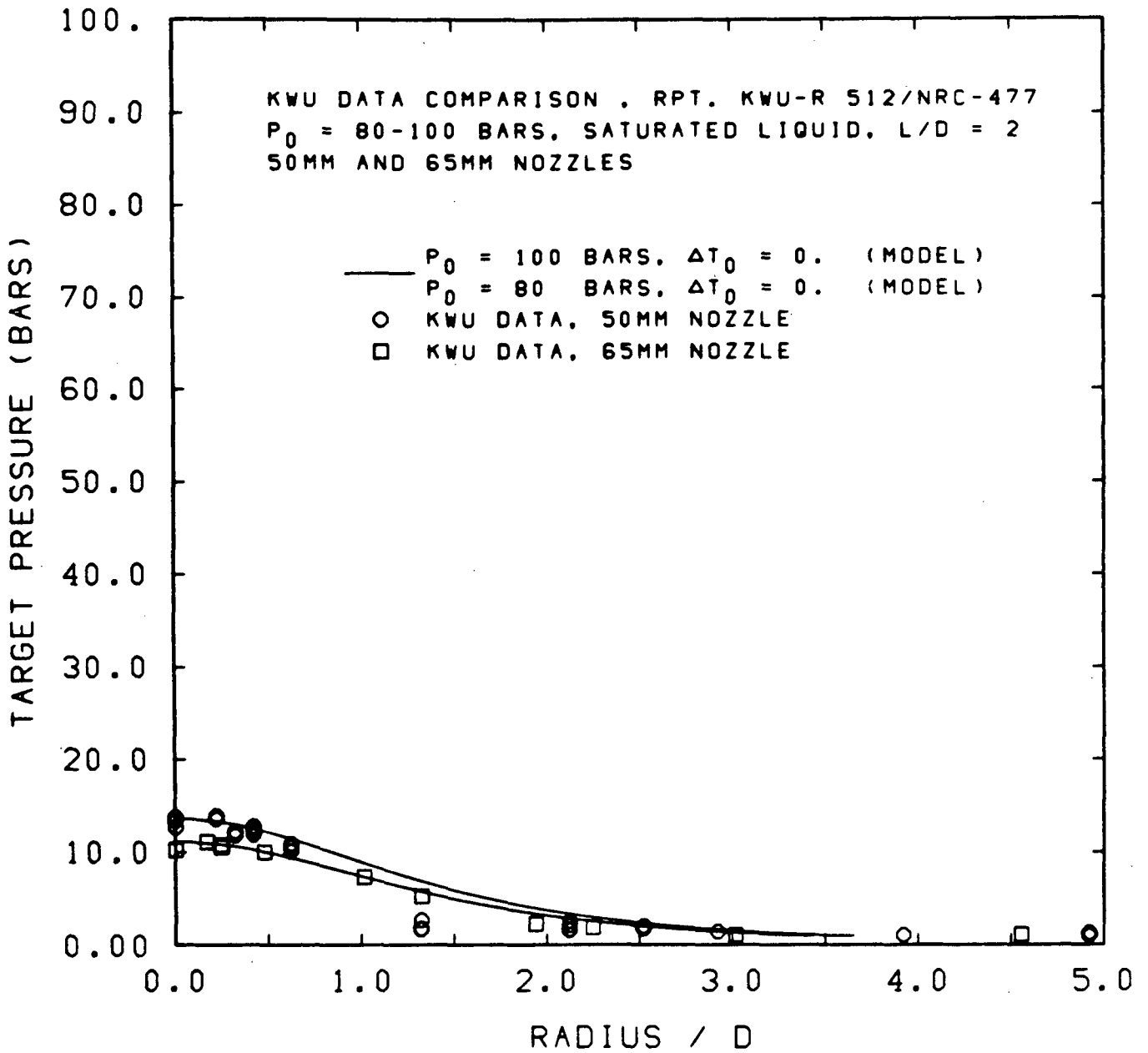
Figure 7.12   Comparison between KWU data and the two-phase jet
load model for L/D = 2.
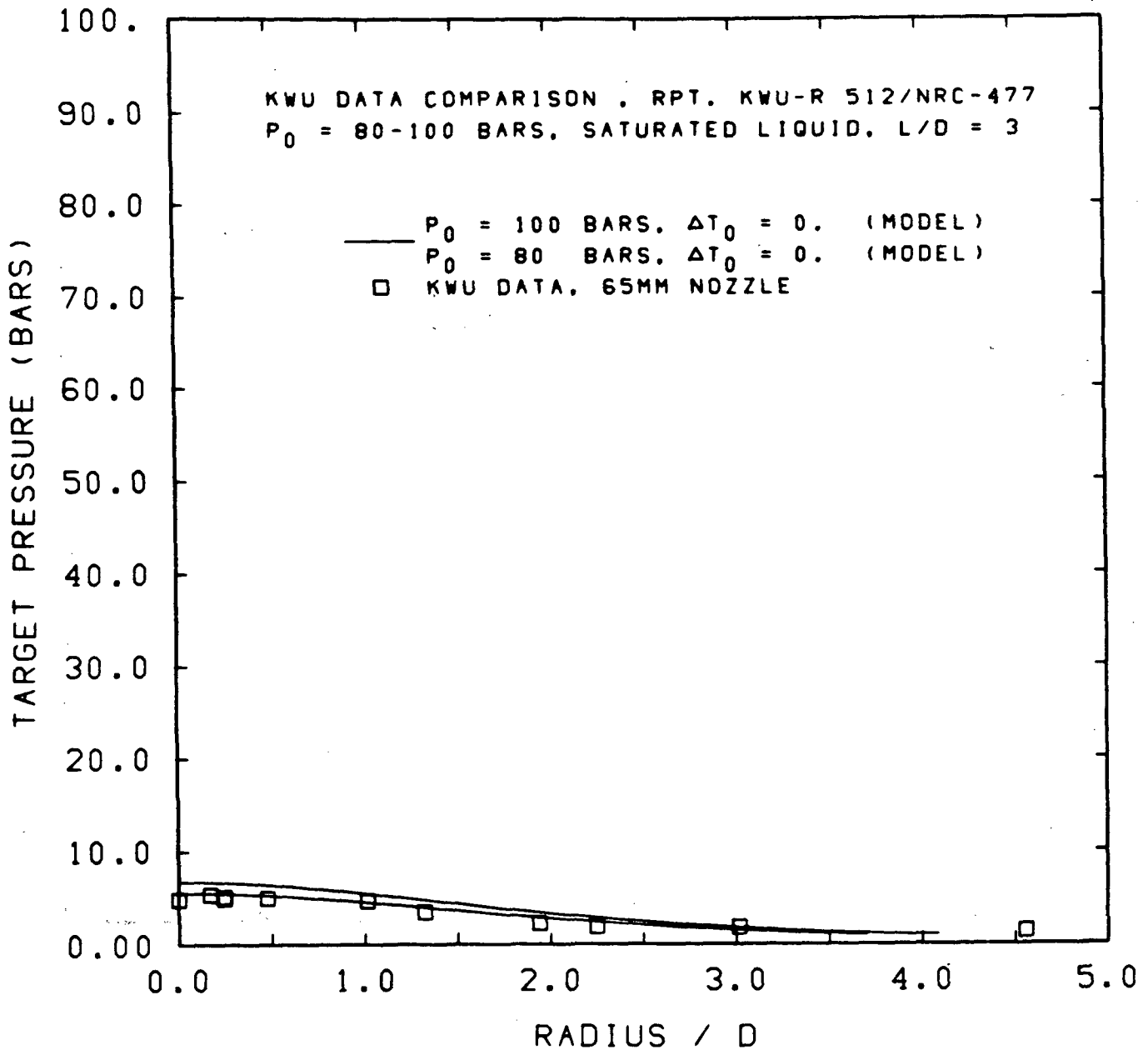
Figure 7.13   Comparison between KWU data and the two-phase jet
load model for L/D = 3.
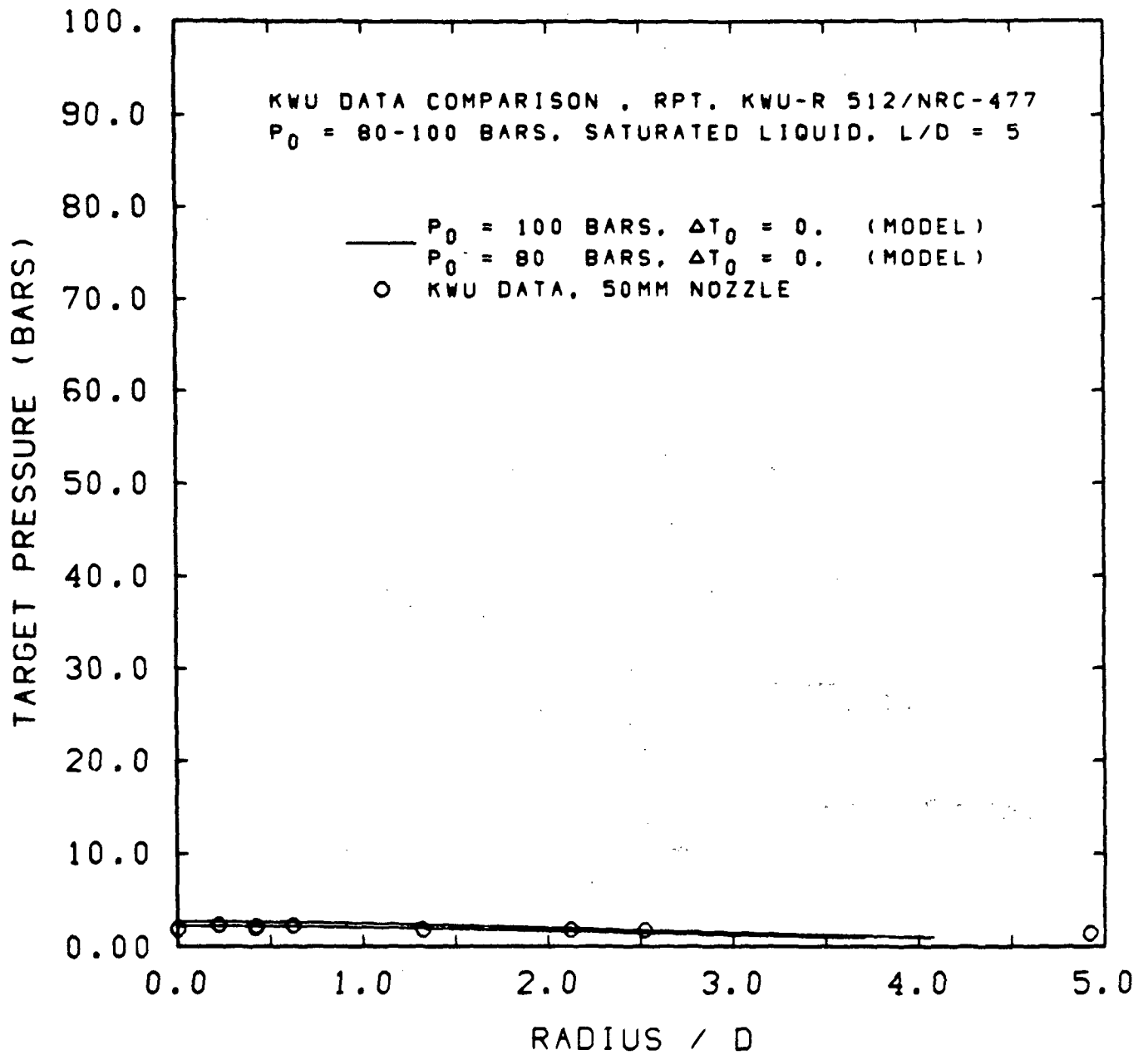
Figure 7.14 Comparison between KWU data and the two-phase jet load model for L/D = 5.

125
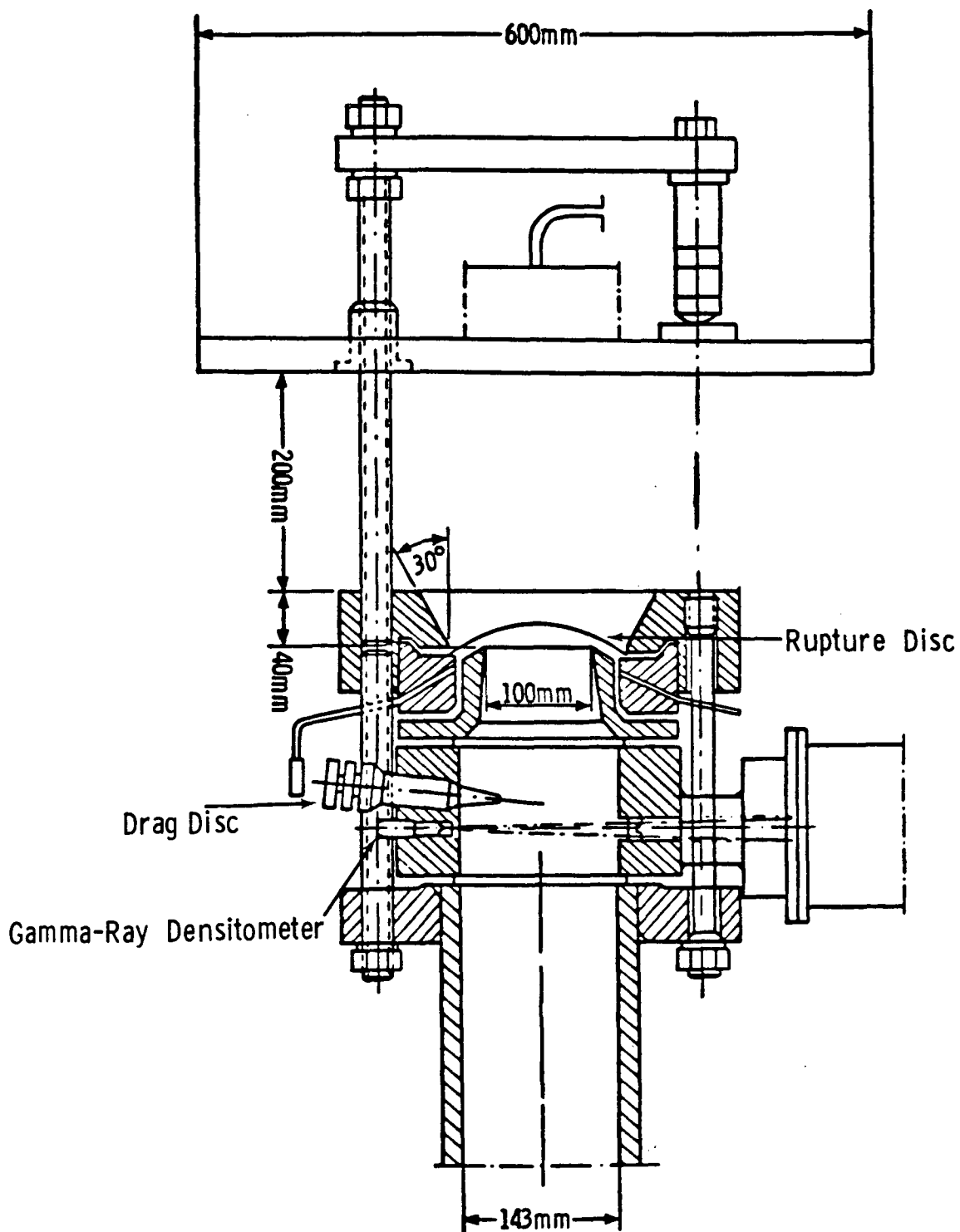
Figure 7.15 Battelle-Frankfurt RS-50 nozzle configuration.

degree of subcooling the closer this effective L/D will come to
2.0. The effect of this nozzle design coupled with the target
location leads to a situation where the target pressures (or load)
are very sensitive to the degree of subcooling. For example
consider conditions not unlike those in the Battelle blow downs:
P_O = 80 bars, ΔT_O = 35°C to 50°C. When this range of
thermodynamic conditions is examined using Figure 4.3 or Figure 7.2,
we find that (L/D - L_C/D) is small, and the slope of the
centerline pressure curve (Figure 7.2) is steep and extremely
sensitive to subcooling. This effect is readily seen in the
Battelle data. In the Battelle C11 experiment (Reference 28) and
C12 experiment (Reference 29) the thermodynamic conditions upstream
of the break are, within experimental accuracy, identical.
However, downstream of the break on the target there are
differences in target pressure, measured at the same time and
location in the blow down, of 30 bars or more (see Figures 7.17 and
7.18). These differences are caused by the sensitivity of the
experiment to subcooling and subsequent differences in effective
L/D. The extreme sensitivity displayed by Figures 7.1 to 7.6 of the
target conditions for subcooled flows at small L/D to small changes
in thermodynamic conditions can explain widely varying target
pressures or loads for "identical" vessel conditions. In fact
Figures 7.1 to 7.6 explain experimental results that have in the
past been incorrectly interpreted as dynamic effects.

As indicated above the experimental reports C11 and C12 did not
contain the small vessel conditions; the data comparisons were,
therefore, performed by two methods. First, experimental pressures
and temperatures measured near the small vessel were assumed to be
representative of the small vessel conditions, and secondly, the
small vessel conditions were taken from a CSQ model of the Battelle
experiment.

The data comparisons to be shown here are the centerline
pressure on a target as a function of the blow-down time, t. The
load model theory used in making these comparisons is given in
Section 7.1. Although some radial profile information exists for
the Battelle experiments, these comparisons were not performed. The
centerline pressures are the most difficult to predict and will
govern any radial comparisons.

In case one the pressure in the pipe connecting the large and
small vessels (PS 194) and the temperature at the break exit (TS270)
were assumed to be representative of the small vessel conditions
(jet stagnation conditions); these two curves are given in Figure
7.16. The error introduced by this assumption is unknown. The
pressure trace, PS194, was subject to considerable fluctuation while
the temperature, TS270, in the exit was relatively constant.
Consequently, the data comparisons were performed by plotting the
target pressure resulting from the upper and lower bound on the PS

127
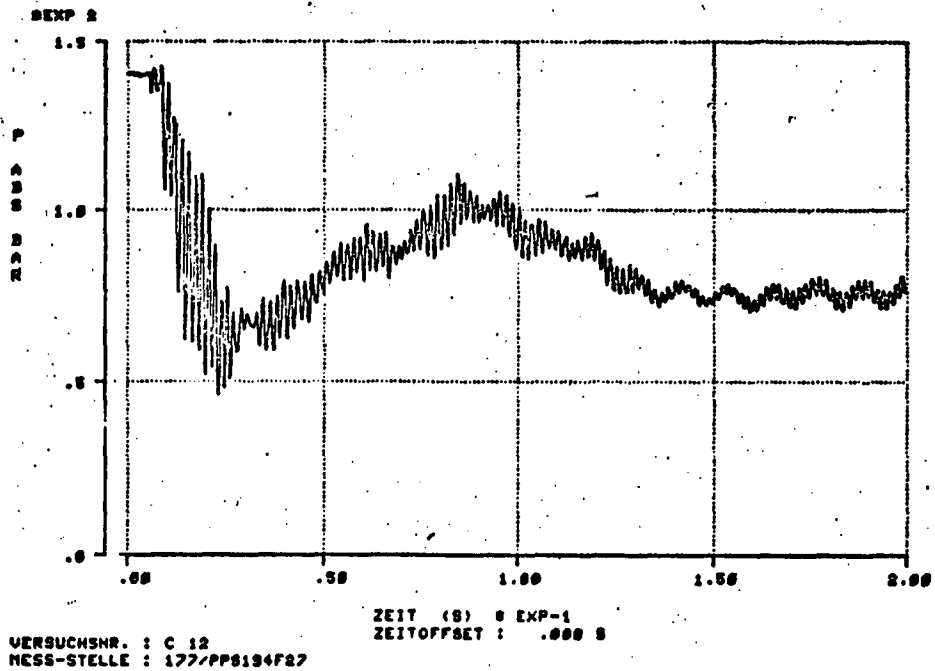
(a)
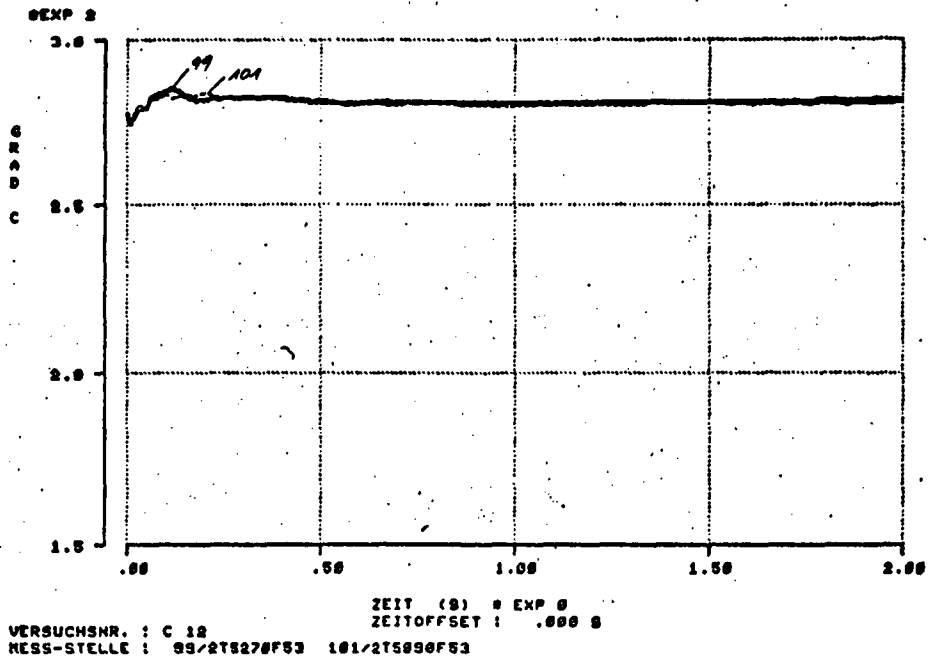
(b)

Figure 7.16   Pressure and temperature measured for
experiment RS-50-Cl2 and used to evaluate
the upper and lower bound stagnation
conditions for Figures 6.17 and 6.18.
(a) PS194, (b) TS270.

128

194 pressure trace; moreover, the results were plotted for a target L/D of 2.0 (effective L/D equal to 2.0). Figures 7.17 and 7.18 show these comparisons for the C11 and C12 experiments; these curves show the load model predictions plotted on the C11 and C12 target pressure histories taken from References 28 and 29. These comparisons illustrate the strong influence of subcooling (pressure). This comparison is actually quite good when one considers the wide variation in the target data for C11 and C12 experiments, which have "identical" initial conditions. The shape of both curves is predicted, and for the most part the C11 amplitude is predicted. In Figures 7.17 and 7.18 the pressure uncertainty resulted in widely differing predictions (70 bars) for the initial portion of the blowdown. This result shows the sensitivity of pressure loading results to the initial thermodynamic conditions for subcooled states. Furthermore, these results show that the discrepencies between tests C11 and C12 are most likely due to small thermodynamic differences in their initial conditions and not any dynamic effects.

The second comparison technique was to use the small vessel conditions predicted with a CSQ model of the Battelle-Frankfurt blow down.[10] These calculations were performed early in the two-phase jet program, and the results showed excellent agreement with pressure and temperature data in the large tank and system piping and the break flows showed good agreement. The centerline target pressures predicted with the load model using the small vessel conditions from the CSQ calculation are given in Figures 7.19 and 7.20 for C11 and C12, respectively. Again, the model predictions are plotted on the C11 and C12 target pressure histories taken from References 28 and 29. The comparison is given by L/D's of 2.0 and 2.4, thus bounding the range of effective L/D. Again, in view of the wide variation that exists between the C11 and C12 target data, the comparison is quite good; the shape of both curves is predicted and for the most part the amplitude in C11 is predicted.

Finally, Figures 7.21 and 7.22 show the load model pressure prediction for the saturated portion of the blow down (t > .3 to .4 s). The agreement is excellent. Recall that the effective L/D will be nearest L/D = 2.4 in the case of saturated, small-vessel conditions.
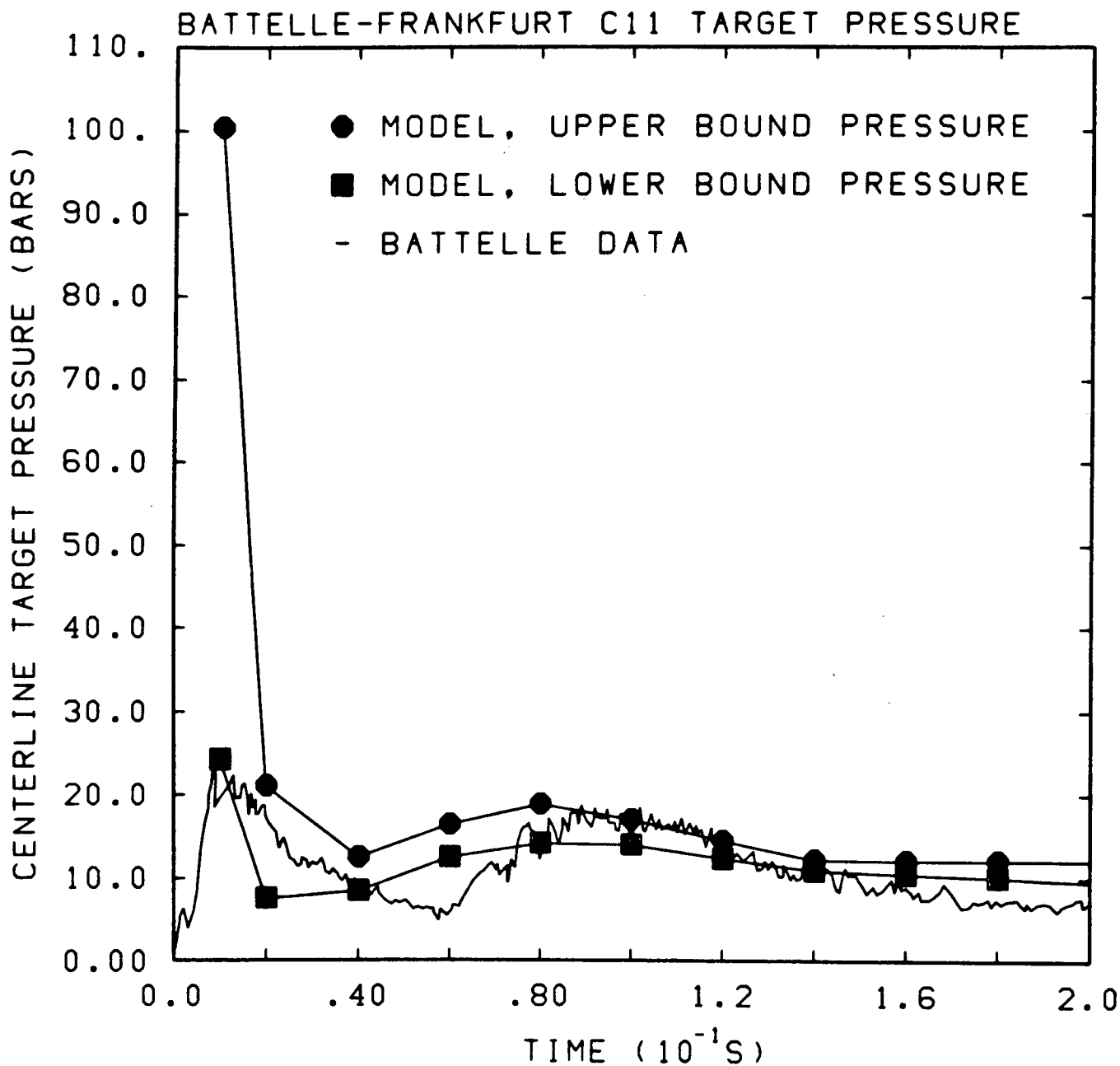
Figure 7.17   Two-phase jet load model and Battelle-Frankfurt
RS-50-C11 data comparison. Stagnation conditions
were approximated using RS-50 measurements;
upper and lower bound approximations were made.

130
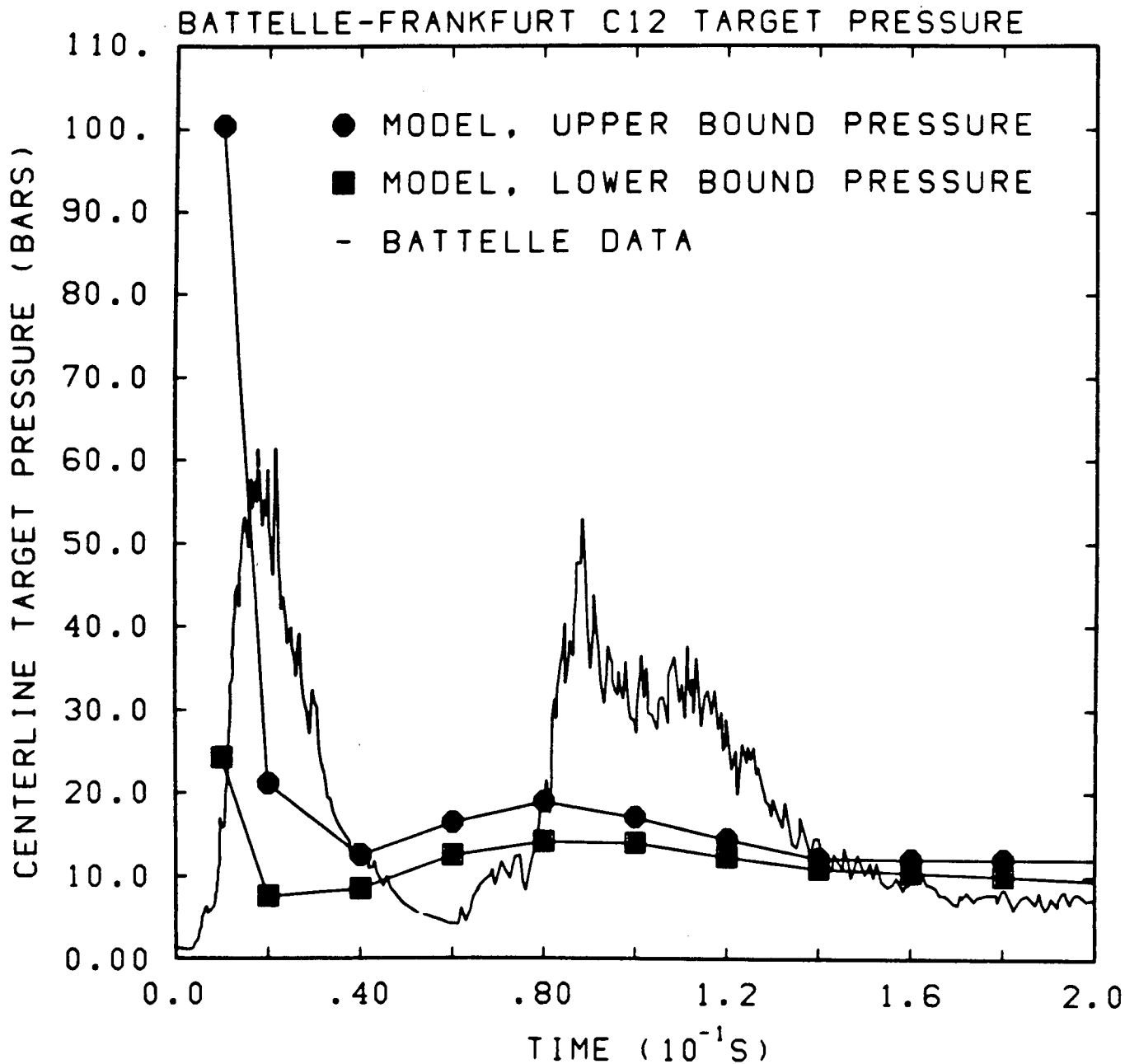
Figure 7.18   Two-phase jet load model and Battelle-Frankfurt
RS-50-Cl2 data comparison. Stagnation conditions
were approximated using RS-50 measurements;
upper and lower bound approximations were made.

131

Figure 7.19   Two-Phase jet load model and Battelle-Frankfurt
RS-50-C11 data comparison. Stagnation
conditions were provided from a CSQ model of
the C11 experiment.

132
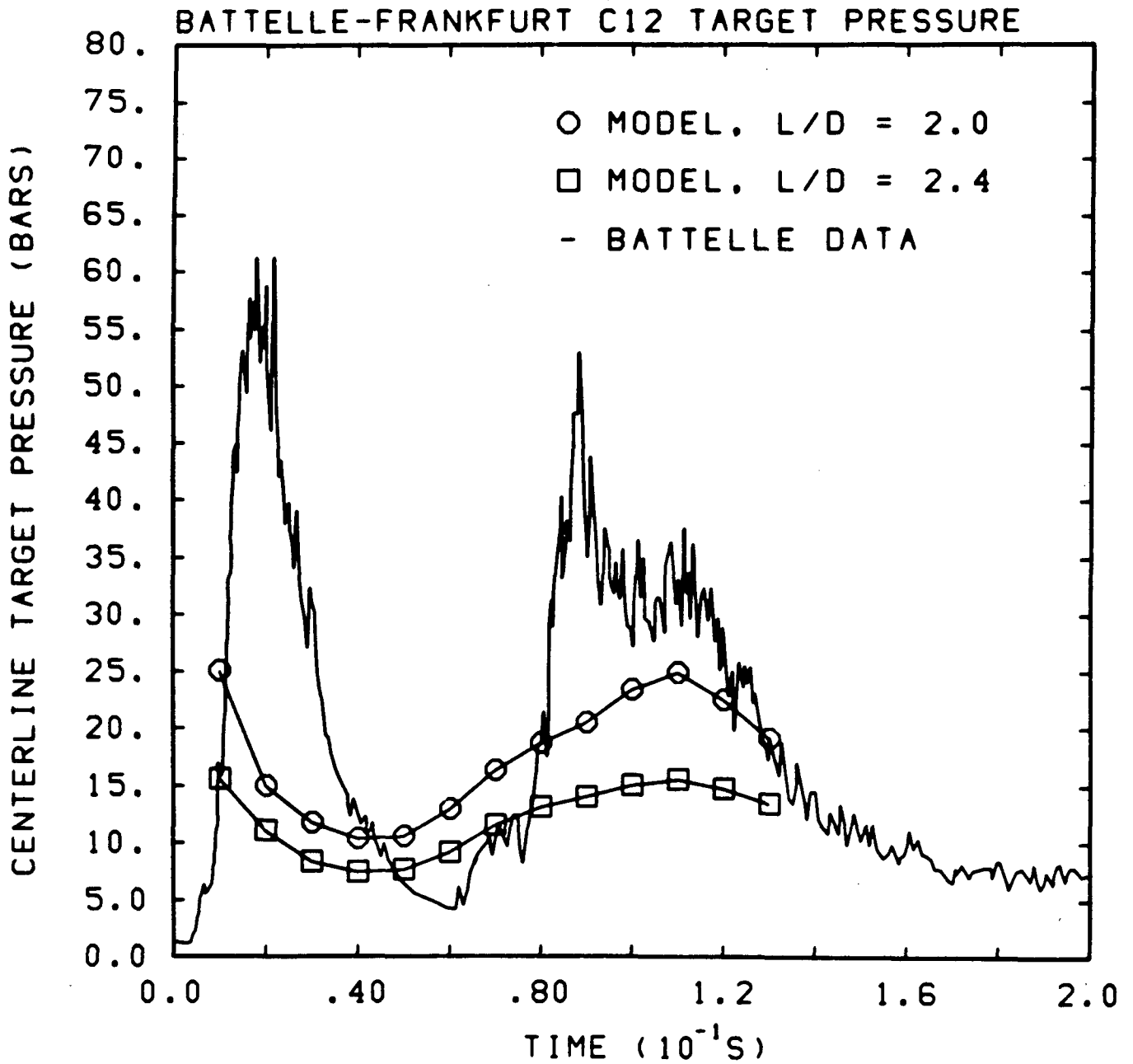
Figure 7.20   Two-phase jet load model and Battelle-Frankfurt
RS-50-Cl2 data comparison. Stagnation conditions
were provided from a CSQ model of the Cl2
experiment.

Figure 7.21   Two-phase jet load model and Battelle-Frankfurt
RS-50-C11 data comparison. Stagnation
conditions were saturated and were provided
by measurements at the exit nozzle.

134
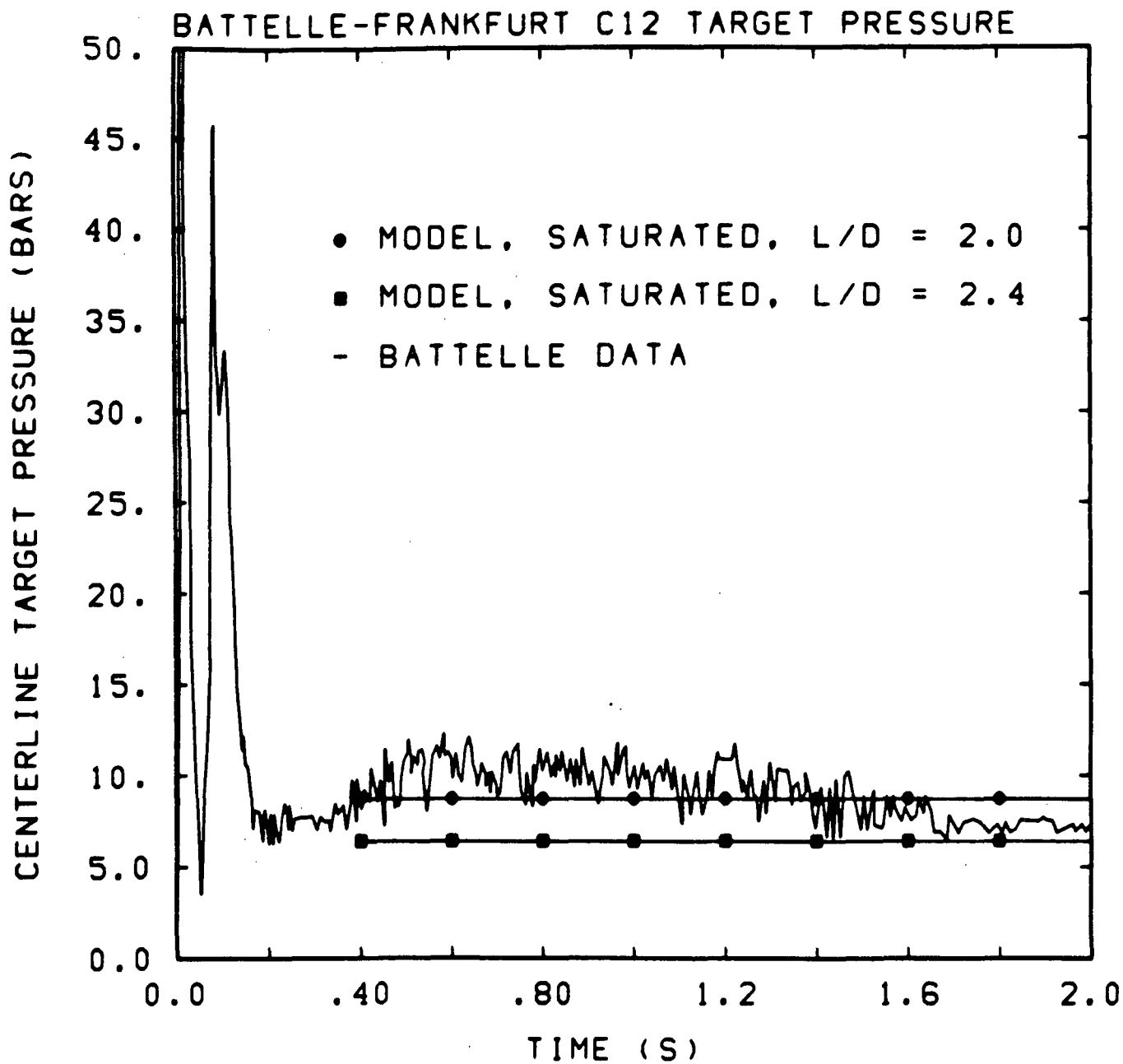
Figure 7.22   Two-phase jet load model and Battelle-Frankfurt
RS-50-C12 data comparison. Stagnation
conditions were saturated and were provided
by measurements at the nozzle exit.

REFERENCES

1. Moody, F. J., "Fluid Reaction and Impingement Loads," Specialty Conference on Structural Design of Nuclear Plant Facilities, Vol. 1, Chicago, Illinois, December, 1973.

2. American National Standard: Design Basis for Protection of Light Water Nuclear Power Plants Against Effects of Postulated Pipe Rupture, ANSI/ANS-58.2-1980, American Nuclear Society, LaGrange Park, IL, 1980; or see

   Watts Bar Nuclear Plant Final Safety Analysis Report, Section 3.6, Tennessee Valley Authority; or see

   Grand Gulf Nuclear Station Final Safety Analysis Report, Section 3.6, Middle South Utilities Systems.

3. U. S. Nuclear Regulatory Commission, Standard Review Plan for the Review of Safety Analysis Reports for Nuclear Power Plants, LWR Edition, NUREG-0800, Section 3.6.2, Office of Nuclear Reactor Regulation, July, 1981.

4. TRAC-P1A: An Advanced Best Estimate Computer Program for PWR LOCA Analysis, LA-7777-MS (NUREG/CR-0665), Safety Code Development Group, Energy Division, Los Alamos Scientific Laboratory, Los Alamos, NM, May 1979.

5. RELAP4/MOD6, A Computer Program for Transient Thermal/Hydraulic Analysis of Nuclear Reactors and Related Systems, User's Manual, CDAP TR-003, Idaho National Engineering Laboratory, January 1979.

6. RETRAN - A Program for One-Dimensional Transient Thermal-Hydraulic Analysis of Complex Fluid Flow Systems, EPRI CCM-5, Energy Incorporated, Idaho Falls, Idaho, 1978.

7. Centi, R., Faravelli, M., Gaspari, G. P., and Lo Nigro, F., "Fog Test Facility Performances, Programs, and Results," Workshop on Jet Impingement and Pipe Whip, Genoa, Italy, June 29-July 1, 1981, Ansaldo Impianti, SIS-81-R-06, July 1981.

8. The Marviken Project, "The Marviken Full-Scale Jet Impingement Tests, Fourth Series," Report Series MXD-200[S], Joint Reactor Safety Experiments in the Marviken Power Station, Sweden, 1980-1981.

9. Thompson, S. L., Thermal/Hydraulic Analysis Research Program Quarterly Report, April-June 1980, SAND80-1091, Sandia National Laboratories, Albuquerque, NM, August 1980.

10. Thompson, S. L., Thermal/Hydraulic Analysis Research Program Quarterly Report, July-September 1980, SAND80-1091, Sandia National Laboratories, Albuquerque, NM, November 1980.

11. Tomasko, D., Two-Phase Jet Loads Fiscal Year 1979 Annual Report, SAND 80-0267, Sandia National Laboratories, Albuquerque, NM, March 1980.

12. Thompson, S. L., Thermal/Hydraulic Analysis Research Program Quarterly Report, January-March 1980, SAND80-1091, Sandia National Laboratories, Albuquerque, NM, May 1980.

13. Broadus, C. R., James, S. W., Lee, W. H., Lime, J. F., and Pate, R. A., BEACON/MOD2: A CDC 7600 Computer Program for Analyzing the Flow of Mixed Air, Steam, and Water in a Containment System, CDAP-TR-002, Idaho National Engineering Laboratory, December 1977.

14. Broadus, C. R., et. al., BEACON/MOD3: A Computer Program for Thermal/Hydraulic Analysis of Nuclear Reactor Containments - Users Manual, NUREG/CR-1148, EGG-2008, EG&G Idaho Inc., Idaho Falls, Idaho, April 1980.

15. Hirt, C. W., Romero, N. C., Torrey, and Travis, J. R., SOLA-DF: A Solution Algorithm For Nonequilibrium Two-Phase Flow, LA-7725-MS, NUREG/CR-0690, Los Alamos Scientific Laboratory, Los Alamos, NM.

16. Thompson, S. L., CSQ-II - An Eulerian Finite Difference Program for Two-Dimensional Material Response, Part I Materials Section, SAND77-1339, Sandia National Laboratories, Albuquerque, NM, January 1979.

17. Keenan, J. H., Keys, F. G., Hill, P. G., and Moore, J. G., Steam Tables, Wiley-Interscience Publications, New York, 1978.

18. Travis, J. R., Hirt, C. W., Rivard, W. C., "Multidimensional Effects in Critical Two-Phase Flow," Nuclear Science and Engineering, Vol. 68, pp. 338-348, 1978.

19. Moody, F. J., "Maximum Flow Rate of a Single Component, Two-Phase Mixture," Trans. of ASME, J. of Heat Transfer, Vol. 87, pp 134-142, 1965.

20. Moody, F. J., "Maximum Two-Phase Vessel Blowdown From Pipes," Trans. of ASME, J. of Heat Transfer, Vol. 88, pp. 285-295, 1966.

21. Henry, R. E. and Fauske, H. K., "The Two-Phase Critical Flow of One-Component Mixtures in Nozzles, Orfices, and Short Tubes," Trans. of ASME, J. of Heat Transfer, Vol. 93, 1971.

22. Hall, D. G., _An Inventory of the Two-Phase Critical Flow Experimental Data Base_, EGG-CAAP-5140, Idaho National Engineering Laboratory, EG&G Idaho, Inc., Idaho Falls, ID, 1980.

23. Liepmann, W. H., and Roshko, K., Elements of Gasdynamics, John Wiley and Sons, Inc., New York, 1957.

24. McGlaun, J. M., _Improvements in CSQII: An Improved Numerical Convection Algorithm_, SAND82-0051, Sandia National Laboratories, Albuquerque, NM, January 1982.

25. Shin, K. S., "Ontario-Hydro Jet Tests - Results of Free Jet Tests," Technical Memorandum, CWTM-067-FD, Westinghouse Canada, Inc., Atomic Power Division, July 1980.

26. More, J. J., "The Levenberg-Marquardt Algorithm, Implementation and Theory," _Numerical Analysis_, G. A. Watson (ed), Lecture Notes in Mathematics 630, Springer-Verlag, 1977.

27. Eichler, R., Kastner, W., Lochner, H., and Riedle, K., _Safety Project in the Area of Light Water Reactors, Studies on Critical Two-Phase Flow_, NRC-477 (translation, 1978) KWU-R-512, Kraftwerk Union, FRG, 1975.

28. Vorhaben RS 50, Untersuchung der Vorgange in einen mehrfach unterteilten Containment beim Bruch einer Kuhlmittelleitung wassergekuhlter Reaktoren, Technischer Bericht BF RS 50-32-C11-1, Battelle-Frankfurt, FRG, 1976.

29. Vorhaben RS 50, Untersuchung der Vorgange in einen mehrfach unterteilten Containment beim Bruch einer Kuhlmittelleitung wassergekuhlter Reaktoren, Technischer Bericht BF RS 50-32-C12-1, Battelle-Frankfurt, FRG, 1976.

APPENDIX A

TWO PHASE JET LOAD MODEL

This appendix contains the target pressure distribution, load distribution, and target pressure contours for two-phase jets impinging on axisymmetric targets. A complete description of these charts is provided in Chapter 2. Chapter 2 also provides instruction concerning their application.
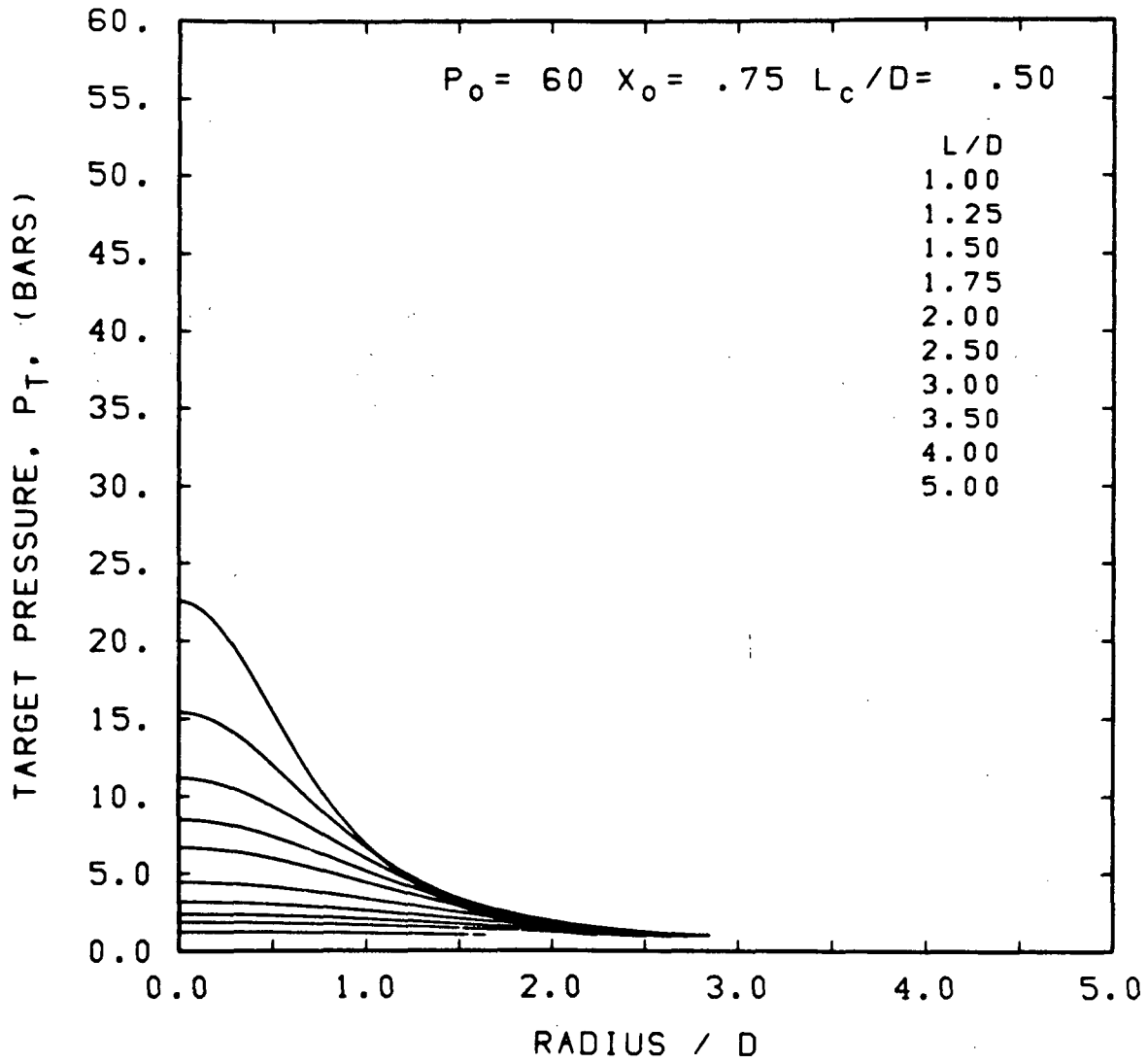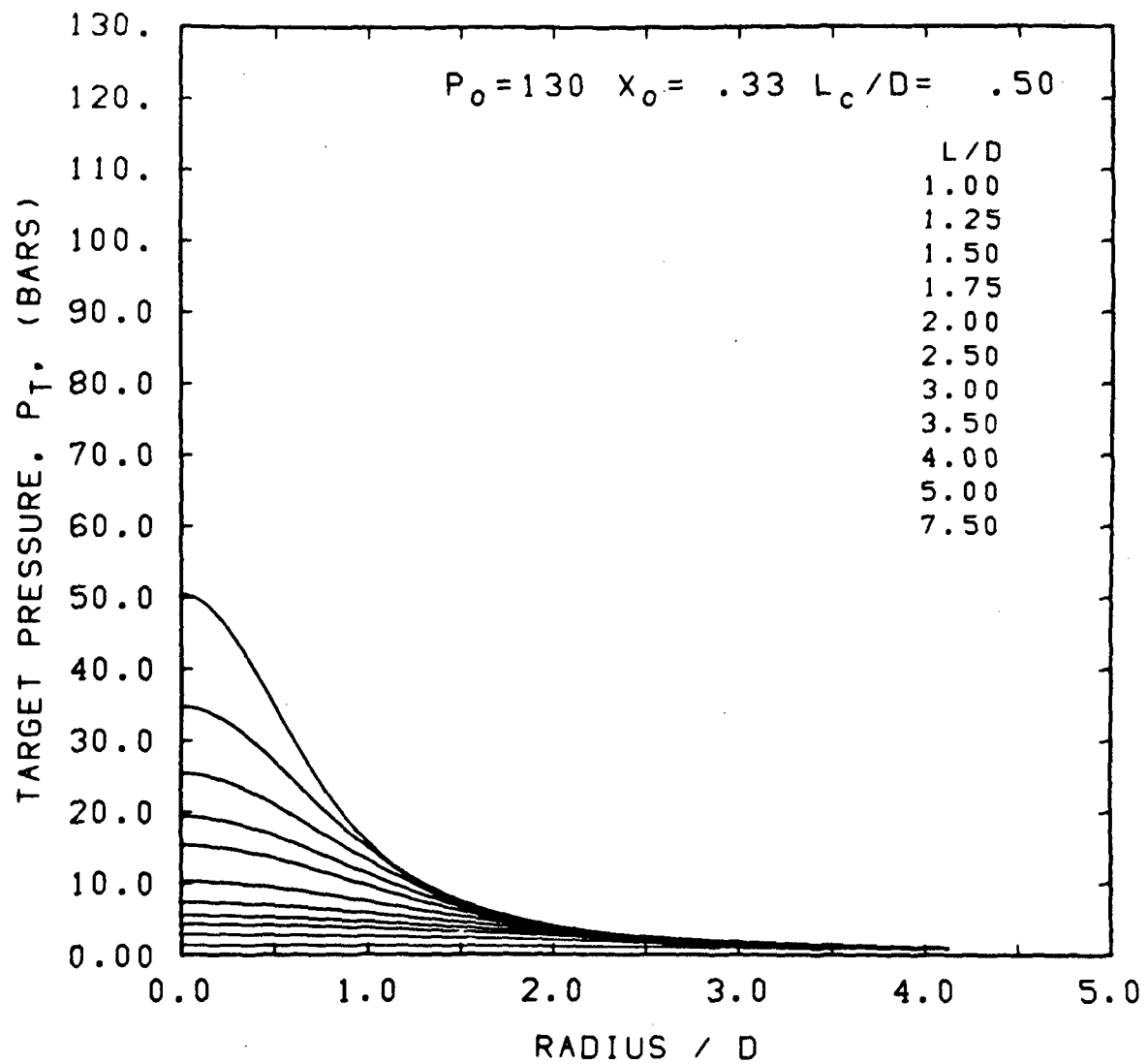
FIGURE A.1   TARGET PRESSURE DISTRIBUTIONS

140
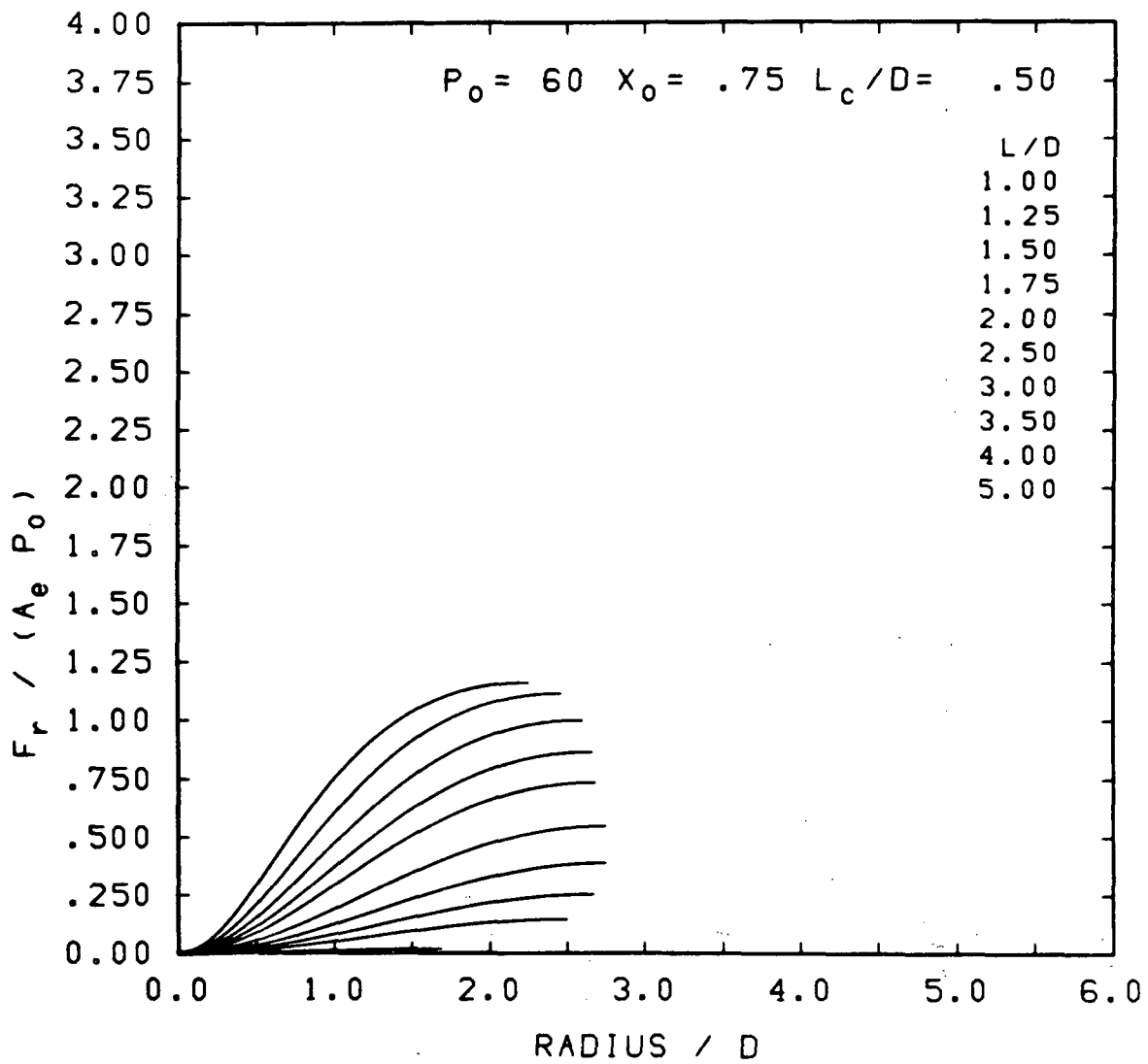
FIGURE A.2   TARGET LOAD DISTRIBUTIONS

```
                                        (BARS)
                                    A =   1.0
                                    B =   2.5
   7 +                              C =   5.0
                                    D =  10.0
                                    E =  15.0
   6 +                              F =  20.0
                                    G =  25.0
                                    H =  30.0
   5 +              A               I =  35.0
                                    J =  40.0
                                    K =  45.0
   4 +                    A         L =  50.0
                                    M =  55.0
D                         A         N =  60.0
/  3 +          A         A         O =  65.0
                                    P =  70.0
L            C         A   A        Q =  75.0
   2 +      C         A     A       R =  80.0
            C         B
      B     C         B   A
   1 +  F  B  C     B     A
                               Po = 60  Xo = .75  Lc/D =   .50
   0 +  1     2     3     4     5     6
              RADIUS / D
```
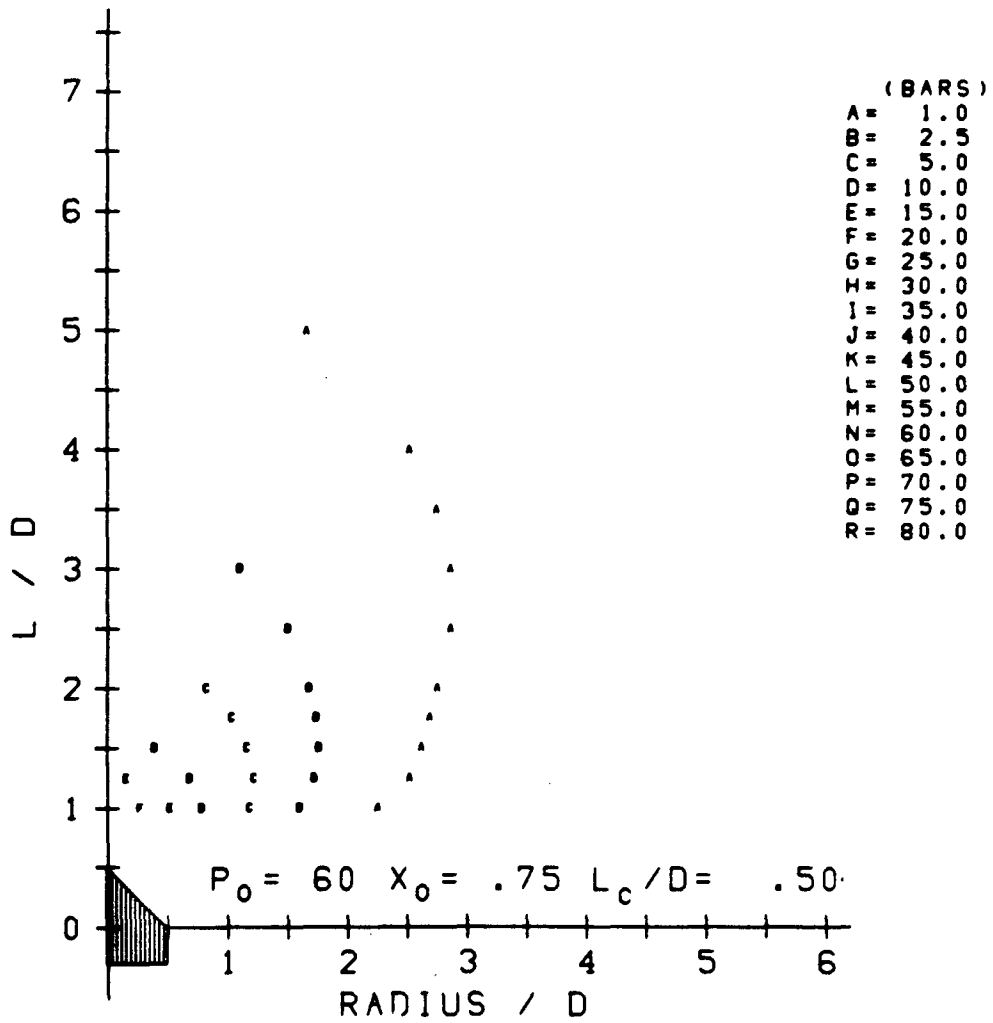
FIGURE A.3   COMPOSITE TARGET PRESSURE CONTOURS
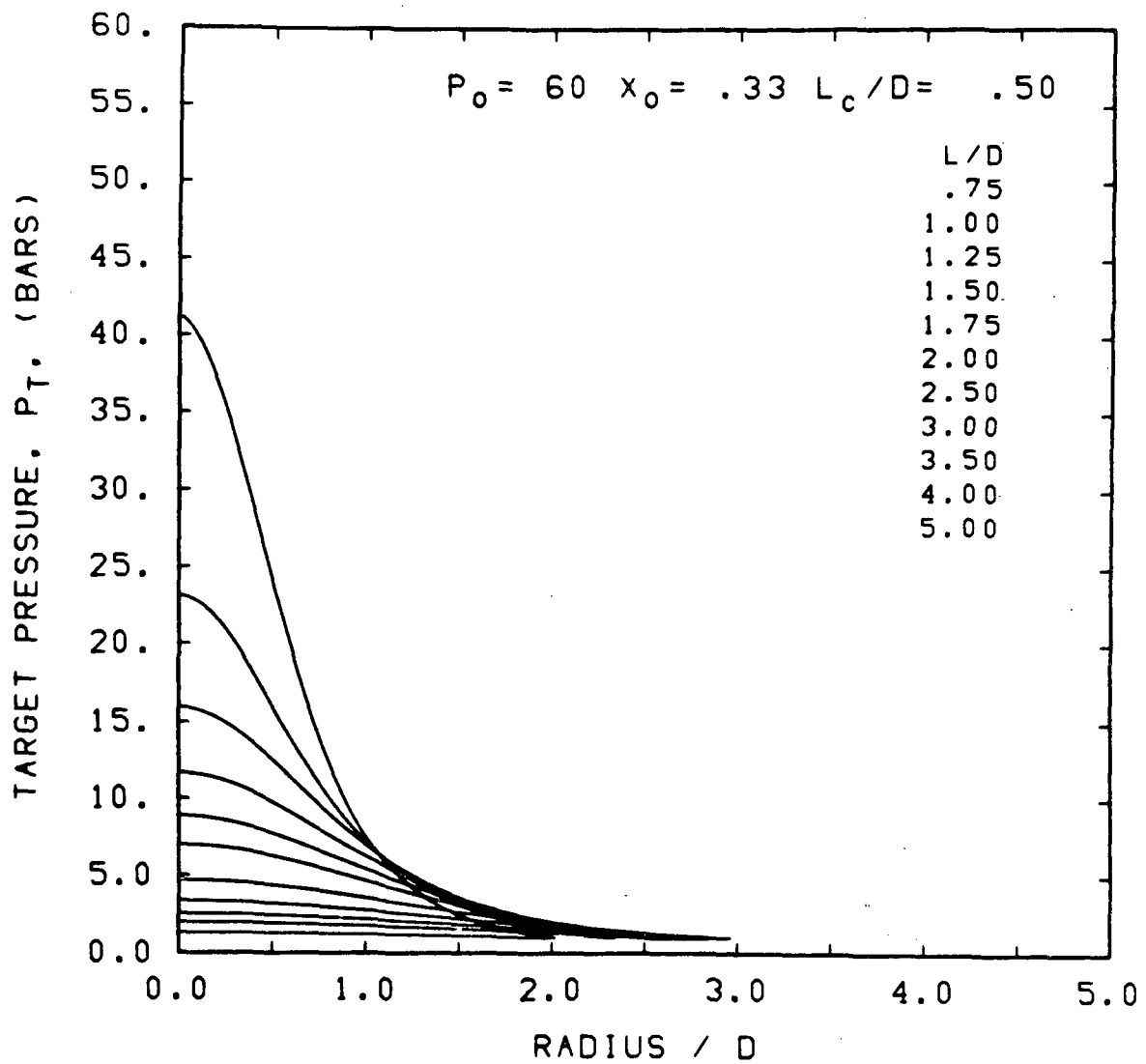
FIGURE A.4   TARGET PRESSURE DISTRIBUTIONS

143
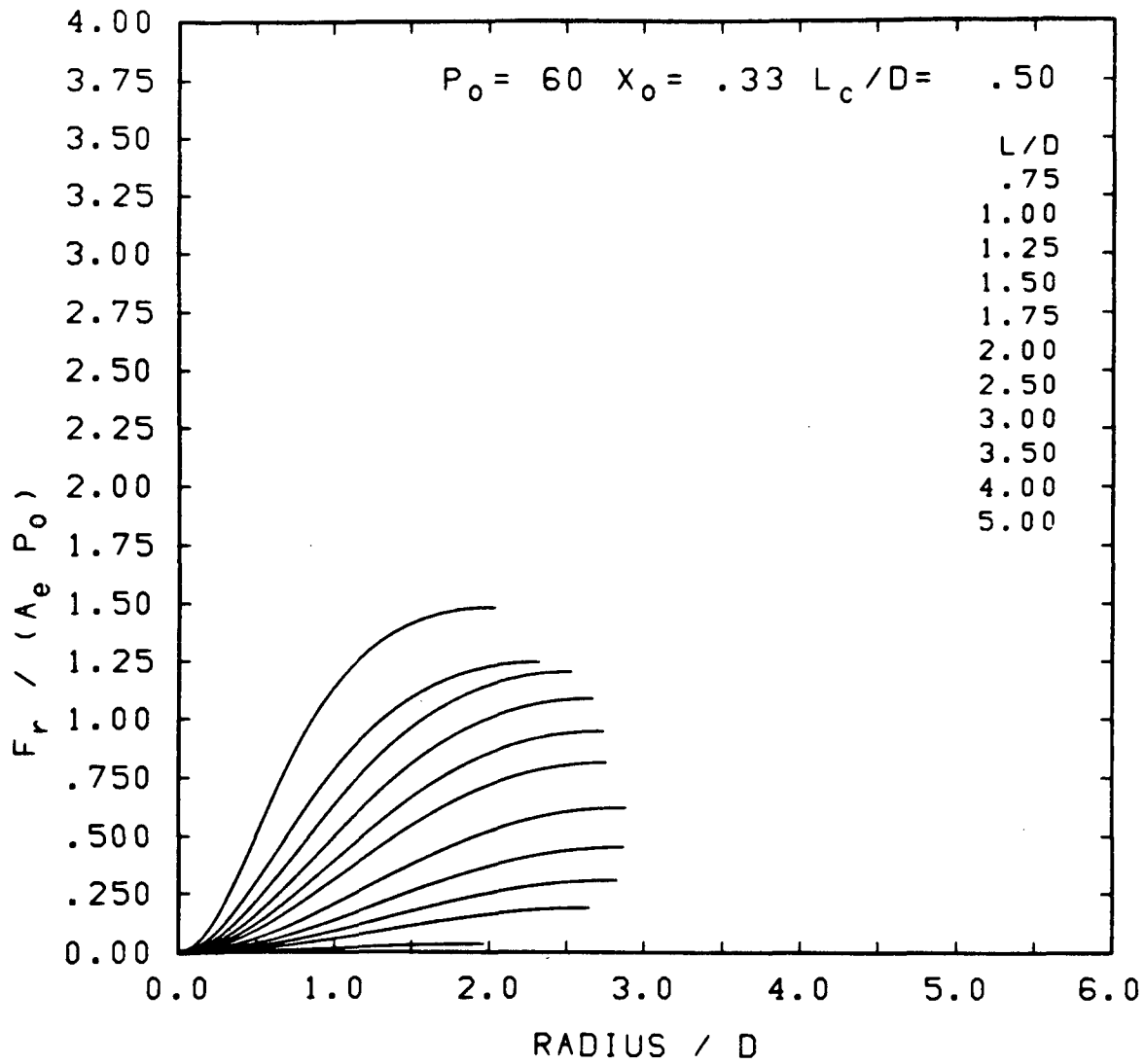
FIGURE A.5   TARGET LOAD DISTRIBUTIONS
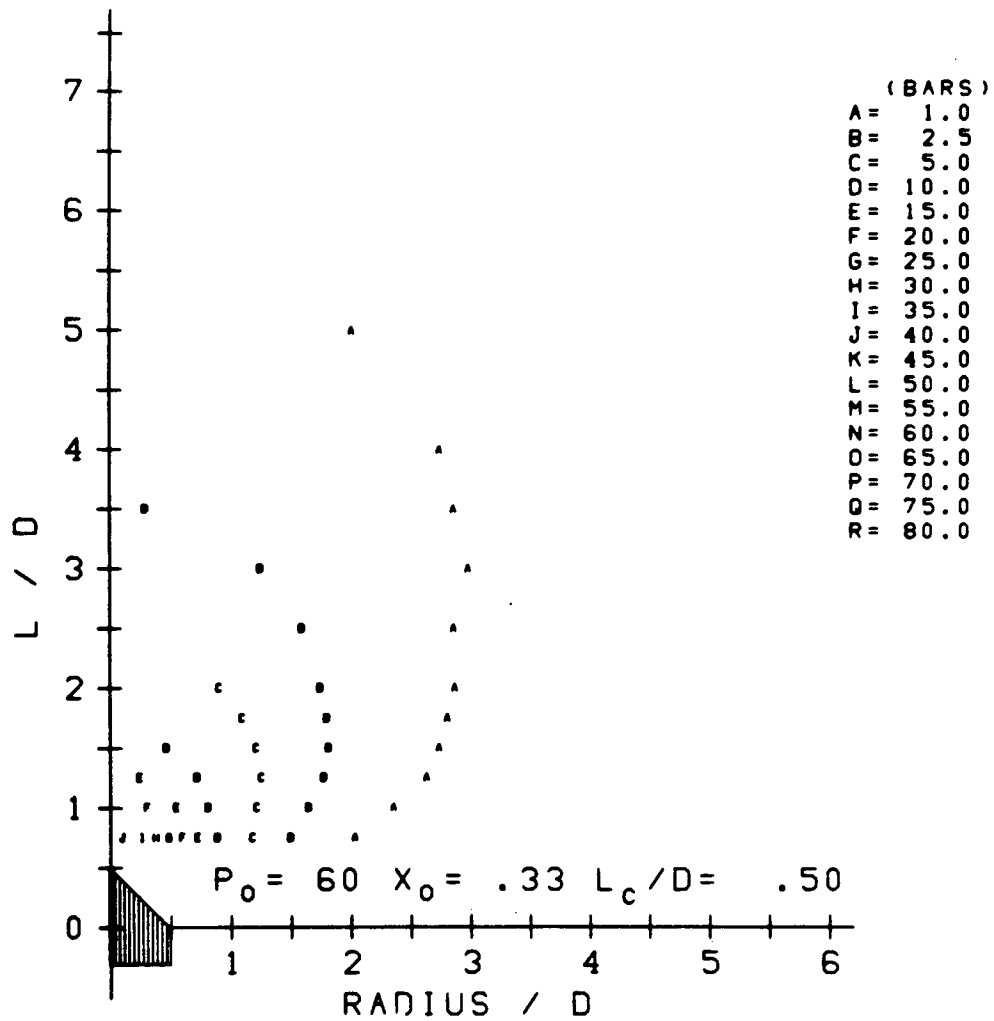
FIGURE A.6 COMPOSITE TARGET PRESSURE CONTOURS
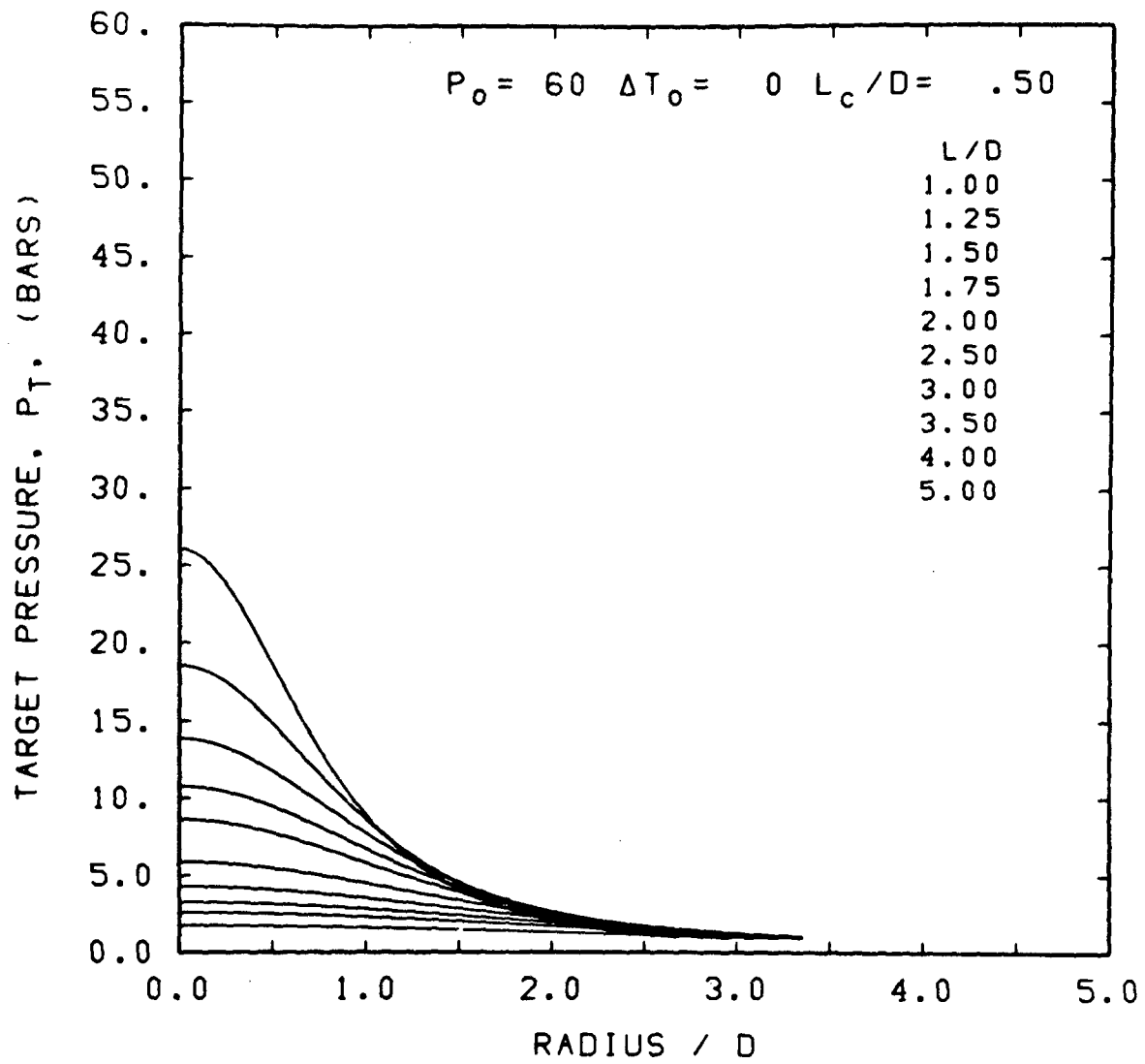
FIGURE A.7   TARGET PRESSURE DISTRIBUTIONS
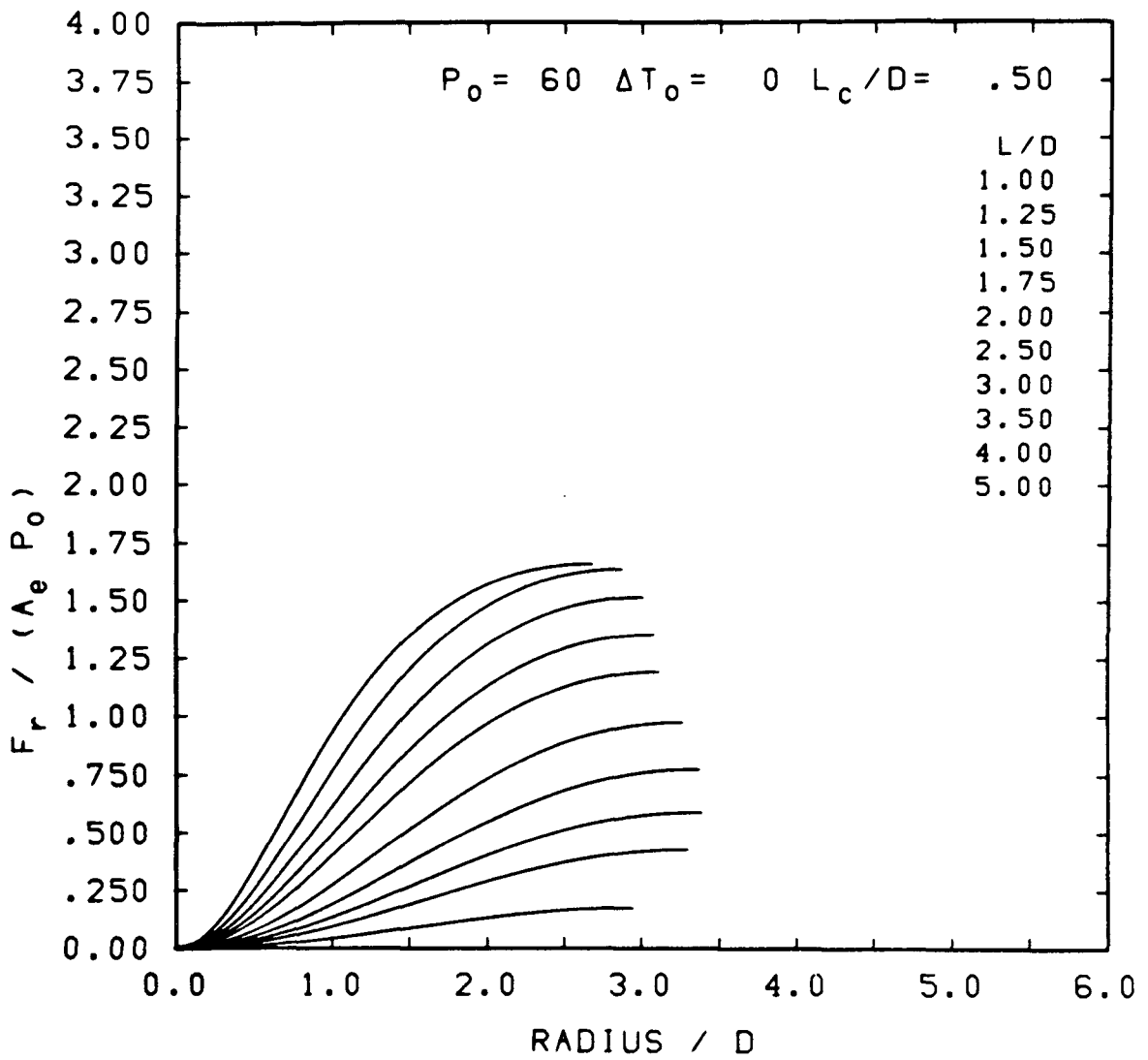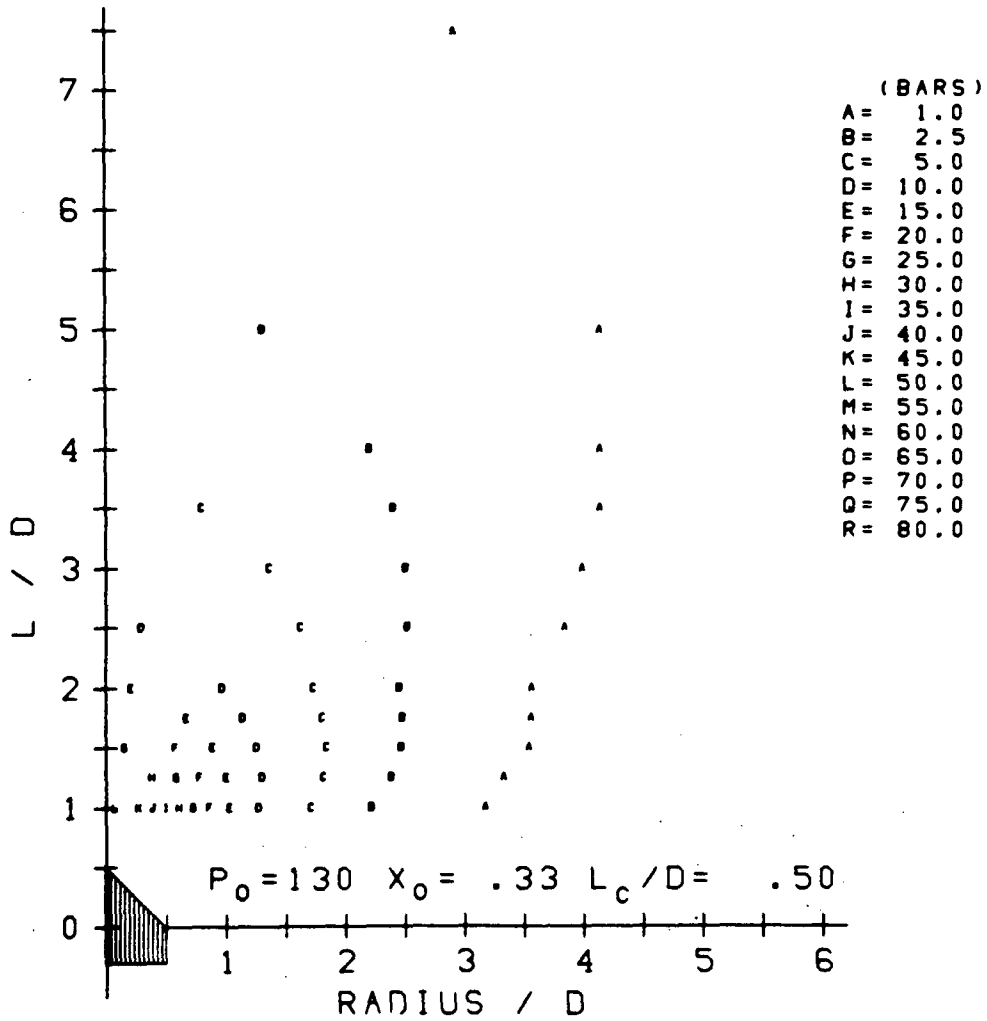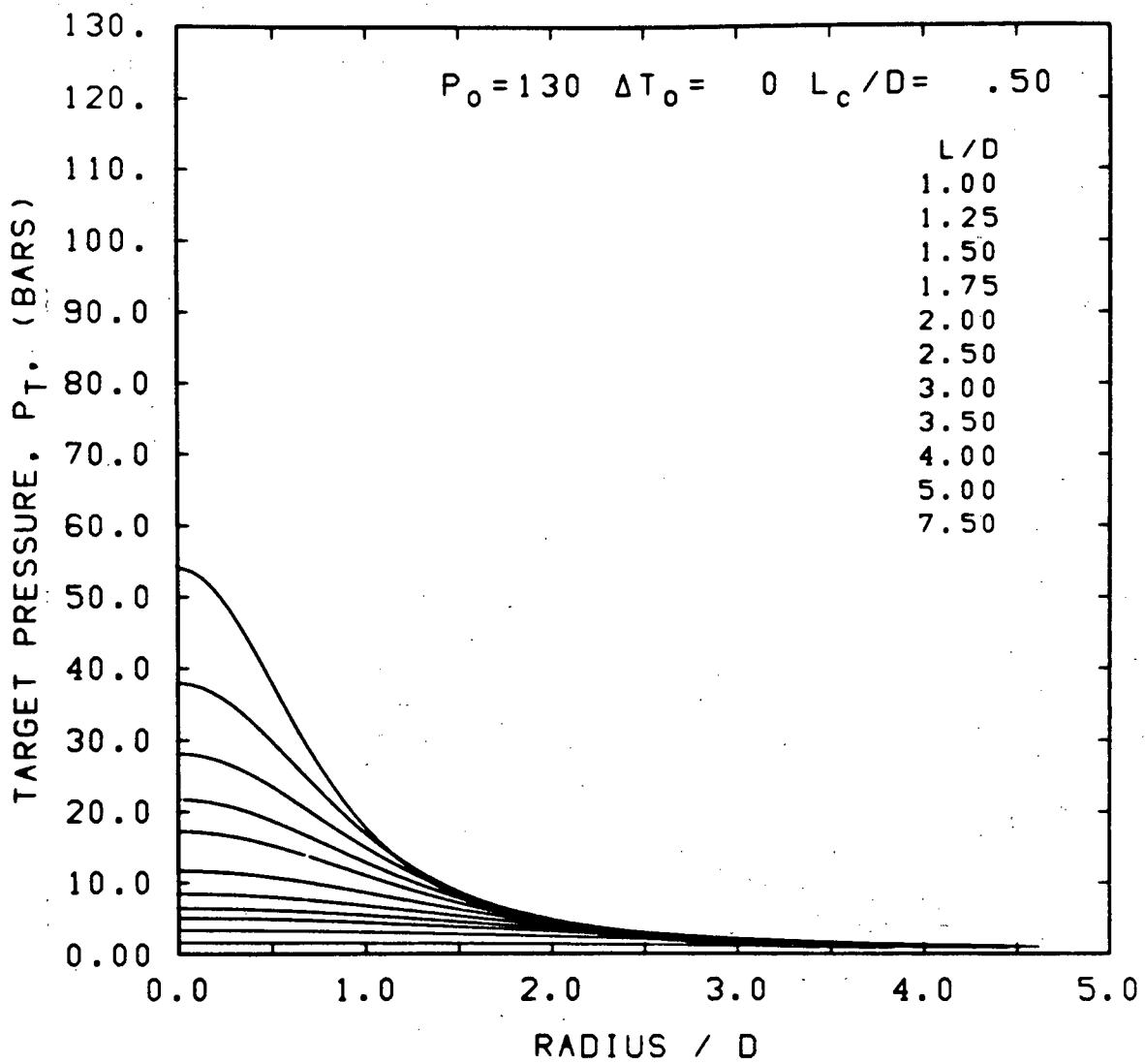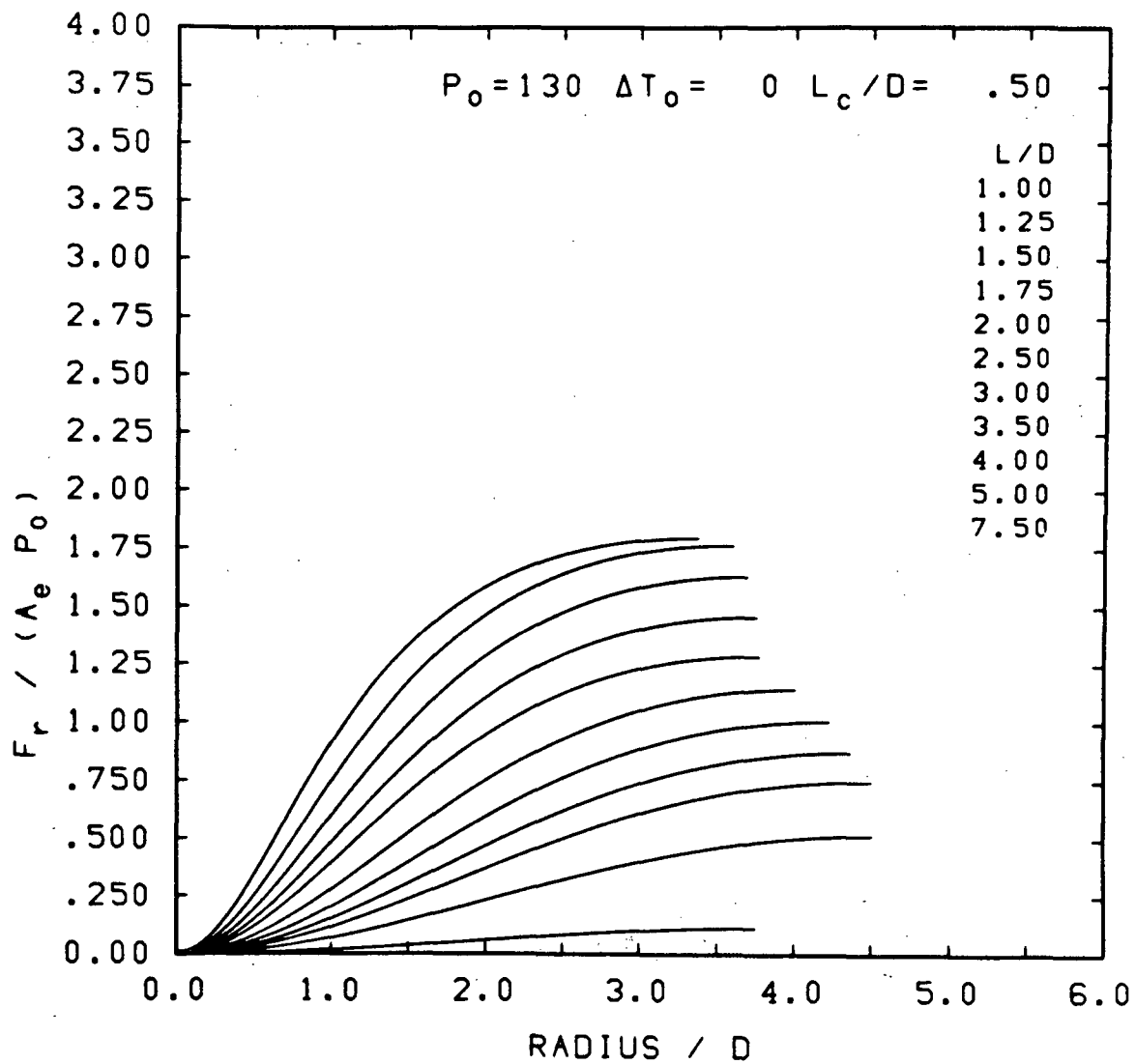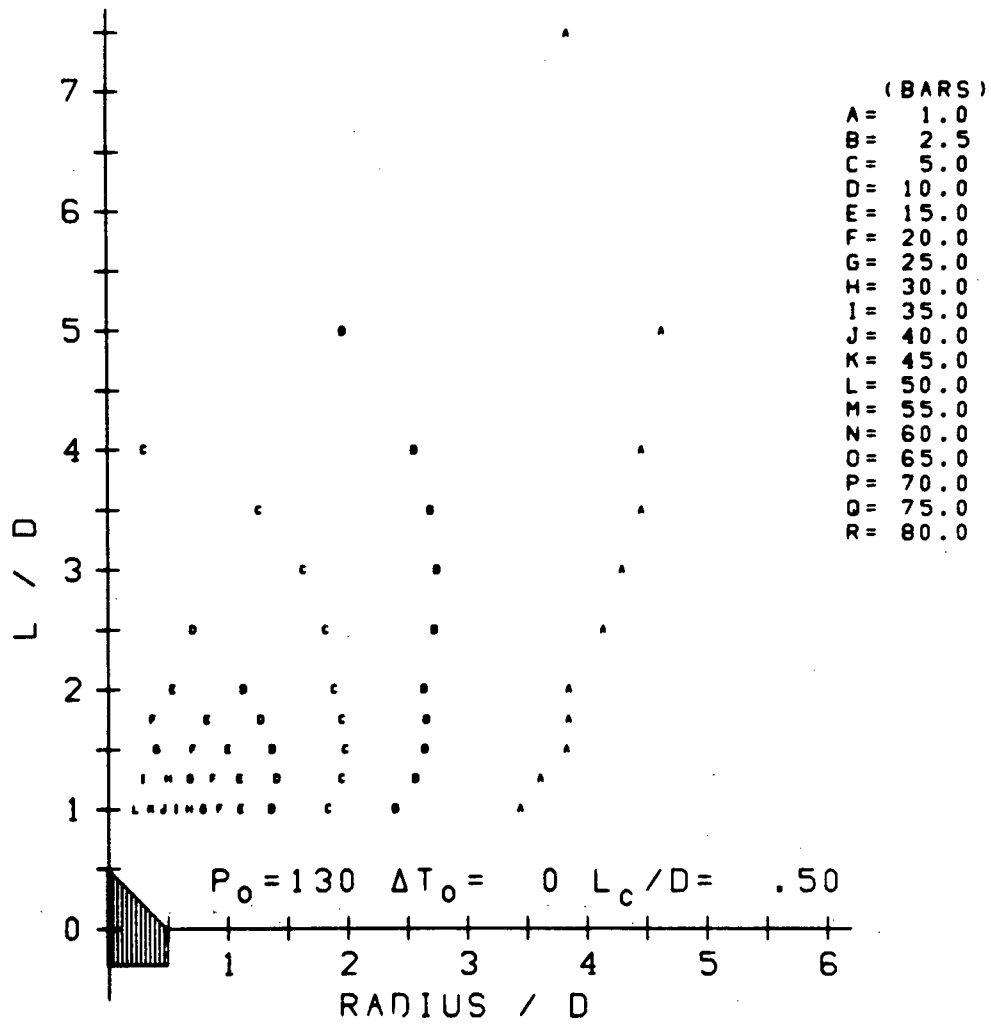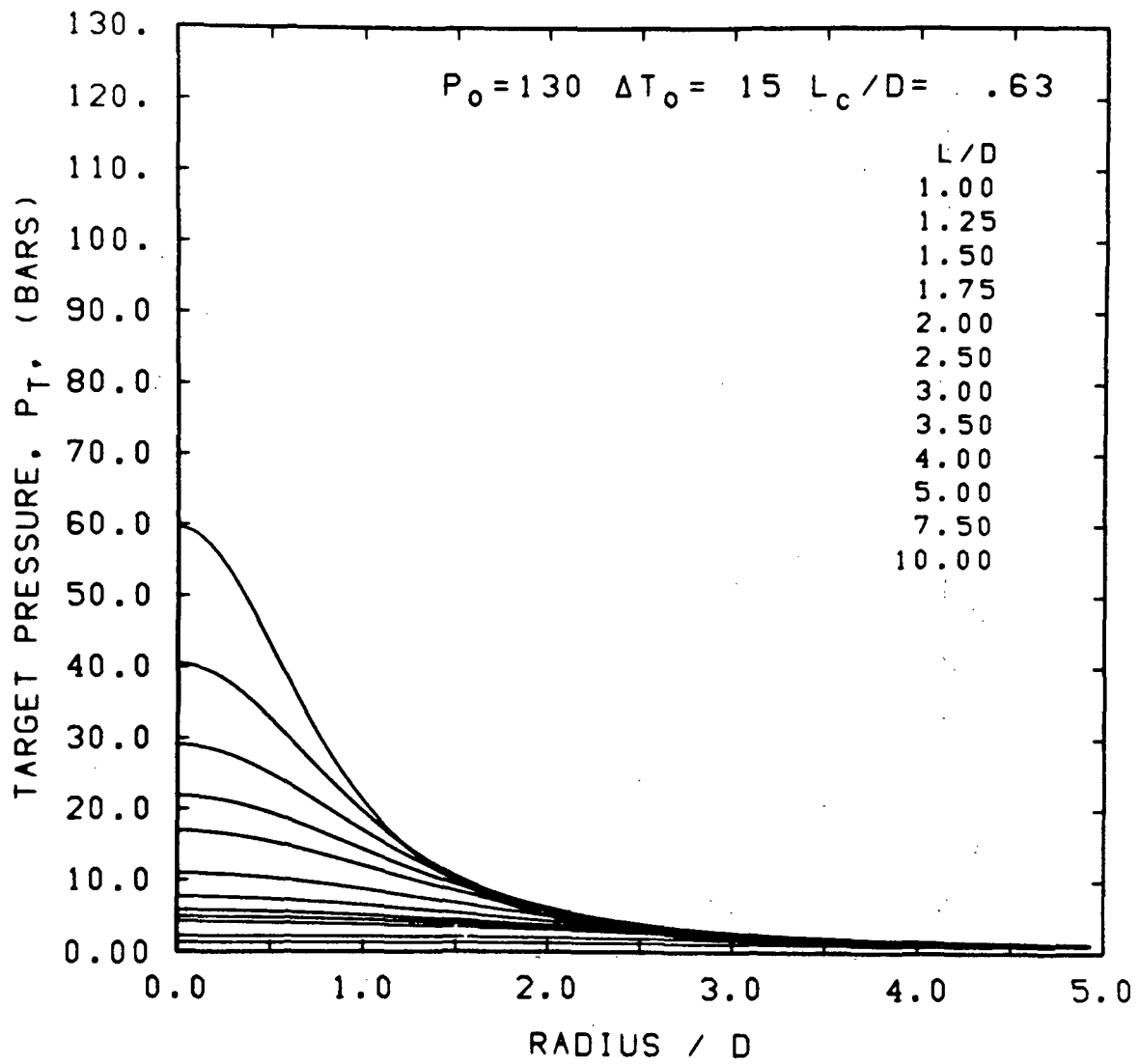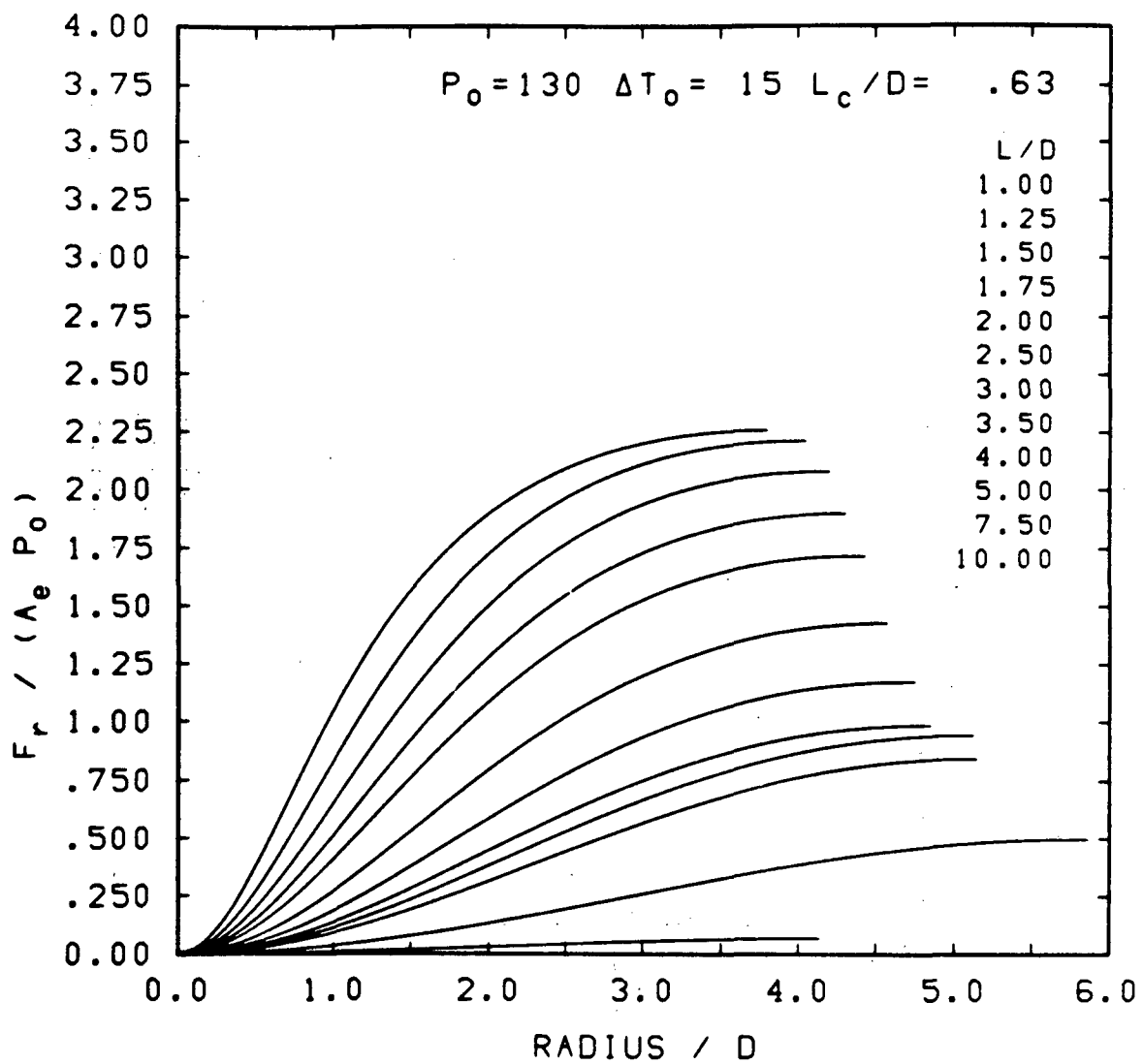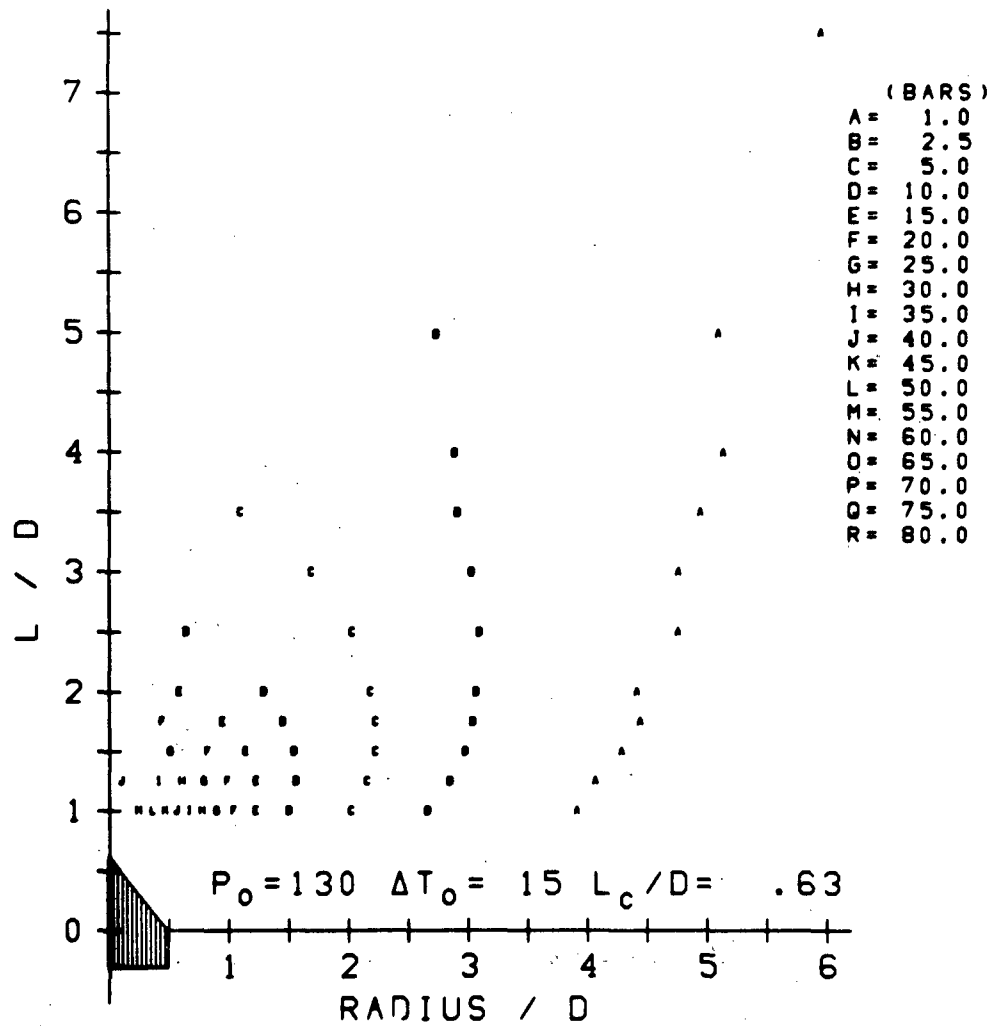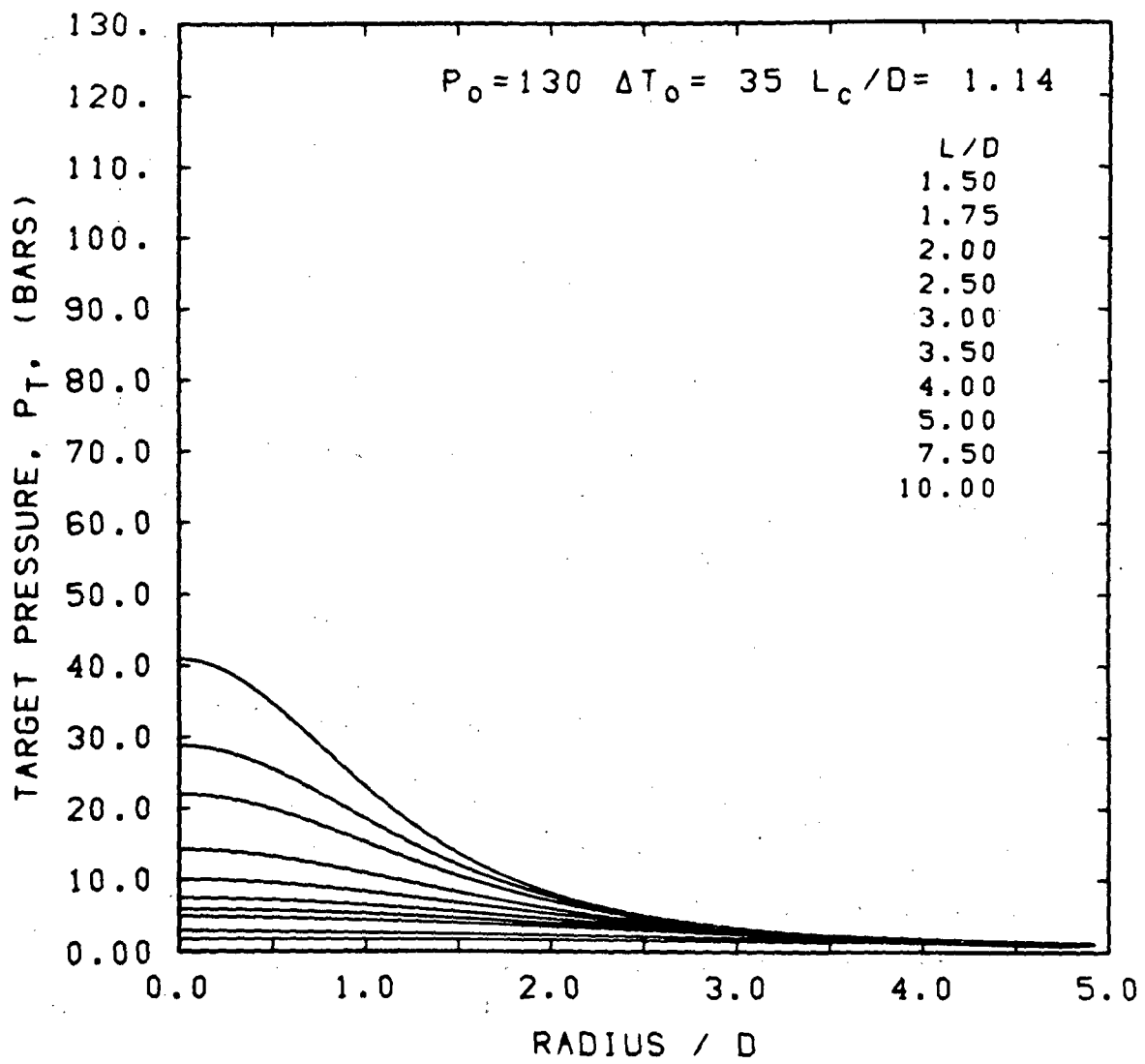
FIGURE A.8   TARGET LOAD DISTRIBUTIONS
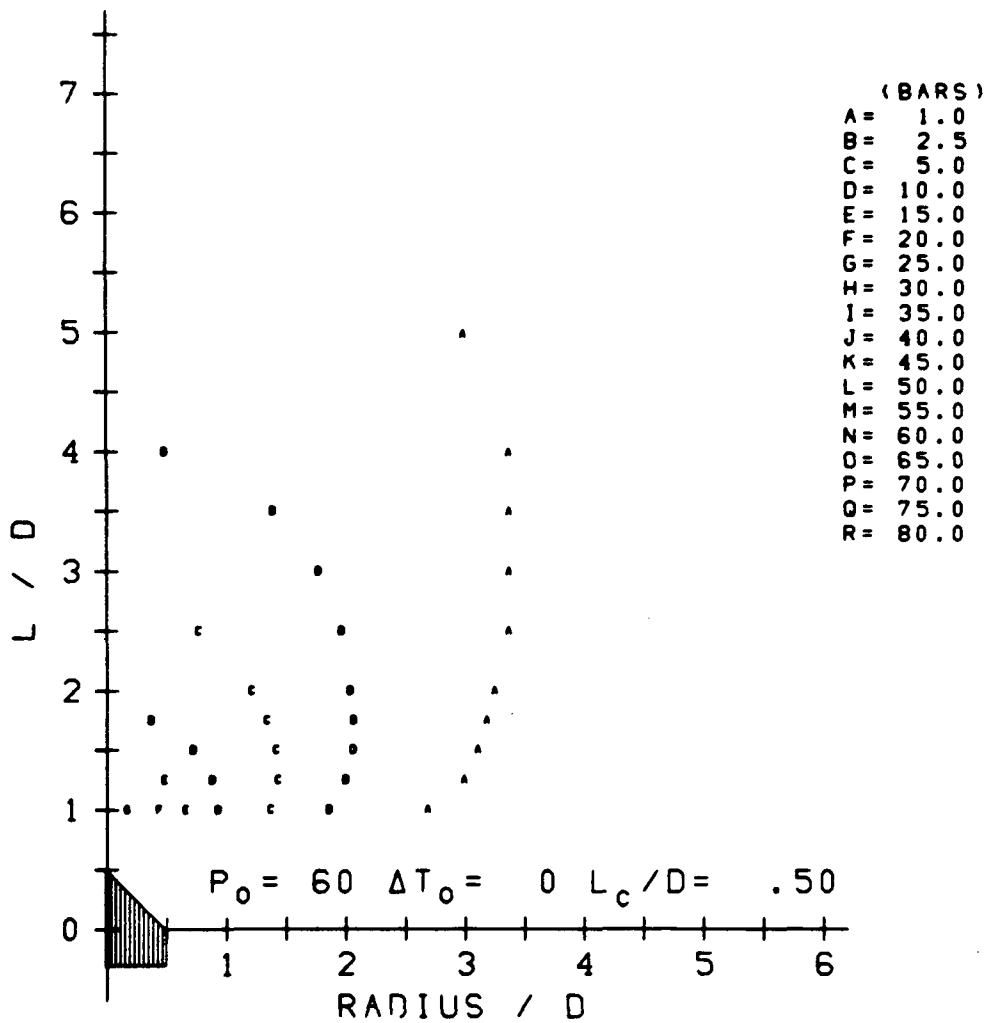
FIGURE A.9   COMPOSITE TARGET PRESSURE CONTOURS
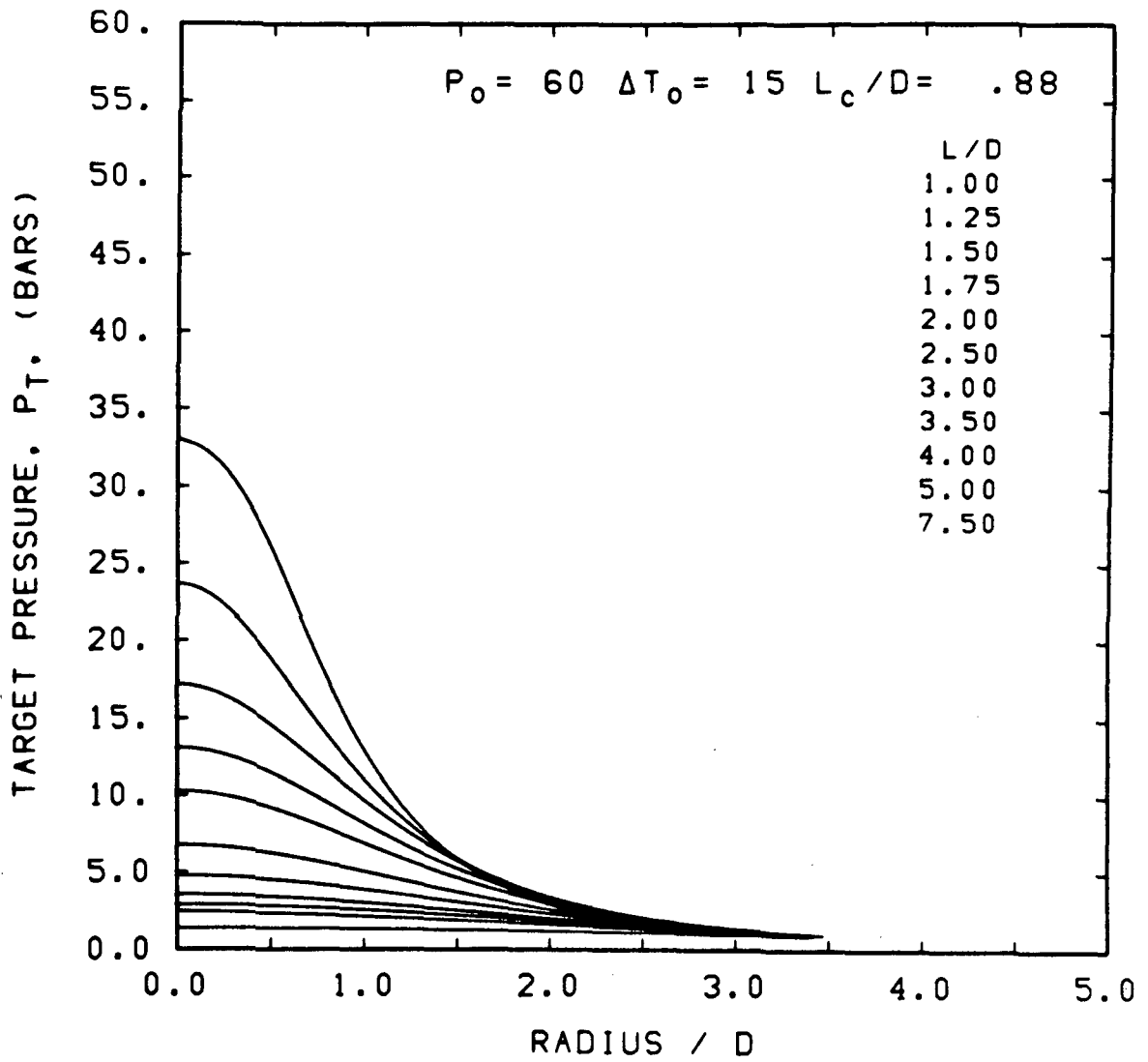
FIGURE A.10   TARGET PRESSURE DISTRIBUTIONS
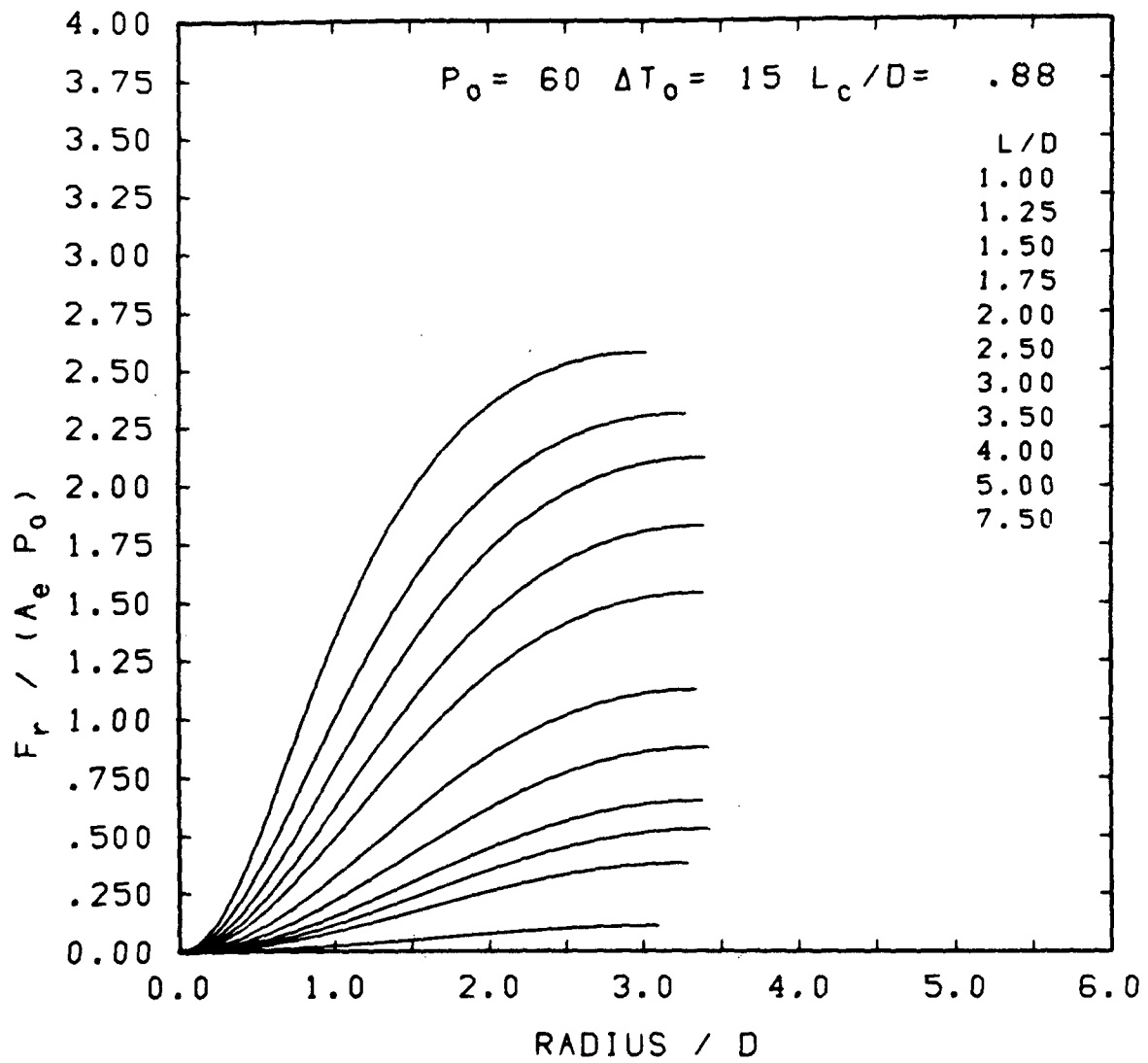
FIGURE A.11   TARGET LOAD DISTRIBUTIONS

150
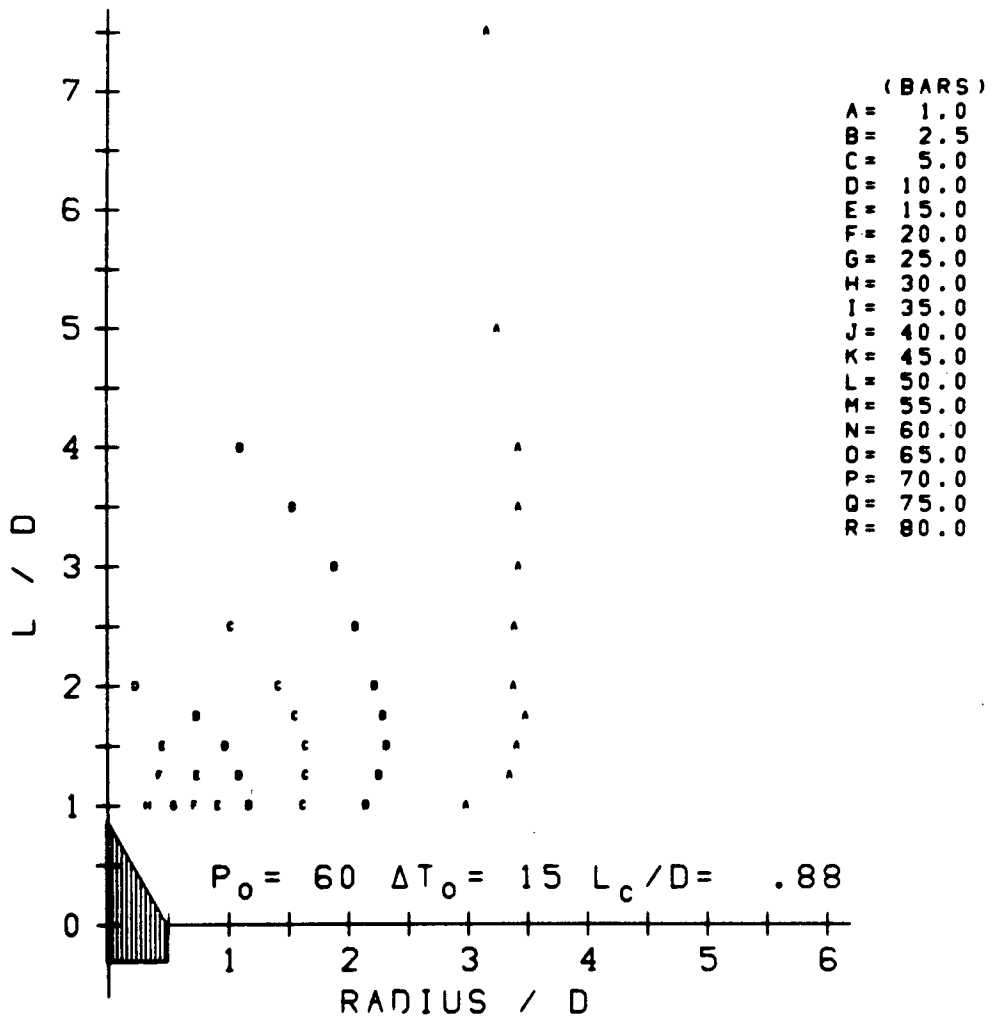
FIGURE A.12 COMPOSITE TARGET PRESSURE CONTOURS
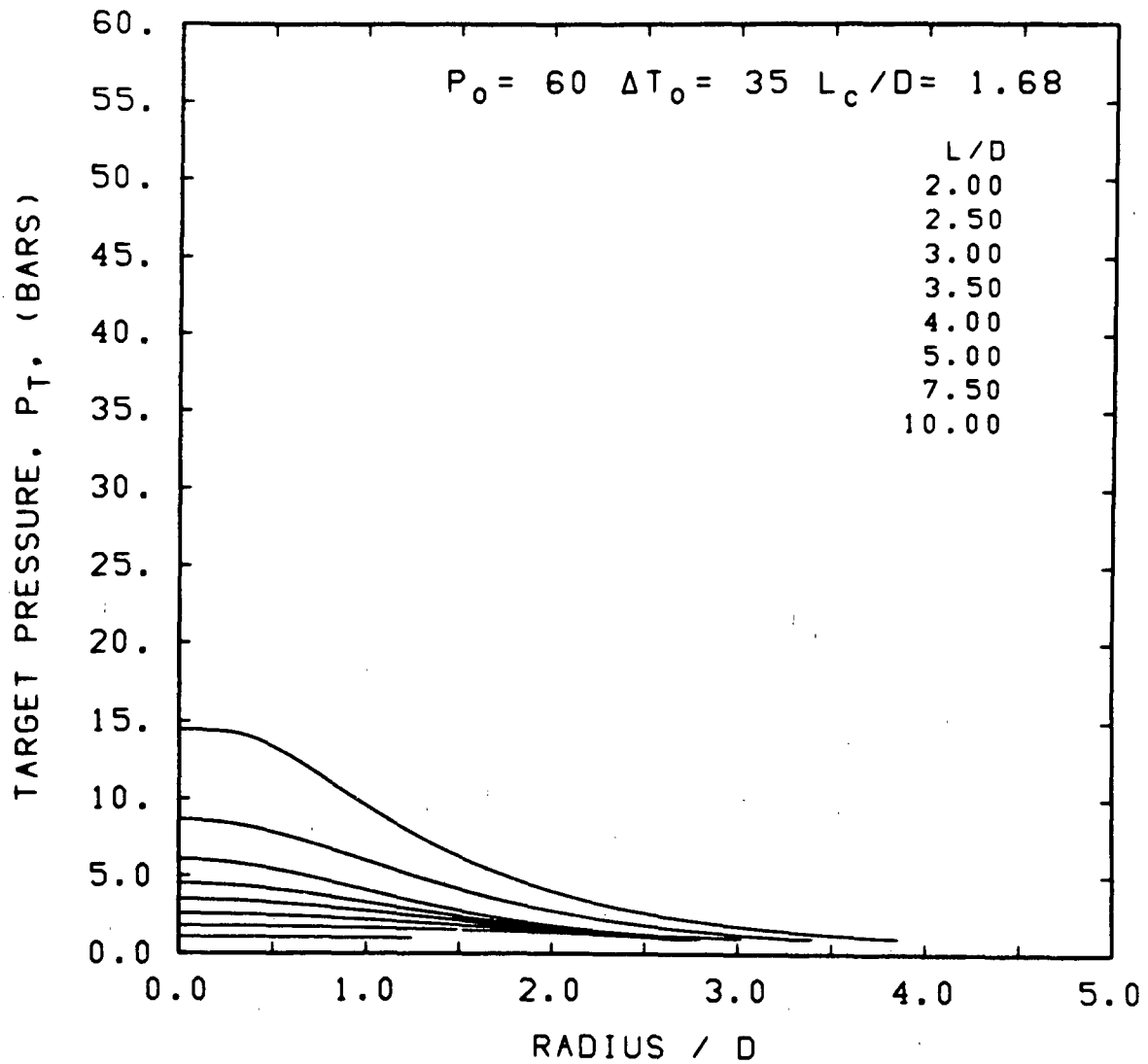
FIGURE A.13 TARGET PRESSURE DISTRIBUTIONS

152
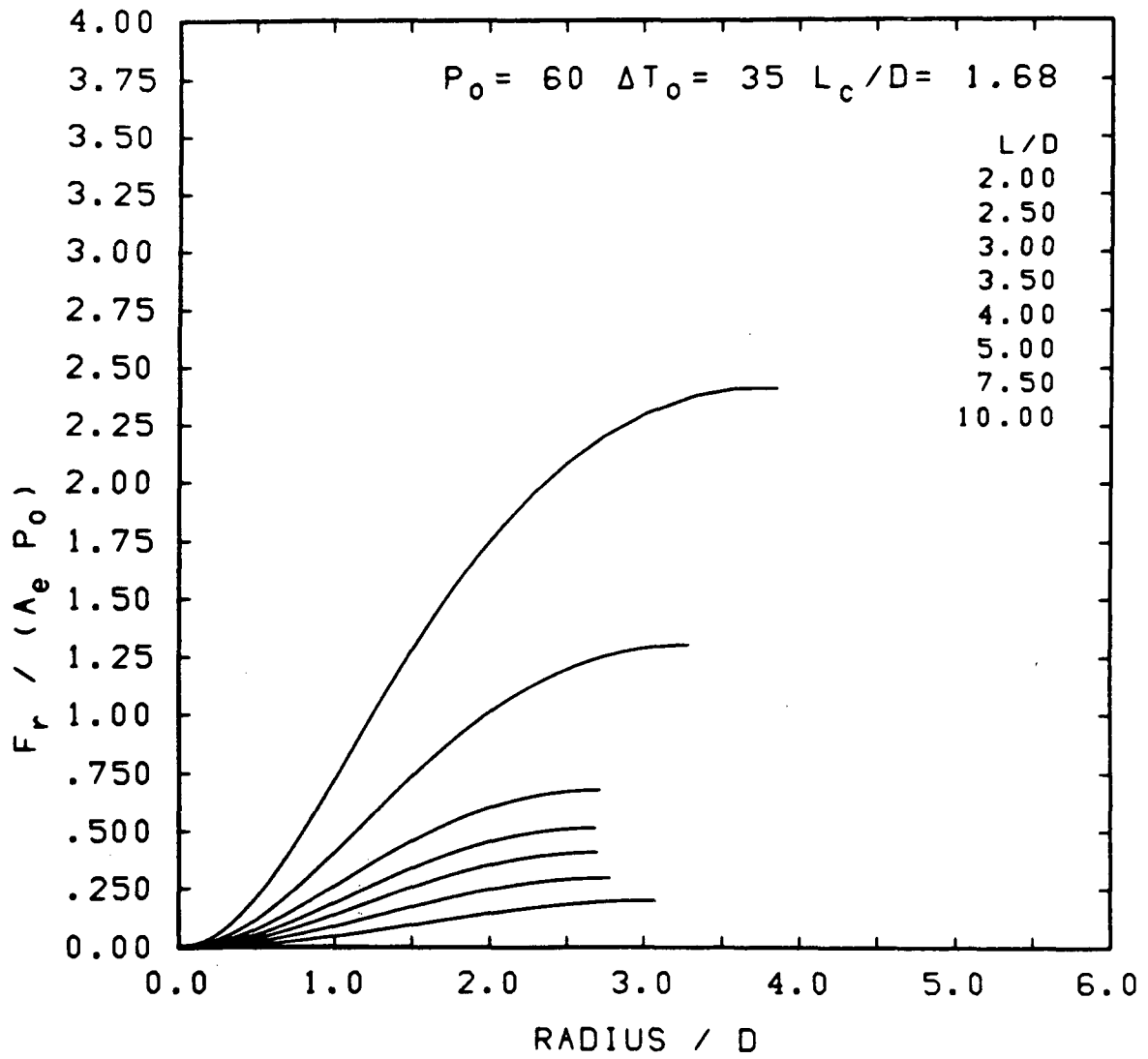
FIGURE A.14   TARGET LOAD DISTRIBUTIONS
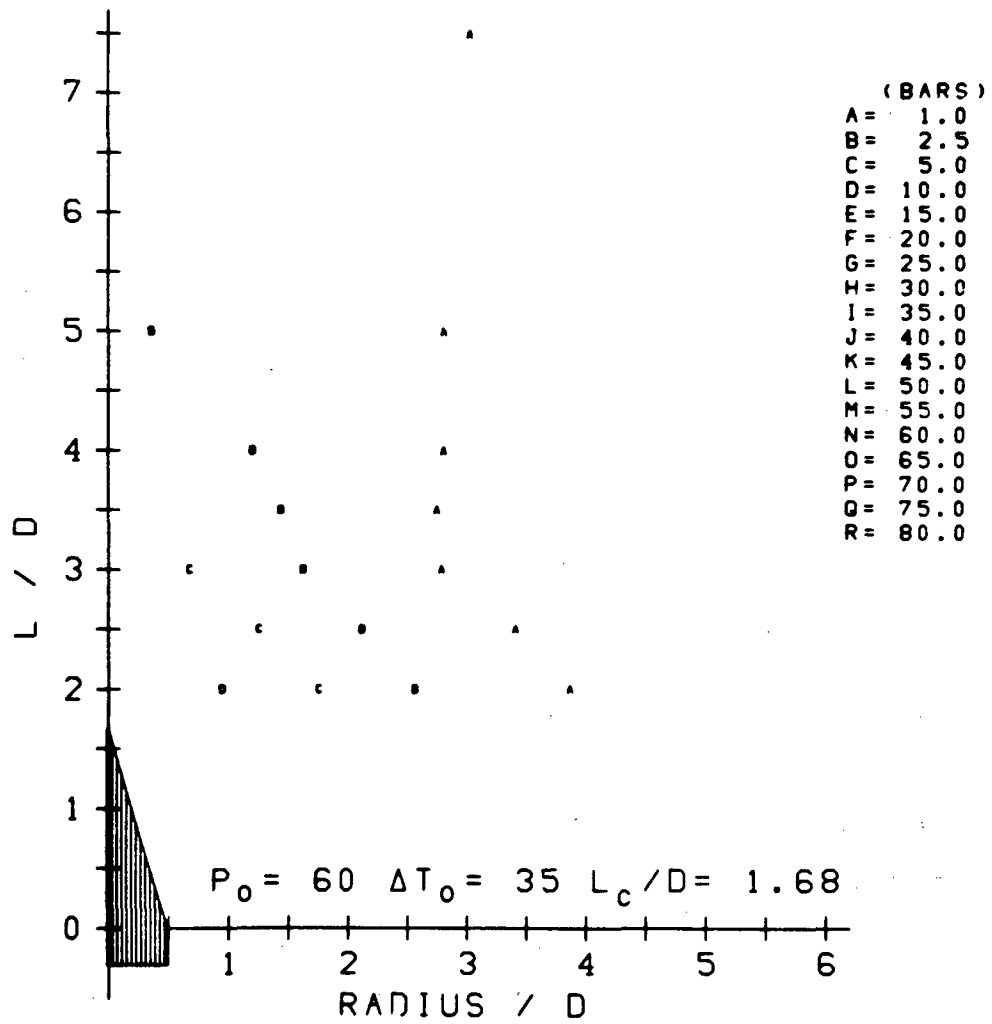
FIGURE A.15 COMPOSITE TARGET PRESSURE CONTOURS
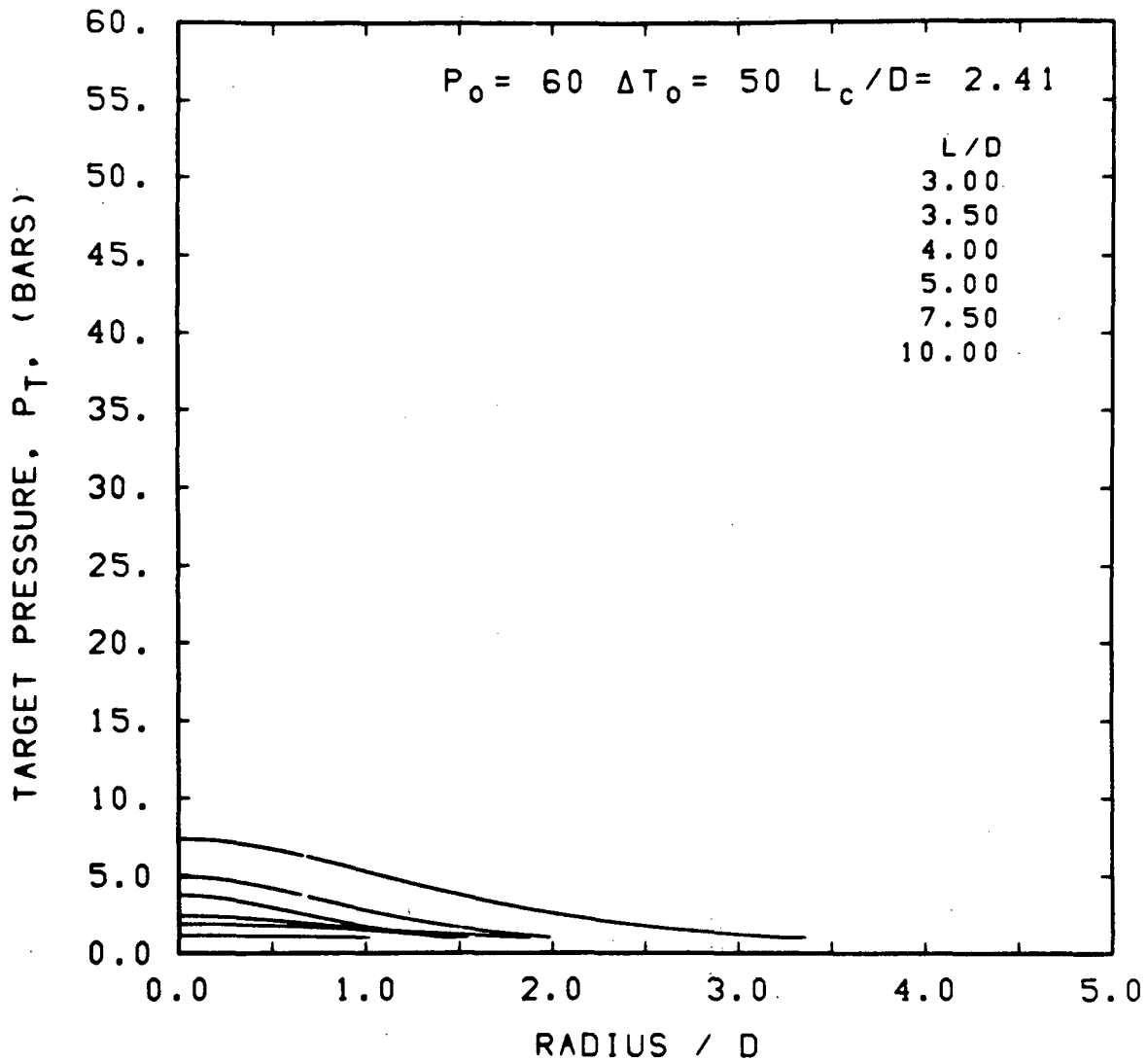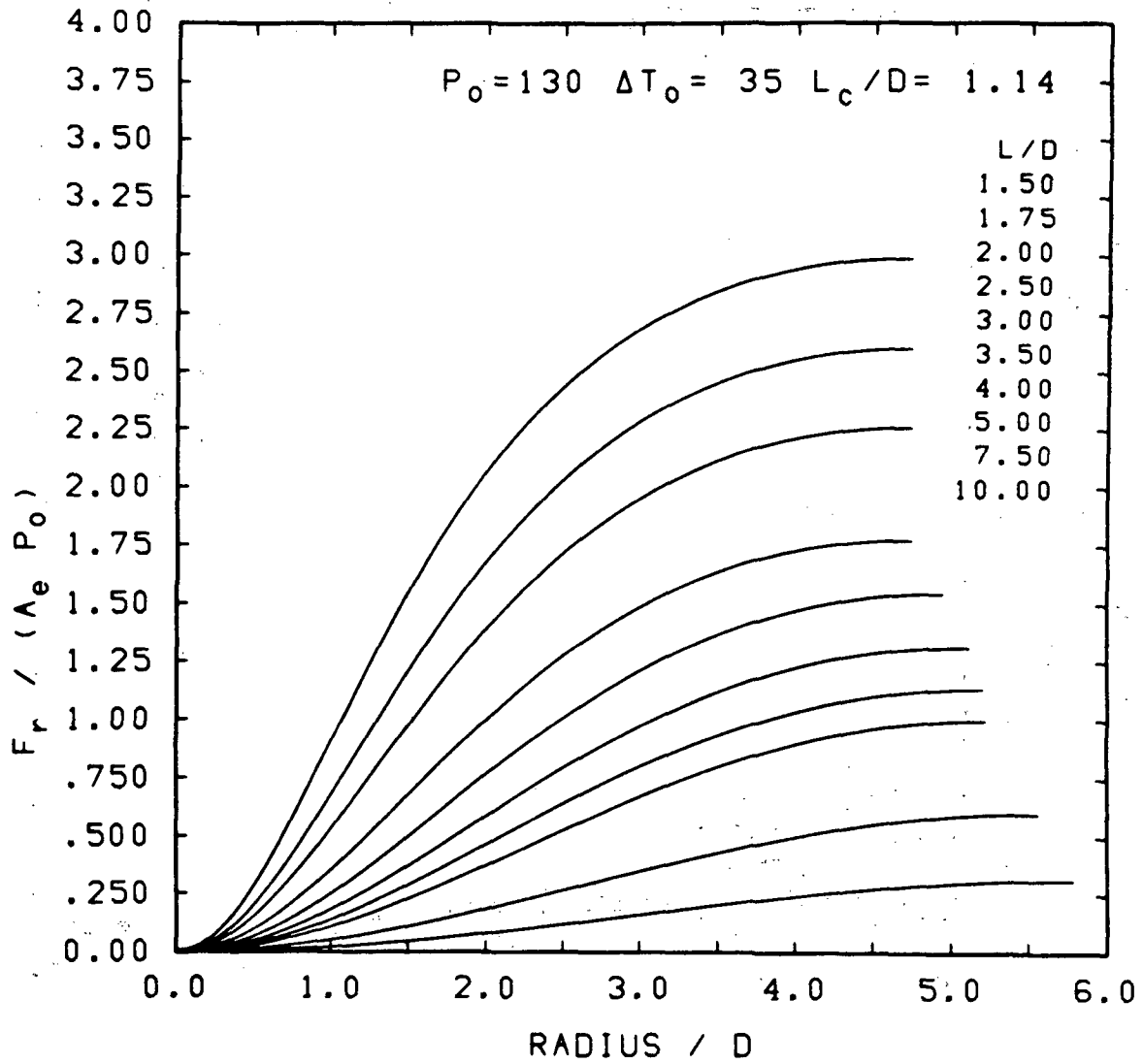
FIGURE A.16   TARGET PRESSURE DISTRIBUTIONS
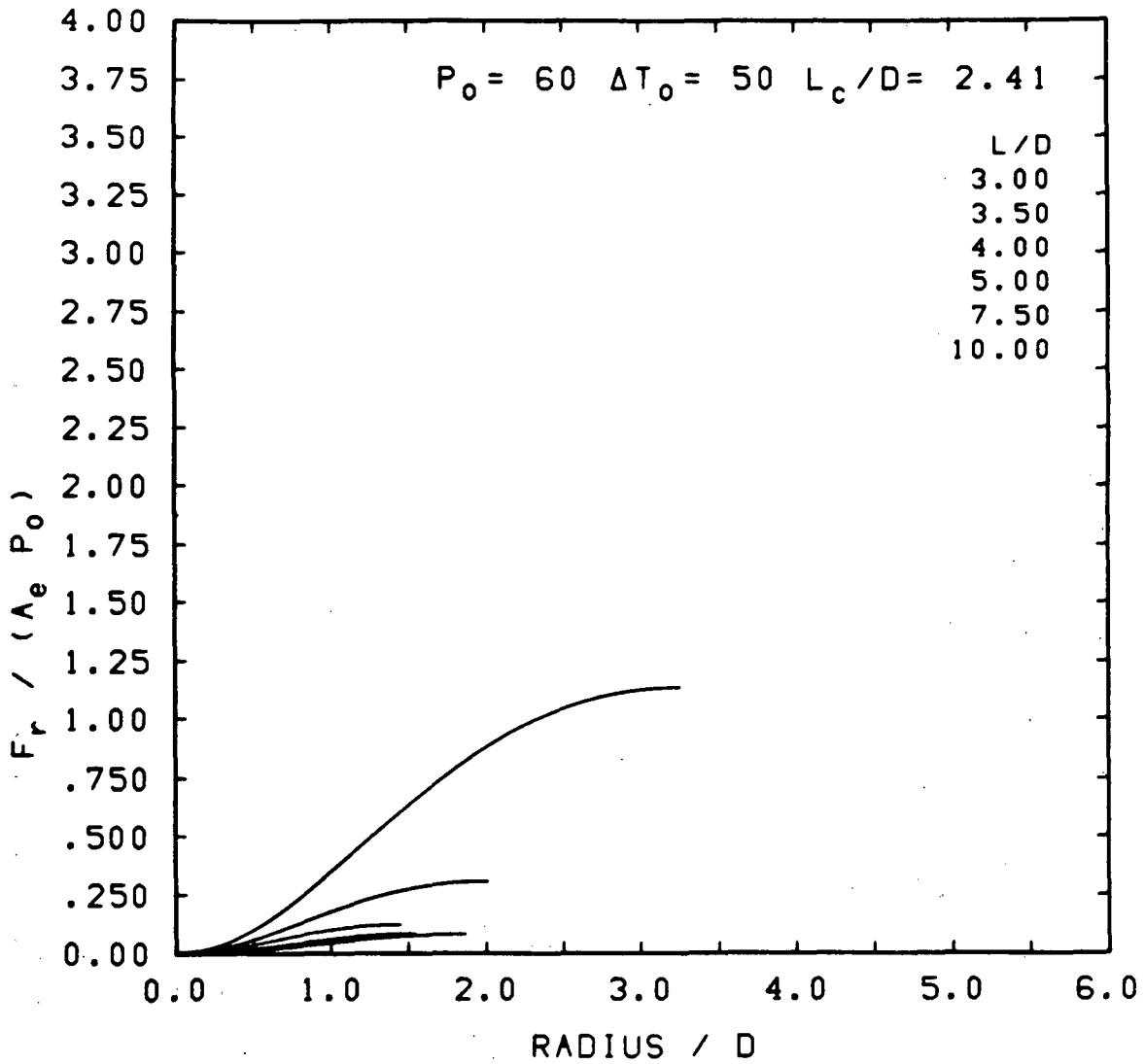
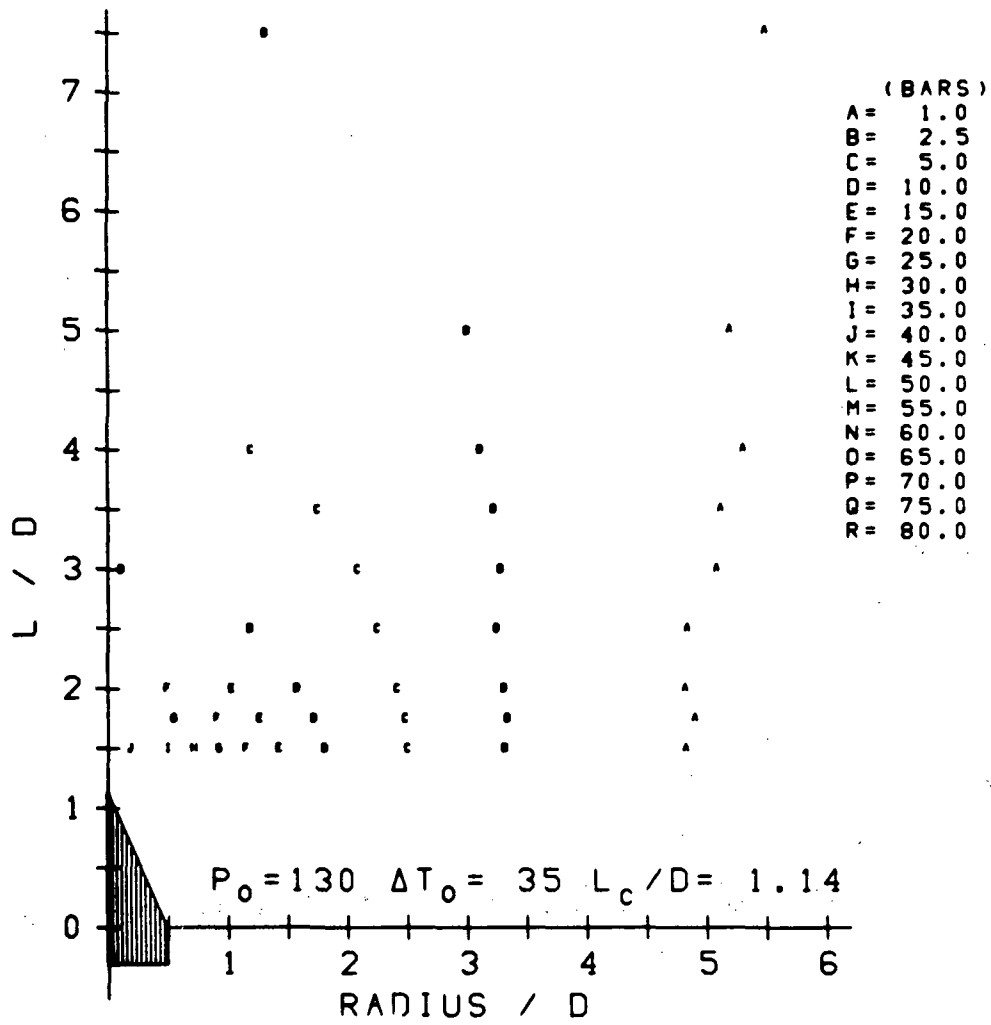FIGURE A.17 TARGET LOAD DISTRIBUTIONS
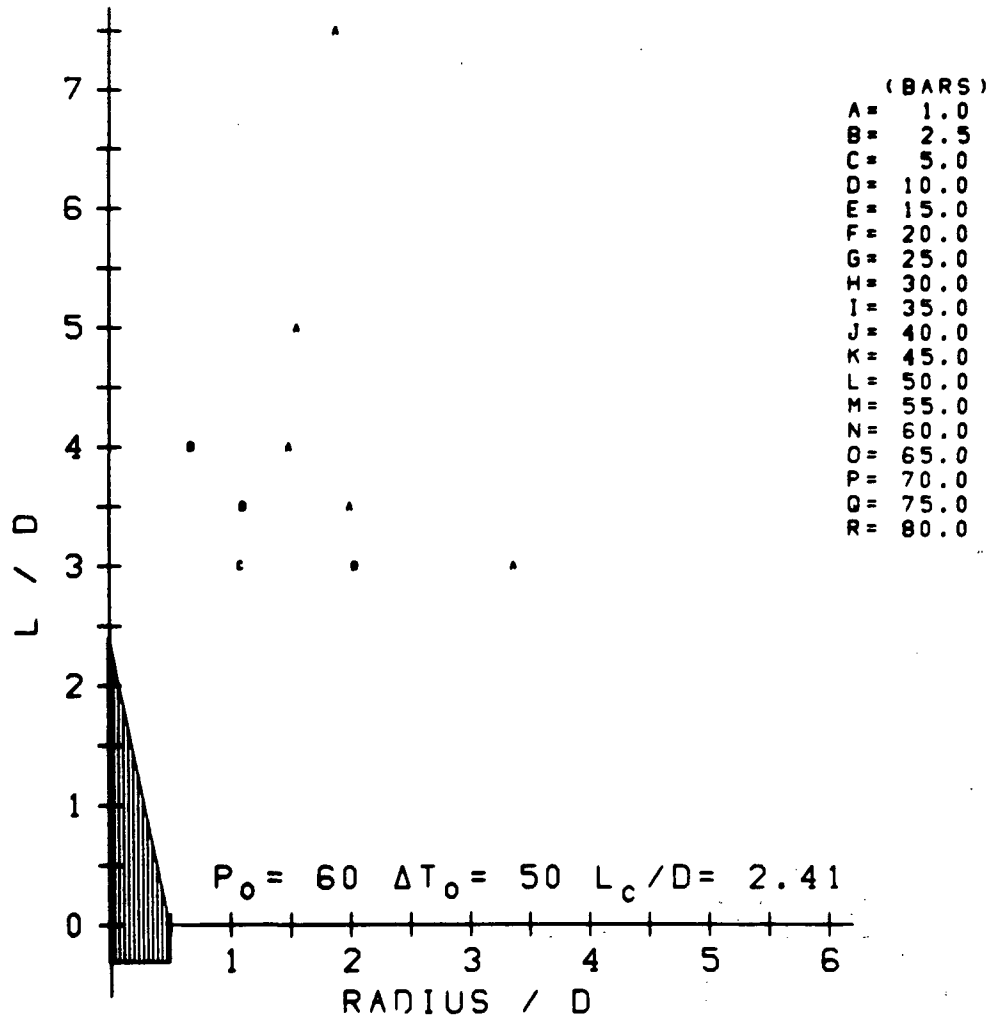
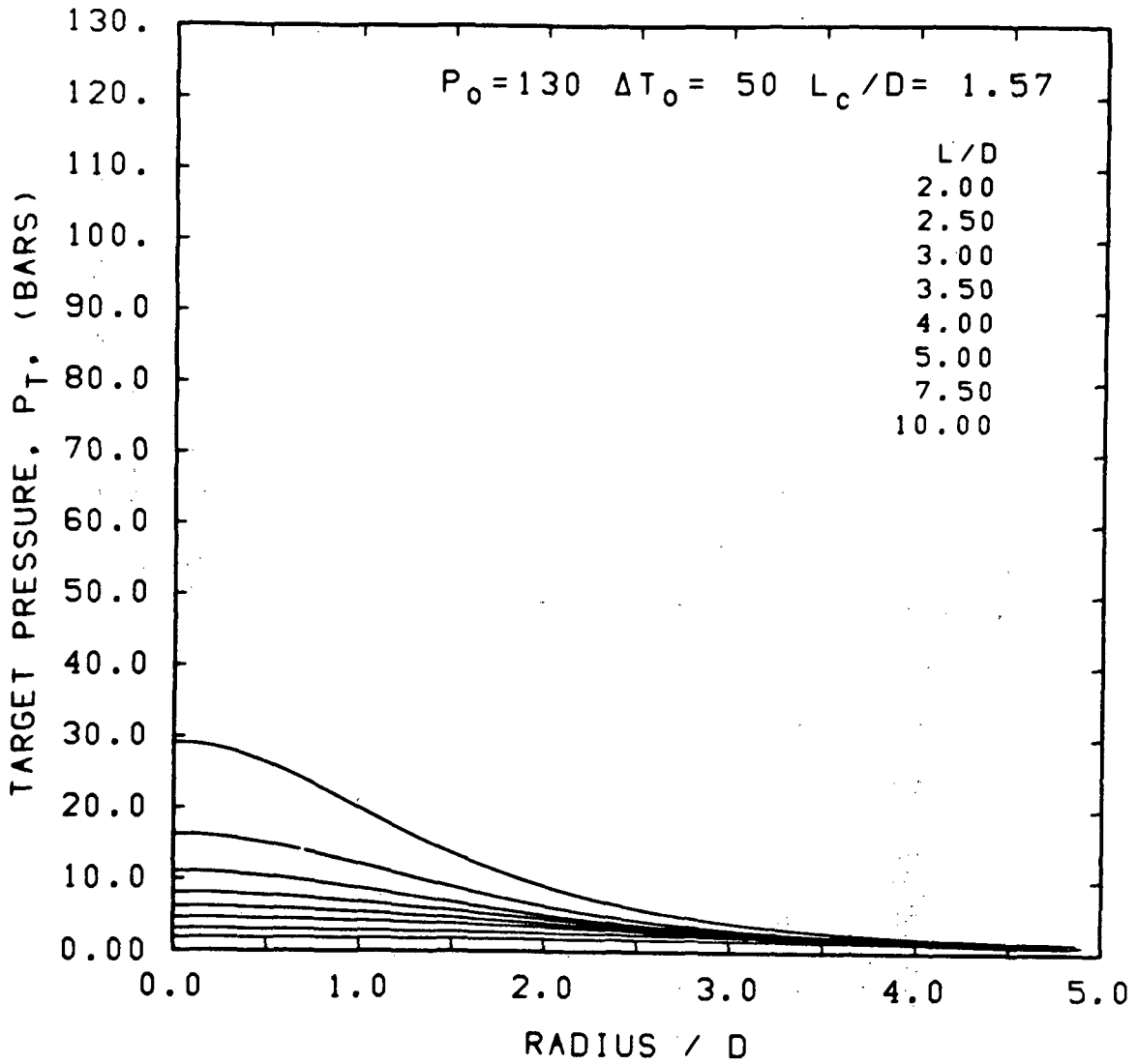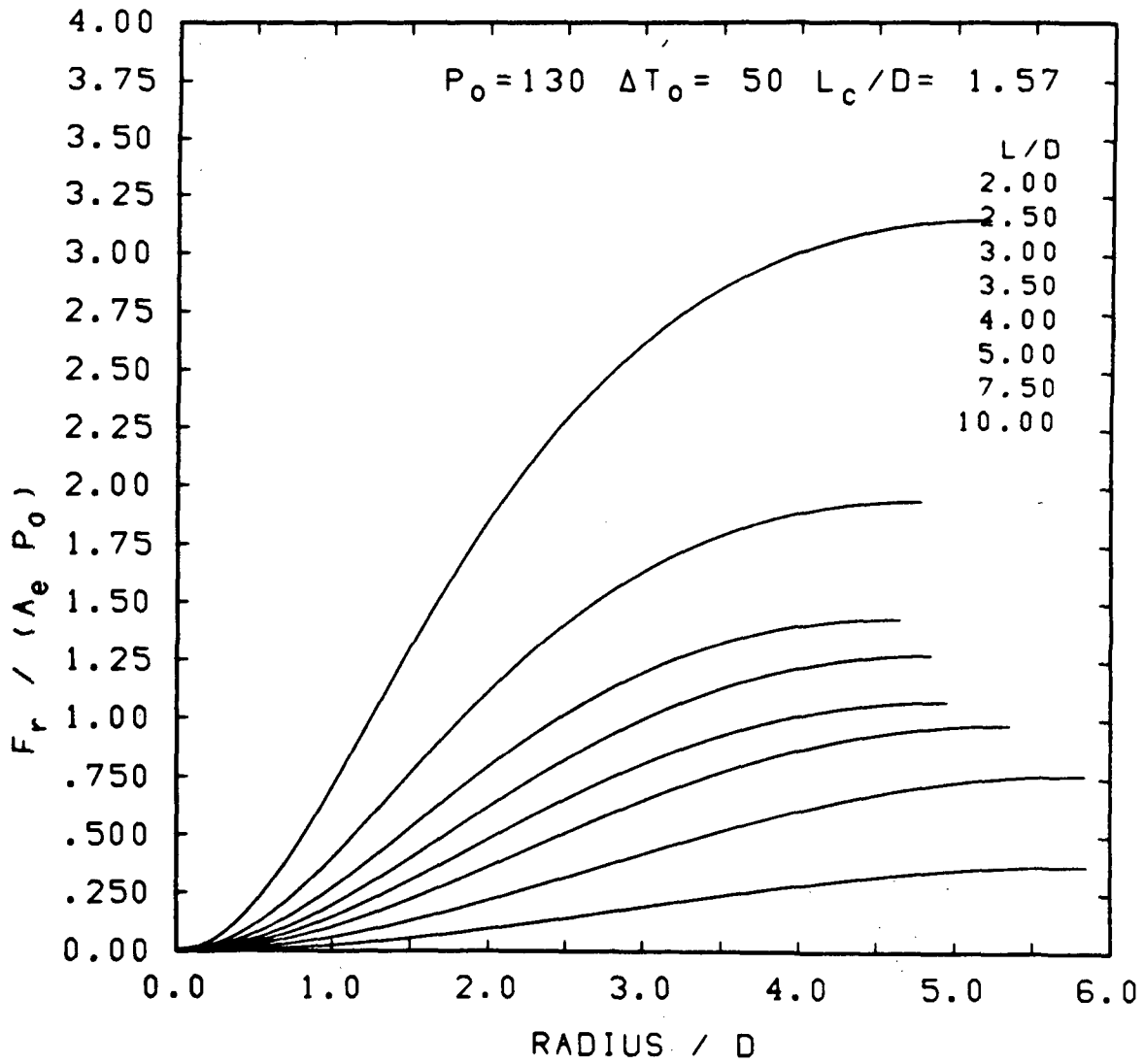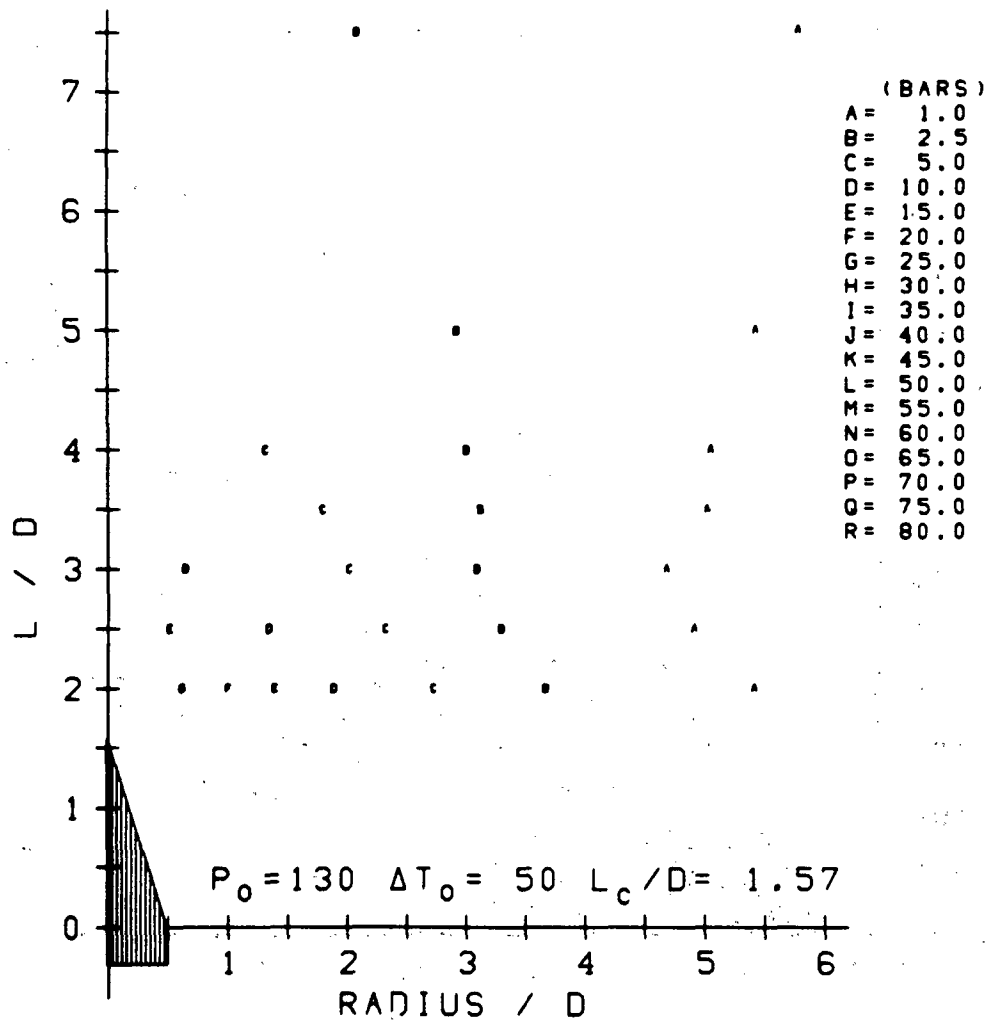FIGURE A.18   COMPOSITE TARGET PRESSURE CONTOURS
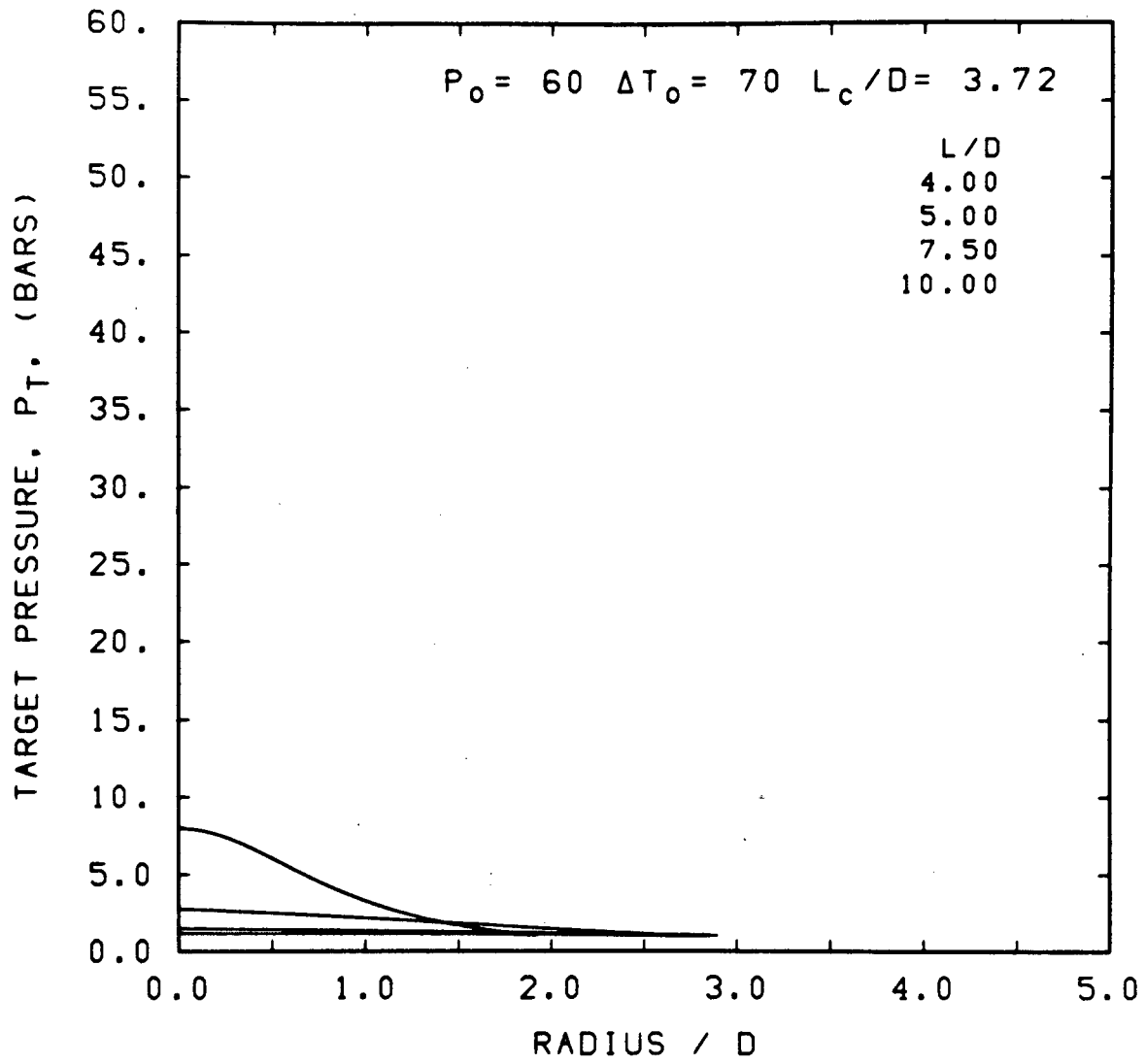
FIGURE A.19   TARGET PRESSURE DISTRIBUTIONS
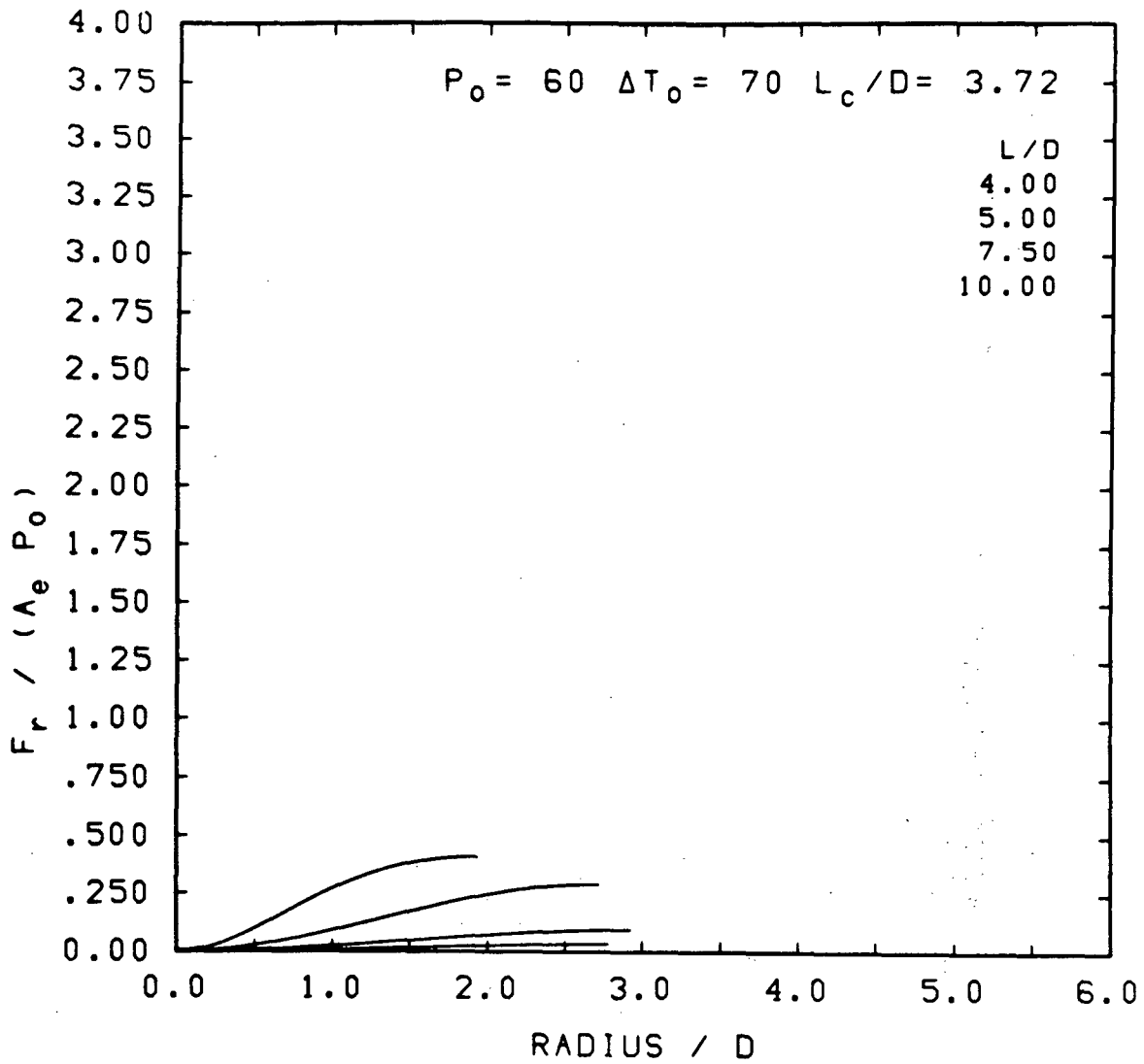
FIGURE A.20   TARGET LOAD DISTRIBUTIONS
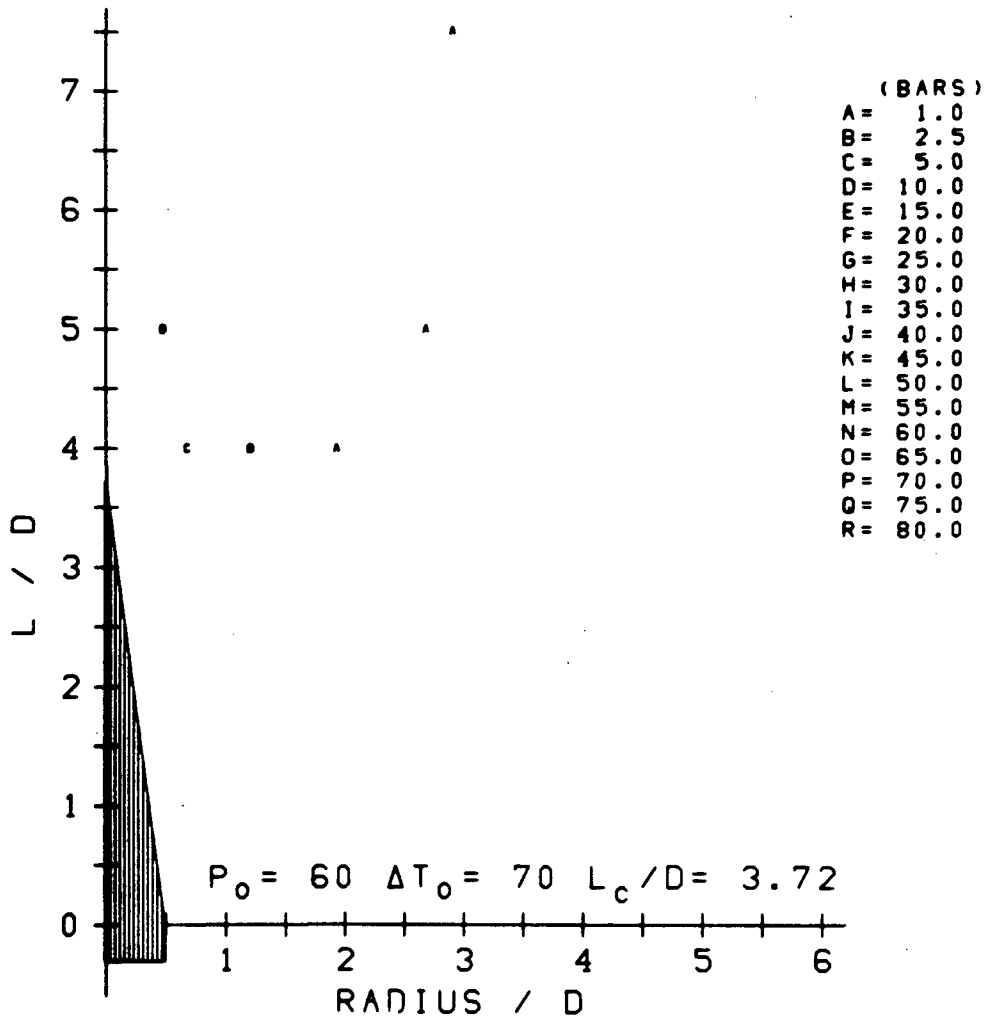
FIGURE A.21   COMPOSITE TARGET PRESSURE CONTOURS

(BARS)
A = 1.0
B = 2.5
C = 5.0
D = 10.0
E = 15.0
F = 20.0
G = 25.0
H = 30.0
I = 35.0
J = 40.0
K = 45.0
L = 50.0
M = 55.0
N = 60.0
O = 65.0
P = 70.0
Q = 75.0
R = 80.0

$P_o = 60$ $\Delta T_o = 70$ $L_c/D = 3.72$
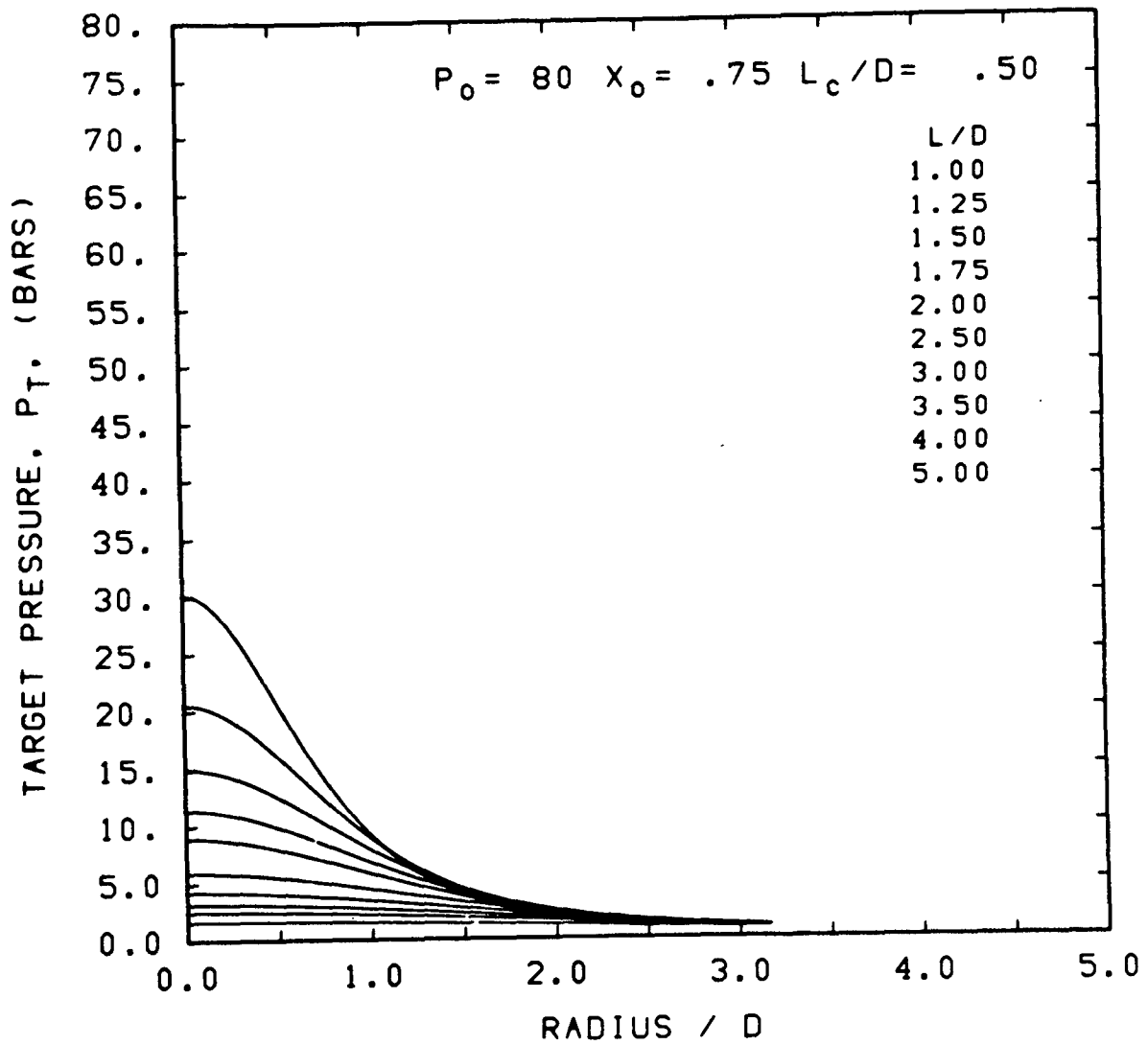
FIGURE A.22 TARGET PRESSURE DISTRIBUTIONS

161
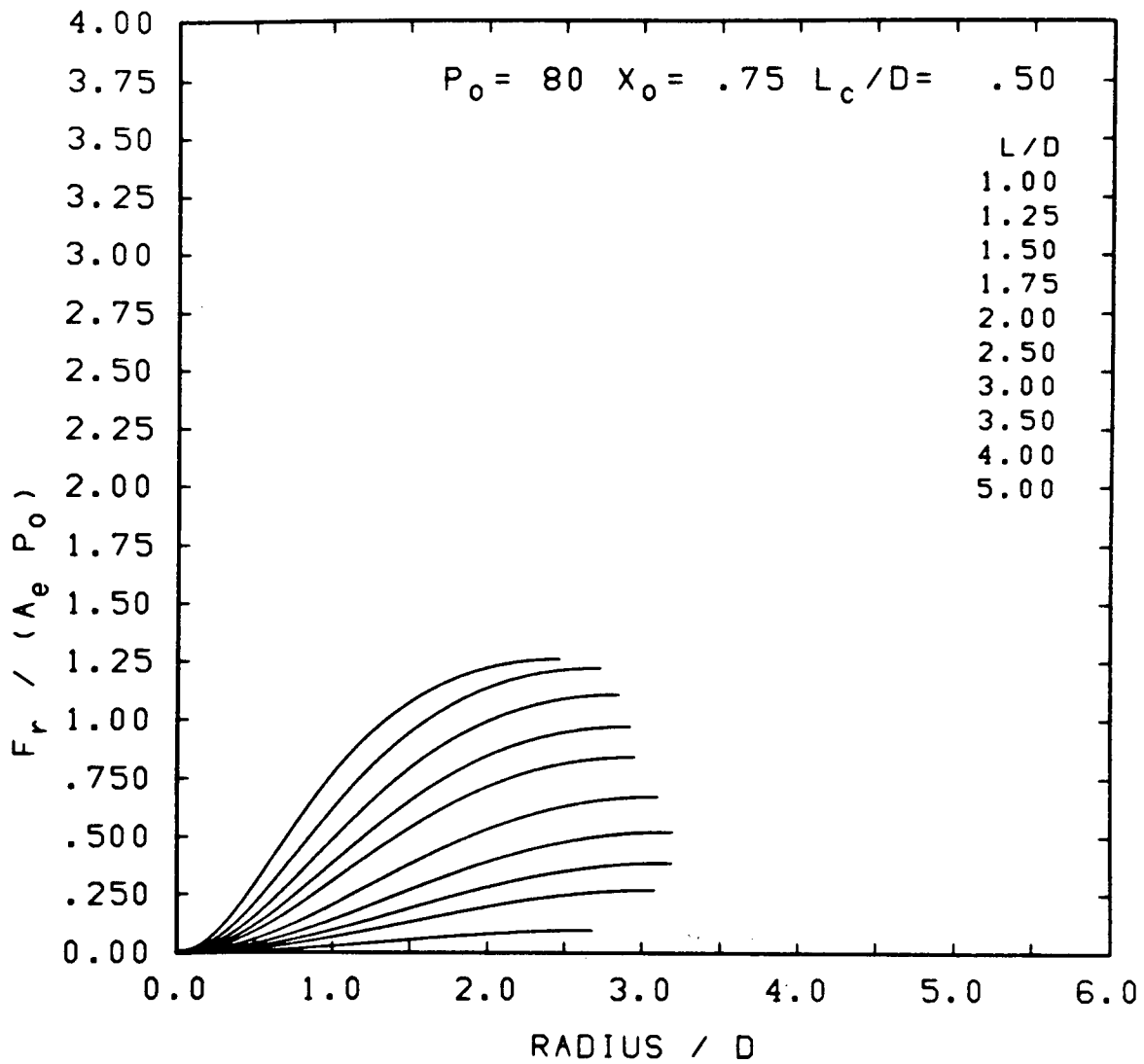
FIGURE A.23 TARGET LOAD DISTRIBUTIONS

162
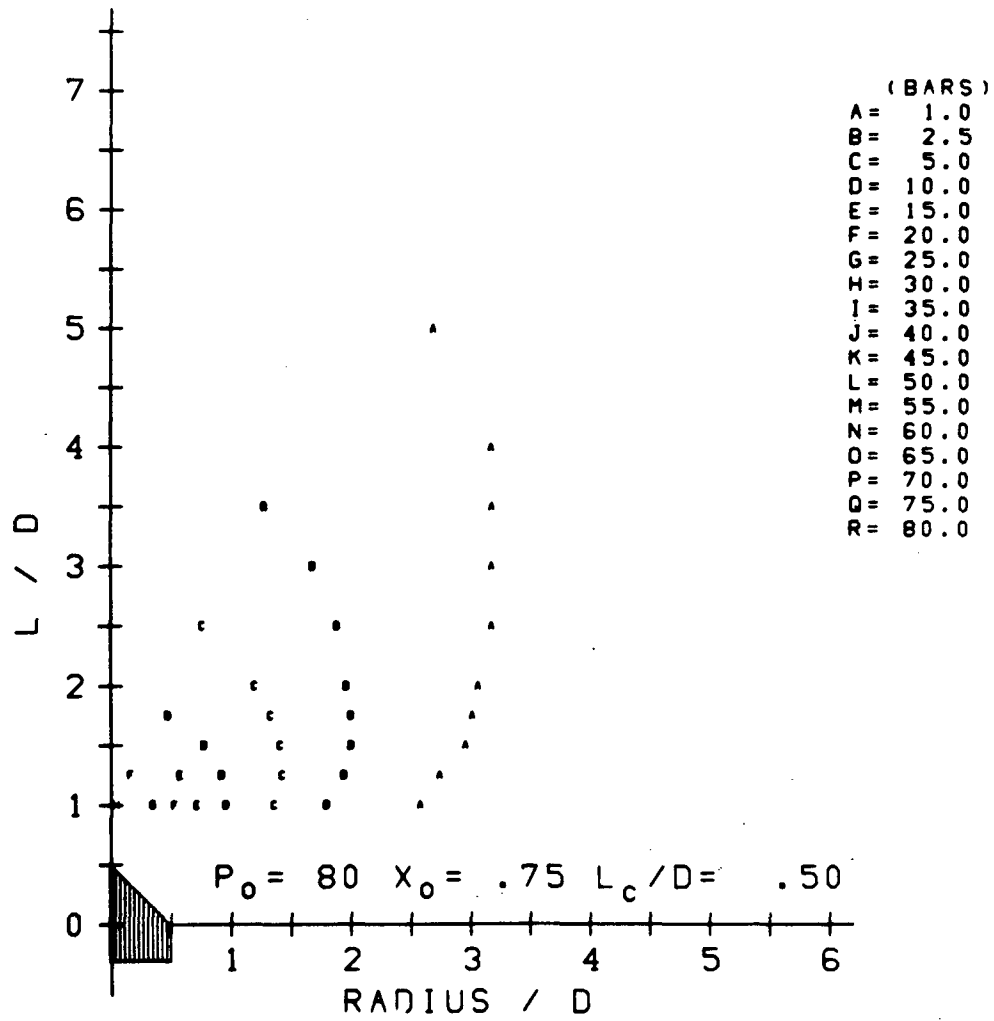
FIGURE A.24   COMPOSITE TARGET PRESSURE CONTOURS

163
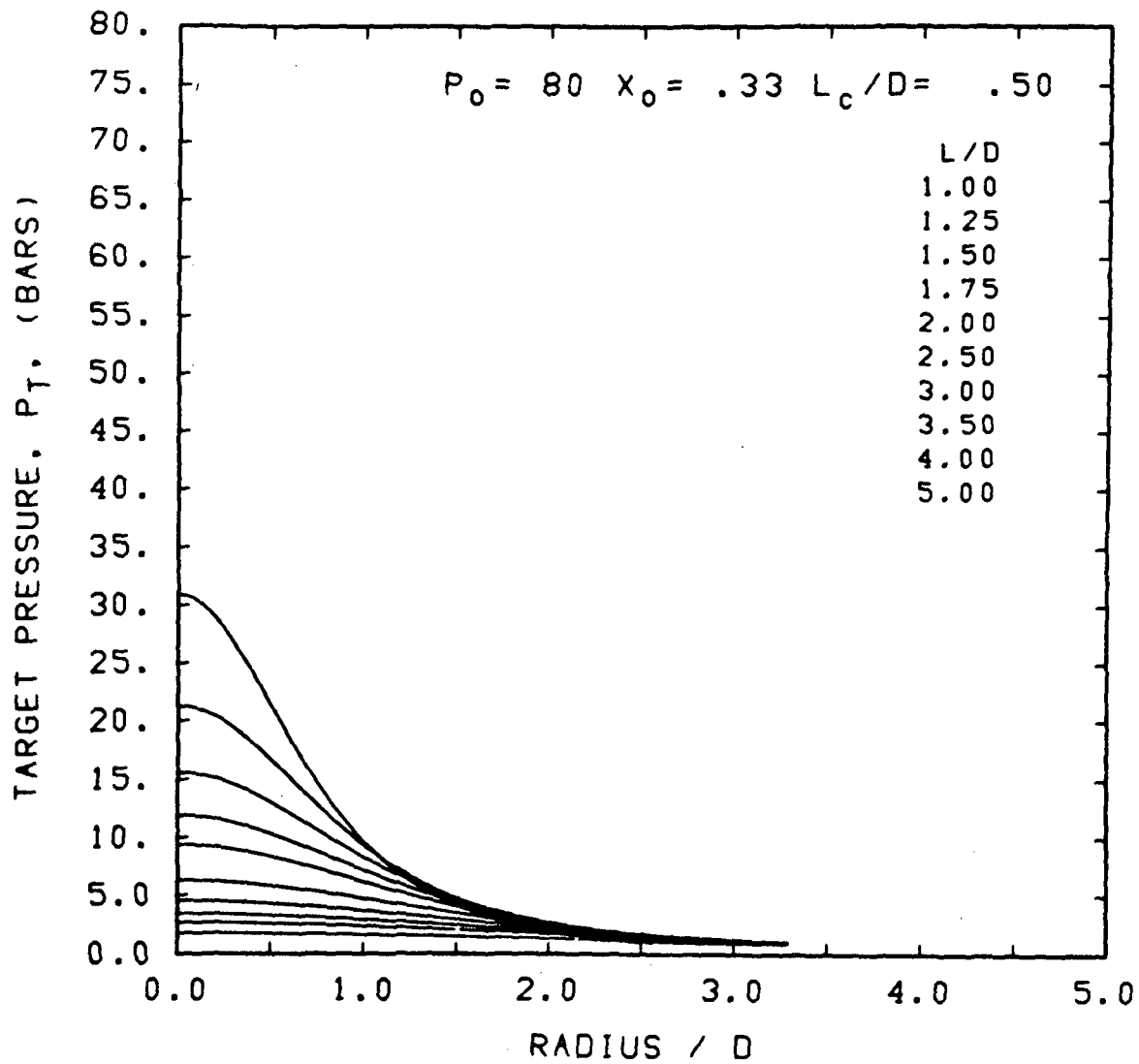
FIGURE A.25   TARGET PRESSURE DISTRIBUTIONS

The figure shows target pressure distributions with the following parameters and legend:

$P_0 = 80$ $X_0 = .33$ $L_c/D = .50$

L/D
1.00
1.25
1.50
1.75
2.00
2.50
3.00
3.50
4.00
5.00

The vertical axis is labeled TARGET PRESSURE, P_T, (BARS) with values 0.0, 5.0, 10., 15., 20., 25., 30., 35., 40., 45., 50., 55., 60., 65., 70., 75., 80.

The horizontal axis is labeled RADIUS / D with values 0.0, 1.0, 2.0, 3.0, 4.0, 5.0
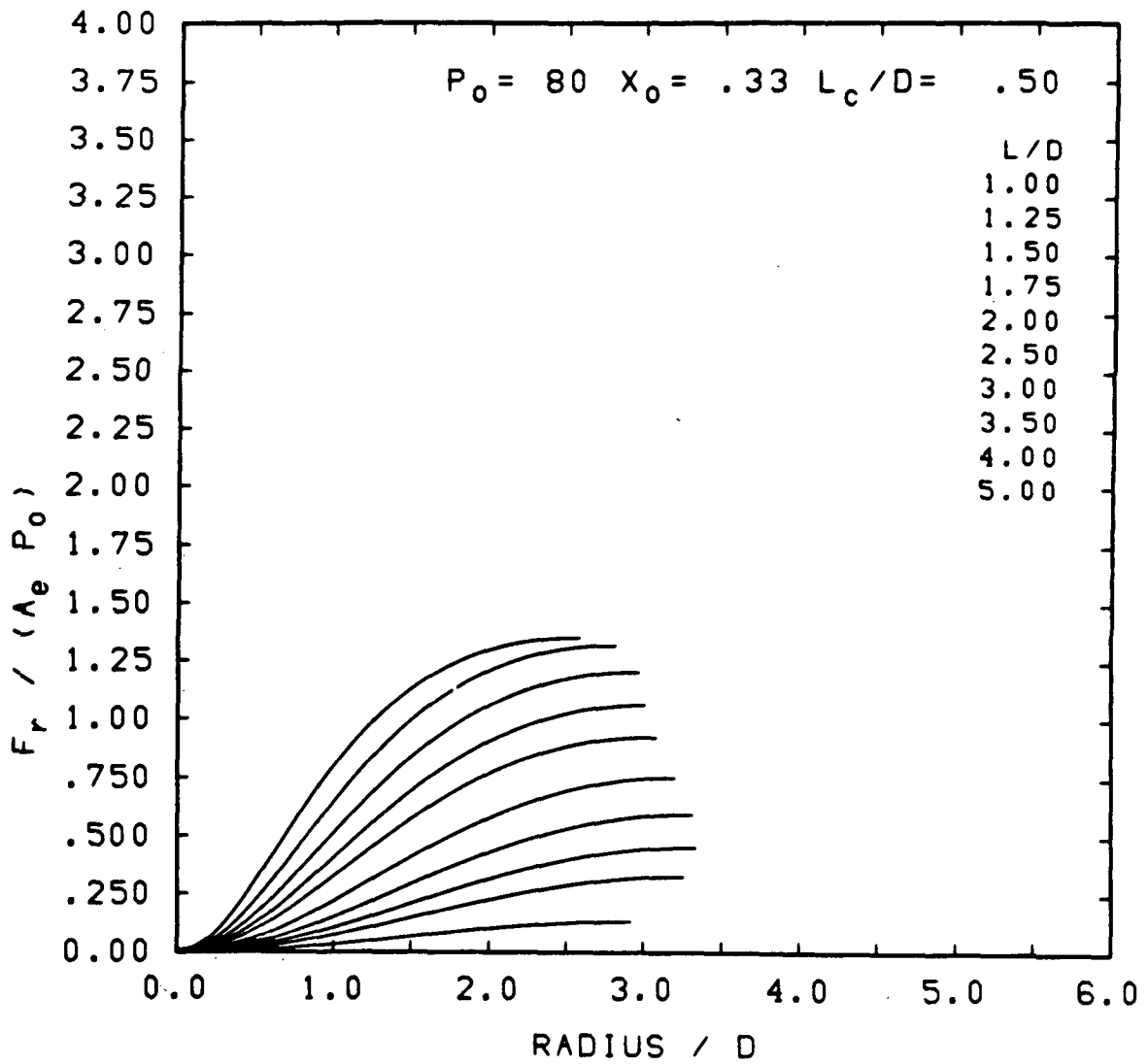
FIGURE A.26   TARGET LOAD DISTRIBUTIONS
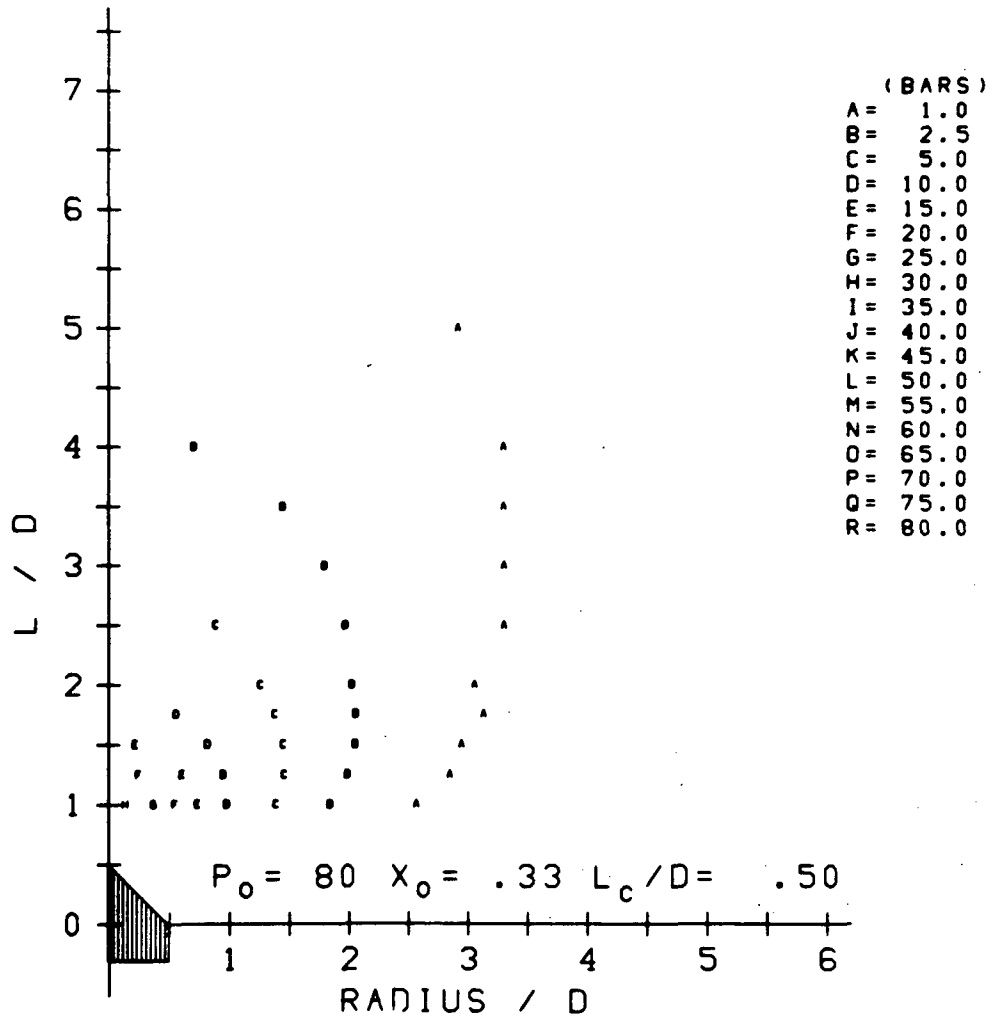
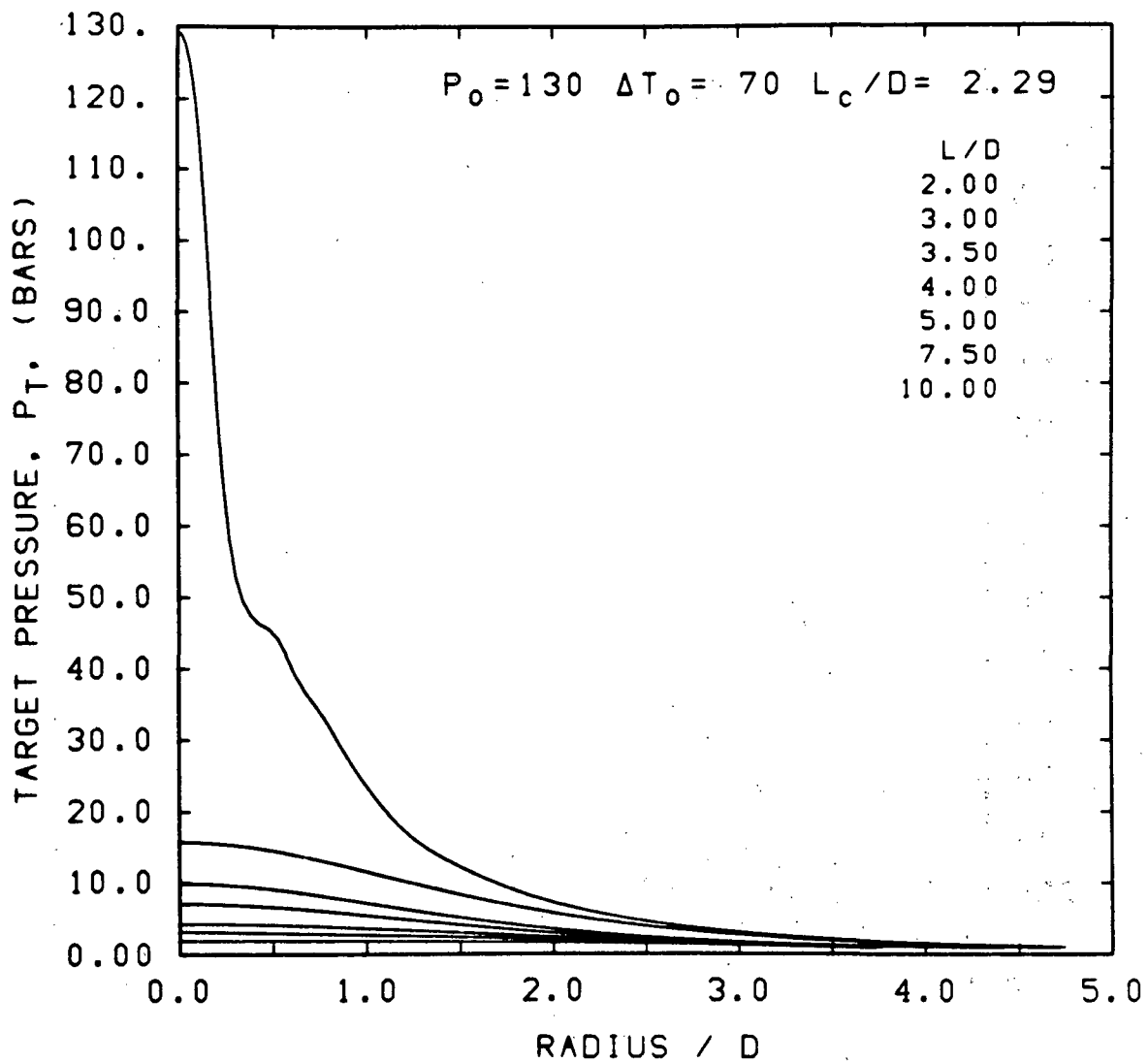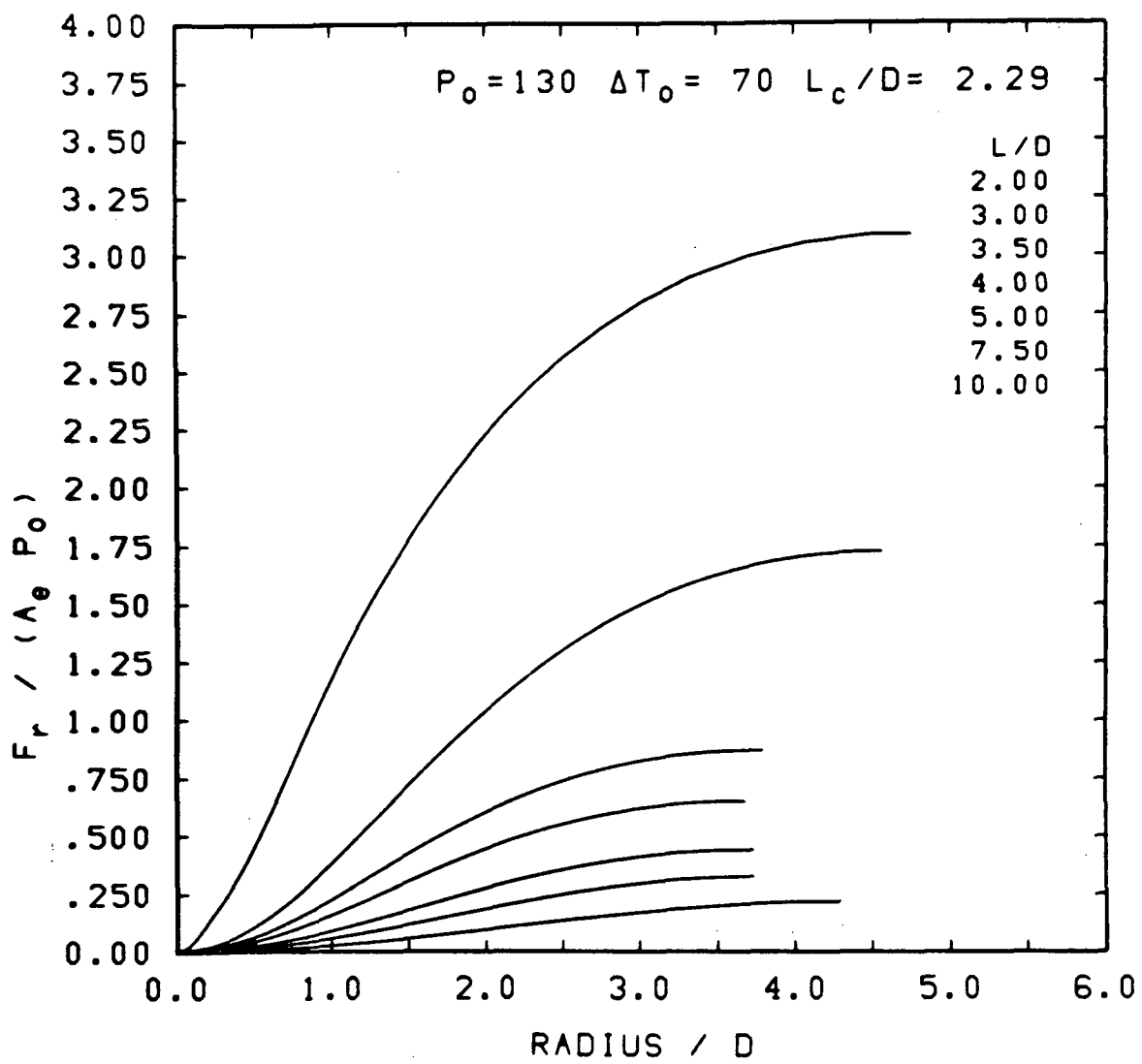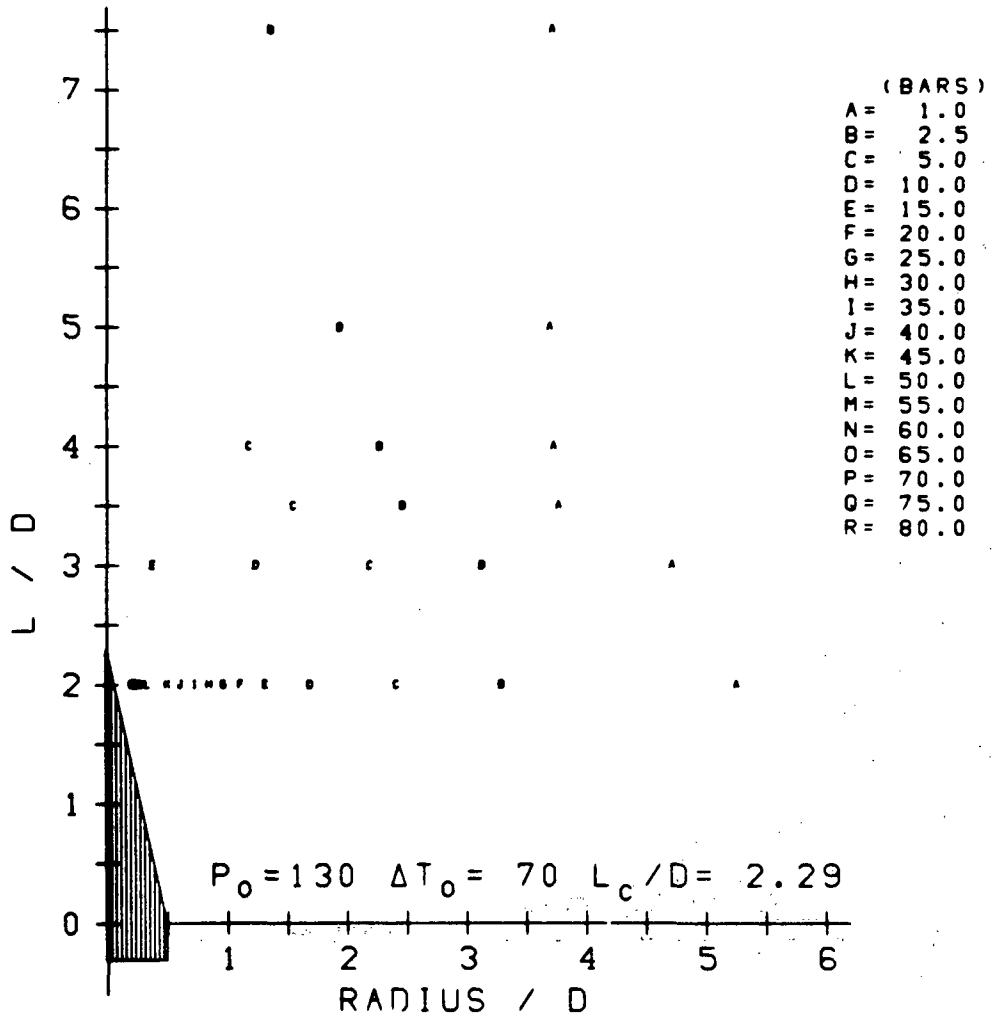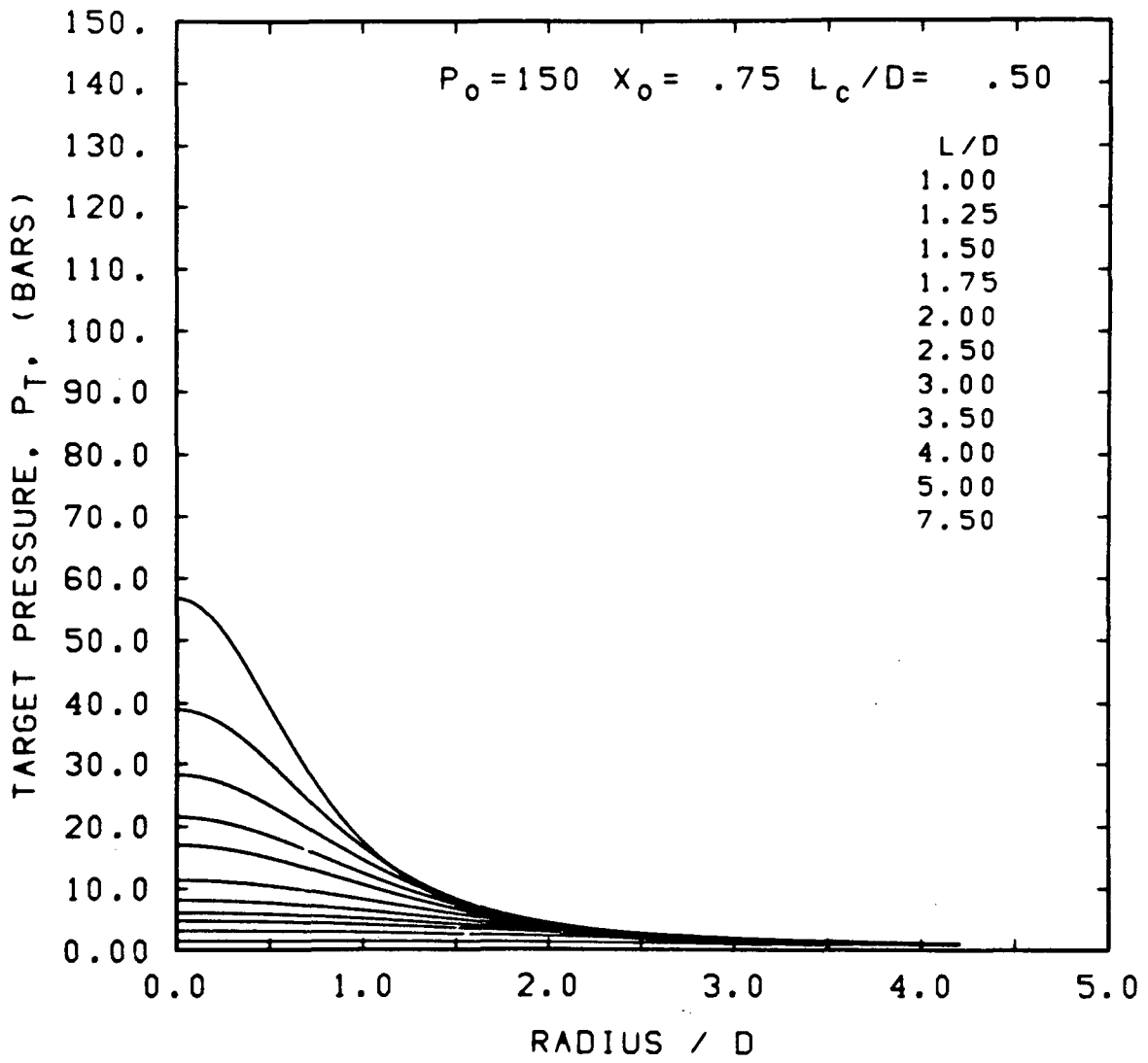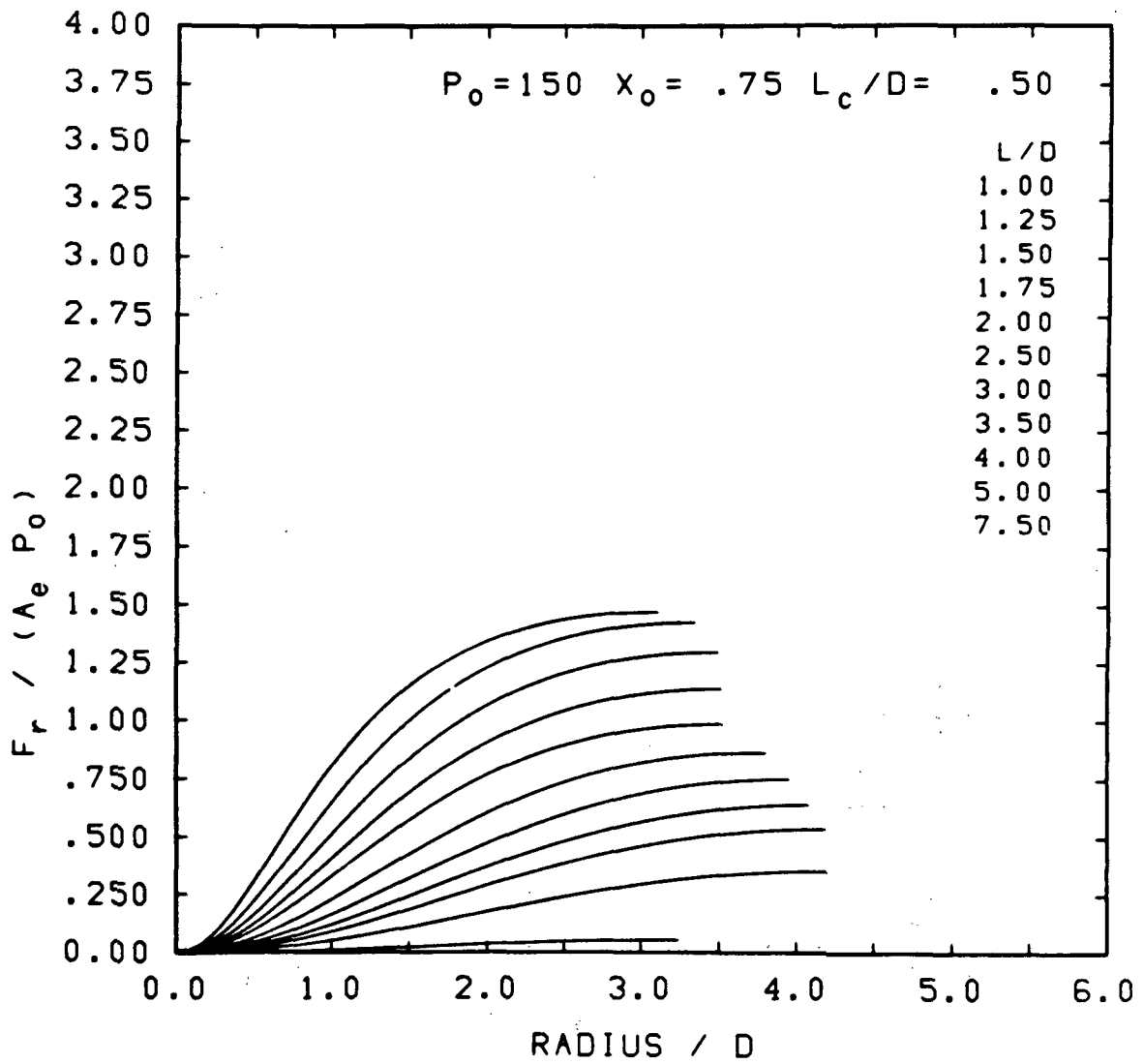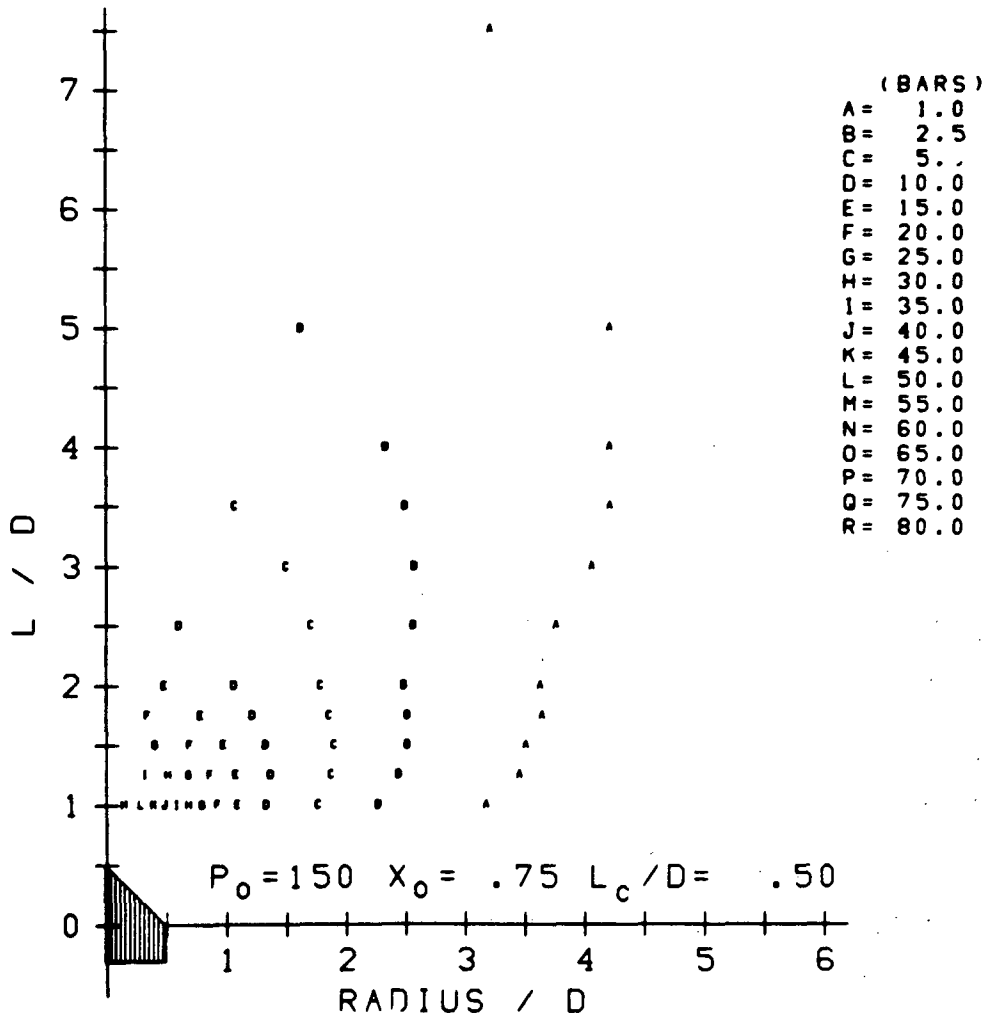FIGURE A.27   COMPOSITE TARGET PRESSURE CONTOURS
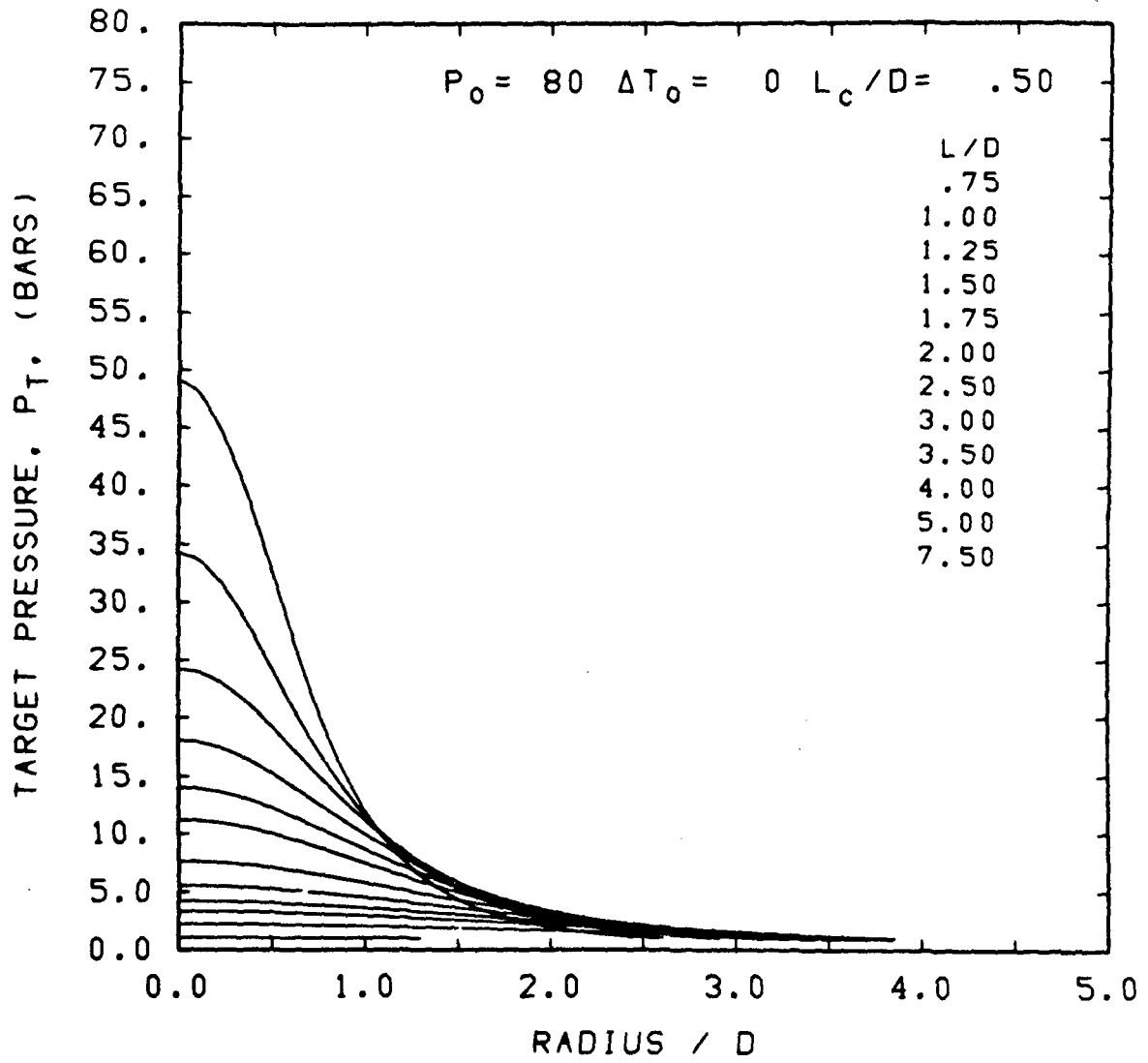
FIGURE A.28   TARGET PRESSURE DISTRIBUTIONS
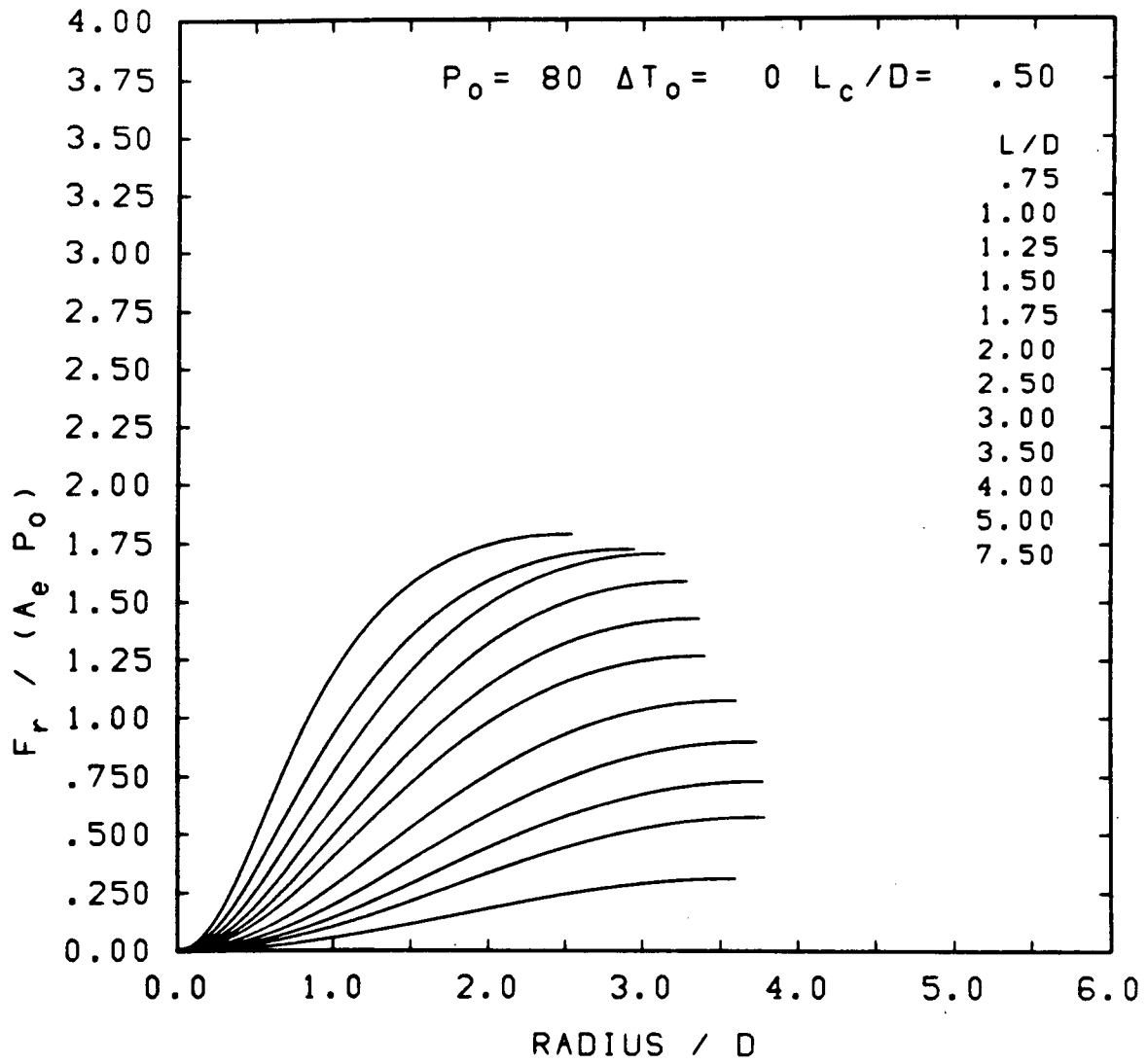
FIGURE A.29   TARGET LOAD DISTRIBUTIONS
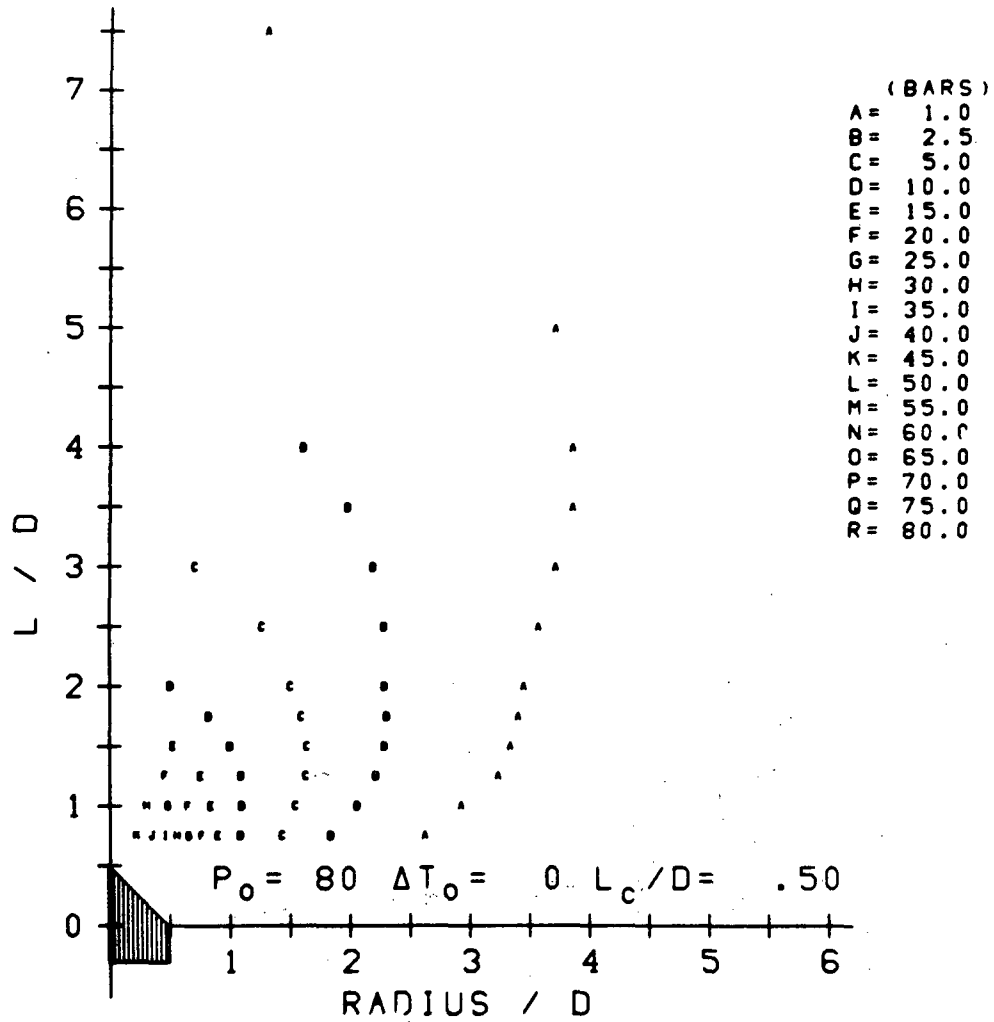
FIGURE A.30   COMPOSITE TARGET PRESSURE CONTOURS

(BARS)
A = 1.0
B = 2.5
C = 5.0
D = 10.0
E = 15.0
F = 20.0
G = 25.0
H = 30.0
I = 35.0
J = 40.0
K = 45.0
L = 50.0
M = 55.0
N = 60.0
O = 65.0
P = 70.0
Q = 75.0
R = 80.0

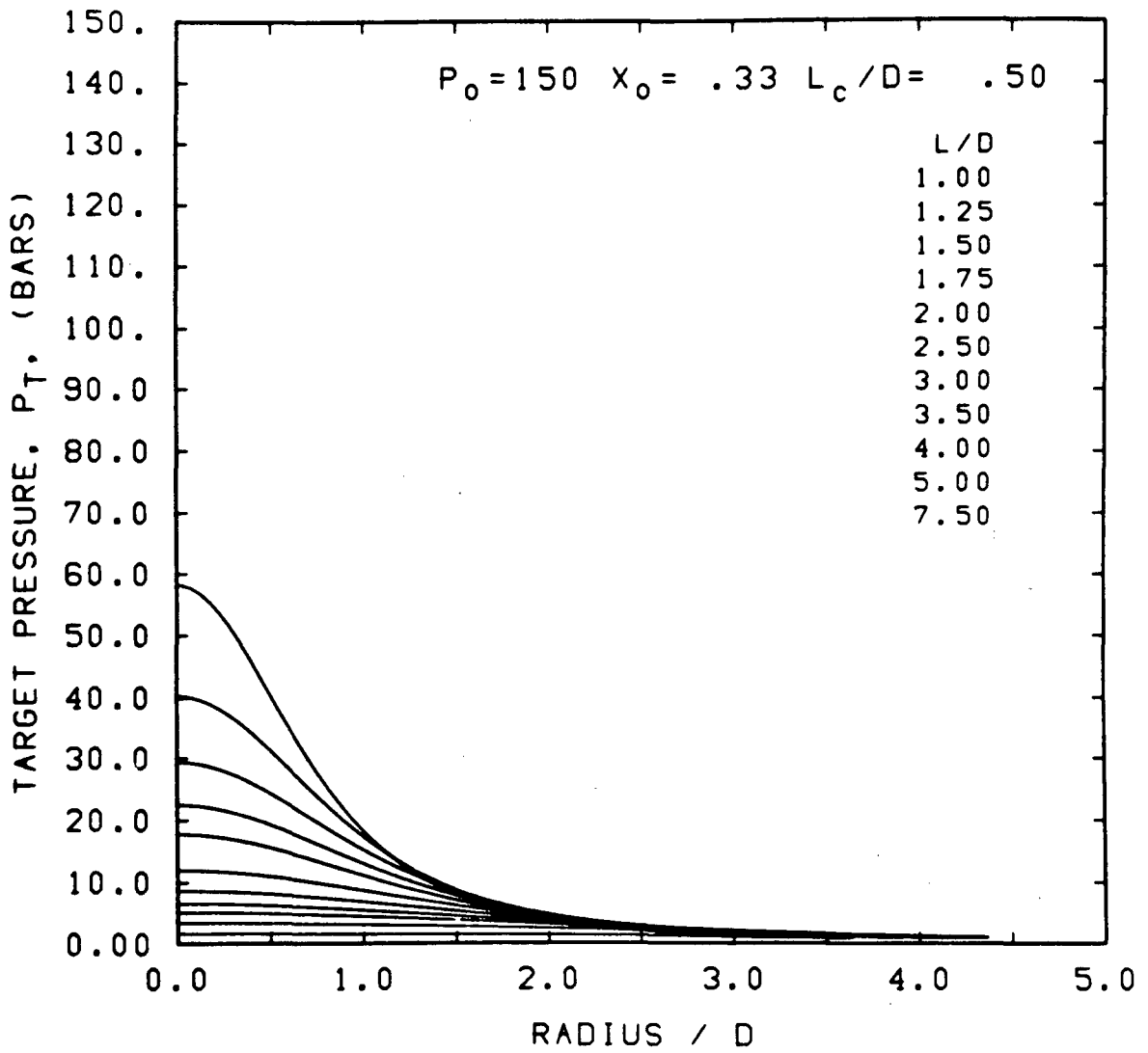$P_o = 80$ $\Delta T_o = 0$ $L_c/D = .50$

L / D

RADIUS / D
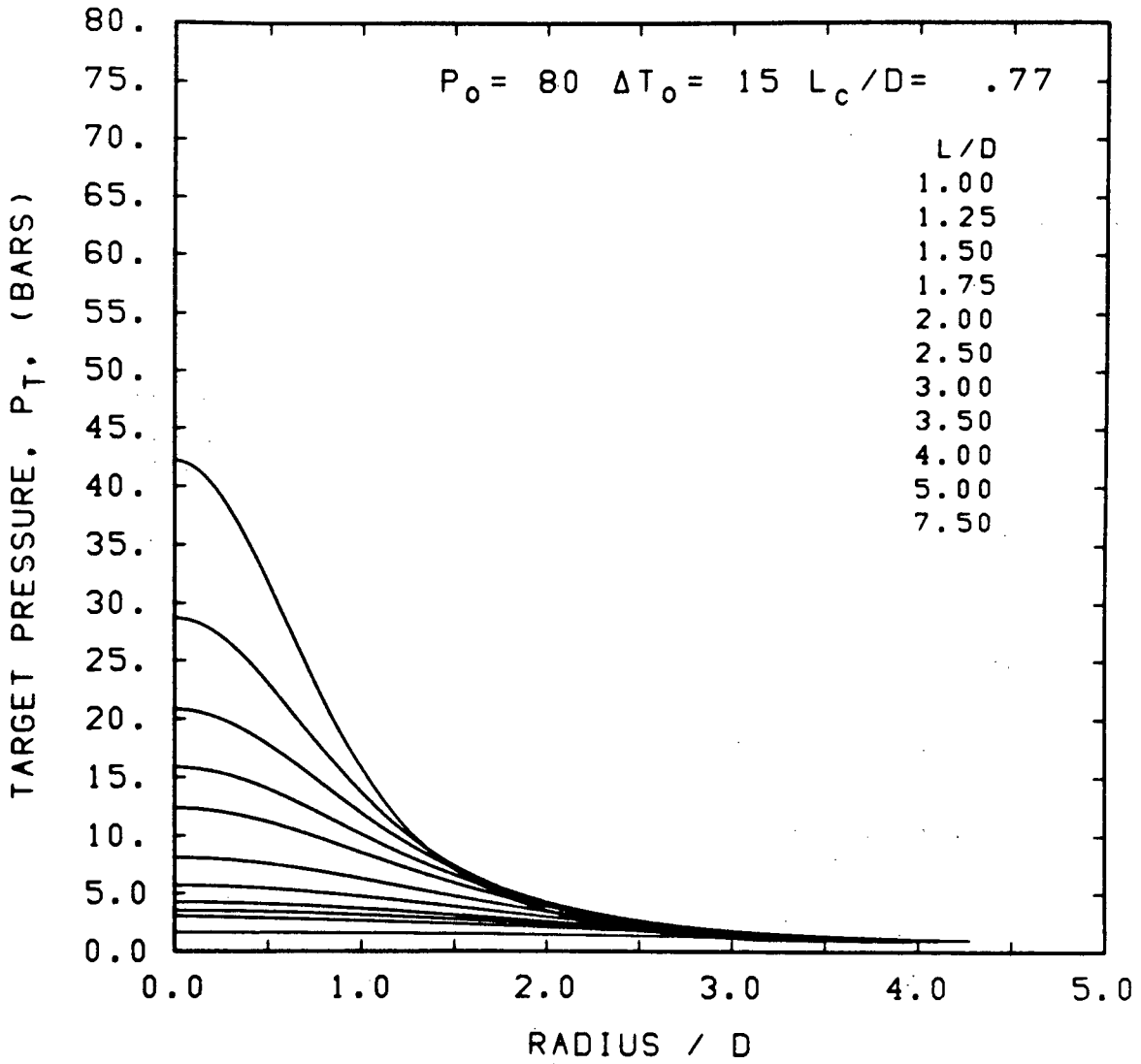
FIGURE A.31   TARGET PRESSURE DISTRIBUTIONS
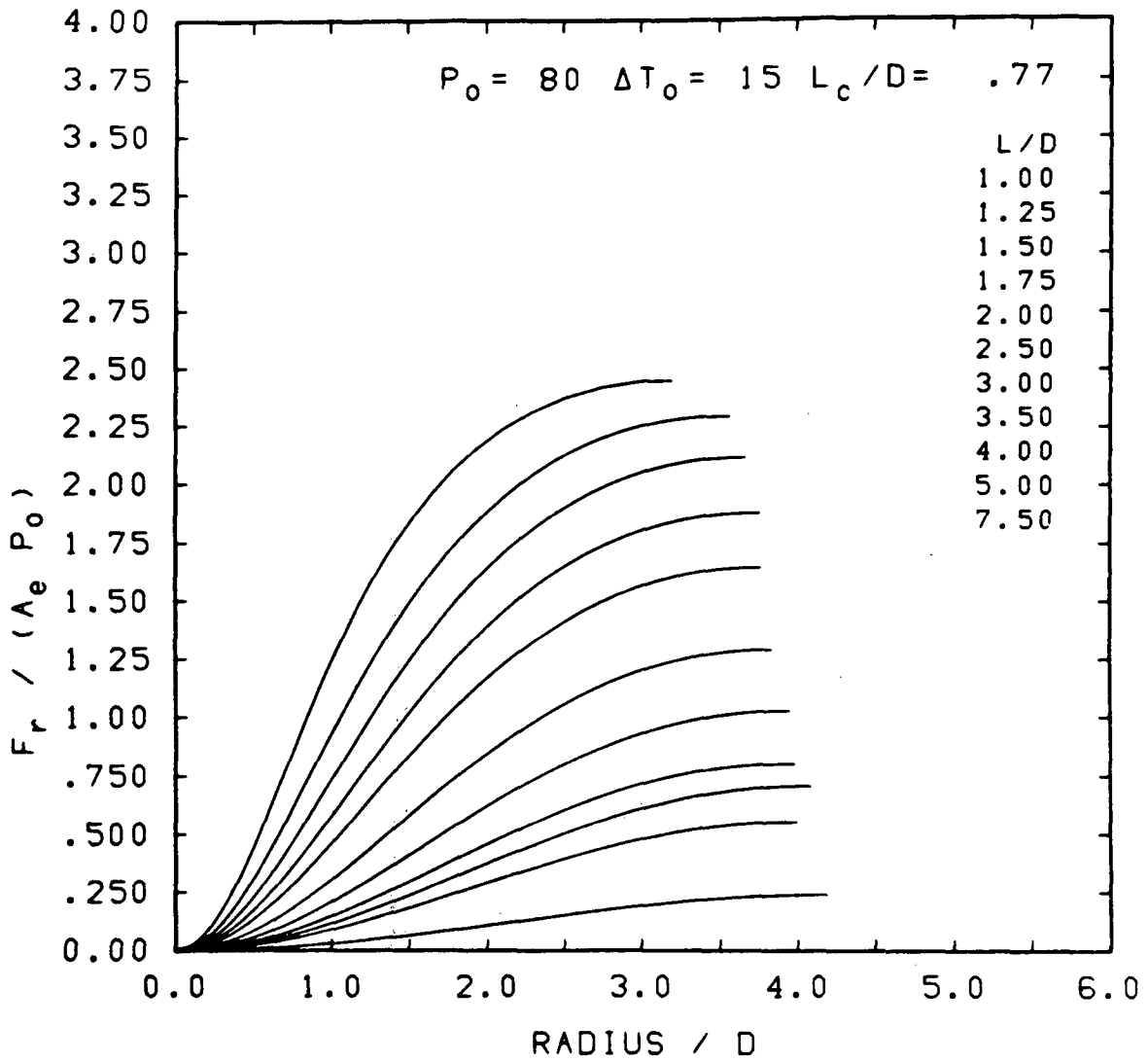
FIGURE A.32   TARGET LOAD DISTRIBUTIONS
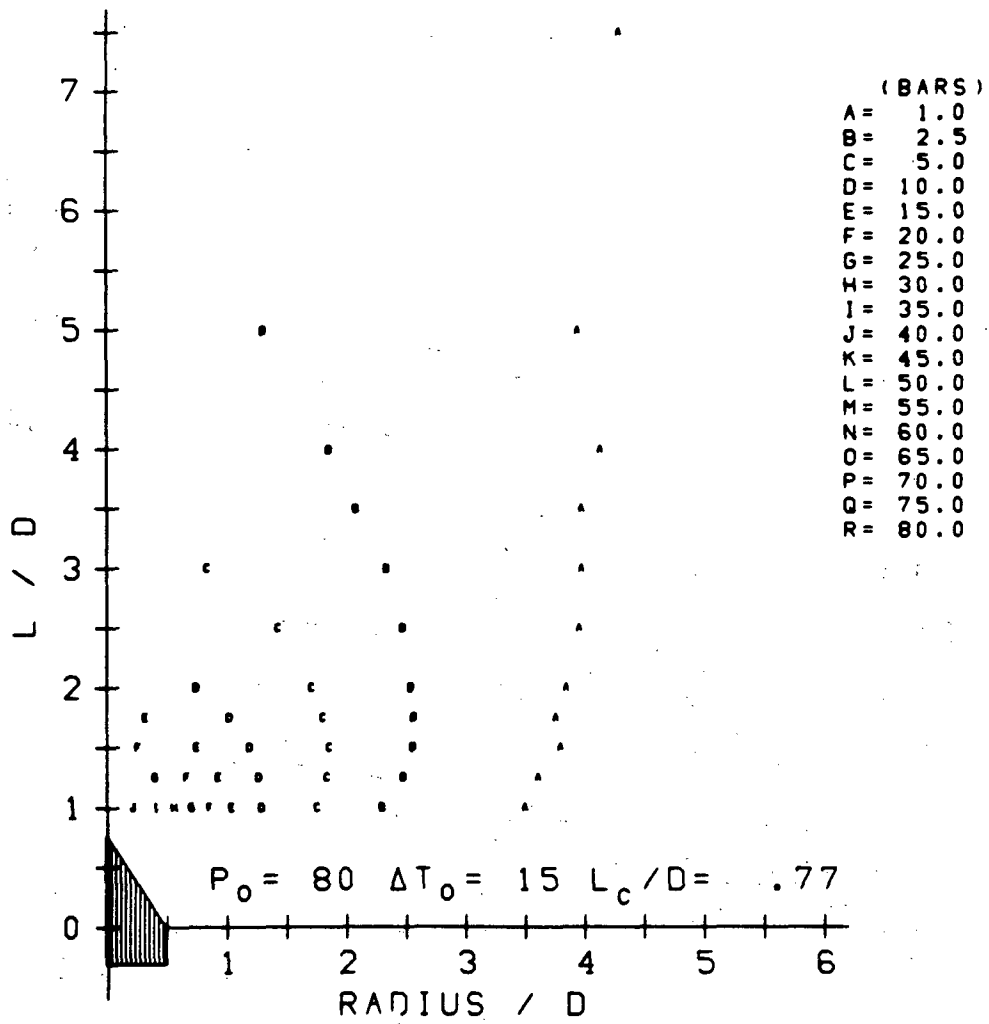
FIGURE A.33   COMPOSITE TARGET PRESSURE CONTOURS

172
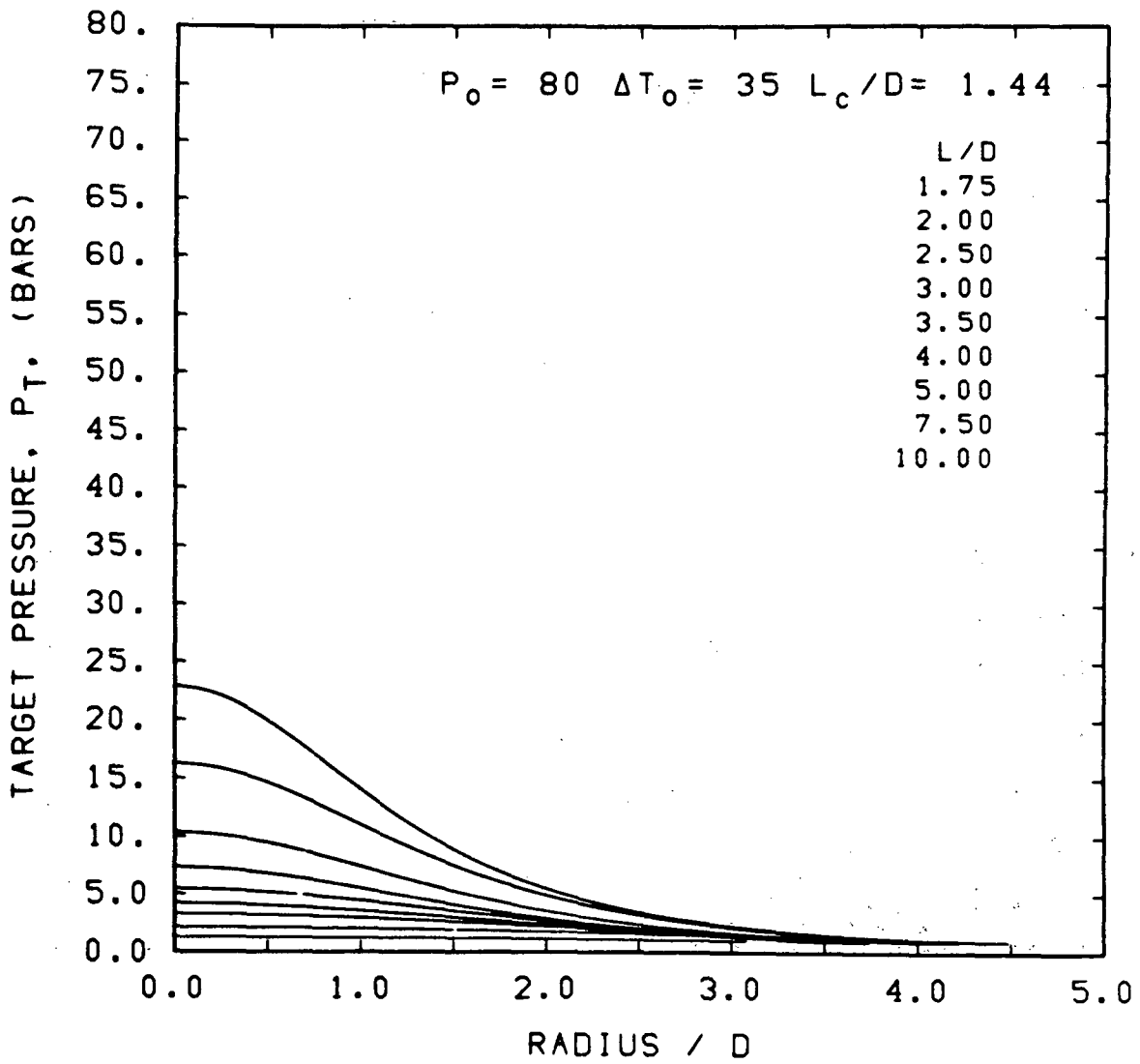
FIGURE A.34   TARGET PRESSURE DISTRIBUTIONS

$P_o = 80 \quad \Delta T_o = 35 \quad L_c/D = 1.44$

L/D
1.75
2.00
2.50
3.00
3.50
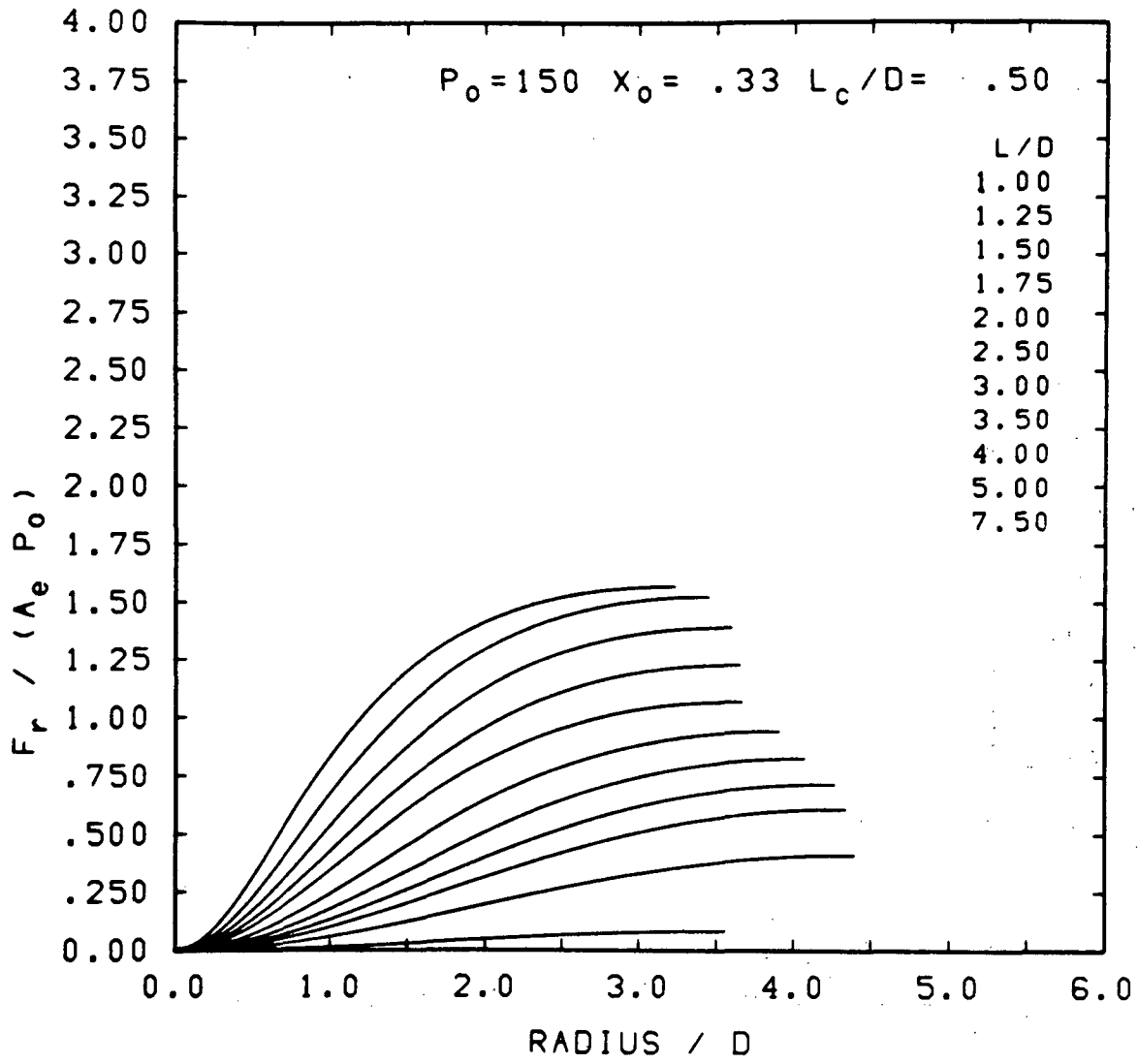4.00
5.00
7.50
10.00
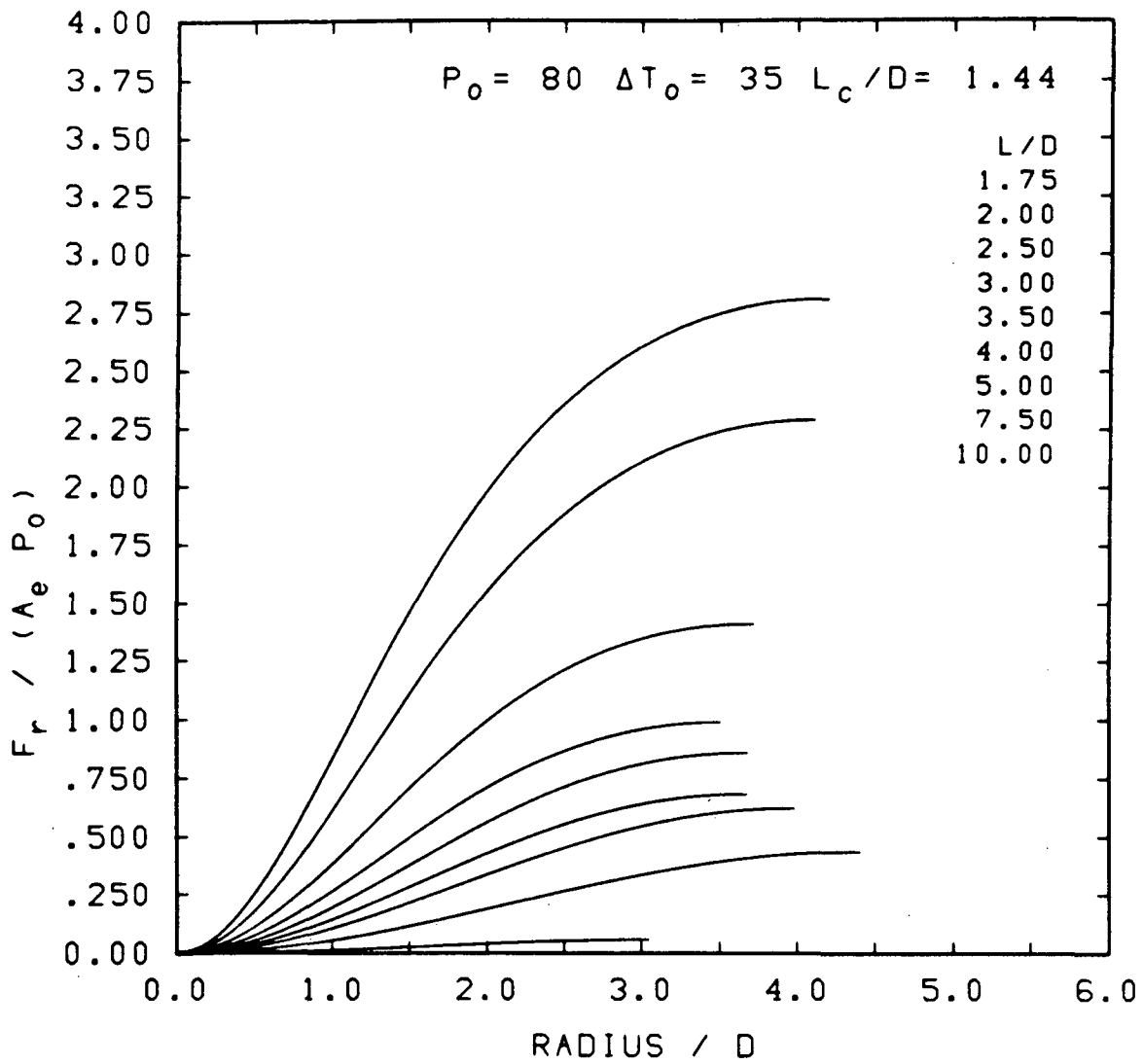
FIGURE A.35   TARGET LOAD DISTRIBUTIONS
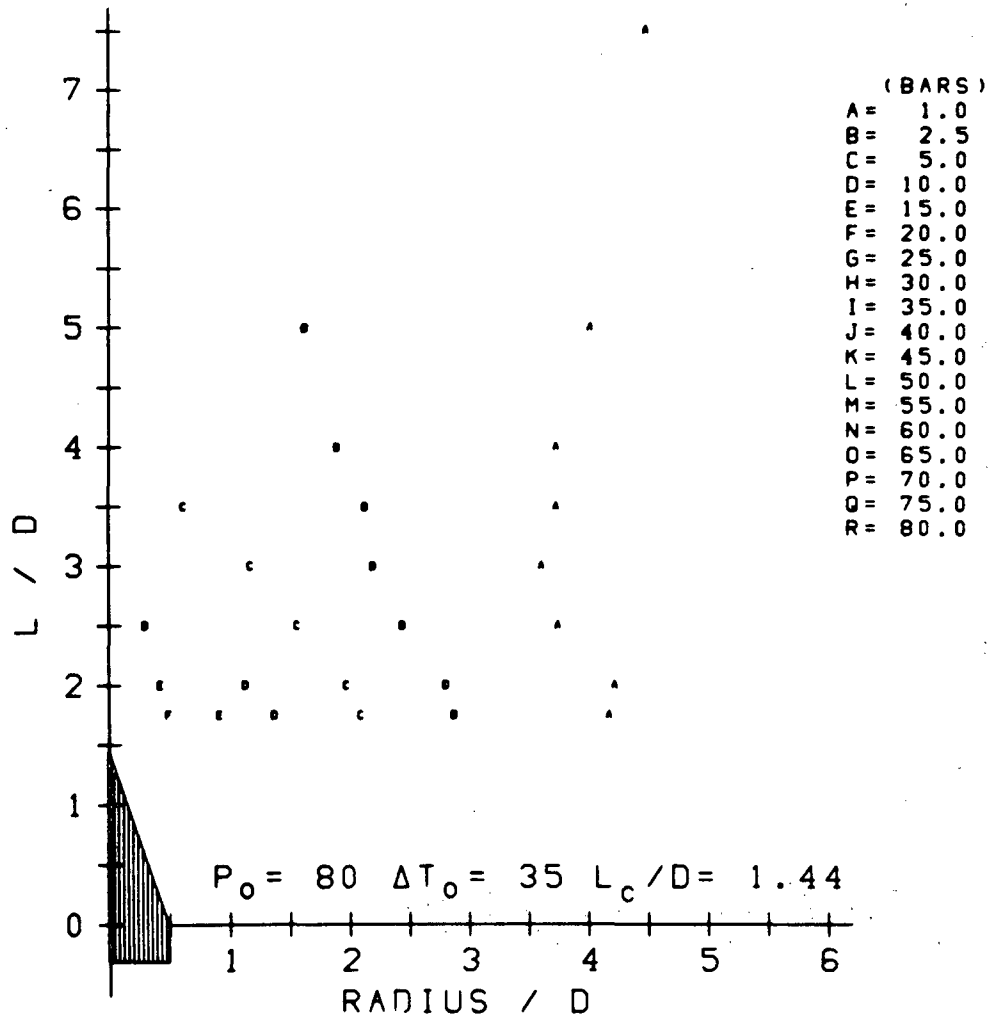
FIGURE A.36   COMPOSITE TARGET PRESSURE CONTOURS
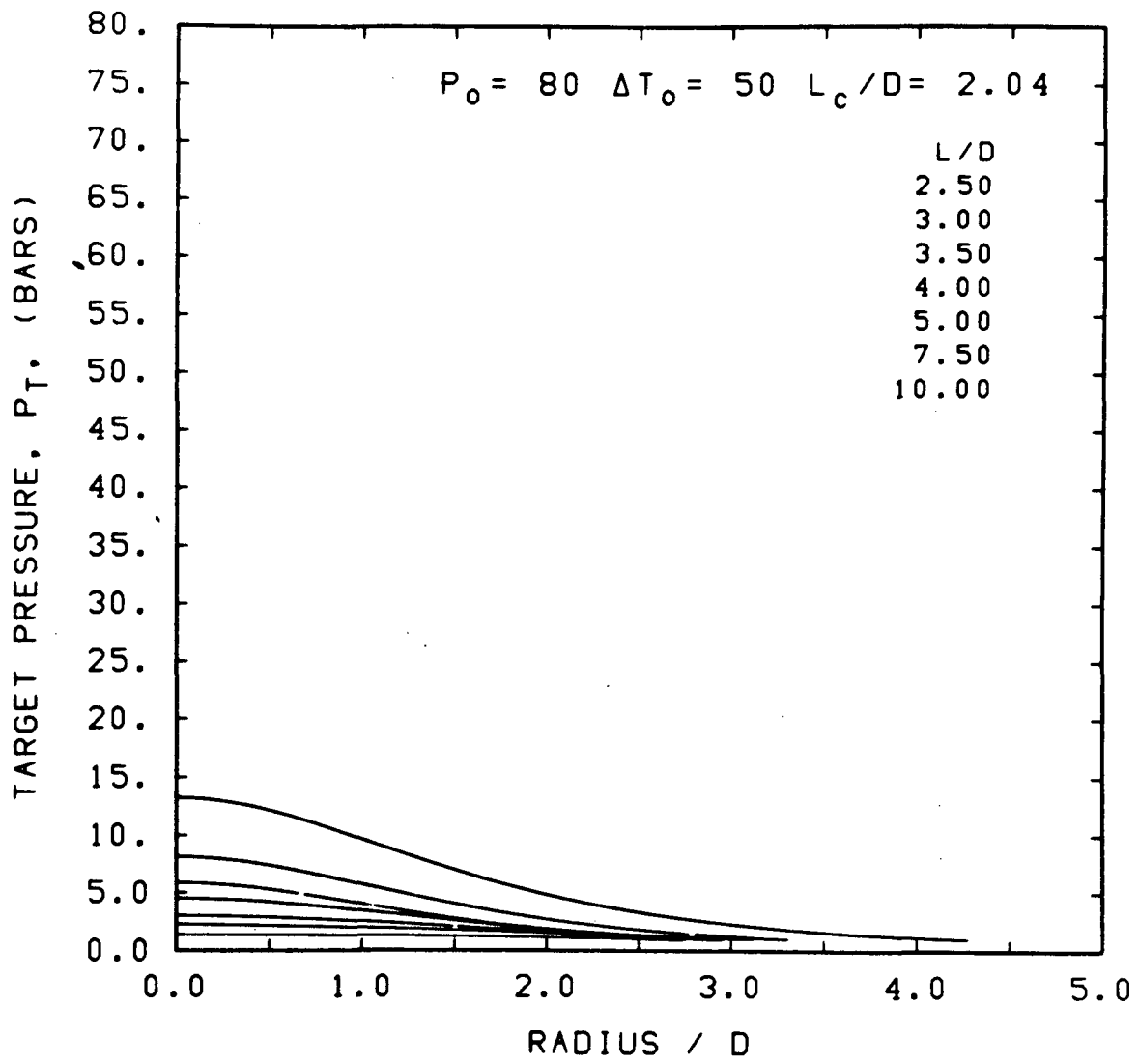
FIGURE A.37   TARGET PRESSURE DISTRIBUTIONS
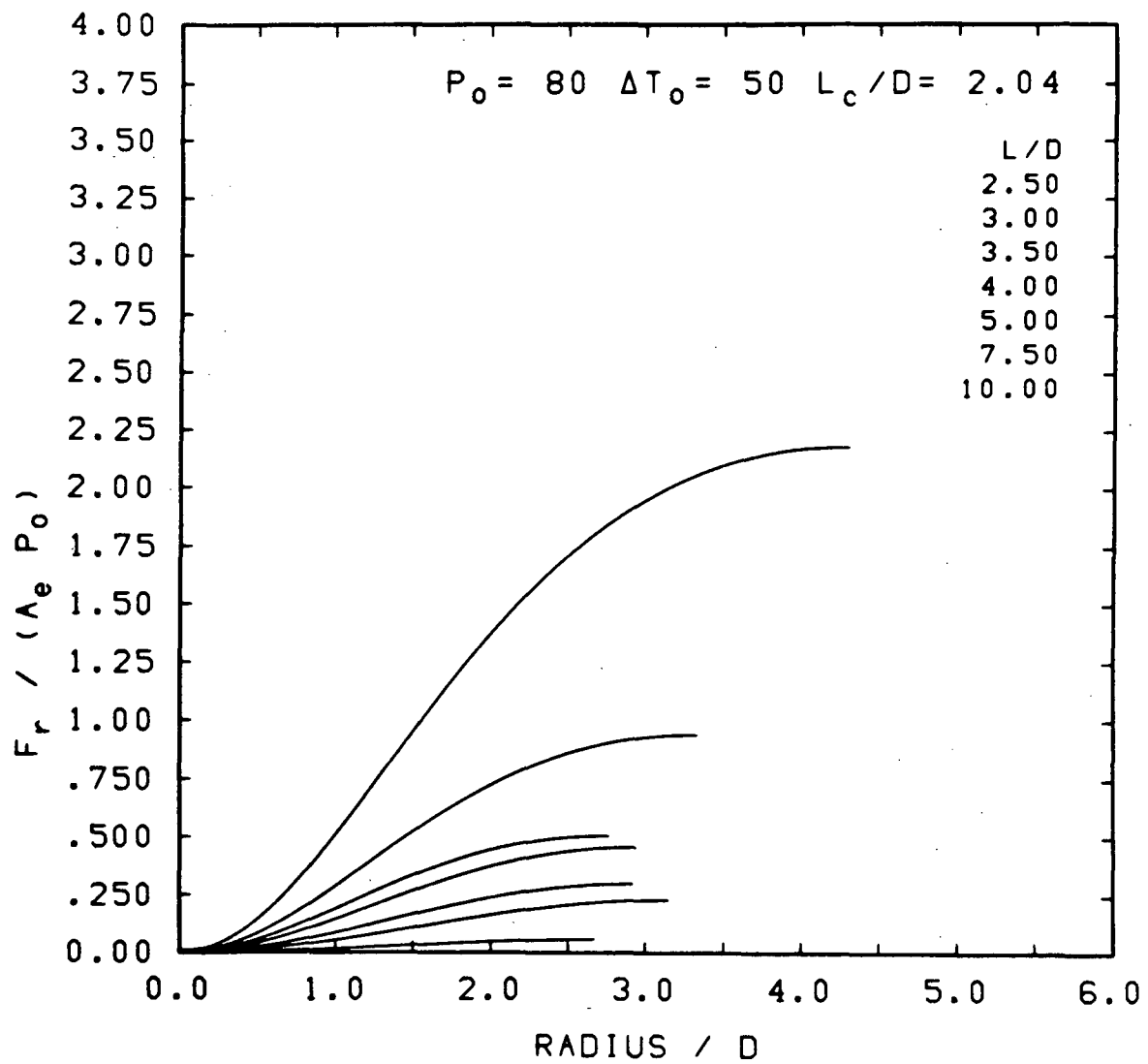
FIGURE A.38   TARGET LOAD DISTRIBUTIONS

177
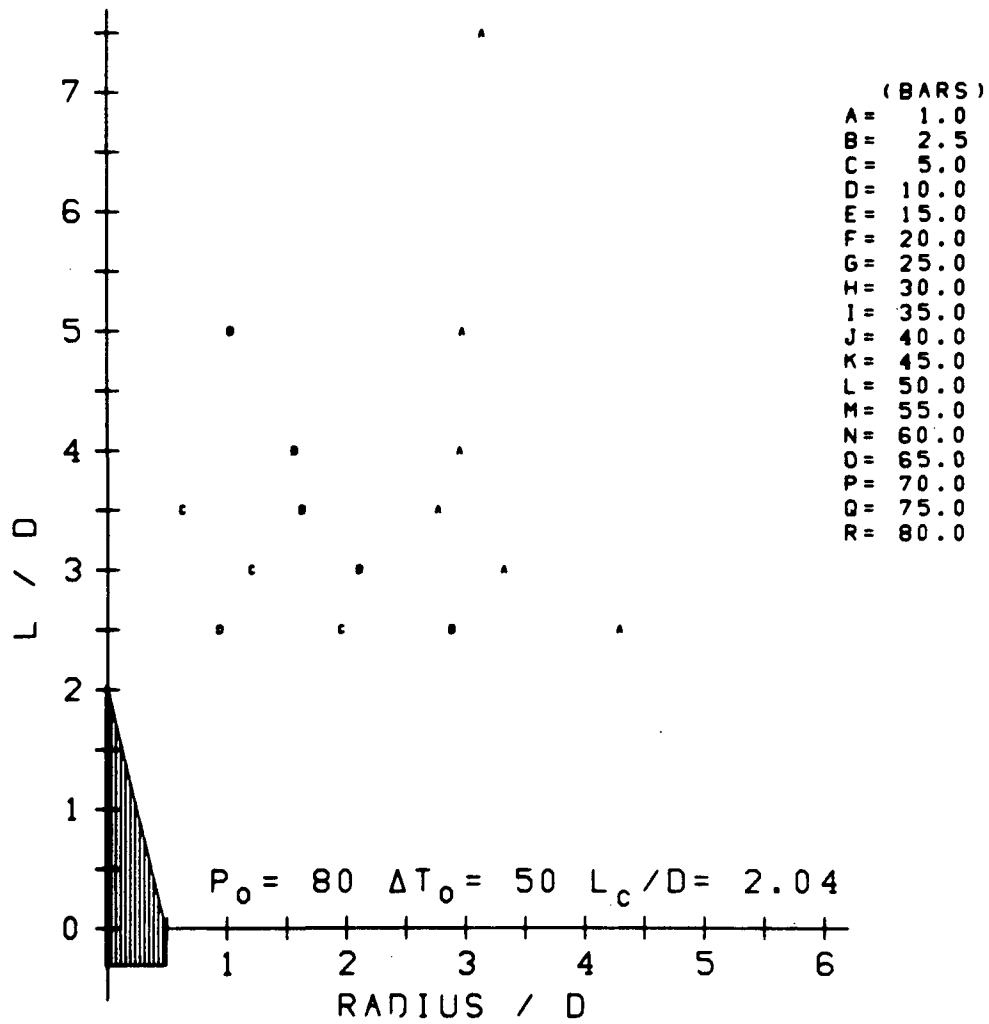
FIGURE A.39 COMPOSITE TARGET PRESSURE CONTOURS

178
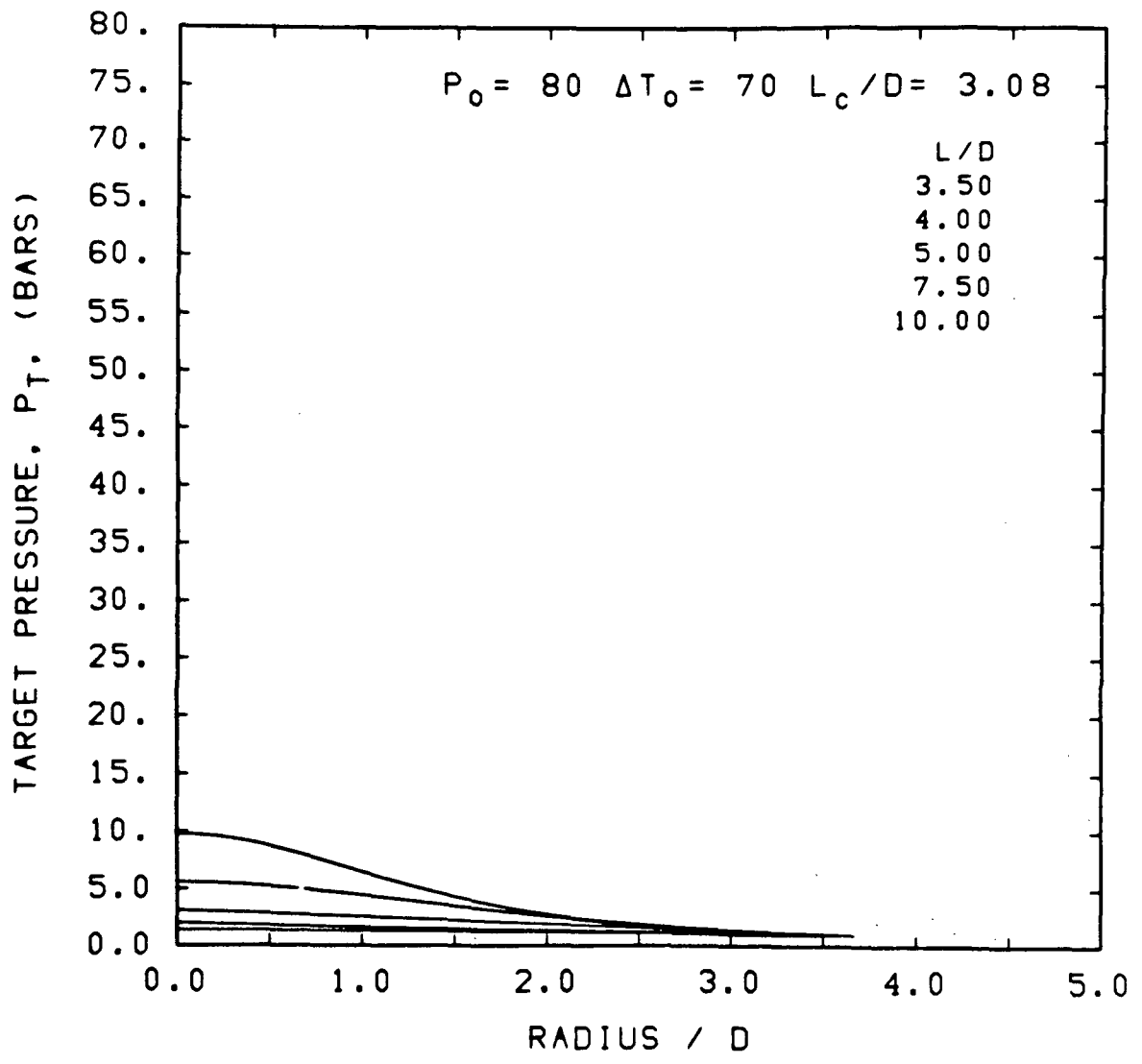
FIGURE A.40   TARGET PRESSURE DISTRIBUTIONS
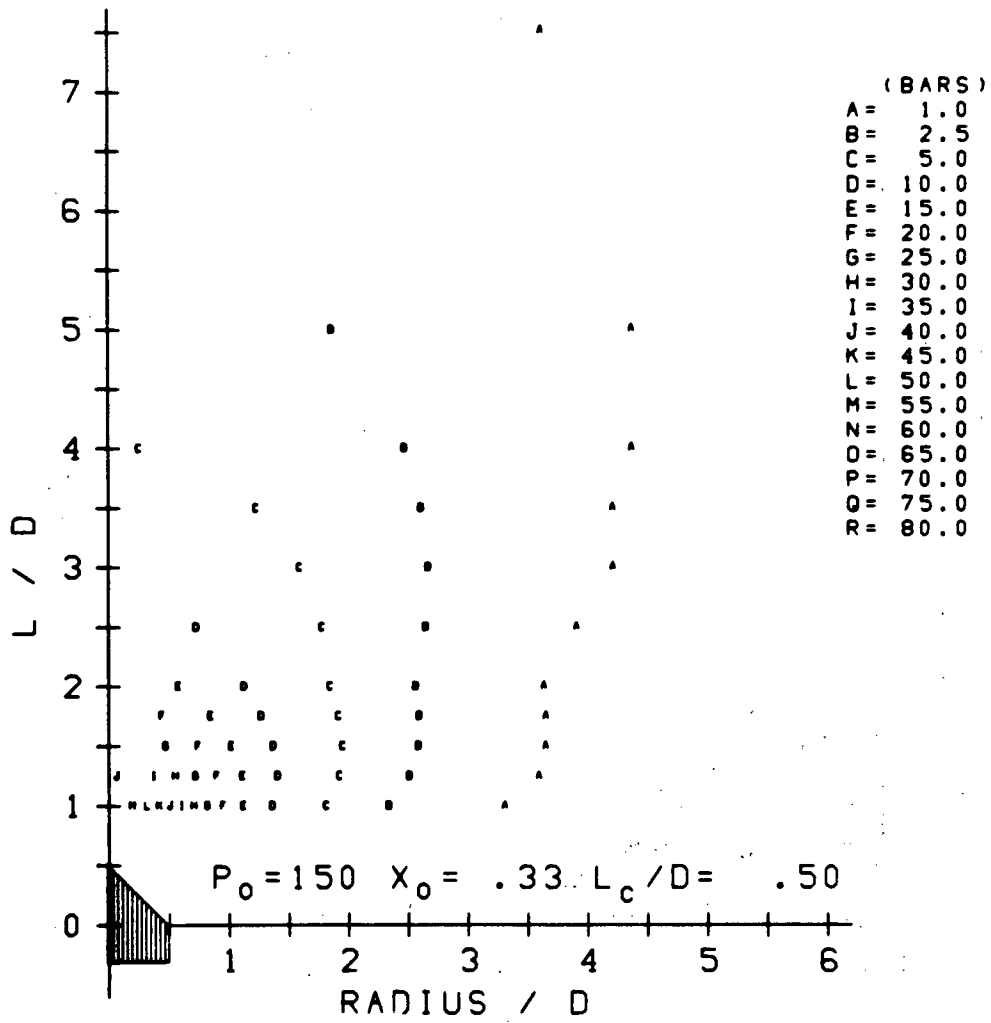
179
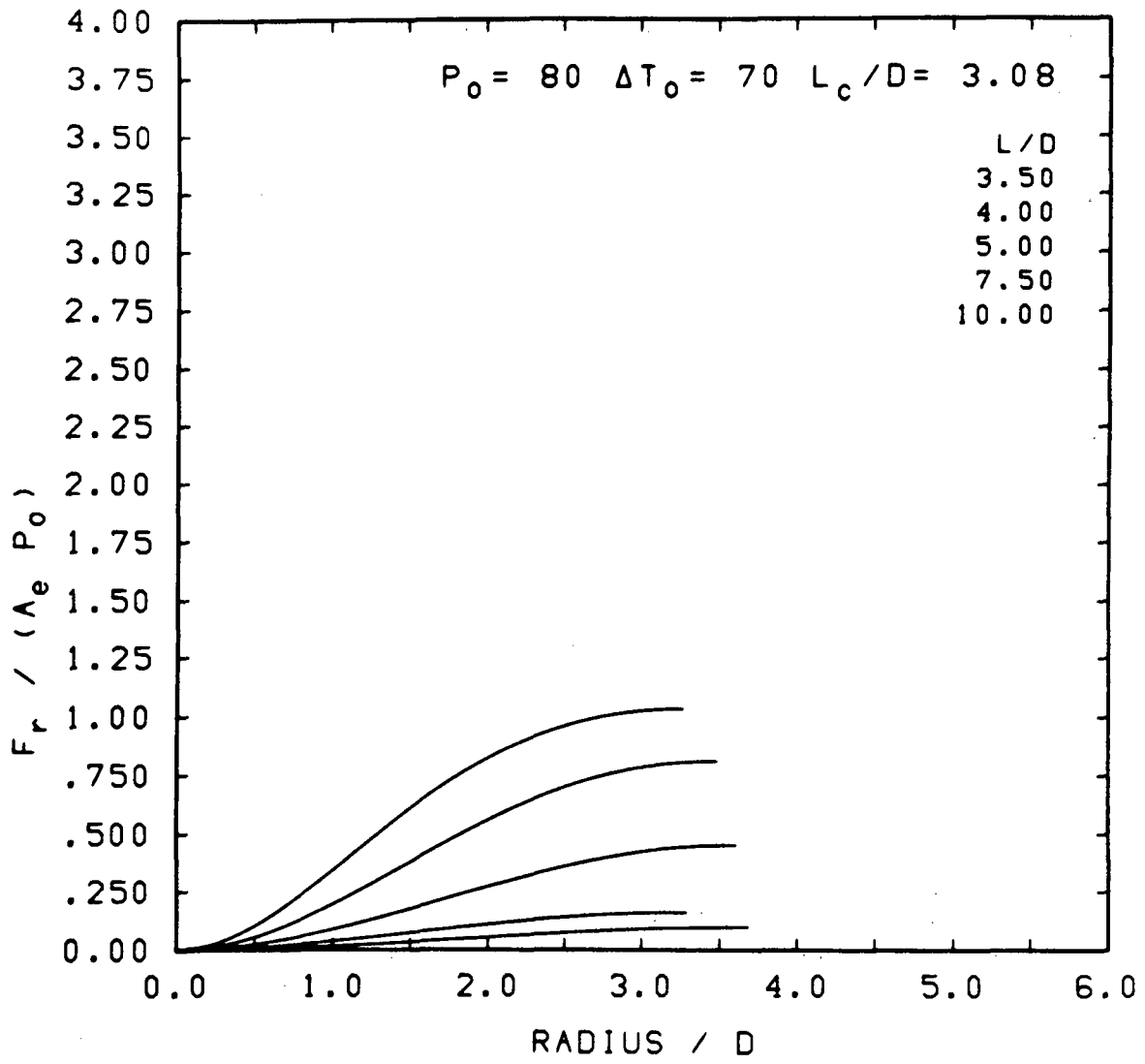
FIGURE A.41   TARGET LOAD DISTRIBUTIONS
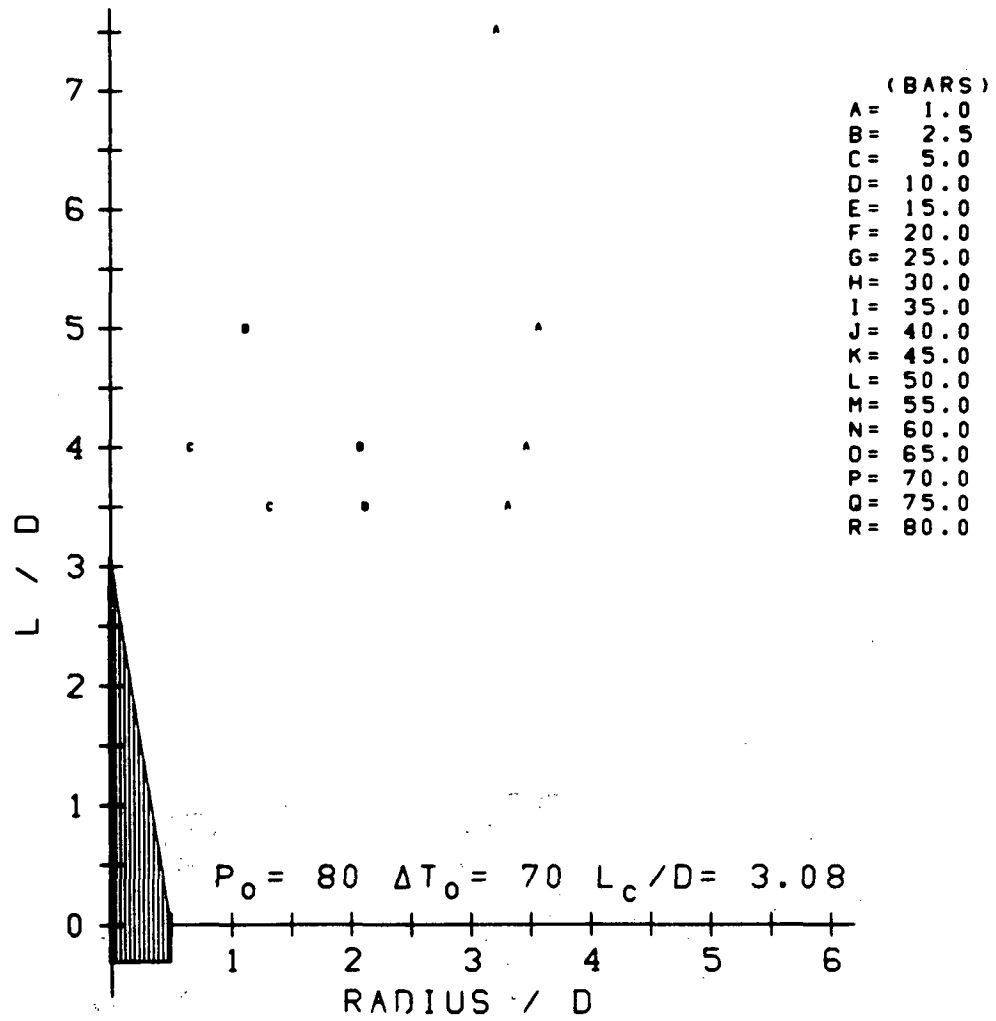
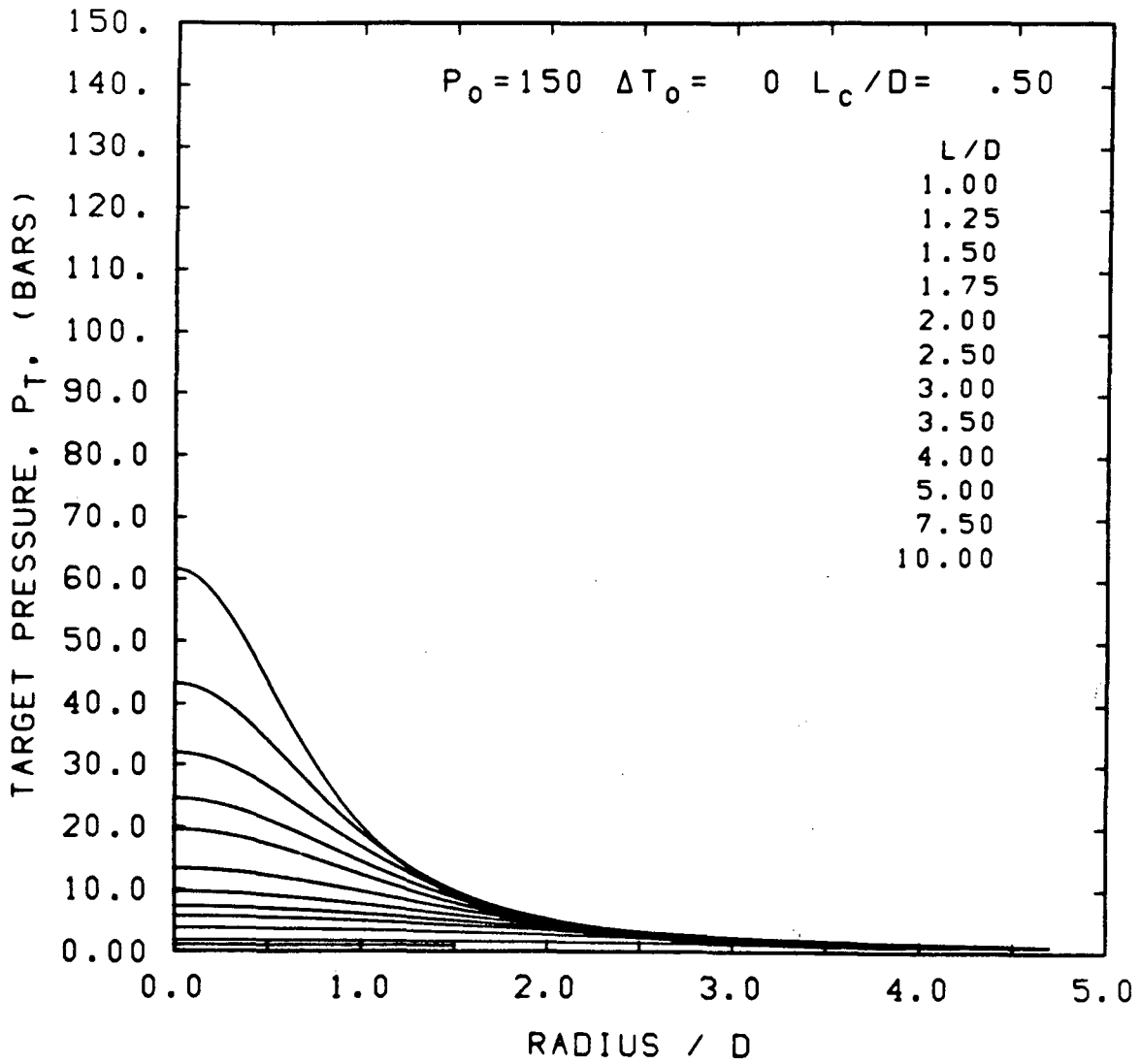FIGURE A.42   COMPOSITE TARGET PRESSURE CONTOURS
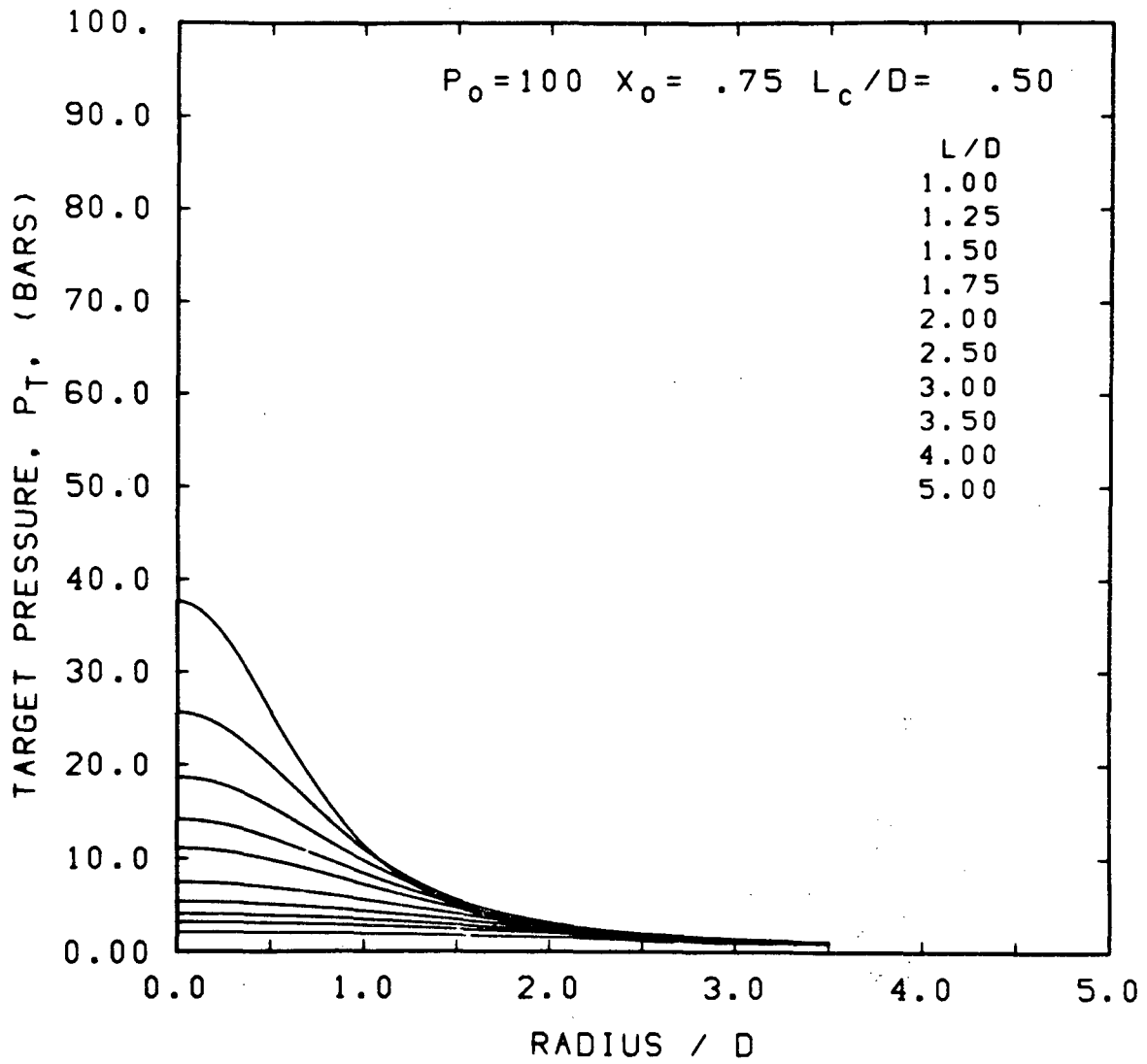
FIGURE A.43   TARGET PRESSURE DISTRIBUTIONS
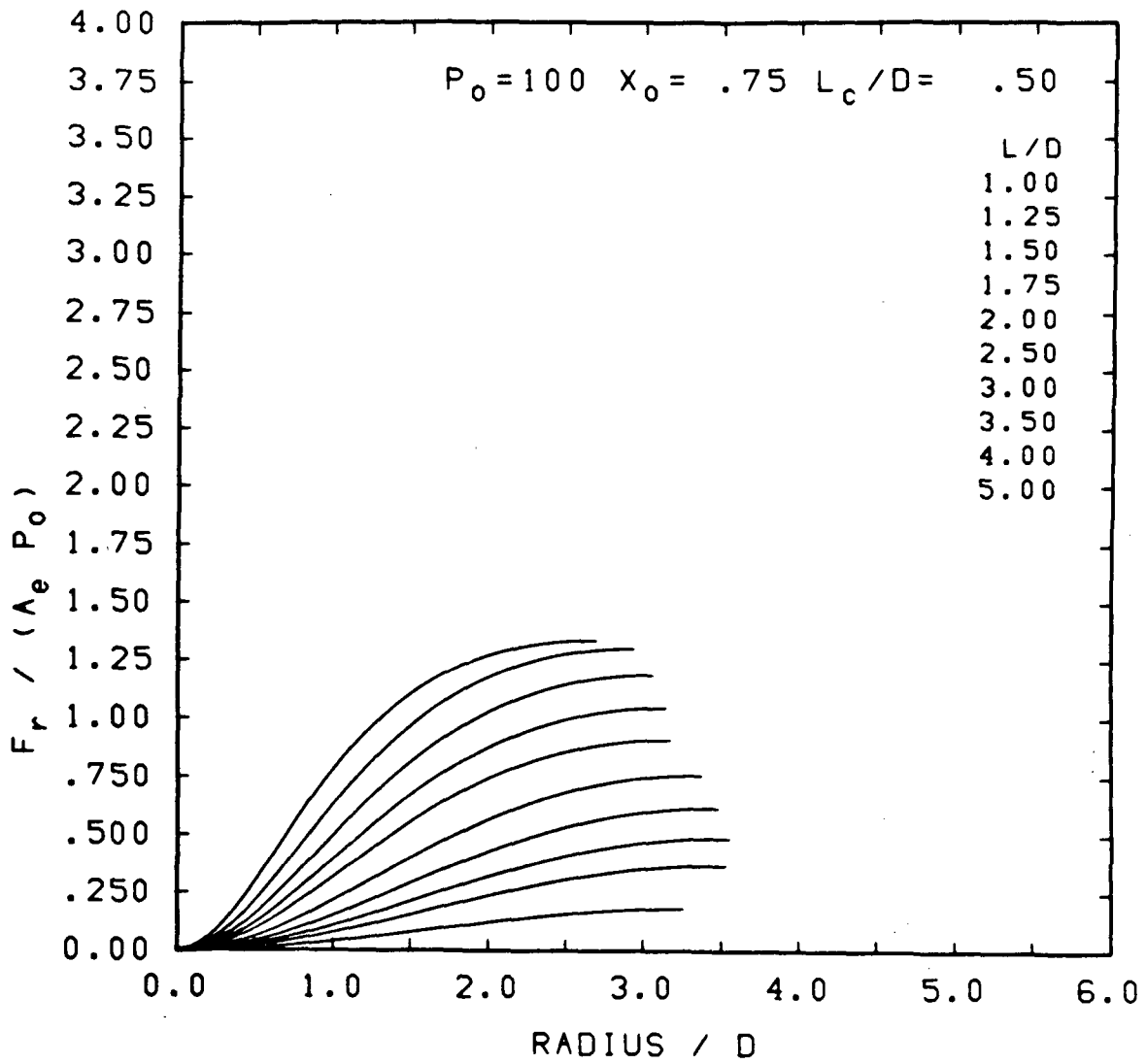
FIGURE A.44 TARGET LOAD DISTRIBUTIONS
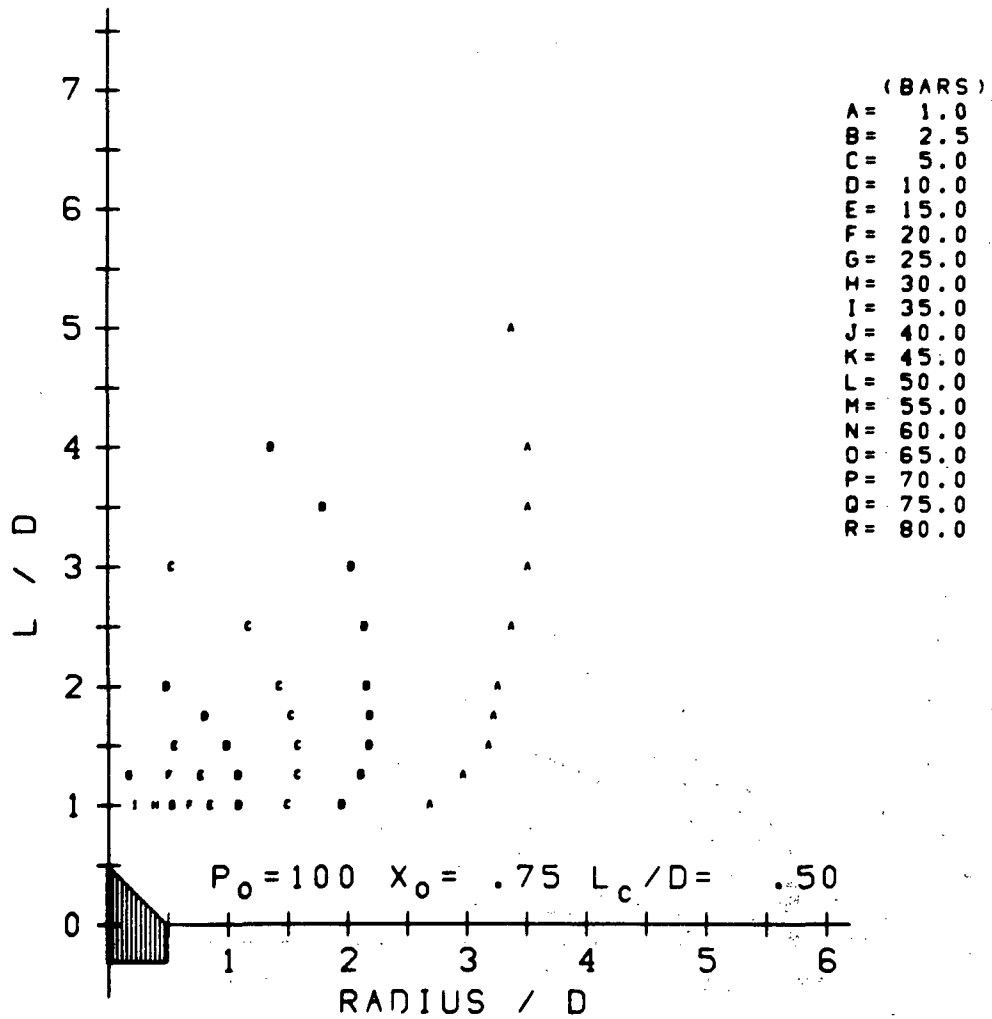
FIGURE A.45 COMPOSITE TARGET PRESSURE CONTOURS
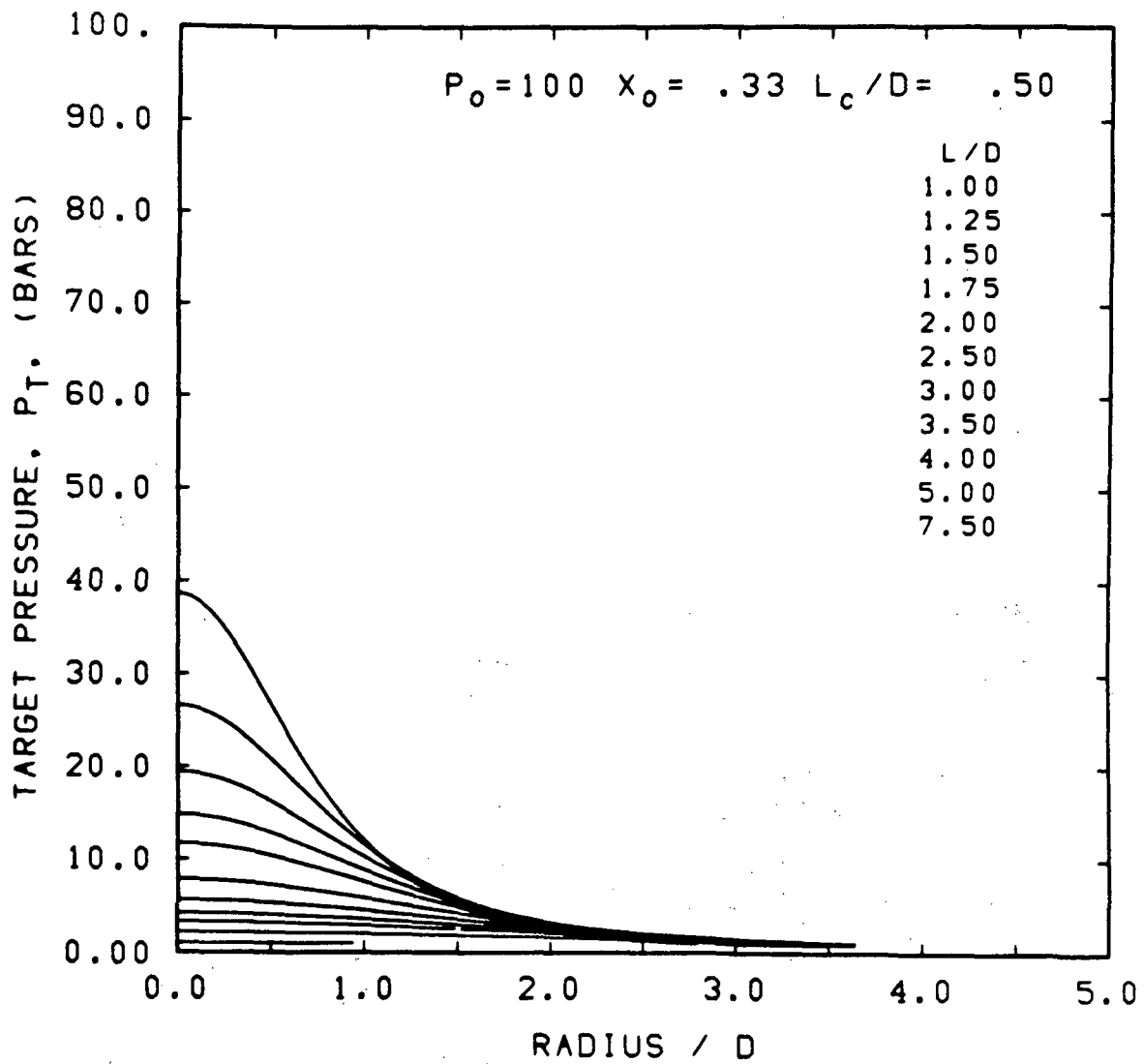
FIGURE A.46 TARGET PRESSURE DISTRIBUTIONS
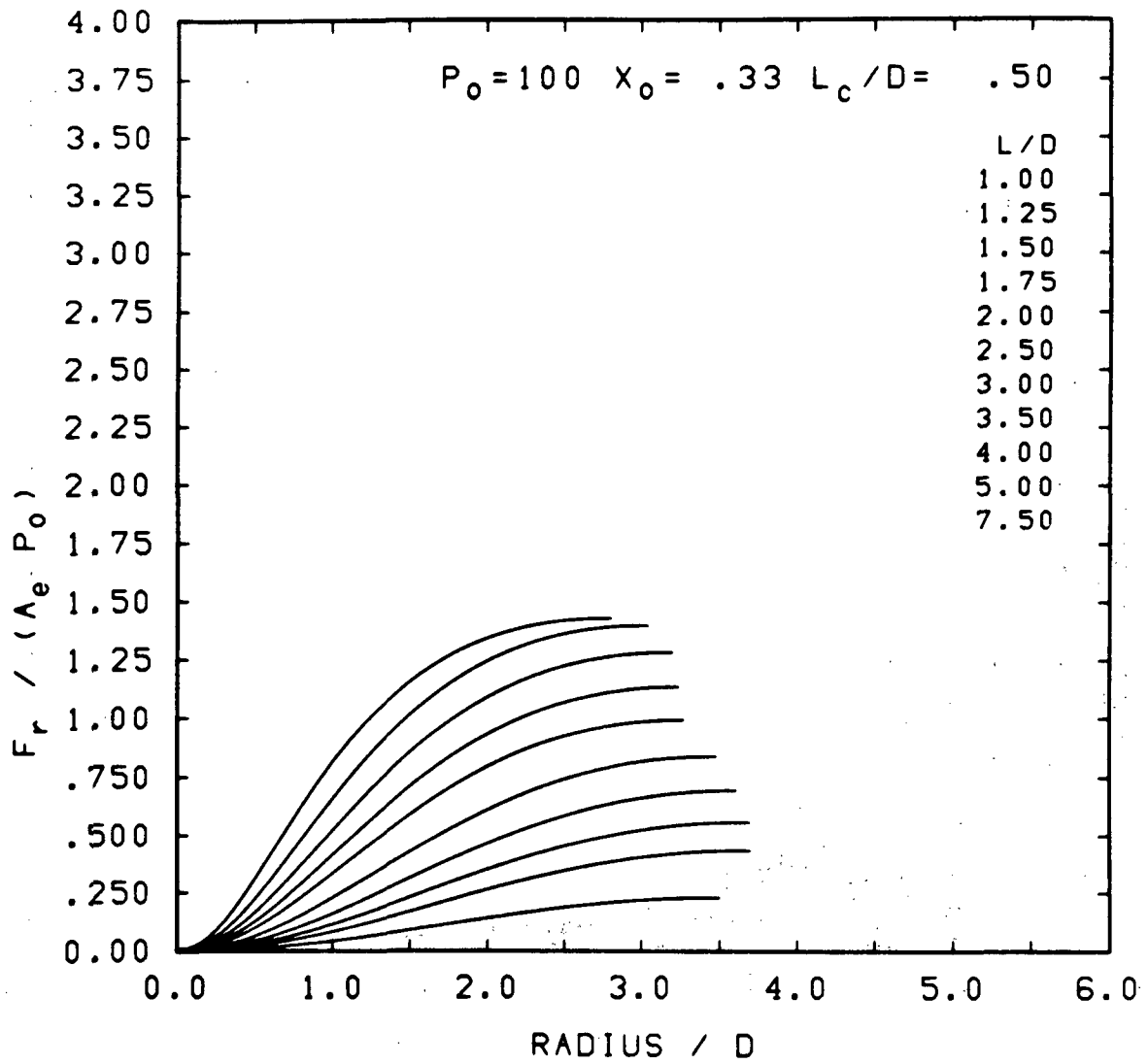
FIGURE A.47   TARGET LOAD DISTRIBUTIONS

186
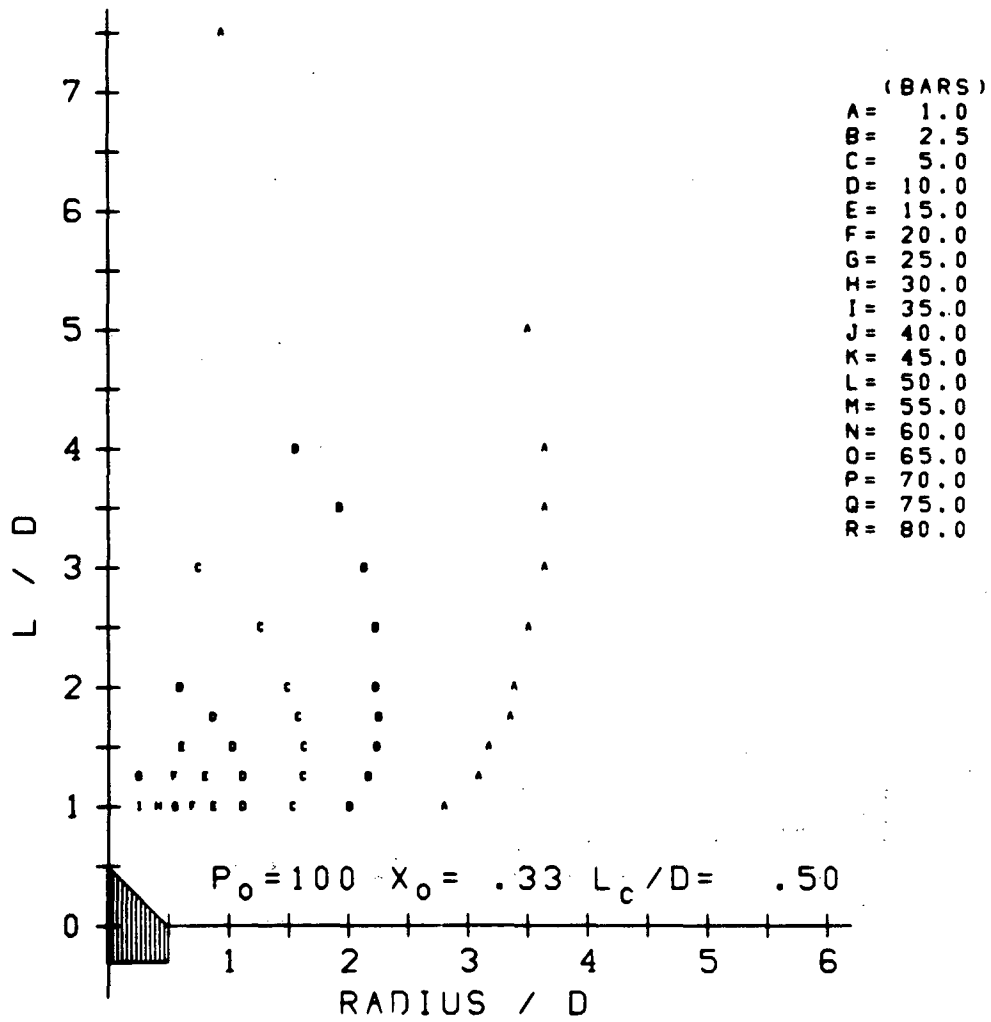
FIGURE A.48   COMPOSITE TARGET PRESSURE CONTOURS
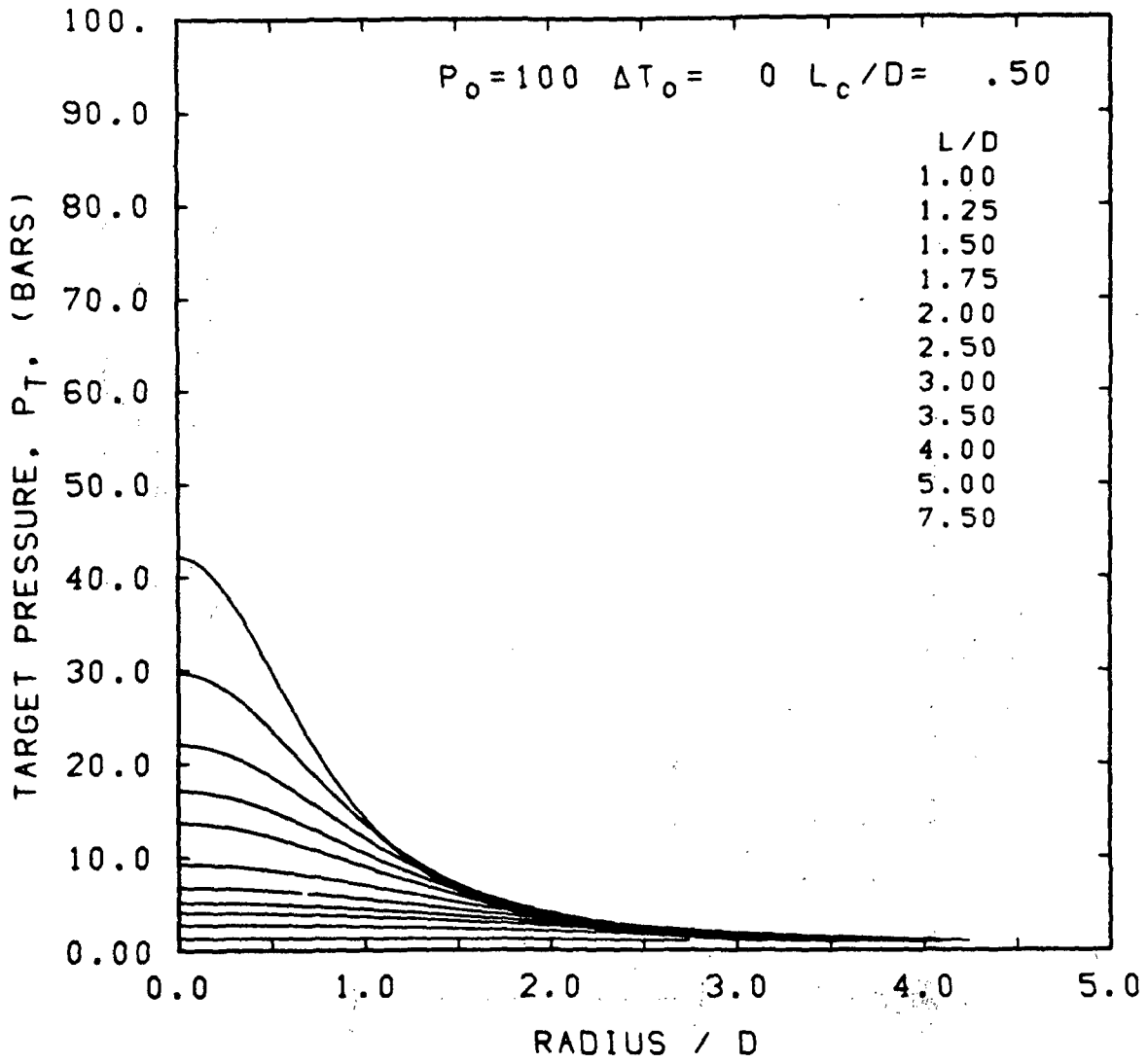
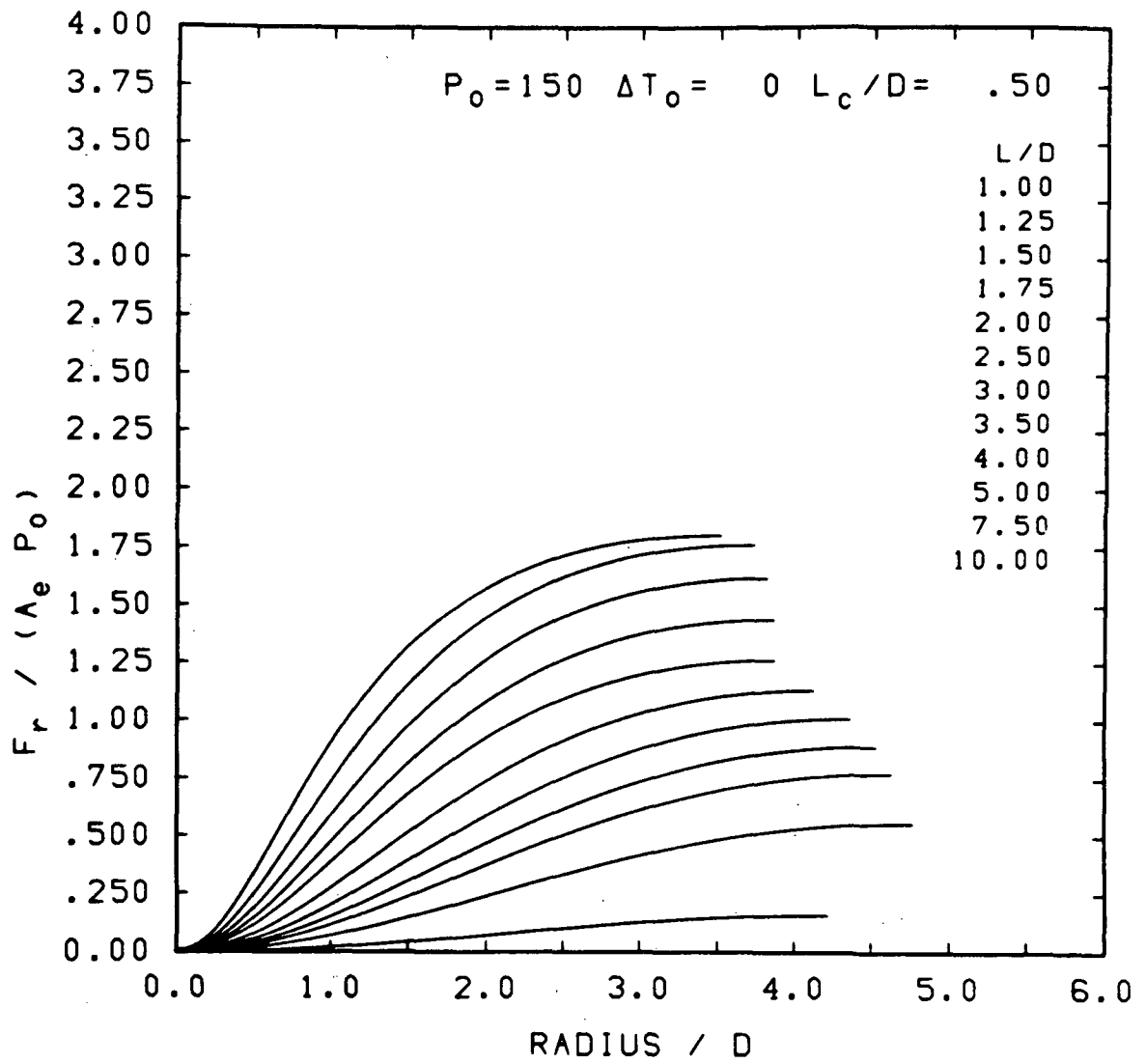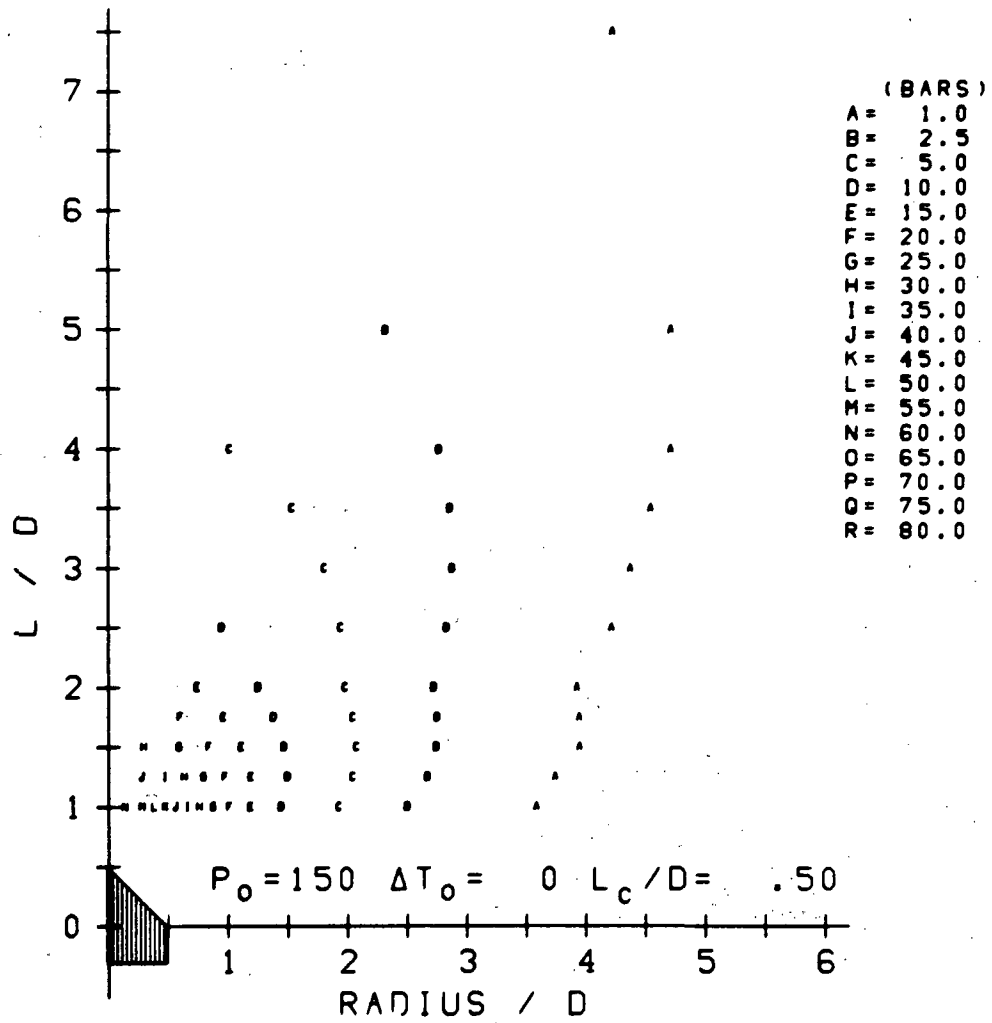FIGURE A.49   TARGET PRESSURE DISTRIBUTIONS
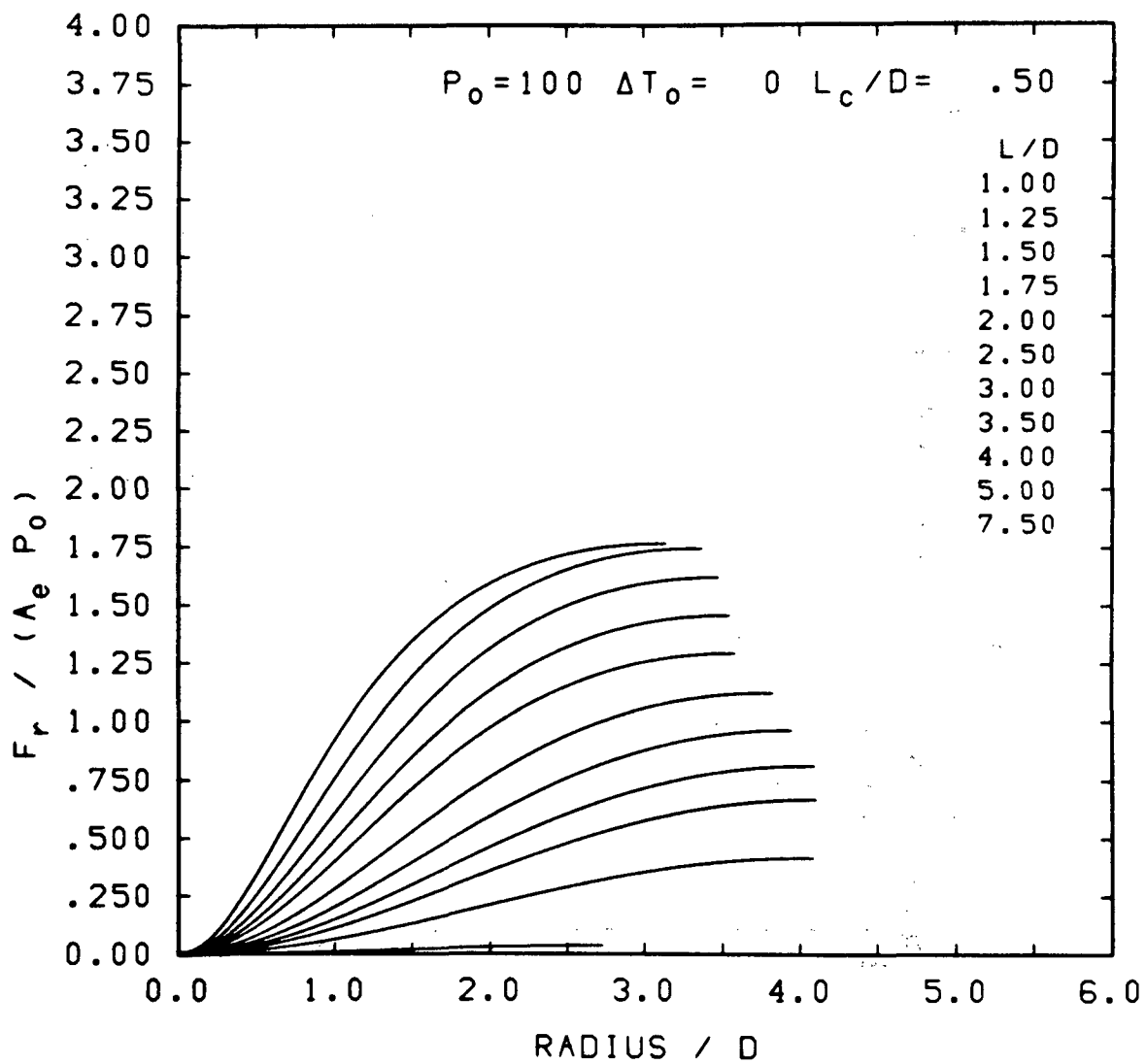
FIGURE A.50   TARGET LOAD DISTRIBUTIONS
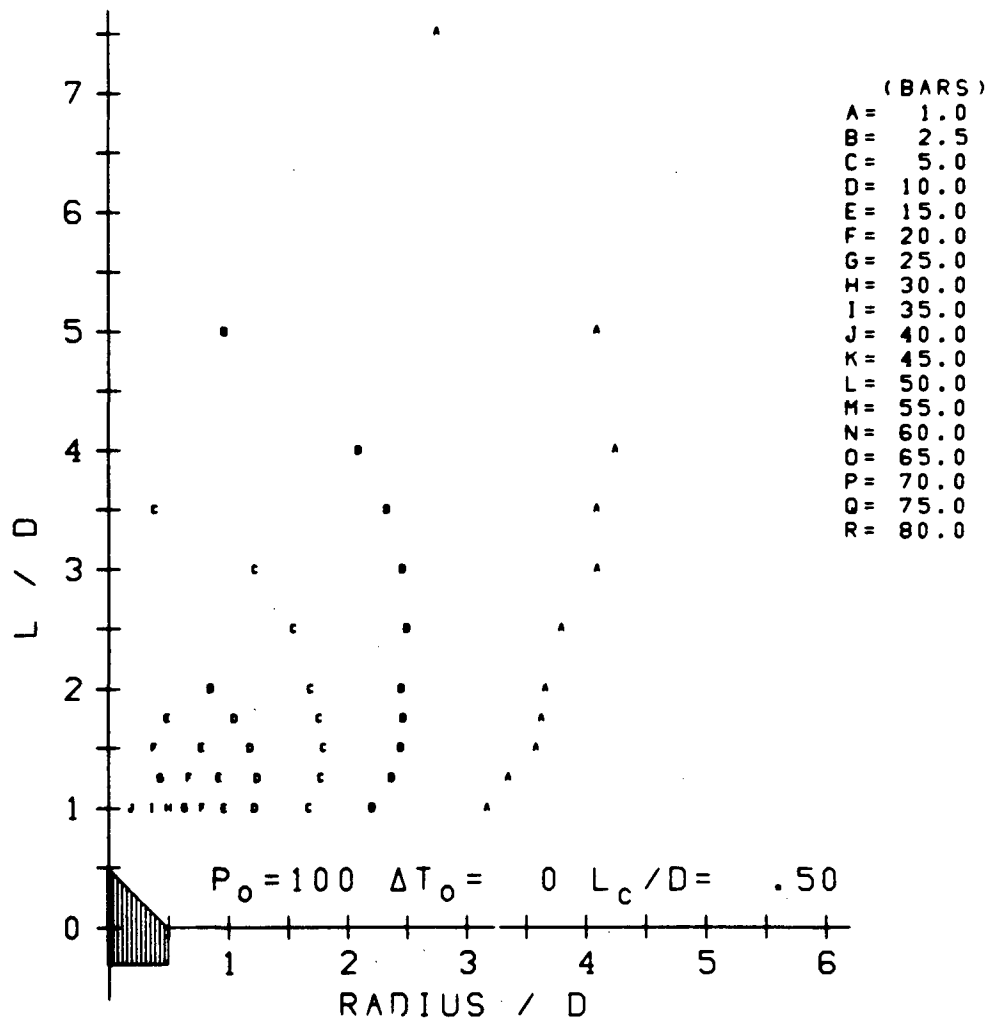
FIGURE A.51   COMPOSITE TARGET PRESSURE CONTOURS
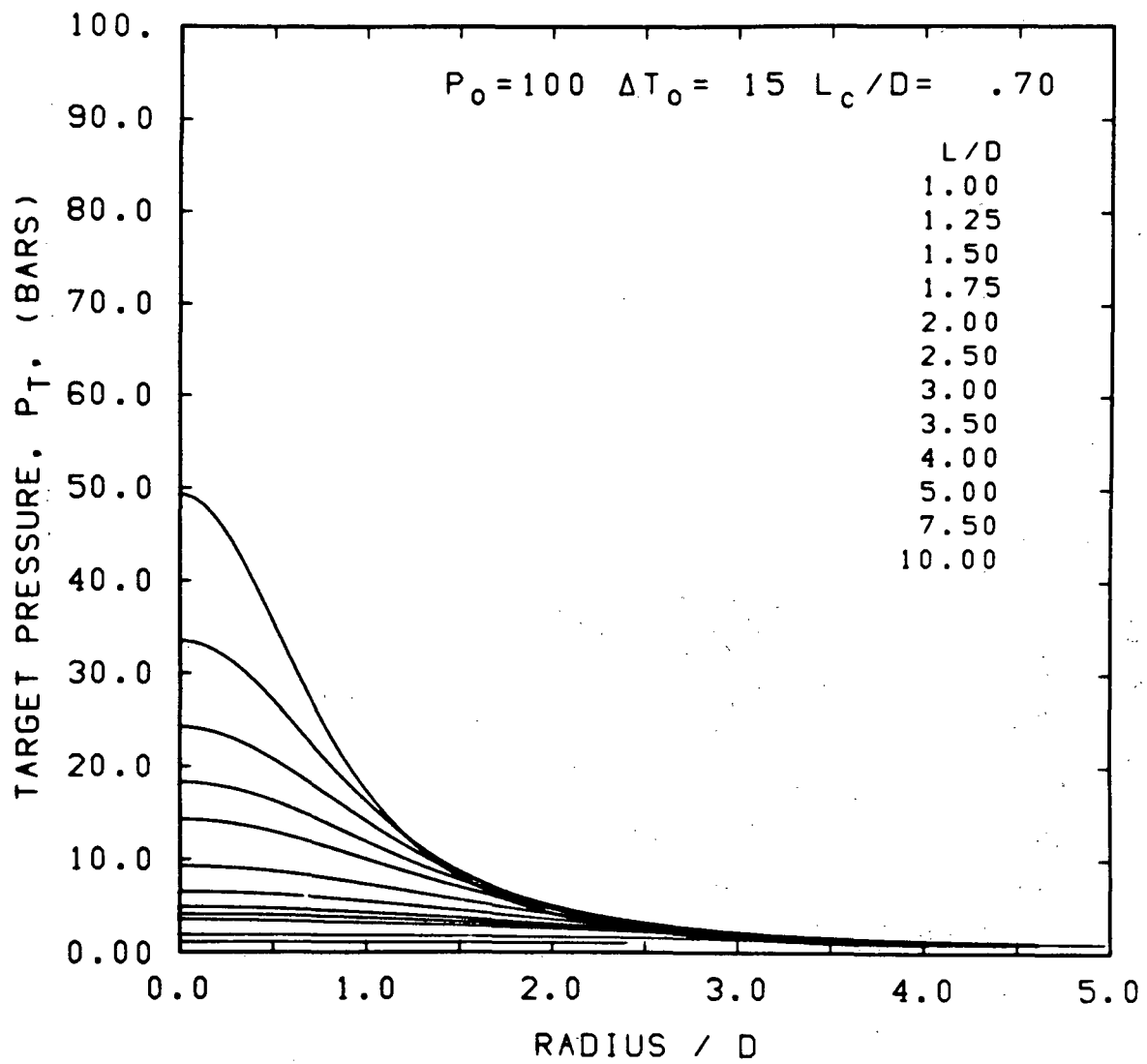
FIGURE A.52   TARGET PRESSURE DISTRIBUTIONS
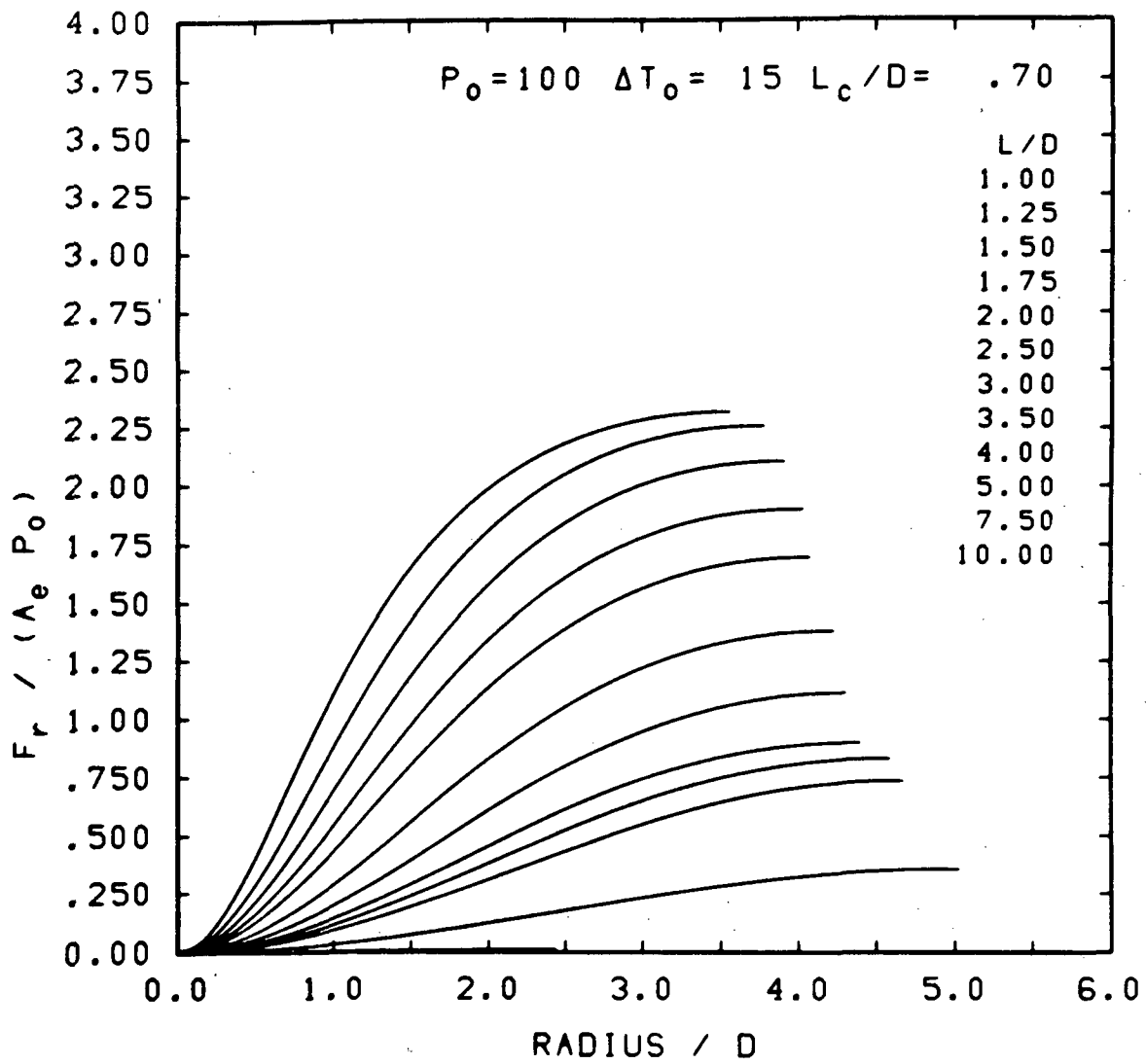
FIGURE A.53   TARGET LOAD DISTRIBUTIONS
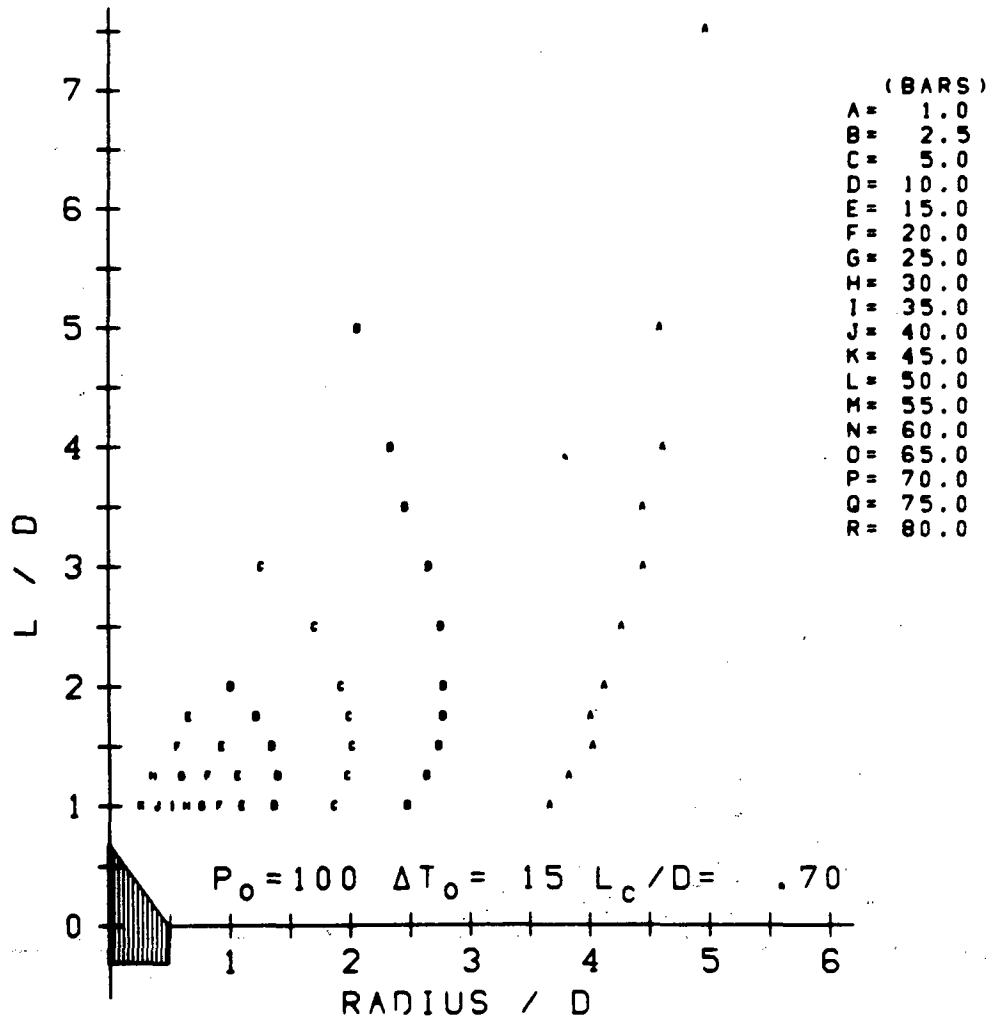
FIGURE A.54   COMPOSITE TARGET PRESSURE CONTOURS
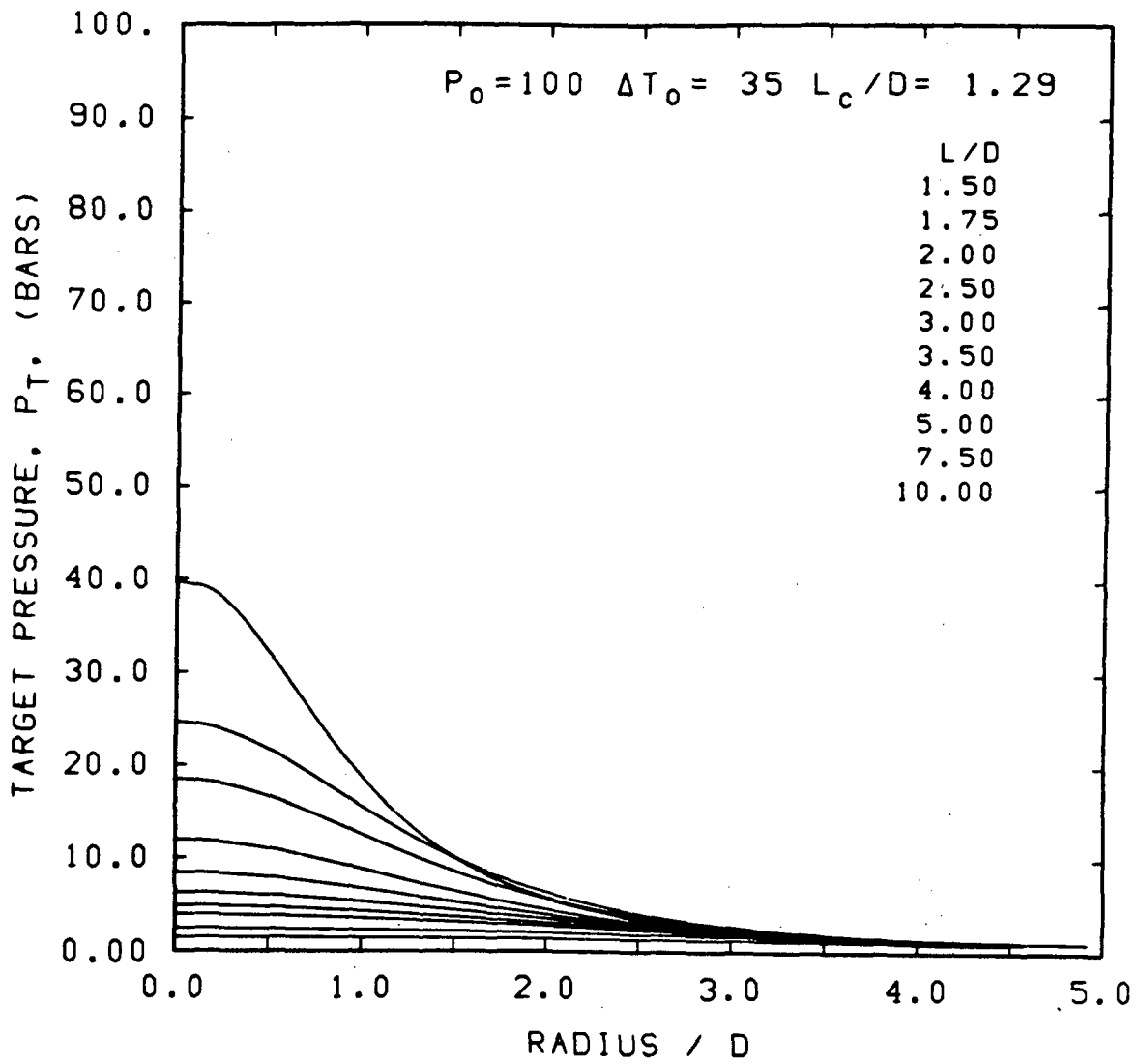
FIGURE A.55   TARGET PRESSURE DISTRIBUTIONS

194
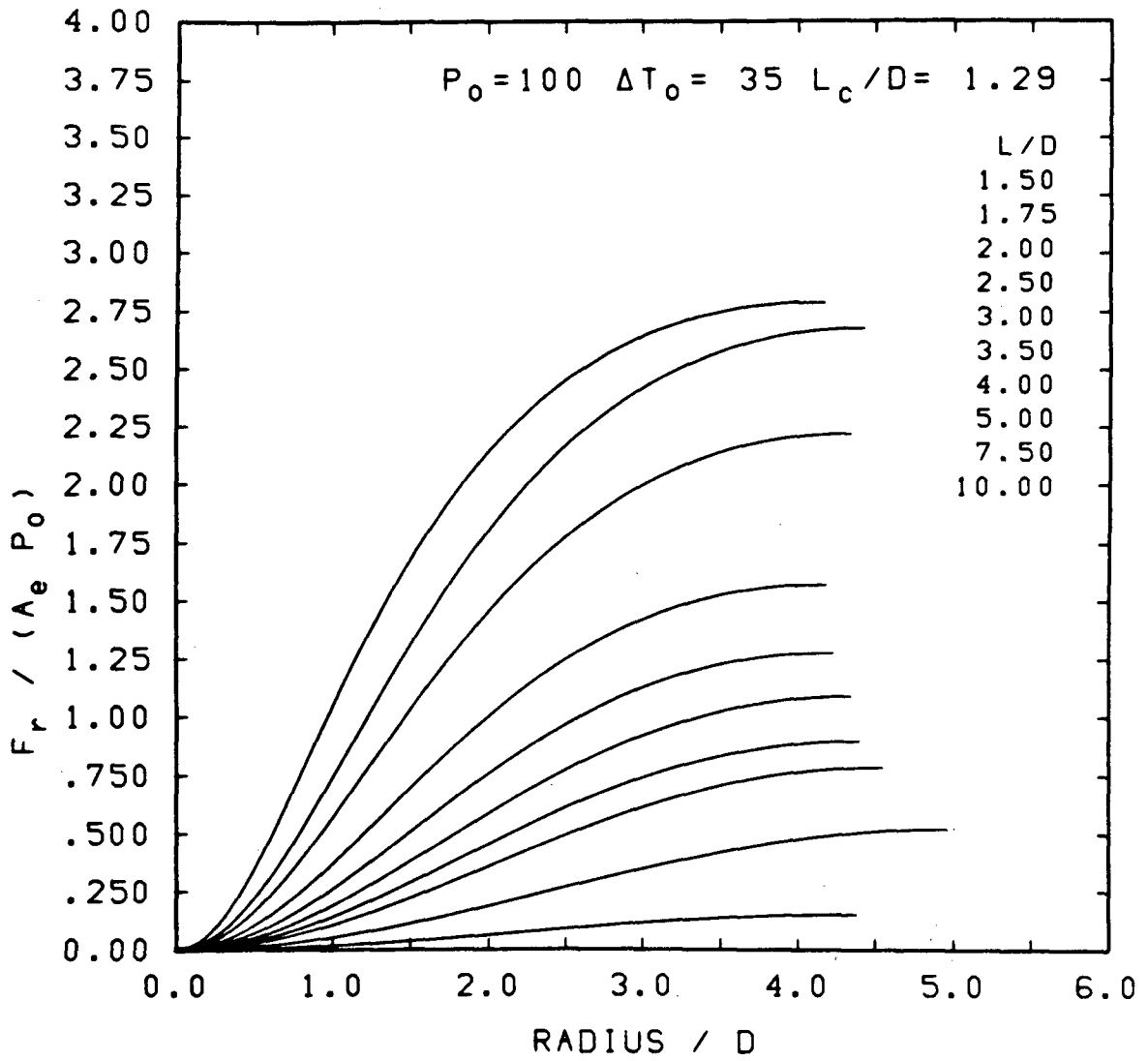
FIGURE A.56   TARGET LOAD DISTRIBUTIONS
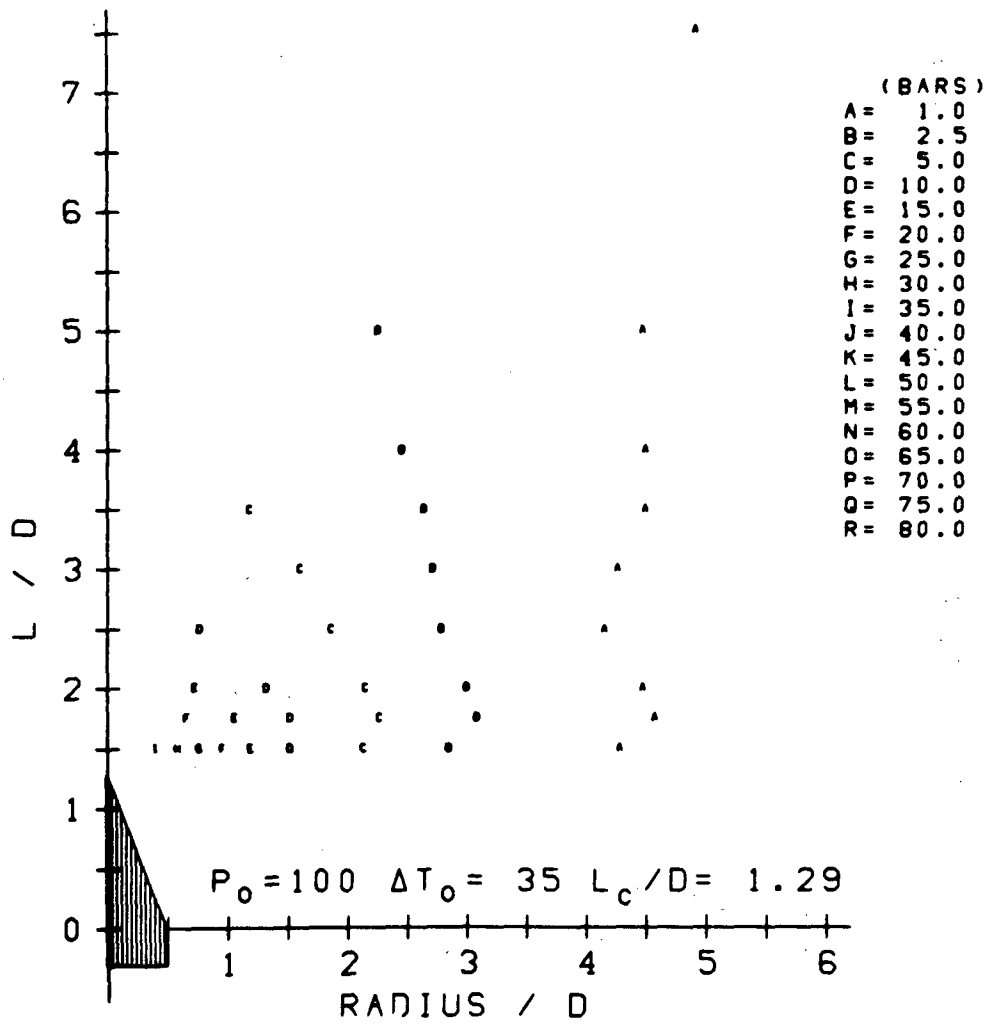
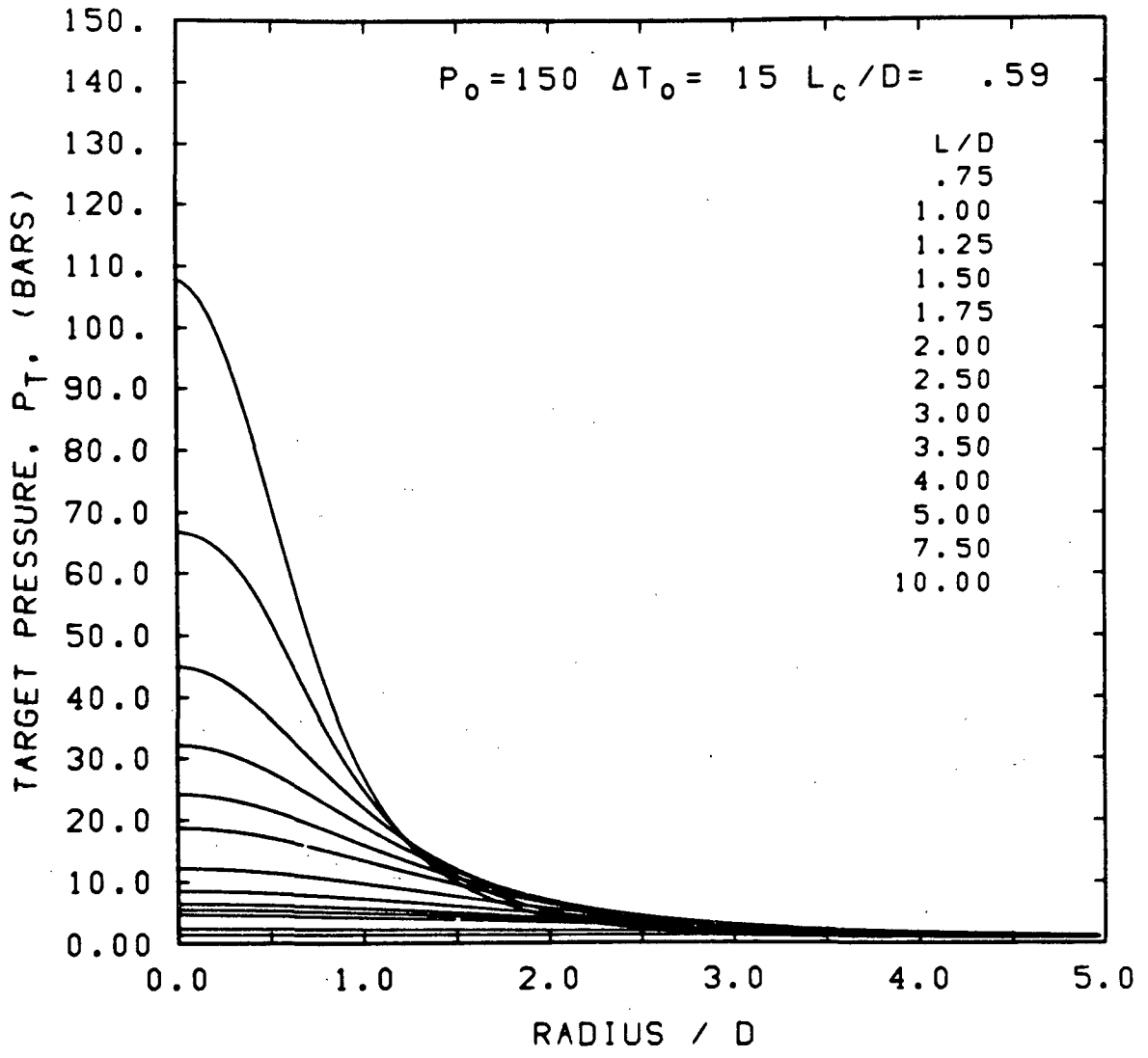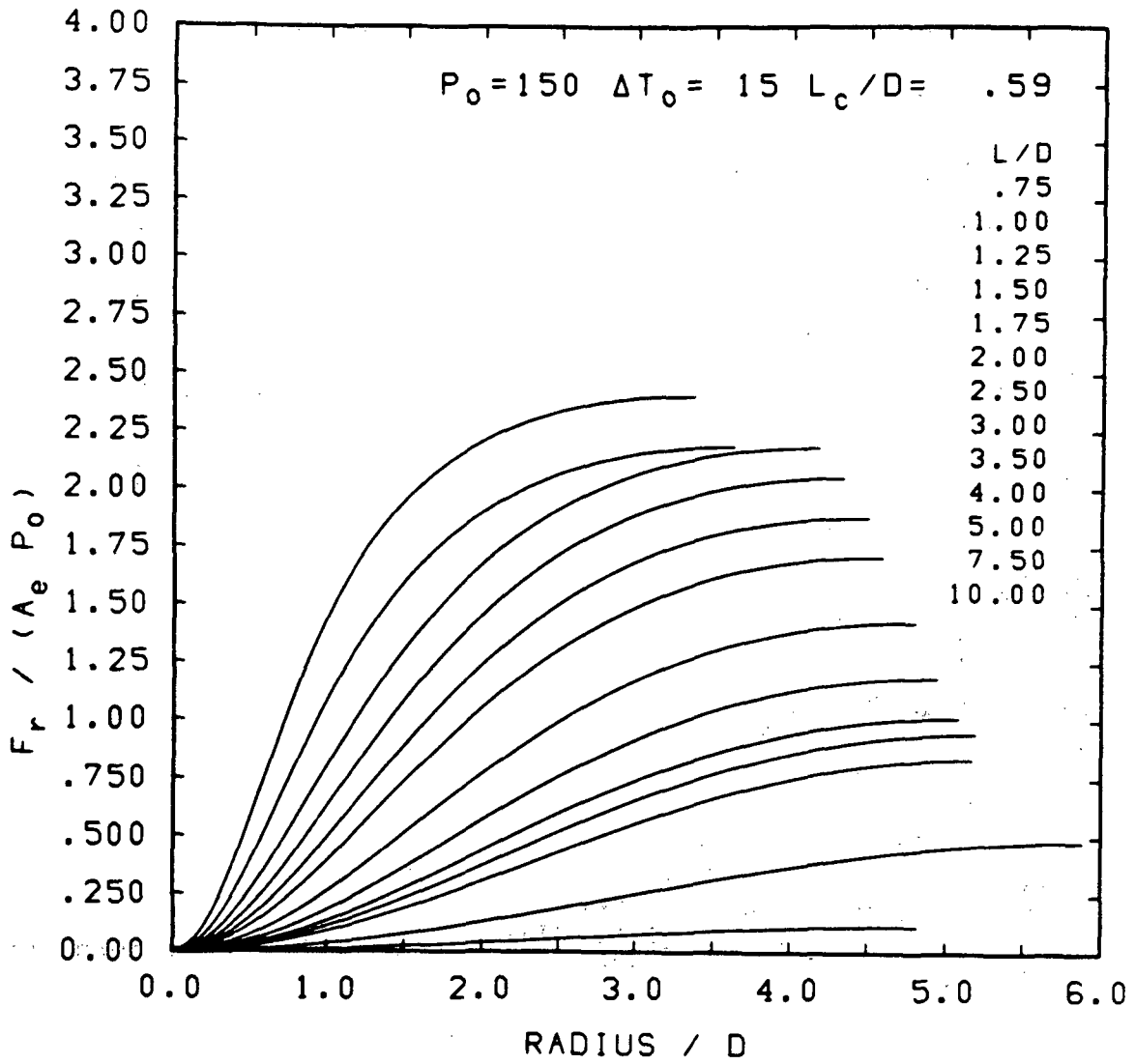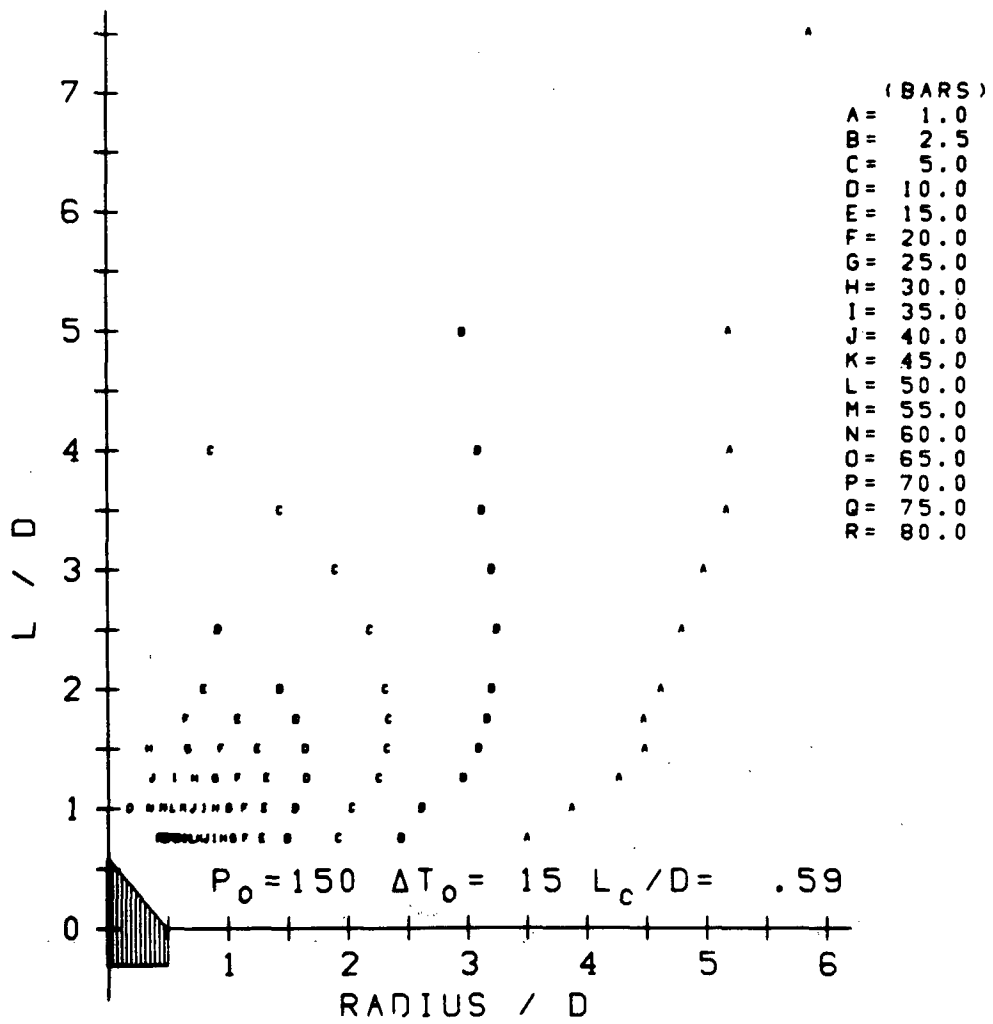FIGURE A.57   COMPOSITE TARGET PRESSURE CONTOURS
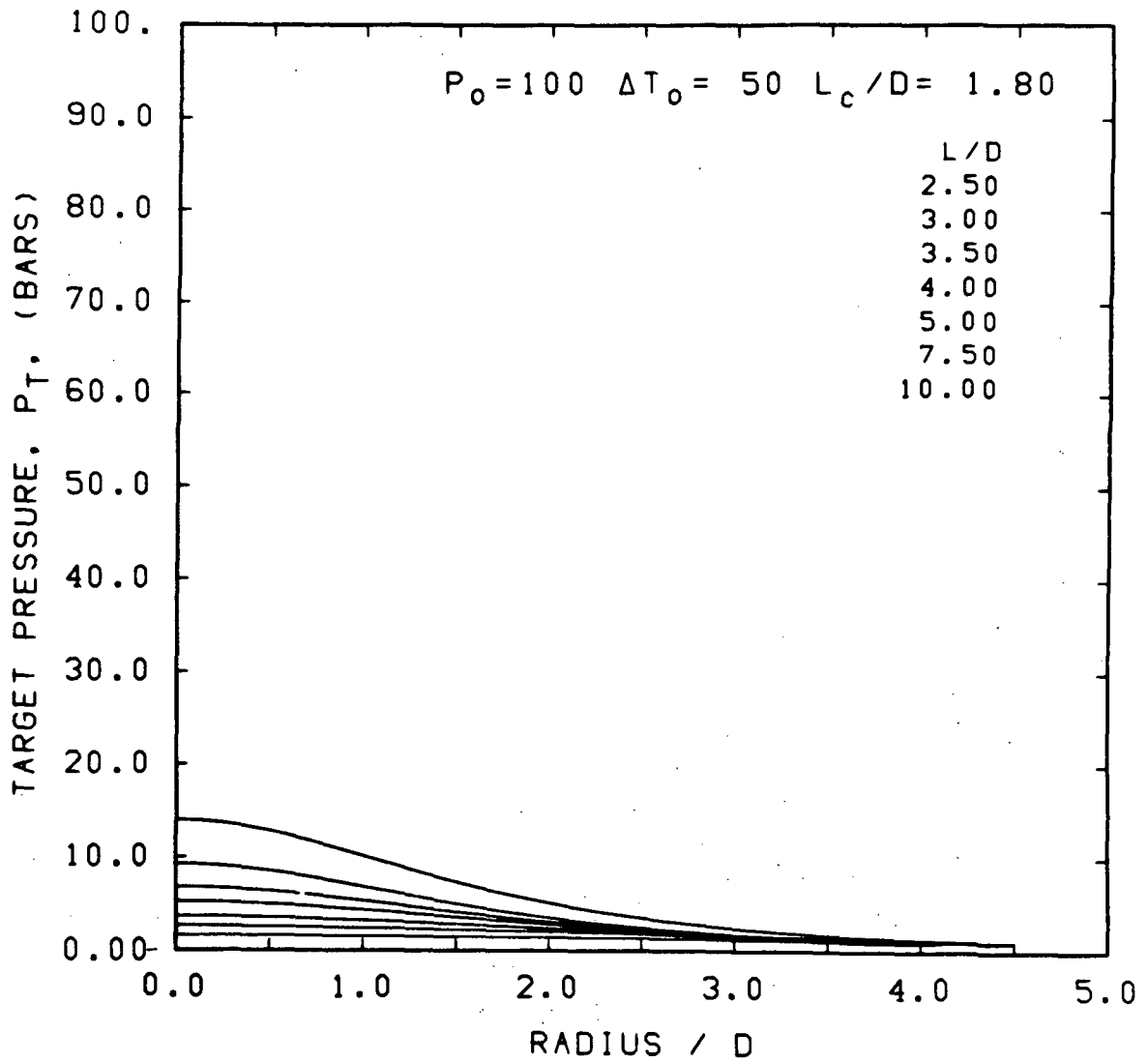
FIGURE A.58   TARGET PRESSURE DISTRIBUTIONS

197
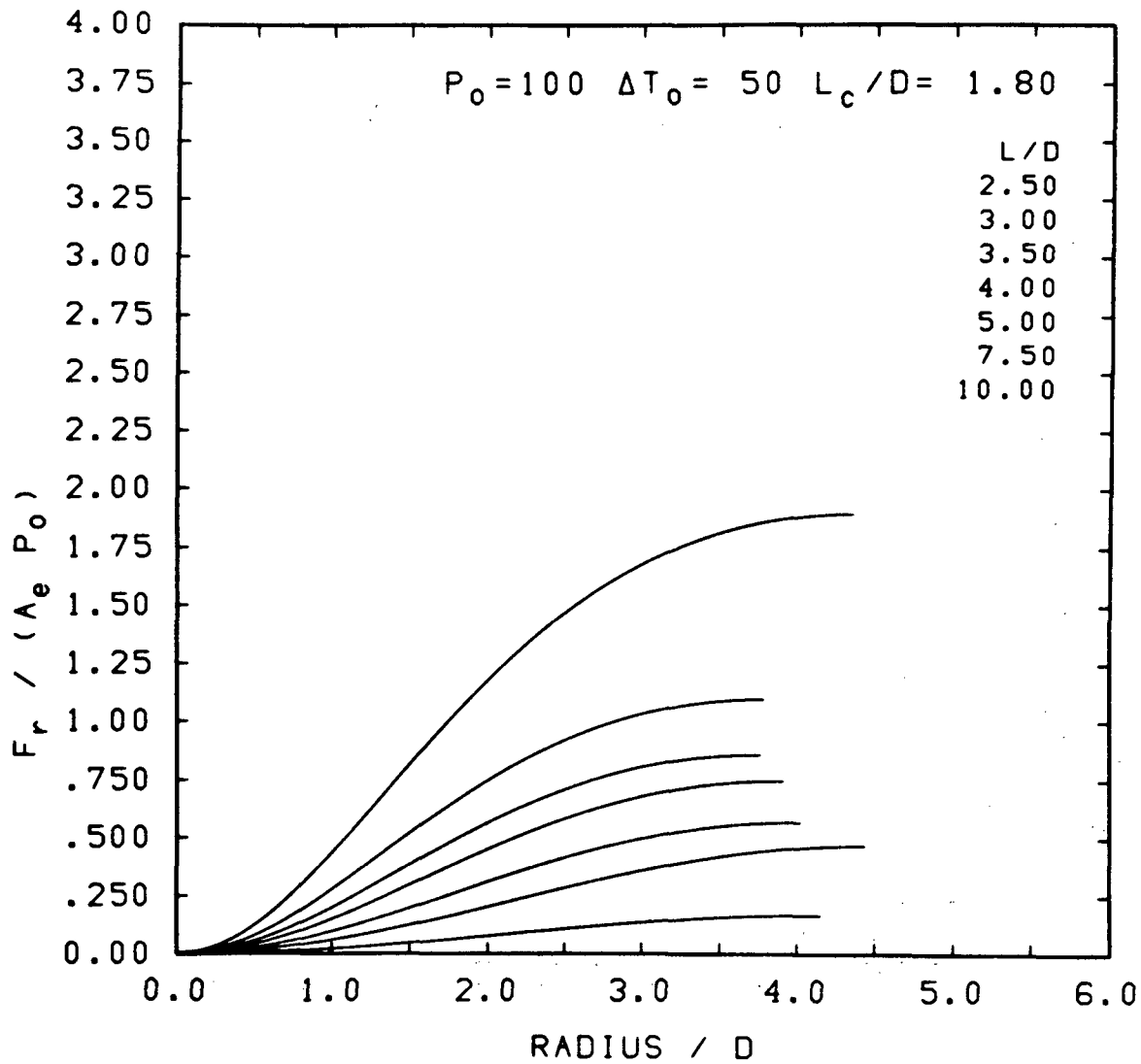
FIGURE A.59   TARGET LOAD DISTRIBUTIONS
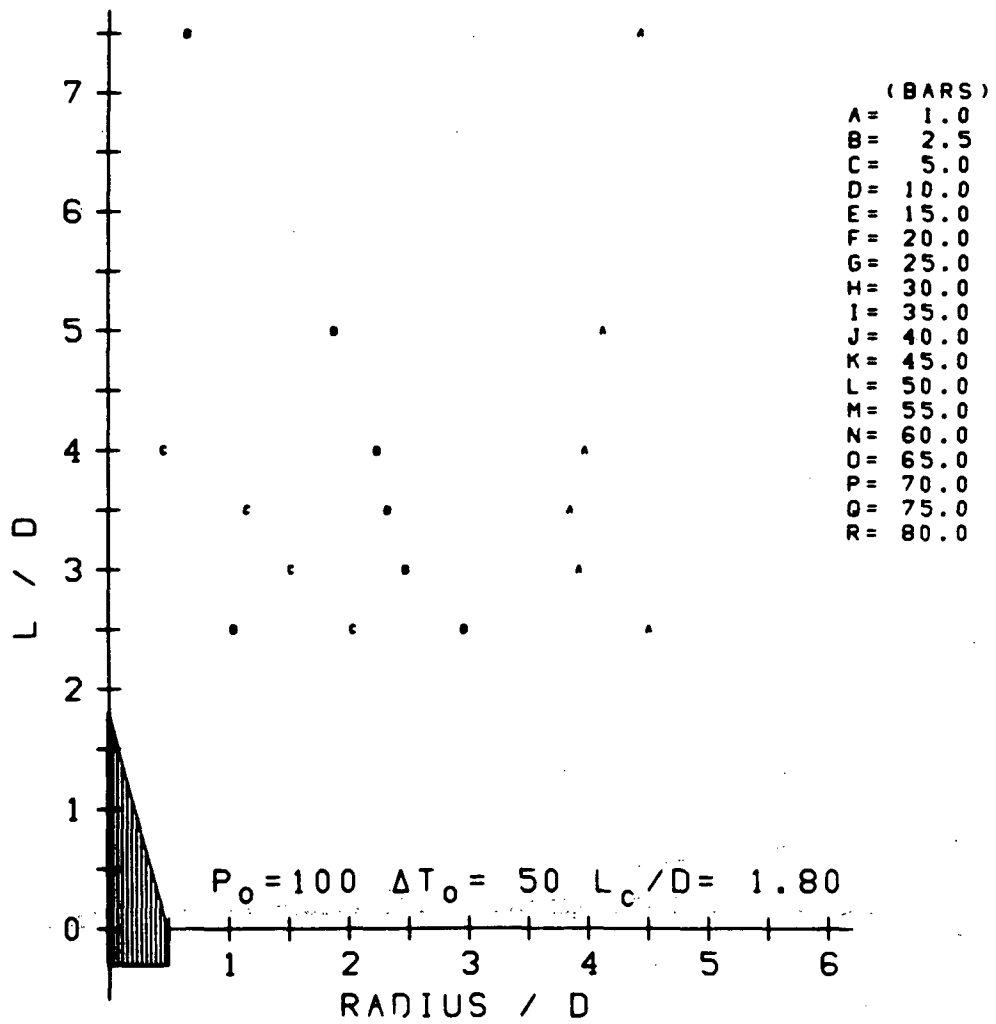
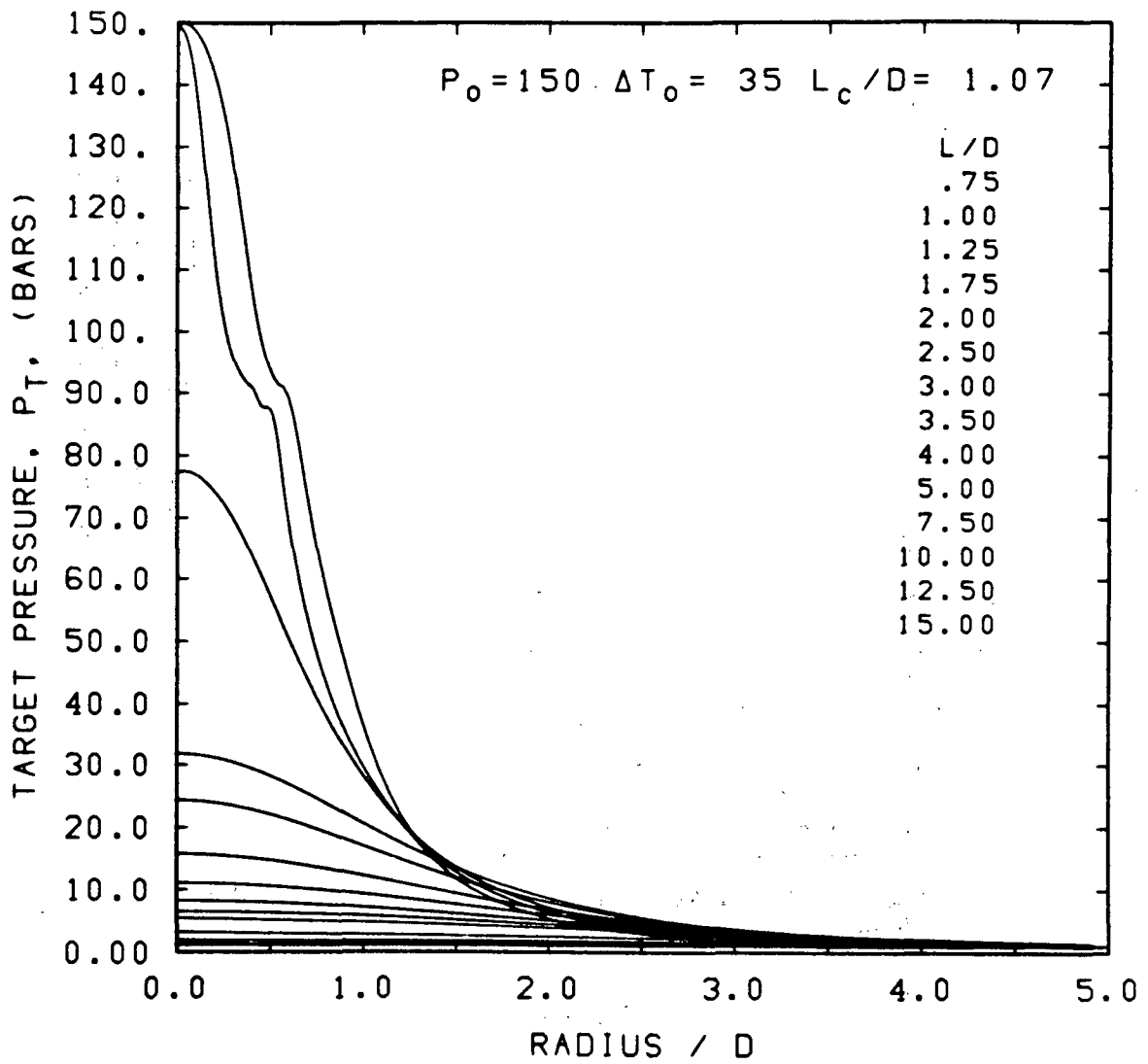FIGURE A.60   COMPOSITE TARGET PRESSURE CONTOURS

199
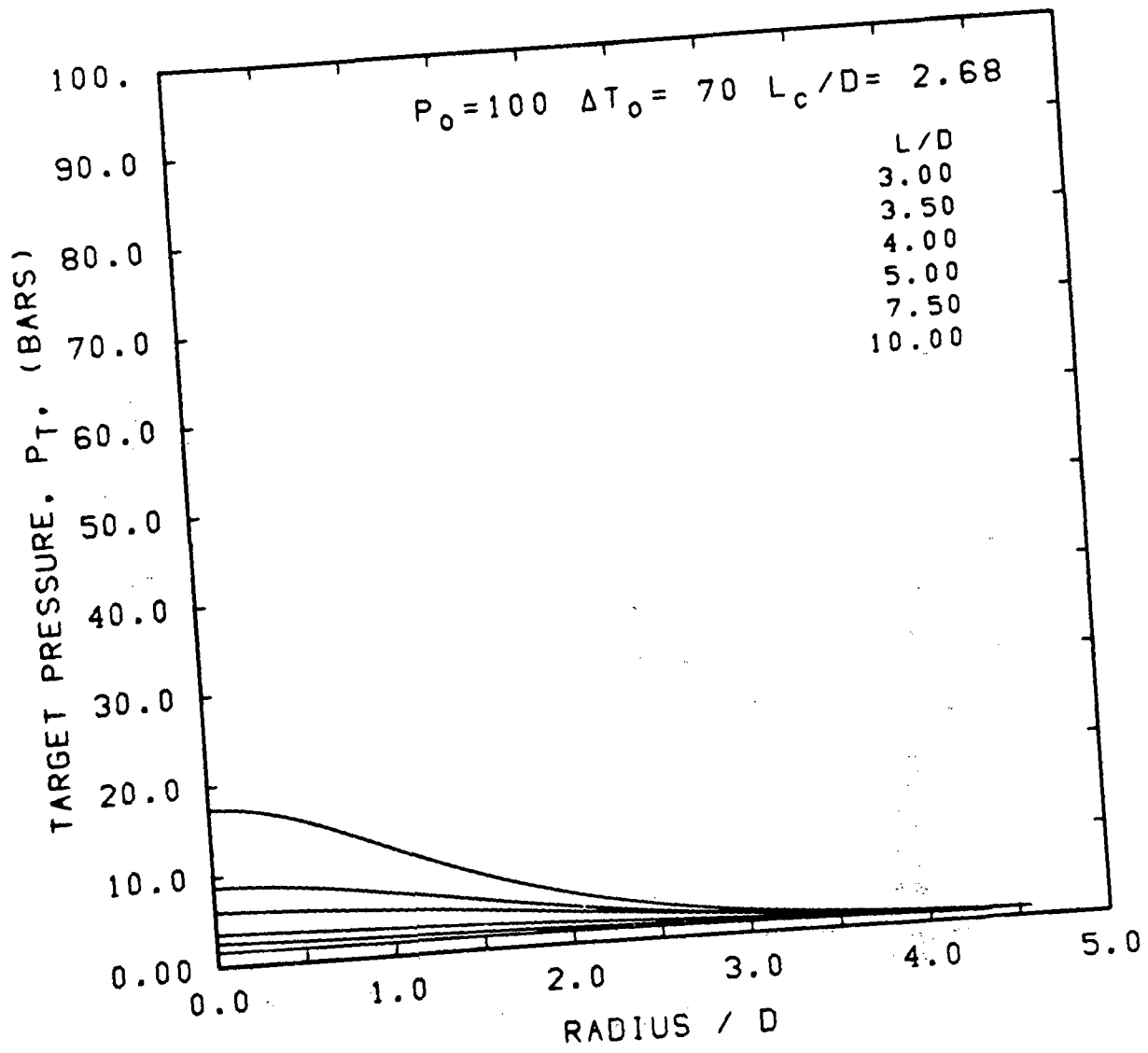
FIGURE A.61 TARGET PRESSURE DISTRIBUTIONS
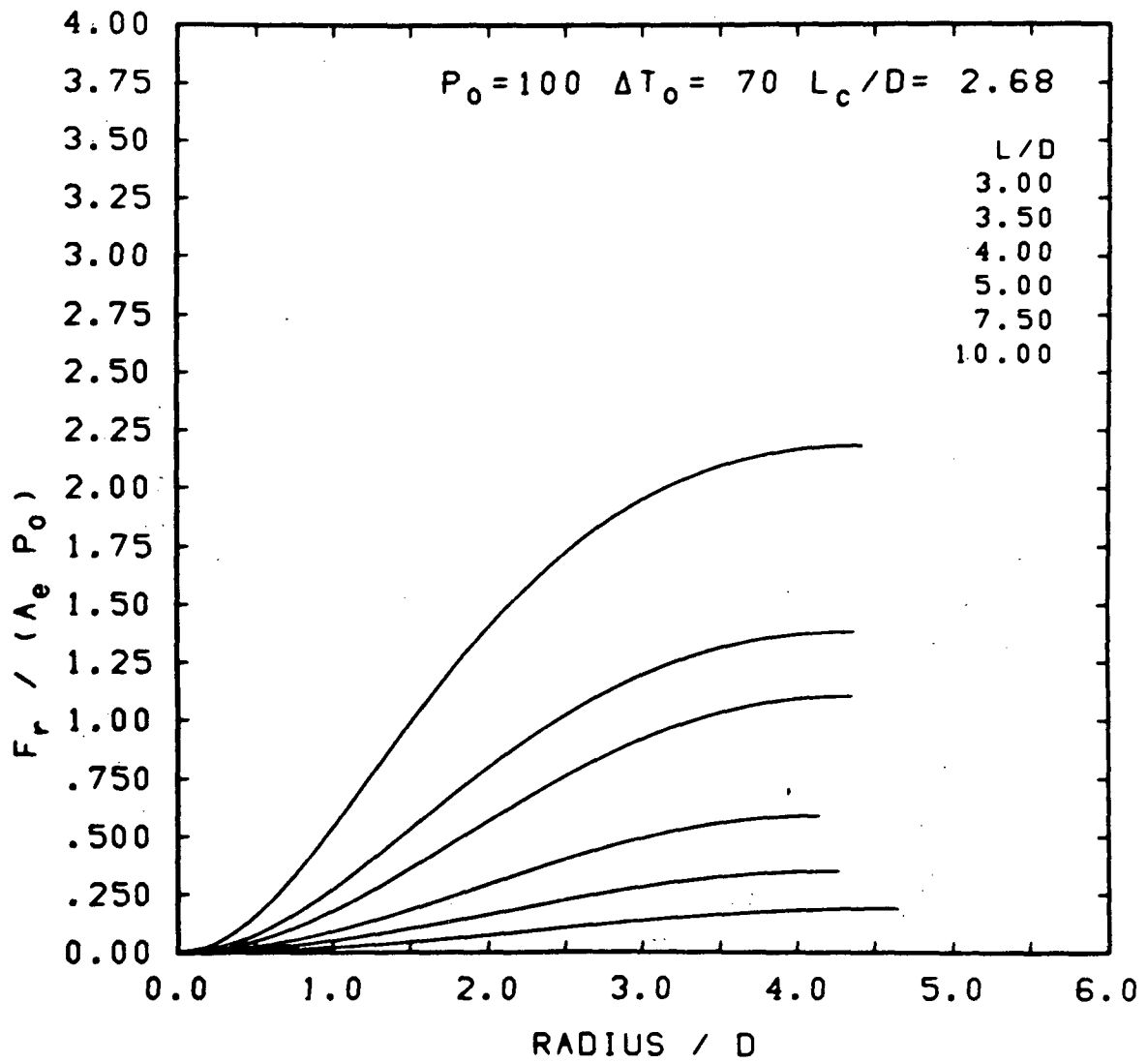
FIGURE A.62   TARGET LOAD DISTRIBUTIONS
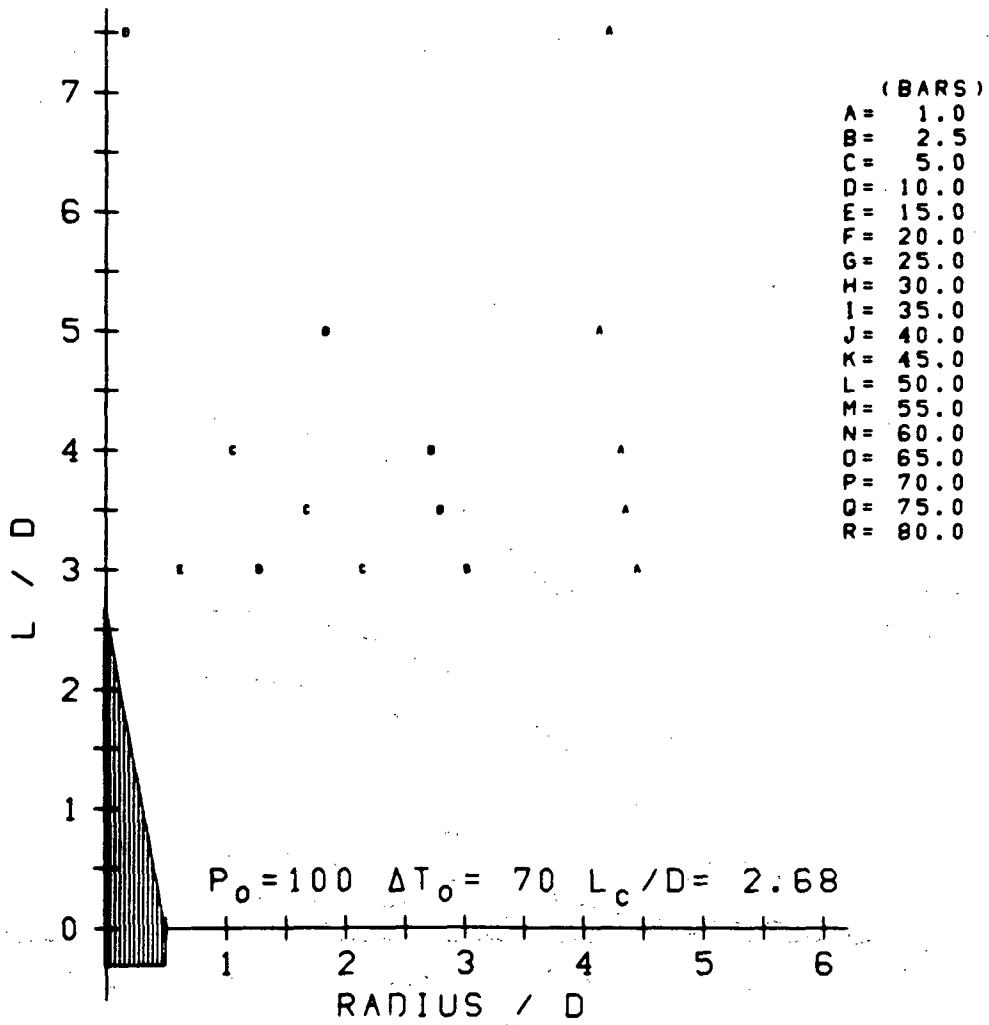
FIGURE A.63 COMPOSITE TARGET PRESSURE CONTOURS
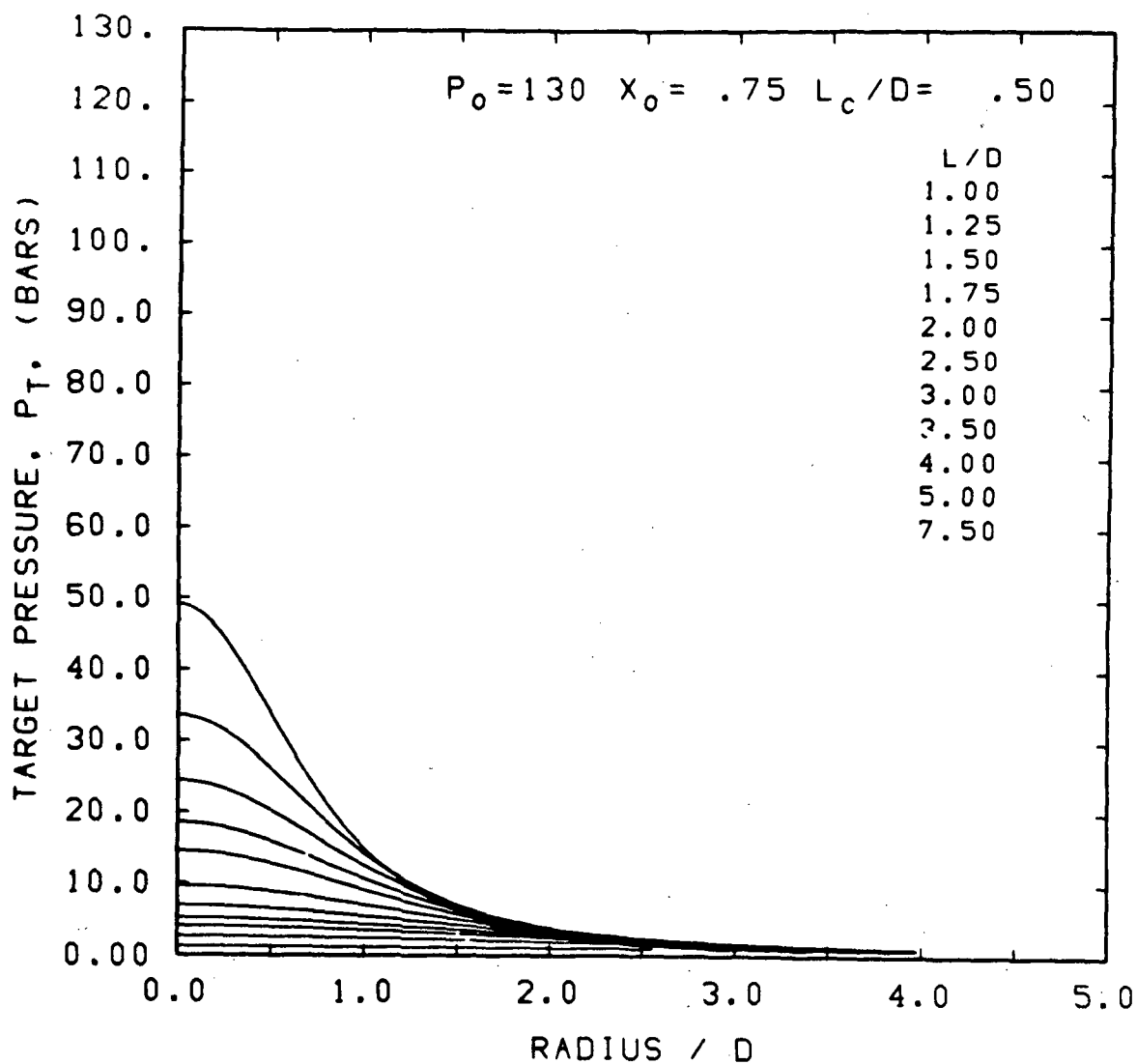
FIGURE A.64 TARGET PRESSURE DISTRIBUTIONS

The figure shows a plot with the following parameters and legend:

$P_o = 130$ $X_o = .75$ $L_c/D = .50$

L/D
1.00
1.25
1.50
1.75
2.00
2.50
3.00
3.50
4.00
5.00
7.50

Y-axis: TARGET PRESSURE, P_T, (BARS) ranging from 0.00 to 130.
X-axis: RADIUS / D ranging from 0.0 to 5.0
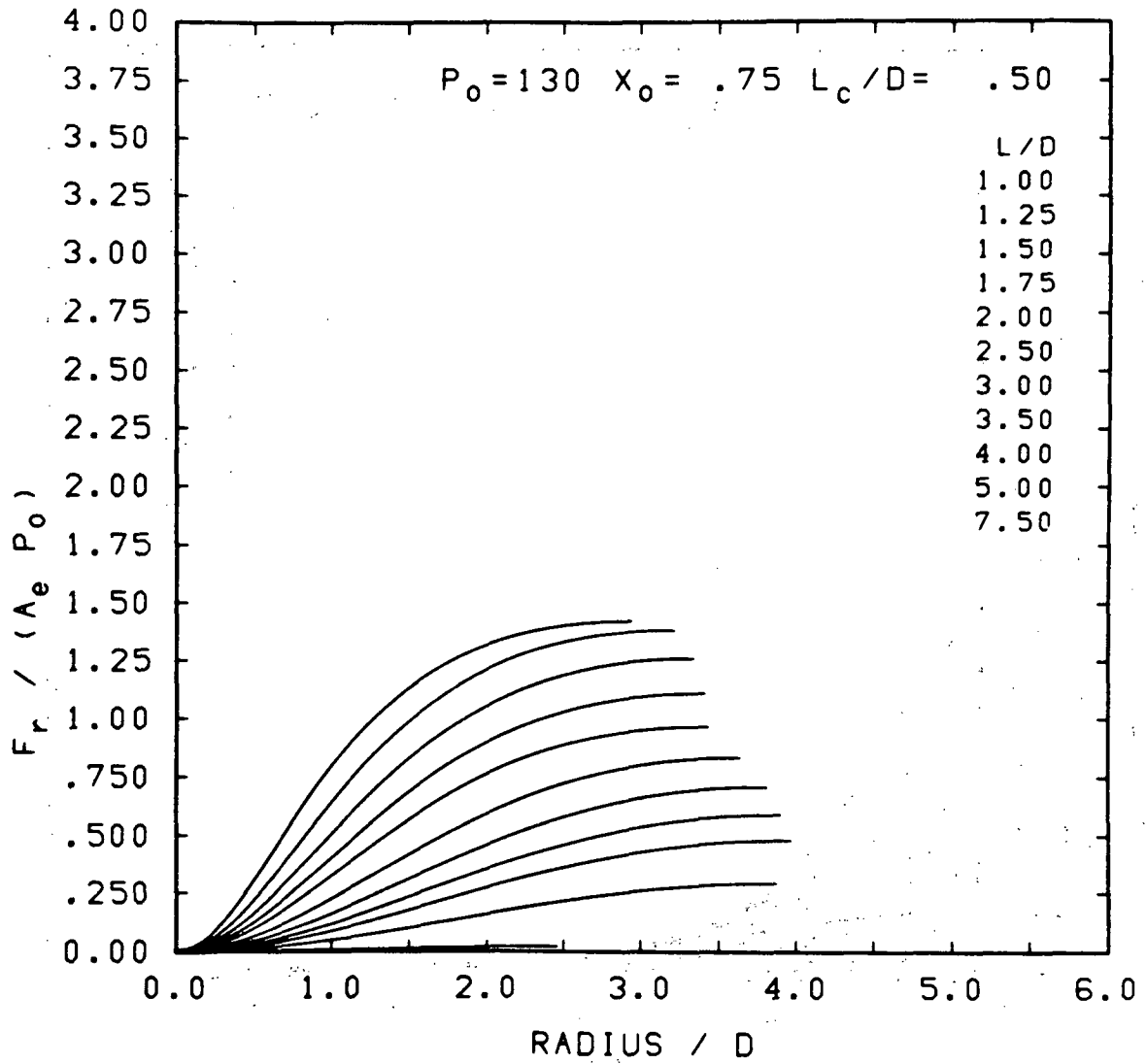
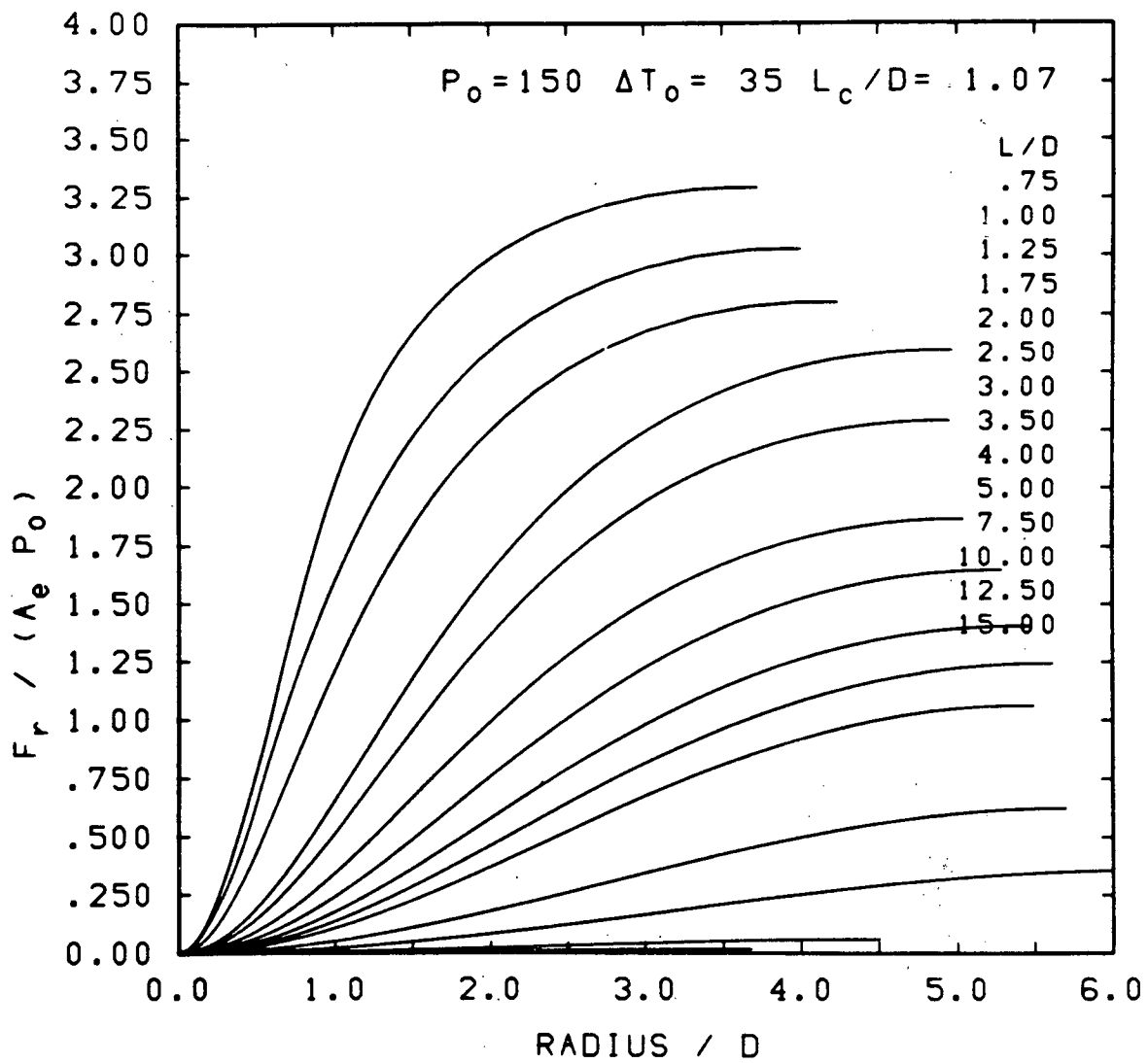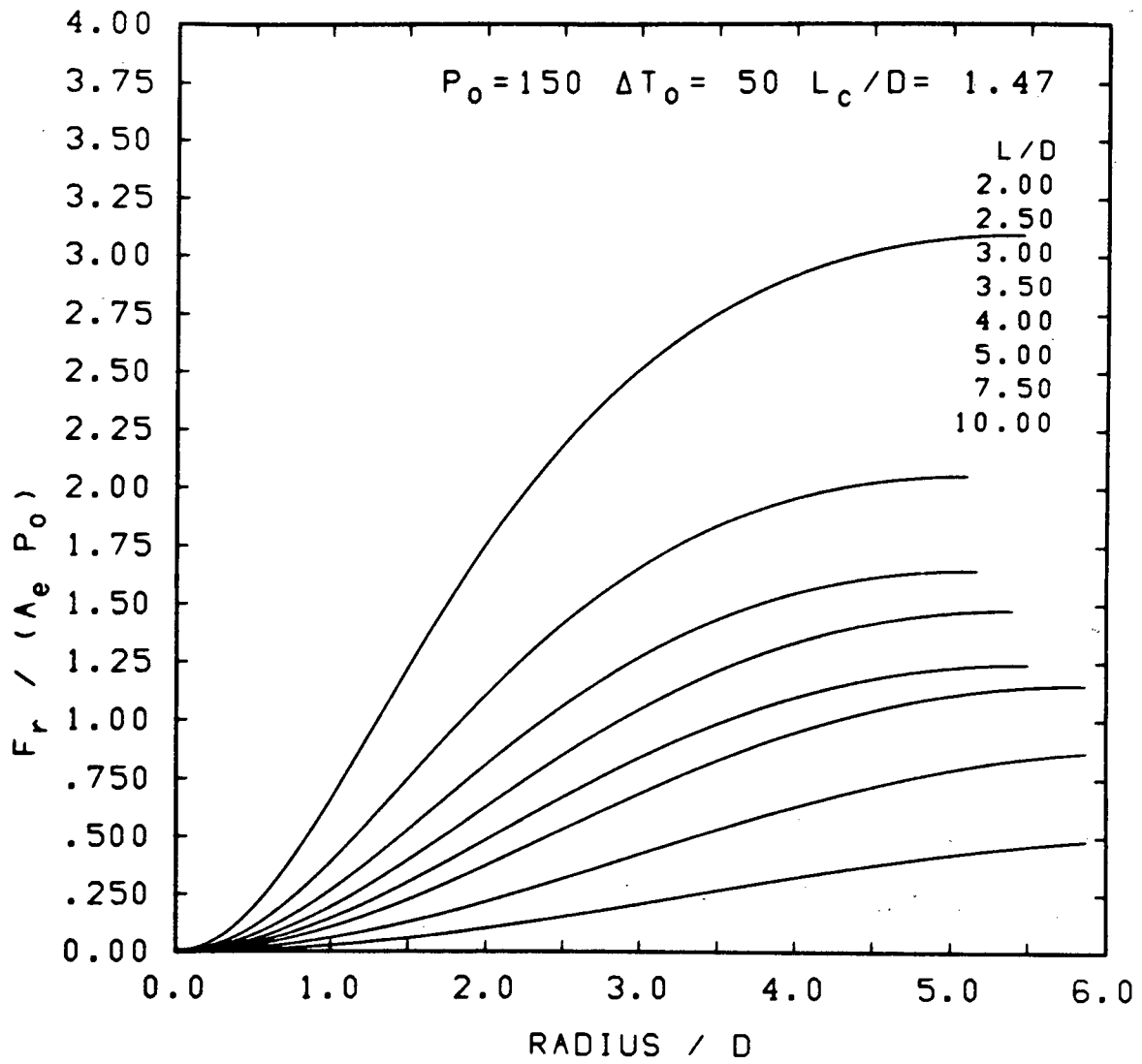FIGURE A.65   TARGET LOAD DISTRIBUTIONS
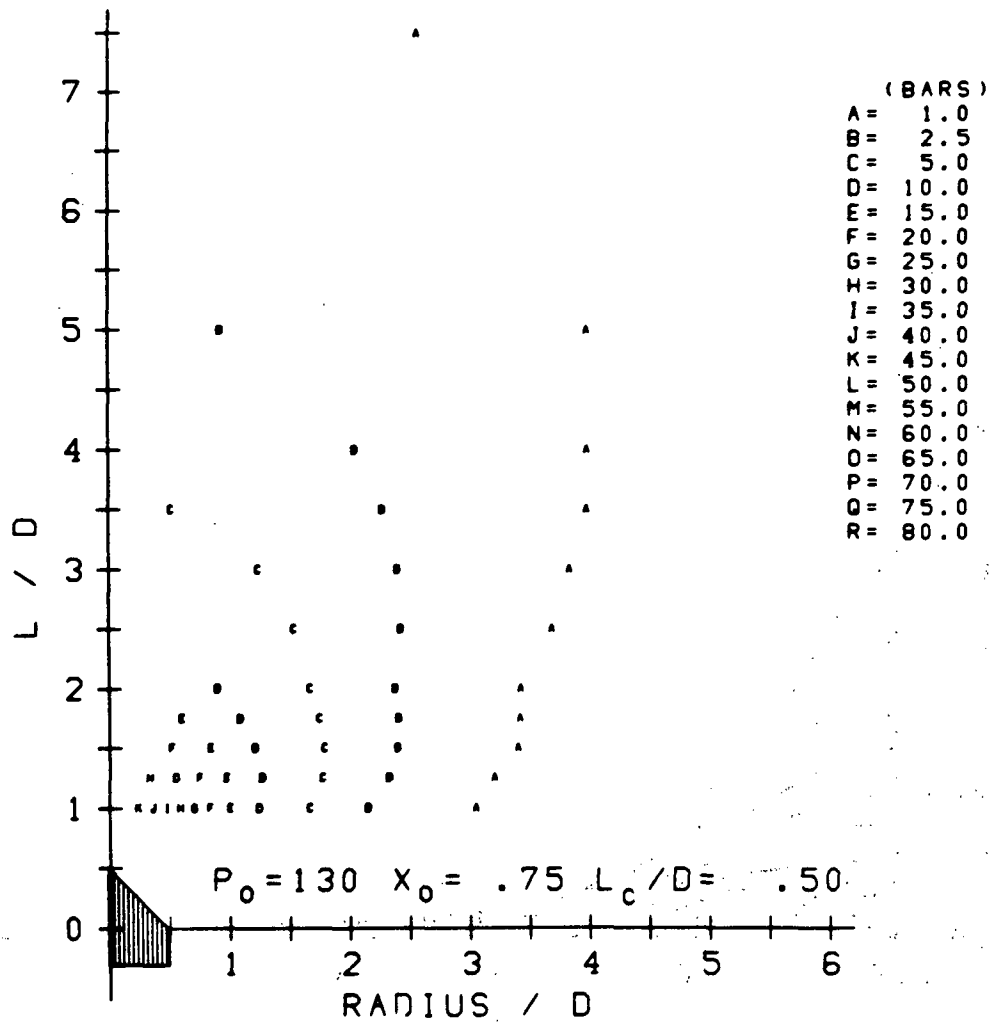
FIGURE A.66 COMPOSITE TARGET PRESSURE CONTOURS

FIGURE A.67   TARGET PRESSURE DISTRIBUTIONS

The figure shows target pressure distributions with axes:
- Y-axis: TARGET PRESSURE, P_T, (BARS), ranging from 0.00 to 130.
- X-axis: RADIUS / D, ranging from 0.0 to 5.0

Parameters: $P_o = 130$ $X_o = .33$ $L_c/D = .50$

L/D values:
1.00
1.25
1.50
1.75
2.00
2.50
3.00
3.50
4.00
5.00
7.50
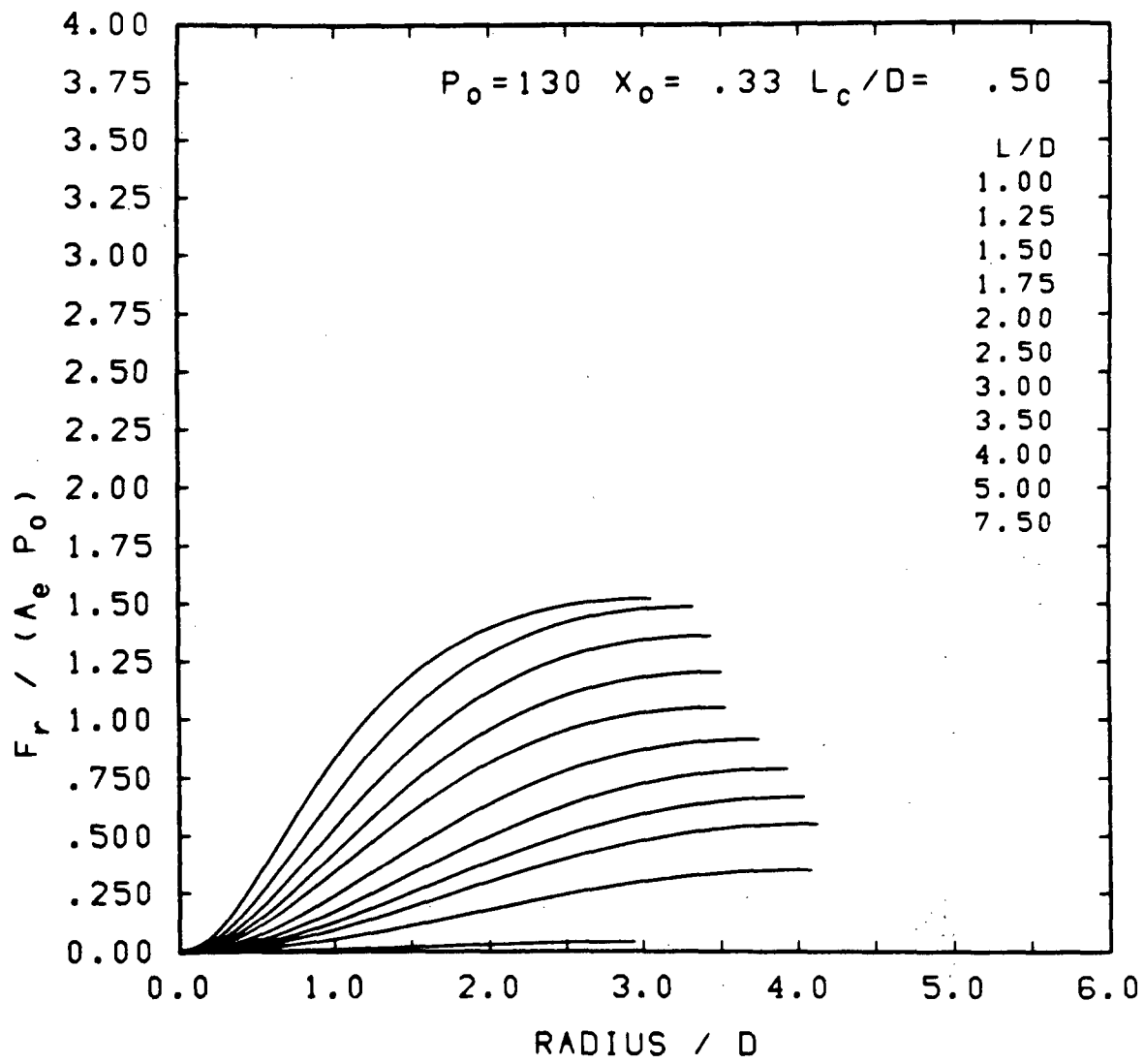
FIGURE A.68   TARGET LOAD DISTRIBUTIONS

The figure shows curves of $F_r / (A_e P_o)$ versus RADIUS / D with parameters $P_o = 130$, $X_o = .33$, $L_c / D = .50$, and L/D values of 1.00, 1.25, 1.50, 1.75, 2.00, 2.50, 3.00, 3.50, 4.00, 5.00, 7.50.
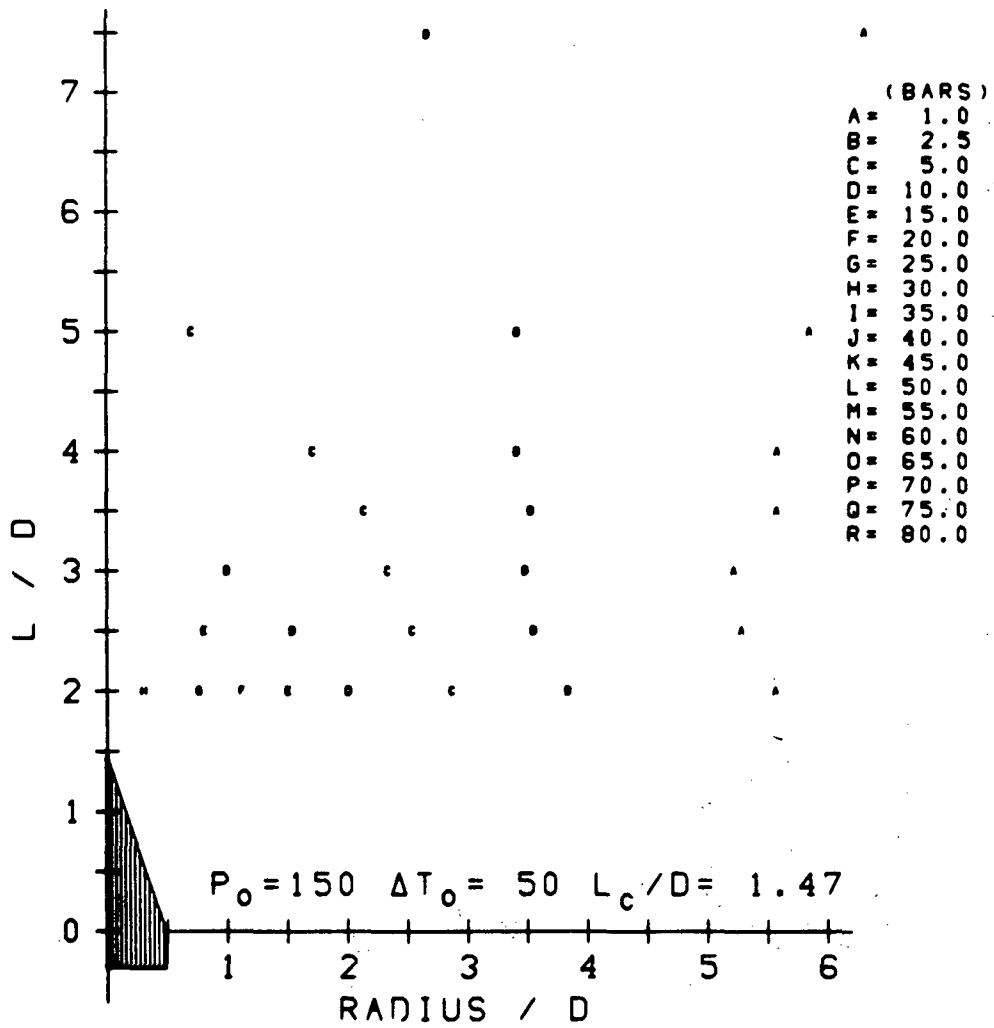
FIGURE A.69   COMPOSITE TARGET PRESSURE CONTOURS

FIGURE A.70   TARGET PRESSURE DISTRIBUTIONS

209

FIGURE A.71   TARGET LOAD DISTRIBUTIONS

(BARS)
A = 1.0
B = 2.5
C = 5.0
D = 10.0
E = 15.0
F = 20.0
G = 25.0
H = 30.0
I = 35.0
J = 40.0
K = 45.0
L = 50.0
M = 55.0
N = 60.0
O = 65.0
P = 70.0
Q = 75.0
R = 80.0

$P_o = 130$ $\Delta T_o =$ 0 $L_c/D =$ .50

L / D

RADIUS / D

FIGURE A.72   COMPOSITE TARGET PRESSURE CONTOURS

FIGURE A.73   TARGET PRESSURE DISTRIBUTIONS

The plotted curves carry the header:

$P_O = 130$ $\Delta T_O = 15$ $L_c/D = .63$

L/D
1.00
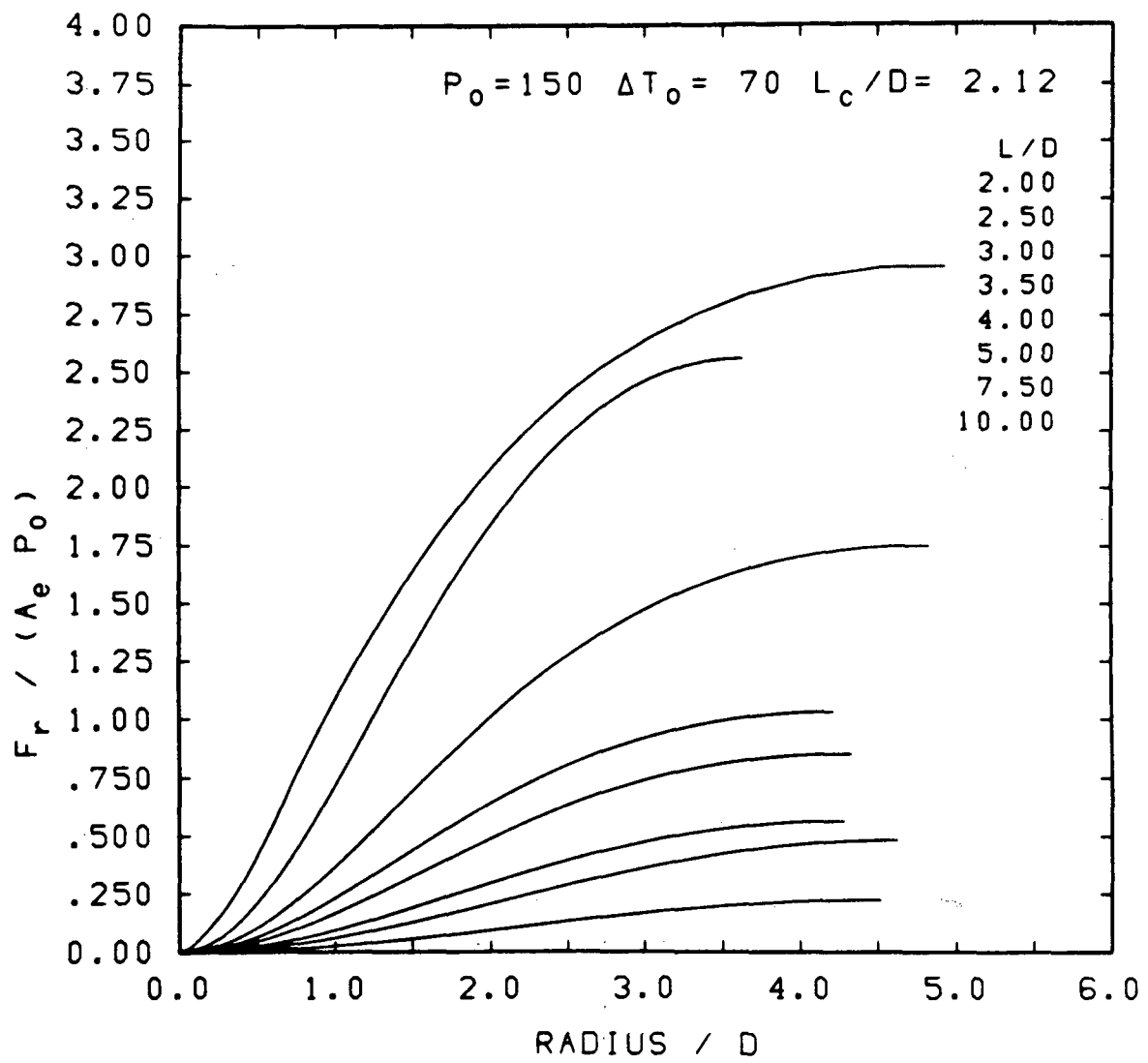1.25
1.50
1.75
2.00
2.50
3.00
3.50
4.00
5.00
7.50
10.00

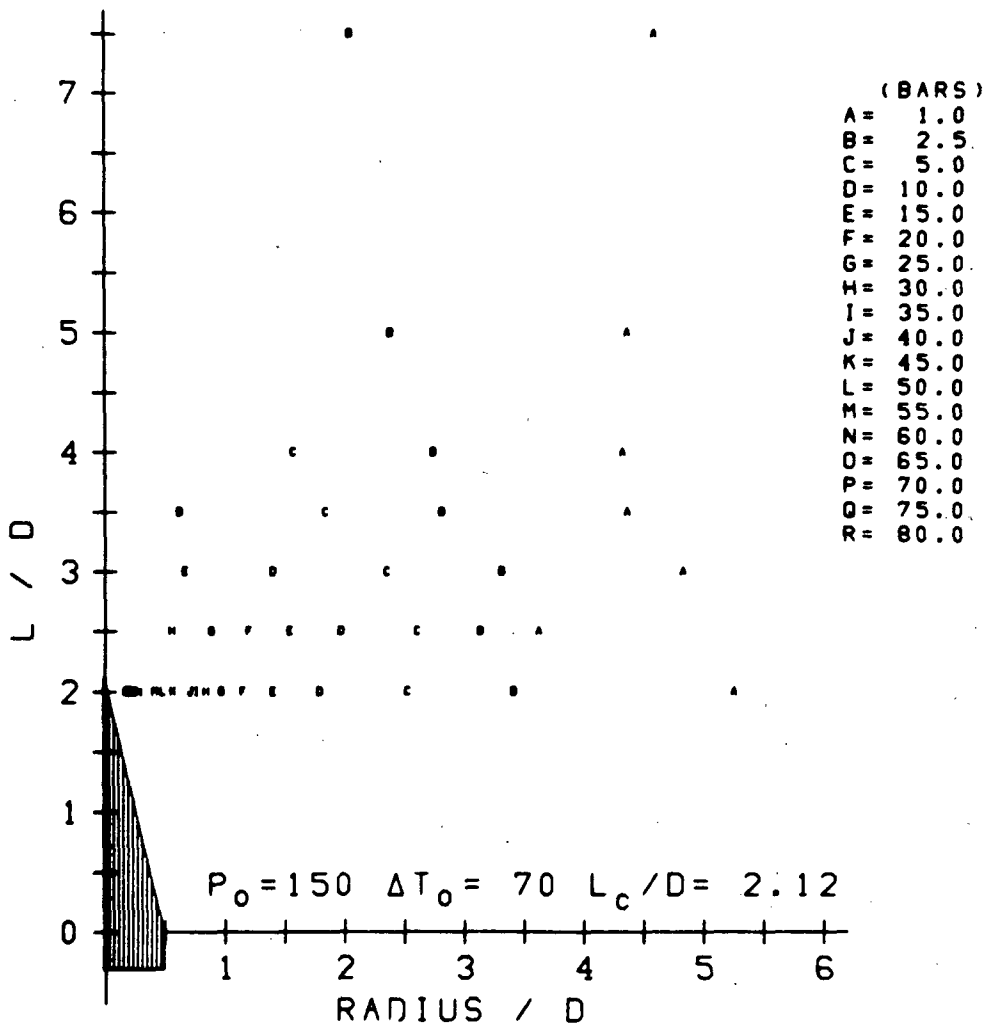FIGURE A.74 TARGET LOAD DISTRIBUTIONS

FIGURE A.75 COMPOSITE TARGET PRESSURE CONTOURS

FIGURE A.76   TARGET PRESSURE DISTRIBUTIONS

215

FIGURE A.77 TARGET LOAD DISTRIBUTIONS

216
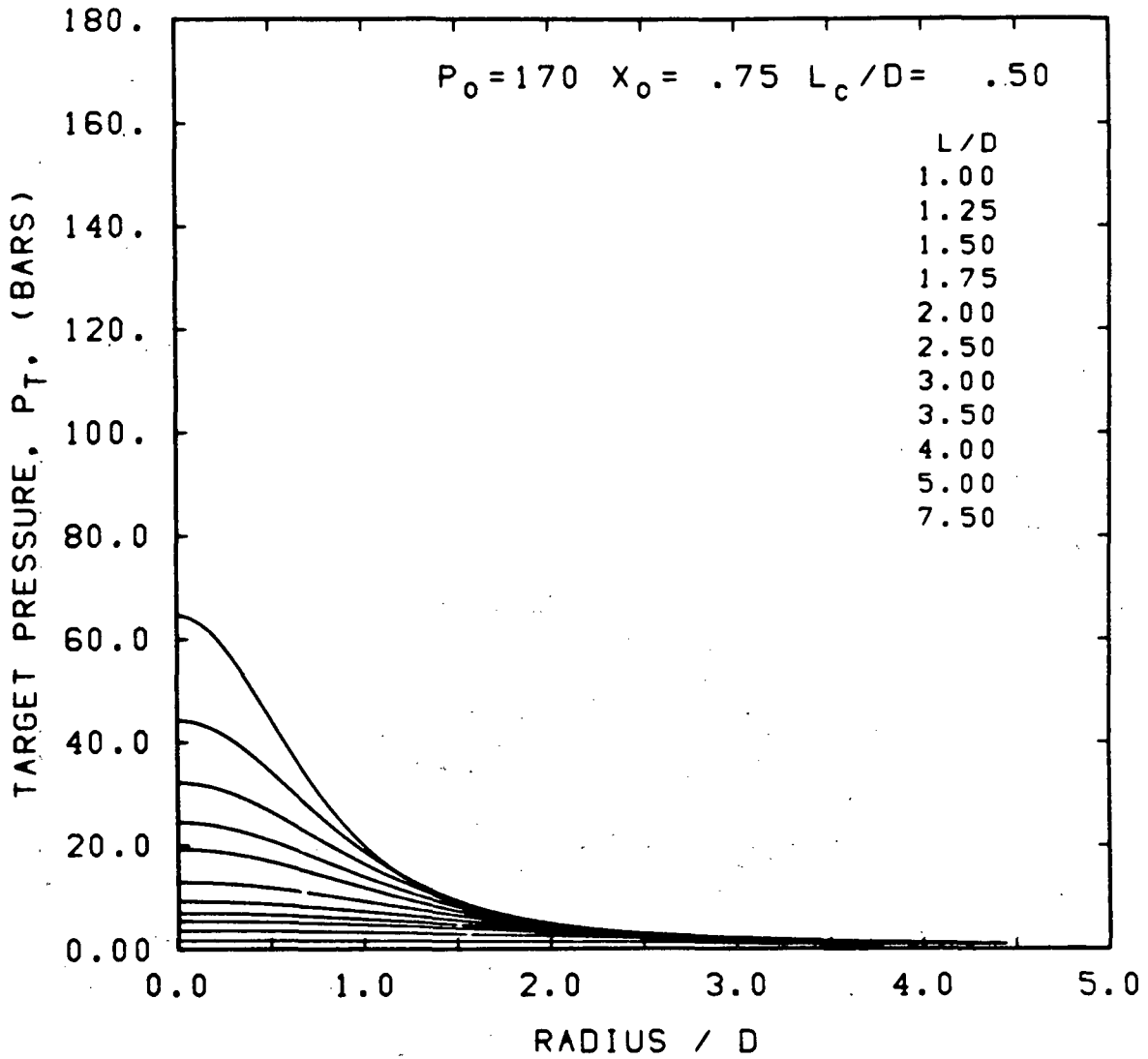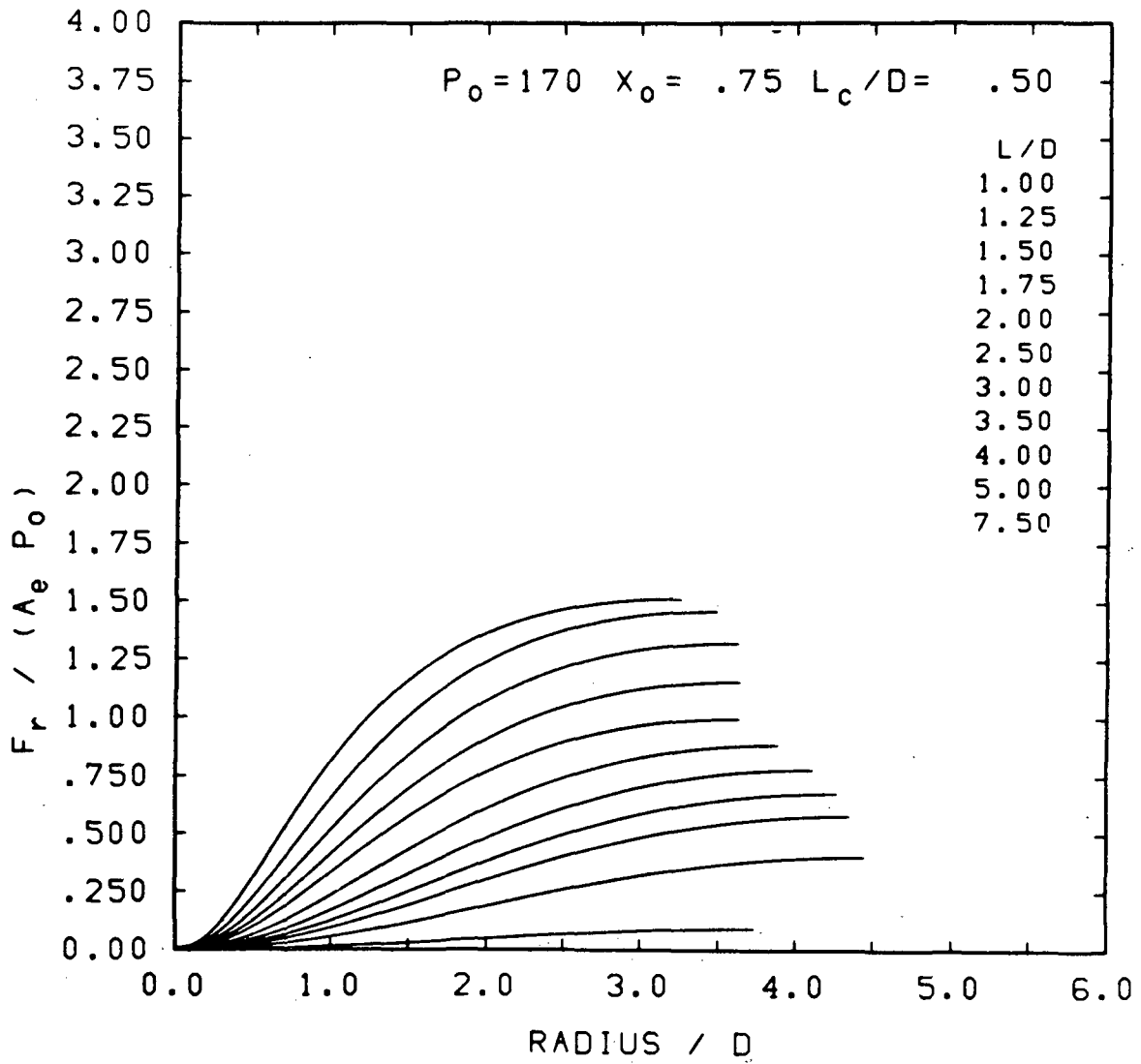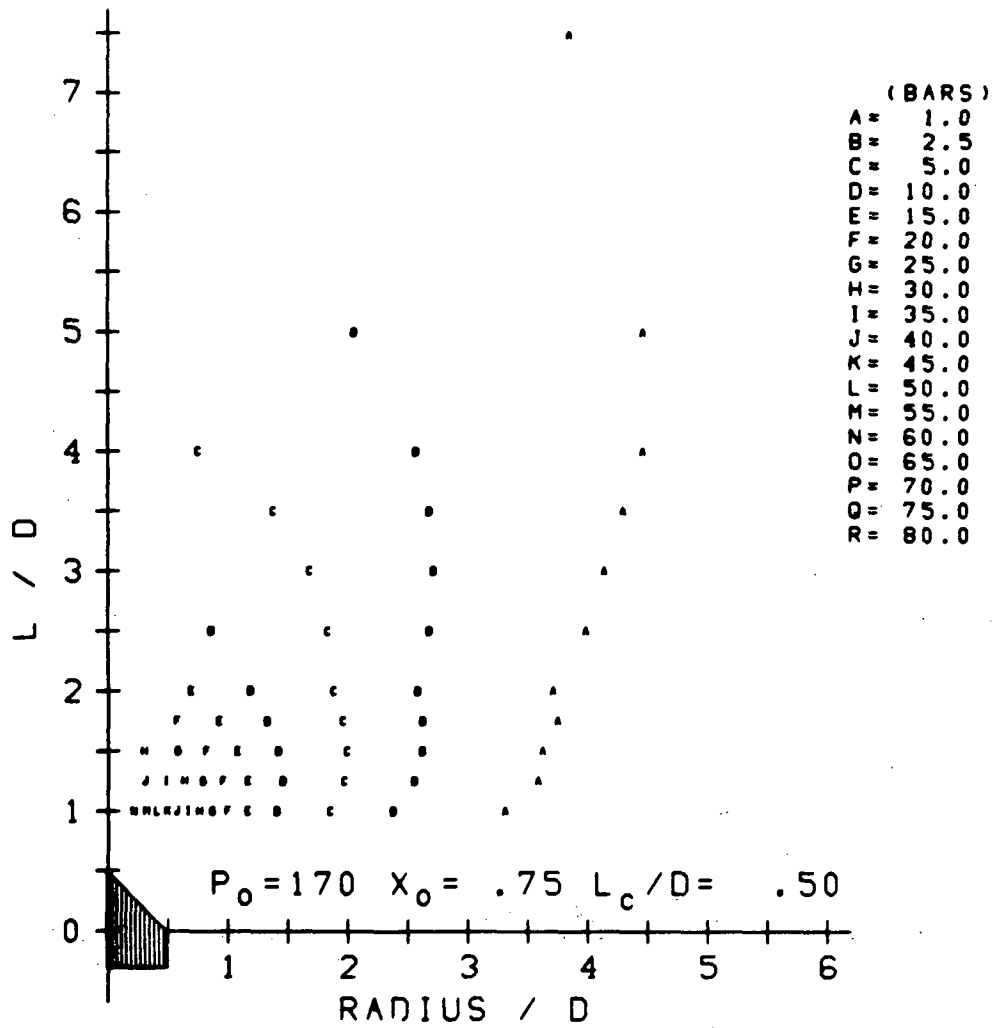
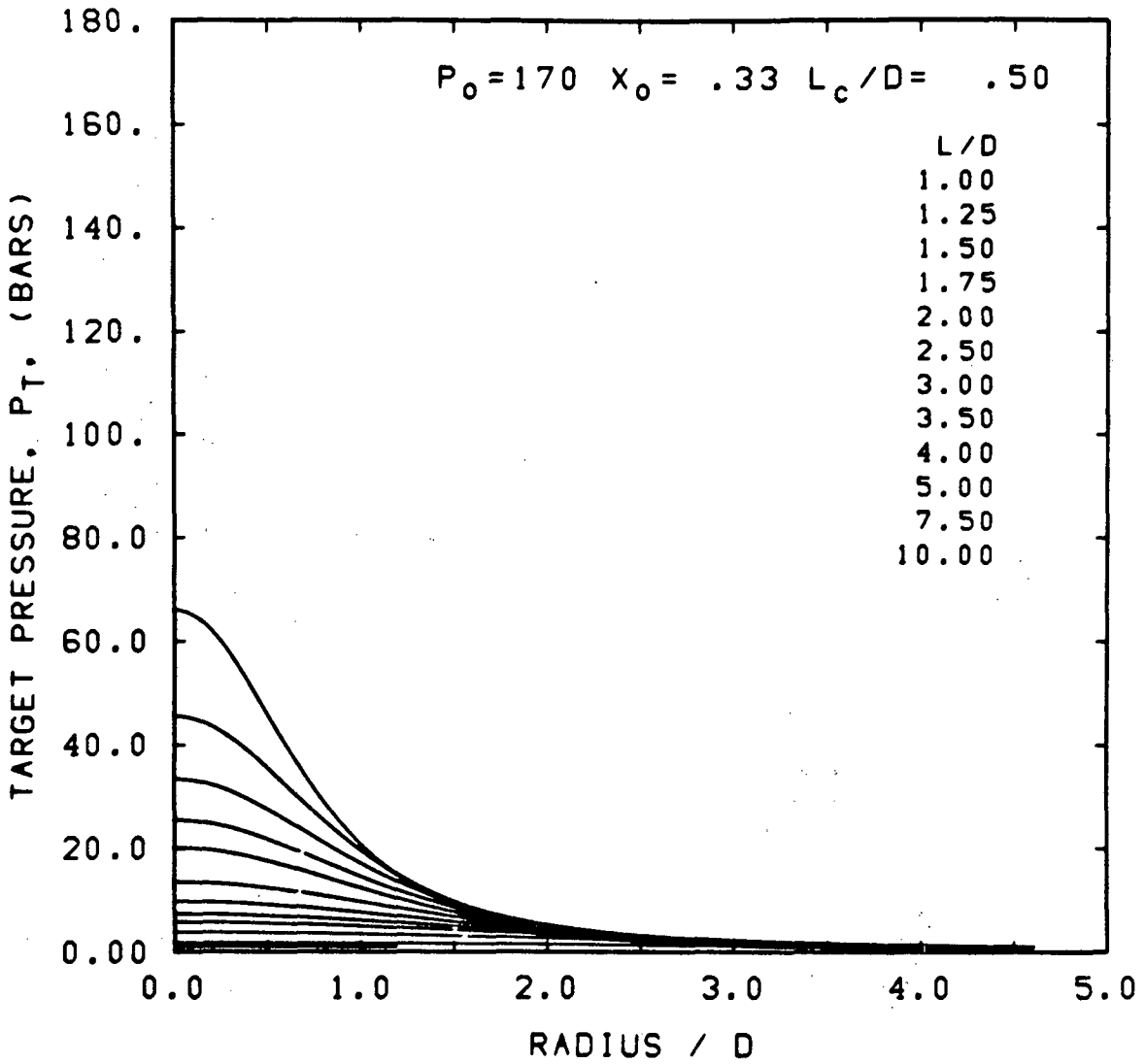FIGURE A.78 COMPOSITE TARGET PRESSURE CONTOURS

FIGURE A.79 TARGET PRESSURE DISTRIBUTIONS

218

FIGURE A.80   TARGET LOAD DISTRIBUTIONS

FIGURE A.81   COMPOSITE TARGET PRESSURE CONTOURS

FIGURE A.82   TARGET PRESSURE DISTRIBUTIONS

FIGURE A.83 TARGET LOAD DISTRIBUTIONS

FIGURE A.84 COMPOSITE TARGET PRESSURE CONTOURS

$P_o = 130$ $\Delta T_o = 70$ $L_c/D = 2.29$

(BARS)
A = 1.0
B = 2.5
C = 5.0
D = 10.0
E = 15.0
F = 20.0
G = 25.0
H = 30.0
I = 35.0
J = 40.0
K = 45.0
L = 50.0
M = 55.0
N = 60.0
O = 65.0
P = 70.0
Q = 75.0
R = 80.0

L / D

RADIUS / D

FIGURE A.85   TARGET PRESSURE DISTRIBUTIONS

224

FIGURE A.86   TARGET LOAD DISTRIBUTIONS

FIGURE A.87   COMPOSITE TARGET PRESSURE CONTOURS

FIGURE A.88   TARGET PRESSURE DISTRIBUTIONS
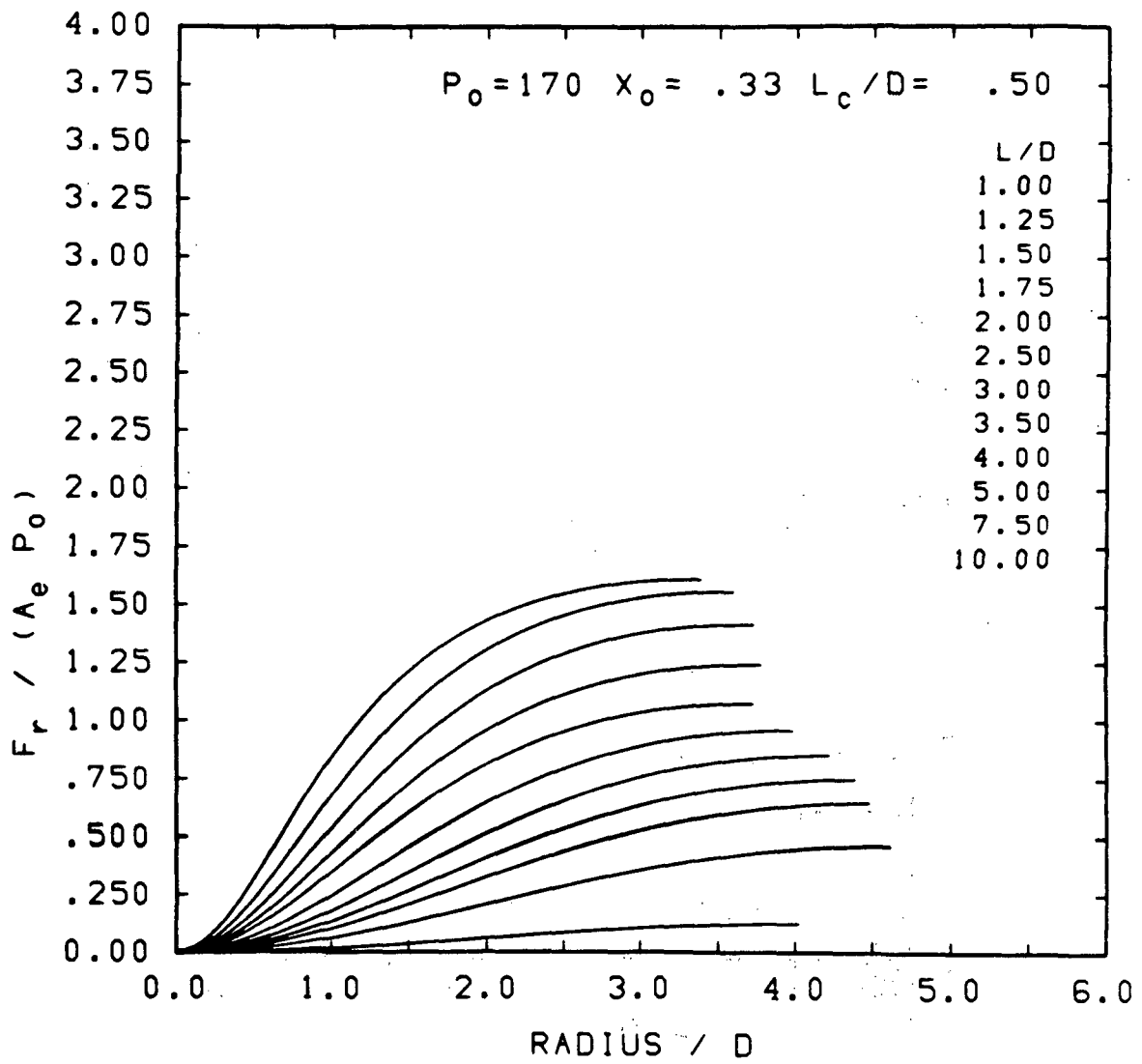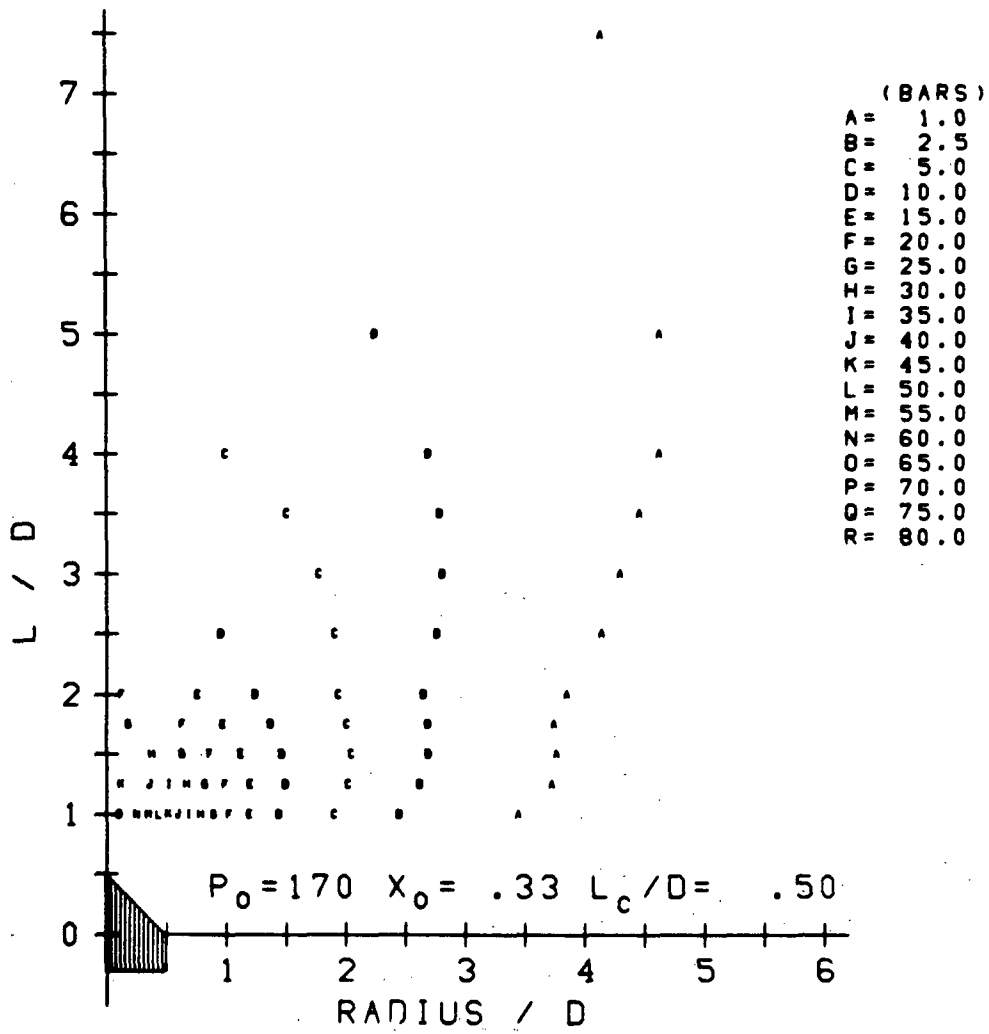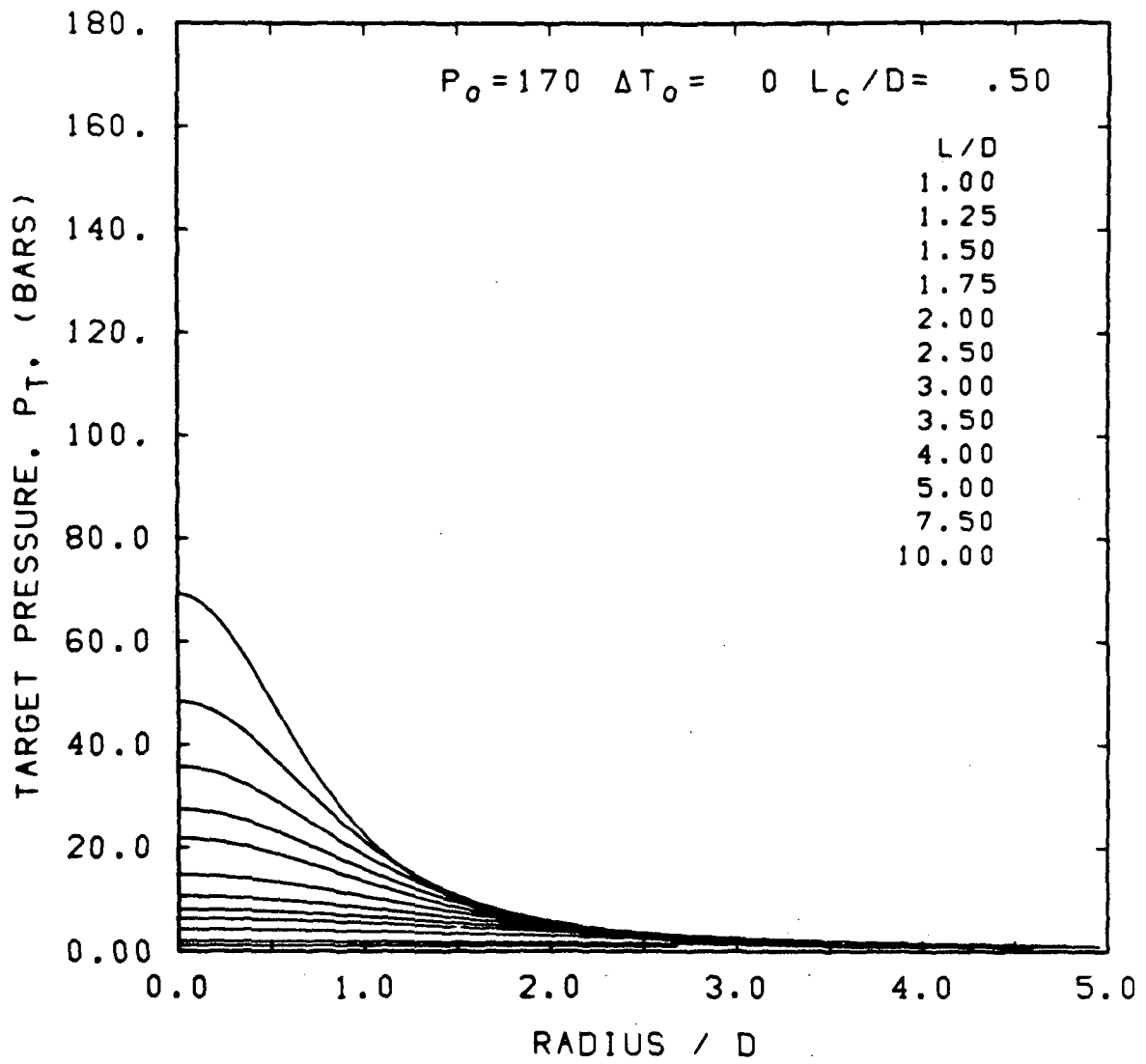
FIGURE A.89   TARGET LOAD DISTRIBUTIONS

FIGURE A.90 COMPOSITE TARGET PRESSURE CONTOURS

FIGURE A.91 TARGET PRESSURE DISTRIBUTIONS

FIGURE A.92   TARGET LOAD DISTRIBUTIONS

FIGURE A.93 COMPOSITE TARGET PRESSURE CONTOURS
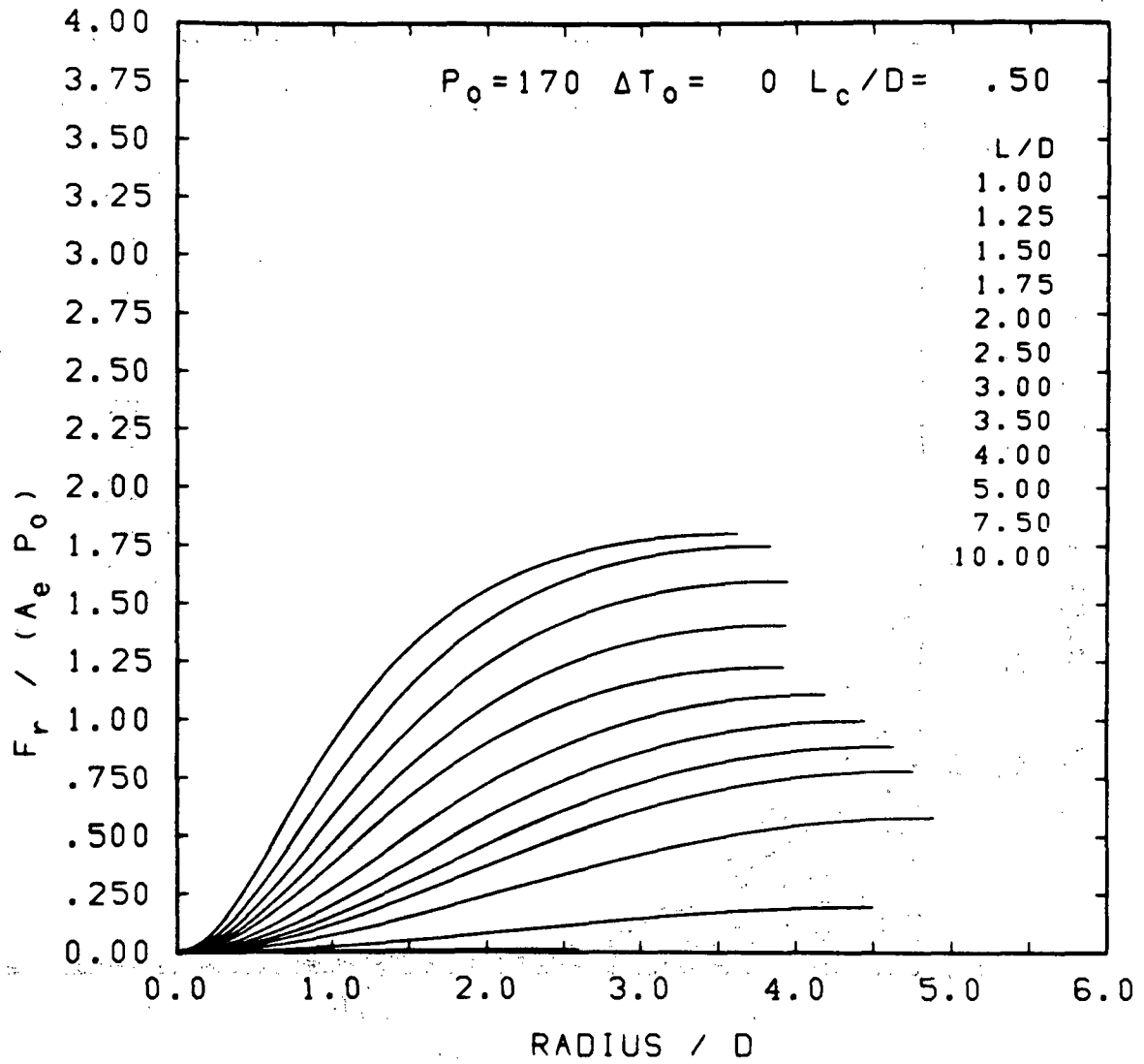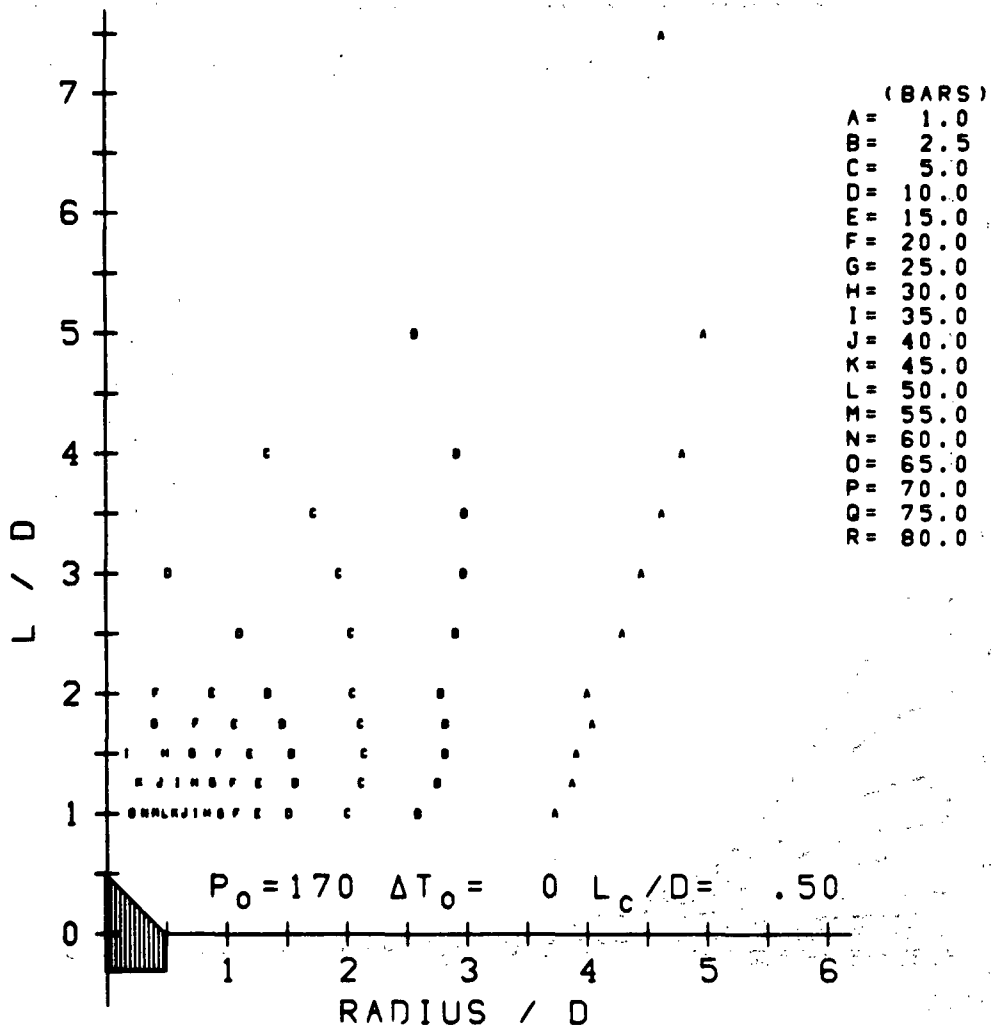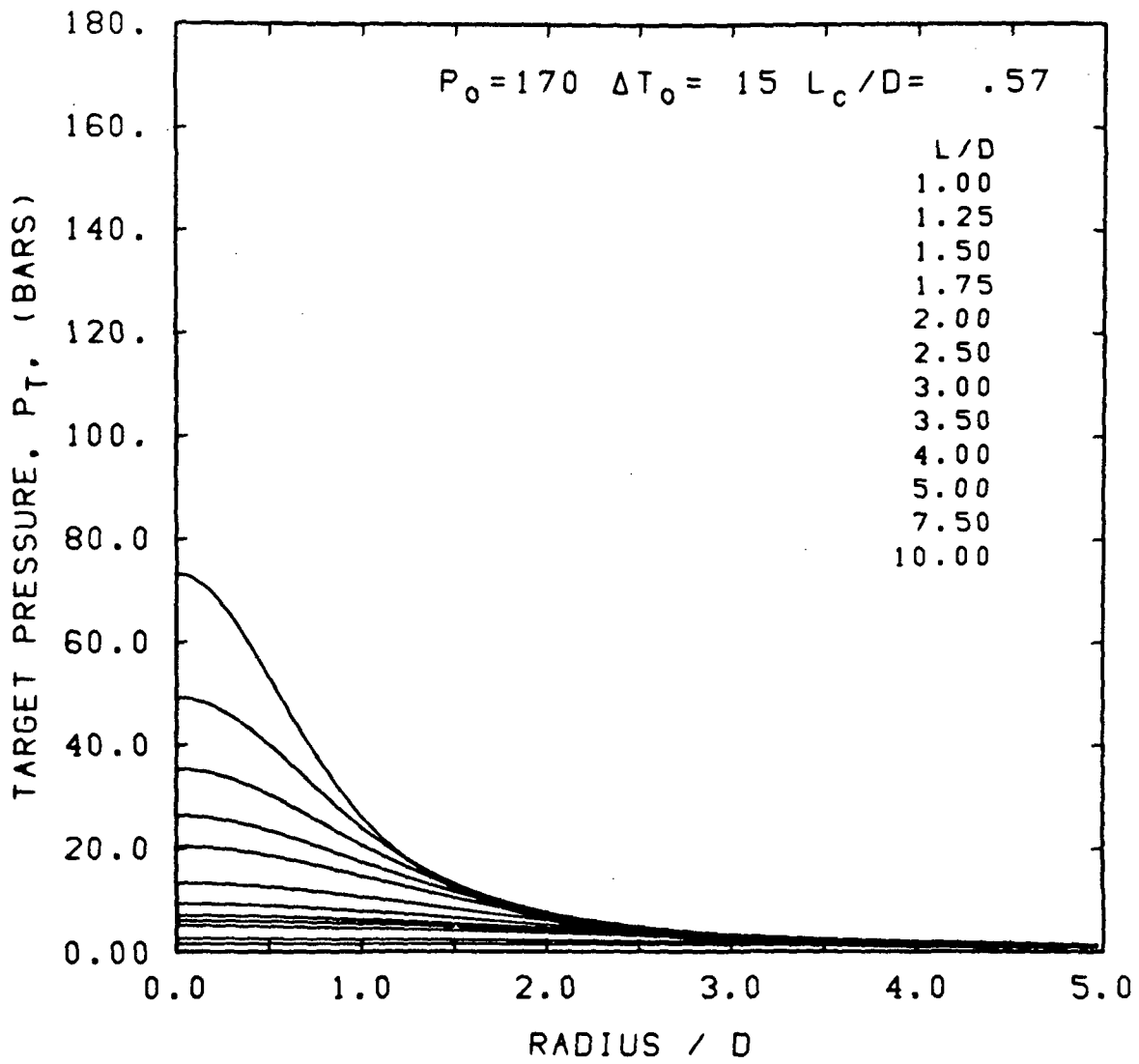
FIGURE A.94   TARGET PRESSURE DISTRIBUTIONS

FIGURE A.95 TARGET LOAD DISTRIBUTIONS

FIGURE A.96 COMPOSITE TARGET PRESSURE CONTOURS

FIGURE A.97 TARGET PRESSURE DISTRIBUTIONS

FIGURE A.98   TARGET LOAD DISTRIBUTIONS
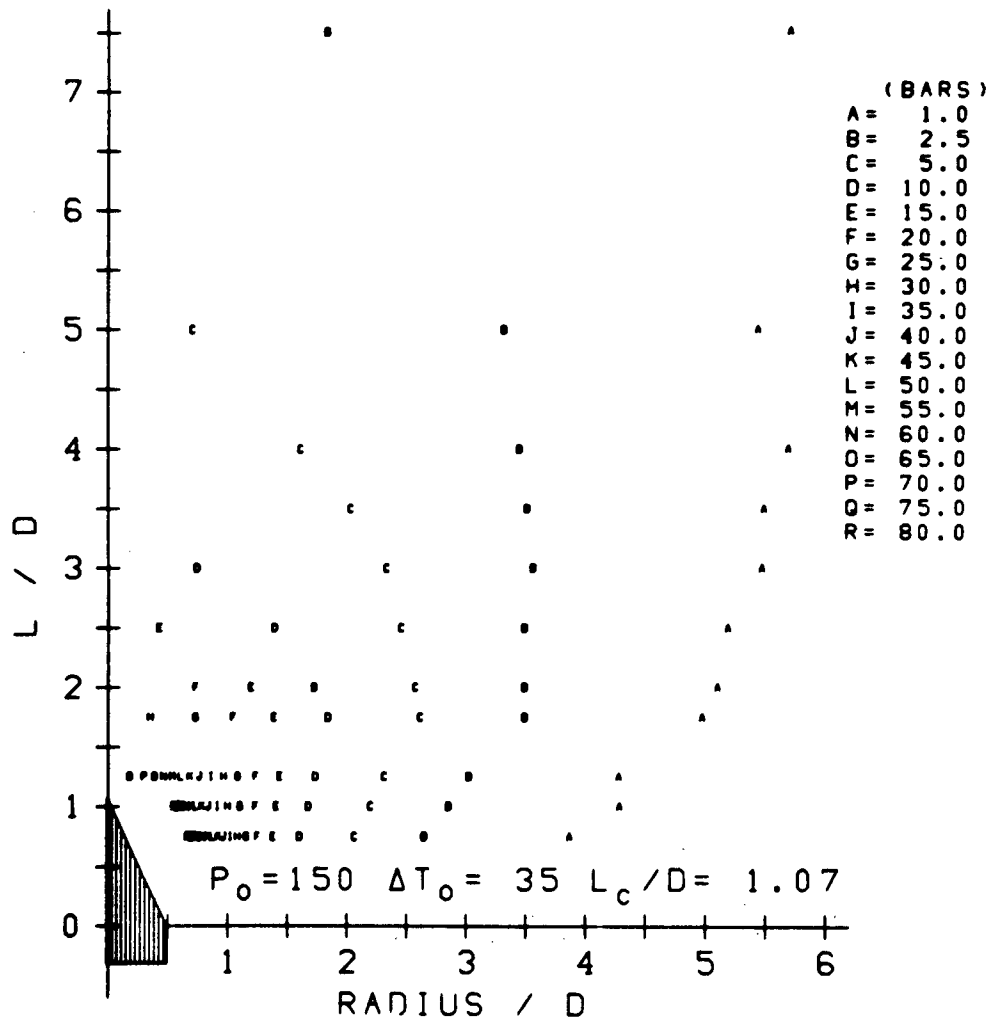
FIGURE A.99 COMPOSITE TARGET PRESSURE CONTOURS

238
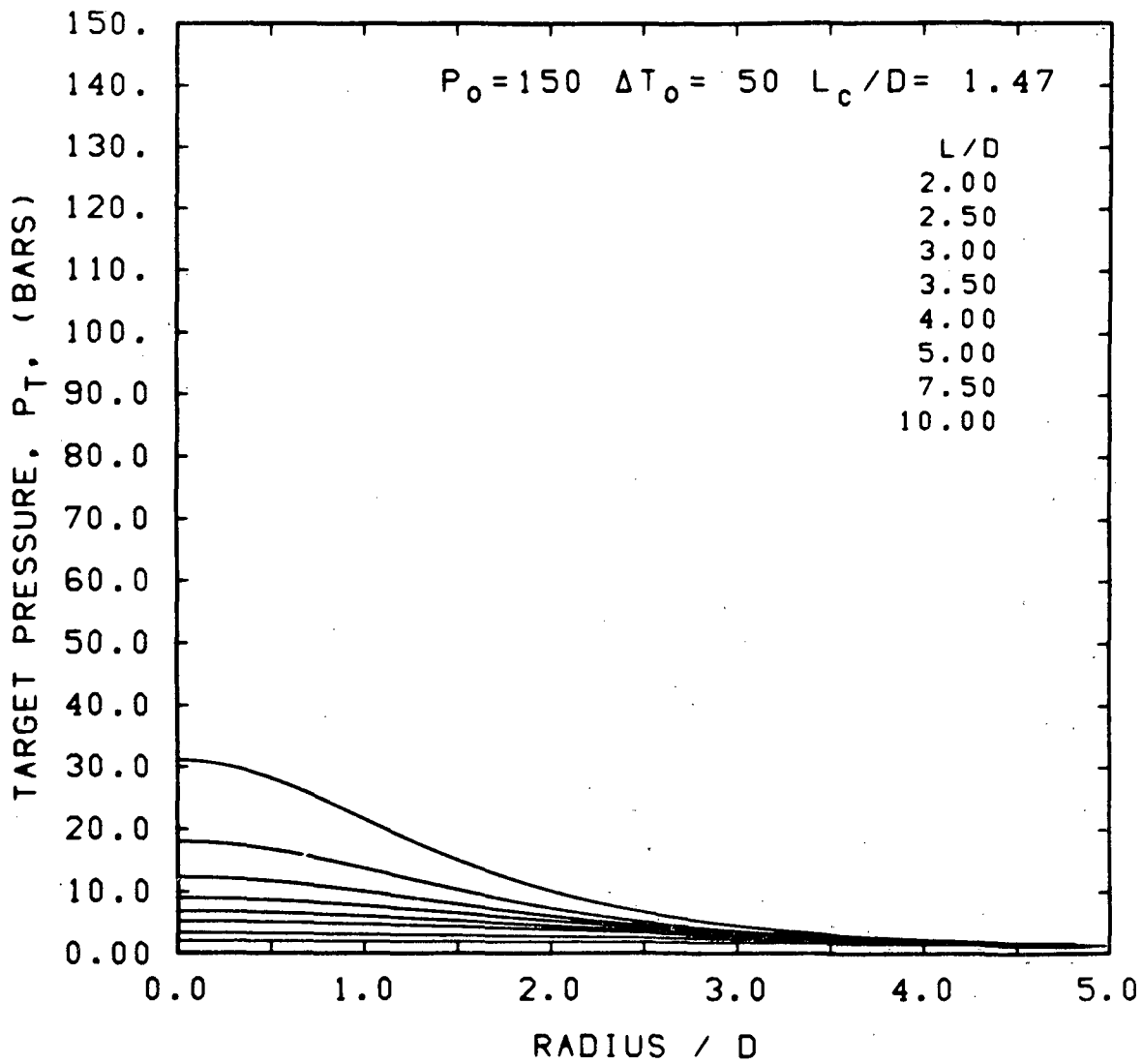
FIGURE A.100   TARGET PRESSURE DISTRIBUTIONS

The figure shows a plot of TARGET PRESSURE, P_T, (BARS) on the vertical axis (0.00 to 150.) versus RADIUS / D on the horizontal axis (0.0 to 5.0).

Plot annotations:
$P_o = 150$ $\Delta T_o = 50$ $L_c/D = 1.47$

L/D
2.00
2.50
3.00
3.50
4.00
5.00
7.50
10.00

FIGURE A.101 TARGET LOAD DISTRIBUTIONS

FIGURE A.102   COMPOSITE TARGET PRESSURE CONTOURS

241
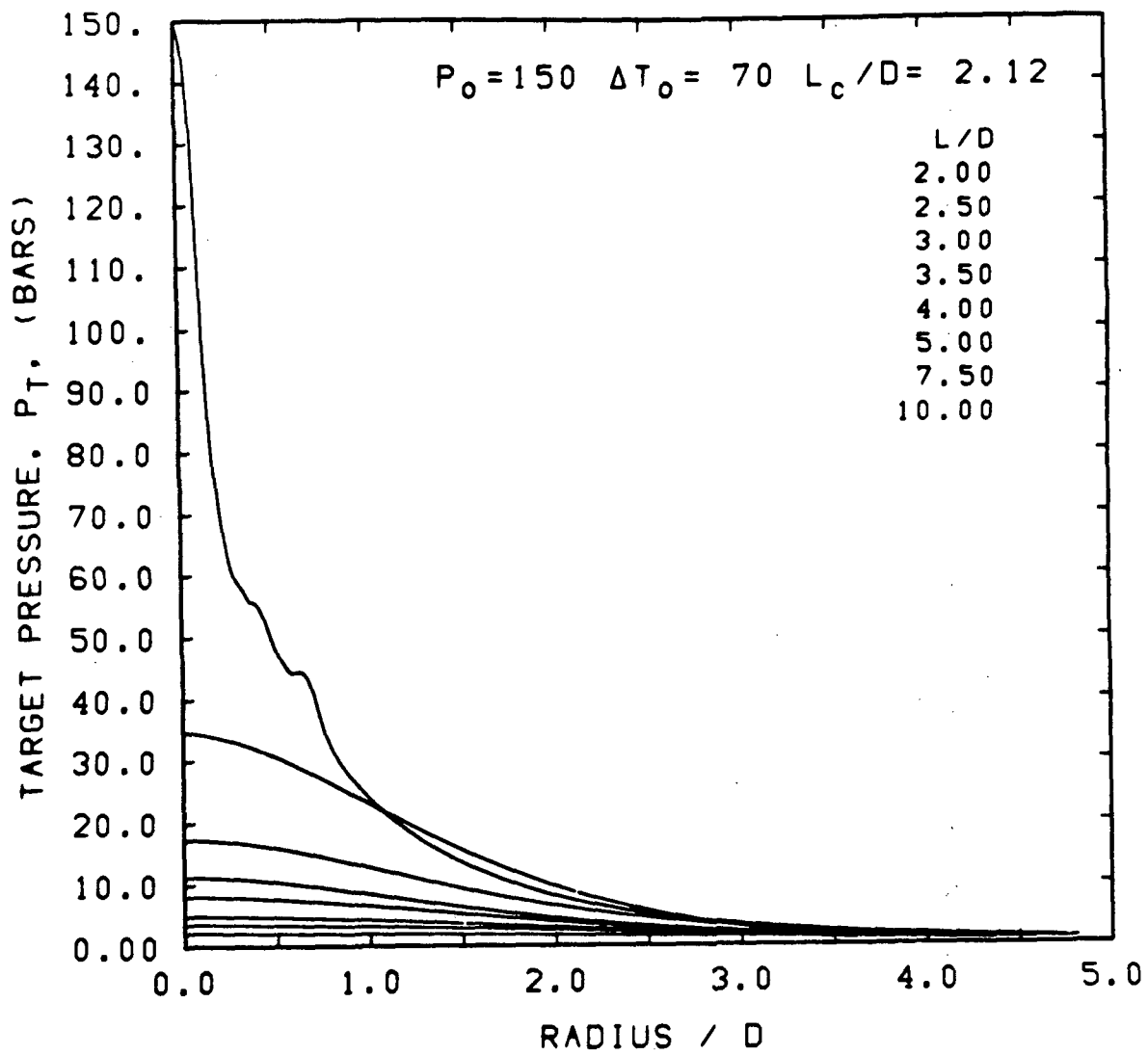
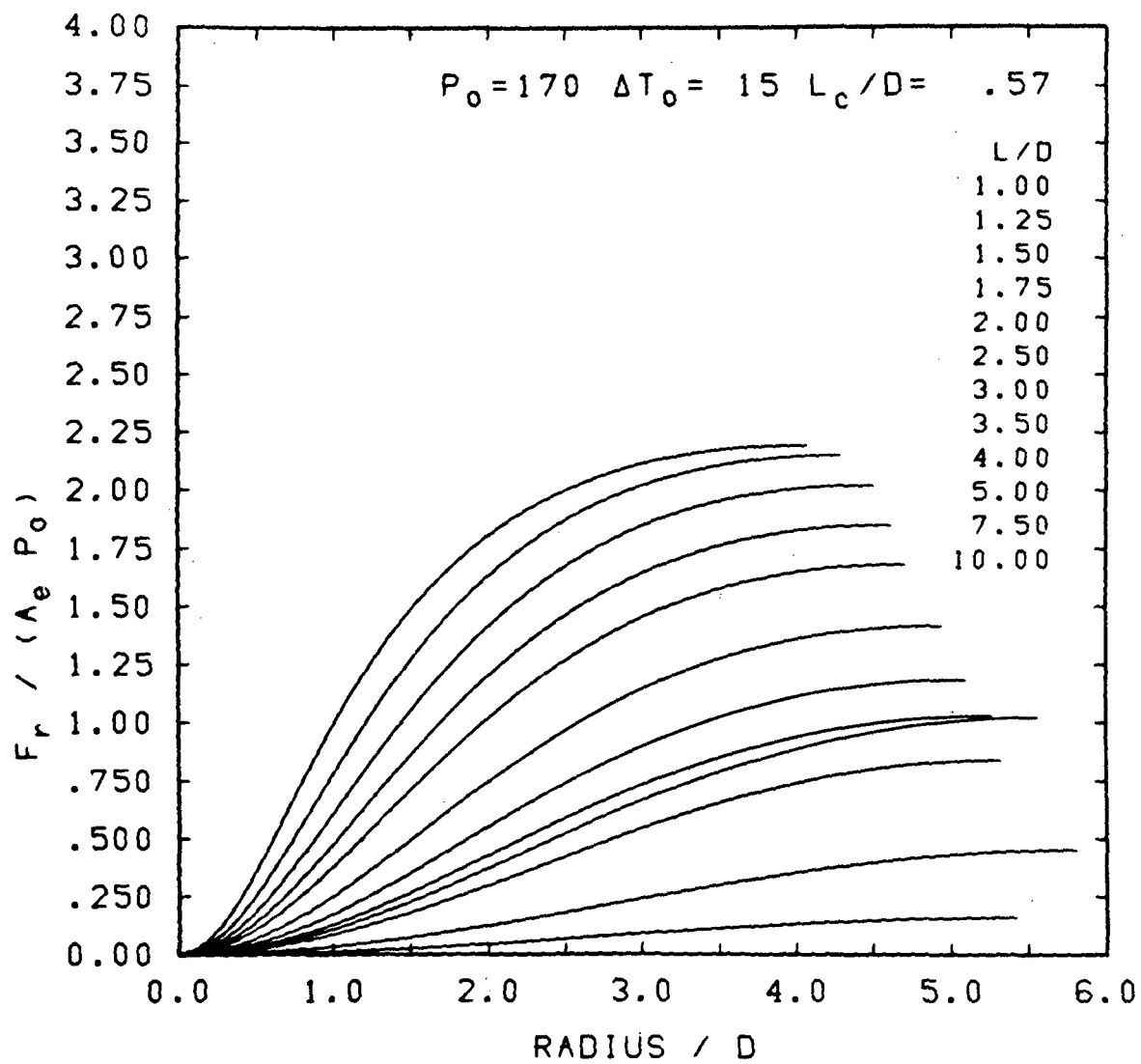FIGURE A.103   TARGET PRESSURE DISTRIBUTIONS

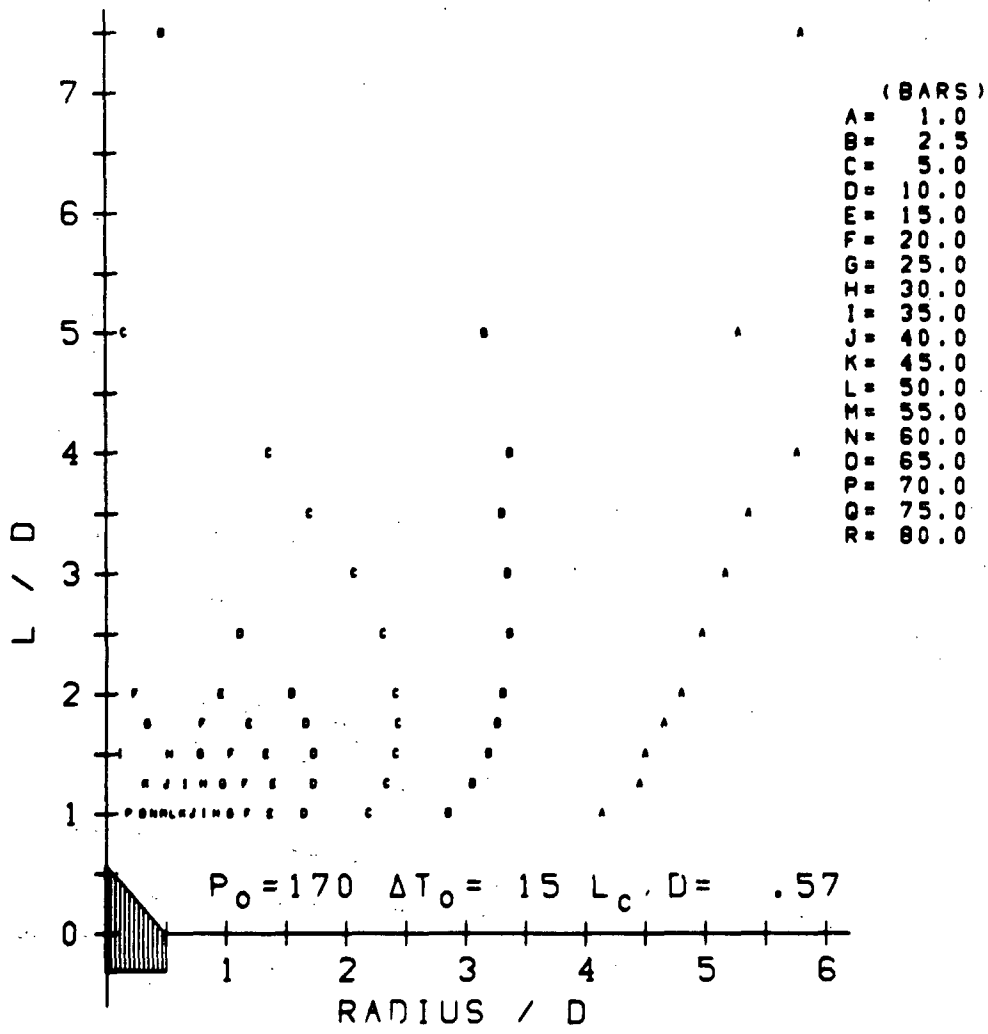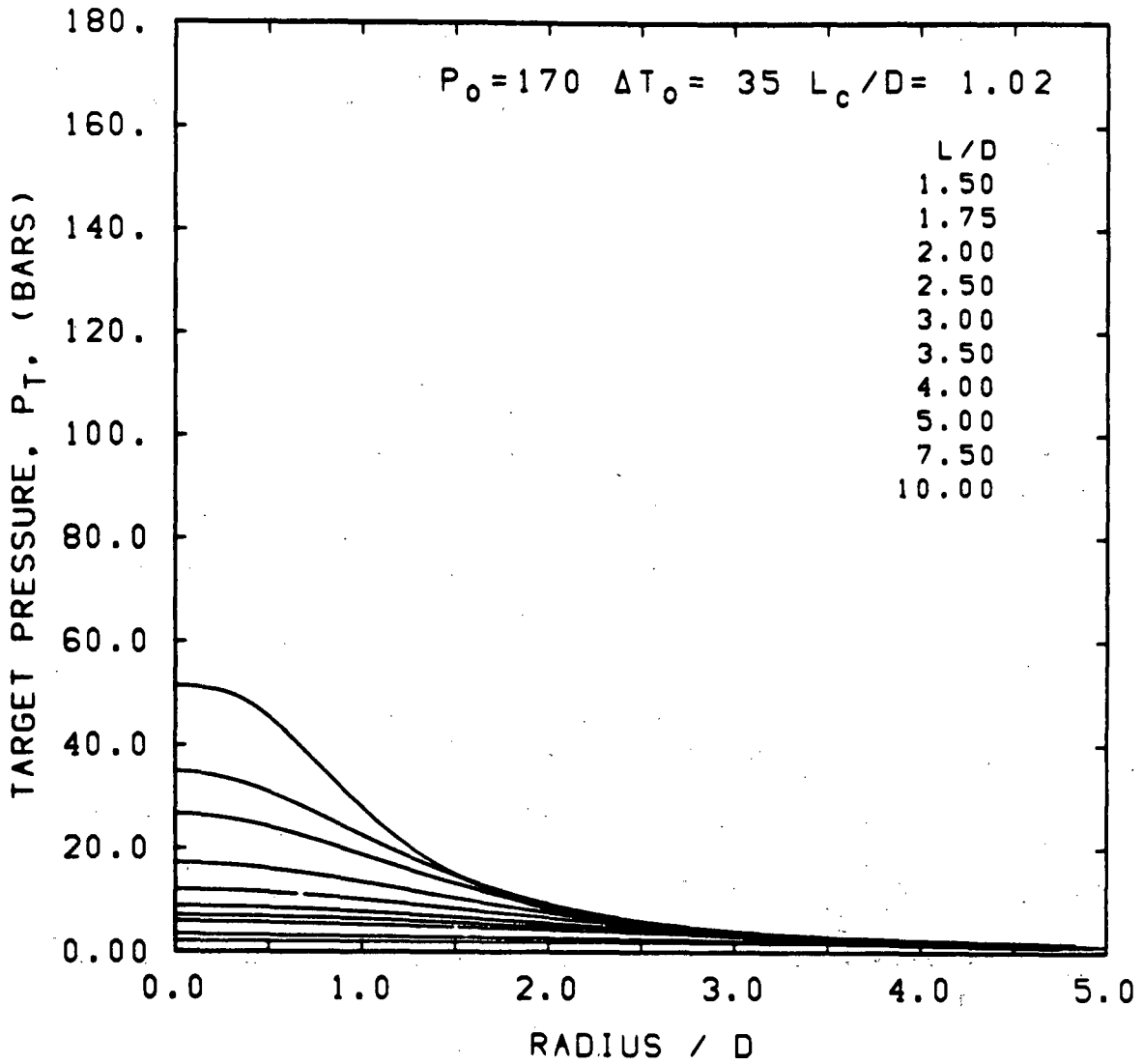FIGURE A.104   TARGET LOAD DISTRIBUTIONS

FIGURE A.105 COMPOSITE TARGET PRESSURE CONTOURS

FIGURE A.106   TARGET PRESSURE DISTRIBUTIONS

FIGURE A.107   TARGET LOAD DISTRIBUTIONS

FIGURE A.108 COMPOSITE TARGET PRESSURE CONTOURS

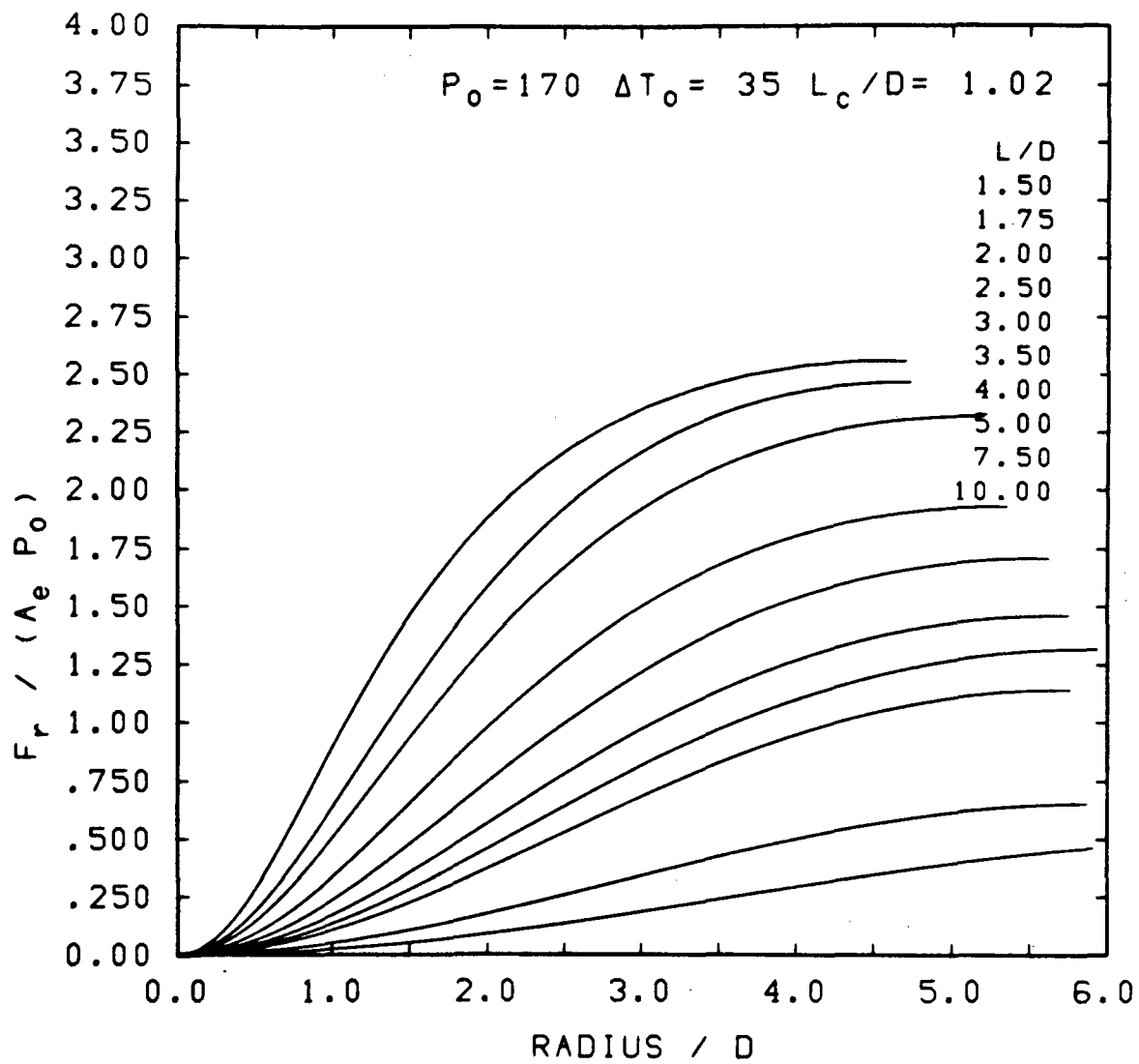FIGURE A.109   TARGET PRESSURE DISTRIBUTIONS

248

FIGURE A.110 TARGET LOAD DISTRIBUTIONS

FIGURE A.111 COMPOSITE TARGET PRESSURE CONTOURS

FIGURE A.112   TARGET PRESSURE DISTRIBUTIONS
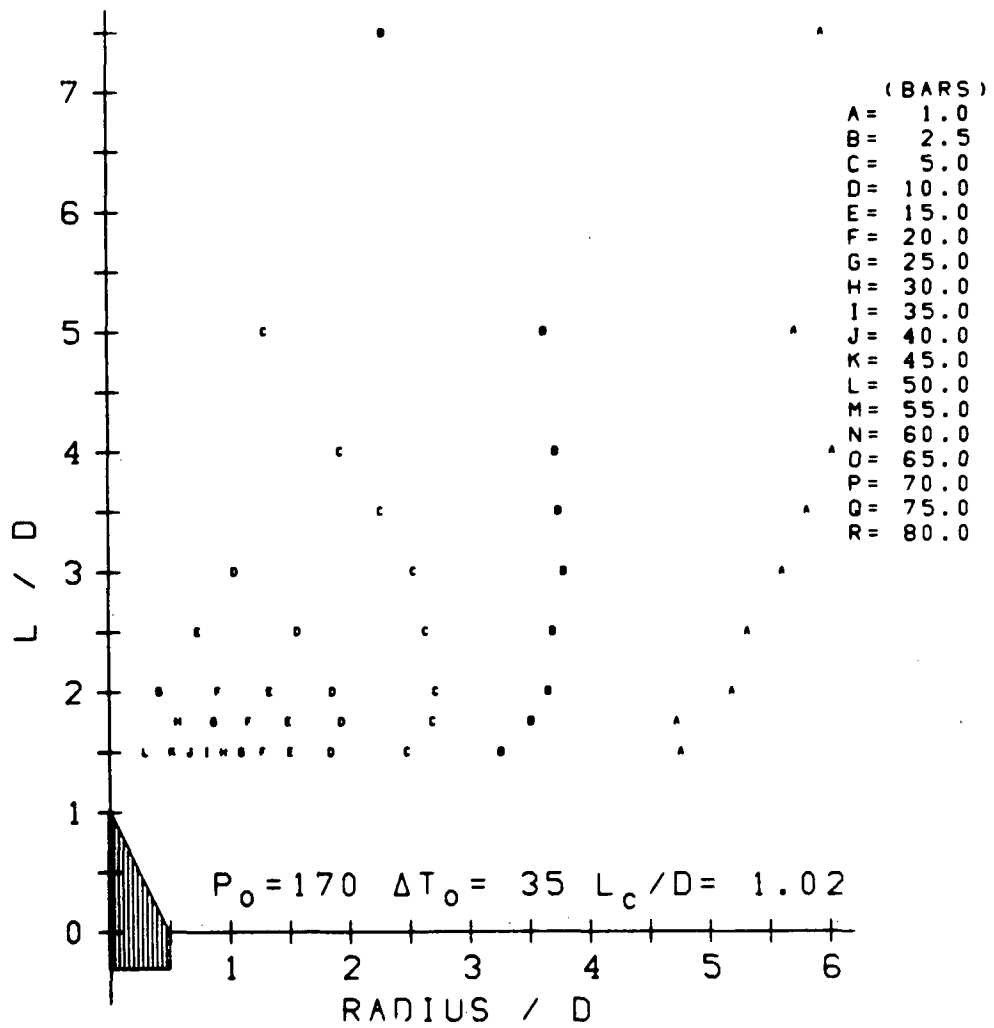
251

FIGURE A.113   TARGET LOAD DISTRIBUTIONS

FIGURE A.114 COMPOSITE TARGET PRESSURE CONTOURS

FIGURE A.115   TARGET PRESSURE DISTRIBUTIONS

FIGURE A.116   TARGET LOAD DISTRIBUTIONS

FIGURE A.117 COMPOSITE TARGET PRESSURE CONTOURS

FIGURE A.118   TARGET PRESSURE DISTRIBUTIONS

FIGURE A.119 TARGET LOAD DISTRIBUTIONS

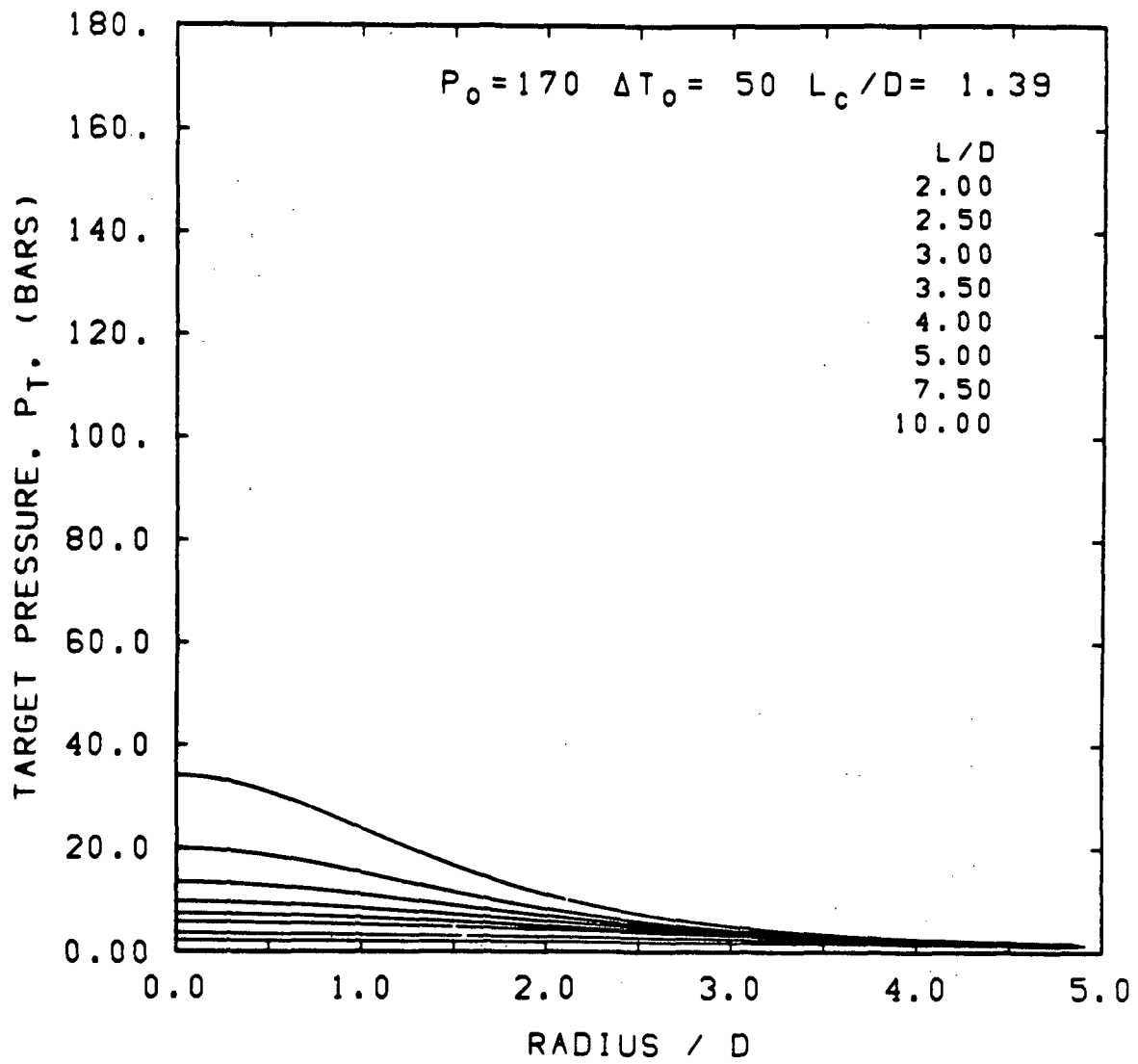FIGURE A.120   COMPOSITE TARGET PRESSURE CONTOURS

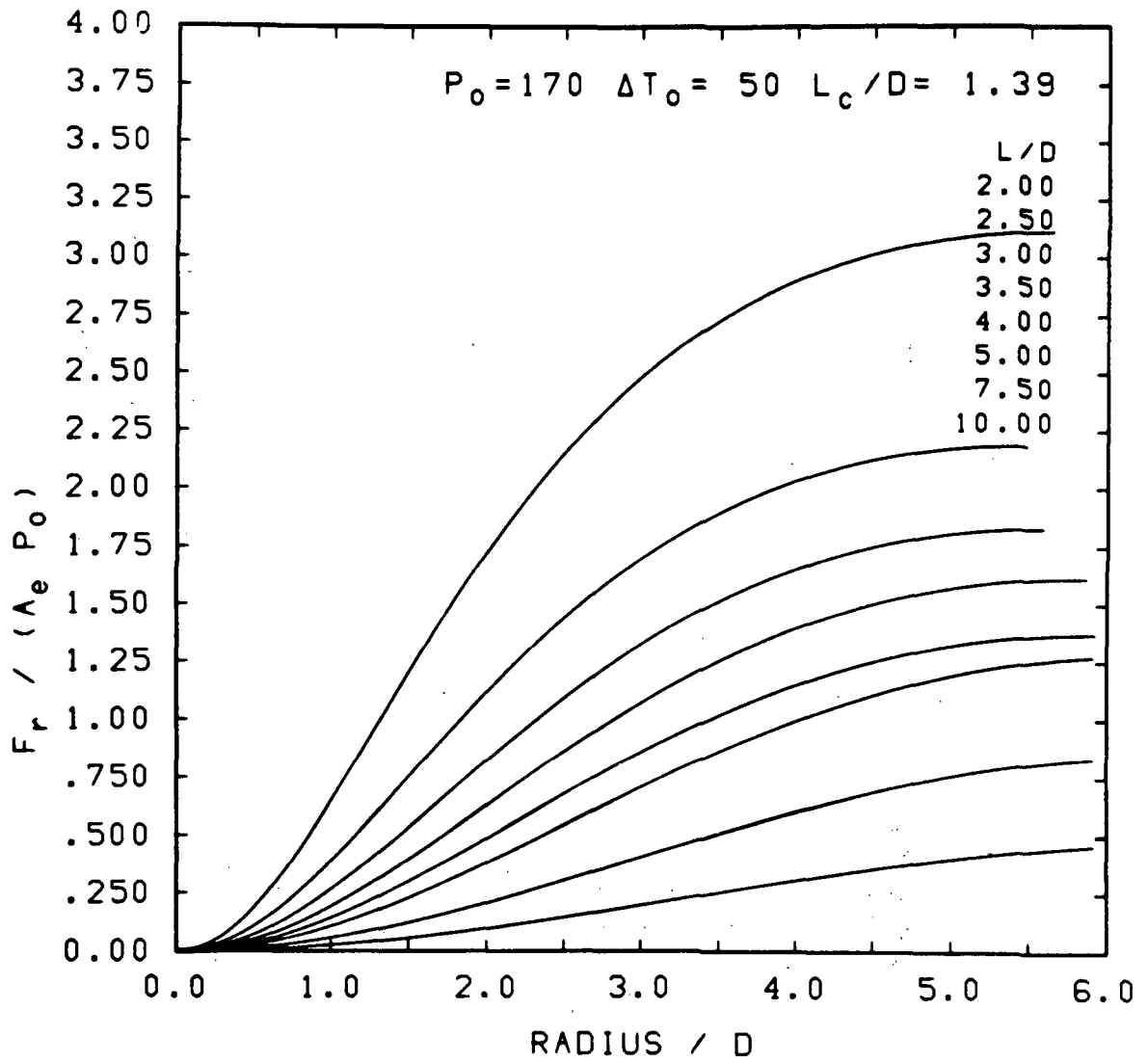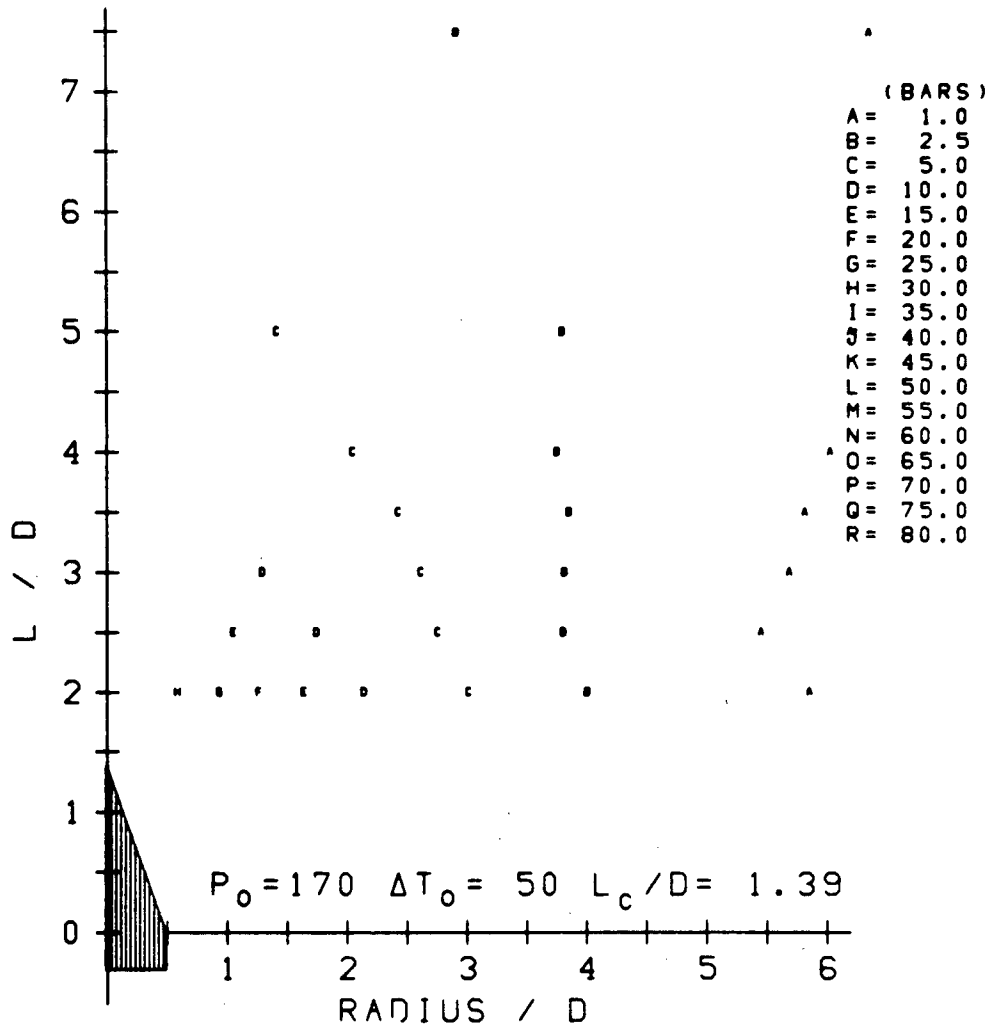FIGURE A.121   TARGET PRESSURE DISTRIBUTIONS

FIGURE A.122 TARGET LOAD DISTRIBUTIONS

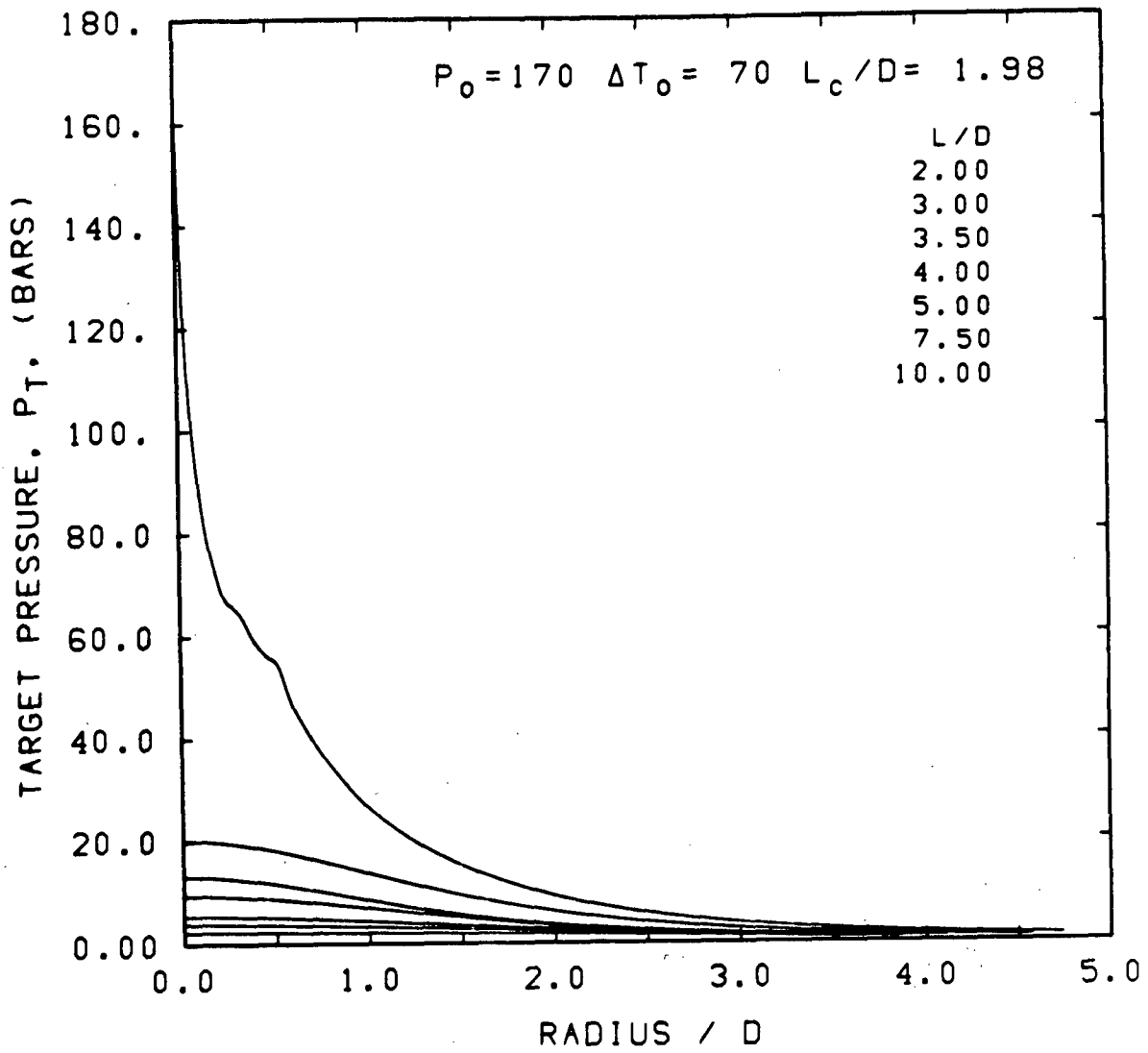FIGURE A.123   COMPOSITE TARGET PRESSURE CONTOURS

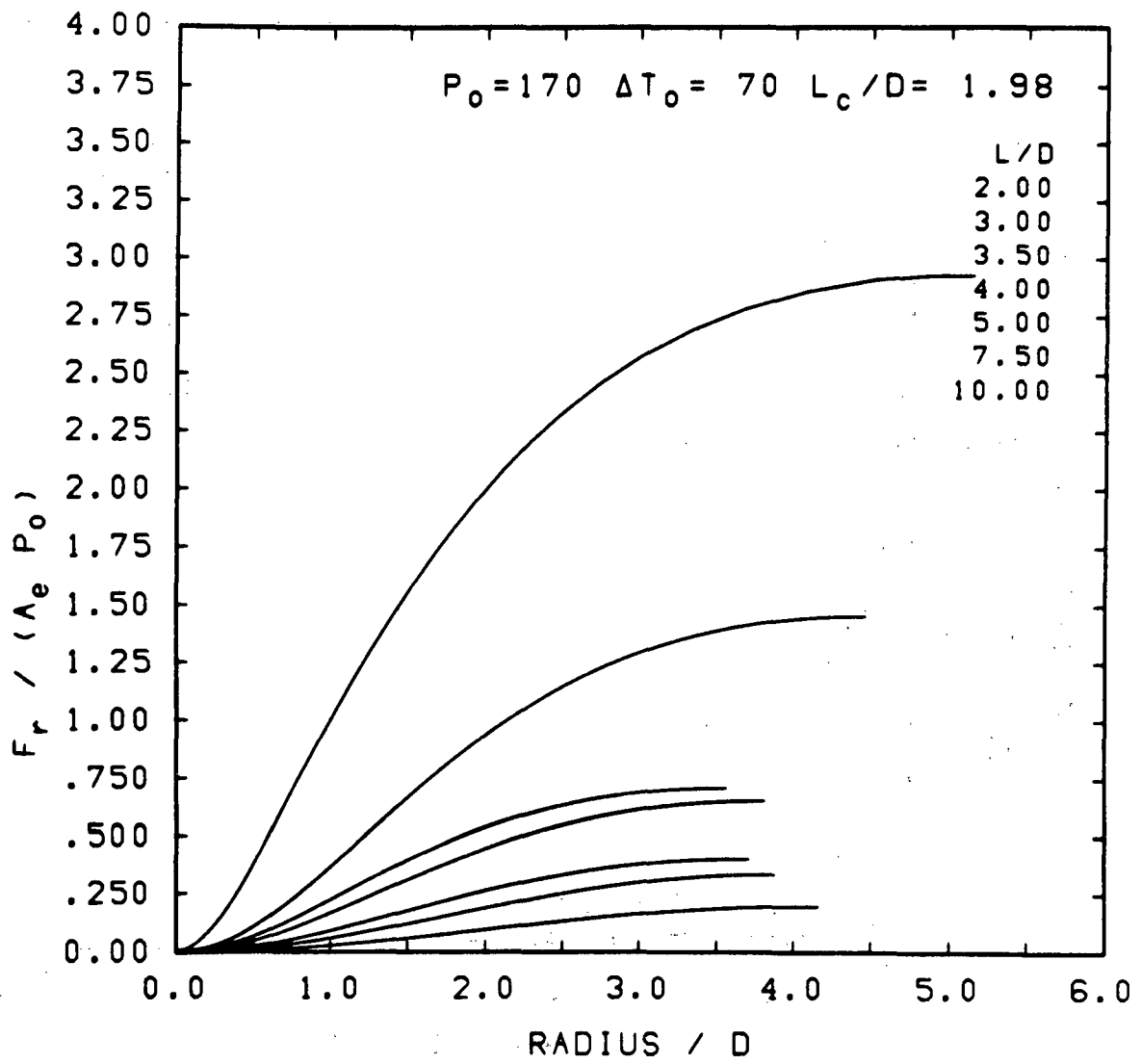FIGURE A.124   TARGET PRESSURE DISTRIBUTIONS

263

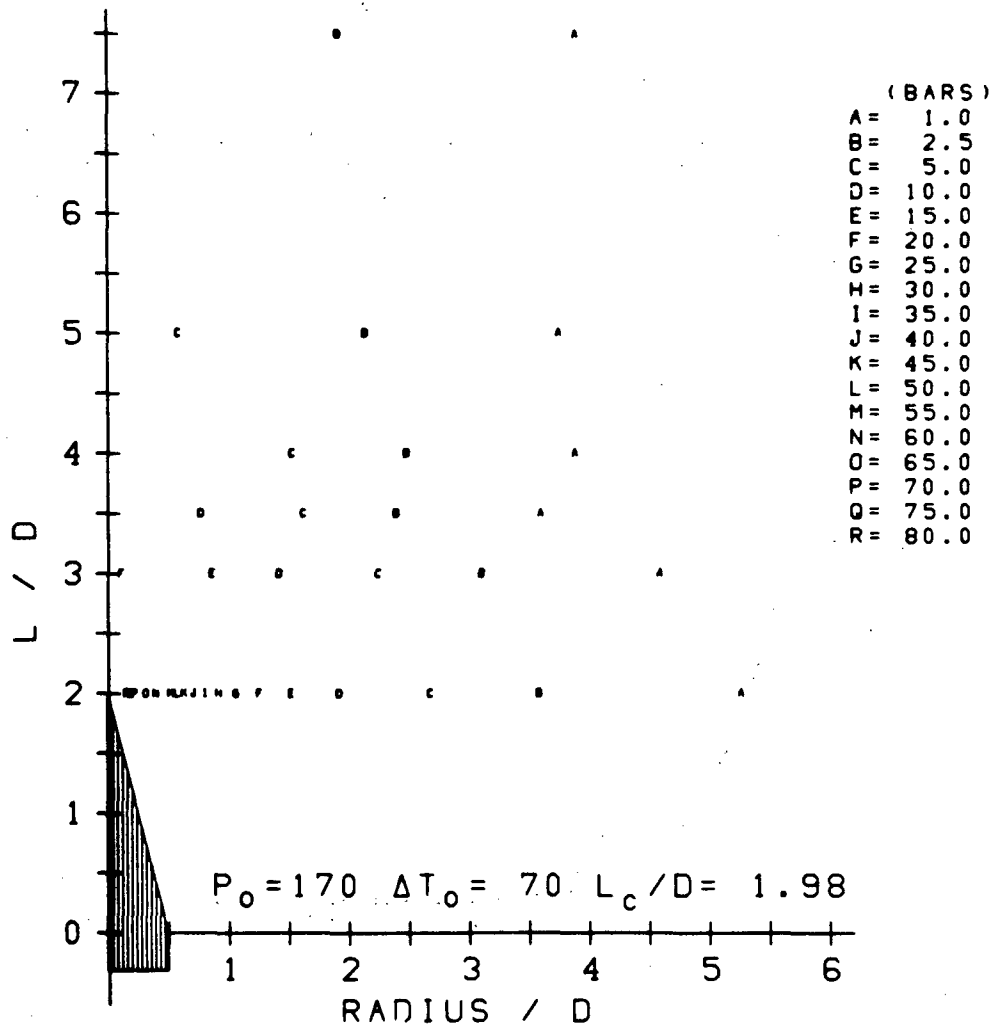FIGURE A.125 TARGET LOAD DISTRIBUTIONS

FIGURE A.126   COMPOSITE TARGET PRESSURE CONTOURS

APPENDIX B

CENTERLINE TARGET PRESSURE DISTRIBUTIONS

This appendix contains a series of figures showing the centerline target pressures as functions of the distance to the target and stagnation properties. A complete description of these figures is provided in Chapter 6.

Figure B.1   Centerline target pressure as a function of
              the distance to the target (L/D) and the
              stagnation properties.

Figure B.2   Centerline target pressure as a function of the
distance to the target (L/D) and the stagnation
properties.

$P_0 = 100$ BARS

$\Delta T_0 = 70$
$\Delta T_0 = 50$
$\Delta T_0 = 35$
$\Delta T_0 = 15$
$\Delta T_0 = 0$
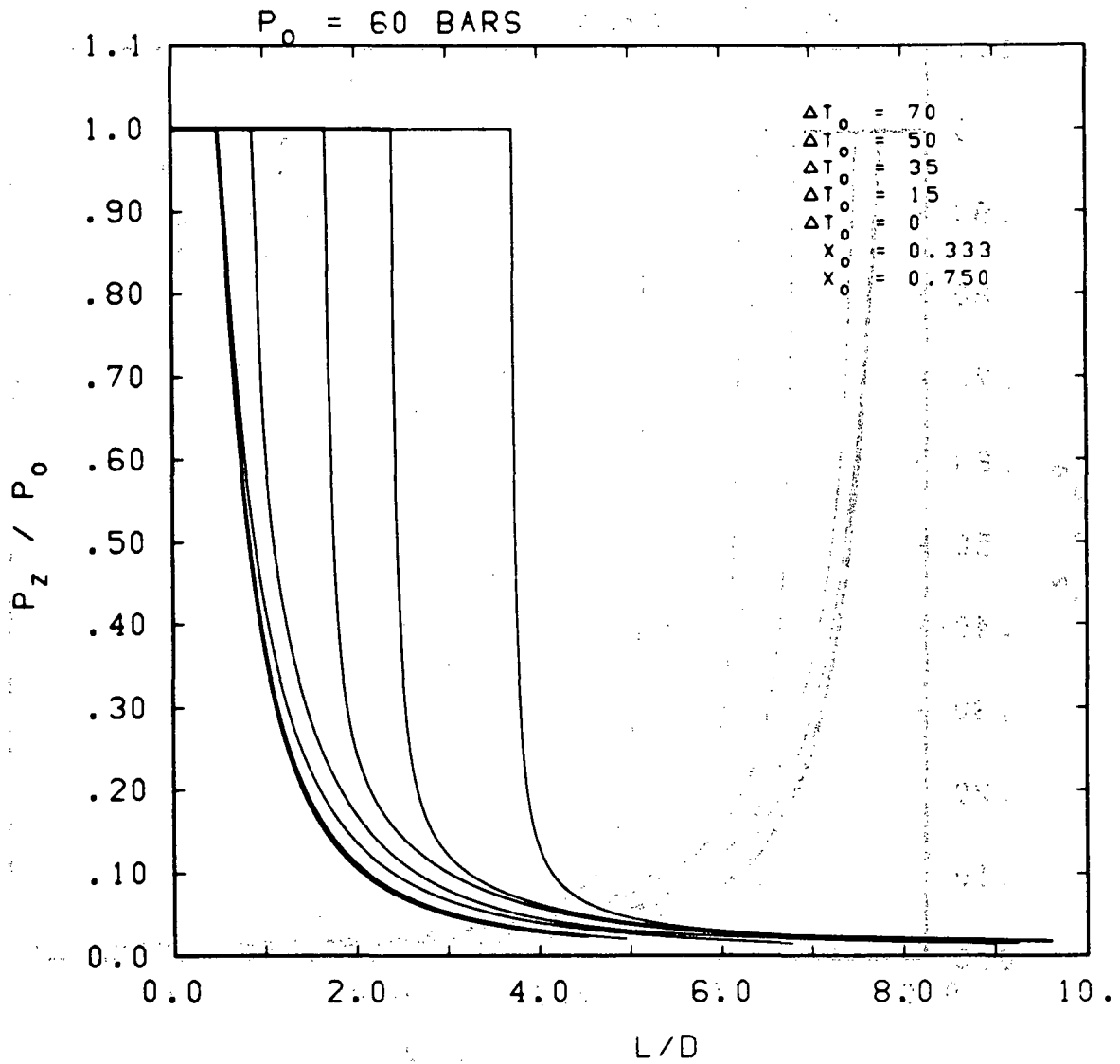$X_0 = 0.333$
$X_0 = 0.750$

P_z / P_0

L/D

Figure B.3   Centerline target pressure as a function of the distance to the target (L/D) and the stagnation properties.

Figure B.4   Centerline target pressure as a function of the
distance to the target (L/D) and the stagnation
properties.

$P_0 = 150$ BARS

P_z / P_o vs L/D

$\Delta T_o = 70$
$\Delta T_o = 50$
$\Delta T_o = 35$
$\Delta T_o = 15$
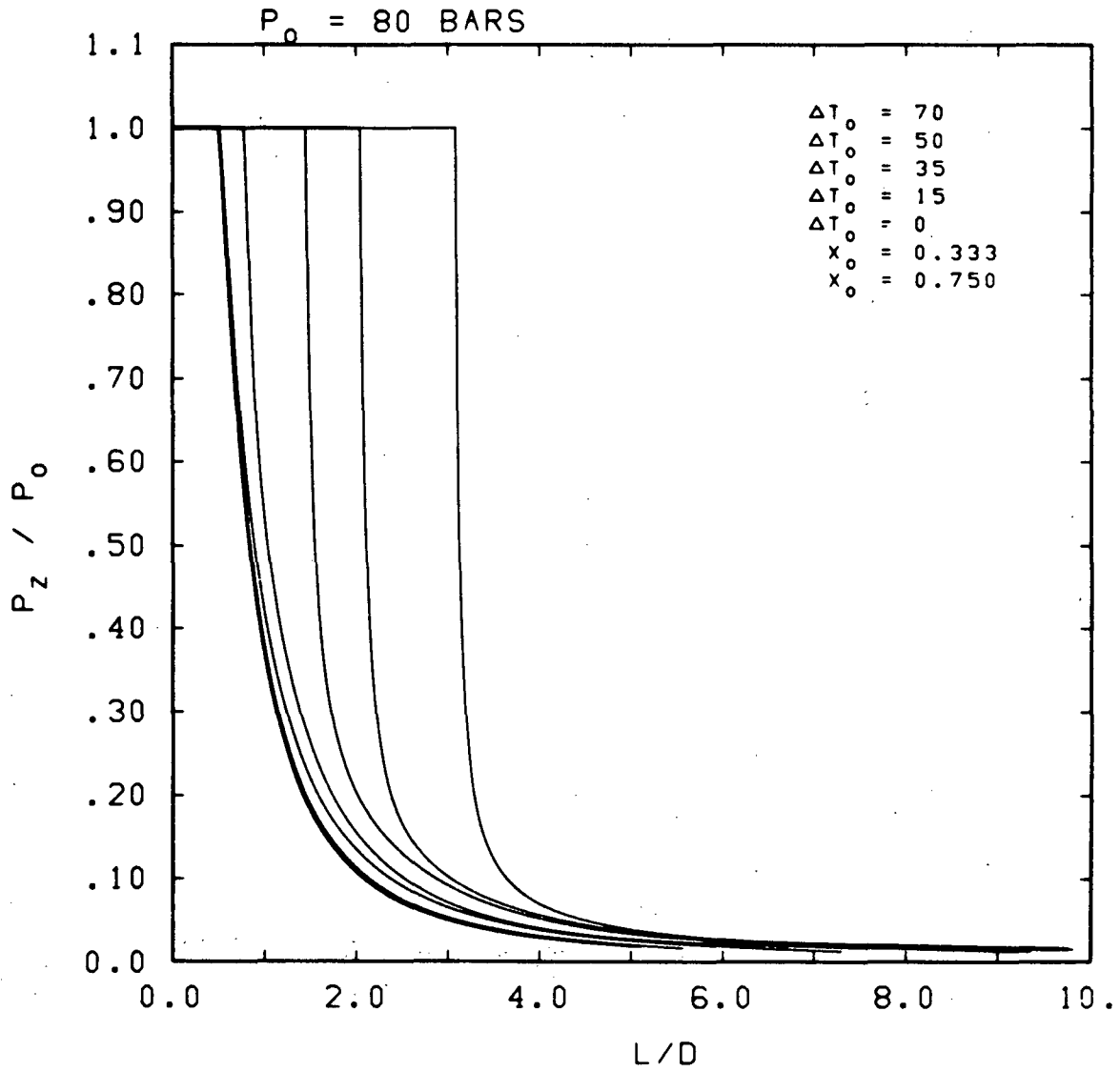$\Delta T_o = 0$
$X_o = 0.333$
$X_o = 0.750$
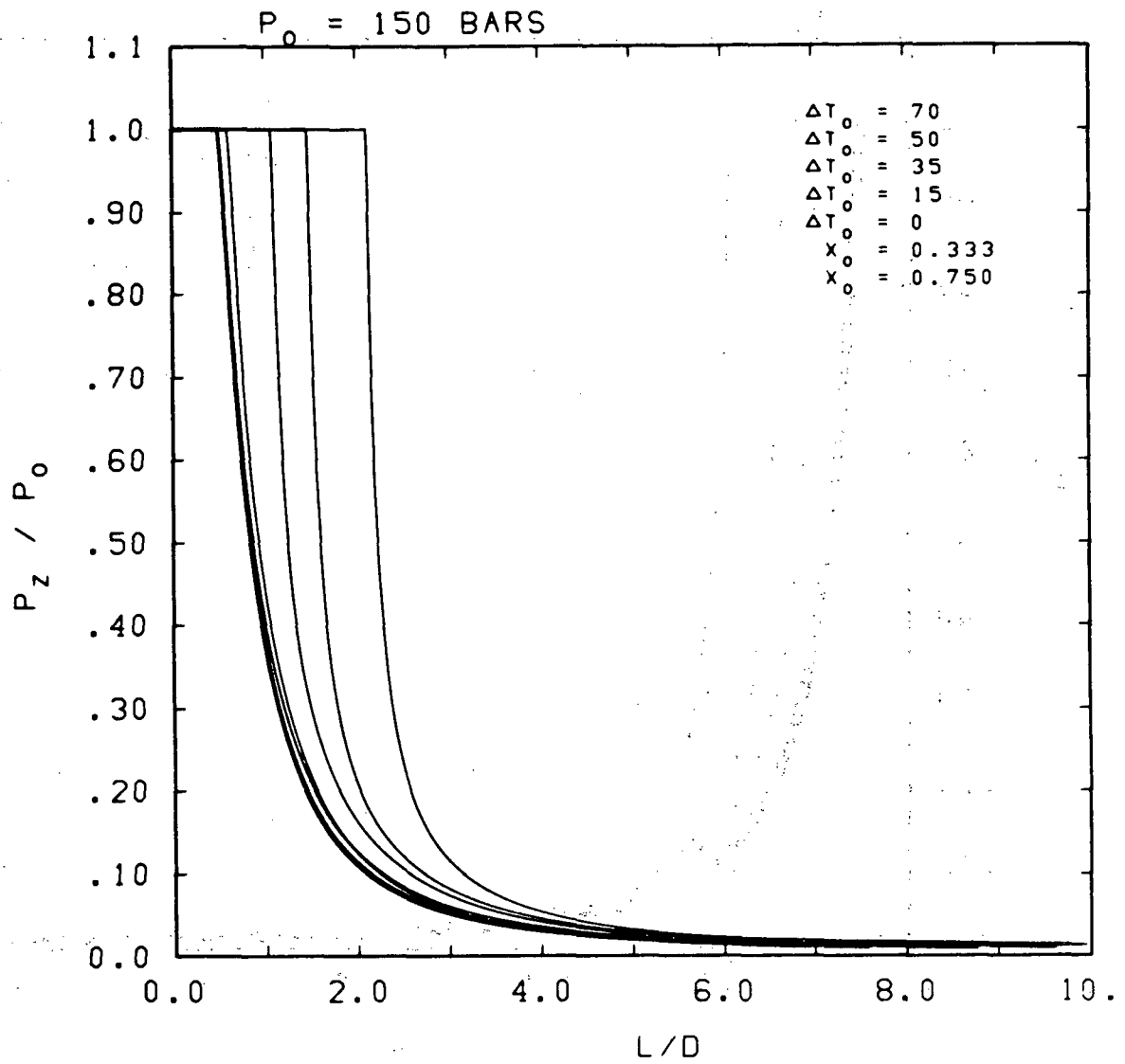
Figure B.5   Centerline target pressure as a function of the distance to the target (L/D) and the stagnation properties.
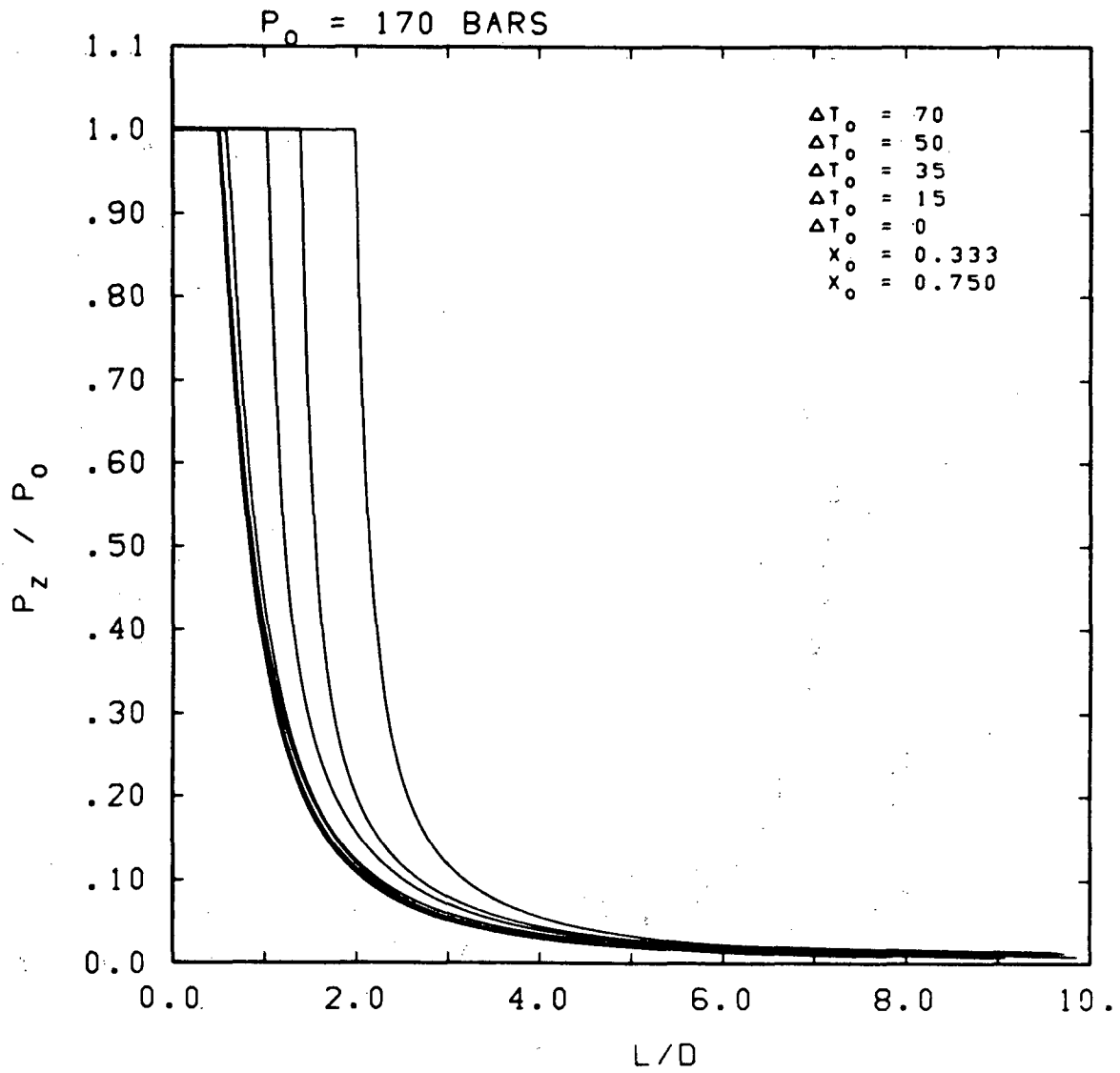
Figure B.6   Centerline target pressure as a function of the
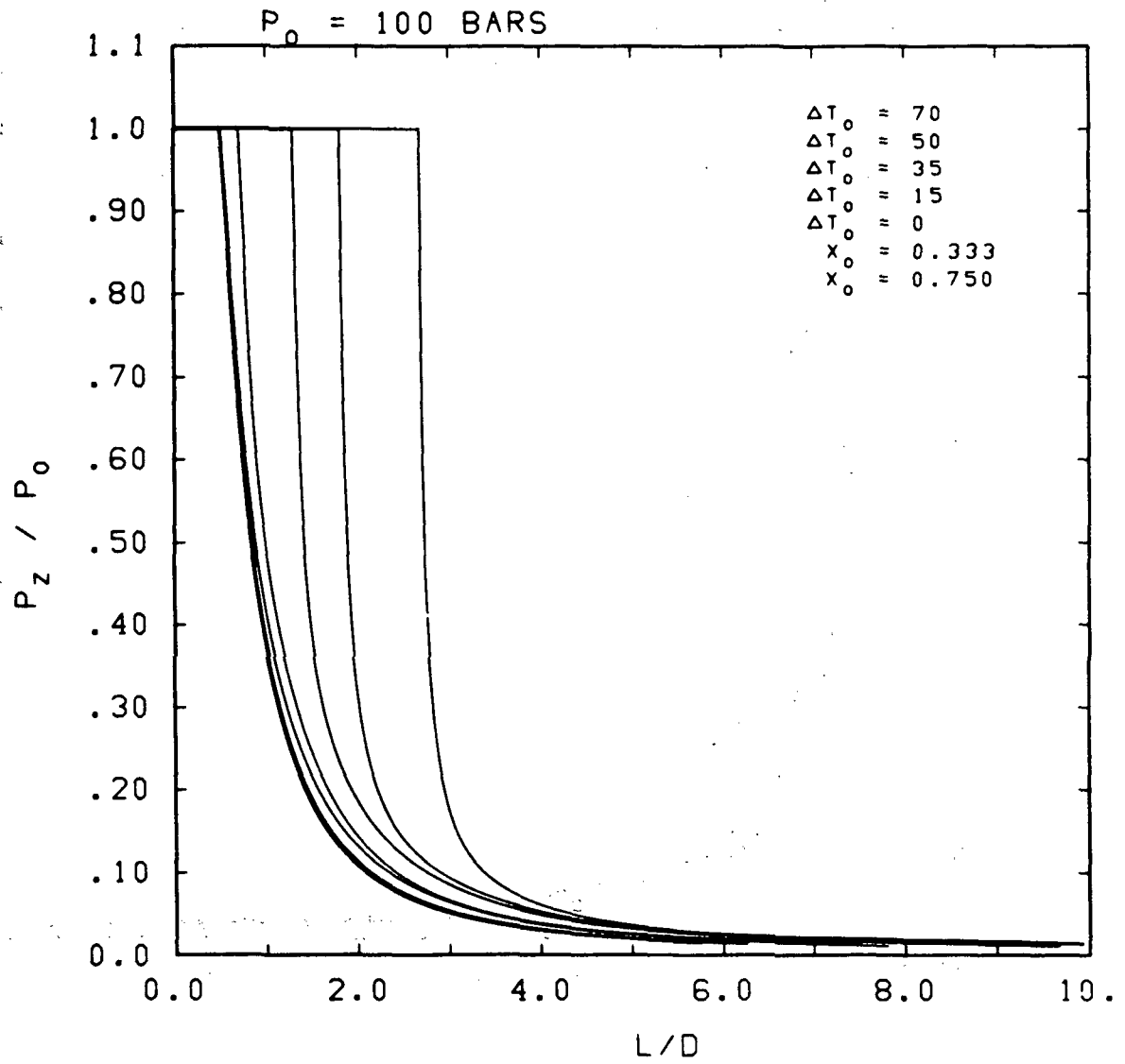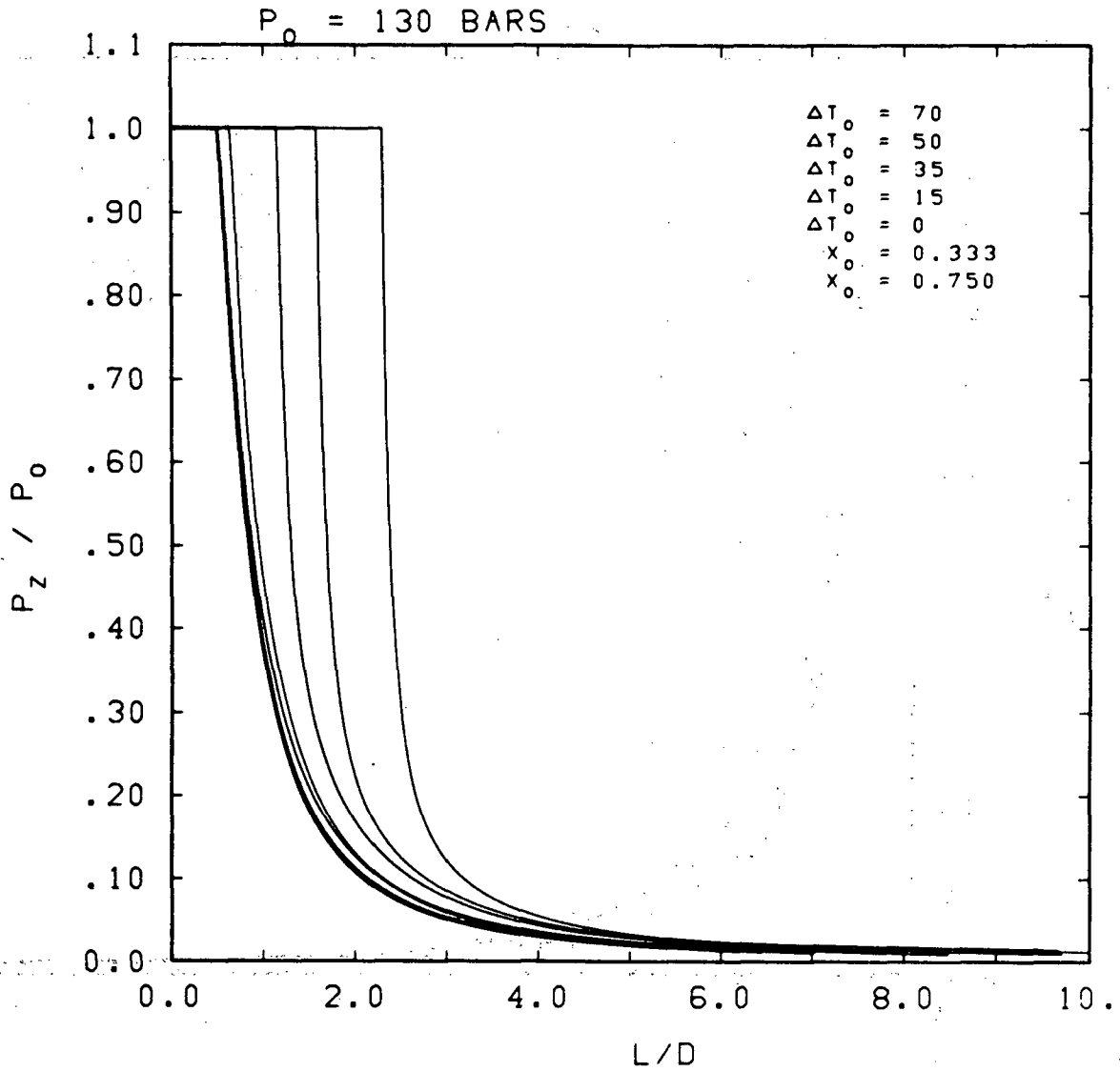distance to the target (L/D) and the stagnation
properties.

APPENDIX C

TWO-PHASE JET-EXIT CORE LENGTHS

This appendix contains the jet exit core length (L_C/D) for various vessel conditions. A complete description of these curves is given in Sections 3.6 and 4.2.
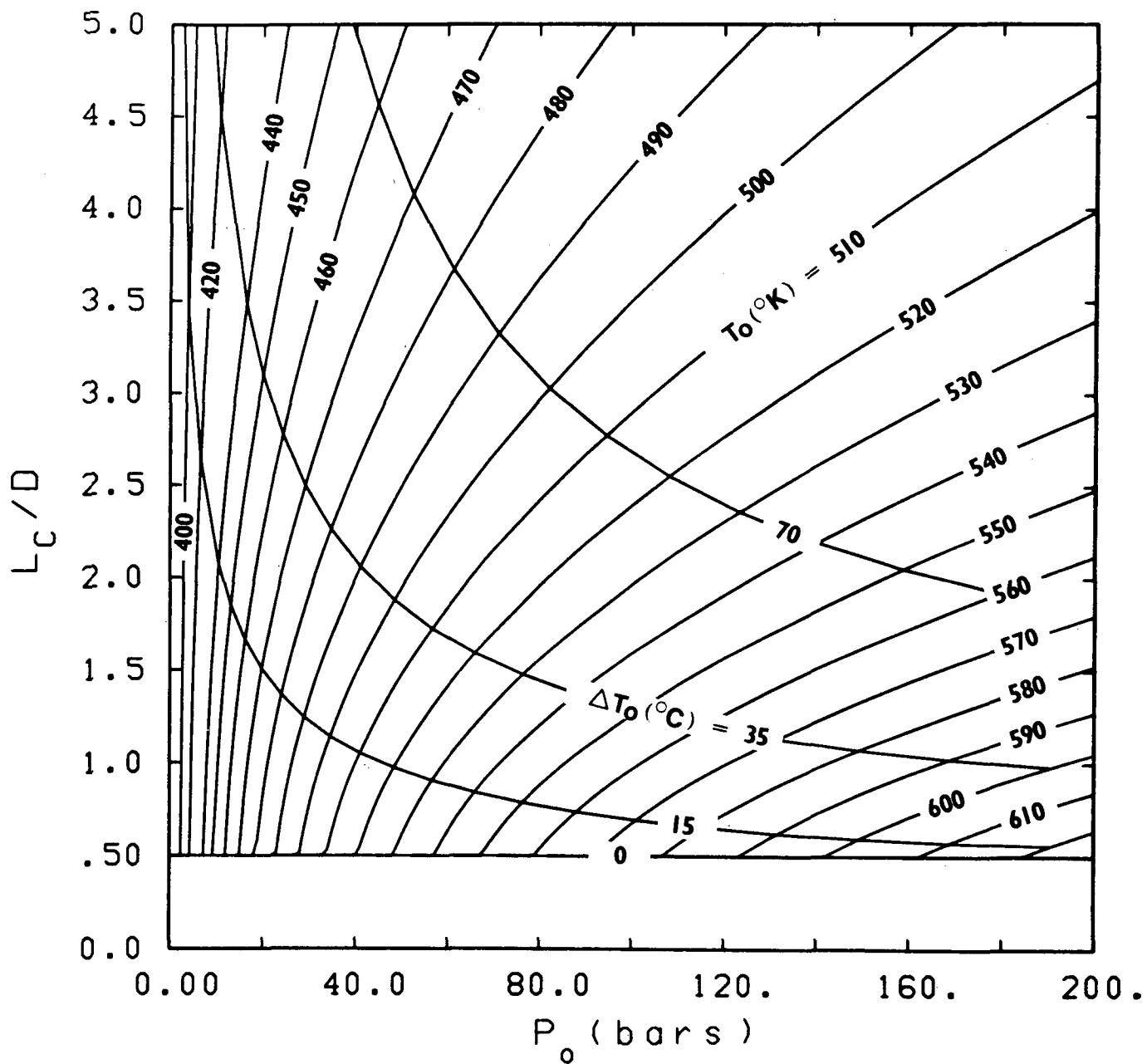
Figure C.1   Two-phase, jet-exit core (L_c/D) as a function of
stagnation pressure and stagnation temperature
or subcooling.
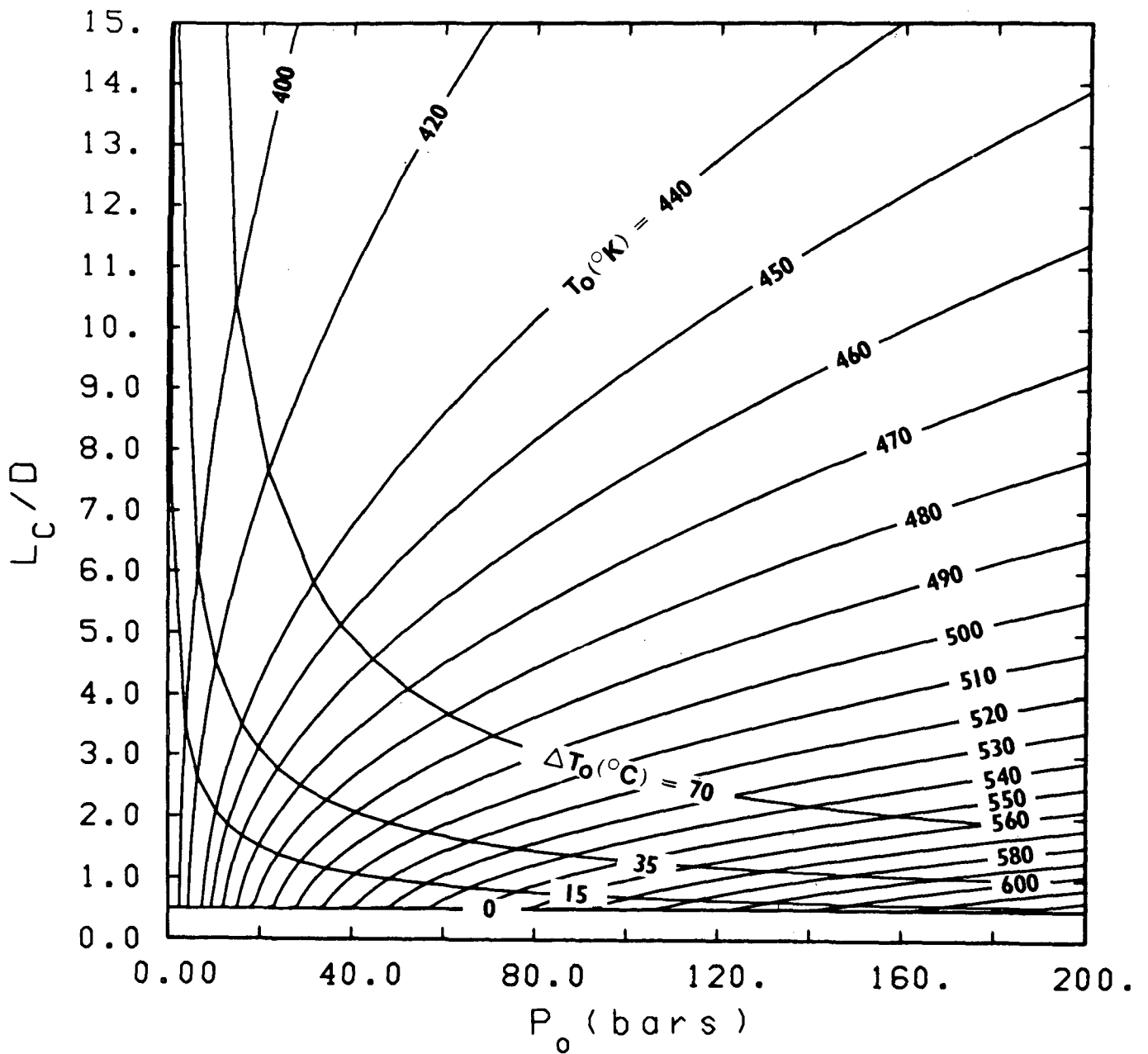
Figure C.2   Two-phase, jet-exit core (L_C/D) as a function of stagnation pressure and stagnation temperature or subcooling.

APPENDIX D

WATER PROPERTIES AND HEM CRITICAL FLOW PROPERTIES

This appendix contains figures showing the thermodynamic properties of water and the HEM critical flow for water as a function of thermodynamic conditions. A description of the curves is given in Chapters 3 and 5.
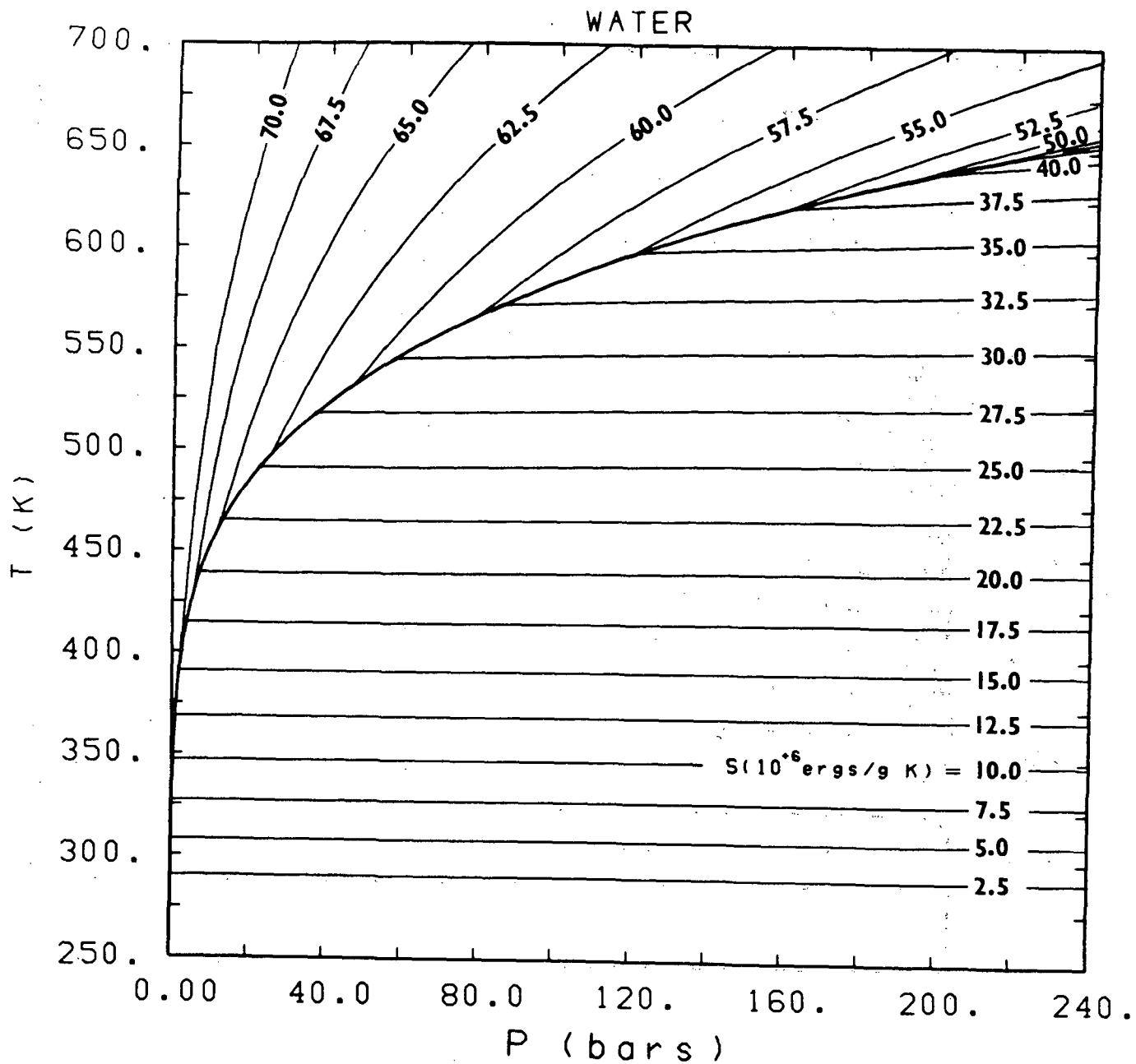
Figure D.1   Thermodynamic properties of water.
Temperature as a function of pressure and
entropy for a range of pressure and entropy
that emphasizes subcooled conditions.
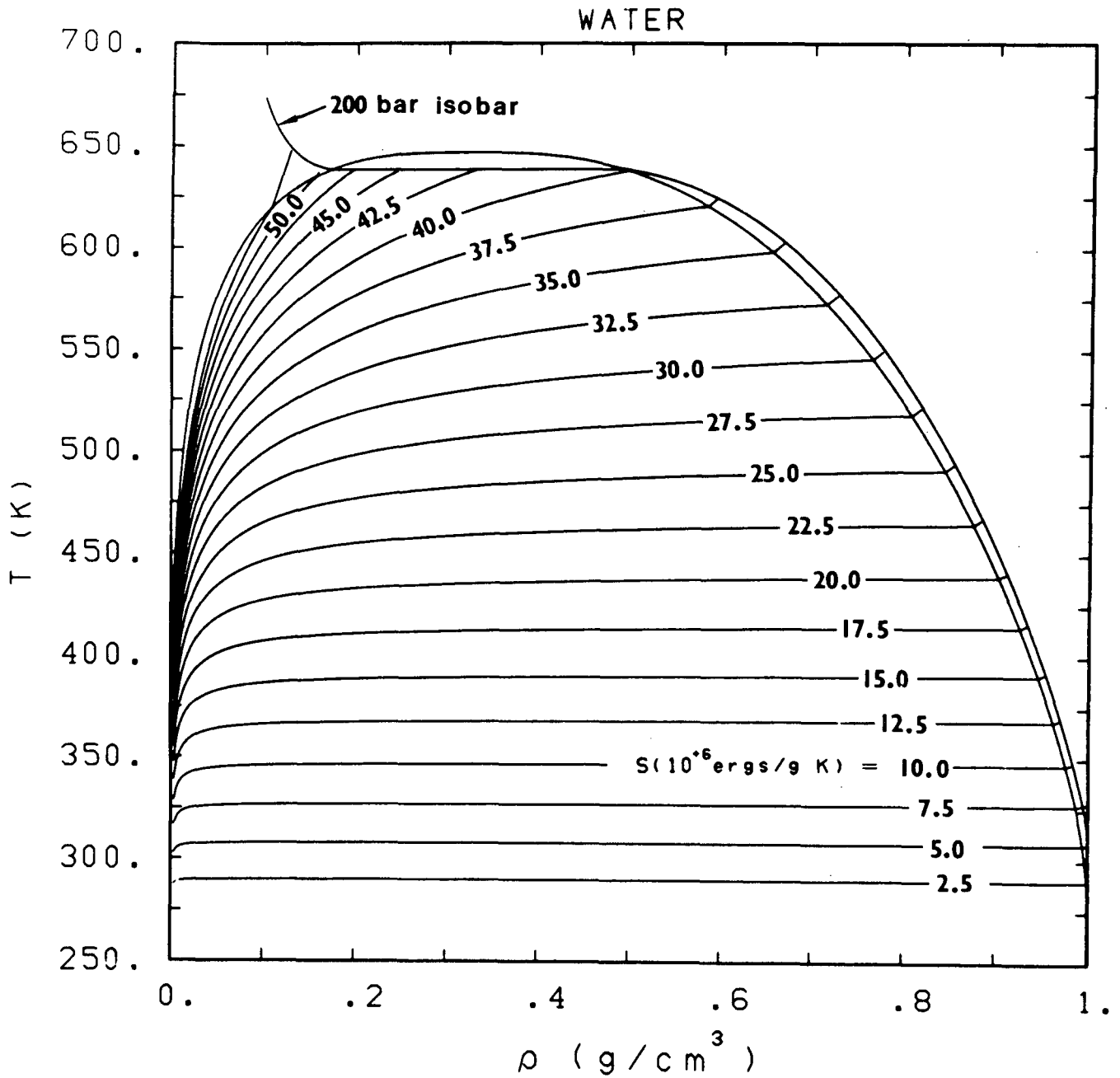
Figure D.2 Thermodynamic properties of water.
Temperature as a function of density and
entropy for a range of density and entropy
that emphasizes saturated conditions.
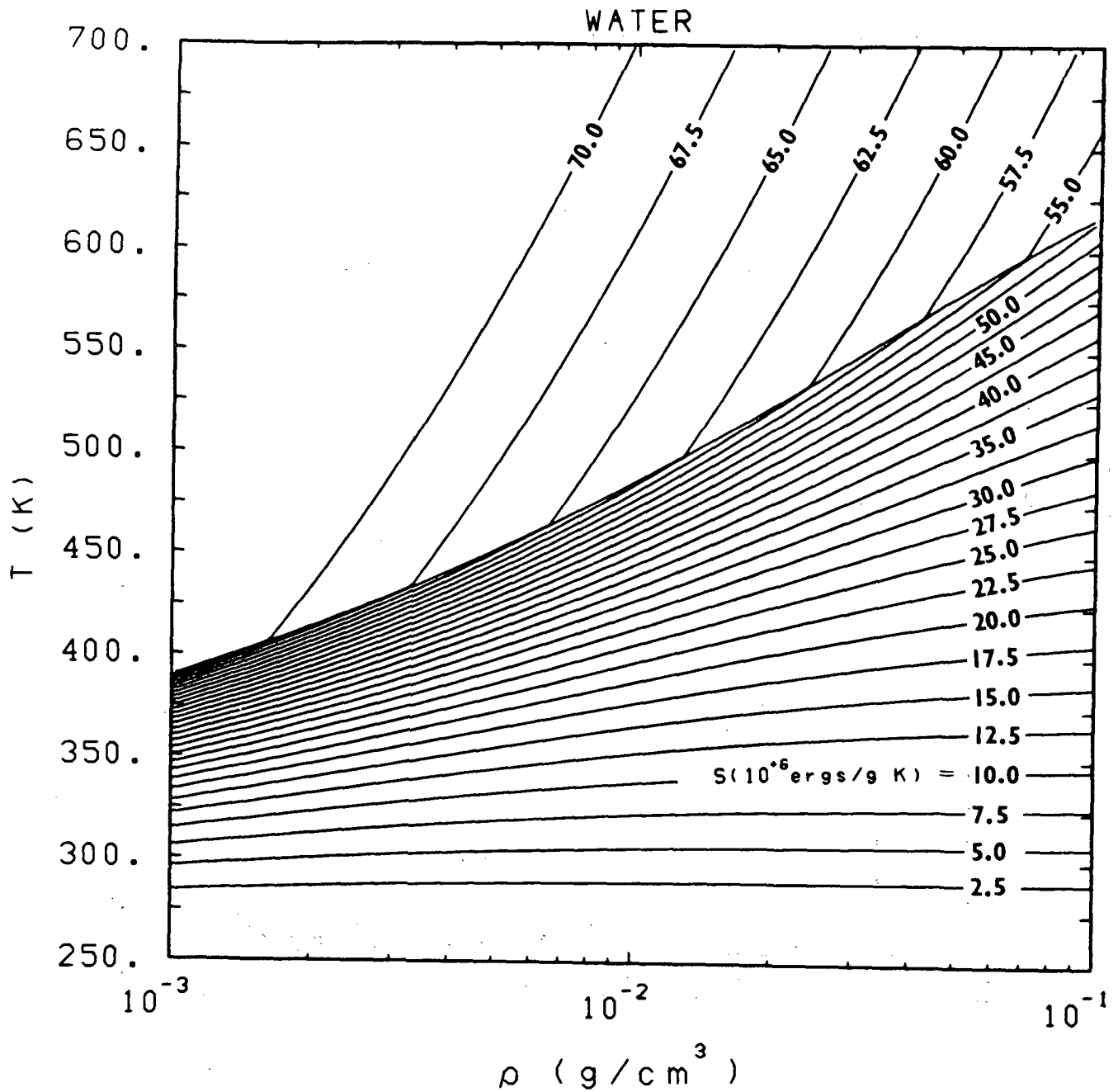
Figure D.3   Thermodynamic properties of water.
             Temperature as a function of density and
             entropy for low densities.
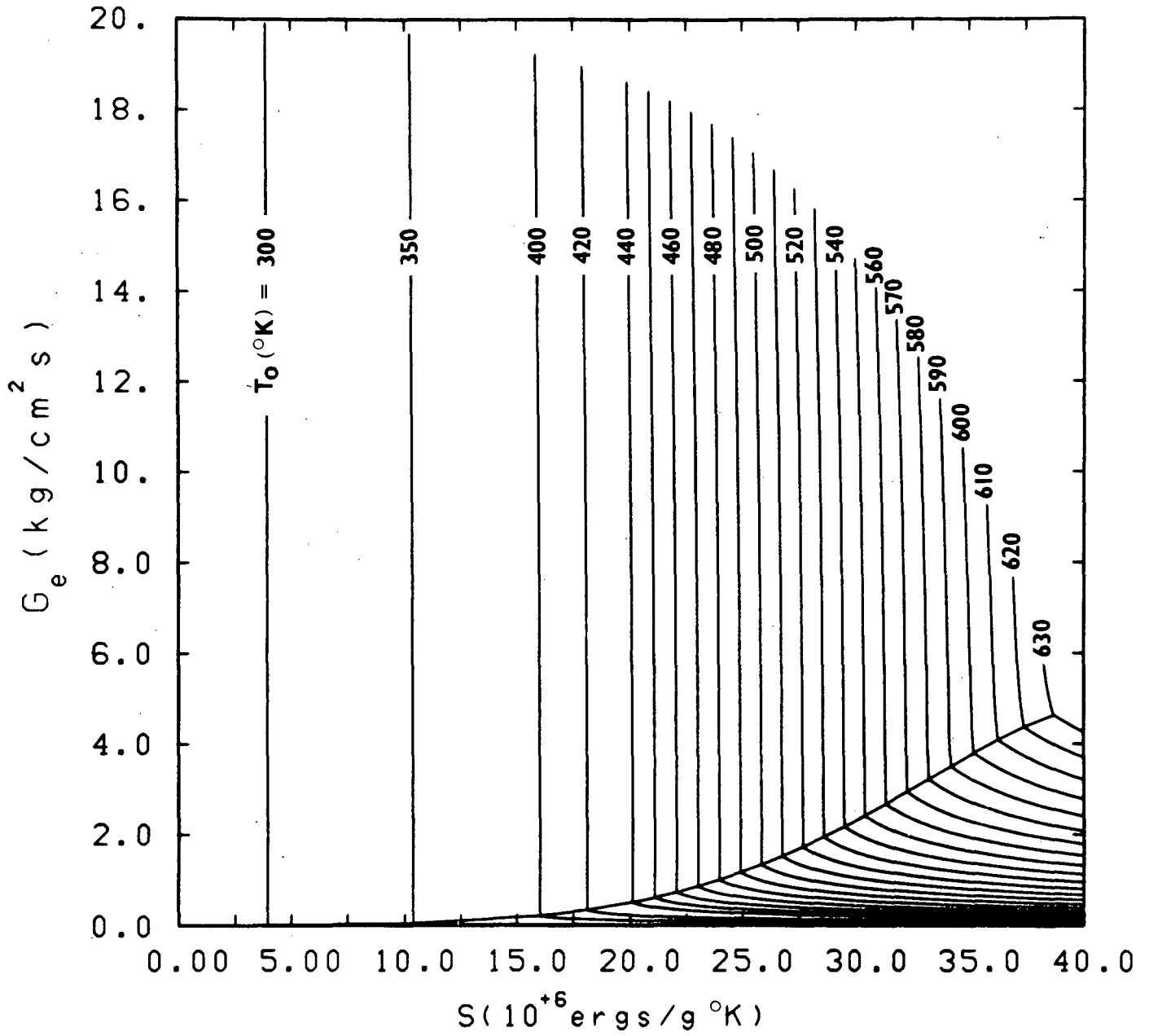
Figure D.4   HEM mass flux as a function of entropy and
stagnation temperature for a range of entropy
which emphasizes subcooled stagnation conditions.
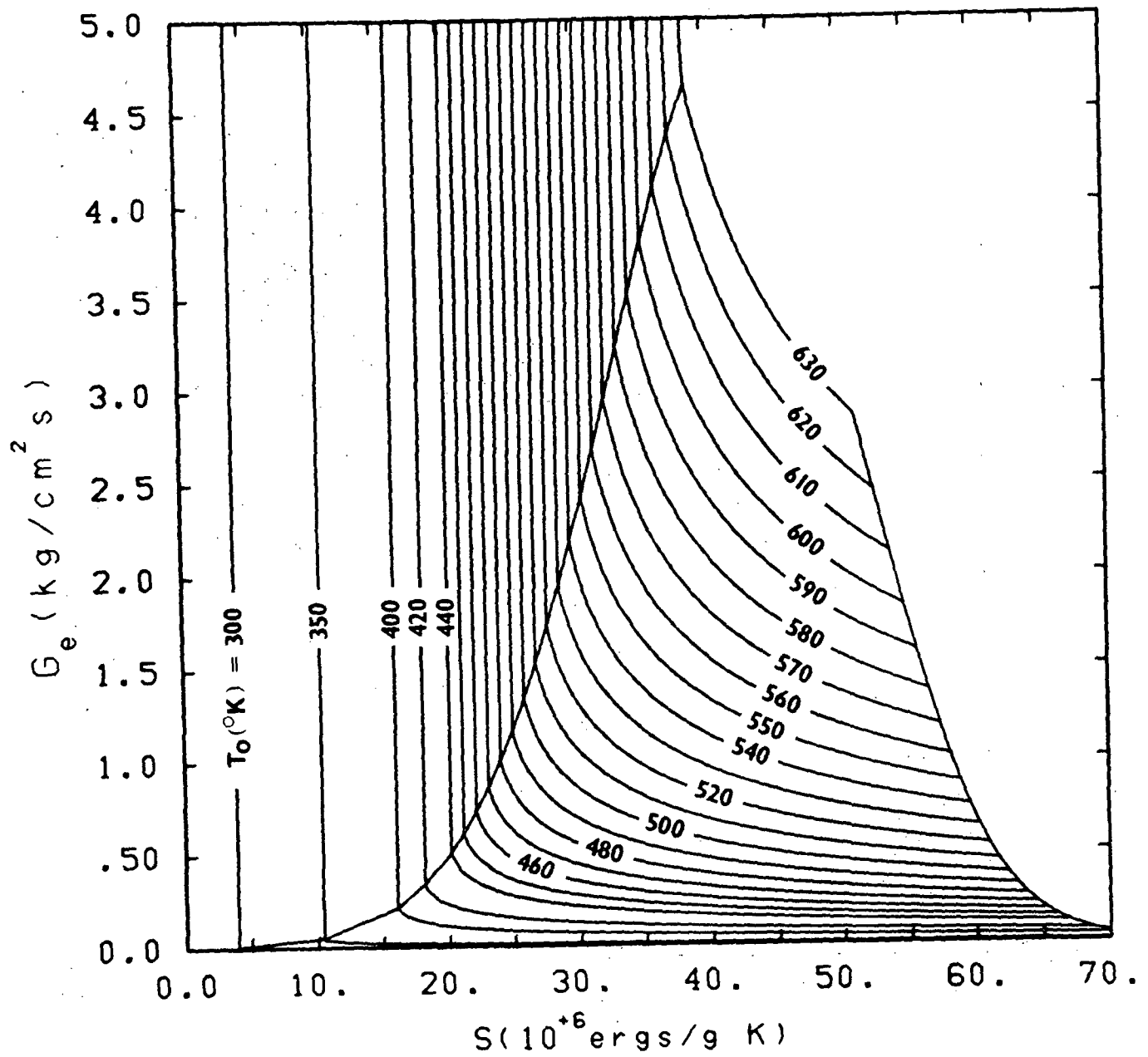
Figure D.5 HEM mass flux as a function of entropy and
stagnation temperature for a range of entropy
which emphasizes saturated stagnation conditions.

281
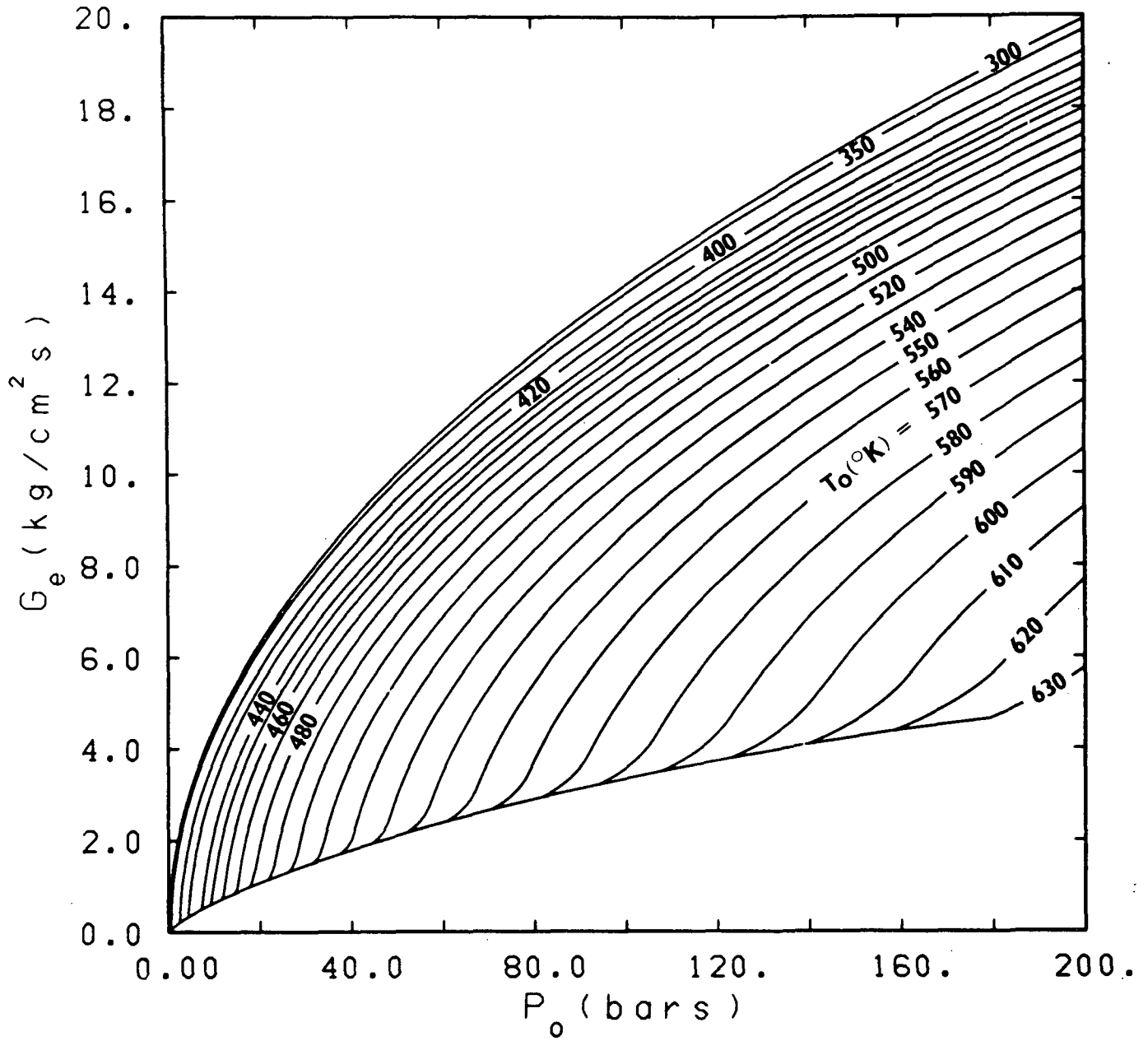
Figure D.6   HEM mass flux as a function of stagnation
pressure and stagnation temperature.
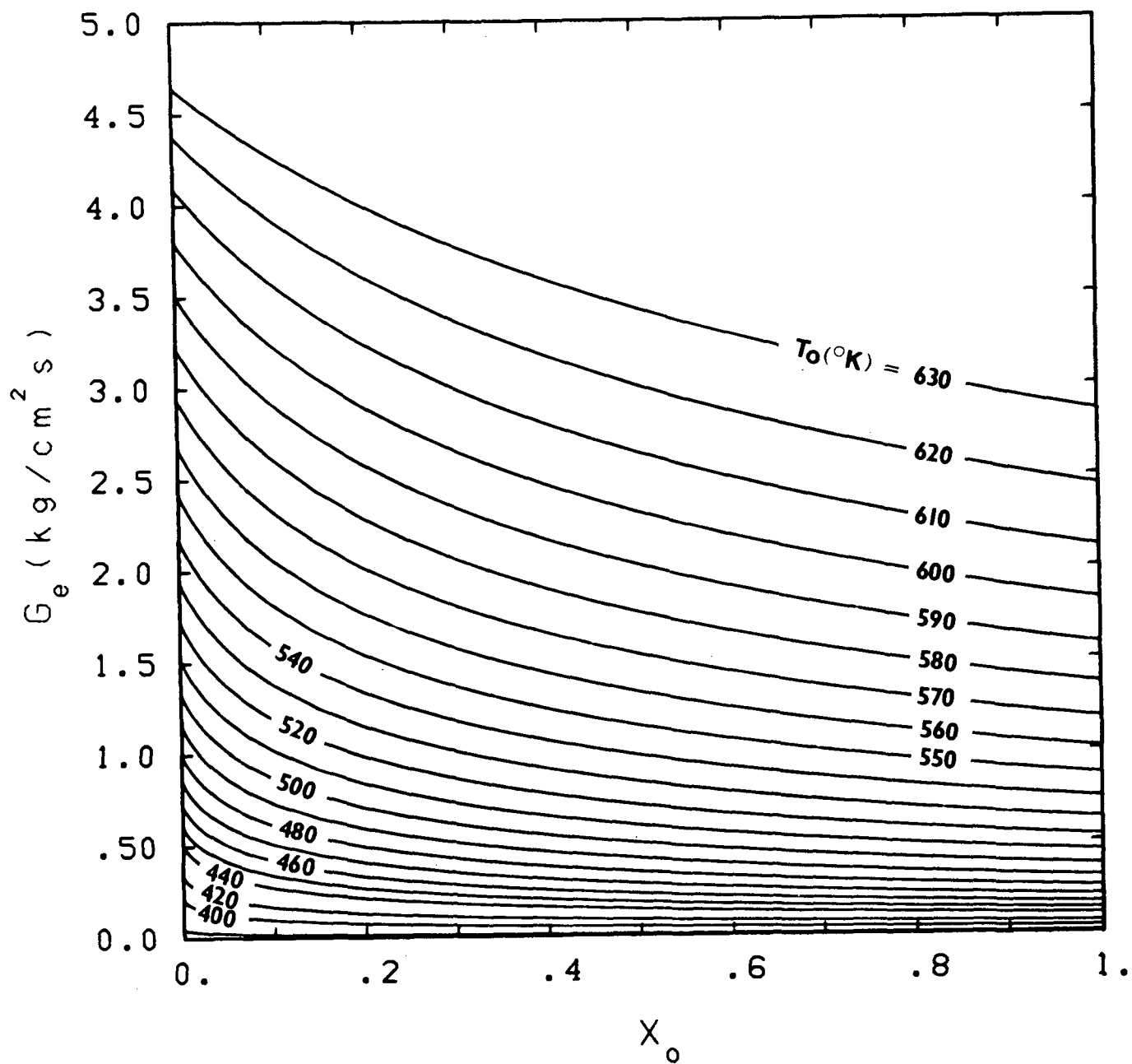
Figure D.7   HEM mass flux as a function of stagnation quality
             and stagnation temperature.
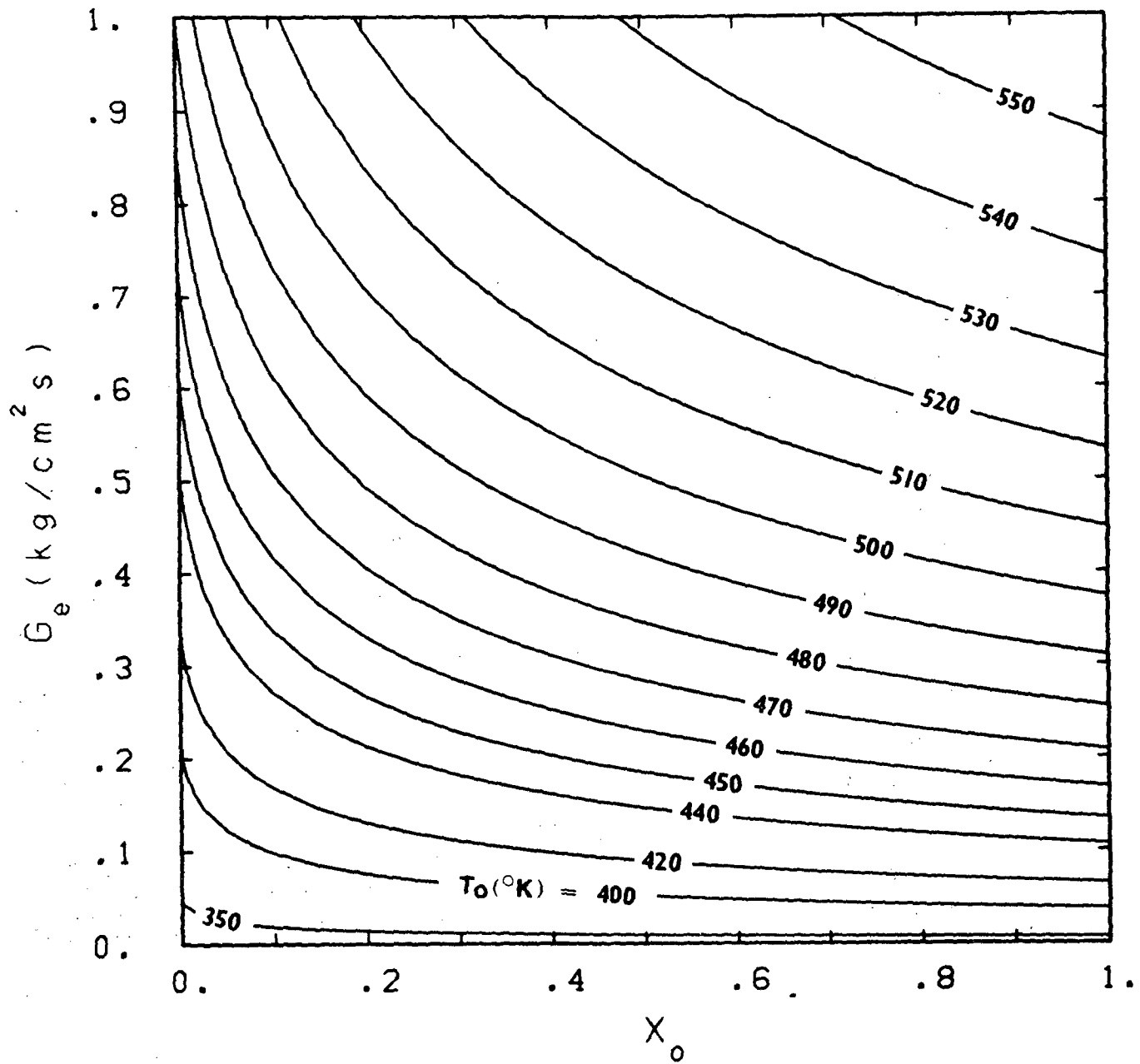
Figure D.8   HEM mass flux as a function of the stagnation
quality and stagnation temperature.
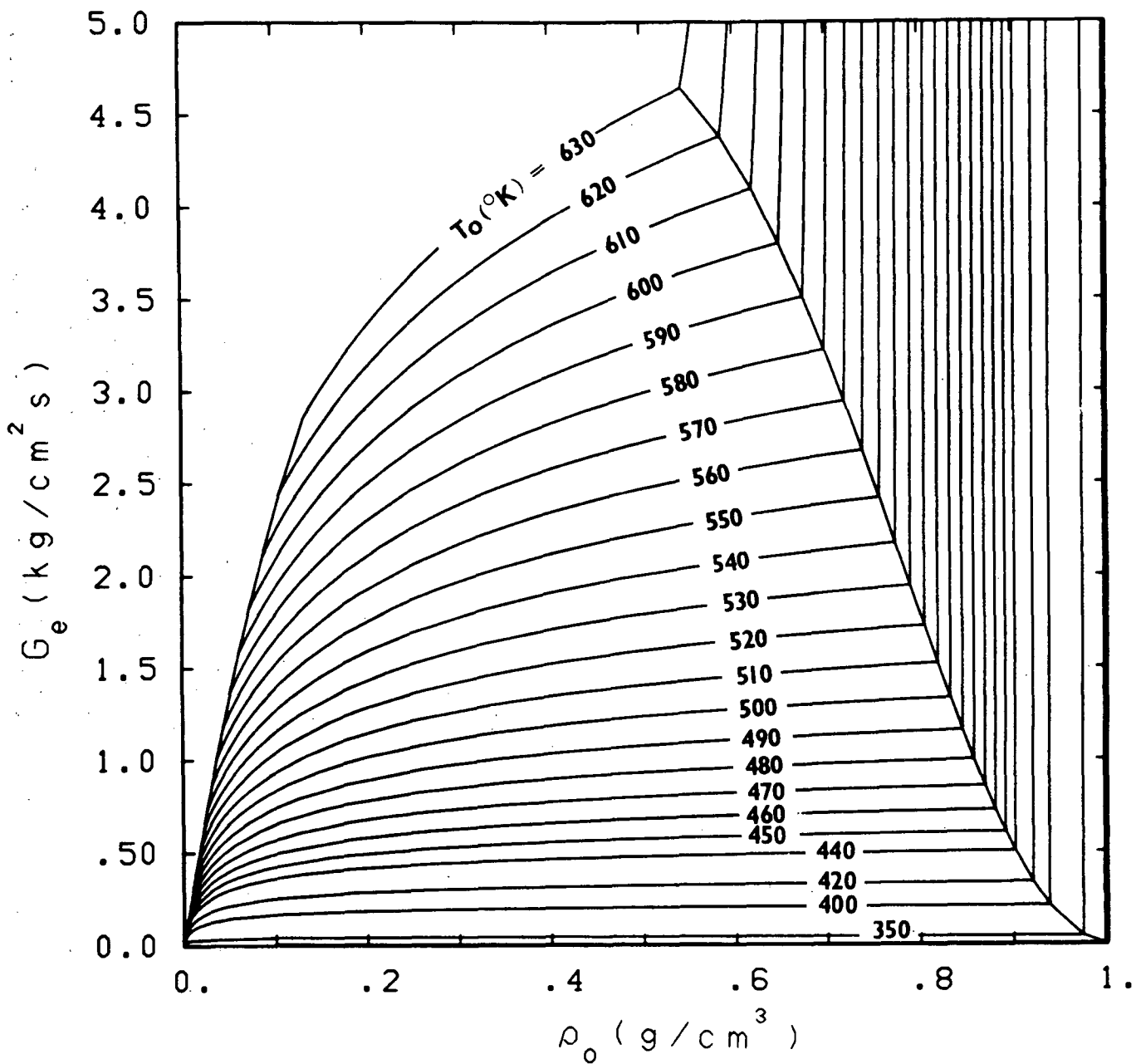
Figure D.9 HEM mass flux as a function of the stagnation density and stagnation temperature.
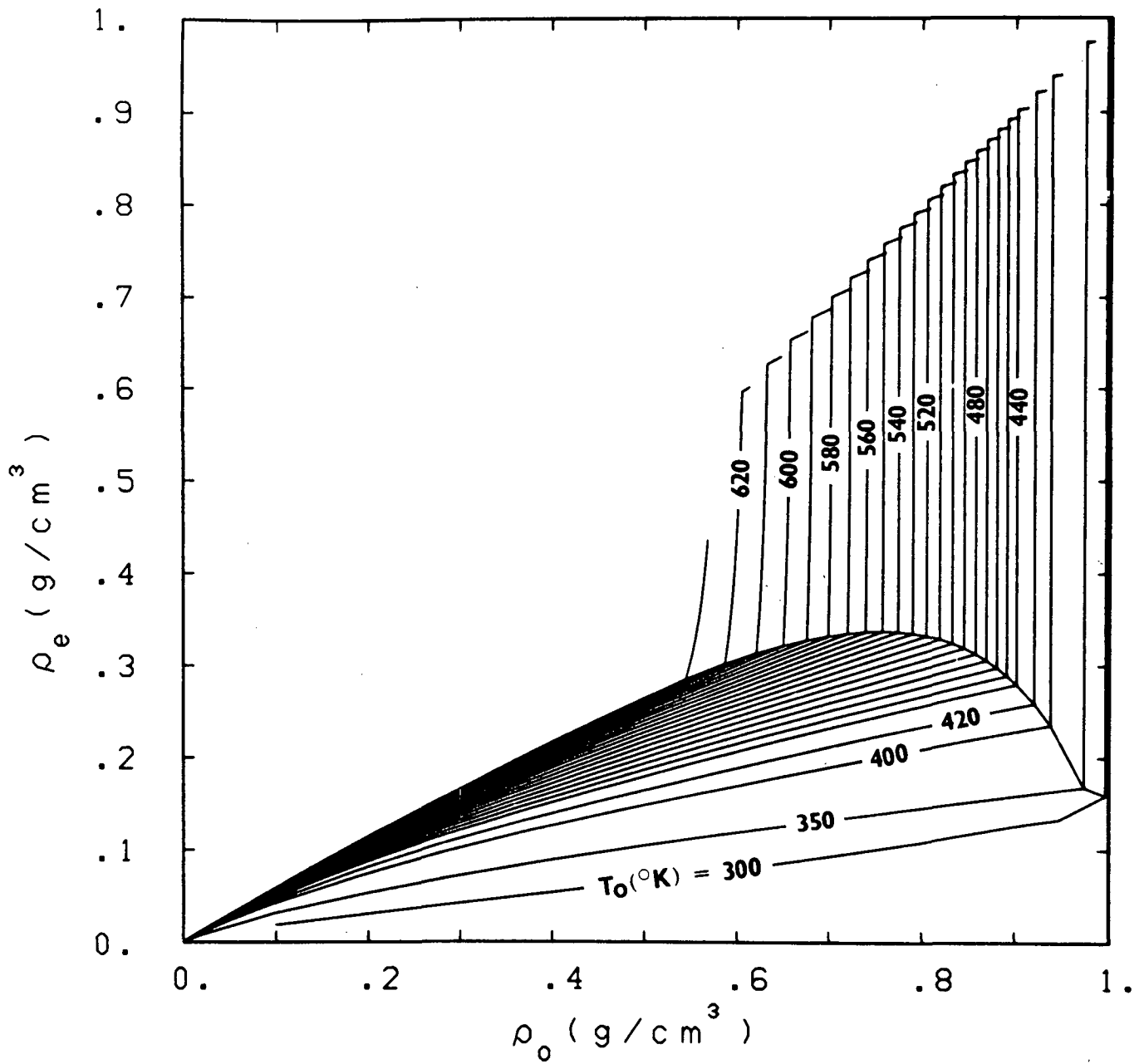
Figure D.10   HEM critical flow density as a function of
stagnation density and stagnation temperature.

DISTRIBUTION:

U. S. NRC Distribution Contractor (CDSI)   (360)
7300 Pearl Street
Bethesda, MD 20014
     335 copies for R4
      25 copies for NTIS

List available from author   (39)

9268 - D. Tomasko
9400 - A. W. Snyder
9410 - D. J. McCloskey
9411 - F. Eric Haskin
9420 - J. V. Walker
9424 - M. J. Clauser
9440 - D. A. Dahlgren
9441 - M. Berman
9441 - A. L. Camp
9442 - W. A. Von Riesemann
9443 - D. D. Carlson
9443 - P. O. Strom
9444 - S. L. Thompson   (25)
9444 - L. D. Buxton
9444 - R. K. Byers
9444 - D. Dobranich
9444 - L. N. Kmetyk
9444 - R. Knight
9444 - K. McFadden
9444 - J. M. McGlaun
9444 - J. Orman
9444 - G. C. Padilla
9444 - A. C. Peterson
9444 - W. H. Schmidt
9444 - R. M. Summers
9444 - G. G. Weigand   (40)
9444 - C. C. Wong
9445 - L. O. Cropp
9446 - B. Bader
9450 - J. A. Reuscher
8214 - M. A. Pound
3141 - L. J. Erickson   (5)
3151 - W. L. Garner   (3)

4. TITLE AND SUBTITLE (Add Volume No., if appropriate) TWO-PHASE JET LOADS	2. (Leave blank)
	3. RECIPIENT'S ACCESSION NO. ---

7. AUTHOR(S) G. G. Weigand, S. L. Thompson, D. Tomasko	5. DATE REPORT COMPLETED

	MONTH	YEAR
	January	1983

9. PERFORMING ORGANIZATION NAME AND MAILING ADDRESS (Include Zip Code) Organization 9444 Sandia National Laboratories P. O. Box 5800 Albuquerque, New Mexico 87185	DATE REPORT ISSUED

	MONTH	YEAR
	January	1983

	6. (Leave blank)
	8. (Leave blank)

12. SPONSORING ORGANIZATION NAME AND MAILING ADDRESS (Include Zip Code) U.S. Nuclear Regulatory Commission Office of Nuclear Regulatory Research Mechanical/Structural Engineering Branch Division of Engineering Technology Washington, DC 20555	10. PROJECT/TASK/WORK UNIT NO.
	11. FIN NO. A-1205

13. TYPE OF REPORT Technical	PERIOD COVERED (Inclusive dates) ---

15. SUPPLEMENTARY NOTES	14. (Leave blank)

16. ABSTRACT (200 words or less)

A model has been developed for predicting two-phase, water jet loadings on axisymmetric targets. The model ranges in application from 60 to 170 bars pressure and 70°C subcooled liquid to 0.75 (or greater) quality -- completely covering the range of interest in pressurized water or boiling water reactors. The model was developed using advanced two-dimensional computational techniques to solve the governing equations of mass, momentum, and energy. The model displays in a series of tables and charts the target load and pressure distributions as a function of vessel (or break) conditions; this enables fast yet accurate "look up" for answers. For many situations of practical interest, the model can predict sub-cooled and saturated loadings in excess of the simple control volume upper bounds of $2P_oA_e$ for nonflashing liquid and $1.26P_oA_e$ for steam. Also, the results indicate that the area of the loading on a flat target is often larger than assumed by simplier models. Finally, approximate models are given for estimating two-phase jet flow, expansion character-istics, shock strengths, and stagnation pressures. These approximate models could be used for estimating pressures on targets not specifically addressed in this study.

17. KEY WORDS AND DOCUMENT ANALYSIS	17a. DESCRIPTORS

17b. IDENTIFIERS/OPEN-ENDED TERMS

18. AVAILABILITY STATEMENT	19. SECURITY CLASS (This report) Uncl	21. NO. OF PAGES 492
	20. SECURITY CLASS (This page) Uncl	22. PRICE S

Org.	Bldg.	Name	Rec'd by	Org.	Bldg.	Name	Rec'd by

Sandia National Laboratories